METALLIC ALLOYS IN MEDICAL APPLICATIONS

EDITED BY: Liqiang Wang, Lechun Xie and Daixiu Wei

PUBLISHED IN: Frontiers in Bioengineering and Biotechnology and
Frontiers in Materials

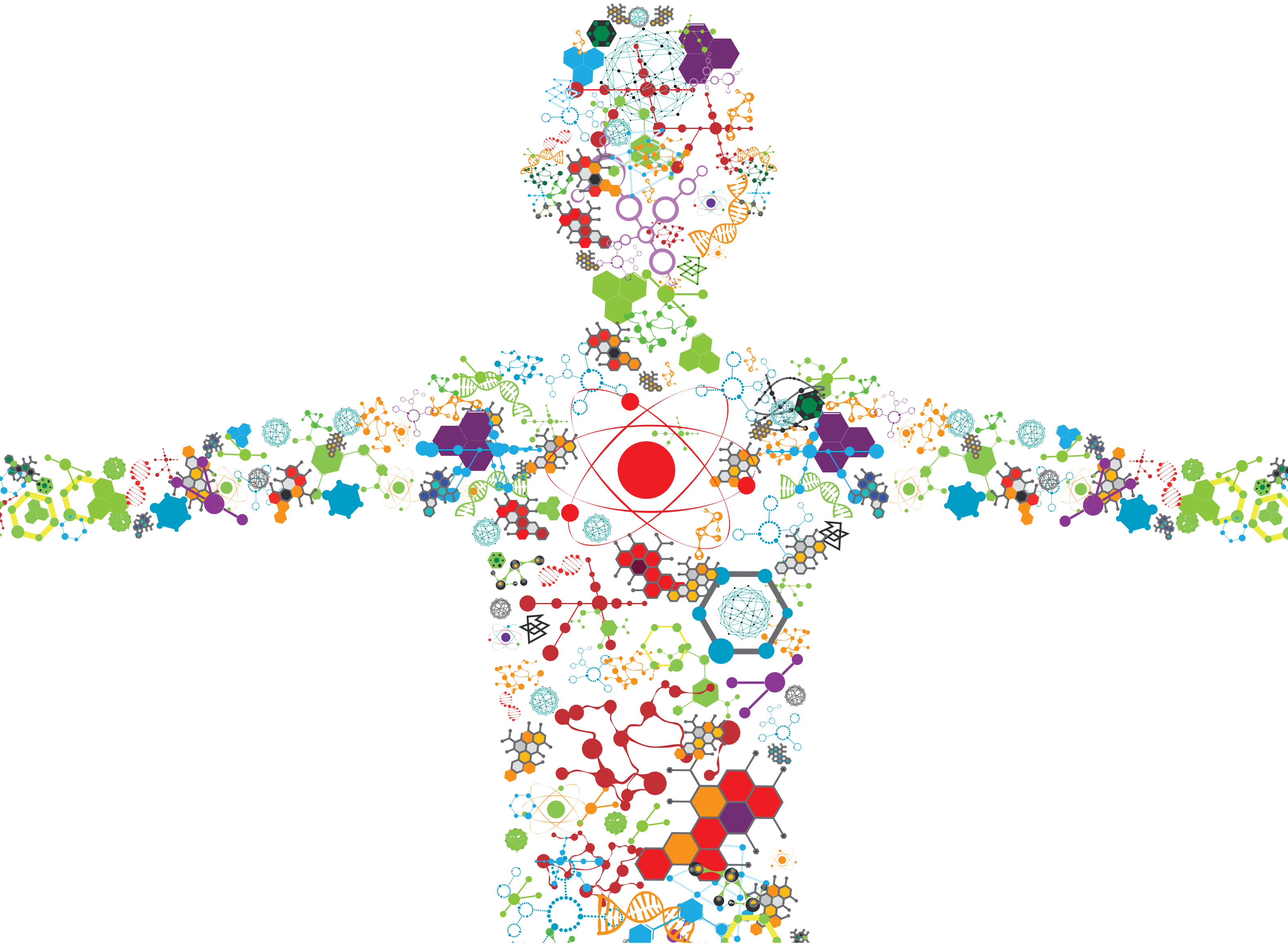

frontiers Research Topics

ISSN 1664-8714
ISBN 978-2-83250-550-2
DOI 10.3389/978-2-83250-550-2

About Frontiers

Frontiers is more than just an open-access publisher of scholarly articles: it is a pioneering approach to the world of academia, radically improving the way scholarly research is managed. The grand vision of Frontiers is a world where all people have an equal opportunity to seek, share and generate knowledge. Frontiers provides immediate and permanent online open access to all its publications, but this alone is not enough to realize our grand goals.

Frontiers Journal Series

The Frontiers Journal Series is a multi-tier and interdisciplinary set of open-access, online journals, promising a paradigm shift from the current review, selection and dissemination processes in academic publishing. All Frontiers journals are driven by researchers for researchers; therefore, they constitute a service to the scholarly community. At the same time, the Frontiers Journal Series operates on a revolutionary invention, the tiered publishing system, initially addressing specific communities of scholars, and gradually climbing up to broader public understanding, thus serving the interests of the lay society, too.

Dedication to Quality

Each Frontiers article is a landmark of the highest quality, thanks to genuinely collaborative interactions between authors and review editors, who include some of the world's best academicians. Research must be certified by peers before entering a stream of knowledge that may eventually reach the public - and shape society; therefore, Frontiers only applies the most rigorous and unbiased reviews.
Frontiers revolutionizes research publishing by freely delivering the most outstanding research, evaluated with no bias from both the academic and social point of view. By applying the most advanced information technologies, Frontiers is catapulting scholarly publishing into a new generation.

What are Frontiers Research Topics?

Frontiers Research Topics are very popular trademarks of the Frontiers Journals Series: they are collections of at least ten articles, all centered on a particular subject. With their unique mix of varied contributions from Original Research to Review Articles, Frontiers Research Topics unify the most influential researchers, the latest key findings and historical advances in a hot research area! Find out more on how to host your own Frontiers Research Topic or contribute to one as an author by contacting the Frontiers Editorial Office: frontiersin.org/about/contact

METALLIC ALLOYS IN MEDICAL APPLICATIONS

Topic Editors:
Liqiang Wang, Shanghai Jiao Tong University, China
Lechun Xie, Wuhan University of Technology, China
Daixiu Wei, Tohoku University, Japan

Citation: Wang, L., Xie, L., Wei, D., eds. (2022). Metallic Alloys in Medical Applications. Lausanne: Frontiers Media SA. doi: 10.3389/978-2-83250-550-2

Table of Contents

frontiers | Frontiers in Bioengineering and Biotechnology

TYPE Editorial
PUBLISHED 06 October 2022
DOI 10.3389/fbioe.2022.1041295

EDITED AND REVIEWED BY
Hasan Uludag,
University of Alberta, Canada

*CORRESPONDENCE
Lechun Xie,
lechunxie@yahoo.com

†These authors have contributed equally to this work

SPECIALTY SECTION
This article was submitted to Biomaterials,
a section of the journal
Frontiers in Bioengineering and Biotechnology

RECEIVED 10 September 2022
ACCEPTED 23 September 2022
PUBLISHED 06 October 2022

CITATION
Wang L, Xie L and Wei D (2022), Editorial: Metallic alloys in medical applications. *Front. Bioeng. Biotechnol.* 10:1041295.
doi: 10.3389/fbioe.2022.1041295

Editorial: Metallic alloys in medical applications

Liqiang Wang[1†], Lechun Xie[2,3*†] and Daixiu Wei[4†]

[1]State Key Laboratory of Metal Matrix Composites, School of Materials Science and Engineering, Shanghai Jiao Tong University, Shanghai, China, [2]Hubei Key Laboratory of Advanced Technology for Automotive Components, Wuhan University of Technology, Wuhan, China, [3]Hubei Collaborative Innovation Center for Automotive Components Technology, Wuhan University of Technology, Wuhan, China, [4]Institute for Materials Research, Tohoku University, Sendai, Japan

KEYWORDS

Biomaterials, biomedical, Bioengineering, Biotechnology, metal alloy

Editorial on the Research Topic
Metallic alloys in medical applications

Biomaterials are natural or artificial materials used to manufacture implants to replace lost or diseased biological structures in order to restore form and function. Biomaterials that require long-term service, such as orthopedic implants, need good physical and chemical stability, such as stainless steel and titanium alloys. While biomaterials that need to disappear after a certain period of time such as vascular stents need biodegradability, such as magnesium alloys. In recent years, biomedical high entropy alloys (HEAs) as novel alloy systems are considered to have a greater potential in the biomedical field. In addition, there is an urgent need to use simulation and computation in the design and fabrication process of metallic implants for individual patient requirements.

In terms of traditional biomedical metals such as 316L stainless steel (316L SS) and Mg alloy, Li et al. prepared several 316L SS specimens with different angles (0°, 15°, 30°, 45°, 60°, 75°, and 90°) relative to the substrate by selective laser melting (SLM) and investigated the effects of different angles on the microstructure evolution, tensile properties, and corrosion resistance of 316L SS. The specimens with 90° relative to the substrate show higher toughness and corrosion resistance due to a higher volume fraction of low-angle grain boundaries and finer grains. Zhang et al. reviewed the recent developments in Mg alloys in optimizing composition and microstructure, enhancing mechanical properties, controlling degradation rates, and elucidating corrosion mechanisms. They pointed out that surface modification techniques should be utilized to improve the corrosion resistance of Mg alloys on the basis of ensuring biocompatibility and mechanical properties. Yang et al.prepared a mixture of metallic Fe and Mg in a layered composite using a one-step dip-coating method and evaluated the morphology, composition, crystal structure, and corrosion behavior of Mg/Fe sheets. Long-term open-circuit potential measurements showed that the Mg/Fe sheet specimens exhibited a "self-healing" effect in Dulbecco's modified Eagle medium, which provides a new method to control the corrosion rate of Mg/Fe. Åhman et al. investigated the effect of powder bed laser melting and subsequent hot isostatic pressing (HIP) on the microstructure and weave of the specimens in different orientations and explored the corrosion behavior of Mg-Y-Nd-Zr alloys compared to the extruded specimens. The results show that more and coarser secondary phases lead to higher local corrosion rates in the powder bed laser melt specimens and HIPed specimens. Yang et al. prepared Mg-Ti composites with a bicontinuous interpenetrating phase structure by infiltrating Mg melt into 3D printed Ti scaffolds and explored its degradation behavior and effects on mouse embryonic osteoblast precursor cells. They found that Mg-Ti composite preferentially started to degrade near the interface and significantly enhanced osteogenic activity due to the positive effect of a moderate amount of Mg^{2+}.

In the aspect of novel alloy systems, for example, Liu et al. summarized the superior mechanical properties and biocompatibility of biomedical HEAs. Moreover, biomedical HEAs show both high strength and low elastic modulus, which can meet the strength requirements and avoid stress shielding, and some of them exhibit good superelasticity. Regarding the biological properties, biomedical HEAs focus on the elements with good biocompatibility, such as Ti, Ta, Nb, Zr, and Hf. However, the biological behaviors of biomedical HEAs are currently limited to *in vitro* cell viability experiments, and relevant *in vivo* experiments still need to be carried out. Feng et al. summarized the composition of biomedical HEAs in recent years, introduced their biocompatibility and the mechanical properties matching with human bone, and gave suggestions for future directions. They concluded that there is a demand for advancing theoretical and simulation studies on the compositional design of biomedical HEAs, quantifying the effects of composition, process, and post-treatment on the performance of biomedical HEAs, as well as focusing on the depletion of biomedical HEAs under actual use conditions.

To meet individual service requirements, multi-level simulation and computation are utilized in the design of biomedical metallic implants. Hou et al. systematically investigated the phase stability, elastic modulus, and electronic structure of the body-centered cubic structure of β-TiX (X = Nb, Ta) alloy with the aid of first-principles calculations. The results show that the bonding strength between Ti and X atoms increases with the increase of the alloying element X content, which leads to an increase in phase stability and elastic modulus. Lv et al. designed porous scaffolds based on triply periodic minimal surface structures with the same porosity and different pore strategies by changing the minimal surface equation. They systematically investigated the effects of the pore strategy on the microstructure, mechanical properties, and permeability of the porous scaffolds, and the results showed that the continuous gradient distribution of pore size altered the stress distribution inside the scaffolds. Liang et al. proposed a reasonable cervical intervertebral range of motion after anterior cervical discectomy and fusion (ACDF) to offset the increased intervertebral facet joint forces and intradiscal pressures in the non-fusion segment after anterior cervical discectomy fusion. This study provides a new method to estimate reasonable range of motion after ACDF surgery from a biomechanical perspective, and further *in vitro* and clinical studies are needed for validation.

The contributions of the above work were summarized as follows: the traditional biomedical metals, especially 316L SS and Mg alloys (Li et al.; Zhang et al.; Yang et al.; Åhman et al.; Yang et al.); novel alloy system, biomedical HEAs (Liu et al.; Feng et al.); and simulation and computational methods (Hou et al.; Lv et al.; Liang et al.). This Research Topic focused on the recent development of metallic biomaterials for medical applications, which can promote the development of metallic biomaterials.

Author contributions

All authors listed have made a substantial, direct, and intellectual contribution to the work and approved it for publication.

Conflict of interest

The authors declare that the research was conducted in the absence of any commercial or financial relationships that could be construed as a potential conflict of interest.

Publisher's note

frontiers in Bioengineering and Biotechnology

ORIGINAL RESEARCH
published: 03 November 2021
doi: 10.3389/fbioe.2021.778332

Study on Mechanism of Structure Angle on Microstructure and Properties of SLM-Fabricated 316L Stainless Steel

Xiaofeng Li[1,2]*, Denghao Yi[1,3†], Xiaoyu Wu[1†], Jinfang Zhang[1,2], Xiaohui Yang[4], Zixuan Zhao[2], Jianhong Wang[1], Bin Liu[2] and Peikang Bai[1]

[1]School of Materials Science and Engineering, North University of China, Taiyuan, China, [2]The State Key Laboratory of Powder Metallurgy, Central South University, Changsha, China, [3]Institute of Laser Engineering, Faculty of Materials and Manufacturing, Beijing University of Technology, Beijing, China, [4]Instrumental Analysis Center, Taiyuan University of Science and Technology, Taiyuan, China

Edited by:
Daixiu Wei,
Tohoku University, Japan

Reviewed by:
Weidong Zhang,
Hunan University, China
Kaiyang Li,
University of Alberta, Canada

***Correspondence:**
Xiaofeng Li
lxf@nuc.edu.cn

†These authors have contributed equally to this work and share first authorship

Specialty section:
This article was submitted to Biomaterials, a section of the journal Frontiers in Bioengineering and Biotechnology

Received: *16 September 2021*
Accepted: *23 September 2021*
Published: *03 November 2021*

Citation:
Li X, Yi D, Wu X, Zhang J, Yang X, Zhao Z, Wang J, Liu B and Bai P (2021) Study on Mechanism of Structure Angle on Microstructure and Properties of SLM-Fabricated 316L Stainless Steel. Front. Bioeng. Biotechnol. 9:778332. doi: 10.3389/fbioe.2021.778332

In this study, seven 316L stainless steel (316L SS) bulks with different angles (0°, 15°, 30°, 45°, 60°, 75°, and 90°) relative to a build substrate were built *via* selective laser melting (SLM). The influences of different angles on the metallography, microstructure evolution, tensile properties, and corrosion resistance of 316L SS were studied. The 0° sample showed the morphology of corrugated columnar grains, while the 90° sample exhibited equiaxed grains but with a strong <101> texture. The 60° sample had a good strength and plasticity: the tensile strength with 708 MPa, the yield strength with 588 MPa, and the elongation with 54.51%. The dislocation strengthening and grain refinement play a vital role in the mechanical properties for different anisotropy of the SLM-fabricated 316L SS. The 90° sample had greater toughness and corrosion resistance, owing to the higher volume fraction of low-angle grain boundaries and finer grains.

Keywords: selective laser melting, construction angles, 316L SS, tensile properties, grain refinement

INTRODUCTION

Additive manufacturing (AM) has great development prospects in the medical, automotive, aerospace, and mold industries and is currently a global manufacturing trend, as stated by Song S. et al. (2020). Selective laser melting (SLM), as one of the AM technology, "prints" materials and components directly from a computer-aided design file, thereby offering unique advantages of design freedom for complex parts without the need for molds (Shu et al., 2020). As SLM is a layer-by-layer building technology, it provides ample opportunities for tailoring the microstructure and then mechanical properties (Xing et al., 2020). At present, the powder materials suitable for SLM technology mainly include 316L stainless steel, AlSi10Mg, Inconel 718, Inconel 625, and TC4 (Harun et al., 2018; Kreitcberg et al., 2017; Li et al., 2021; Luo et al., 2019; Yu et al., 2020).

Notably, 316L stainless steel (316L SS) has excellent comprehensive mechanical properties, corrosion resistance, good biocompatibility, and good SLMed formability (Kong et al., 2018a; Shin et al., 2021; Xu et al., 2021), but the release of Ni element may cause adverse health problems. Therefore, the important factor for the application of 316L SS in the biological field is the corrosion and element release of the SLM-formed part in the biological environment. The SLM-processed 316L SS had been extensively studied, including relative density, surface roughness, microstructure, and mechanical properties (Liverani et al., 2017; Agrawal et al., 2020; Marattukalam et al., 2020).

However, the SLM-fabricated 316L SS displays microstructure anisotropy. Specifically, the difference of columnar grains of the vertical plane and equiaxed grains of the horizontal plane could cause anisotropy of mechanical properties and corrosion resistance. Additionally, defect distribution, residual stress, deformation mechanism, and melt pool boundary are affected by the performance anisotropy of the SLM-prepared 316L SS (Yin et al., 2018; Chen et al., 2019; Shifeng et al., 2014; Blinn et al., 2020). In order to alleviate this, some researchers have decreased defects in the SLM-processed 316L SS, such as cracks and pores, by optimizing the process parameters (Liverani et al., 2017). Several studies have changed the laser-scanning strategy and increased the preheating temperature to improve the residual stress level and the microstructure anisotropy within the SLM-fabricated 316L SS (Song Y.n. et al., 2020). AlMangour et al. (2017) have added nano-scale TiC particles to improve the SLM-processed 316L SS' mechanical performances by refining the microstructure and increasing dislocation density. Additionally, many researchers have implemented post-processing techniques, such as heat treatment, promoting the homogenization of microstructures and improving the mechanical performances anisotropy from the SLM-formed 316L SS (Hong et al., 2021). Kong et al. (2018a) found that 316L SS formed under high laser power has a thicker passivation film and higher cell proliferation ability than that formed at low laser power.

It is crucial to study the influence of the construction angle on the SLM-prepared 316L SS' microstructure evolution, mechanical performances, and corrosion under stable process parameters. During SLM, the relationship between the placement of the sample and the gas–flow direction can affect the relative density of the formed part (Agius et al., 2017). Build orientation, local heat input, and rapid solidification can change the grain orientation of SLM-prepared 316L SS. Additionally, Wen et al. (2019) found that the spatial orientation of the molten pool boundary affected the SLM-fabricated 316L SS' toughness. The fatigue–crack direction of SLM-fabricated 316L SS was correlated with the laser scanning angle, and the formation of defects impacts the type of fractures (Zhang et al., 2019). Liu et al. (2020) reported that the crystal plasticity model accurately captured and forecasted the yield strength anisotropy behavior of SLM-fabricated 316L, which is mainly influenced by the crystallographic structure. During deformation, the vertical sample was deformed by grain extension then dislocation slip and had the stability of work hardening, whereas grain rotation occurred through slipping and massive twinning in the horizontal sample, which exhibited a smaller effective grain size (Bahl et al., 2019; Liu et al., 2020; Kale et al., 2021). Thus, the 0° sample had higher yield strength than the 90° sample. Atapour et al. (2020) studied the corrosion resistance of SLM-formed 316L SS from different build orientations before and after heat treatment in dilute hydrochloric acid (HCl, PH = 1.5). Compared with as-built, the heat-treated sample could release more Ni element, which may be attributed to the reduction of the surface oxide layer thickness.

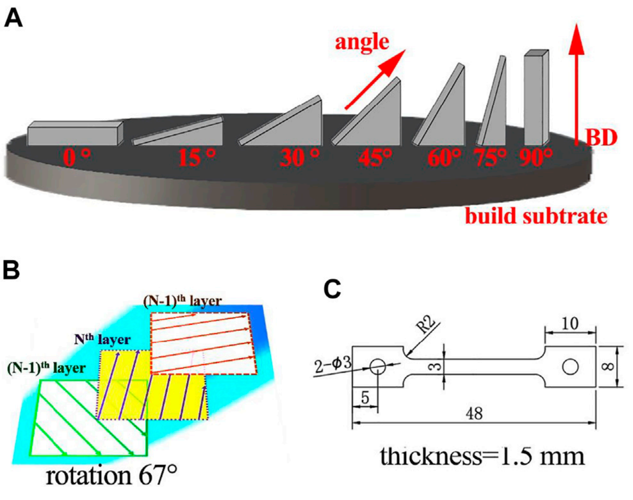

FIGURE 1 | Model design: **(A)** 45° sample, **(B)** 75° sample, **(C)** selected laser scanning strategy, and **(D)** dimensions (in mm) used in the fabrication of the tensile samples.

In this study, seven groups of 316L SS samples with different angles relative to a build substrate were designed and then formed through SLM technology using optimized process parameters. The effects of construction angles (from 0° to 90° relative to build plate) on the microstructure evolution, texture, tensile properties, and corrosion resistance of SLM-prepared 316L samples were researched. This study drew an outlook on the gradient in microstructure evolution, tensile properties, and corrosion resistance from different construction angles relative to the build substrate in SLM-fabricated 316L SS.

EXPERIMENT

SLM Technique

A gas-atomized 316L stainless steel powder with a particle size ranging from 20 to 50 μm was produced by Avimetal Powder Metallurgy Technology Co., Ltd. The SLM samples were prepared employing the Renishaw AM 400 system. The beam size of laser was 70 μm in diameter. The SLM processes were proceeded in high-purity Ar (≥99.99%) gas atmosphere with an O_2 content below 0.1%. Optimized printing parameters of 50-μm powder layer thickness, 185-W laser power, 100-μs exposure time, and 120-μm hatch distance were used to ensure good material density. The selection of optimal parameters was determined on the basis of a large number of experiments. During the SLM process, a rotation of 67° laser scanning strategy between successive layers was used, as shown in **Figure 1C**. Seven samples with different angles relative to the build plate were manufactured. One sample was prepared every 15° from 0° to 90°. **Figure 1A,B** shows the models of the 45° sample and 75° sample. There was no dangling part in the SLM-processed sample, and the deposition area of the sample (construction angle from 0° to 90°) gradually decreased with the increase in the built height. Among them, the 0° sample had the largest

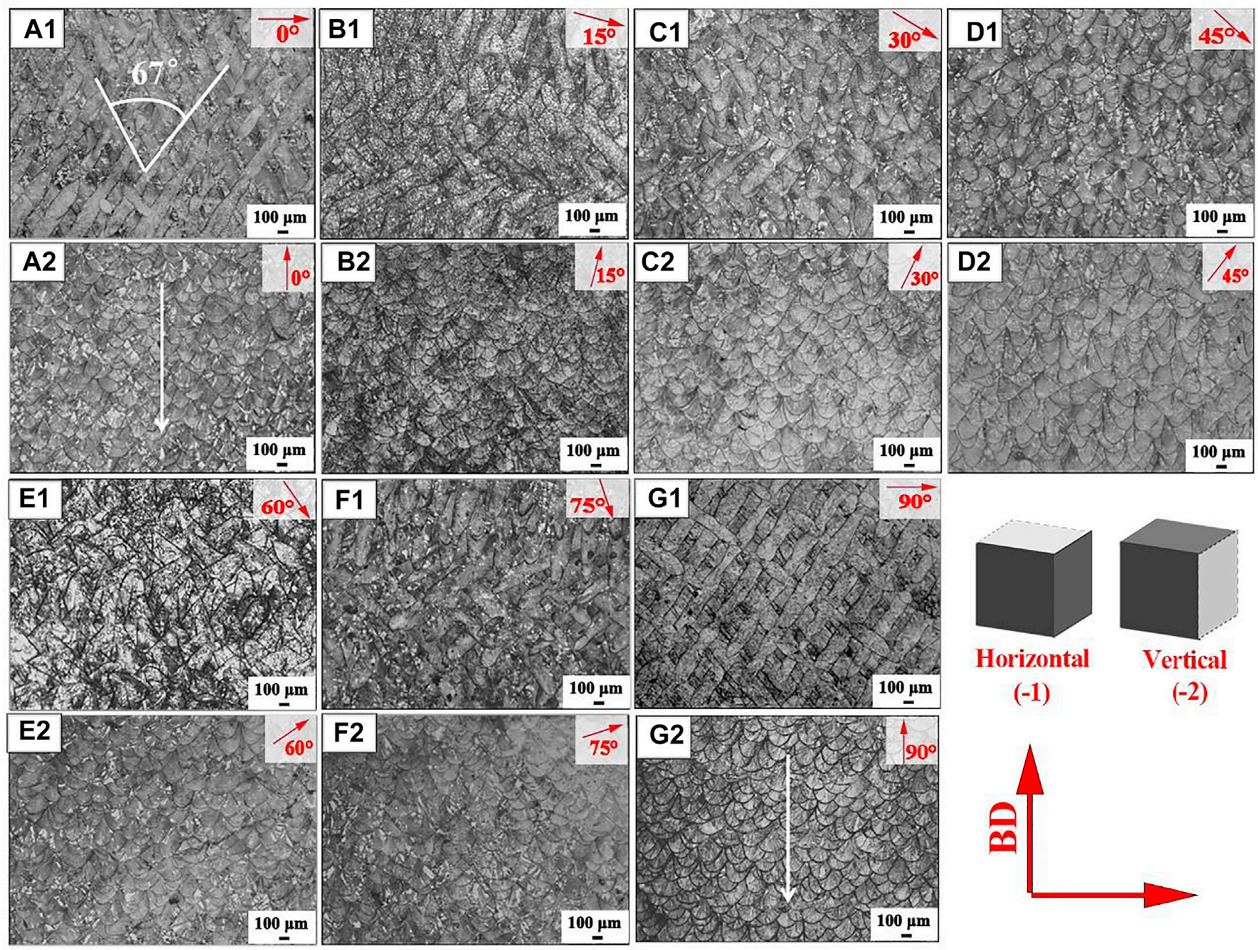

FIGURE 2 | OM images of SLM-processed 316L SS from different angles relative to the build substrate: (a_1-g_1) cross section and (a_2-g_2) longitudinal section.

deposition area (55 × 10 mm), and the 90° sample had the largest *Z*-axis dimension (55 mm).

Microstructure Characterization and Mechanical Properties

To experimentally study the mechanical anisotropy, tensile samples were fabricated along different construction angles relative to the build subtrate: 0°, 15°, 30°, 45°, 60°, 75°, and 90°. The selection of the construction angles was conducive to a more comprehensive understanding of the force on each part of the SLM-fabricated sample. Blocks close to the net dimension were cut out of each sample *via* electric discharge machining (EDM) and used for producing tensile samples. **Figure 1D** shows the three-dimensional size of a tensile sample. The cut blocks were ground using SiC paper, polished by diamond suspension, and etched with an acid mixture ($HCl:HNO_3$ = 3:1). Using an Axiovert 200MAT optical microscope (OM) and a TESCAN VEGA3 scanning electron microscope (SEM), we observed the macrostructure or microstructure of each samples. Electron backscatter diffraction (EBSD) results were obtained on a Hitachi S-3400N SEM equipped with an HKL EBSD. The EBSD measurements were done on extractions from the 0°, 45°, 60°, and 90° samples, and the test plane was selected to be perpendicular to the load–direction plane. Using a calibrated E43.504 electronic universal testing machine, we performed the tensile tests of each sample at room temperature, with a 2 mm/min tensile speed. Samples were tested in triplicate to ensure accuracy.

Electrochemical Testing

The electrochemical measurements were performed in 3.5 wt% NaCl solution at 25°C, and the etching surface zone was 5 mm × 5 mm. A three-electrode arrangement was used: the sample is the working electrode, saturated calomel is the reference electrode, and a Pt is the counter electrode. All of the samples were welded by a copper wire and then embedded in the epoxy resin. The working surfaces were ground with SiC paper, polished, ultrasonically cleaned in absolute ethyl alcohol for 3 min, and air-dried before testing. The corrosion resistance of all samples was characterized by polarization curves. The corrosion current and sweep

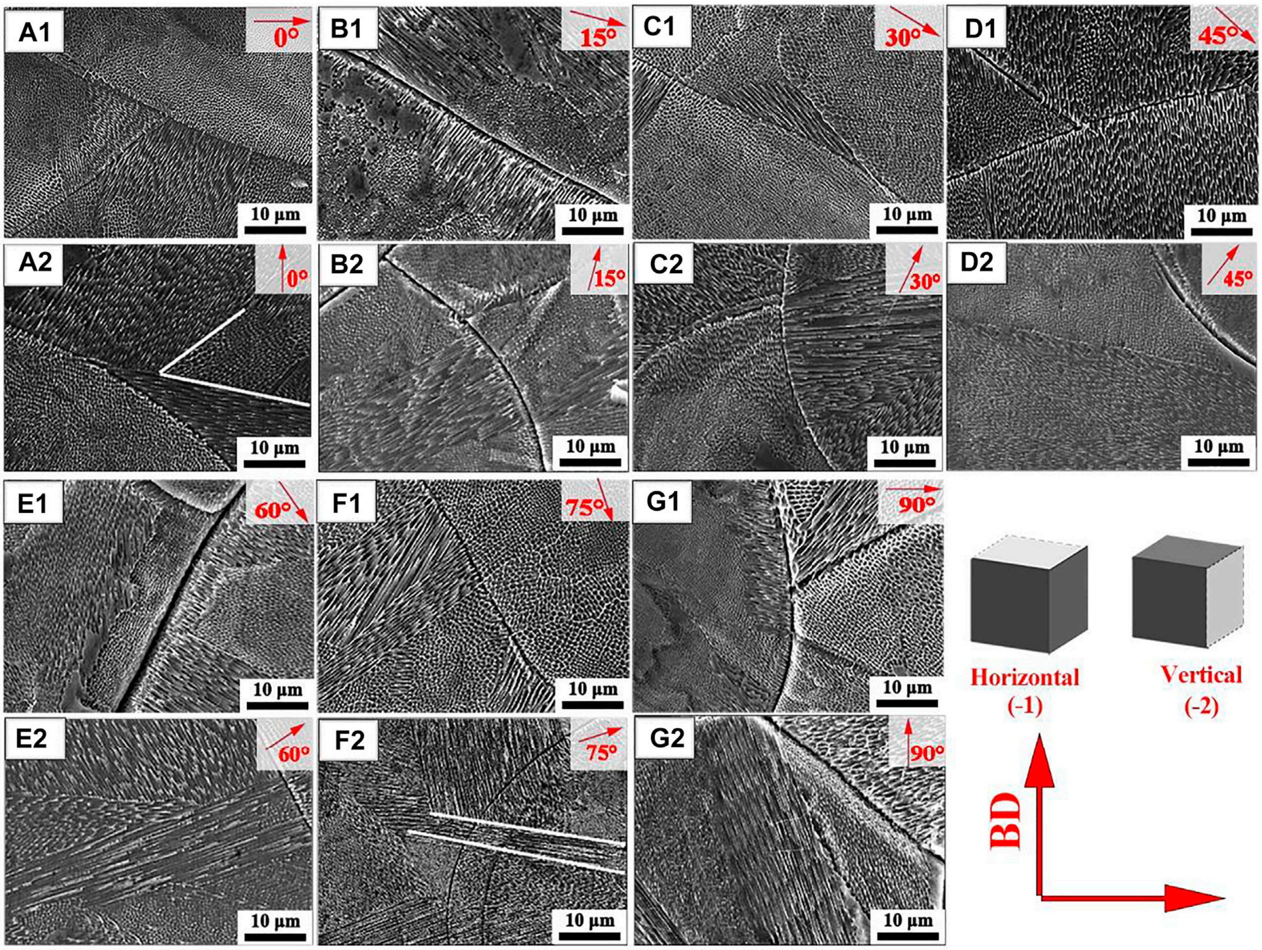

FIGURE 3 | SEM images of SLM-processed 316L SS with from different angles relative to the build substrate: (a_1-g_1) cross section and (a_2-g_2) longitudinal section.

potential of each sample were analyzed by CHI604E software. Each sample's current density is based on the total current divided by the exposed area during the corrosion test. The surface roughness is not generally considered in the calculation. The calculation can be expressed as follows:

$$i_{\mathrm{corr}} = \frac{I_{corr}}{A},$$

where i_{corr} is current density with A/cm^2, I_{corr} is total anodic current with unit of A.

RESULTS

Macrostructure Evolution

In **Figure 2**, the OM images show the morphologies form in the horizontal and vertical planes of the SLM-formed 316L SS from different angles (relative to build subtrate). **Figure 2A$_1$**-g_1 shows the "track–track" overlap trajectory that was the overlapping trajectory between the nth laser track and the (n+1)th laser track. Consistent with the scanning pattern, the laser track of samples with different construction angles displayed intersection angles of 67° (shown by the white line in **Figure 2A$_1$**). Shortened and even overlapped average laser tracks were observed for each set of construction angle samples (for which the sum of construction angles = 90°) with the construction angle changes. The sets of construction angles were: 0° and 90° samples, 15° and 75° samples, and 30° and 60° samples. The laser track of the horizontal plane of the 45° sample showed a semicircular melt channel, similar to the shape of the molten pool.

Figure 2A$_2$-g_2 shows the microscopic morphology of the vertical planes of the SLM-formed 316L SS from different angles (relative to build subtrate). Fish scale–like melt pools were observed in the vertical plane of all samples and were repeatedly stacked to form dense SLM-processed parts. Each sample showed similar melt pool morphology, which showed a "layer–layer" overlap. The tilt angle of the melt pools between the adjacent layers also changed with the construction angle. The melt pool orientation of the 0° and 90° samples was perpendicular to the build plate, see in **Figure 2A$_2$** and g_2, while a part of the melt pool orientation from the 15° sample was at an angle of 15° relative to the build plate; other samples followed similar patterns.

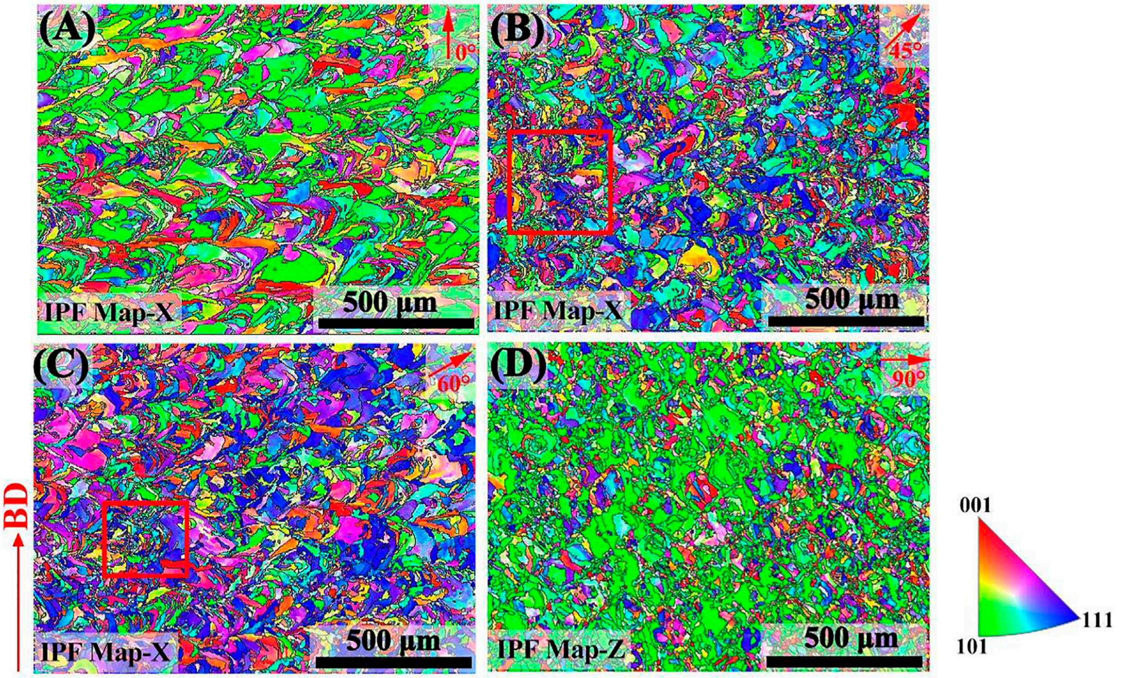

FIGURE 4 | EBSD inverse pole figures of SLM-processed 316L SS from different angles relative to the build substrate: **(A–D)** angle of 0, 45, 60, and 90.

Microstructure Evolution

As shown in **Figure 3**$\mathbf{A}_1$-g_1, the SEM morphology of the cross section from the SLM-formed 316L SS with different angles (relative to build subtrate) were exhibited. The grains of SLM-formed 316L SS were mainly composed of columnar subcrystals, cellular subcrystals, and cellular dendrite subcrystals. The 60° samples exhibited finer cellular subcrystals and cellular dendrite subcrystals, followed by the 45°, 30°, 0°, and 15° samples in the order of fineness. The 75° and 90° samples had larger cellular subcrystals and cellular dendrite subcrystals. Cellular dendrite subcrystals were observed in the 0° sample and 60° sample, while columnar subcrystals of different orientations appeared in the 30° sample, 45° sample, and 75° sample. The 15° sample and 90° sample displayed columnar subcrystals perpendicular to the molten pool boundary.

Figure 3$\mathbf{A}_2$-g_2 exhibits the SEM morphology of the longitudinal section from the SLM-formed 316L SS with different construction angles. There were cellular subcrystals inside the melt pool of the 0° and 45° samples, and a small number of cellular dendrite subcrystals outside the melt pool boundary (MPB). The 15° sample displayed cellular dendrite sub-grains inside the melt pool. **Figure 3**$\mathbf{C}_2$ shows that the columnar subcrystals were perpendicular to the MPB from the 30° sample. The 60° sample and 90° sample exhibited mostly cellular dendrite subcrystals and cellular subcrystals. The cellular dendrite subcrystals of the 60° sample were of an uniform size, while the cellular dendrite subcrystals of the 90° sample were slightly larger, as shown in **Figure 3**$\mathbf{E}_2$ and g_2.

Comparing the SEM images in **Figure 3**$\mathbf{A}_1$-g_1, the proportion of columnar sub-grains in the longitudinal section was higher than that in the cross section, especially in the 75° and 90° samples. The proportion of dendrite sub-grains increased in order of 15°, 0°, 60°, 30°, and 45° samples. The orientation of dendrite sub-grains from 75° sample and 90° sample exhibited obvious differences, as shown in **Figure 3**$\mathbf{F}_2$ and g_2. **Figure 3**$\mathbf{F}_2$ shows the epitaxial growth of dendrites in the 75° sample. The dendrite grains inside the melt pool continued to cross and grow along the melt pool boundary to a new melt pool, and dendrite grains of different orientations appeared.

Figure 4 shows the inverse pole figures (IPF) of the sample with different angles of 0°, 45°, 60°, and 90°. The microtexture was analyzed based on the EBSD data obtained from a plane perpendicular to the load direction. The grain orientation maps were mainly identified by three color: red is <001>, green is <101>, and blue is <111> (Kale et al., 2021). No sign of MPBs appears due to epitaxial grain growth in remelted zones, shown in **Figure 4A**. The 0° sample' grains show a ripple pattern and a strong <101> texture (represented by green) obtained parallel to the build direction. The 45° and 60° sample exhibited a non-uniform grain structure and numerous finer grains appeared, as shown in the red boxes in **Figure 4B,C**. The portion of <111> oriented grains (displayed by blue color) of the 45° sample was higher than those of the 0° and 90° samples, while the portion of <111> oriented grains of the 60° sample was higher compared with the 45° sample. The <111> oriented grains showed an increasing trend with the increase in the construction angle. The 90° sample showed rectangular beam–shaped grains, which were marked with equiaxed grains in the scanning direction, and an intense <101> texture was acquired along

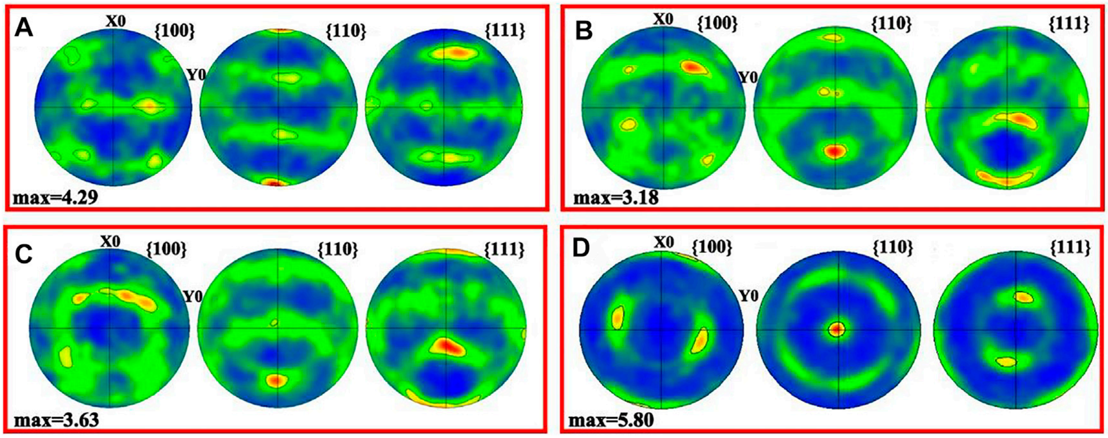

FIGURE 5 | PF of SLM-processed 316L SS from different angles relative to the build substrate: **(A–D)** angle of 0, 45, 60, and 90.

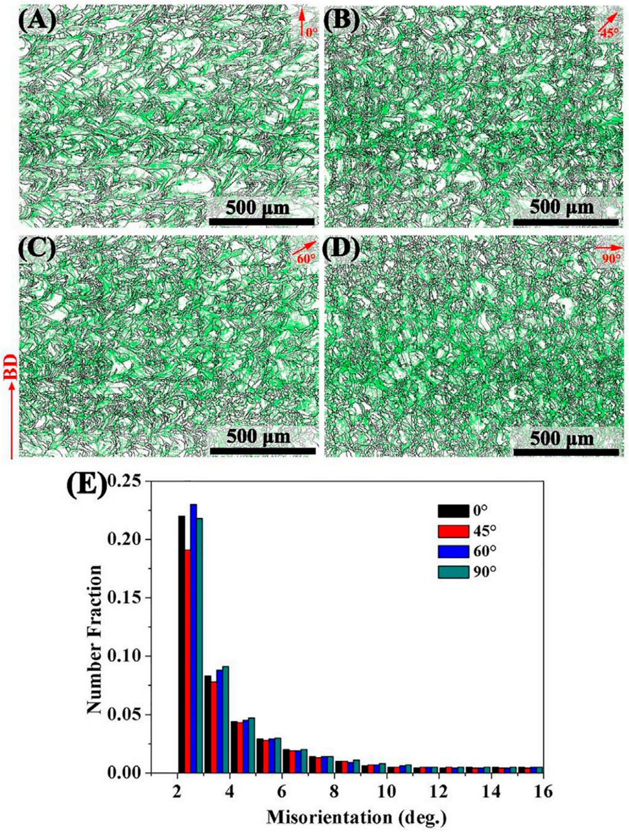

FIGURE 6 | Grain boundary misorientation angles of SLM-processed 316L SS from different angles relative to the build substrate: **(A–D)** angle of 0, 45, 60, and 90 and **(E)** the proportion of LAGBs in each sample.

the scan direction. An additional, minor <001> texture component was visible in all the samples.

According to the EBSD data, the 0°, 45°, 60°, and 90° samples included 1,929, 2,980, 2,583, and 3,316 crystal grains, respectively. The average grain sizes of these samples were 25.18, 20.19, 22.49, and 19.93 μm, as measured by the interception method. The proportions of grains smaller than 11.0 μm in the 0°, 45°, 60°, and 90° samples were 5.02, 0.00, 5.13, and 5.94%, respectively. In addition, the aspect ratios of grains from the 0°, 45°, 60°, and 90° samples were 3.12, 2.45, 2.52, and 2.18, respectively. The larger the aspect ratio of the grains, the higher the proportion of columnar grains in the plane (Spittle, 2013). Therefore, the 0° sample showed a high proportion of columnar grains, followed by the 60° sample, and the 45° sample.

Figure 5 shows the pole figures (PF) of each samples with different angles of 0°, 45°, 60°, and 90°, corresponding to the 0° sample, 45° sample, 60° sample, and 90° sample. The grains of the 0° sample were symmetrically arranged in parallel to the X0 axis, and an intense <110> crystallographic texture was acquired parallel to the BD. The 90° sample showed a preferred <110> texture perpendicular to the XY plane. The diffusion ring seen from the {110} PF demonstrated a fiber texture parallel to the X-orientation. Based on the Channel 15 analysis, the maximum texture was a shear texture of 45° with the build direction, as shown in the {110} PF of the 45° sample. **Figure 5C** shows that the maximum texture was a shear texture of 60° with the build direction in the {110} PF of the 60° sample. It illustrated that the grain orientation of the different angle planes was related to the build direction. The multiple of the uniform density (MUD) value depicts the relative texture strength of a particular orientation in a sample. The 90° sample showed a larger MUD value (5.80), followed by the 0° sample (MUD = 4.29). The MUD of the 60° sample was 3.63, and the 45° sample had the minimum mud value of 3.18.

Figure 6 shows the grain boundary misorientation angle distribution of SLM-formed 316L SS with different angles of 0°, 45°, 60°, and 90°, corresponding to the 0° sample, 45° sample, 60° sample, and 90° sample, respectively. The green and black lines in **Figure 6** correspond to the locations of LAGBs and HAGBs, respectively. Among them, grain boundaries with an orientation angle less than 15° were defined as LAGBs, while the

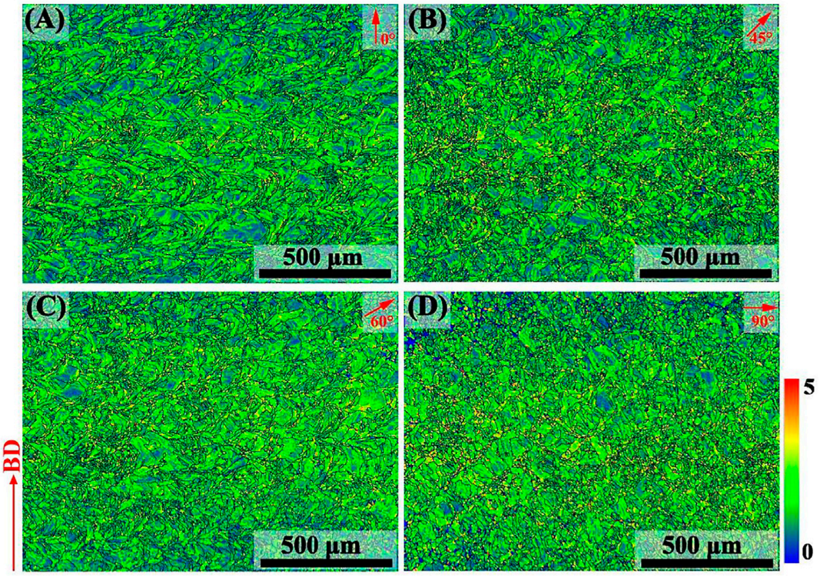

FIGURE 7 | KAM map of SLM-processed 316L SS from different angles relative to the build substrate: **(A–D)** angle of 0, 45, 60, and 90.

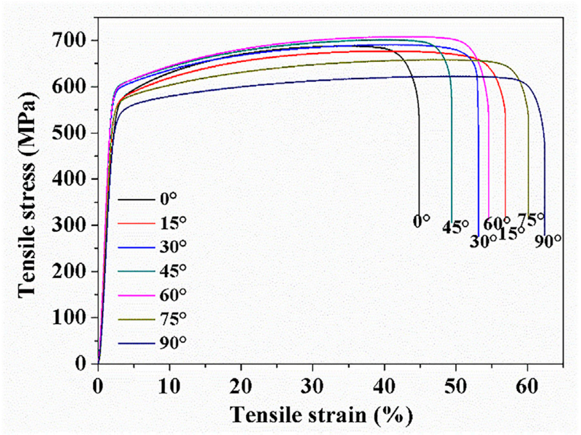

FIGURE 8 | Stress–strain curve of SLM-processed 316L SS from different angles relative to the build substrate.

rest were defined as HAGBs. The statistical results are summarized in **Figure 6E**. The linear fractions of LAGBs from the 0°, 45°, 60°, and 90° samples were 45.4, 41.6, 46.9, and 47.1%, respectively. Of them, the linear fractions of LAGBs were the lowest in the 45° sample, while the 60° and 90° samples had similar linear fractions of LAGBs.

The kernel average misorientation (KAM) diagrams represent the average misorientation of a given point relative to the third nearest neighbor (upper limit of 5°), as shown in **Figure 7**. The green color corresponds to a high stress concentration and high degree of plastic deformation. Based on the qualitative analysis of the KAM image, the SLM-prepared 316L SS exhibited high residual stress, which results from multiple thermal cycles and especially thermal shrinkage stress during rapid melting and solidification. To convert local misorientation into the density of geometrically necessary dislocation (GND), the following formula is used:

TABLE 1 | Tensile properties of SLM-processed 316L SS with different angles relative to the build substrate.

Construction angle (°)	UTS (MPa)	YS (MPa)	Elongation%
0	688	538	45.21
15	677	551	57.94
30	691	566	53.66
45	701	586	49.25
60	708	588	54.51
75	658	560	60.92
90	623	513	62.57

$$\rho^{GND} = \frac{2\theta}{ub},$$

where ρ^{GND} is the GND density at points, θ denotes the local misorientation angle (Gao et al., 2020), b represents the Burger's vector (0.25 nm), and u is the scan step (3 μm) of EBSD. The average ρ^{GND} of the 0°, 45°, 60°, and 90° samples were 3.89×10^{15} m^{-2}, 4.26×10^{15} m^{-2}, 4.29×10^{15} m^{-2}, and 4.56×10^{15} m^{-2}, respectively.

Tensile Performance and Fracture Examination

Figure 8 depicts the stress and strain curves of all samples, and the corresponding ultimate tensile strength (UTS), yield strength (YS), and elongation are listed in **Table 1**. The samples with different construction angles showed obvious mechanical

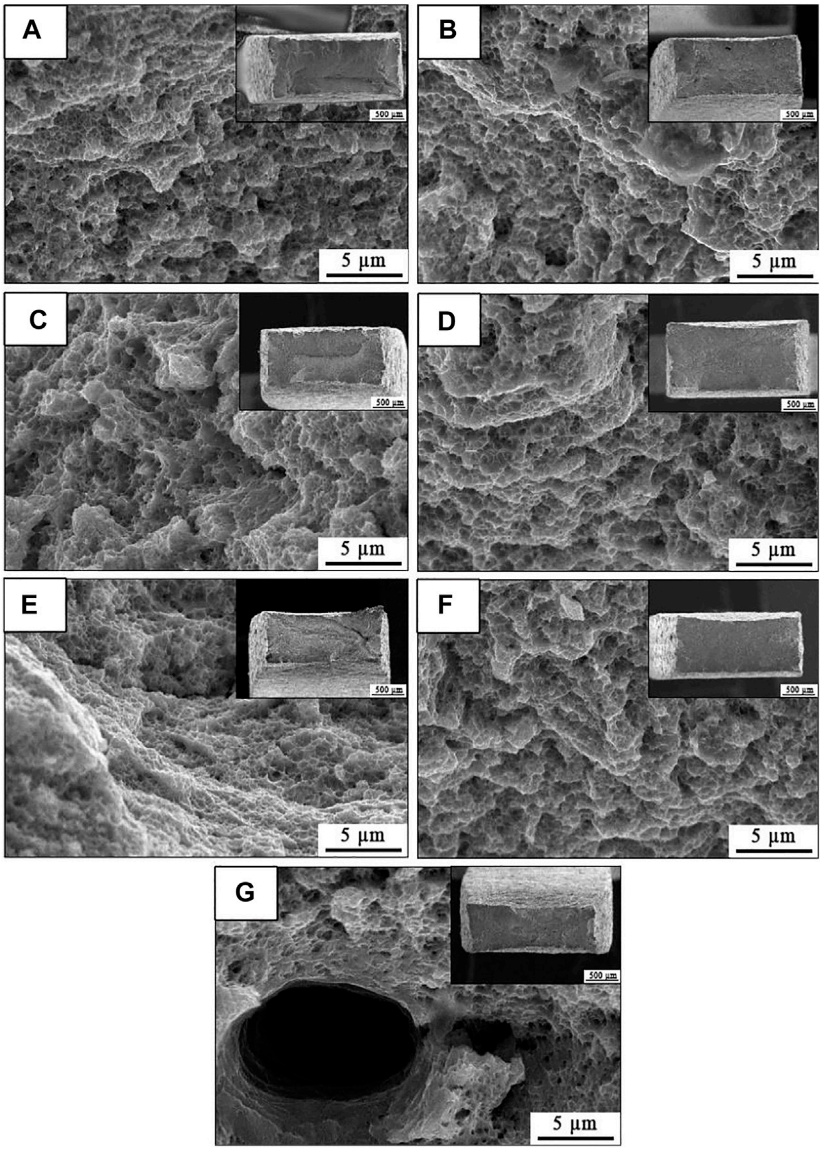

FIGURE 9 | Characterization of fracture surface of the SLM-processed 316L SS from different angles relative to the build substrate: **(A–G)** angle of 0, 15, 30, 45, 60, 75, and 90.

anisotropy. The 45° and 60° samples exhibited the maximum tensile strengths of 701 and 708 MPa, respectively. This tensile strength was significantly better than the SLM-formed 316L SS of Song Y.n. et al. (2020) and Chao et al. (2021). The 90° sample had lower tensile strength (623 MPa) than the other samples. The 45° sample and 60° sample had approximately equal yield strength, with values of 586 and 588 MPa, respectively. The 0° and 90° specimens showed lower yield strength, with values of 538 and 513 MPa, respectively. The 90° sample displayed the best plasticity, with a maximum elongation of 62.57%. The elongation of the 45° sample (49.25%) was only slightly better than that of the 0° sample (45.21%).

Figure 9 displays the fracture morphologies of the SLM-formed 316L SS from different angles relative to the build substrate, and the illustrations show the corresponding macroscopic fracture morphology. It can be seen that the fractures of each sample were smooth fracture facets, showing the necking phenomenon. The 0° sample and 45° sample exhibited slight necking, while the 75° and 90° samples displayed more necking, corresponding to the stronger plasticity. The 45°, 75°, and 90° samples were relatively flat in the fracture surface, while the 0°, 30°, and 60° samples had fine cracks, which results from the necking stage causing the fast fracture of a sample. Pores were visible in the fracture plane of the 15° sample, indicating that stress preferentially accumulated at the pore. A dimple morphology was observed in every alloy, indicating that the SLM-processed 316L SS had good plasticity. The 60° sample displayed relatively smaller and uniform dimples,

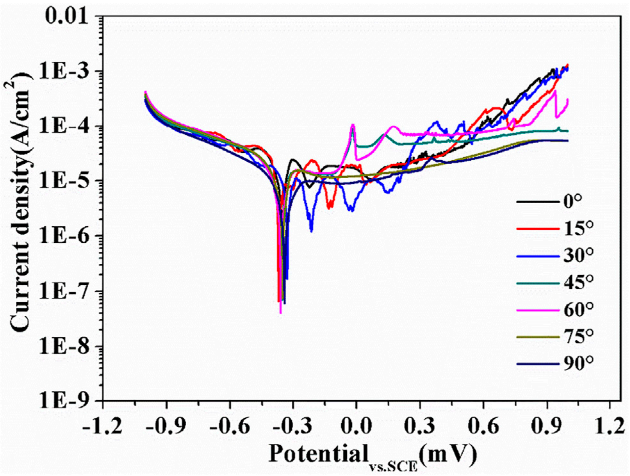

FIGURE 10 | Potentiodynamic polarization curves of SLM-processed 316L SS from different angles relative to the build substrate in a 3.5 wt% NaCl solution.

indicating uniformity of the microstructure. The 90° sample had large and deep dimples with a diameter of about 5 μm, indicating that the sample had a great capability to lose stability locally. Thus, the 90° sample had high plasticity.

Corrosion Resistance

Figure 10 depicts the polarization curve of all sample. The current density was not stable with the increase of sweep potential, which indicates the formation of an unstable passive film in the surface. **Table 2** generalizes the sweep potential (E_{corr}) and current density (I_{corr}) of each sample. The sweep potential range of each sample was between −0.33 V and −0.37 V, and the 30° specimen displayed the largest sweep potential of −0.33 V. According to thermodynamics, the greater the sweep potential, the better the corrosion resistance of the sample (Zhang et al., 2012). Additionally, the current density of all samples ranged from 1.12×10^{-5} A/cm^2 to 2.20×10^{-5} A/cm^2, except for the 90° sample (8.8×10^{-6} A/cm^2). The corrosion rate was directly proportional to the I_{corr} (Zhang et al., 2012). Therefore, the 90° sample had the lowest corrosion rate.

DISCUSSIONS

Effect of Angles Relative to Build Substrate on Microstructure Evolution

Reasonable process parameters can ensure that the powder is melted, and the spheroidization does not appear, which could ensure the full density of all samples, and offer high mechanical strength and corrosion resistance. Then the premature fracture or pinning corrosion would not appear due to pores during service.

The microstructure of the sample (construction angle relative to build plate) was affected due to the change of the construction angle, and the morphology of the horizontal plane was similar for each set of construction angle samples. In addition, the laser radiation and remelting of the plane of the same area increased, which caused shortened and even overlapped average laser tracks of each sample with the increase of the construction angle. When construction angle is 45°, the melt pool morphology of the vertical plane from the sample was almost the same as the laser trace of the horizontal plane. This might indicate that two samples (45° and 135° relative to the build plate) had less differences between the microstructures.

TABLE 2 | Potentiodynamic polarization results of SLM-formed 316L SS.

Construction angles	I_{corr}/(A/cm^2)	E_{corr}/V
0°	1.96×10^{-5}	−0.35
15°	2.20×10^{-5}	−0.37
30°	1.12×10^{-5}	−0.33
45°	2.04×10^{-5}	−0.35
60°	1.64×10^{-5}	−0.36
75°	2.04×10^{-5}	−0.35
90°	8.8×10^{-6}	−0.34

When the construction height increased, the deposition layer was continuously preheated and remelted, causing continuous accumulation of heat, while the temperature gradient and the degree of subcooling on the next layer decreased. Thus, the sub-grains nucleated and grew, leading to a larger grain size. During solidification, the growth of adjacent dendrites was inhibited due to fast cooling. Thus, columnar sub-grains were formed with obvious orientation. Portions of the columnar sub-grains exhibited epitaxial growth because of continuous remelting. During cooling, the sub-grains at the MPB continued to grow along the growth direction of the initial sub-grains inside of molten pool. The columnar grains crossed and grew further beyond the MPB. Due to the large temperature gradient during solidification, a part of the columnar grains possessed a strong epitaxial growth trend, even passing through the multilayer melt pool boundary.

The columnar sub-grains were largely different in each direction plane (relative to build plate) in SLM-fabricated 316L stainless steel. The proportion of columnar sub-grains decreased with the increase of the angle when the inclination angle of the plane was less than 45° (compared to build plate). In contrast, the proportion of columnar grains slightly increased when the inclination of the plane ranged from 45 to 60° (relative to build plate). During solidification, the heat flow dissipated through the deposited layer or the argon gas. The direction of heat transfer was parallel to the direction of grain growth, leading to competitive growth between grains (Larimian et al., 2020). Thus, the columnar grains grew upward along the BD, while the equiaxed grains appeared on the horizontal surface, but the heat transfer of each deposition layer changed with the increase in the construction angle. Based on rapid solidification, the Marangoni convection affected the heat and solute diffusion at the tip of the dendrite sub-grains, causing different aspect ratios of columnar grains in different planes (Spittle, 2013).

Nguyen et al. (2018) prepared Inconel 718 alloy with different powder layer thickness by SLM technology. When the powder layer is 20 μm, the sample exhibits a stable three-dimensional size, fine grain size, and high tensile properties. With the increase of the powder layer thickness, the porosity of the sample increases under the same process parameters. The sample exhibited partial unfused defects when the layer thickness is 50 μm. During the SLM process, when a thin powder layer is used, the sample could experience more thermal cycles. Meanwhile, the sufficient marangoni convection is conducive to a more uniform microstructure and element distribution. Compared with the thick powder layer, the columnar crystals could display the tendency of epitaxial growth in the molten pool when thin powder layer is used to build the same height, during SLM.

Figure 4 shows that <101> orientated grains decreased with the increase in the construction angle (<60°). During SLM processing, with the construction angle increases, the processing area of the block gradually decreases, that is, the area of the deposition layer decreases, which affects the liquid phase isotherm of the powder (Liu et al., 2018). During solidification, the direction of energy dissipation is affected by the building height of each sample. The growth direction of some dendrite sub-grains was perpendicular to the liquid phase isotherm, while some had a certain angle with the liquid phase isotherm. Thermal diffusivity and conductivity and element segregation led to changes of the thermal field at the melt pool. Therefore, the orientations of the grains changed. A similar phenomenon was reported in SLM-fabricated Inconel 718 (Du et al., 2019). In addition, the crystal lattice rotation due to deformation and nitriding affects texture evolution (Poulsen et al., 2003; Stinville et al., 2010). Based on the SLM process, remelting and differences in thermal fields may cause lattice rotation. Similar to the grain orientation in the build direction, the grains of different angle planes might also have undergone lattice rotation. Thus, the different planes exhibited various grain orientations.

Based on rapid melting and solidification, numerous dislocations were accumulated inside the cellular grain and columnar grain. The dislocation density gradually increased, intertwining to form dislocation walls, and further evolved into sub-grain boundaries. As the stress accumulated to a certain critical value, the sub-grain boundaries continued to absorb dislocations and then dynamic recrystallization occurred. Finally, the sub-grain boundaries gradually transformed into HAGBs (Wen et al., 2019). As the built height increased, the temperature gradient along the build direction changed greatly, increasing the density of geometrically necessary dislocation inside the sample (Mercelis and Kruth, 2006).

Effect of Angles Relative to Build Substrate on Mechanical Properties

In this study, the yield strength (YS) of the SLM-fabricated 316 SS with different construction angles exceeded 510 MPa, much higher than that of cold-rolled 316L SS (Shin et al., 2021). This may have been related to grain refinement, solid solution strengthening, and dislocation strengthening.

TABLE 3 | Contribution of each strengthening mechanism on the yield strength of the SLM-fabricated 316L SS with different angles relative to the build substrate based on the models.

Strength (MPa)	0° sample	45° sample	60° sample	90° sample
$\Delta\sigma_{GB}$	242.8	249.2	245.9	249.6
$\Delta\sigma_d$	243.2	254.5	255.4	263.4
$\Delta\sigma_{ss}$	115.4	115.4	115.4	115.4
σ	601.4	619.1	616.7	628.4

During the deformation process, grain boundaries can hinder the sliding of dislocations, causing accumulation of dislocations. Therefore, the need for greater stress promoted plastic deformation and even fracture of the material. The average grain size of each sample was below 26 μm, and the volume fraction of finer grains was greater than 5% except for the 45° sample. Based on the Hall–Petch formula:

$$\Delta\sigma_{GB} = \sigma_0 + k_y d_m^{-1/2},$$

where σ_0 is the friction stress (≈188 MPa), k is the strength coefficient (275 MPa·μm1/2 for 316L steel), and dm represents the average grain size (Li et al., 2018; Kumar et al., 2020). For most alloys, yield strength improves with a decreasing grain size. The theoretical yield strengths of the samples due to Hall–Petch contribution were 242.8, 249.2, 245.9, and 249.6 MPa, in order of increasing construction angles (**Table 3**).

Each samples had a high proportion of LAGBs and dislocation densities. During the load process, LAGBs became the nucleation center of dislocations; dislocations slipped, entangled, and formed dense dislocation walls, resulting in many secondary interfaces and leading to strain hardening. In addition, the LAGBs were related to the KAM diagram. Based on the KAM diagram, many dislocations and dislocation loops appeared in each sample. During the deformation process, the grain boundaries inhibited the movement of the dislocations, thereby leading to a high YS of the material. The dislocation strengthening is described as:

$$\Delta\mathrm{\sigma_d} = \mathrm{BbG_m}\sqrt{\mathrm{\rho}},$$

where B for FCC materials is taken as 0.2, Gm is the shear modulus of the 316L steel (77 GPa), b is burgers vector, and ρ represents the dislocation density, which includes GNDs, estimated by the KAM analysis (Li et al., 2020). Based on theoretical calculations, the σ_d of each sample were 243.2, 254.5, 255.4, and 263.4 MPa, in order of increasing construction angles (**Table 3**).

The solid solution atoms (alloying elements) dissolved in the 316L stainless steel affected yield strength. The solid solution strengthening is given by:

$$\Delta\mathrm{\sigma_{ss}} = \mathrm{k_i c_i},$$

where ki is the strengthening coefficient and ci is the i-th alloying element's concentration (Mohd Yusuf et al., 2020). Mohd Yusuf et al. (2020) calculated σ_{ss} to be 115.4 MPa.

After theoretical calculation, the theoretical yield strength of 316L stainless steel can be expressed as follows:

$$\sigma = \Delta\sigma_{GB} + \Delta\sigma_d + \Delta\sigma_{ss}.$$

Grain refinement and dislocation strengthening played key roles in YS improvement of the SLM-processed 316L SS, as shown in **Table 3**. The results show that the theoretical strength of each sample was larger than the experimental strength. This might be attributed to the effects of defects, micro-textures, the spatial orientation of the melt pool boundary, and element segregation. Among them, the 90° sample contained large pore, which affects the yield strength of the sample.

In addition, the plasticity of the SLM-processed 316L SS was greater than 45% in this study. Some researchers consider that the high ductility of SLM-prepared 316L SS is owed to the interaction between deformation twins and dislocations in the unit cell. The strain-induced texture evolution played a character in improving the ductility of SLM-processed 316L SS before deformation (Dryepondt et al., 2021). Pham et al. (2017) found that the twinning activity was very active near the necking area, and the slip could re-orient the twinning direction. During deformation, the microstructure of the 316L SS underwent grain rotation, slipping, and twinning (Liu et al., 2020). The dispersion of the refined grain structure could improve the strength and ductility of the alloy. In addition, the association of both fine grains and coarse grains was beneficial to improve the elongation (Agius et al., 2017). All the samples exhibited a combination of fine grains and coarse grains, except for the 45° sample, which ensured the high elongation of the SLM-processed 316L SS. During the deformation process, a greater accumulation of dislocations occurred near the grain boundaries in the 90° sample due to the differences in grain sizes. Meanwhile, based on the rough-induced crack termination mechanism, friction stress occurred and slowed the propagation of cracks in the 90° sample, thus the 90° sample had higher ductility than the other samples (Koyama et al., 2017).

The strength and toughness of each set of construction angle samples (for which the sum of the construction angles was 90°) seemed to be similar (within the error of 20 MPa or 3%, respectively), except for the 0° and 90° specimens. Each set of construction angle samples (for which the sum of construction angles = 90°) showed similar macrostructure on the vertical plane and the horizontal plane. This shows that the SLM-processed 316L SS had similar macrostructures on planes with different angles, for which the sum of the construction angles = 90° (relative to build plate). During SLM, the laser acted on the powder layer, melting the metal powder, which solidified and formed a good metallurgical bond. The horizontal plane of each sample shows the morphology of "track–track," and the vertical plane of each sample shows the morphology of "layer–layer," which is the typical macrostructure morphology of SLM-processed samples. Based on rapid cooling, the SLM-processed samples had a fine microstructure and few element segregations at the grain boundaries. Thus, the 316L SS showed strength and plasticity comparable to forging.

Effect of Angles Relative to Build Substrate on Corrosion Resistance

During corrosion, the oxide bonding of the passive film became weak and dissolved when Cl^- ions attacked through the pores of the 316L SS sample surface. The passive film could rupture, thereby affecting the corrosion properties. In addition, based on ASTM G102, the corrosion rate of each sample is calculated by Faraday's law, and the mass loss rate (MR) is calculated as follow:

$$MR = K_2 i_{corr} EW,$$

where MR is given in g/m^2d, i_{corr} in A/m^2, K_2 is a constant (0.8953 g/Ad), ρ is the density of materials, and EW may be thought of as the mass of metal, which may be oxidized. According to the i_{corr} in **Table 2**, the mass loss rate of each sample is different. It can be related to the pore, dislocation density, grain size, and microstructure.

The few of pores had an important role in improving corrosion performance (Mohd Yusuf et al., 2018). The metastable pits were more easily transformed into stable pits due to grain refinement. Therefore, the austenitic stainless steel was hardly affected by corrosion (Abbasi Aghuy et al., 2015). Based on rapid melting and solidification, manganese sulfide (MnS) inclusions were eliminated or significantly refined in the SLM-formed 316L SS, which improved the corrosion resistance (Laleh et al., 2019a).

The higher the proportion of LAGBs in the sample, the stronger the corrosion resistance due to the low interface energy of LAGBs (Laleh et al., 2019b). The greater dislocation density in SLM-formed 316L SS provided further nucleation sites for the passive film (Wang et al., 2015). The increased grain boundary density was conducive to enhancing the formation and adhesion of the passive film on the sample surface (Al-Mamun et al., 2020). The performance of the passive film directly affected the corrosion resistance of each sample. The passive film of 316L SS is made up of Fe oxide on the outer layer and Cr oxide on the inside layer, which has semiconductor properties (Kong et al., 2018b). When the semiconductor was immersed in the NaCl solution, a Helmholtz layer formed on the solution side while a space–charge layer formed on the semiconductor side. The surface of the p-type semiconductor electrode (Cr oxide) had a negative residual charge, and the Helmholtz layer was a cationic layer, which prevented the adsorption of Cl on the sample and thus the passive film's erosion (Hatakeyama et al., 2020). Hence, the 90° sample had high LAGBs, dislocation density, and finer grains, thus it exhibited good corrosion resistance.

CONCLUSION

In this study, the effects of construction angles (from 0° to 90° relative to build plate) on the microstructure evolution, texture, tensile properties, and corrosion resistance of SLM-prepared 316L samples were researched. The main conclusions are made as follows:

1) With the increase of angle, "track–track" overlap track showed various variations on the horizontal surface. Each set of construction angle samples (for which the sum of

construction angles = 90°) exhibited shortening and even overlapping of the laser track.

2) Increasing the angle relative to the build substrate gradually changed the grain morphology of the 316L SS from columnar grains to equiaxed grains. The 0° sample and 90° sample showed a strong <101 > texture. The grain orientation showed a trend from <101> to <111> with an increasing construction angle (<60°).
3) A good unity of high strength (UTS = 708 MPa, YS = 588 MPa) and ductility (54.51%) exhibited in the 60° sample.
4) The 90° sample showed higher elongation (62.57%) and corrosion resistance than the other samples. The passive film had more nucleation sites and formed on the sample surface, by reason of the higher dislocation density and a refined grain structure.

DATA AVAILABILITY STATEMENT

The raw data supporting the conclusions of this article will be made available by the authors, without undue reservation.

AUTHOR CONTRIBUTIONS

XL, DY, and XW collected the experimental data, performed data analysis, and wrote the manuscript. JZ and XY performed a part of data analysis. ZZ, JW, and BL oversaw the project and performed the overall editing of the manuscript. PB provided the financial support for this work.

FUNDING

This work was financially supported by the National Natural Science Foundation of China (No. 52071299 and 51804280), Key R&D program of Shanxi Province (International Cooperation, 201903D421075), the Major Science and Technology Projects of Shanxi Province, China (No. 20181101009), Scientific and Technological Innovation Programs of Higher Education Institutions in Shanxi (No. 2019L0556), and the Support Program for Young Academic Leaders of North University of China, China (No. QX201802).

REFERENCES

Abbasi Aghuy, A., Zakeri, M., Moayed, M. H., and Mazinani, M. (2015). Effect of Grain Size on aitting Corrosion of 304L Austenitic Stainless Steel. *Corrosion Sci.* 94, 368–376. doi:10.1016/j.corsci.2015.02.024

Agius, D., Kourousis, K. I., Wallbrink, C., and Song, T. (2017). Cyclic Plasticity and Microstructure of As-Built SLM Ti-6Al-4V: The Effect of Build Orientation. *Mater. Sci. Eng. A* 701, 85–100. doi:10.1016/j.msea.2017.06.069

Agrawal, A. K., Meric de Bellefon, G., and Thoma, D. (2020). High-throughput Experimentation for Microstructural Design in Additively Manufactured 316L Stainless Steel. *Mater. Sci. Eng. A* 793, 139841. doi:10.1016/j.msea.2020.139841

Al-Mamun, N. S., Mairaj Deen, K., Haider, W., Asselin, E., and Shabib, I. (2020). Corrosion Behavior and Biocompatibility of Additively Manufactured 316L Stainless Steel in a Physiological Environment: the Effect of Citrate Ions. *Additive Manufacturing* 34, 101237. doi:10.1016/j.addma.2020.101237

AlMangour, B., Grzesiak, D., and Yang, J.-M. (2017). In-situ Formation of Novel TiC-Particle-Reinforced 316L Stainless Steel Bulk-form Composites by Selective Laser Melting. *J. Alloys Compounds* 706, 409–418. doi:10.1016/j.jallcom.2017.01.149

Atapour, M., Wang, X., Färnlund, K., Odnevall Wallinder, I., and Hedberg, Y. (2020). Corrosion and Metal Release Investigations of Selective Laser Melted 316L Stainless Steel in a Synthetic Physiological Fluid Containing Proteins and in Diluted Hydrochloric Acid. *Electrochimica Acta* 354, 136748. doi:10.1016/j.electacta.2020.136748

Bahl, S., Mishra, S., Yazar, K. U., Kola, I. R., Chatterjee, K., and Suwas, S. (2019). Non-equilibrium Microstructure, Crystallographic Texture and Morphological Texture Synergistically Result in Unusual Mechanical Properties of 3D Printed 316L Stainless Steel. *Additive Manufacturing* 28, 65–77. doi:10.1016/j.addma.2019.04.016

Blinn, B., Krebs, F., Ley, M., Teutsch, R., and Beck, T. (2020). Determination of the Influence of a Stress-Relief Heat Treatment and Additively Manufactured Surface on the Fatigue Behavior of Selectively Laser Melted AISI 316L by Using Efficient Short-Time Procedures. *Int. J. Fatigue* 131, 105301. doi:10.1016/j.ijfatigue.2019.105301

Chao, Q., Thomas, S., Birbilis, N., Cizek, P., Hodgson, P. D., and Fabijanic, D. (2021). The Effect of post-processing Heat Treatment on the Microstructure, Residual Stress and Mechanical Properties of Selective Laser Melted 316L Stainless Steel. *Mater. Sci. Eng. A* 821, 141611. doi:10.1016/j.msea.2021.141611

Chen, W., Voisin, T., Zhang, Y., Florien, J.-B., Spadaccini, C. M., McDowell, D. L., et al. (2019). Microscale Residual Stresses in Additively Manufactured Stainless Steel. *Nat. Commun.* 10, 1–12. doi:10.1038/s41467-019-12265-8

Dryepondt, S., Nandwana, P., Fernandez-Zelaia, P., and List, F. (2021). Microstructure and High Temperature Tensile Properties of 316L Fabricated by Laser Powder-Bed Fusion. *Additive Manufacturing* 37, 101723. doi:10.1016/j.addma.2020.101723

Du, D., Dong, A., Shu, D., Zhu, G., Sun, B., Li, X., et al. (2019). Influence of Build Orientation on Microstructure, Mechanical and Corrosion Behavior of Inconel 718 Processed by Selective Laser Melting. *Mater. Sci. Eng. A* 760, 469–480. doi:10.1016/j.msea.2019.05.013

Gao, S., Hu, Z., Duchamp, M., Krishnan, P. S. S. R., Tekumalla, S., Song, X., et al. (2020). Recrystallization-based Grain Boundary Engineering of 316L Stainless Steel Produced via Selective Laser Melting. *Acta Materialia* 200, 366–377. doi:10.1016/j.actamat.2020.09.015

Harun, W. S. W., Manam, N. S., Kamariah, M. S. I. N., Sharif, S., Zulkifly, A. H., Ahmad, I., et al. (2018). A Review of Powdered Additive Manufacturing Techniques for Ti-6al-4v Biomedical Applications. *Powder Technology* 331, 74–97. doi:10.1016/j.powtec.2018.03.010

Hatakeyama, T., Ida, S., Sekido, N., and Yoshimi, K. (2020). Significant Improvement of the Oxidation Resistance of MoSiBTiC-Based Multiphase Alloys by Ti Enrichment. *Corrosion Sci.* 176, 108937. doi:10.1016/j.corsci.2020.108937

Hong, Y., Zhou, C., Zheng, Y., Zhang, L., and Zheng, J. (2021). The Cellular Boundary with High Density of Dislocations Governed the Strengthening Mechanism in Selective Laser Melted 316L Stainless Steel. *Mater. Sci. Eng. A* 799, 140279. doi:10.1016/j.msea.2020.140279

Kale, A. B., Alluri, P., Singh, A. K., and Choi, S.-H. (2021). The Deformation and Fracture Behavior of 316L SS Fabricated by SLM under Mini V-Bending Test. *Int. J. Mech. Sci.* 196, 106292. doi:10.1016/j.ijmecsci.2021.106292

Kong, D., Ni, X., Dong, C., Lei, X., Zhang, L., Man, C., et al. (2018b). Bio-functional and Anti-corrosive 3D Printing 316L Stainless Steel Fabricated by Selective Laser Melting. *Mater. Des.* 152, 88–101. doi:10.1016/j.matdes.2018.04.058

Kong, D., Ni, X., Dong, C., Zhang, L., Man, C., Xiao, K., et al. (2018a). Heat Treatment Effect on the Microstructure and Corrosion Behavior of 316L Stainless Steel Fabricated by Selective Laser Melting for Proton Exchange Membrane Fuel Cells. *Electrochimica Acta* 276, 293–303. doi:10.1016/j.electacta.2018.04.188

Koyama, M., Zhang, Z., Wang, M., Ponge, D., Raabe, D., Noguchi, H., et al. (2017). Bone-like Crack Resistance in Hierarchical Metastable Nanolaminate Steels. *Science* 355, 1055–1057. doi:10.1126/science.aal2766

Kreitcberg, A., Brailovski, V., and Turenne, S. (2017). Elevated Temperature Mechanical Behavior of IN625 alloy Processed by Laser Powder-Bed Fusion. *Mater. Sci. Eng. A* 700, 540–553. doi:10.1016/j.msea.2017.06.045

Kumar, P., Jayaraj, R., Suryawanshi, J., Satwik, U. R., McKinnell, J., and Ramamurty, U. (2020). Fatigue Strength of Additively Manufactured 316L

Austenitic Stainless Steel. *Acta Materialia* 199, 225–239. doi:10.1016/j.actamat.2020.08.033

Laleh, M., Hughes, A. E., Xu, W., Gibson, I., and Tan, M. Y. (2019a). Unexpected Erosion-Corrosion Behaviour of 316L Stainless Steel Produced by Selective Laser Melting. *Corrosion Sci.* 155, 67–74. doi:10.1016/j.corsci.2019.04.028

Laleh, M., Hughes, A. E., Xu, W., Haghdadi, N., Wang, K., Gibson, I., et al. (2019b). On the Unusual Intergranular Corrosion Resistance of 316L Stainless Steel Additively Manufactured by Selective Laser Melting. *Corrosion Sci.* 161, 108189. doi:10.1016/j.corsci.2019.108189

Larimian, T., Kannan, M., Grzesiak, D., AlMangour, B., and Borkar, T. (2020). Effect of Energy Density and Scanning Strategy on Densification, Microstructure and Mechanical Properties of 316L Stainless Steel Processed via Selective Laser Melting. *Mater. Sci. Eng. A* 770, 138455. doi:10.1016/j.msea.2019.138455

Li, H., Wang, X., Chai, L., Wang, H., Chen, Z., Xiang, Z., et al. (2018). Microstructure and Mechanical Properties of an In-Situ TiB2/Al-Zn-Mg-Cu-Zr Composite Fabricated by Melt-SHS Process. *Mater. Sci. Eng. A* 720, 60–68. doi:10.1016/j.msea.2018.02.025

Li, X., Yi, D., Liu, B., Zhang, J., Yang, X., Feng, Y., et al. (2020). Graphene-strengthened Inconel 625 Alloy Fabricated by Selective Laser Melting. *Mater. Sci. Eng. A* 798, 140099. doi:10.1016/j.msea.2020.140099

Li, X., Yi, D., Wu, X., Zhang, J., Yang, X., Feng, Y., et al. (2021). Effect of Construction Angles on Microstructure and Mechanical Properties of AlSi10Mg alloy Fabricated by Selective Laser Melting. *J. Alloys Compounds* 881, 160459. doi:10.1016/j.jallcom.2021.160459

Liu, M., Takata, N., Suzuki, A., and Kobashi, M. (2018). Microstructural Characterization of Cellular AlSi10Mg alloy Fabricated by Selective Laser Melting. *Mater. Des.* 157, 478–491. doi:10.1016/j.matdes.2018.08.005

Liu, Q., Wang, G., and Qiu, C. (2020). On the Role of Dynamic Grain Movement in Deformation and Mechanical Anisotropy Development in a Selectively Laser Melted Stainless Steel. *Additive Manufacturing* 35, 101329. doi:10.1016/j.addma.2020.101329

Liverani, E., Toschi, S., Ceschini, L., and Fortunato, A. (2017). Effect of Selective Laser Melting (SLM) Process Parameters on Microstructure and Mechanical Properties of 316L Austenitic Stainless Steel. *J. Mater. Process. Technology* 249, 255–263. doi:10.1016/j.jmatprotec.2017.05.042

Luo, S., Huang, W., Yang, H., Yang, J., Wang, Z., and Zeng, X. (2019). Microstructural Evolution and Corrosion Behaviors of Inconel 718 alloy Produced by Selective Laser Melting Following Different Heat Treatments. *Additive Manufacturing* 30, 100875. doi:10.1016/j.addma.2019.100875

Marattukalam, J. J., Karlsson, D., Pacheco, V., Beran, P., Wiklund, U., Jansson, U., et al. (2020). The Effect of Laser Scanning Strategies on Texture, Mechanical Properties, and Site-specific Grain Orientation in Selective Laser Melted 316L SS. *Mater. Des.* 193, 108852. doi:10.1016/j.matdes.2020.108852

Mercelis, P., and Kruth, J. P. (2006). Residual Stresses in Selective Laser Sintering and Selective Laser Melting. *Rapid Prototyping J.* 12, 254–265. doi:10.1108/13552540610707013

Mohd Yusuf, S., Chen, Y., Yang, S., and Gao, N. (2020). Microstructural Evolution and Strengthening of Selective Laser Melted 316L Stainless Steel Processed by High-Pressure Torsion. *Mater. Characterization* 159, 110012. doi:10.1016/j.matchar.2019.110012

Mohd Yusuf, S., Nie, M., Chen, Y., Yang, S., and Gao, N. (2018). Microstructure and Corrosion Performance of 316L Stainless Steel Fabricated by Selective Laser Melting and Processed through High-Pressure Torsion. *J. Alloys Compounds* 763, 360–375. doi:10.1016/j.jallcom.2018.05.284

Nguyen, Q. B., Luu, D. N., Nai, S. M. L., Zhu, Z., Chen, Z., and Wei, J. (2018). The Role of Powder Layer Thickness on the Quality of SLM Printed Parts. *Arch. Civil Mech. Eng.* 18, 948–955. doi:10.1016/j.acme.2018.01.015

Pham, M. S., Dovgyy, B., and Hooper, P. A. (2017). Twinning Induced Plasticity in Austenitic Stainless Steel 316L Made by Additive Manufacturing. *Mater. Sci. Eng. A* 704, 102–111. doi:10.1016/j.msea.2017.07.082

Poulsen, H. F., Margulies, L., Schmidt, S., and Winther, G. (2003). Lattice Rotations of Individual Bulk Grains. *Acta Materialia* 51, 3821–3830. doi:10.1016/S1359-6454(03)00206-4

Shifeng, W., Shuai, L., Qingsong, W., Yan, C., Sheng, Z., and Yusheng, S. (2014). Effect of Molten Pool Boundaries on the Mechanical Properties of Selective Laser Melting Parts. *J. Mater. Process. Technology* 214, 2660–2667. doi:10.1016/j.jmatprotec.2014.06.002

Shin, W.-S., Son, B., Song, W., Sohn, H., Jang, H., Kim, Y.-J., et al. (2021). Heat Treatment Effect on the Microstructure, Mechanical Properties, and Wear Behaviors of Stainless Steel 316L Prepared via Selective Laser Melting. *Mater. Sci. Eng. A* 806, 140805. doi:10.1016/j.msea.2021.140805

Shu, T., Zhang, Y., Sun, G., Pan, Y., He, G., Cheng, Y., et al. (2020). Enhanced Osseointegration by the Hierarchical Micro-nano Topography on Selective Laser Melting Ti-6Al-4V Dental Implants. *Front. Bioeng. Biotechnol.* 8, 621601. doi:10.3389/fbioe.2020.621601

Song, S., Wang, X., Wang, T., Yu, Q., Hou, Z., Zhu, Z., et al. (2020a). Additive Manufacturing of Nerve Guidance Conduits for Regeneration of Injured Peripheral Nerves. *Front. Bioeng. Biotechnol.* 8, 590596. doi:10.3389/fbioe.2020.590596

Song, Y. n., Sun, Q., Guo, K., Wang, X., Liu, J., and Sun, J. (2020b). Effect of Scanning Strategies on the Microstructure and Mechanical Behavior of 316L Stainless Steel Fabricated by Selective Laser Melting. *Mater. Sci. Eng. A* 793, 139879. doi:10.1016/j.msea.2020.139879

Spittle, J. A. (2013). Columnar to Equiaxed Grain Transition in as Solidified Alloys. *Int. Mater. Rev.* 51, 247–269. doi:10.1179/174328006x102493

Stinville, J. C., Villechaise, P., Templier, C., Rivière, J. P., and Drouet, M. (2010). Lattice Rotation Induced by Plasma Nitriding in a 316L Polycrystalline Stainless Steel. *Acta Materialia* 58, 2814–2821. doi:10.1016/j.actamat.2010.01.002

Wang, X., Nie, M., Wang, C. T., Wang, S. C., and Gao, N. (2015). Microhardness and Corrosion Properties of Hypoeutectic Al-7Si alloy Processed by High-Pressure Torsion. *Mater. Des.* 83, 193–202. doi:10.1016/j.matdes.2015.06.018

Wen, S., Chen, K., Li, W., Zhou, Y., Wei, Q., and Shi, Y. (2019). Selective Laser Melting of Reduced Graphene oxide/S136 Metal Matrix Composites with Tailored Microstructures and Mechanical Properties. *Mater. Des.* 175, 107811. doi:10.1016/j.matdes.2019.107811

Xing, H., Li, R., Wei, Y., Ying, B., Li, D., and Qin, Y. (2020). Improved Osteogenesis of Selective-Laser-Melted Titanium Alloy by Coating Strontium-Doped Phosphate with High-Efficiency Air-Plasma Treatment. *Front. Bioeng. Biotechnol.* 8, 367. doi:10.3389/fbioe.2020.00367

Xu, D., Qian, J., Guan, X., Ren, L., Yang, K., Zhang, S., et al. (2021). Copper-Containing Alloy as Immunoregulatory Material in Bone Regeneration via Mitochondrial Oxidative Stress. *Front. Bioeng. Biotechnol.* 8, 620629. doi:10.3389/fbioe.2020.620629

Yin, Y. J., Sun, J. Q., Guo, J., Kan, X. F., and Yang, D. C. (2019). Mechanism of High Yield Strength and Yield Ratio of 316 L Stainless Steel by Additive Manufacturing. *Mater. Sci. Eng. A* 744, 773–777. doi:10.1016/j.msea.2018.12.092

Yu, J., Kim, D., Ha, K., Jeon, J. B., and Lee, W. (2020). Strong Feature Size Dependence of Tensile Properties and its Microstructural Origin in Selectively Laser Melted 316L Stainless Steel. *Mater. Lett.* 275, 128161. doi:10.1016/j.matlet.2020.128161

Zhang, J., Xu, J., Cheng, W., Chen, C., and Kang, J. (2012). Corrosion Behavior of Mg-Zn-Y Alloy with Long-Period Stacking Ordered Structures. *J. Mater. Sci. Technology* 28, 1157–1162. doi:10.1016/S1005-0302(12)60186-8

Zhang, Z., Chu, B., Wang, L., and Lu, Z. (2019). Comprehensive Effects of Placement Orientation and Scanning Angle on Mechanical Properties and Behavior of 316L Stainless Steel Based on the Selective Laser Melting Process. *J. Alloys Compounds* 791, 166–175. doi:10.1016/j.jallcom.2019.03.082

Conflict of Interest: The authors declare that the research was conducted in the absence of any commercial or financial relationships that could be construed as a potential conflict of interest.

frontiers in Materials

ORIGINAL RESEARCH
published: 08 December 2021
doi: 10.3389/fmats.2021.786650

Preliminary Studies for One-Step Fabrication of Metallic Iron-Based Coatings on Magnesium as Temporary Protection in Biodegradable Medical Application

Yuyun Yang[1,2,3], Zizhong Shi[1], Xiufang Cui[1], Yuejun Liu[1], Guo Jin[1], Sannakaisa Virtanen[3], Aldo R. Boccaccini[2] and Peng She[4]**

[1]Department of Material Science and Chemical Engineering, Institute of Surface/Interface Science and Technology, Harbin Engineering University, Harbin, China, [2]Department of Materials Science and Engineering, Institute of Biomaterials, University of Erlangen-Nuremberg, Erlangen, Germany, [3]Department of Materials Science and Engineering, Institute for Surface Science and Corrosion, University of Erlangen-Nuremberg, Erlangen, Germany, [4]Department of Orthopaedics, The Seventh Affiliated Hospital of Sun Yat-sen University, Shenzhen, China

Edited by:
Lechun Xie,
Wuhan University of Technology,
China

Reviewed by:
Lin Mao,
University of Shanghai for Science and Technology, China
Jun Wang,
Deakin University, Australia
Davod Seifzadeh,
University of Mohaghegh Ardabili, Iran

***Correspondence:**
Xiufang Cui
cuixiufang@hrbeu.edu.cn
Peng She
shep@mail.sysu.edu.cn

Specialty section:
This article was submitted to Biomaterials, a section of the journal Frontiers in Materials

Received: *30 September 2021*
Accepted: *15 November 2021*
Published: *08 December 2021*

Citation:
Yang Y, Shi Z, Cui X, Liu Y, Jin G, Virtanen S, Boccaccini AR and She P (2021) Preliminary Studies for One-Step Fabrication of Metallic Iron-Based Coatings on Magnesium as Temporary Protection in Biodegradable Medical Application. Front. Mater. 8:786650. doi: 10.3389/fmats.2021.786650

Iron and magnesium are being considered as promising candidates for biodegradable materials in medical applications, both materials having their specific advantages and challenges. A hybrid of metallic iron and magnesium in a layered composite is studied in the present work, to combine the merits of both metals. A single-step dip-coating method was employed to prepare the layered composite material. Morphology, composition, crystal structure and corrosion behavior of the Mg/Fe sheet were assessed by SEM, EDX, XRD, and electrochemical measurements. The Mg/Fe layered composite sheet is composed of the magnesium substrate, a 1–2 μm metallic iron coating, and a pompon-like $Mg(OH)_2$/MgO top layer. Long-term open-circuit potential measurements revealed that the Mg/Fe sheet samples exhibit a "self-healing" effect in Dulbecco's modified Eagle's medium.

Keywords: iron, magnesium, one-step fabrication, composite, "self-healing" effect

1 INTRODUCTION

Since Lane introduced the application of metal plates for bone fracture fixation 100 years ago, metallic biomaterials have achieved huge development for a variety of biomedical applications (Hornberger et al., 2012; Mao et al., 2017; Li et al., 2019). The most well-known metallic biomaterials are high corrosion-resistant materials, such as 316 stainless steel (Tan et al., 2003; Shih et al., 2004; Patnaik et al., 2020), cobalt-chromium alloys (Ducheyne and Healy, 1988; Que and Topoleski, 2000; Kereiakes et al., 2003; Watanabe et al., 2021), titanium and its alloys (Helary et al., 2009; Huang et al., 2010; Niinomi et al., 2012; Jin et al., 2015; Lourenço et al., 2020), tantalum alloys (Miyazaki et al., 2000; Shimko et al., 2005; Zhou et al., 2007; Rodriguez-Contreras et al., 2021), as well as precious alloys (O'Brien, 1997; Chen et al., 2005; Niinomi et al., 2015). Another group of metals consists of biodegradable materials, such as pure iron and a variety of Fe-based alloys as well as pure magnesium and Mg alloys (Wu et al., 2016; Mao et al., 2017; Yang et al., 2018; Gorejová et al., 2019; Costantino et al., 2020; Zhu et al., 2021).

In the meantime, elements such as Fe and Mg are also considered as essential trace elements participating in a wide variety of metabolic processes, such as enzyme catalysis, oxygen transport, energy metabolism, and DNA and RNA synthesis (Zhang et al., 2018; Lee et al., 2021). Released Fe and Mg ions during biodegradation reactions directly incorporate into the metabolic processes, affecting the metabolic functions and the biodegradation of metallic implants.

Compared with non-degradable materials, biodegradable metals should not cause permanent physical irritation and they avoid the need to remove a temporary implant in a second operation (Schinhammer et al., 2013; Mao et al., 2017). In principle, a controllable degradation rate should be achieved as this is a key requirement for degradable metallic biomaterials. Regarding degradation, Mg (Mg alloys) and Fe (Fe alloys) present different challenges. For example, the high dissolution rate of magnesium in biological environments largely limits its biomedical application (Fischerauer et al., 2013). Therefore, various surface modification and coating methods (Rajabalizadeh and Seifzadeh, 2014; Seifzadeh and Farhoudi, 2016; Nezamdoust et al., 2019; Abdi-Alghanab et al., 2020; Ouyang et al., 2020; Chen et al., 2021) are applied to tailor the undesired fast degradation rate into a moderate one to fulfill the therapeutic tasks. For instance, Zhu (Zhu et al., 2021) prepared a poly (d,l-lactic acid)-coated magnesium alloy-based rapamycin drug-eluting bioresorbable stent. *In vivo* and *in vitro* studies showed that the polymeric coatings provided a suitable degradation rate of magnesium alloy stents.

Compared with Mg-based alloys, pure iron and its alloys exhibit better mechanical properties and cause no excessive hydrogen evolution during degradation. On the contrary, several studies have been performed to increase the degradation rate of Fe-based materials for the possible application in temporary implants, as Fe-based materials show a too slow corrosion rate in biological environments (Abou Neel et al., 2005; Moravej et al., 2010; Zhang et al., 2010; Francis et al., 2015; Gorejová et al., 2019; Lee et al., 2021). For example in the research of Lee et al. (Lee et al., 2021) a novel combination of nanostructured surface topography and galvanic reaction was reported to achieve a uniform and accelerated degradation of a Fe implant.

Based on related research work on tailoring the degradation behavior of both biodegradable Mg materials (to decrease degradation) and Fe materials (to increase degradation), the idea of combining Mg and Fe together, especially by using iron coating as temporary protection of Mg substrates, is a feasible approach. In this design, two biocompatible metallic materials are introduced in one system, which greatly enhances the biocompatibility of the combined material for further investigation. On the other hand, the metallic iron serving as temporary protection on Mg would achieve the goal of tailoring the degradation rate of both Mg and Fe at the same time. Metallic iron coatings could protect magnesium substrates from aggressive corrosion attacks in the physiological environment until the metallic iron coatings are fully biodegraded. Meanwhile, by comparing with the degradation performance of bulk Fe materials, the degradation behavior of Fe coatings will be intensively affected by their thickness and structure.

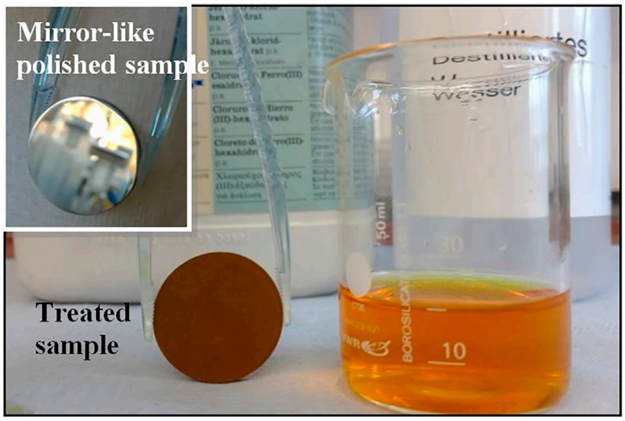

FIGURE 1 | Evidence of the change of the Mg sample surface upon treatment in Fe-bearing coating solution.

Hence, in this study, metallic iron coatings are produced on magnesium substrates by a simple single-step dip-coating method. The reactions taking place in an aqueous solution are spontaneously driven by the electrochemical properties of the participating elements Mg and Fe, and no external energy was introduced during the process (Yan and Xue, 2006). This approach is in contrast to previous attempts to produce metallic coatings via several deposition ways, such as high velocity oxygen fuel, plasma spraying, physical vapor deposition, laser cladding, sol-gel, and kinetic spraying (Livsey, 1981; Liu et al., 2009; Nezamdoust and Seifzadeh, 2017; Dayani et al., 2018; Ferrández-Montero et al., 2019; Lin et al., 2021; Akhter et al., 2022). In most of these methods, fine powders as feedstock and a complex apparatus are needed to fabricate the metallic coatings on the substrate. The here explored one-step dip-coating method combines biodegradable metallic magnesium and iron together in one composite, and the different degradation behaviors of the two metals are exploited. The principle of the coating process is the immersion plating of Fe, taking advantage of the difference in the electrochemical potentials of the substrate and the coating material.

2 EXPERIMENTAL

2.1 Materials Preparation

Commercially pure magnesium rod of 25.4 mm diameter and 99.9% purity, (Chempur Feinchemikalien und Forschungsbedarf GmbH, Germany) was cut into 2–4 mm thickness slices to be used as substrates. A 1200 grit Microcut fleece (Buehler GmbH, Germany) was used for grinding with an ethanol/glycerol (3:1) mixture as lubricant. After that, the samples were cleaned in ultra-sonic bath in ethanol for 3 min. Subsequently, the samples were polished in three steps with diamond paste (6 µm, 3 µm, 1 µm) and a lubricant which consisted of distilled water/ethanol/neutral soap (1,000 ml:250 ml:10 g), followed by ultrasonic cleaning immediately after each polishing step. All samples were rinsed with ethanol and dried with hot air stream.

The fabrication of the layered composite coating was carried out by a dip-coating method. According to the electrochemical series of the elements, a metal cation in an electrolyte can be reduced by any metal with a lower electrochemical potential. In this study, a less noble Mg substrate was applied to reduce Fe^{3+} into Fe and, as a consequence, Mg was oxidized into Mg^{2+} during the dipping process. The chemical reaction is according to **Eq. 1**.

$$3Mg + 2Fe^{3+} \rightarrow 3Mg^{2+} + 2Fe \quad (1)$$

For this process, 1 g iron (III) chloride hexahydrate (Sigma-Aldrich) was completely dissolved in 20 ml de-ionized water under magnetic stirring for 5 min. The Mg substrates were immersed in the coating solution. The dip coating procedure was carried out at room temperature for 90 s. Immediately after being taken out from the suspension, the samples were rinsed in ethanol for 20 s and dried with hot air stream. As shown in **Figure 1**, mirror-like polished magnesium samples were completely covered by a brown composite coating after the treatment. A thin outer oxidized iron layer formed after taking the samples out from the suspension which could contribute to the brown color.

2.2 Microstructure and Composition of the Coatings

The surface and cross-section morphology and the chemical composition of the fabricated layered composite coatings were examined *via* a scanning electron microscope (SEM, model Auriga, Zeiss) equipped with energy-dispersive X-ray spectroscopy (EDX). The cross-sectional samples were prepared by Ar ion milling system (IM4000, HITACHI). X-ray diffraction (XRD) was performed using an X'pert Philips MPD instrument (equipped with Panalytical X'celerator detector, Germany) employing graphite monochromized Cu Kα radiation (Wavelength 1.54056 Å).

2.3 Electrochemical Measurements

Electrochemical behavior of the samples was investigated by using an electrochemical workstation "IM6eX" (Zahner-Elektrik GmbH and Co. KG, Kronach, Germany). Dulbecco's modified Eagle's medium (DMEM, Biochrome AG) was used as the electrolyte. The measurements were carried out in a conventional three-electrode cell assembly which consisted of the coated sample as the working electrode, a platinum plate as the auxiliary electrode and an Ag/AgCl electrode in 3-M KCl as the reference electrode. Long-term open-circuit potential (OCP) was monitored continuously up to 8 h in DMEM at room temperature. DMEM was refreshed every 8 h to mimic the physical buffering environment. To accelerate corrosoin, the samples were potentiodynamically polarized with sweep rate of 3 mV/s into the anodic direction.

3 RESULTS AND DISCUSSION

3.1 Microstructure and Composition

Morphology and elemental composition of freshly prepared samples were studied via SEM coupled with EDX and representative results are shown in **Figure 2**. EDX analysis was carried out on the whole surface and at special locations to determine the composition of the layered composite coating. Clusters, as magnified in **Figure 2A**, precipitated randomly on the entire surface. These clusters were principally composed of metallic iron, such as at Spot 2 in **Figure 2B**. The iron signal indicates successful chemical conversion reaction, namely reduction of Fe^{3+} into Fe by the less noble Mg substrate (subsequent XRD results confirm this observation as discussed below). In the general survey 62.43 wt% iron was detected, with 25.73 wt% of O, 8.27 wt% of Mg, and 3.57 wt% of Cl. The small amount of chlorine is incorporated in the coating as a contamination from the reaction solution. The weight percentage of Mg at Spot 1 in **Figure 2A**, that is the rather flat area between the clusters, represents the highest value (12.34 wt%) compared with that of the whole area and that in Spot 2. In any case, the surface of the sample mostly consists of iron.

3.2 Crystal Structure of the Coatings

XRD measurements were conducted to characterize the crystal structure of the formed coatings. **Figure 3** shows the XRD patterns of pure Mg, pure Fe and the treated sample. All peaks in the pattern of the hybrid laminate appear in the exactly corresponding position to those of pure Mg and pure Fe substrates. Besides, a weak peak at approx. 60°, 2θ are assigned to $Mg(OH)_2$. XRD results therefore confirm that the layered composite coating is mainly composed of metallic Mg and Fe, and small amount of $Mg(OH)_2$, which is in good agreement with the EDX results.

The proposed formation mechanism of the particular structure shown in **Figure 2A** is schematically illustrated in **Figure 4**. The chemical reactions occurring during the dipping process are schematically shown to explain the mechanism. As Mg is less noble than Fe, metallic Fe can be formed on Mg from the Fe^{3+} ion containing solution. Therefore, upon immersion of pure Mg samples in $FeCl_3$ solution, the following chemical reactions take place:

$$3Mg + 2Fe^{3+} \rightarrow 2Fe + 3Mg^{2+}$$
$$Mg + 2H_2O \rightarrow Mg(OH)_2\downarrow + H_2\uparrow$$

The sites of Fe^{3+} ion reduction and deposition as metallic Fe coincide with the sites of metallic Mg oxidation into Mg^{2+} and its dissolution. Simultaneously, with the hydrolysis of water, H_2 is produced and OH^- released. Mg^{2+} can easily precipitate with OH^- as $Mg(OH)_2$, hence depositing on the surface as well.

After 2 weeks storage in air, the surface morphology and chemical composition of the prepared samples were observed again by SEM coupled with EDX, as shown in **Figure 5**. Compared with the fresh sample, a characteristic "pompon-like" structure is formed at the sites between clusters, for instance near Spot 3 and framed areas in **Figure 5A**. The framed areas are shown in magnification to reveal the nano scale features on the surface, showing the presence of nano needles or nano wires branching out in all directions from the center of the pompon. EDX analysis revealed that the locations of the pompons are primarily enriched with Mg (35.89 wt%) and O (57.98 wt%), but contain only traces of Fe (0.1 wt%), such as in Spot 3. Conversely, much less Mg (4.61 wt%) and O (4.04 wt%) are detected in other areas, such as in Spot 5, where the random disorganized clusters are observed, while 84.43 wt% Fe is discovered in this spot. As regards the chemical composition in

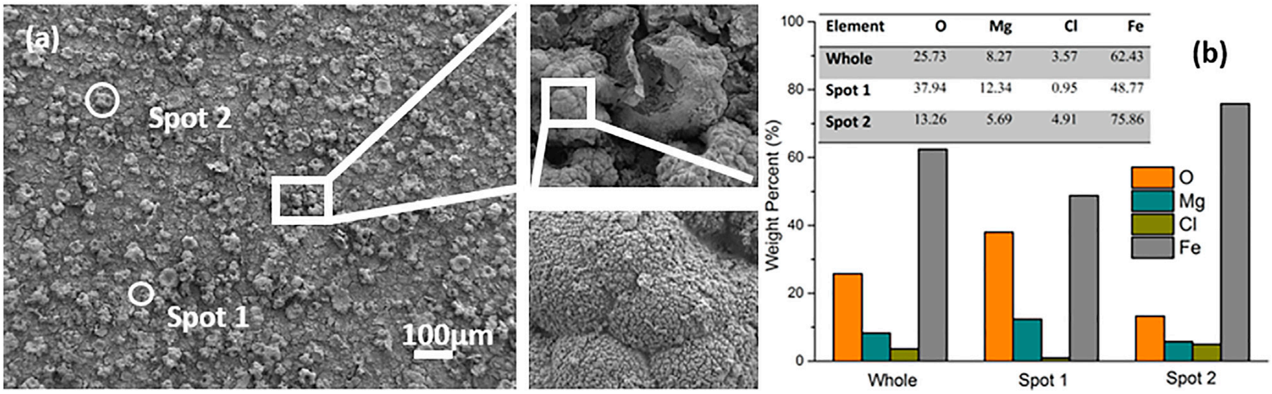

Element	O	Mg	Cl	Fe
Whole	25.73	8.27	3.57	62.43
Spot 1	37.94	12.34	0.95	48.77
Spot 2	13.26	5.69	4.91	75.86

FIGURE 2 | SEM images. **(A)** with EDX analysis **(B)** of a freshly prepared sample.

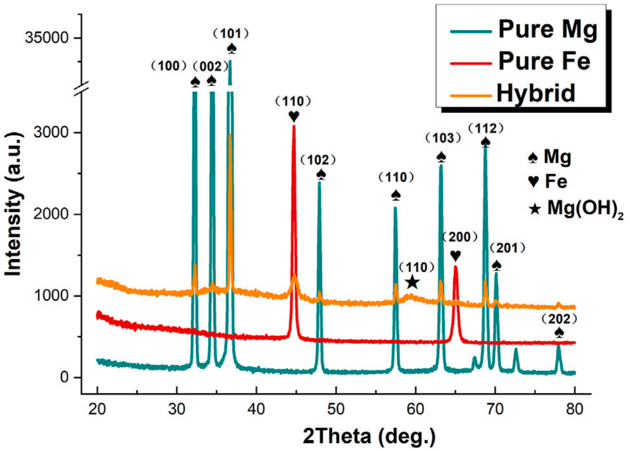

FIGURE 3 | X-ray diffraction patterns of pure Mg, pure Fe and the freshly prepared composite laminate.

Spot 4, the total weight percentage of Mg and O takes up more than 99% throughout the coating. In addition, many fine cracks are observed, which is a typical observation for conversion coatings on magnesium (Cui et al., 2012). Storage in air results in strongly increasing amounts of O and Mg on the whole surface, namely, from 25.73 wt% and 8.27 wt% in the fresh sample (in **Figure 2B**) up to 49.79 wt% and 37.32 wt% after lying in air (**Figure 5B**). Since Mg is more active than Fe under atmospheric conditions, galvanic corrosion has occurred between these two metals. As a result, Mg has been oxidized into pompon-like MgO/$Mg(OH)_2$ structures gradually forming on the whole surface, and metallic iron has remained unattacked. The process is schematically shown in **Figure 6**. Eventually, the resulting structure is a metallic Fe coating buried under a $Mg(OH)_2$ layer, as shown by the cross-sectional element mapping in **Figure 7**.

3.3 Cross-Section Morphology and Composition

For observing the morphology and element distribution from cross sections of the hybrid laminate after 2-week exposure to ambient air, SEM observations and EDX elemental mapping were carried out, as shown in **Figure 7**. The total thickness of the coating was determined to be approximately 19.4 µm. Elemental mapping of the cross-section revealed an uneven distribution of Mg, O, Fe, and Cl through the thickness of the coating. The top layer contains mainly Mg and O, this layer also shows cracks which are typical for MgO/$Mg(OH)_2$ surface layers. In addition,

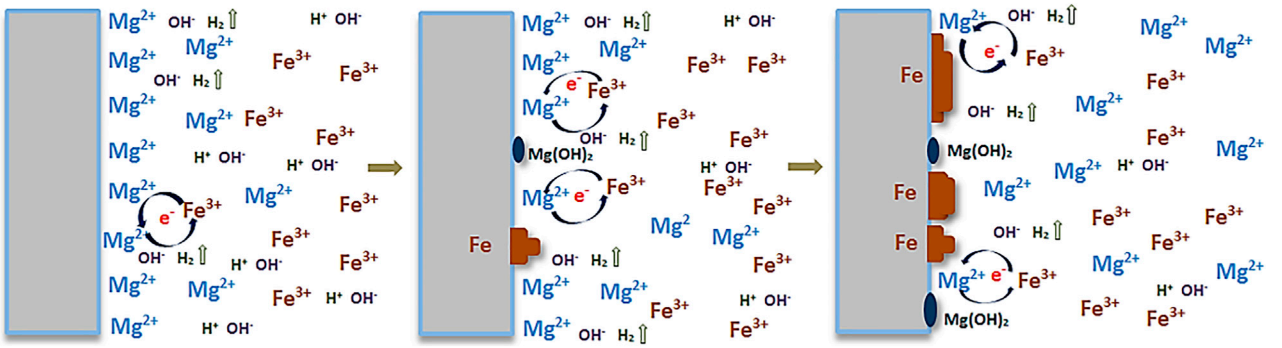

FIGURE 4 | Schematic illustration for the formation of the coating.

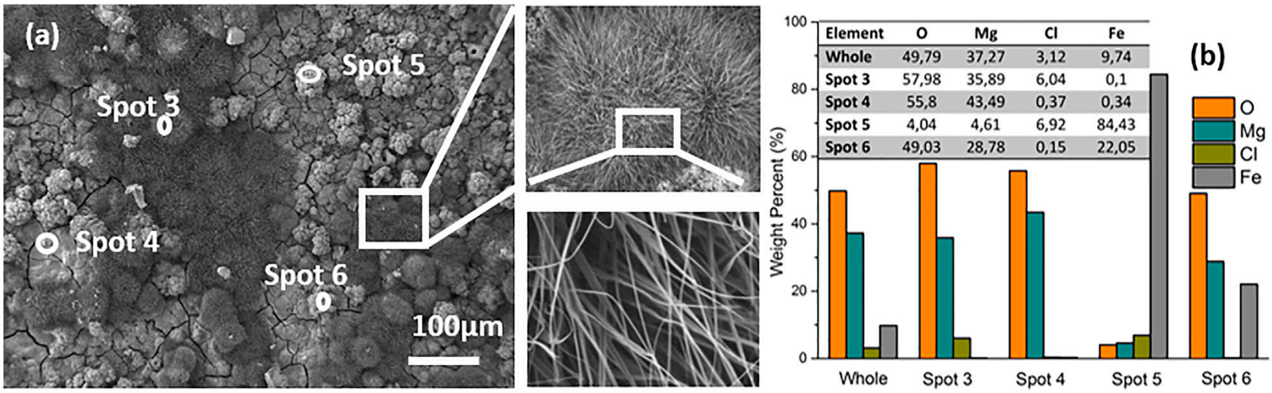

Element	O	Mg	Cl	Fe
Whole	49,79	37,27	3,12	9,74
Spot 3	57,98	35,89	6,04	0,1
Spot 4	55,8	43,49	0,37	0,34
Spot 5	4,04	4,61	6,92	84,43
Spot 6	49,03	28,78	0,15	22,05

FIGURE 5 | SEM images. **(A)** of the surface and EDX analysis. **(B)** of a sample after 2 weeks exposure to air.

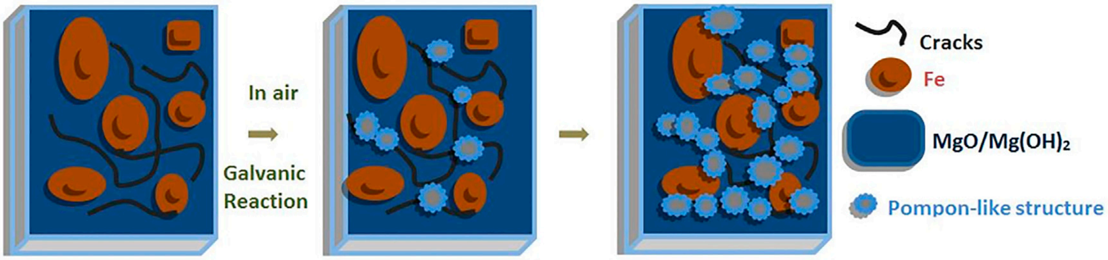

FIGURE 6 | Schematic illustration to represent the oxidation process on investigated samples.

the chlorine contamination is only present in the uppermost part of the surface layer. Interestingly, the Fe coating with a thickness of 1–2 µm is buried under the top $MgO/Mg(OH)_2$ layer, as suggested in the schematic diagram in **Figure 6**. Additional $MgO/Mg(OH)_2$ formation can be seen at sites of cracks through the top $MgO/Mg(OH)_2$ and the Fe layers.

3.4 Corrosion Behavior

3.4.1 OCP Measurements

To investigate the corrosion behavior of the new layered metals, long-term open-circuit potential (OCP) measurements were carried out in DMEM for the coated sample, as well as for pure Fe and pure Mg. The OCP variation as a function of time for the different samples is shown in **Figure 8**. Clearly, pure Mg and pure Fe samples reach a rather stable value around −1.75 V after 2500 s and −0.7 V after 4000 s, respectively, whereas the OCP of the coated sample fluctuated markedly between −0.2 V and −1.2 V during the first 8 h immersion time. However, interestingly, the OCP always recovered back to near −0.2 V every time after a sharp drop down to values close to −1.2 V. These oscillations in the OCP indicate breakdown events in the coating (sharp drop of OCP), followed by "self-healing" of the coating, for instance by precipitation of $Mg(OH)_2$ or other corrosion products blocking the sites of coating breakdown. Similar oscillations occurred again during the 27–35 h OCP observation, but the potential in this case recovers back to around -500mV and the fluctuation frequency is reduced compared with that during the first 0–8 h of immersion. After 46 h immersion in DMEM, OCP dropped down to around -1200mV and stayed stable in the following 4 h.

The "self-healing" effect in OCP curves mainly embodies the "pulling up" of the dropped OCP values to a much higher OCP level. It can be speculated that the pulling-up and dropping-down processes shown in OCP curves are strongly linked to the initiating and hindering of the galvanic reactions which are non-continuously happening between the magnesium substrate and the iron coating in DMEM. In the first 8 h of OCP measurement, the upper level of OCP curves was maintained at around −0.2 V. This upper level of OCP values was even less negative than that of pure iron, which stayed at around −0.7 V after 8 h tests. The reason behind this unique phenomenon might be the existence of iron oxides and other depositions in DMEM precipitating on the surface of the magnesium substrate. Meanwhile, galvanic reactions would be initiated at the defect sites where the magnesium substrate was not fully coated by metallic iron coatings and the deposited products. At this stage, the OCP curve demonstrates a sharp drop-down to a lower level, which reflects the proceeding of galvanic reactions. The galvanic reaction products, mainly composed of $Mg(OH)_2$ and other hydrated and carbonated (Mg,Ca)-phosphate (Wagener and Virtanen, 2016) formed near the micro-crack sites, would separate the connection between the magnesium substrate and the iron coating in the medium and impeding the galvanic reaction process. The prevailed "OFF" mode of the galvanic reaction induces the "self-healing" effect in OCP curves and the

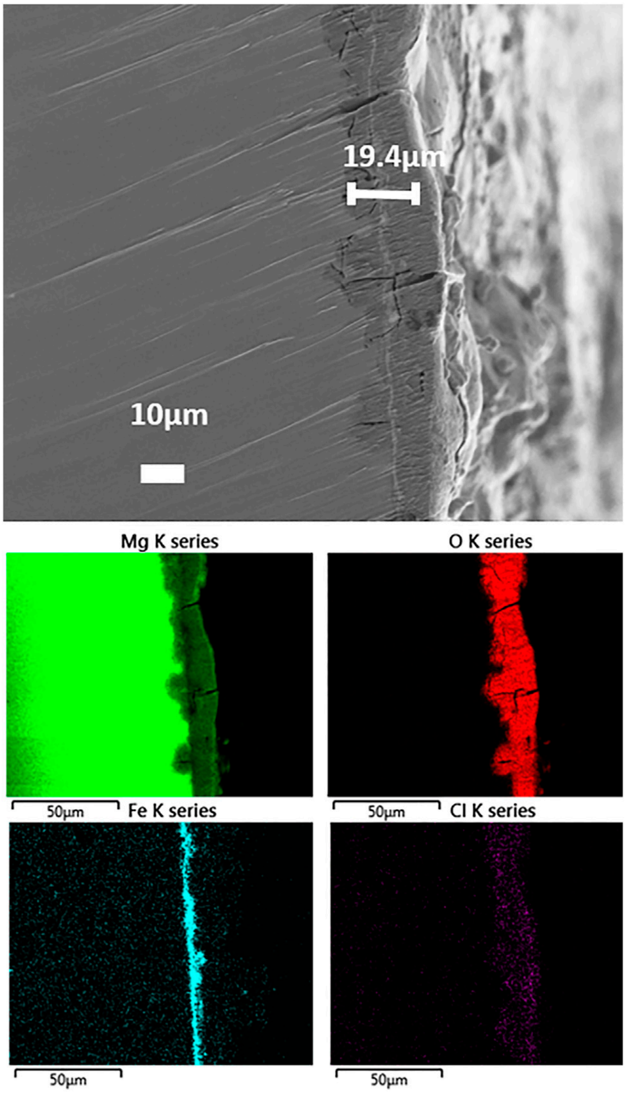

FIGURE 7 | SEM images and EDX mapping of the cross-section of the hybrid laminate after 2 weeks exposure to air.

occasional "ON" mode of the galvanic reaction leads to the lower OCP level. The similar case can also be found in the curves of 27–35 h OCP, only the sharp potential dropping-down times and upper level of OCP decrease. The pH variation curve during the first 6 h of immersion and the potentiodynamic polarization curves of samples are displayed in the Supporting Information part.

In order to investigate changes in the morphology during the long-term OCP immersion experiment, samples were observed after 8 h (in **Figures 9A,B**) and 50 h (in **Figures 9C,D**) OCP monitoring in DMEM. As shown in **Figure 9A**, randomly distributed clusters are still displayed on the whole surface after 8 h OCP measurement. In the magnified images, many precipitates deposited on the surface can be observed. A typical magnesium conversion coating morphology with cracks is observed after 50 h OCP monitoring in **Figure 9C**. Protuberances, such as in Spot 11, could be seen on the separated pieces of the cracked coating in high magnification images in **Figure 9C**. The results in **Figure 9B,D** show the coating composition in overview for the whole surface and for three different sites. Since the depositions formed on the top surface, EDX data in **Figures 9B,D** shows a nearly 50% reduced iron signals as compared with a fresh sample (in **Figure 2B**). On the other hand, the O content increased significantly from 25.73 wt% in **Figure 2B** to about 50 wt% in **Figures 9B,D**. With longer immersion time in DMEM, the weight percentage of Mg increased from ca. 10 wt % at 8 h up to 30 wt% at 50 h. The growing amount of O and Mg coincides with the formation of the typical cracked coating, as observed in **Figure 9C**.

Compounds containing Na, P, K, and Ca are incorporated in the surface layer and stem from the DMEM solution, which was employed as electrolyte for the OCP measurements. Overall, the levels of Na, P, K and Ca decrease from the values at 8 h in **Figure 9B** to the values at 50 h in **Figure 9D**. The decreasing trend might be due to the fact that the compounds containing such elements are buried by the subsequently formed $Mg(OH)_2$ on top.

3.4.2 Micromorphology and Composition After Electrochemical Measurements

To demonstrate the coating behavior under a highly accelerated corrosion scenario, the coated samples were polarized up to +1 V (this condition does not correspond to a normal corrosion scenario of Mg alloys, but the experiment was carried out to indicate a worst-case behavior). Corrosion products after the electrochemical measurement were examined by SEM along with EDX to determine the morphology and chemical composition. As shown in **Figure 10A**, the coating is still present on the surface, exhibiting some large clusters of compact precipitates. The tiny cracks spread between or through the clusters on the rough surface. The chemical composition of the corrosion products was analyzed by EDX. The results in **Figure 10** 2) show the composition in overview for the whole surface and for three different sites. For the overview, strong signals for Fe (54.53 wt%) and O (34.17 wt%) are observed, with some Ca (5.17%) and minor amounts of Mg, Na, Cl, P and K (in total 5 wt%). A similar case for element distribution is found at Spot 13 and Spot 14 in **Figure 10B**. The Fe content in Spot 12 (73.69 wt%)

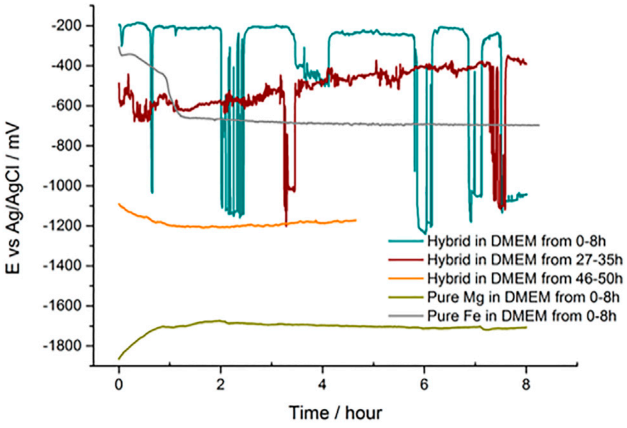

FIGURE 8 | Open-circuit potential as a function of immersion time in DMEM.

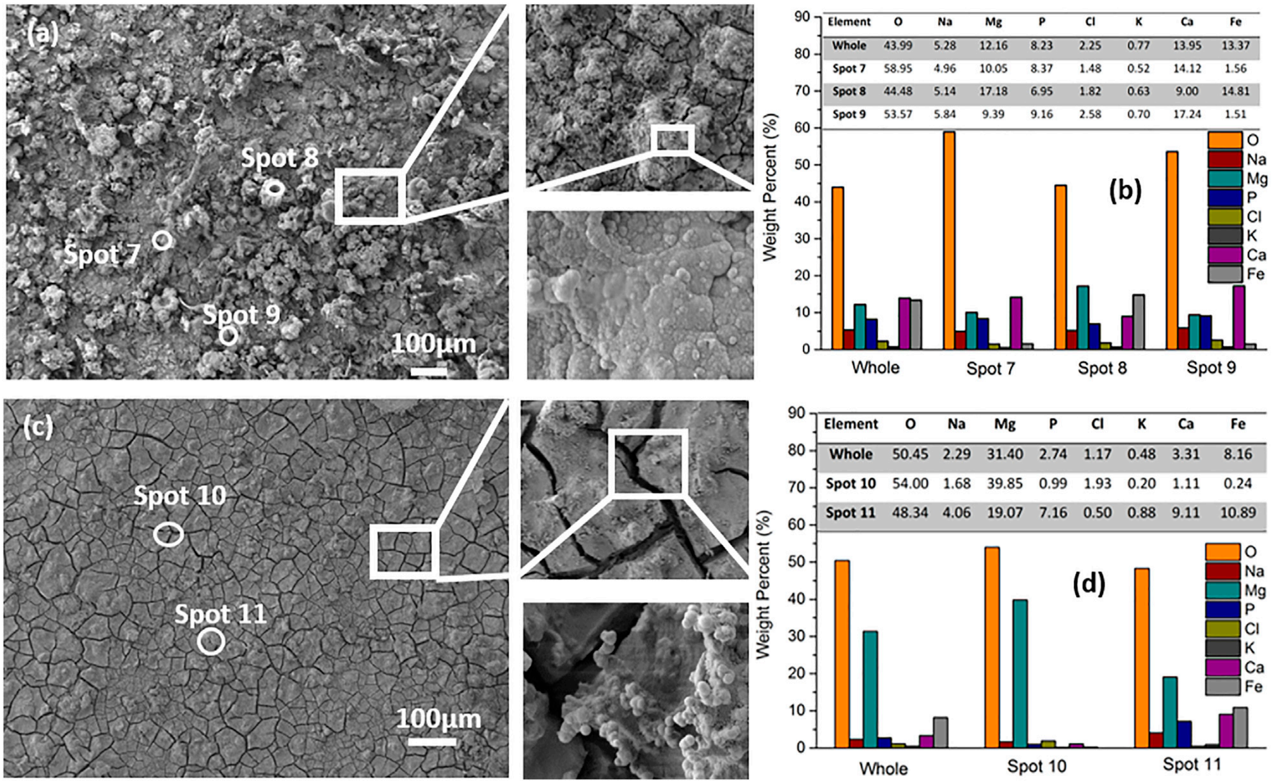

Element	O	Na	Mg	P	Cl	K	Ca	Fe
Whole	43.99	5.28	12.16	8.23	2.25	0.77	13.95	13.37
Spot 7	58.95	4.96	10.05	8.37	1.48	0.52	14.12	1.56
Spot 8	44.48	5.14	17.18	6.95	1.82	0.63	9.00	14.81
Spot 9	53.57	5.84	9.39	9.16	2.58	0.70	17.24	1.51

Element	O	Na	Mg	P	Cl	K	Ca	Fe
Whole	50.45	2.29	31.40	2.74	1.17	0.48	3.31	8.16
Spot 10	54.00	1.68	39.85	0.99	1.93	0.20	1.11	0.24
Spot 11	48.34	4.06	19.07	7.16	0.50	0.88	9.11	10.89

FIGURE 9 | SEM images with EDX analysis of the hybrid layers after 8 h **(A,B)** and 50 h **(C,D)** OCP monitoring in DMEM.

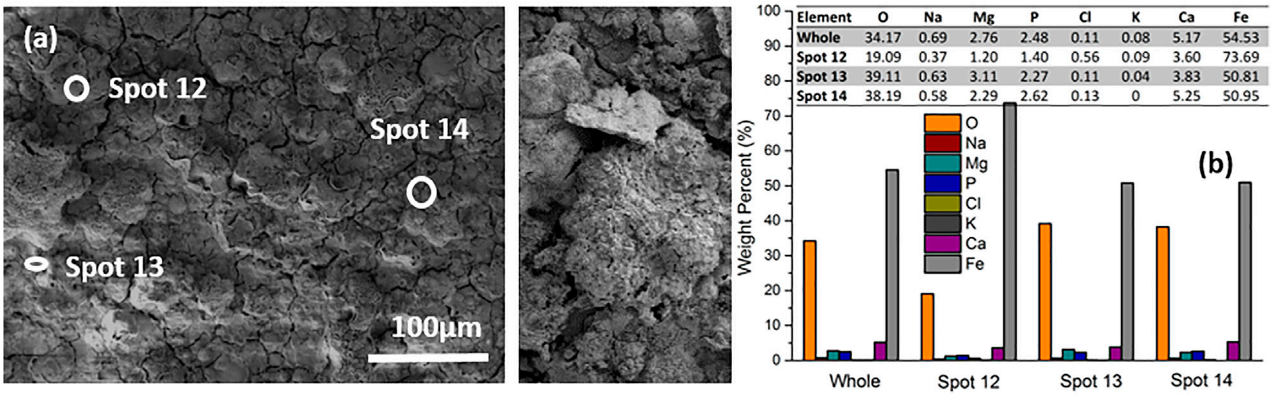

Element	O	Na	Mg	P	Cl	K	Ca	Fe
Whole	34.17	0.69	2.76	2.48	0.11	0.08	5.17	54.53
Spot 12	19.09	0.37	1.20	1.40	0.56	0.09	3.60	73.69
Spot 13	39.11	0.63	3.11	2.27	0.11	0.04	3.83	50.81
Spot 14	38.19	0.58	2.29	2.62	0.13	0	5.25	50.95

FIGURE 10 | SEM image **(A)** and EDX result **(B)** of the surface morphology of hybrid laminate after electrochemical tests.

is even higher than in the whole surface. The comparable presence of Fe and the significant decreased Mg content after the electrochemical measurement as compared with the average amount present in the fresh treated samples (see **Figure 2B**) may be attributed to the unstable MgO or $Mg(OH)_2$ and other components in the top layer that have dissolved during the testing period in DMEM, exposing the underlying Fe compact coating, as shown in **Figure 10A**. Noteworthy is that the Fe coating has not been destroyed by polarization up to + 1 V in DMEM. The Fe coating will work as a barrier against the penetration of external corrosive ions onto the magnesium substrate. Furthermore, the weight percentage ratio of oxygen to iron in the fresh sample (**Figure 2**) and after electrochemical tests (**Figure 10**) increases approximately from 1:3 to 1:2, revealing partial oxidation of the metallic iron.

4 CONCLUSION AND OUTLOOK

A simple, single-step dip coating process was used to fabricate a layered composite coating composed of metallic Fe and $Mg(OH)_2$

on a Mg substrate. A metallic Fe coating with a thickness of 1–2 μm is formed between the Mg substrate and a $Mg(OH)_2$/MgO top layer. Under immersion conditions in DMEM, the open-circuit potential of the coated samples shows large oscillations, indicating local breakdown events followed by a self-healing behavior of the coated samples.

The simple coating process developed here; based on spontaneous electrochemical reactions, combined with the self-healing nature of the composite coating, represent a promising approach for tackling the challenge of controlling the corrosion rate of both Mg and Fe. Further research will focus on attempting to increase the thickness of the coatings and decrease the presence of cracks in the coatings, as well as on further elucidation of the degradation mechanisms and the origin of the self-healing property of the coatings.

DATA AVAILABILITY STATEMENT

The original contributions presented in the study are included in the article/**Supplementary Material**, further inquiries can be directed to the corresponding author.

AUTHOR CONTRIBUTIONS

YY, SV, and AB have substantial contributions to the conception and design of the work. YY collected, analyzed, and interpretation of data for the work. XC, GJ, and PS organized the structure of the manuscript. ZS and YL were responsible for the experiments of pH variation and potentiodynamic polarization during the revision period. All authors contributed to manuscript revision, read, and approved the submitted version.

FUNDING

YY would like to acknowledge China Postdoctoral Science Foundation (No. 3236310536), Heilongjiang Postdoctoral Science Foundation (No. 002100830603), and Fundamental Research Funds for the Central Universities (No. 3072021CF1005).

ACKNOWLEDGMENTS

The authors would like to thank Lei Wang (Chair for Surface Science and Corrosion) and Martin Weiser (Chair for Surface Science and Corrosion) from University of Erlangen-Nuremberg, Germany, for XRD and cross-section experimental supports.

SUPPLEMENTARY MATERIAL

The Supplementary Material for this article can be found online at: https://www.frontiersin.org/articles/10.3389/fmats.2021.786650/full#supplementary-material

REFERENCES

Abdi-Alghanab, K., Seifzadeh, D., Rajabalizadeh, Z., and Habibi-Yangjeh, A. (2020). High Corrosion Protection Performance of the LDH/Ni-P Composite Coating on AM60B Magnesium Alloy. *Surf. Coat. Technol.* 397, 125979. doi:10.1016/j.surfcoat.2020.125979

Abou Neel, E. a., Ahmed, I., Blaker, J. J., Bismarck, a., Boccaccini, a. R., Lewis, M. P., et al. (2005). Effect of Iron on the Surface, Degradation and Ion Release Properties of Phosphate-Based Glass Fibres. *Acta Biomater.* 1 (5), 553–563. doi:10.1016/j.actbio.2005.05.001

Akhter, R., Bendavid, A., and Munroe, P. (2022). Effect of Ni Content on the Microstructure and Mechanical Properties of TiNiN Coatings. *Appl. Surf. Sci.* 573, 151536. doi:10.1016/j.apsusc.2021.151536

Chen, J., Wiley, B., Li, Z.-Y., Campbell, D., Saeki, F., Cang, H., et al. (2005). Gold Nanocages: Engineering Their Structure for Biomedical Applications. *Adv. Mater.* 17 (18), 2255–2261. doi:10.1002/adma.200500833View/save

Chen, Y., Wu, L., Yao, W., Zhong, Z., Chen, Y., Wu, J., et al. (2021). One-Step *In Situ* Synthesis of Graphene Oxide/MgAl-Layered Double Hydroxide Coating on a Micro-arc Oxidation Coating for Enhanced Corrosion Protection of Magnesium Alloys. *Surf. Coat. Technol.* 413, 127083. doi:10.1016/j.surfcoat.2021.127083

Costantino, M. D., Schuster, A., Helmholz, H., Meyer-Rachner, A., Willumeit-Römer, R., and Luthringer-Feyerabend, B. J. C. (2020). Inflammatory Response to Magnesium-Based Biodegradable Implant Materials. *Acta Biomater.* 101, 598–608. doi:10.1016/j.actbio.2019.10.014

Cui, X., Jin, G., Yang, Y., Liu, E., Lin, L., and Zhong, J. (2012). The Formation of Neodymium Conversion Coating and the Influence of Post-Treatment. *Appl. Surf. Sci.* 258 (7), 3249–3254. doi:10.1016/j.apsusc.2011.11.073

Dayani, S. B., Shaha, S. K., Ghelichi, R., Wang, J. F., and Jahed, H. (2018). The Impact of AA7075 Cold Spray Coating on the Fatigue Life of AZ31B Cast Alloy. *Surf. Coat. Technol.* 337, 150–158. doi:10.1016/J.SURFCOAT.2018.01.008

Ducheyne, P., and Healy, K. E. (1988). The Effect of Plasma-Sprayed Calcium Phosphate Ceramic Coatings on the Metal Ion Release from Porous Titanium and Cobalt-Chromium Alloys. *J. Biomed. Mater. Res.* 22 (12), 1137–1163. doi:10.1002/jbm.820221207

Ferrández-Montero, A., Lieblich, M., González-Carrasco, J. L., Benavente, R., Lorenzo, V., Detsch, R., et al. (2019). Development of Biocompatible and Fully Bioabsorbable PLA/Mg Films for Tissue Regeneration Applications. *Acta Biomater.* 98, 114–124. doi:10.1016/J.ACTBIO.2019.05.026

Fischerauer, S. F., Kraus, T., Wu, X., Tangl, S., Sorantin, E., Hänzi, a. C., et al. (2013). *In Vivo* Degradation Performance of Micro-arc-oxidized Magnesium Implants: A Micro-CT Study in Rats. *Acta Biomater.* 9 (2), 5411–5420. doi:10.1016/j.actbio.2012.09.017

Francis, A., Yang, Y., Virtanen, S., and Boccaccini, A. R. (2015). Iron and Iron-Based Alloys for Temporary Cardiovascular Applications. *J. Mater. Sci. Mater. Med.* 26, 138. doi:10.1007/s10856-015-5473-8

Gorejová, R., Haverová, L., Oriňaková, R., Oriňak, A., and Oriňak, M. (2019). Recent Advancements in Fe-Based Biodegradable Materials for Bone Repair. *J. Mater. Sci.* 54 (3), 1913–1947. doi:10.1007/s10853-018-3011-z

Helary, G., Noirclere, F., Mayingi, J., and Migonney, V. (2009). A New Approach to Graft Bioactive Polymer on Titanium Implants: Improvement of MG 63 Cell Differentiation onto This Coating. *Acta Biomater.* 5 (1), 124–133. doi:10.1016/j.actbio.2008.07.037

Hornberger, H., Virtanen, S., and Boccaccini, A. R. (2012). Biomedical Coatings on Magnesium Alloys - A Review. *Acta Biomater.* 8 (7), 2442–2455. doi:10.1016/j.actbio.2012.04.012

Huang, H.-L., Chang, Y.-Y., Lai, M.-C., Lin, C.-R., Lai, C.-H., and Shieh, T.-M. (2010). Antibacterial TaN-Ag Coatings on Titanium Dental Implants. *Surf. Coat. Technology* 205 (5), 1636–1641. doi:10.1016/j.surfcoat.2010.07.096

Jin, G., Qin, H., Cao, H., Qiao, Y., Zhao, Y., Peng, X., et al. (2015). Zn/Ag Micro-galvanic Couples Formed on Titanium and Osseointegration Effects in the Presence of S. Aureus. *Biomaterials* 65, 22–31. doi:10.1016/j.biomaterials.2015.06.040

Kereiakes, D. J., Cox, D. A., Hermiller, J. B., Midei, M. G., Bachinsky, W. B., Nukta, E. D., et al. (2003). Usefulness of a Cobalt Chromium Coronary Stent Alloy. *Am. J. Cardiol.* 92 (4), 463–466. doi:10.1016/S0002-9149(03)00669-6

Lee, M. K., Lee, H., Park, C., Kang, I. G., Kim, J., Kim, H. E., et al. (2021). Accelerated Biodegradation of Iron-Based Implants via Tantalum-Implanted Surface Nanostructures. *Bioact. Mater.* 9, 239–250. doi:10.1016/j.bioactmat.2021.07.003

Li, C., Guo, C., Fitzpatrick, V., Ibrahim, A., Zwierstra, M. J., Hanna, P., et al. (2019). Design of Biodegradable, Implantable Devices towards Clinical Translation. *Nat. Rev. Mater.* 5, 61–81. doi:10.1038/s41578-019-0150-z

Lin, T. J., Sheu, H. H., Lee, C. Y., and Lee, H. Bin. (2021). The Study of Mechanical Properties and Corrosion Behavior of the Fe-Based Amorphous Alloy Coatings Using High Velocity Oxygen Fuel Spraying. *J. Alloys Compd.* 867, 159132. doi:10.1016/j.jallcom.2021.159132

Liu, X. Q., Zheng, Y. G., Chang, X. C., Hou, W. L., Wang, J. Q., Tang, Z., et al. (2009). Microstructure and Properties of Fe-Based Amorphous Metallic Coating Produced by High Velocity Axial Plasma Spraying. *J. Alloys Compd.* 484 (1–2), 300–307. doi:10.1016/j.jallcom.2009.04.086

Livsey, C. (1981). Apparatus for Application of Metallic Coatings to Metallic Substrates. *Patent* 4, 300474.

Lourenço, M. L., Cardoso, G. C., Sousa, K. d. S. J., Donato, T. A. G., Pontes, F. M. L., and Grandini, C. R. (2020). Development of Novel Ti-Mo-Mn Alloys for Biomedical Applications. *Sci. Rep.* 10 (1), 1–8. doi:10.1038/s41598-020-62865-4

Mao, L., shen, L., Chen, J., Zhang, X., Kwak, M., Wu, Y., et al. (2017). A Promising Biodegradable Magnesium Alloy Suitable for Clinical Vascular Stent Application. *Sci. Rep.* 7 (1), 46343. doi:10.1038/srep46343

Miyazaki, T., Kim, H.-M., Miyaji, F., Kokubo, T., Kato, H., and Nakamura, T. (2000). Bioactive Tantalum Metal Prepared by NaOH Treatment. *J. Biomed. Mater. Res.* 50 (1), 35–42. doi:10.1002/(sici)1097-4636(200004)50:1<35:aid-jbm6>3.0.co;2-8

M. Niinomi, T. Narushima, and M. Nakai (Editors) (2015). *Advances in Metallic Biomaterials; Springer Series in Biomaterials Science and Engineering* (New York, United States: Springer). doi:10.1007/978-3-662-46842-5

Moravej, M., Purnama, a., Fiset, M., Couet, J., and Mantovani, D. (2010). Electroformed Pure Iron as a New Biomaterial for Degradable Stents: *In Vitro* Degradation and Preliminary Cell Viability Studies. *Acta Biomater.* 6 (5), 1843–1851. doi:10.1016/j.actbio.2010.01.008

Nezamdoust, S., and Seifzadeh, D. (2017). Application of CeH–V/Sol–Gel Composite Coating for Corrosion Protection of AM60B Magnesium Alloy. *Trans. Nonferrous Met. Soc. China (English Ed.* 27 (2), 352–362. doi:10.1016/S1003-6326(17)60039-6

Nezamdoust, S., Seifzadeh, D., and Rajabalizadeh, Z. (2019). Application of Novel Sol–Gel Composites on Magnesium Alloy. *J. Magnes. Alloy.* 7 (3), 419–432. doi:10.1016/j.jma.2019.03.004

Niinomi, M., Nakai, M., and Hieda, J. (2012). Development of New Metallic Alloys for Biomedical Applications. *Acta Biomater.* 8 (11), 3888–3903. doi:10.1016/j.actbio.2012.06.037

O'Brien, W. (1997). *Dental Materials and Their Selection*. Chicago: Quintessence.

Ouyang, Y., Li, L. X., Xie, Z. H., Tang, L., Wang, F., and Zhong, C. J. (2020). A Self-Healing Coating Based on Facile PH-Responsive Nanocontainers for Corrosion Protection of Magnesium Alloy. *J. Magnes. Alloy.* doi:10.1016/j.jma.2020.11.007

Patnaik, L., Ranjan Maity, S., and Kumar, S. (2020). Status of Nickel Free Stainless Steel in Biomedical Field: A Review of Last 10 Years and what Else Can Be Done. *Mater. Today Proc.* 26, 638–643. doi:10.1016/j.matpr.2019.12.205

Que, L., and Topoleski, L. D. T. (2000). Third-Body Wear of Cobalt-Chromium-Molybdenum Implant Alloys Initiated by Bone and Poly(Methyl Methacrylate) Particles. *J. Biomed. Mater. Res.* 50 (3), 322–330. doi:10.1002/(sici)1097-4636(20000605)50:3<322:aid-jbm5>3.0.co;2-u

Rajabalizadeh, Z., and Seifzadeh, D. (2014). The Effect of Copper Ion on Microstructure, Plating Rate and Anticorrosive Performance of Electroless Ni-P Coating on AZ61 Magnesium Alloy. *Prot. Met. Phys. Chem. Surf.* 50 (4), 516–523. doi:10.1134/S2070205114040157

Rodriguez-Contreras, A., Moruno, C. M., Fernandez-Fairen, M., Rupérez, E., Gil, F. J., and Manero, J. M. (2021). "Other Metallic Alloys: Tantalum-Based Materials for Biomedical Applications," in *Structural Biomaterials* (Amsterdam, Netherlands: Elsevier), 229–273. doi:10.1016/b978-0-12-818831-6.00007-0

Schinhammer, M., Steiger, P., Moszner, F., Löffler, J. F., and Uggowitzer, P. J. (2013). Degradation Performance of Biodegradable Fe-Mn-C(-Pd) Alloys. *Mater. Sci. Eng. C. Mater. Biol. Appl.* 33 (4), 1882–1893. doi:10.1016/j.msec.2012.10.013

Seifzadeh, D., and Farhoudi, L. (2016). Electroless Co-P Plating on Magnesium Alloy and its Anti-corrosion Properties. *Surf. Eng.* 32 (5), 348–355. doi:10.1179/1743294415Y.0000000034

Shih, C.-C., Shih, C.-M., Su, Y.-Y., Su, L. H. J., Chang, M.-S., and Lin, S.-J. (2004). Effect of Surface Oxide Properties on Corrosion Resistance of 316L Stainless Steel for Biomedical Applications. *Corrosion Sci.* 46 (2), 427–441. doi:10.1016/S0010-938X(03)00148-3

Shimko, D. A., Shimko, V. F., Sander, E. A., Dickson, K. F., and Nauman, E. A. (2005). Effect of Porosity on the Fluid Flow Characteristics and Mechanical Properties of Tantalum Scaffolds. *J. Biomed. Mater. Res.* 73B (2), 315–324. doi:10.1002/jbm.b.30229

Tan, Q., Ji, J., Barbosa, M. A., Fonseca, C., and Shen, J. (2003). Constructing Thromboresistant Surface on Biomedical Stainless Steel via Layer-By-Layer Deposition Anticoagulant. *Biomaterials* 24 (25), 4699–4705. doi:10.1016/S0142-9612(03)00363-6

Wagener, V., and Virtanen, S. (2016). Protective Layer Formation on Magnesium in Cell Culture Medium. *Mater. Sci. Eng. C* 63, 341–351. doi:10.1016/j.msec.2016.03.003

Watanabe, K., Fukuzaki, S., Sugino, A., Benson, N., Metcalf, N., Nakamura, M., et al. (2021). Cobalt-Chromium Alloy Has Superior Antibacterial Effect Than Titanium Alloy. *Spine (Phila. Pa. 1976)* 46 (17), E911–E915. doi:10.1097/BRS.0000000000003970

Wu, Y., He, G., Zhang, Y., Liu, Y., Li, M., Wang, X., et al. (2016). Unique Antitumor Property of the Mg-Ca-Sr Alloys with Addition of Zn. *Nat. Publ. Gr.* 6, 21736. doi:10.1038/srep21736

Yan, C., and Xue, D. (2006). General, Spontaneous Ion Replacement Reaction for the Synthesis of Micro- and Nanostructured Metal Oxides. *J. Phys. Chem. B* 110 (4), 1581–1586. doi:10.1021/jp056373+

Yang, Y., Zhou, J., Detsch, R., Virtanen, S., Taccardi, N., Heise, S., et al. (2018). Biodegradable Nanostructures: Degradation Process and Biocompatibility of Iron Oxide Nanostructured Arrays. *Mater. Sci. Eng. C* 85 (October 2017), 203–213. doi:10.1016/j.msec.2017.12.021

Zhang, C., Lin, J., and Liu, H. (2018). Magnesium-Based Biodegradable Materials for Biomedical Applications. *MRS Adv.* 3 (40), 2359–2364. doi:10.1557/adv.2018.488

Zhang, E., Chen, H., and Shen, F. (2010). Biocorrosion Properties and Blood and Cell Compatibility of Pure Iron as a Biodegradable Biomaterial. *J. Mater. Sci. Mater. Med.* 21 (7), 2151–2163. doi:10.1007/s10856-010-4070-0

Zhou, Y.-L., Niinomi, M., Akahori, T., Nakai, M., and Fukui, H. (2007). Comparison of Various Properties between Titanium-Tantalum Alloy and Pure Titanium for Biomedical Applications. *Mater. Trans.* 48 (3), 380–384. doi:10.2320/matertrans.48.380

Zhu, J., Zhang, X., Niu, J., Shi, Y., Zhu, Z., Dai, D., et al. (2021). Biosafety and Efficacy Evaluation of a Biodegradable Magnesium-Based Drug-Eluting Stent in Porcine Coronary Artery. *Sci. Rep.* 11 (1), 1–12. doi:10.1038/s41598-021-86803-0

Conflict of Interest: The authors declare that the research was conducted in the absence of any commercial or financial relationships that could be construed as a potential conflict of interest.

frontiers | Frontiers in Bioengineering and Biotechnology

ORIGINAL RESEARCH
published: 08 June 2022
doi: 10.3389/fbioe.2022.910475

Pore Strategy Design of a Novel NiTi-Nb Biomedical Porous Scaffold Based on a Triply Periodic Minimal Surface

Yuting Lv[1,2]*, Guohao Liu*[1]*, Binghao Wang*[1]*, Yujin Tang*[3]**, Zhengjie Lin*[4]*, Jia Liu*[3]**,*
Guijiang Wei[2,3] *and Liqiang Wang*[2]***

[1]College of Mechanical and Electronic Engineering, Shandong University of Science and Technology, Qingdao, China, [2]State Key Laboratory of Metal Matrix Composites, Shanghai Jiao Tong University, Shanghai, China, [3]Affiliated Hospital of Youjiang Medical University for Nationalities, Baise, China, [4]3D Printing Clinical Translational and Regenerative Medicine Center, Shenzhen Shekou People's Hospital, Shenzhen, China

The pore strategy is one of the important factors affecting the biomedical porous scaffold at the same porosity. In this work, porous scaffolds were designed based on the triply periodic minimal surface (TPMS) structure under the same porosity and different pore strategies (pore size and size continuous gradient distribution) and were successfully prepared using a novel $Ni_{46.5}Ti_{44.5}Nb_9$ alloy and selective laser melting (SLM) technology. After that, the effects of the pore strategies on the microstructure, mechanical properties, and permeability of porous scaffolds were systematically investigated. The results showed that the $Ni_{46.5}Ti_{44.5}Nb_9$ scaffolds have a low elastic modulus (0.80–1.05 GPa) and a high ductility (15.3–19.1%) compared with previous works. The pore size has little effect on their mechanical properties, but increasing the pore size significantly improves the permeability due to the decrease in specific surfaces. The continuous gradient distribution of the pore size changes the material distribution of the scaffold, and the smaller porosity structure has a better load-bearing capacity and contributes primarily to the high compression strength. The local high porosity structure bears more fluid flow, which can improve the permeability of the overall scaffold. This work can provide theoretical guidance for the design of porous scaffolds.

Keywords: additive manufacturing, triply periodic minimal surfaces, NiTi-Nb, porous scaffolds, pore strategy

Edited by:
Roman Surmenev,
Tomsk Polytechnic University, Russia

Reviewed by:
Xu Song,
The Chinese University of Hong Kong, China
Qiang Wang,
China Medical University, China

***Correspondence:**
Yujin Tang
tangyujin196709@163.com
Jia Liu
liujia0111@live.cn
Liqiang Wang
wang_liqiang@sjtu.edu.cn

Specialty section:
This article was submitted to Biomaterials,
a section of the journal Frontiers in Bioengineering and Biotechnology

Received: *01 April 2022*
Accepted: *06 May 2022*
Published: *08 June 2022*

Citation:
Lv Y, Liu G, Wang B, Tang Y, Lin Z, Liu J, Wei G and Wang L (2022) Pore Strategy Design of a Novel NiTi-Nb Biomedical Porous Scaffold Based on a Triply Periodic Minimal Surface. Front. Bioeng. Biotechnol. 10:910475. doi: 10.3389/fbioe.2022.910475

INTRODUCTION

Biomedical metal materials are one of the ideal materials for treating bone defects because of their high strength, corrosion resistance, and biocompatibility (Wang et al., 2020; Guo et al., 2022), but the solid metal material has a much higher elastic modulus than that of human bone, easily resulting in "stress shielding" and degradation of the bone tissue around the implant (Geetha et al., 2009). The porous scaffolds can be used to replace the solid materials, which can not only reduce the elastic modulus but can also promote cell adhesion and the growth of bone tissue (Chen et al., 2020; Mao et al., 2022). The traditional processing methods are difficult to achieve the preparation of complex porous structures, limiting the development of metal porous scaffolds. The development of additive manufacturing technology provides a solution for the preparation of complex porous structures. Additive manufacturing can both personalize bone scaffolds with precise dimensions to match the shape of the bone defect and precisely control their porosity, pore size, and distribution (Wang et al., 2020). Therefore, additive manufacturing of metal porous scaffolds has great potential in the field of bone defect treatment.

The structure design of porous scaffolds is one of the focuses of scientists in various countries. Previous studies have mainly focused on lattice structures based on the CAD method and topology optimization (Wang et al., 2016; Wang et al., 2019). The common types of lattice structural units are the diamond structure (Zhang et al., 2018; Cutolo et al., 2020; Li et al., 2020), body-centered cubic (BCC) structure (Arabnejad et al., 2016; Li et al., 2019), and dodecahedral structure (Liu et al., 2017; Guo et al., 2020). However, the lattice structures have an uneven transition of structural units, stress concentration, and difficult parametric design, which makes it difficult to meet the requirements of high-performance porous scaffolds (Giannitelli et al., 2014). Triply periodic minimal surfaces (TPMSs) are surfaces with the periodic distribution of zero mean curvature in three-dimensional space (Yuan et al., 2019). Zhang et al. (2020) designed a Ti6Al4V scaffold with a single directional gradient variation by changing the minimal surface equation and found that the scaffold had good mechanical properties and permeability matching those of natural bone tissue. Previous investigations have indicated that the minimal surface method has significant advantages in improving the mechanical properties and parametric design of scaffolds (Lv et al., 2021).

The human bone has a porous structure, and the different areas have various pore sizes and size distribution (Onal et al., 2018). The porous scaffold prepared by different pore strategies can be used to simulate human bone pore size features. Ran et al. (2018) found that the mechanical properties of the scaffolds decreased with the increase in the pore size and porosity, and the small pore was favorable for cell adhesion, and the large pore was favorable for cell proliferation; when the pore size was 600 μm, the scaffolds showed the optimal bone tissue growing-in ability. Therefore, from the present investigations, increasing the pore size or porosity can match the biomechanical properties of bone tissue and improve the biological properties of the scaffold (Ouyang et al., 2019). Under the same porosity, the pore strategy is the main factor affecting the mechanical properties and permeability of porous scaffolds, which includes pore size and pore size distribution. However, as far as we know, the effect of pore strategy based on the triply periodic minimal surface structure on the mechanical properties and permeability of porous scaffolds has rarely been mentioned.

NiTi system alloy has superelasticity, shape-memory function, good biocompatibility, and corrosion resistance; thus it is a good functional biomedical material (Habijan et al., 2012; Li et al., 2014). However, the Ni_4Ti_3 second phase in the NiTi alloy reduces the toughness and ductility of the alloy, so it is necessary to introduce a high strength second phase to improve the mechanical properties. It is well-known that Nb is a typical wide hysteresis phase transformation element and also has good biocompatibility. Therefore, the addition of Nb can not only change the microstructures (Lin et al., 2013; Gu et al., 2019) but can also improve the biocompatibility of NiTi alloy (Guo et al., 2021). The research on the additive manufactured NiTi-Nb alloy is still in the initial stage, and it is mainly prepared as a bulk alloy. Liu et al. (2020) prepared NiTi-Nb eutectic bulk alloy by additive manufacturing and found that Nb particles could accelerate the eutectic phase transition and the precipitation of the β-Nb phase, which improved the mechanical properties of the scaffold. However, the study of additive manufacturing of NiTi-Nb porous scaffolds has not been reported.

Therefore, in this work, the porous scaffolds were designed and simulated by human bone pore size features based on minimal surface structures under the same porosity and different pore strategies, including uniform scaffolds with different pore sizes and scaffolds with continuous gradient distribution of pore sizes. The porous scaffolds were successfully prepared using a novel $Ni_{46.5}Ti_{44.5}Nb_9$ alloy and selective laser melting (SLM) technology, and the effects of the pore strategies on the formability, mechanical properties, and permeability of the porous scaffolds were systematically investigated.

MATERIALS AND METHODS

Design and Preparation of the Scaffolds

In this work, porous scaffolds with the same porosity and different pore strategies were obtained by controlling minimal surface structural units, including three uniform distributed porous scaffolds with different pore sizes (500, 750, and 900 μm) and two porous scaffolds with a gradient distribution of pore sizes along the radial direction (pore sizes of 500–900 μm from inside to outside and 900–500 μm from inside to outside). Correspondingly, the scaffolds were named G500, G750, G900, G500-900, and G900-500, and the designed models are shown in **Figure 1**.

The G-structure of the minimal surface was selected to prepare the scaffolds. The equation of the G-structure is as follows:

$$\begin{aligned}\varphi(x,y,z)_G &= \sin\left(\frac{2\pi}{L}x\right)\cos\left(\frac{2\pi}{L}y\right)+\sin\left(\frac{2\pi}{L}z\right)\cos\left(\frac{2\pi}{L}x\right)\\ &\quad+\sin\left(\frac{2\pi}{L}y\right)\cos\left(\frac{2\pi}{L}z\right)\\ &= C,\end{aligned}$$

where L is the period of the minimal surface, i.e., the structure unit size, and C is the threshold, which is used to control the volume of the solid part. At a certain L, the pore size varies over the range (0, L). The structural unit sizes of the uniform scaffolds are 0.845, 1.242, and 1.522 mm, respectively (**Figure 1**). Furthermore, when the C value is replaced with a function related to the radius, a pore size distribution with continuous gradient variation in the radial direction can be obtained. The internal and external porosities (C_{in}, C_{out}) of the G500-900 scaffold are 41 and 90%, respectively, and the opposite is true for the G900-500 scaffold. Eventually, the porosity distribution function of the G-structure is as follows:

$$C_{(x,y)} = (C_{out}-C_{in})\left(\frac{\sqrt{x^2+y^2}}{r}\right)^n + C_{in},$$

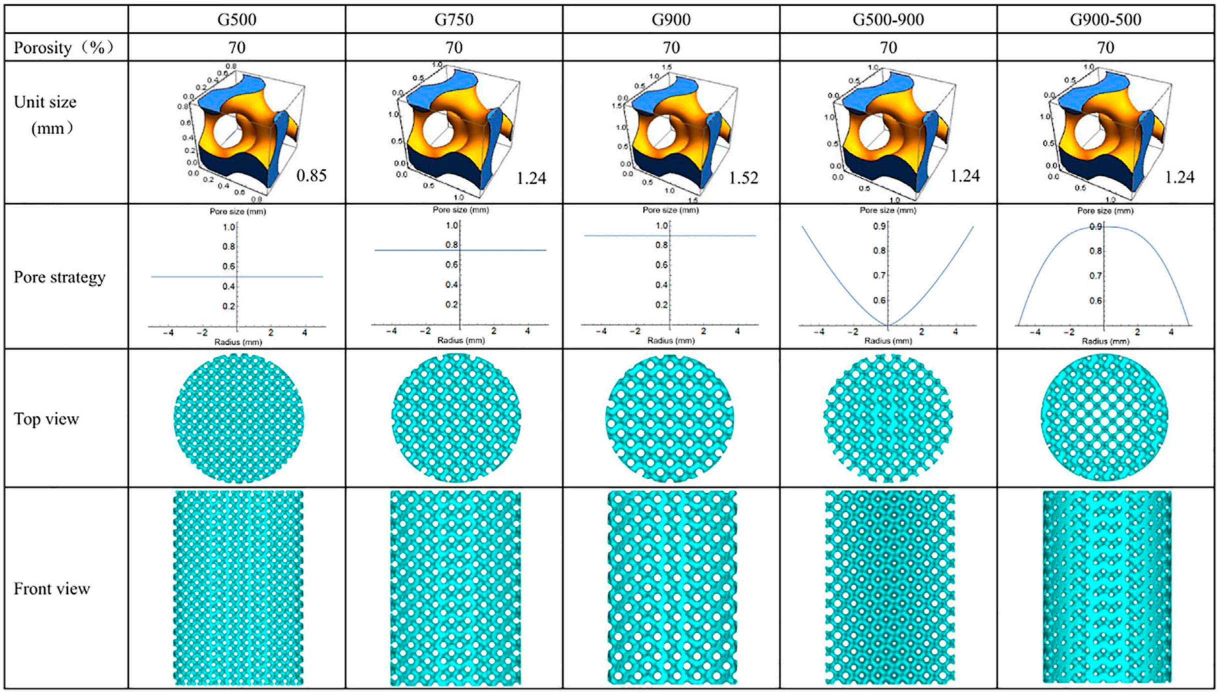

FIGURE 1 | Design model of the scaffold.

The G-structure equations and pore size distribution functions were imported into Mathematica soft to generate the model with a height of 15 mm and a diameter of 10 mm, and then, the models were repaired by importing into MagicSoft before SLM preparation.

NiTi alloy powder and Nb powder were used as raw materials, and the powder ratio was 91:9. Thus, the nominal chemical composition of the blended powder was $Ni_{46.5}Ti_{44.5}Nb_9$. After a high-energy ball mill for 3 h, the blended powder was used to prepare the scaffolds by SLM. The processing parameters were set as follows: the laser power was 200 W, powder layer thickness was 30 μm, spot size was 120 μm, laser scanning speed was 600 mm/s, scanning direction rotated 67° between successive layers, and substrate preheating temperature was 160°C. The scaffolds were washed three times with anhydrous ethanol in an ultrasonic cleaner to remove the unmelted metal powder from the surface.

Macro Morphologies and Microstructure Observation

The Archimedes method and dry weight method were used to calculate the density and porosity of the scaffolds. Micro-CT (PerkinElmer, Quantum GX II) was used to observe the macroscopic morphology of the scaffolds. The scanning voltage and current were 90 Kv and 80 μA, respectively, and the scanning time was 14 min. The 3D reconstruction was carried out using the device's built-in software with the same threshold values. A scanning electron microscope (SEM, JSM-7600F, JEOL) was used to observe the surface morphology and microstructure of the scaffolds. For the microstructure observation, the samples were ground and polished to a mirror finish by standard metallographic procedures and etched by using a reagent (composed of 10 vol% HNO_3, 20 vol% HF, and 70 vol% H_2O) for 15 s.

Compression Tests and Finite Element Simulation

Compression tests were carried out by using an MTS servo-hydraulic press (MTS 810, MTS, USA) at room temperature and a rate of 0.5 mm/min. The elastic modulus, compression strength, and maximum strain of the scaffolds were calculated based on the stress–strain curves.

The mechanical analysis of the G-structure unit with different porosities and the porous scaffolds was performed by ANSYS 16.0. The mesh type for the finite element analysis was a tetrahedral mesh with a size of 0.1 mm. The material model is chosen to be a nonlinear material, which needs to be created in ANSYS software. The material had an elastic modulus of 37 GPa, a compressive strength of 960 MPa, a Poisson's ratio of 0.3, a density of 6,475 kg/m^3, a bulk modulus of 36 GPa, and a shear modulus of 14 GPa. The boundary conditions were set as follows: fixing the bottom of the scaffold, applying a 10% displacement load on the top of the scaffold, and a compression rate of 0.5 mm/min. After the finite element analysis, the stress distribution of the scaffold was the output.

Permeability Tests and Fluid Finite Element Simulation

In order to evaluate the permeability of the scaffold, the permeability was tested by the falling head method, and the schematic diagram of the device is shown in **Figure 2A**. In the

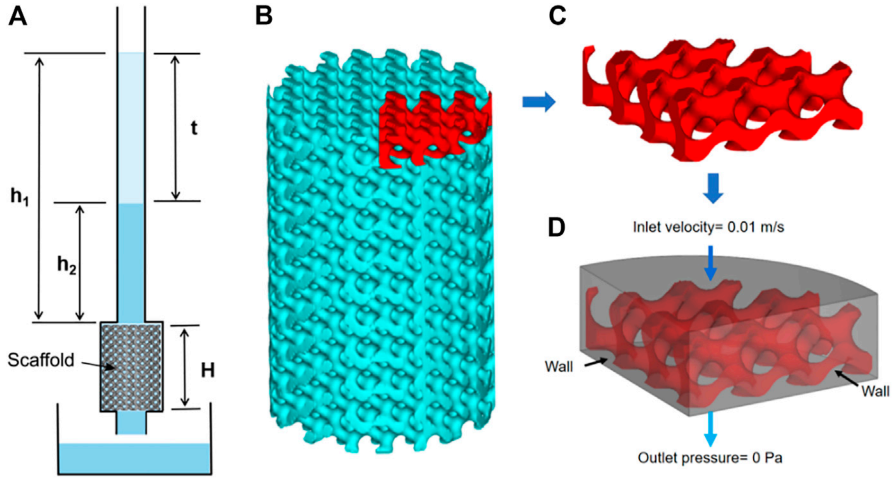

FIGURE 2 | Permeability experiments and finite element simulations: **(A)** schematic representation of the experimental device used in the falling head permeability test, **(B)** scaffold model, **(C)** model for finite element simulation, and **(D)** boundary setting for finite element simulation.

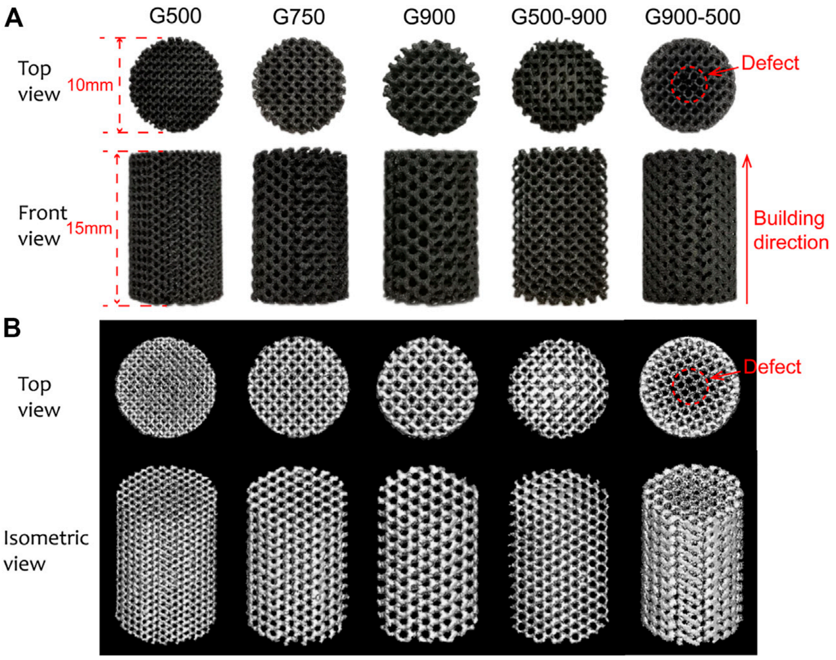

FIGURE 3 | (A) Macroscopic morphologies of $Ni_{46.5}Ti_{44.5}Nb_9$ porous scaffolds and **(B)** micro-CT 3D reconstruction model of the scaffolds.

course of the experiment, the water level in the seepage tube gradually drops from h_1 to h_2, which was kept constant for each test. The permeability K of the scaffolds was calculated from the equation of Darcy's law:

$$K = \frac{\mu H A}{\rho g t a}\ln\left(\frac{h_1}{h_2}\right),$$

where H is the height of the scaffold, A is the cross-sectional areas of the seepage tube, a is the cross-sectional areas of the scaffold, μ is the viscosity of the water, ρ is the density of the water, and g is the acceleration of gravity.

In order to simulate the flow of human body fluids inside the porous scaffold, ANSYS software was used to simulate the permeability of the scaffold using human body fluid as media, as shown in **Figures 2B–D**. The density of the fluid was 1,050 Kg/m^3, the viscosity was 0.0035 Pa⋆s, the inlet flow velocity was set to 0.01 m/s, and the outlet pressure was set to 0 Pa (Truscello et al., 2012). After the finite element simulation, the inlet pressure was

TABLE 1 | Modeling parameters and actual porosity of the scaffolds.

Scaffold	Superficial area (mm^2)	Design mean porosity (%)	Dry weighing porosity (%)	Porosity of the micro-CT reconstruction model (%)
G500	4169.366	70	71.83 ± 0.41	70.28 ± 0.74
G750	2866.860	70	71.07 ± 0.39	67.92 ± 0.21
G900	2367.944	70	68.97 ± 0.31	70.85 ± 0.29
G500-900	2644.182	70	71.67 ± 0.54	67.42 ± 0.53
G900-500	2837.003	70	71.68 ± 0.66	69.01 ± 0.33

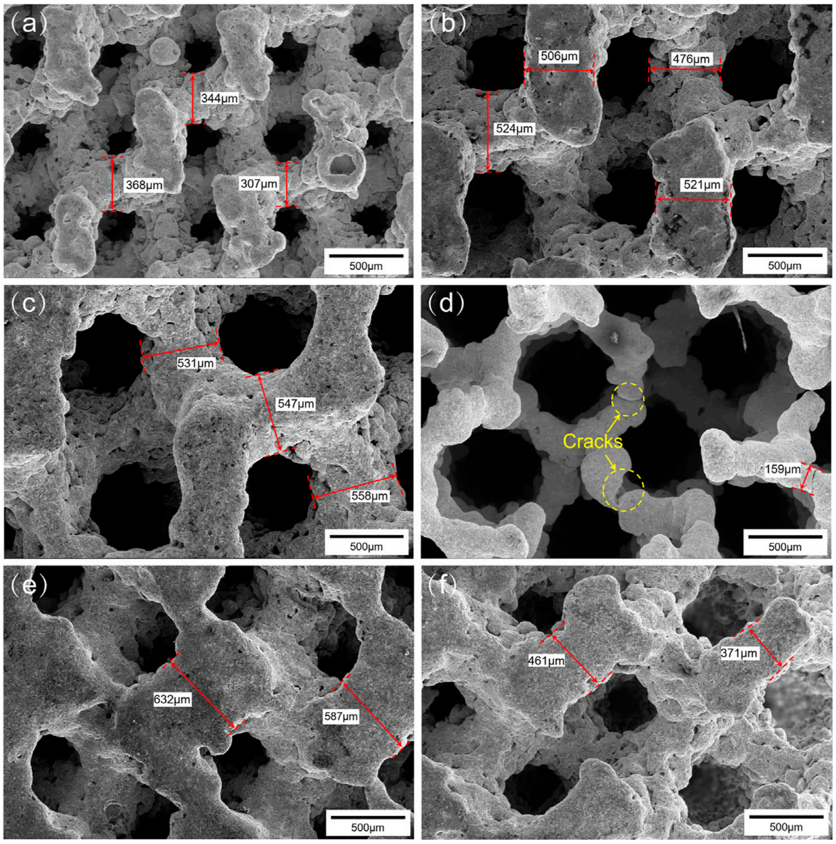

FIGURE 4 | Surface morphologies of the scaffolds: **(A)** G500, **(B)** G750, **(C)** G900, **(D)** G900-500, **(E)** and **(F)** G500-900.

calculated, and the pressure distribution cloud and flow velocity distribution of the fluid model were the output.

RESULTS AND DISCUSSION

Macroscopic Morphology Analysis

Figure 3A shows the macroscopic morphologies of the $Ni_{46.5}Ti_{44.5}Nb_9$ porous scaffolds. As can be seen, except for the G900-500 scaffold, all the scaffolds are structurally intact with no obvious defects. The height and the diameter of the scaffolds are 15.11 ± 0.12 mm and 10.06 ± 0.08 mm, respectively, which are basically consistent with the designed model. The density of the porous scaffold measured by the Archimedes drainage method is 6.62 g/cm^3. The porosity of the scaffold was calculated by the dry weight method and Micro-CT built-in software, as shown in **Table 1**. The porosity of the porous scaffold is basically consistent with the designed porosity. The surface area of the scaffold model is also obtained by Magics software (**Table 1**), and it can be found that the surface area of the scaffold increases with the decrease in the pore size. **Figure 3B** shows the Micro-CT 3D reconstruction image of the porous scaffold, and the results indicated that the prepared porous scaffold has good connectivity, and no pore blockage occurs.

Figures 4A–C show SEM images of the surface morphology of the porous scaffolds with pore size strategy. As can be seen, the surface of the $Ni_{46.5}Ti_{44.5}Nb_9$ porous scaffold is uneven and has an obvious step effect (Cheng et al., 2014). The support

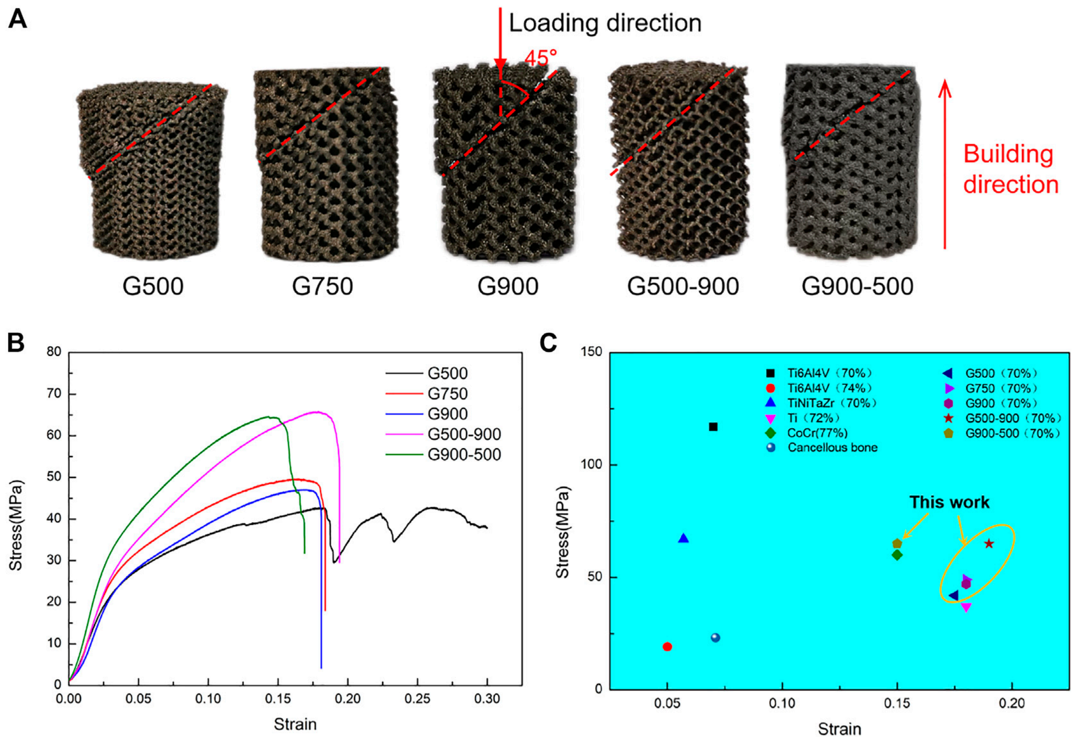

FIGURE 5 | Compression properties of the scaffolds: **(A)** morphologies of the post-compression test, **(B)** compression stress–strain curve, and **(C)** comparison of mechanical properties of the scaffold with different materials under similar porosity (Sevilla et al., 2007; Ataee et al., 2018; Cutolo et al., 2018; Cutolo et al., 2020; Liu et al., 2020; Luo et al., 2020).

TABLE 2 | Mechanical properties of $Ni_{46.5}Ti_{44.5}Nb_9$ scaffolds.

Scaffold	Elastic modulus (GPa)	Compression strength (MPa)	Maximum strain (%)
G500	0.86 ± 0.11	42.3 ± 0.9	17.5 ± 0.3
G750	1.03 ± 0.09	49.3 ± 0.6	18.2 ± 0.5
G900	0.80 ± 0.10	47.7 ± 0.9	18.4 ± 0.5
G500-900	0.96 ± 0.06	65.8 ± 1.6	19.1 ± 0.8
G900-500	1.05 ± 0.05	64.4 ± 0.8	15.3 ± 0.7

TABLE 3 | Modulus of the elastic modulus of G structural units with different porosities.

Porosity (%)	Elastic modulus (GPa)
20	18.563
30	13.770
40	10.057
50	6.968
60	4.442
70	2.175
80	0.568

thicknesses of the scaffolds are found to be larger than the designed dimensions, and the dimensional errors are between 5 and 25%. It should be noted that the center of the G900-500 scaffold shows defect, and the support thickness is also much smaller than the design size (200 μm) (**Figure 4D**), which is due to the fact that the minimum support thickness of the G900-500 scaffold (200 μm) is close to the processing limit of the SLM (80–250 μm) (Tofail et al., 2018), which lead to the generation of cracks. Therefore, the accuracy of the processing and the minimum design size of the scaffold should be considered in the design of the scaffold. **Figures 4E,F** show the surface morphology of the G500-900 scaffold, it can be found that the gradient structure of the scaffold varies significantly.

Compression Property Analysis

Figure 5 illustrates the macroscopic shape and compression performance of $Ni_{46.5}Ti_{44.5}Nb_9$ scaffolds after compression tests. As can be seen from **Figure 5A**, the angle between the fracture surface and the loading direction is 45°; this is because the scaffolds are subjected to shear stress during the compression process (Yan et al., 2015; Liu et al., 2018). The

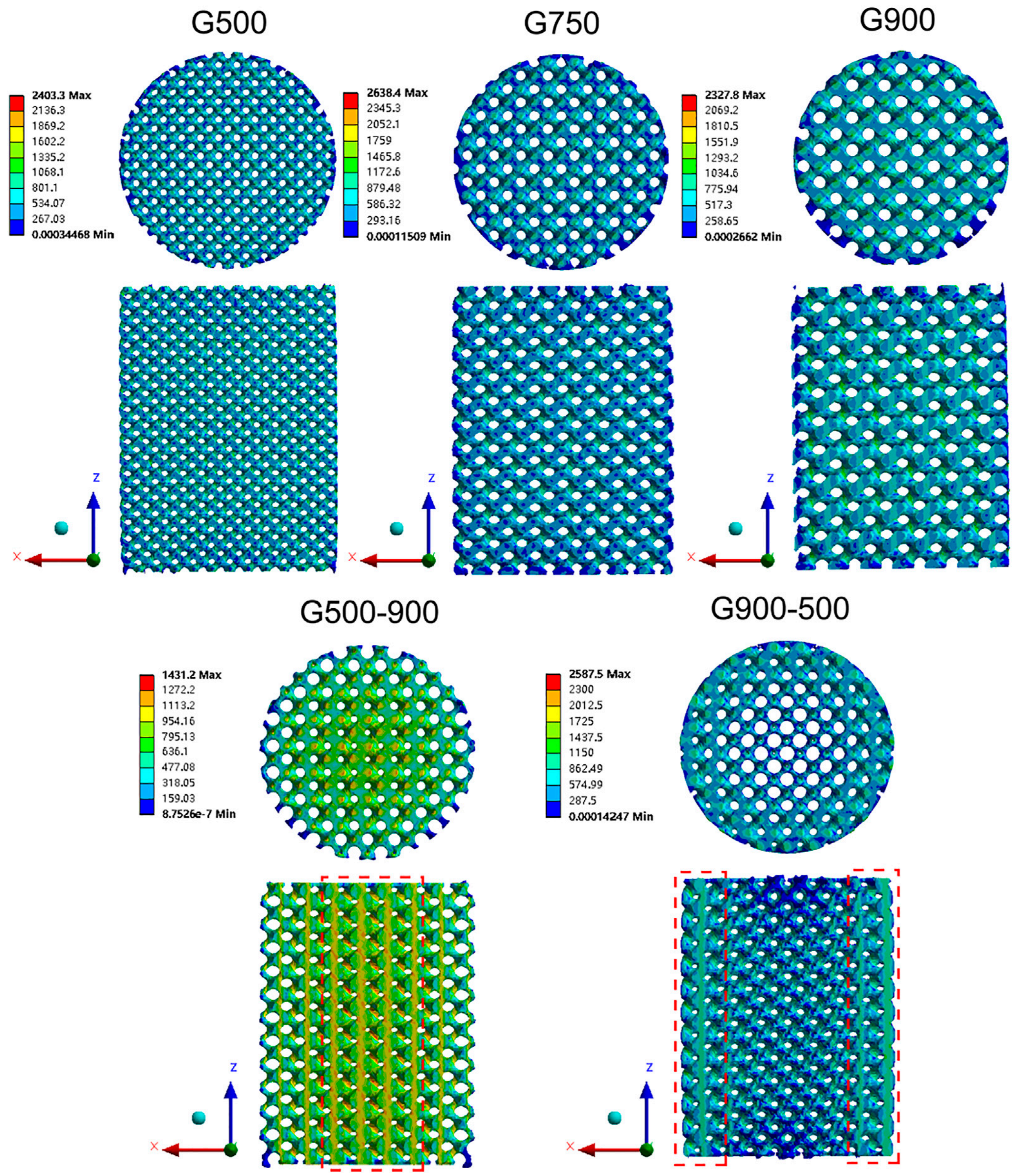

FIGURE 6 | Stress distribution cloud images of the scaffolds under 10% displacement load.

compressive stress–strain curves of the $Ni_{46.5}Ti_{44.5}Nb_9$ scaffolds are shown in **Figure 5B**. Due to the small thickness of support in the G500 scaffold (280 μm), when the stress reached the compressive strength of the scaffold, the local support broke first during the compression process, and the stress dropped sharply. However, the scaffold was not completely broken but was gradually compacted (as shown in **Figure 5A**), and the stress increased again, resulting in stress fluctuation of compressive curves. The mechanical properties of the $Ni_{46.5}Ti_{44.5}Nb_9$ porous scaffold are listed in **Table 2** from which it can be seen that the scaffold has an elastic modulus between 0.80–1.05 GPa, a compressive strength between 42.3–65.8 MPa, and an elongation between 15.3–19.1%. With the same porosity, the difference in mechanical properties of uniform scaffolds with different pore sizes is not significant, indicating that the pore size strategy has little effect on mechanical properties. However, the compression strength of G500-900 and G900-500 scaffolds is significantly higher than that of uniform scaffolds. This is because the radial gradient strategy increases the local support thickness of the scaffolds and improves their load-bearing capacity.

Figure 5C shows the mechanical properties of porous scaffolds of different materials with similar porosity. As can be seen, the $Ni_{46.5}Ti_{44.5}Nb_9$ scaffolds have higher compressive strength than most of the scaffolds of other materials and also have a high elongation (comparable to CoCr and Ti scaffolds).

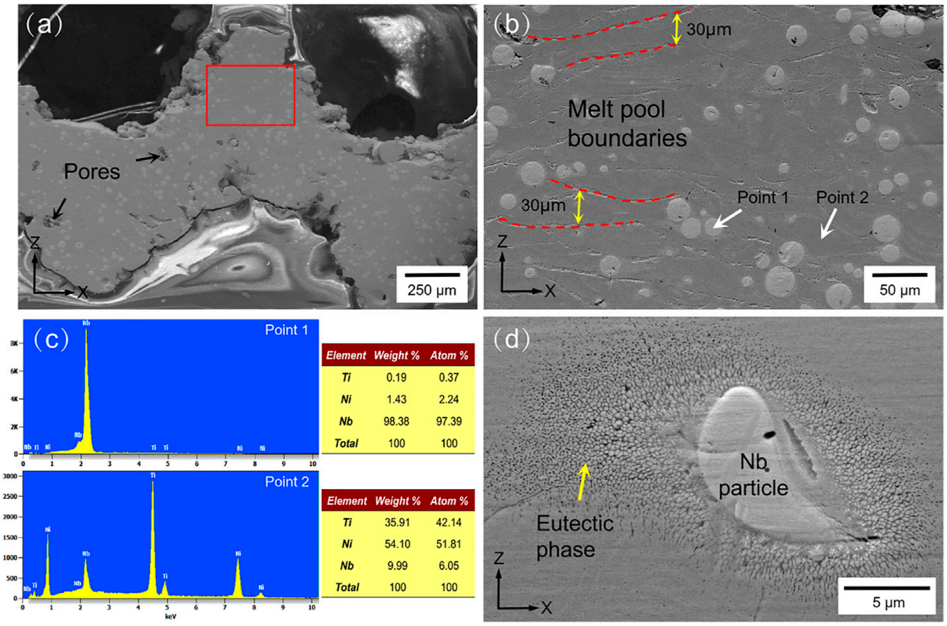

Element	Weight %	Atom %
Ti	0.19	0.37
Ni	1.43	2.24
Nb	98.38	97.39
Total	100	100

Element	Weight %	Atom %
Ti	35.91	42.14
Ni	54.10	51.81
Nb	9.99	6.05
Total	100	100

FIGURE 7 | XRD pattern and microstructure images: **(A)** microstructure images of the scaffold in the XZ section, **(B)** enlarged image of the red rectangle in **(A,C)** and EDS spectrums of points 1 and 2 in **(B,D)** eutectic phase and Nb particles.

The $Ni_{46.5}Ti_{44.5}Nb_9$ porous scaffold with 70% porosity has an elastic modulus matching cancellous bone (0.02–2 GPa) and higher compressive strength than cancellous bone, meeting the performance requirements of bone implants (Sevilla et al., 2007). Lu et al. (2021) also prepared porous scaffolds by SLM using the NiTi shape memory alloy. The elastic modulus of the scaffolds with a porosity of 66% was 1.75–2.45 GPa, which could match cancellous bone and avoid stress masking. The NiTi porous scaffold also has good elongation and superelasticity with a maximum recoverable strain of 5.1%. Therefore, NiTi-based porous scaffolds with high porosity have good potential for cancellous bone repairing.

The elastic modulus of the G-structure unit with different porosities was calculated by the finite element simulation software, and the results are shown in **Table 3**. It can be found that the elastic modulus of the G-structure unit gradually decreases with the increase in porosity, which is consistent with the results obtained by Bartolomeu et al. (2020). The porous scaffolds with different pore size distribution strategies have different porosities. The mechanical properties of the G500-900 scaffold gradually decrease as the porosity increases from the center of the scaffold to the outside. As the porosity of the G900-500 scaffold gradually decreases from the center to the outside of the scaffold, the mechanical properties of gradient scaffolds change gradually along the radius direction. **Figure 6** shows the stress distribution in the scaffolds after the compression simulation. We can also observe that the stress in the uniform scaffolds is evenly distributed, while the stress in the G500-900 and G900-500 scaffolds shows a gradient distribution. The G500-900 scaffold has a small pore size and thick support in the center (red dashed line), which is subjected to more stress during compression. Also, the G900-500 scaffold has a small pore and thickness support on the edge (red dashed line), which increases the load-bearing capacity of the scaffold. As a result, the compression strength of the gradient scaffolds is higher than that of the uniform scaffolds under the same porosity.

Phase Structure and Microstructure Analysis

Figure 7 shows the SEM images of the $Ni_{46.5}Ti_{44.5}Nb_9$ scaffold. As seen in **Figure 7A**, the inside of the scaffold is very dense, no large cracks or inclusions are observed, and only a few voids exist. **Figure 7B** shows an enlarged image of the red rectangle area in **Figure 7A**, which clearly shows the melt pool formed by the layer-by-layer build-up with a pool thickness of approximately 30 μm. The microstructure of the scaffold mainly consists of a matrix and round second phase with particle sizes of 10–30 μm. The EDS energy spectra of the matrix and particles (**Figure 7C**) show that the matrix is mainly NiTi with an Nb content of about 6%, and the particles are Nb particles. This indicates that during the additive manufacturing, part of the Nb is solidly dissolved into the NiTi matrix, forming the solution strengthening. Part of the Nb is retained and uniformly distributed in the matrix, forming second phase strengthening (Liu et al., 2021; Wang et al., 2018). A high magnification image of the Nb particle is shown in **Figure 7D**, where a fine eutectic structure is formed around the Nb. According to the investigation, the higher cooling rate of the SLM process promotes the diffusion of Nb and produces fine

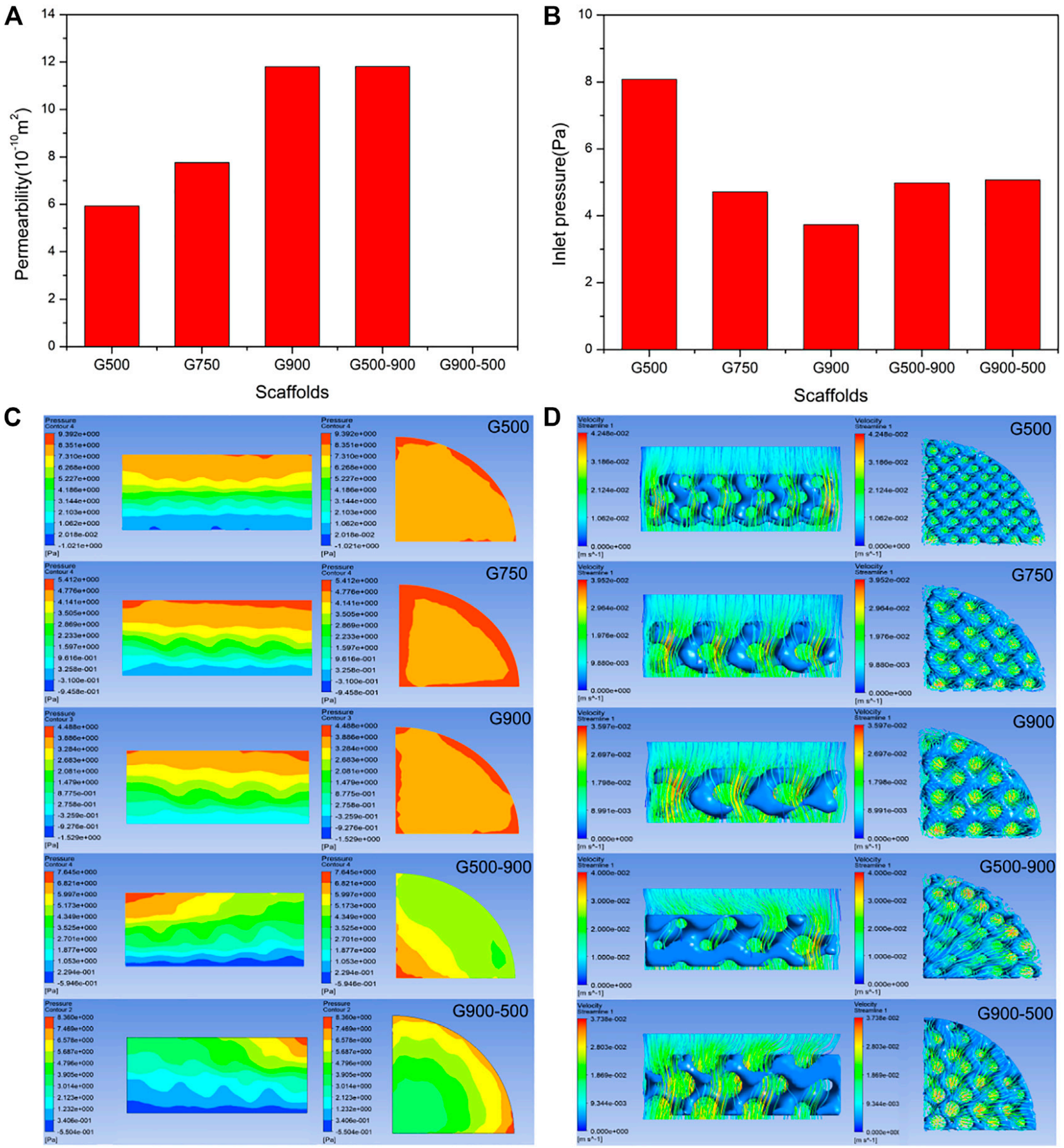

FIGURE 8 | Results of the permeability test and finite element simulation of porous scaffolds: **(A)** permeability test results (the permeability of the G900-500 scaffold is not recorded due to the formation of preparation defects). **(B)** Inlet pressure results are calculated by finite element simulation. **(C)** Fluid pressure distribution cloud diagram. **(D)** Fluid flow velocity distribution diagram. (It should be noted that media of the experiment and simulation are water and human body fluid, respectively).

eutectic microstructures, which can improve the strength and ductility of the porous scaffold (Liu et al., 2020).

Permeability of the Porous Scaffold

Permeability indicates the ability of a fluid to pass through a porous medium and can reflect the ability of the scaffold to transport nutrients and metabolites (Yu et al., 2020). It is an important parameter for biomedical porous scaffolds and is crucial for cell proliferation, differentiation, and the growth of bone tissue (Singh et al., 2009). **Figure 8A** shows the measured permeability of the scaffolds using the falling head method, and it can be seen that the permeability of the uniform scaffolds gradually increases with the increasing pore size. The G500-900 scaffold with a radial gradient structure exhibits comparable permeability to the G900 scaffold. **Figure 8B** shows the inlet pressure of the fluid model. The lower inlet pressure indicates that the porous scaffold has less obstruction to the fluid. For uniform scaffolds, the fluid simulation results are the same as for the falling head method, whereas the permeability of the G500-900 and G900-500 scaffolds are comparable to that of the G750 scaffold. It should be noted that the pore size has significantly affected the permeability and the surface area of the scaffolds (**Table 1**). This is because the surface area of the scaffold decreases with the increasing pore size, which reduces the friction drag of the scaffold during fluid flow, thus increasing the permeability of the scaffold (Ali and Sen, 2018).

To investigate the fluid flow inside the porous scaffold, the pressure and flow velocity clouds of the fluid model were the output *via* ANSYS CFD, as shown in **Figures 8C,D**. In **Figure 8C**, the section of the uniform scaffold in the axial direction has a stable pressure field, and the pressure gradually decreases, which facilitates the entry of body fluids into the scaffold (Ma et al., 2020). It is worth noting that the G500-900 gradient scaffold has the lowest pressure at the edge in the radial direction, where the scaffold has the largest pore size. This may be the reason why the gradient scaffold has a good comparative permeability with the G750 scaffold. **Figure 8D** shows the flow distribution of the scaffold. As can be seen, the G500-900 scaffold has the highest flow velocity at the edge, which improves the permeability of the overall scaffold.

CONCLUSION

In this study, $Ni_{46.5}Ti_{44.5}Nb_9$ porous scaffolds with different strategies were successfully prepared and simulated by human bone pore size features based on the triply periodic minimal surfaces and selective laser melting technology. The microstructures, mechanical properties, and permeability of the scaffolds were systematically investigated, and the main conclusions are obtained as follows:

1) The $Ni_{46.5}Ti_{44.5}Nb_9$ porous scaffolds have a modulus of elasticity of 0.80–1.05 GPa, a compressive strength of 42.3–65.8 MPa, and an elongation of 15.3–19.1%. For the uniform scaffolds, the pore size strategy has little effect on the mechanical properties of porous scaffolds, and porosity with a continuous gradient distribution can significantly improve the mechanical properties. This is because continuous gradient scaffolds have a low porosity area in the inner or outer regions, and the denser part can bear more stress, thus improving the mechanical properties of the scaffolds.
2) The microstructures of the $Ni_{46.5}Ti_{44.5}Nb_9$ porous scaffolds mainly contain NiTi matrix and Nb particles. The addition of Nb to the NiTi alloy can promote the formation of the eutectic microstructure and precipitation of the rich Nb phase, thus simultaneously increasing the strength and toughness of the alloy.
3) Under the same porosity, increasing the pore size can improve the permeability of porous scaffolds due to the decrease in the specific surface. The local high porosity structure in the continuous gradient scaffolds bears more fluid flow, which can improve the permeability of the overall scaffold.

DATA AVAILABILITY STATEMENT

The raw data supporting the conclusions of this article will be made available by the authors, without undue reservation.

AUTHOR CONTRIBUTIONS

YL carried out the conception of the idea of the manuscript. YT and JL provided the data and advice. BW and GL collected and collated the data. YL wrote the original draft. ZL reviewed and revised the original draft. GW provided guidance for the revision of the manuscript. LW provided the financial support for the project to this publication. All the authors contributed to the manuscript and approved the submitted version.

ACKNOWLEDGMENTS

The authors would like to acknowledge the financial supports provided by the National Science Foundation (Grant No. 51801115) and the China Postdoctoral Science Foundation (Grant No. 2020M671112).

REFERENCES

Ali, D., and Sen, S. (2018). Computational Fluid Dynamics Study of the Effects of Surface Roughness on Permeability and Fluid Flow-Induced Wall Shear Stress in Scaffolds. *Ann. Biomed. Eng.* 46, 2023–2035. doi:10.1007/s10439-018-2101-z

Arabnejad, S., Burnett Johnston, R., Pura, J. A., Singh, B., Tanzer, M., and Pasini, D. (2016). High-strength Porous Biomaterials for Bone Replacement: A Strategy to Assess the Interplay between Cell Morphology, Mechanical Properties, Bone Ingrowth and Manufacturing Constraints. *Acta Biomater.* 30, 345–356. doi:10.1016/j.actbio.2015.10.048

Ataee, A., Li, Y., Fraser, D., Song, G., and Wen, C. (2018). Anisotropic Ti-6Al-4V Gyroid Scaffolds Manufactured by Electron Beam Melting (EBM) for Bone Implant Applications. *Mater. Des.* 137, 345–354. doi:10.1016/j.matdes.2017.10.040

Bartolomeu, F., Costa, M. M., Alves, N., Miranda, G., and Silva, F. S. (2020). Engineering the Elastic Modulus of NiTi Cellular Structures Fabricated by Selective Laser Melting. *J. Mech. Behav. Biomed. Mater.* 110, 103891. doi:10.1016/j.jmbbm.2020.103891

Chen, Z., Yan, X., Yin, S., Liu, L., Liu, X., Zhao, G., et al. (2020). Influence of the Pore Size and Porosity of Selective Laser Melted Ti6Al4V ELI Porous Scaffold on Cell Proliferation, Osteogenesis and Bone Ingrowth. *Mater. Sci. Eng. C* 106, 110289. doi:10.1016/j.msec.2019.110289

Cheng, A., Humayun, A., Cohen, D. J., Boyan, B. D., and Schwartz, Z. (2014). Additively Manufactured 3D Porous Ti-6Al-4V Constructs Mimic Trabecular Bone Structure and Regulate Osteoblast Proliferation, Differentiation and Local Factor Production in a Porosity and Surface Roughness Dependent Manner. *Biofabrication* 6 (4), 045007. doi:10.1088/1758-5082/6/4/045007

Cutolo, A., Engelen, B., Desmet, W., and Van Hooreweder, B. (2020). Mechanical Properties of Diamond Lattice Ti-6Al-4V Structures Produced by Laser Powder Bed Fusion: On the Effect of the Load Direction. *J. Mech. Behav. Biomed. Mater.* 104, 103656. doi:10.1016/j.jmbbm.2020.103656

Cutolo, A., Neirinck, B., Lietaert, K., de Formanoir, C., and Van Hooreweder, B. (2018). Influence of Layer Thickness and Post-process Treatments on the Fatigue Properties of CoCr Scaffolds Produced by Laser Powder Bed Fusion. *Addit. Manuf.* 23, 498–504. doi:10.1016/j.addma.2018.07.008

Geetha, M., Singh, A. K., Asokamani, R., and Gogia, A. K. (2009). Ti Based Biomaterials, the Ultimate Choice for Orthopaedic Implants - A Review. *Prog. Mater. Sci.* 54 (3), 397–425. doi:10.1016/j.pmatsci.2008.06.004

Giannitelli, S. M., Accoto, D., Trombetta, M., and Rainer, A. (2014). Current Trends in the Design of Scaffolds for Computer-Aided Tissue Engineering. *Acta Biomater.* 10 (2), 580–594. doi:10.1016/j.actbio.2013.10.024

Gu, H., Ding, Z., Yang, Z., Yu, W., Zhang, W., Lu, W., et al. (2019). Microstructure Evolution and Electrochemical Properties of TiO2/Ti-35Nb-2Ta-3Zr Micro/nano-Composites Fabricated by Friction Stir Processing. *Mater. Des.* 169, 107680. doi:10.1016/j.matdes.2019.107680

Guo, L., Ataollah Naghavi, S., Wang, Z., Nath Varma, S., Han, Z., Yao, Z., et al. (2022). On the Design Evolution of Hip Implants: A Review. *Mater. Des.* 216, 110552. doi:10.1016/j.matdes.2022.110552

Guo, S., Zhang, H., Chen, Y., Liu, Q., Wu, R., Ma, W., et al. (2021). A Sandwich-Structured Nb/NiTi Composite with Good Bio-Compatibility, Near-Linear-Elastic Deformation and Large Elastic Admissible Strain. *Compos. Part B Eng.* 207, 108586. doi:10.1016/j.compositesb.2020.108586

Guo, Z., Wang, C., Du, C., Sui, J., and Liu, J. (2020). Effects of Topological Structure on Antibacterial Behavior and Biocompatibility of Implant. *Procedia CIRP* 89, 126–131. doi:10.1016/j.procir.2019.12.003

Habijan, T., Haberland, C., Meier, H., Frenzel, J., Wittsiepe, J., Wuwer, C., et al. (2013). The Biocompatibility of Dense and Porous Nickel-Titanium Produced by Selective Laser Melting. *Mater. Sci. Eng. C* 33 (1), 419–426. doi:10.1016/j.msec.2012.09.008

Li, J., Yang, H., Wang, H., and Ruan, J. (2014). Low Elastic Modulus Titanium-Nickel Scaffolds for Bone Implants. *Mater. Sci. Eng. C* 34, 110–114. doi:10.1016/j.msec.2013.08.043

Li, Y., Ding, Y., Munir, K., Lin, J., Brandt, M., Atrens, A., et al. (2019). Novel β-Ti35Zr28Nb Alloy Scaffolds Manufactured Using Selective Laser Melting for Bone Implant Applications. *Acta Biomater.* 87, 273–284. doi:10.1016/j.actbio.2019.01.051

Li, Y., Pavanram, P., Zhou, J., Lietaert, K., Taheri, P., Li, W., et al. (2020). Additively Manufactured Biodegradable Porous Zinc. *Acta Biomater.* 101, 609–623. doi:10.1016/j.actbio.2019.10.034

Lin, Z., Wang, L., Xue, X., Lu, W., Qin, J., and Zhang, D. (2013). Microstructure Evolution and Mechanical Properties of a Ti-35Nb-3Zr-2Ta Biomedical Alloy Processed by Equal Channel Angular Pressing (ECAP). *Mater. Sci. Eng. C* 33 (8), 4551–4561. doi:10.1016/j.msec.2013.07.010

Liu, F., Mao, Z., Zhang, P., Zhang, D. Z., Jiang, J., and Ma, Z. (2018). Functionally Graded Porous Scaffolds in Multiple Patterns: New Design Method, Physical and Mechanical Properties. *Mater. Des.* 160, 849–860. doi:10.1016/j.matdes.2018.09.053

Liu, S., Han, S., Zhang, L., Chen, L.-Y., Wang, L., Zhang, L., et al. (2020). Strengthening Mechanism and Micropillar Analysis of High-Strength NiTi-Nb Eutectic-type Alloy Prepared by Laser Powder Bed Fusion. *Compos. Part B Eng.* 200, 108358. doi:10.1016/j.compositesb.2020.108358

Liu, S., Liu, W., Liu, J., Liu, J., Zhang, L., Tang, Y., et al. (2021). Compressive Properties and Microstructure Evolution in NiTiNb Alloy with Mesh Eutectic Phase. *Mater. Sci. Eng. A* 801, 140434. doi:10.1016/j.msea.2020.140434

Liu, Y. J., Ren, D. C., Li, S. J., Wang, H., Zhang, L. C., and Sercombe, T. B. (2020). Enhanced Fatigue Characteristics of a Topology-Optimized Porous Titanium Structure Produced by Selective Laser Melting. *Addit. Manuf.* 32, 101060. doi:10.1016/j.addma.2020.101060

Liu, Y. J., Wang, H. L., Li, S. J., Wang, S. G., Wang, W. J., Hou, W. T., et al. (2017). Compressive and Fatigue Behavior of Beta-type Titanium Porous Structures Fabricated by Electron Beam Melting. *Acta Mater.* 126, 58–66. doi:10.1016/j.actamat.2016.12.052

Lu, H. Z., Ma, H. W., Luo, X., Wang, Y., Wang, J., Lupoi, R., et al. (2021). Microstructure, Shape Memory Properties, and *In Vitro* Biocompatibility of Porous NiTi Scaffolds Fabricated via Selective Laser Melting. *J. Mater. Res. Technol.* 15, 6797–6812. doi:10.1016/j.jmrt.2021.11.112

Luo, J. P., Huang, Y. J., Xu, J. Y., Sun, J. F., Dargusch, M. S., Hou, C. H., et al. (2020). Additively Manufactured Biomedical Ti-Nb-Ta-Zr Lattices with Tunable Young's Modulus: Mechanical Property, Biocompatibility, and Proteomics Analysis. *Mater. Sci. Eng. C* 114, 110903. doi:10.1016/j.msec.2020.110903

Lv, Y., Wang, B., Liu, G., Tang, Y., Lu, E., Xie, K., et al. (2021). Metal Material, Properties and Design Methods of Porous Biomedical Scaffolds for Additive Manufacturing: A Review. *Front. Bioeng. Biotechnol.* 9, 641130. doi:10.3389/fbioe.2021.641130

Ma, S., Tang, Q., Han, X., Feng, Q., Song, J., Setchi, R., et al. (2020). Manufacturability, Mechanical Properties, Mass-Transport Properties and Biocompatibility of Triply Periodic Minimal Surface (TPMS) Porous Scaffolds Fabricated by Selective Laser Melting. *Mater. Des.* 195, 109034. doi:10.1016/j.matdes.2020.109034

Mao, C., Yu, W., Jin, M., Wang, Y., Shang, X., Lin, L., et al. (2022). Mechanobiologically Optimized Ti-35Nb-2Ta-3Zr Improves Load Transduction and Enhances Bone Remodeling in Tilted Dental Implant Therapy. *Bioact. Mater.* 16, 15–26. doi:10.1016/j.bioactmat.2022.03.005

Onal, E., Frith, J., Jurg, M., Wu, X., and Molotnikov, A. (2018). Mechanical Properties and *In Vitro* Behavior of Additively Manufactured and Functionally Graded Ti6Al4V Porous Scaffolds. *Metals* 8 (4), 200. doi:10.3390/met8040200

Ouyang, P., Dong, H., He, X., Cai, X., Wang, Y., Li, J., et al. (2019). Hydromechanical Mechanism behind the Effect of Pore Size of Porous Titanium Scaffolds on Osteoblast Response and Bone Ingrowth. *Mater. Des.* 183, 108151. doi:10.1016/j.matdes.2019.108151

Ran, Q., Yang, W., Hu, Y., Shen, X., Yu, Y., Xiang, Y., et al. (2018). Osteogenesis of 3D Printed Porous Ti6Al4V Implants with Different Pore Sizes. *J. Mech. Behav. Biomed. Mater.* 84, 1–11. doi:10.1016/j.jmbbm.2018.04.010

Sevilla, P., Aparicio, C., Planell, J. A., and Gil, F. J. (2007). Comparison of the Mechanical Properties between Tantalum and Nickel-Titanium Foams Implant Materials for Bone Ingrowth Applications. *J. Alloys Compd.* 439 (1-2), 67–73. doi:10.1016/j.jallcom.2006.08.069

Singh, R., Lee, P., Lindley, T., Dashwood, R., Ferrie, E., and Imwinkelried, T. (2009). Characterization of the Structure and Permeability of Titanium Foams for Spinal Fusion Devices. *Acta Biomater.* 5, 477–487. doi:10.1016/j.actbio.2008.06.014

Tofail, S. A. M., Koumoulos, E. P., Bandyopadhyay, A., Bose, S., O'Donoghue, L., and Charitidis, C. (2018). Additive Manufacturing: Scientific and Technological Challenges, Market Uptake and Opportunities. *Mater. Today* 21 (1), 22–37. doi:10.1016/j.mattod.2017.07.001

Truscello, S., Kerckhofs, G., Van Bael, S., Pyka, G., Schrooten, J., and Van Oosterwyck, H. (2012). Prediction of Permeability of Regular Scaffolds for Skeletal Tissue Engineering: A Combined Computational and Experimental Study. *Acta Biomater.* 8 (4), 1648–1658. doi:10.1016/j.actbio.2011.12.021

Wang, C., Huang, W., Zhou, Y., He, L., He, Z., Chen, Z., et al. (2020). 3D Printing of Bone Tissue Engineering Scaffolds. *Bioact. Mater.* 5, 82–91. doi:10.1016/j.bioactmat.2020.01.004

Wang, L., Xie, L., Zhang, L.-C., Chen, L., Ding, Z., Lv, Y., et al. (2018). Microstructure Evolution and Superelasticity of Layer-like NiTiNb Porous Metal Prepared by Eutectic Reaction. *Acta Mater.* 143, 214–226. doi:10.1016/j.actamat.2017.10.021

Wang, S., Liu, L., Li, K., Zhu, L., Chen, J., and Hao, Y. (2019). Pore Functionally Graded Ti6Al4V Scaffolds for Bone Tissue Engineering Application. *Mater. Des.* 168, 107643. doi:10.1016/j.matdes.2019.107643

Wang, S., Shi, Z. a., Liu, L., Zhou, X., Zhu, L., and Hao, Y. (2020). The Design of Ti6Al4V Primitive Surface Structure with Symmetrical Gradient of Pore Size in Biomimetic Bone Scaffold. *Mater. Des.* 193, 108830. doi:10.1016/j.matdes.2020.108830

Wang, X., Xu, S., Zhou, S., Xu, W., Leary, M., Choong, P., et al. (2016). Topological Design and Additive Manufacturing of Porous Metals for Bone Scaffolds and Orthopaedic Implants: A Review. *Biomaterials* 83, 127–141. doi:10.1016/j.biomaterials.2016.01.012

Yan, C., Hao, L., Hussein, A., and Young, P. (2015). Ti-6Al-4V Triply Periodic Minimal Surface Structures for Bone Implants Fabricated via Selective Laser Melting. *J. Mech. Behav. Biomed. Mater.* 51, 61–73. doi:10.1016/j.jmbbm.2015.06.024

Yu, G., Li, Z., Li, S., Zhang, Q., Hua, Y., Liu, H., et al. (2020). The Select of Internal Architecture for Porous Ti Alloy Scaffold: A Compromise between Mechanical

Properties and Permeability. *Mater. Des.* 192, 108754. doi:10.1016/j.matdes.2020.108754

Yuan, L., Ding, S., and Wen, C. (2019). Additive Manufacturing Technology for Porous Metal Implant Applications and Triple Minimal Surface Structures: A Review. *Bioact. Mater.* 4 (1), 56–70. doi:10.1016/j.bioactmat.2018.12.003

Zhang, B., Pei, X., Zhou, C., Fan, Y., Jiang, Q., Ronca, A., et al. (2018). The Biomimetic Design and 3D Printing of Customized Mechanical Properties Porous Ti6Al4V Scaffold for Load-Bearing Bone Reconstruction. *Mater. Des.* 152, 30–39. doi:10.1016/j.matdes.2018.04.065

Zhang, S., Li, C., Hou, W., Zhao, S., and Li, S. (2016). Longitudinal Compression Behavior of Functionally Graded Ti-6Al-4V Meshes. *J. Mater. Sci. Technol.* 32 (11), 1098–1104. doi:10.1016/j.jmst.2016.02.008

Zhang, X., Yan, X., Fang, G., and Liu, M. (2020). Biomechanical Influence of Structural Variation Strategies on Functionally Graded Scaffolds Constructed With Triply Periodic Minimal Surface. *Addit. Manuf.* 32, 101015. doi:10.1016/j.addma.2019.101015

Conflict of Interest: The authors declare that the research was conducted in the absence of any commercial or financial relationships that could be construed as a potential conflict of interest.

frontiers | Frontiers in Bioengineering and Biotechnology

ORIGINAL RESEARCH
published: 16 June 2022
doi: 10.3389/fbioe.2022.918032

Biomechanical Analysis of the Reasonable Cervical Range of Motion to Prevent Non-Fusion Segmental Degeneration After Single-Level ACDF

Weishi Liang[†]*, Bo Han*[†]*, Yong Hai*, Jincai Yang and Peng Yin**

Department of Orthopedic Surgery, Beijing Chaoyang Hospital, Capital Medical University, Beijing, China

The compensatory increase in intervertebral range of motion (ROM) after cervical fusion can increase facet joint force (FJF) and intradiscal pressure (IDP) in non-fusion segments. Guiding the post-ACDF patient cervical exercise within a specific ROM (defined as reasonable ROM) to offset the increase in FJF and IDP may help prevent segmental degeneration. This study aimed to determine the reasonable total C0–C7 ROM without an increase in FJF and IDP in non-fusion segments after anterior cervical discectomy and fusion (ACDF). A three-dimensional intact finite element model of C0–C7 generated healthy cervical conditions. This was modified to the ACDF model by simulating the actual surgery at C5–C6. A 1.0 Nm moment and 73.6 N follower load were applied to the intact model to determine the ROMs. A displacement load was applied to the ACDF model under the same follower load, resulting in a total C0–C7 ROM similar to that of the intact model. The reasonable ROMs in the ACDF model were calculated using the fitting function. The results indicated that the intervertebral ROM of all non-fusion levels was increased in the ACDF model in all motion directions. The compensatory increase in ROM in adjacent segments (C4/5 and C6/7) was more significant than that in non-adjacent segments, except for C3/4 during lateral bending. The intervertebral FJF and IDP of C0–C7 increased with increasing ROM. The reasonable ROMs in the ACDF model were 42.4°, 52.6°, 28.4°, and 42.25° in flexion, extension, lateral bending, and axial rotation, respectively, with a decreased ROM of 4.4–7.2%. The postoperative increase in FJF and IDP in non-fusion segments can be canceled out by reducing the intervertebral ROM within reasonable ROMs. This study provided a new method to estimate the reasonable ROMs after ACDF from a biomechanical perspective, and further in vitro and clinical studies are needed to confirm this.

Keywords: anterior cervical discectomy and fusion, range of cervical motion, adjacent segment degeneration (ASD), facet joint force (FJF), intradiscal pressure (IDP), finite element analysis

Edited by:
Liqiang Wang,
Shanghai Jiao Tong University, China

Reviewed by:
Xueqing Wu,
Beihang University, China
Yan Yu,
Tongji Hospital Affiliated to Tongji University, China

****Correspondence:***
Yong Hai
yong.hai@ccmu.edu.cn
Peng Yin
yinpeng3904@126.com

[†] *These authors have contributed equally to this work and co-first authors*

Specialty section:
This article was submitted to Biomechanics,
a section of the journal Frontiers in Bioengineering and Biotechnology

Received: *11 April 2022*
Accepted: *05 May 2022*
Published: *16 June 2022*

Citation:
Liang W, Han B, Hai Y, Yang J and Yin P (2022) Biomechanical Analysis of the Reasonable Cervical Range of Motion to Prevent Non-Fusion Segmental Degeneration After Single-Level ACDF.
Front. Bioeng. Biotechnol. 10:918032.
doi: 10.3389/fbioe.2022.918032

INTRODUCTION

Due to aging, lack of neck muscle exercise, and chronic abnormal use of the cervical spine, cervical degeneration diseases have become a common problem in the middle-aged and elderly population (Buyukturan et al., 2017; Wada et al., 2018; Kumagai et al., 2019; Tamai et al., 2019). Anterior cervical discectomy and fusion (ACDF) has become the standard clinical procedure for the treatment of cervical myelopathy and radiculopathy, which can directly remove the compression of intervertebral discs, posterior longitudinal ligaments, and osteophytes on the spinal cord to relieve the symptoms of nerve compression (Zhu et al., 2013; Findlay et al., 2018). Implantation of an interbody cage plus plate system can effectively restore the stability and normal physiological curvature of the cervical spine (Oliver et al., 2018). Although ACDF is widely accepted by spinal surgeons worldwide, the high incidence of non-fusion segmental degeneration after ACDF surgery, especially adjacent segment degeneration (ASD), is a big challenge. Alhashash et al. followed up on 70 patients treated with ACDF for more than 3 years and found that the incidence of ASD in patients with single-level fusion was 54%, most commonly after C5/6 fusion (28%) (Alhashash et al., 2018).

The postoperative non-fusion segmental degeneration mainly includes disc degeneration, facet joint degeneration, osteophyte formation, endplate abnormalities, and abnormal curvature of the cervical spine (Harada et al., 2021). In addition, many scholars believed that fusion can significantly increase the endplate and disc stress load at the adjacent segments, thereby accelerating segmental degeneration (Eck et al., 2002; Goffin et al., 2004; Lopez-Espina et al., 2006). Many studies have shown that the compensatory increase in the range of motion (ROM) of the non-fusion motion segments in patients after ACDF surgery may increase the intradiscal pressure (IDP), leading to segmental degeneration (Matsunaga et al., 1999; Eck et al., 2002; Elsawaf et al., 2009; Prasarn et al., 2012). Eck et al. (2002) found a significant increase in segmental motion and IDP of the adjacent upper and lower segments after single-level fusion at the C5/6 level with normal cervical ROM. The compensatory increase in the ROM of non-fusion segments can lead to an increase in facet joint force (FJF), which is closely related to the aggravation of segmental degeneration (Cai et al., 2020). In an *in vitro* experiment (Li et al., 2015), it was also demonstrated that the FJFs in the adjacent segments increased after ACDF fusion, which is one of the possible factors that accelerate ASD.

The previous studies demonstrated that the increase in the intervertebral ROM, FJF, and IDP of both the adjacent segments and other non-adjacent segments after ACDF surgery leads to segmental degeneration (Eck et al., 2002; Prasarn et al., 2012; Li et al., 2015; Wong et al., 2020; Choi et al., 2021). As mentioned above, the effect of postoperative ROM compensation on non-fusion segmental degeneration after ACDF surgery has been studied. However, no research has proposed a postoperative prevention method for segmental degeneration. Therefore, we proposed a reasonable cervical ROM based on biomechanism, which can offset the increase in IDP and FJF caused by the abnormal increase in ROM in non-fusion segments (Elsawaf et al., 2009). Guiding the patients to conduct postoperative neck activities within reasonable ROMs to decrease the abnormal load on the facet joints and discs may help delay the progression of non-fusion segment degeneration.

In the present study, we constructed an intact finite element (FE) model and a single-level C5/6 ACDF model of C0–C7. This study aimed to determine the specific total C0–C7 ROM (defined as reasonable total C0–C7 ROM) of the entire cervical spine after single-level ACDF operation without an increase in FJF and IDP and explore the ROM compensation changes of non-fusion segments after fusion and the effect of the increased total C0–C7 ROMs on the FJF and IDP values.

MATERIALS AND METHODS

Establishment of the Intact Finite Element Model

The geometric characteristics of the intact cervical FE model were constructed from computed tomography (CT) images of a healthy woman without cervical spondylosis history and vertebrae abnormities. The FE model of the C0–C7 cervical spine is shown in **Figure 1**. The CT image was first imported into Mimics (Materialise Inc., Belgium) and transformed into a geometric structure of C0–C7. The geometric model was meshed using Hypermesh (Altair Engineering, Inc., United States). The FE models were preprocessed and analyzed using Abaqus (Dassault Systemes Simulia Corporation, United States).

According to the previous studies, the main material properties and element types used in the FE models are presented in **Table 1** (Zhang et al., 2006; Leahy and Puttlitz, 2012; Burkhardt et al., 2018; Lu and Lu, 2019; Herron et al., 2020). A vertebra consists of a cortical bone (thickness, 1 mm), a cancellous bone, and end plates (thickness, 0.5 mm) (Lu and Lu, 2019). The cortical shell and cancellous bone were meshed using tetrahedral elements, while cortical endplates of the facet joints and intervertebral discs were meshed using hexahedral elements. The occiput bones are discretized as rigid bodies. The intervertebral discs comprised the nucleus pulposus and annulus fibrosus. The nucleus pulposus was modeled as a nearly incompressible hyperelastic body, accounting for approximately 40% of the intervertebral volume (Cai et al., 2020). A neo-Hookean material was used to model the annulus ground substance. The annulus fibers of eight layers were created and meshed with truss elements. The angles between the annulus fibers and the mid-height plane were approximately ±30° (Kallemeyn et al., 2010; Chen et al., 2018; Lu and Lu, 2020).

In addition, the tectorial membrane (TM) and transverse ligament (TL) surfaces were modeled using S4 elements with a thickness of 1mm, and the main ligaments were established with nonlinear tension-only spring elements in the appropriate anatomical location: apical ligament, alar ligament, anterior atlanto-occipital membrane, anterior atlantoaxial membrane, posterior atlanto-occipital membrane, posterior atlantoaxial ligament, anterior longitudinal ligament, posterior longitudinal ligament, ligament flavum, interspinous ligament, and facet joint capsules (Herron et al., 2020).

Establishment of the Single-Level ACDF Finite Element Model

The details of the established single-level ACDF FE model are shown in **Figure 2**, and the surgical process was illustrated as follows. At first, the anterior longitudinal ligaments, posterior longitudinal ligaments, and intervertebral disc at the C5/6

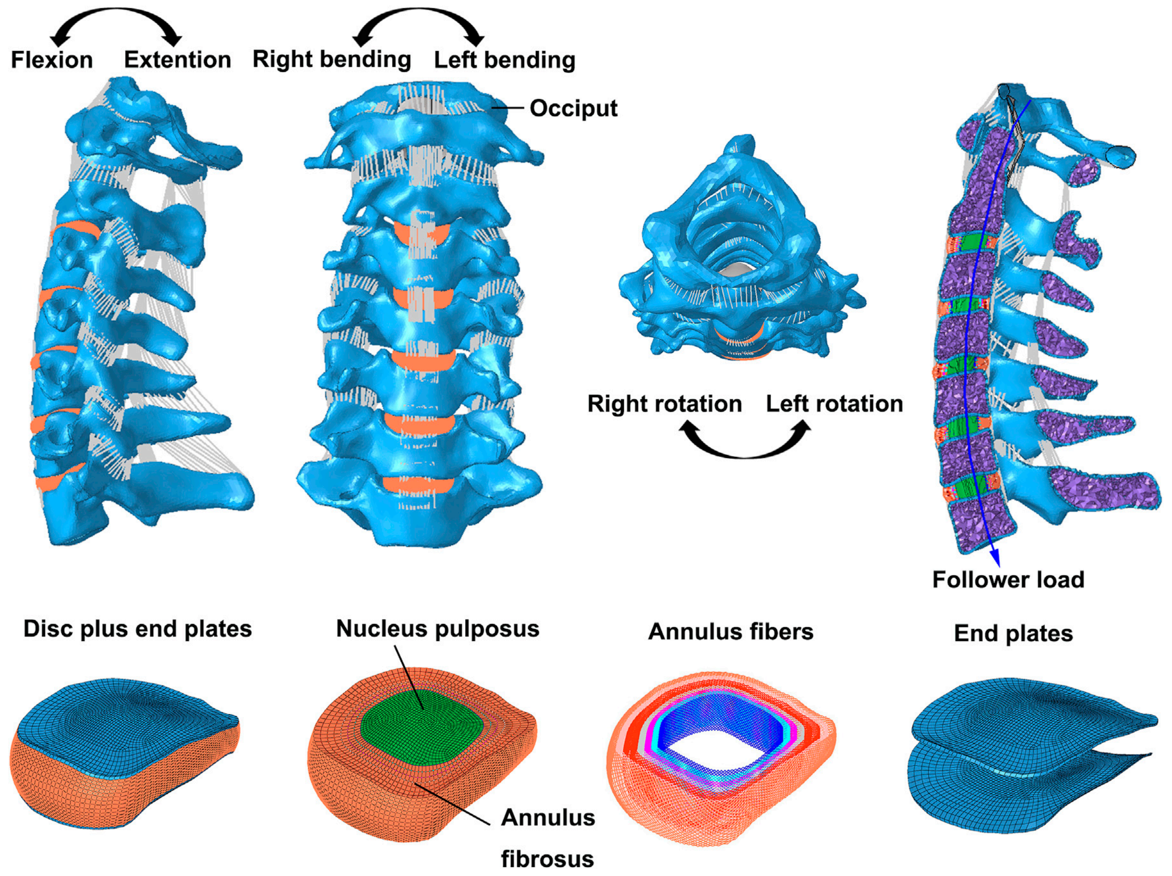

FIGURE 1 | Images of the C0–C7 intact FE model imposed with different direction moment and 73.6 N follower load, and the decomposition views of intervertebral disc plus endplates were listed.

TABLE 1 | Main material properties of the cervical finite element model.

Component	Constitutive model	Young's modulus (MPa)	Poisson's ratio	Element type
Cortical bone	Isotropic elastic	E = 10,000	ν = 0.3	C3D4 C3D8
Cancellous bone	Neo-Hookean	E = 100	ν = 0.3	C3D4
Tectorial membrane	Neo-Hookean	$C_{01} = 13.462$, D = 0.0343	—	S3
Transverse ligament	Neo-Hookean	$C_{10} = 1.923$, D = 0.24	—	S3
Nucleus pulposus	Mooney–Rivlin	$C_{10} = 0.12$, $C_{01} = 0.09$, D = 0	—	C3D8H
Annulus ground substance	Neo-Hookean	C10 = 0.1333, C01 = 0.0333, D = 0.6	—	C3D8H
Annulus fibers	Hypoelastic	350–550	ν = 0.3	T3D2
Cage	PEEK	E = 3,760	ν = 0.38	C3D4
Screws and rods	Titanium alloy	E = 110,000	ν = 0.3	C3D4

segments were completely resected (Liu et al., 2019; Herron et al., 2020; Wong et al., 2020). After decompression, a cage (Medtronic Sofamor Danek USA, Minnesota, United States) was implanted at the C5/6 segments, and both contact surfaces of the cages were ensured to be in complete contact with the corresponding endplates (Liu et al., 2019; Herron et al., 2020; Wong et al., 2020). Finally, an anterior plate-screw structure was placed at C5 and C6 segments to further stabilize the surgical segments, and the ACDF model was successfully established.

Loading and Boundary Conditions

In every FE model, loads were applied to the rigid reference point of C0, while the bottom surface of the lower endplate of C7 was fully fixed in all displacement degrees of freedom, and other vertebrae were not constrained (Zhang et al., 2006; Wong et al., 2020). First, only a pure moment of 1.0 Nm was applied to validate the intact model. A pressure load of 0.1 MPa was applied to each nucleus pulposus to mimic the biomechanical environment of the intervertebral disc during daily life *in vivo*

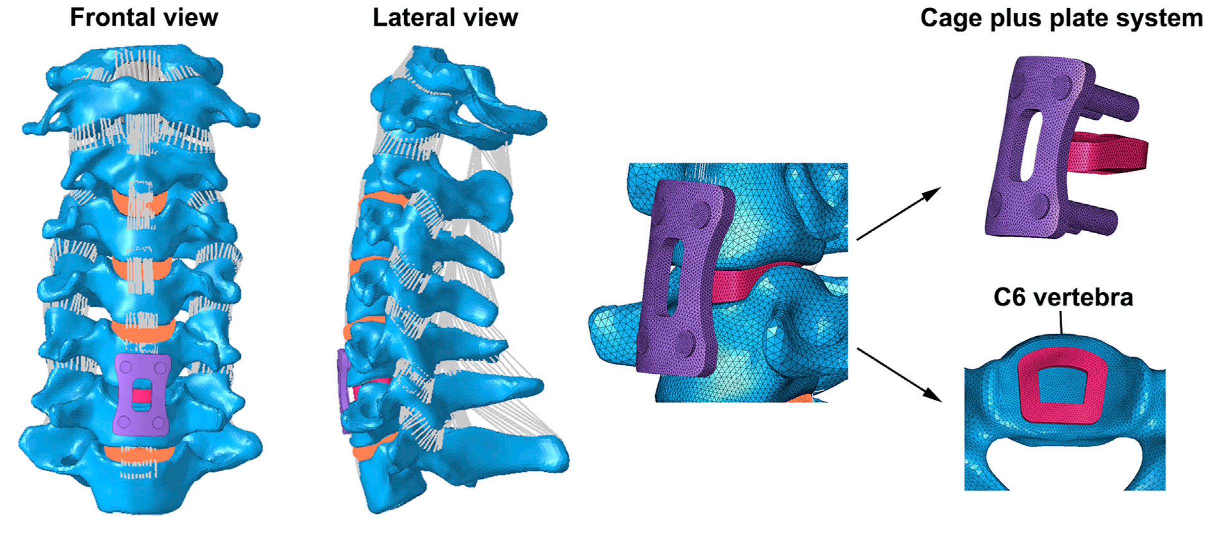

FIGURE 2 | FE model of single-level C5/6 ACDF implanted with a cage plus plate system was shown.

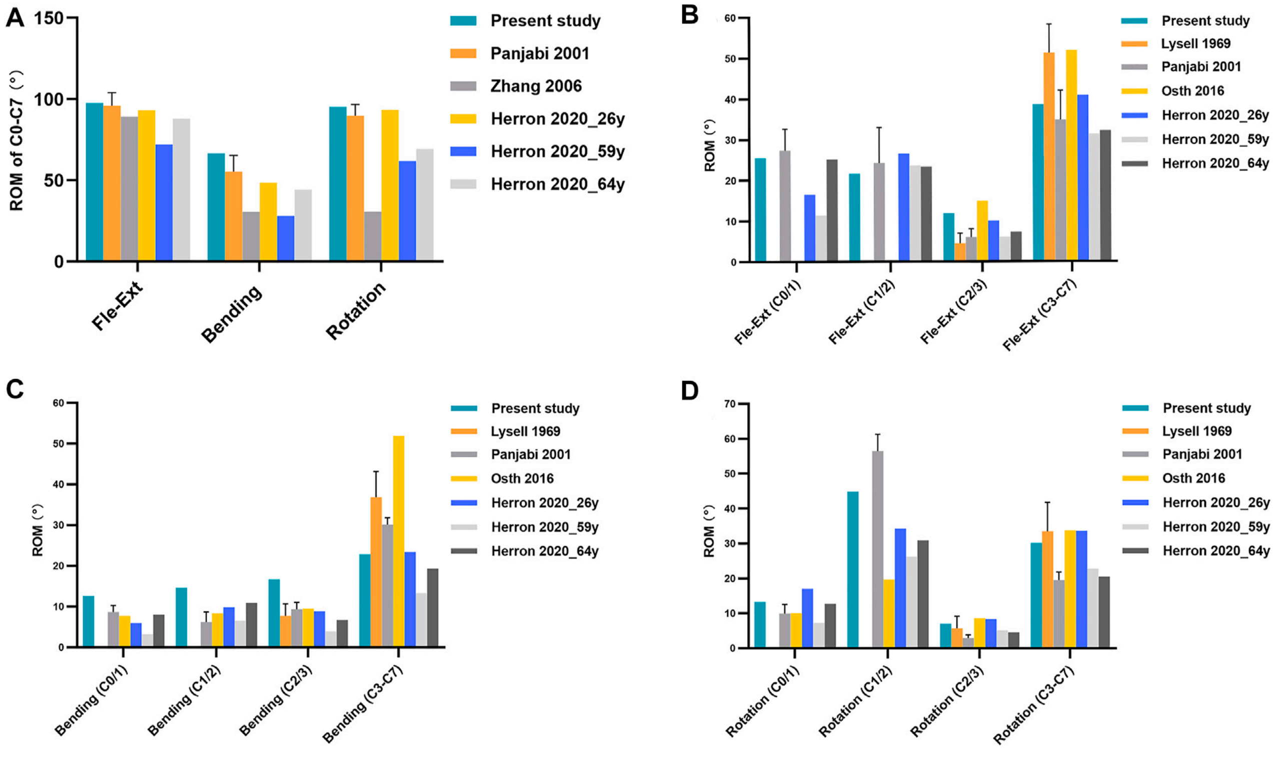

FIGURE 3 | (A) Total C0–C7 ROM, **(B-D)** intervertebral ROM of the upper cervical spine (C0–C3) and the total ROM of the lower cervical spine (C3–C7) in the intact model under a 1.0 Nm moment were compared with those of the previously published studies. Fle-Ext: flexion-extension.

(Wilke et al., 1999). Under a 73.6 N follower load, a 1.0 Nm moment was also applied in the intact model to produce different postures. The follower load of 73.6 N is a physiological compressive load along the physiological curve of the cervical spine to simulate the effect of head weight and muscle force (Mo et al., 2015; Yu et al., 2016; Wong et al., 2020) (**Figure 1**). The connector elements were created by coupling the intermediate nodes of each endplate with the endplate surface. Then, the follower load was applied at each level through the connector elements (Du et al., 2015). Under the same follower load, the ACDF model was subjected to the displacement loads of the three planes to produce different postures. The nodes in the interface

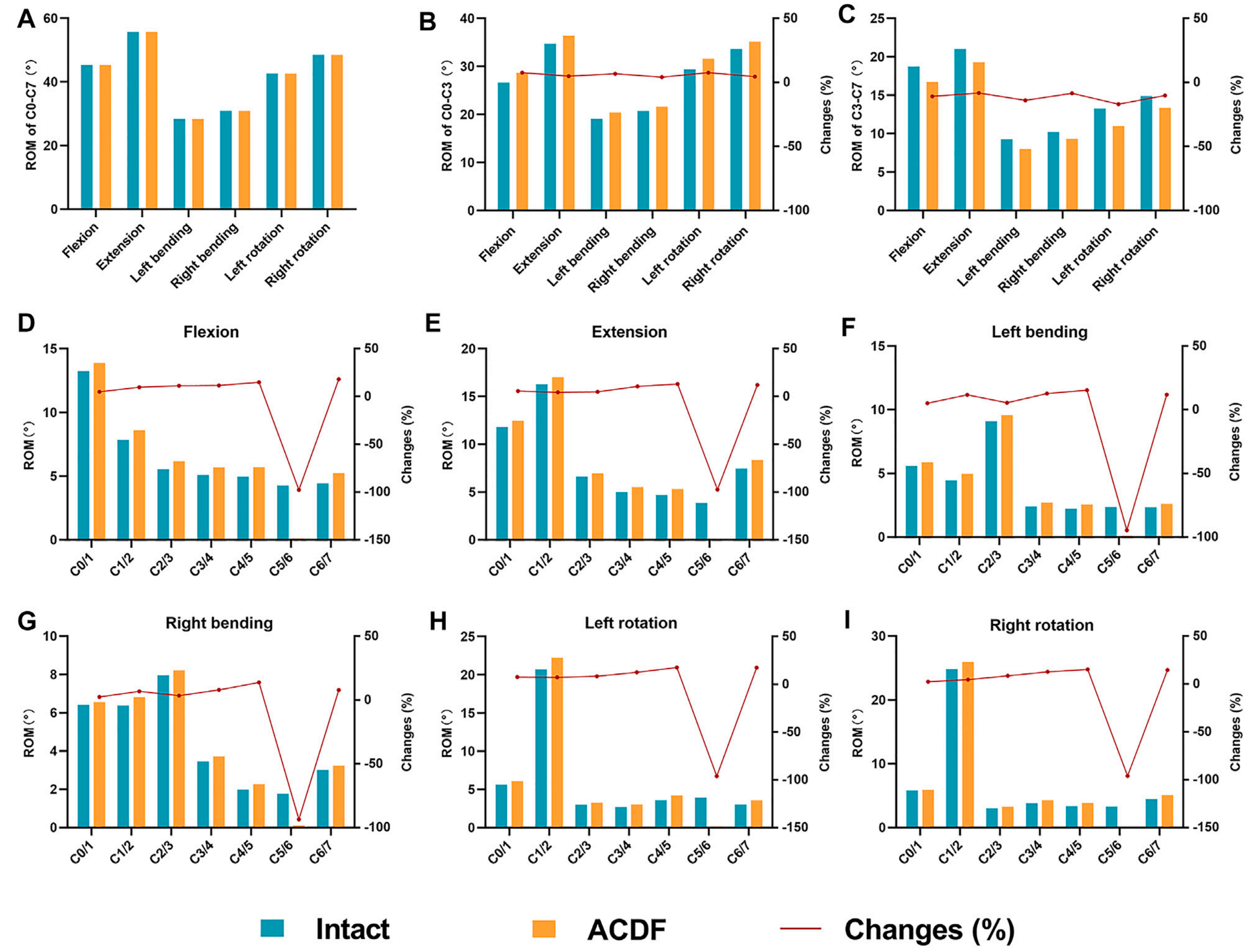

FIGURE 4 | Comparison of the ROM in the intact model and the ACDF model under the same displacement **(A)** Displacement load was applied to the ACDF model under a 73.6 N follower load resulting in a total C0–C7 ROM same as that of the intact model. **(B,C)** Total ROMs of the upper (C0–C3) and the lower (C3–C7) cervical spine **(D–I)** and the intervertebral ROMs of C0–C7 in the six motion directions was shown. Note: changes (%) = (ACDF model value—intact model value)/intact model value × 100%.

region of the screws, plate, and bone were shared to connect them in the ACDF model. Soft and frictionless contact properties were used to simulate the sliding contact between the cortical endplate of the facet joints (Mo et al., 2015). The total C0–C7 ROMs with FJF or IDP constraints in the ACDF model were calculated using the fitting function. First, the FJF or IDP values corresponding to the specific ROM of the ACDF model in the movement process were recorded. These limited numerical points were synthesized into a continuous function, which was used to calculate the function values under the specific ROM values.

RESULTS

Model Validation

To validate the intact model, the total C0–C7 ROM was calculated and compared with two FE studies (Zhang et al., 2006; Herron et al., 2020) and an *in vitro* experimental study (Panjabi et al., 2001) (**Figure 3A**). In the present study, the ROM of total C0–C7 in flexion-extension, lateral bending, and axial rotation was 97.7°, 66.7°, and 95.3°, respectively. Then, the intact model was compared with the FE analysis (Östh et al., 2016; Herron et al., 2020) and *in vitro* experiment (Lysell, 1969; Panjabi et al., 2001) results of the intervertebral ROM of the upper cervical spine (C0–C3) and total ROM of the lower cervical spine (C3–C7) (**Figures 3B–D**). The abovementioned validation results showed that the ROM values in the present intact model are consistent with those of the previously studies, suggesting that the present intact model was successfully constructed and could be used for further FE analysis.

Range of Motion

The intact model was loaded under a 1.0 Nm moment and 73.6 N follower load to determine the ROMs. The total C0–C7 ROMs in the six motion directions are shown in **Figure 4A**. The displacement loads were applied in the ACDF model under the same follower load such that the total C0–C7 ROM matched that of the intact model. In

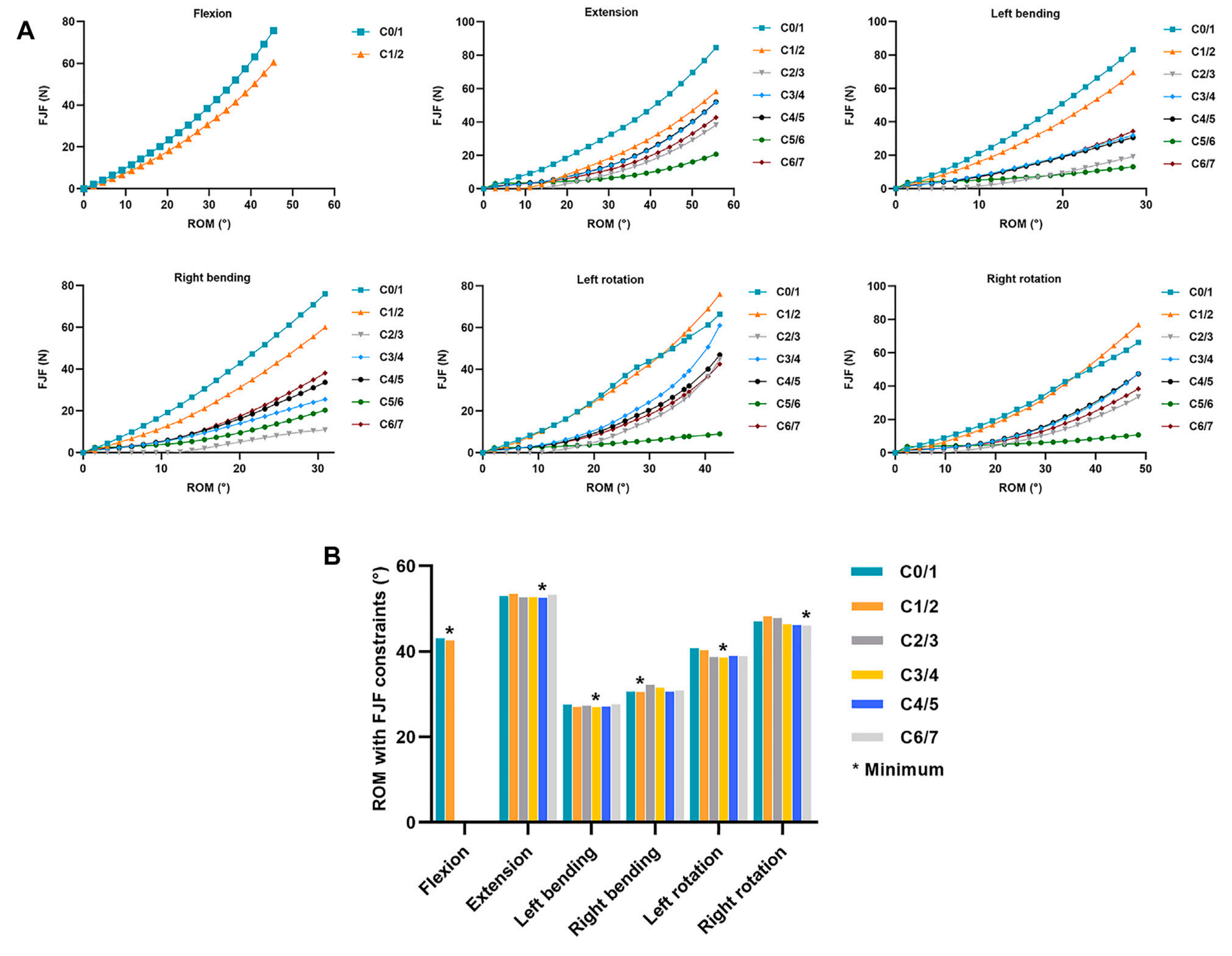

FIGURE 5 | Changes of FJF of non-fused segments in the ACDF model with increasing total C0–C7 ROM **(A)** FJF values in each segment change with increasing total C0–C7 ROM in the ACDF model. **(B)** ROMs were calculated with FJF constraints in the ACDF model, and the minimum ROM in each motion direction was labeled*.

this process, the intervertebral ROM, FJF (**Figure 5**), and IDP (**Figure 6**) and the total C0–C7 ROM in the ACDF model were determined. Compared with the intact model, the total ROM of the upper cervical spine (C0–C3) was compensatorily increased by 4.17–7.64% in the six motion directions (**Figure 4B**). Conversely, the total ROM of the lower cervical spine (C3–C7) was significantly decreased by 8.18–16.94% (**Figure 4C**). Then, the effect of C5/6 fusion on the intervertebral ROM of each segment was explored. Compared with the intact model, the results showed a compensatory increase in intervertebral ROMs in all non-fusion segments in the ACDF model, increasing from 2.04 to 18.15% (**Figures 4D–I**). The intervertebral ROM of the C5/6 surgical segments in the ACDF model was close to 0°. Moreover, the increase in ROM in adjacent segments (C4/5 and C6/7) was more significant than that in non-adjacent segments, except for C3/4 during left and right bending. Furthermore, with the increase in the distance from the surgical fusion segments, the intervertebral ROM compensation revealed a decreasing trend.

Facet Joint Force

For extension and flexion, the FJFs of both the left and right facet joints were recorded and averaged for each level. For lateral bending and axial rotation, only the forces from the loading facet joints were used. In flexion, the FJF values cannot be measured at C2–C7 because the bilateral facet joints were not in contact. Therefore, only the FJF values in the atlanto-occipital (C0/1) and the atlanto-axial (C1/2) joints were recorded during flexion. As shown in **Figure 5A**, the FJF values of each level increased by increasing total C0–C7 ROMs in all six motion directions in the ACDF model. Furthermore, the FJF values of the C0/1 and C1/2 levels were higher than those in the C2/3, C3/4, C4/5, C5/6, and C6/7 levels at the same ROM. As shown in **Figure 5B**, the total C0–C7 ROM of the ACDF model was calculated at the point where the FJF value of the ACDF model reached the maximum FJF value of the intact model. The minimum ROMs with FJF constraints in each motion direction are labeled in **Figure 5B** and are presented in **Table 2**.

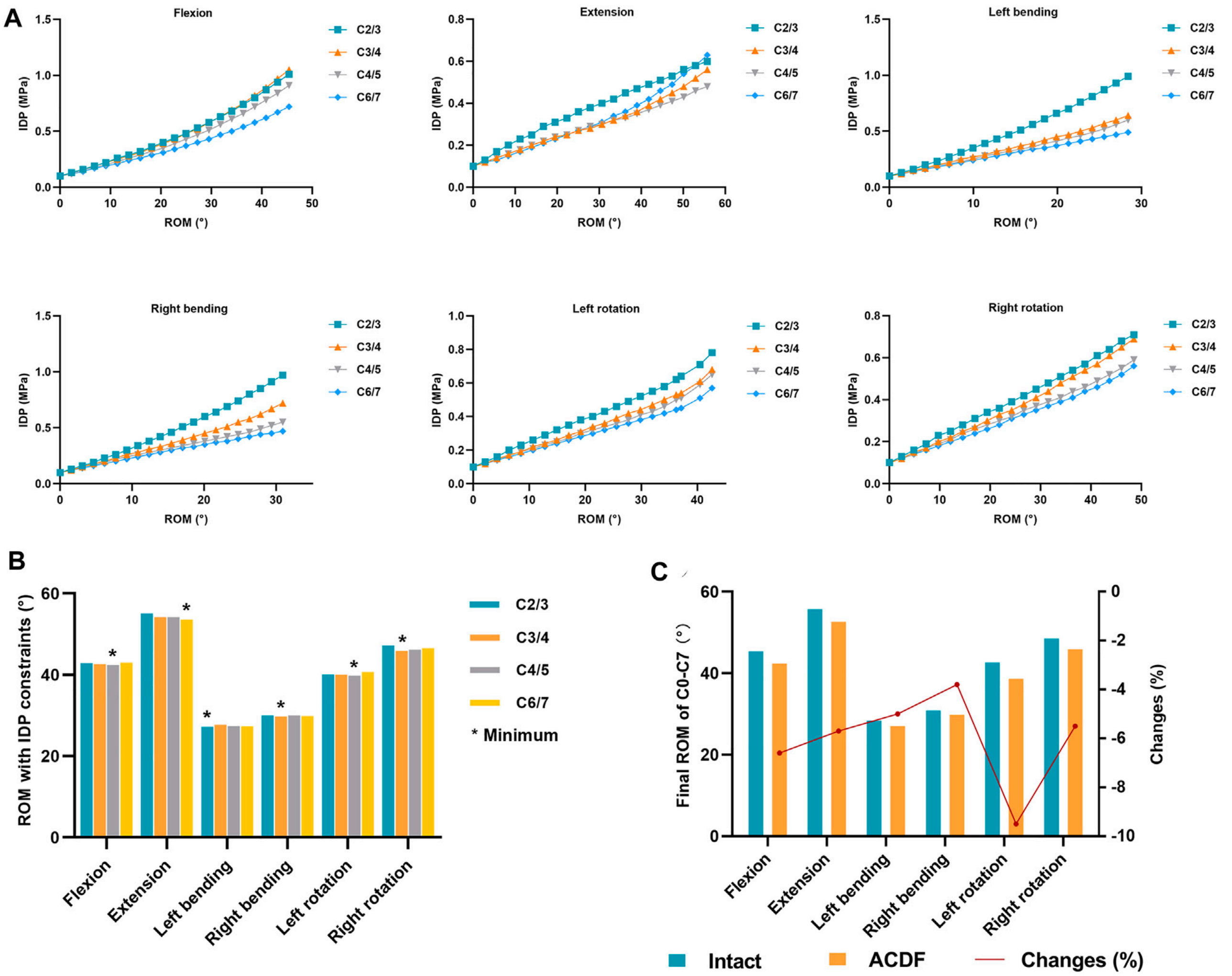

FIGURE 6 | Changes of IDP of non-fused segments in the ACDF model with increasing total C0–C7 ROM and the final reasonable total C0–C7 ROM was calculated **(A)** IDP values of C2/3, C3/4, C4/5, and C6/7 levels change with the increasing total C0–C7 ROM in the ACDF model. **(B)** ROMs were calculated with IDP constraints in the ACDF model, and the minimum ROM in each motion direction was labeled*. **(C)** Reasonable total C0–C7 ROM with FJF and IDP constraints was shown. Note: changes (%) = (ACDF model value—intact model value)/intact model value × 100%.

TABLE 2 | Reasonable total C0–C7 ROM with FJF and IDP constraints.

Subject	Flexion	Extension	Left bending	Right bending	Left rotation	Right rotation
ROM with FJF constraints (°)	42.6	52.6	27.0	30.5	38.6	46.1
ROM with IDP constraints (°)	42.4	53.6	27.2	29.8	39.8	45.9
Reasonable ROM (°)	42.4	52.6	27.0	29.8	38.6	45.9
Mean reasonable ROM (°)	42.4	52.6	28.4		42.3	
Changes (%)	6.6	5.6	4.4		7.2	

Note: changes (%) = (ACDF model value—intact model value)/intact model value × 100%.

Intradiscal Pressure

The relationship between the IDP values and the increase in total C0–C7 ROMs in the ACDF model was explored (**Figure 6A**). Because there is no disc in the C0/1 and C1/2 levels and the discs at C5/6 levels were removed in the ACDF model, only four intervertebral levels (C2/3, C3/4, C4/5, and C6/7) were analyzed. In all motion directions, the IDP values increased with increasing total C0–C7 ROMs. During flexion, left bending, right bending, left rotation, and right rotation, the IDP values of C2/3 and C3/4 levels were higher than those in the C4/5 and C6/7 levels. As shown in **Figure 6B**, the total C0–C7 ROM of the ACDF model was calculated at the point where the IDP value of the ACDF model reached the maximum IDP value of the intact model. The minimum ROMs with IDP constraints in each motion direction are labeled in **Figure 6B** and are presented in **Table 2**.

Reasonable Total C0–C7 Range of Motion After ACDF

The reasonable total C0–C7 ROMs of the ACDF model satisfied the "ROM with FJF constraint" and "ROM with IDP constraint" items, and the lower minimum total C0–C7 ROM value of each motion direction in the two constraint items was selected as the reasonable ROM (**Table 2**). As a result, the reasonable total C0–C7 ROMs were 42.4°, 52.6°, 28.4°, and 42.3° in flexion, extension, lateral bending, and axial rotation, respectively. When compared with the intact model, the reasonable ROMs of the ACDF model decreased by 4.4–7.2% (**Figure 6C**; **Table 2**).

DISCUSSION

The long-term follow-up studies of patients with ACDF surgery have shown different degrees of degeneration in non-fusion cervical segments, which are closely related to postoperative biomechanical changes in the cervical spine (Carrier et al., 2013). However, previous studies have not proposed further corresponding strategies to prevent postoperative segmental degeneration. The C5–C6 segments are found to be the most flexible segments and have a high incidence of degeneration (Miyazaki et al., 2008). To find a good way to decrease abnormally increased load on the facet joints and intervertebral disc after ACDF, we constructed a single-level C5/6 ACDF FE model of C0–C7 to determine the reasonable total C0–C7 ROMs.

Anatomically, the upper cervical vertebra was defined as the C1 and C2 vertebra. To reflect the compensatory increase in intervertebral ROM between C0/1, C1/2, and C2/3 levels of the upper cervical vertebra, the ROM of the upper cervical vertebra measured in this study was defined as C0–C3, while the ROM of the lower cervical vertebra was measured at C3–C7. Under the displacement load and 73.6 N follower loads, we found that the total ROM of the upper cervical spine was increased in the ACDF model and the total ROM of the lower cervical spine was decreased, indicating that the upper cervical spine compensated for the partial loss of C5/6 ROM.

Some studies suggested that ROMs of the adjacent segments and other non-adjacent segments showed an apparent compensatory increase after ACDF surgery (Hua et al., 2020; Wong et al., 2020; Choi et al., 2021). Many researchers have recognized that the increase in intervertebral ROM in non-fusion segments after ACDF surgery is accompanied by an increase in FJF and IDP (Eck et al., 2002; Prasarn et al., 2012; Li et al., 2015). The results of the present study were consistent with those of previous studies. Our results showed that the intervertebral ROMs of all non-fusion segments were increased for the loss of C5/6 ROM in the ACDF model when compared with the intact model. Notably, the ROM compensatory increases in adjacent segments (C4/5 and C6/7) were more significant than those in the non-adjacent segments, except for C3/4 during lateral bending. Previous studies also reported the phenomenon of more ROM compensatory in non-adjacent segments versus adjacent segments (Hua et al., 2020; Choi et al., 2021). Our results also indicated that non-adjacent segments close to the fusion segments were more likely to have more compensation for intervertebral ROM, which may result in a greater risk of degeneration.

The *in vitro* experiments have demonstrated that FJF values significantly increased in non-fusion segments after fusion, which may be the initial factor for the occurrence of segmental degeneration (Chang et al., 2007; Li et al., 2015). It was reported that when the ROM of the degenerative cervical segment was small, the segment's FJF did not significantly increase (Cai et al., 2020). However, when the ROM of the degenerative segments was increased to a certain extent, the FJF value increased significantly. This finding is consistent with the results of the present study, wherein the FJF values of each non-fusion segment increased with an increase in the total C0–C7 ROM in the ACDF model, showing a significant positive correlation. Arokoski et al. (2000) revealed that an abnormal increase in stress rate and load in daily activities leads to structural damage and mechanical failure of the articular cartilage, suggesting that changes in cervical motion state before and after ACDF surgery may lead to facet joint degeneration. Therefore, studying the reasonable motion method after cervical fusion is beneficial for finding a new solution to slow down facet joint degeneration. Moreover, the studies have shown that FJF increases with increasing disc degeneration, which may be related to the disc's abnormal morphology and reduced height (Matsunaga et al., 1999; Hussain et al., 2010).

Non-fusion segment degeneration is also always accompanied by intervertebral disc degeneration, although it remains inconclusive whether disc or facet joint degeneration occurs first (Li et al., 2015). In an *in vitro* study, Eck et al. (2002) found that a part of the disappeared ROM of the fusion segment led to a significant increase in the intervertebral disc pressure at the adjacent level, which may be the mechanism of early disc degeneration after cervical fusion. This also revealed that the IDP values increased with increasing total C0–C7 ROM in all six motion directions in the ACDF model. The increased IDP values were directly associated with a compensatory increase in intervertebral ROM at the same level. Moreover, the IDP values of the C2/3 and C3/4 segments were higher than those in the C4/5 and C6/7 segments, which may be due to the smaller stress area of C2/3 and C3/4 intervertebral discs. The mid-disc cross-sectional area at C2/3, C3/4, C4/5, and C6/7 levels were 260.00, 253.10, 283.1^2, and 310.34 mm^2, respectively.

As the main result of this study, reasonable ROMs of total C0–C7 in the ACDF model without an increase in FJF and IDP were determined. The reasonable total C0–C7 ROMs of all six motion directions decreased by 4.4–7.2% compared with those in the intact model. This result was consistent with the view that reducing intervertebral ROM compensation can reduce IDP and FJF, thereby slowing down the degeneration progress in non-fusion segments (Li et al., 2015; Cai et al., 2020; Wong et al., 2020). The present study may provide scientific guidance for postoperative rehabilitation exercise and help solve the clinical problems associated with postoperative non-fusion segment degeneration.

There are several limitations to the present study. First, the cervical spine FE model was developed based on the geometric information of the cervical spine from a single healthy person, which cannot calculate the statistical significance. Second, the neck muscles were not constructed in this model, although a widely recognized physiological follower load (Mo et al., 2015; Yu et al., 2016; Wong et al., 2020) was applied to simulate the effect of head weight and muscle force. Nevertheless, the follower load could not entirely replace the muscle functions, which might have more complex contributions to cervical motion. Third, the FE models were constructed without considering the degenerative changes such as facet hyperplasia, annular tearing, endplate sclerosis, or vertebral osteoporosis.

CONCLUSION

The present study proposed reasonable cervical ROMs to offset the increase in intervertebral FJF and IDP in non-fusion segments after ACDF. Guiding patients to perform postoperative neck exercises within reasonable ROMs to decrease the abnormal load on the facet joints and disc may help delay non-fusion segment degeneration progression. This biomechanical research approach for reasonable cervical ROMs still needs to be investigated in various single- or multi-level ACDF in the future. More relative biomechanical and clinical studies are necessary to verify the results presented in this study.

DATA AVAILABILITY STATEMENT

The original contributions presented in the study are included in the article/Supplementary Material; further inquiries can be directed to the corresponding authors.

AUTHOR CONTRIBUTIONS

All authors contributed to the research conception and design. The first draft of the manuscript was written by WL. FE model establishment, data calculation, and analyses were performed by WL and BH. The work was critically revised by YH, PY, and JY. All authors commented on previous versions of the study and read and approved the final version.

FUNDING

This work was supported by the National Key Research and Development Program of China (No. 2019YFC0120604), and Youth Science Fund of Beijing Municipal Natural Science Foundation (No. 7204264).

ACKNOWLEDGMENTS

We appreciate the guidance and support from YH and PY on this study.

REFERENCES

Alhashash, M., Shousha, M., and Boehm, H. (2018). Adjacent Segment Disease After Cervical Spine Fusion. *Spine (Phila Pa 1976)* 43 (9), 605–609. doi:10.1097/brs.0000000000002377

Arokoski, J. P. A., Jurvelin, J. S., Väätäinen, U., and Helminen, H. J. (2000). Normal and Pathological Adaptations of Articular Cartilage to Joint Loading. *Scand. J. Med. Sci. Sports* 10 (4), 186–198. doi:10.1034/j.1600-0838.2000.010004186.x

Burkhardt, B. W., Simgen, A., Wagenpfeil, G., Reith, W., and Oertel, J. M. (2018). Adjacent Segment Degeneration After Anterior Cervical Discectomy and Fusion with an Autologous Iliac Crest Graft: A Magnetic Resonance Imaging Study of 59 Patients with a Mean Follow-Up of 27 Years. *Neurosurgery* 82 (6), 799–807. doi:10.1093/neuros/nyx304

Buyukturan, B., Guclu-Gunduz, A., Buyukturan, O., Dadali, Y., Bilgin, S., and Kurt, E. E. (2017). Cervical Stability Training With and Without Core Stability Training for Patients with Cervical Disc Herniation: A Randomized, Single-Blind Study. *Eur. J. Pain* 21 (10), 1678–1687. doi:10.1002/ejp.1073

Cai, X. Y., Sang, D., Yuchi, C. X., Cui, W., Zhang, C., Du, C. F., et al. (2020). Using Finite Element Analysis to Determine Effects of the Motion Loading Method on Facet Joint Forces after Cervical Disc Degeneration. *Comput. Biol. Med.* 116, 103519. doi:10.1016/j.compbiomed.2019.103519

Carrier, C. S., Bono, C. M., and Lebl, D. R. (2013). Evidence-Based Analysis of Adjacent Segment Degeneration and Disease After ACDF: A Systematic Review. *Spine J.* 13 (10), 1370–1378. doi:10.1016/j.spinee.2013.05.050

Chang, U. K., Kim, D. H., Lee, M. C., Willenberg, R., Kim, S.-H., and Lim, J. (2007). Changes in Adjacent-Level Disc Pressure and Facet Joint Force After Cervical Arthroplasty Compared with Cervical Discectomy and Fusion. *J. Neurosurg. Spine* 7 (1), 33–39. doi:10.3171/spi-07/07/033

Chen, W. M., Jin, J., Park, T., Ryu, K. S., and Lee, S. J. (2018). Strain Behavior of Malaligned Cervical Spine Implanted with Metal-On-Polyethylene, Metal-On-Metal, and Elastomeric Artificial Disc Prostheses - A Finite Element Analysis. *Clin. Biomech.* 59, 19–26. doi:10.1016/j.clinbiomech.2018.08.005

Choi, H., Purushothaman, Y., Baisden, J. L., Rajasekaran, D., Jebaseelan, D., and Yoganandan, N. (2021). Comparative Finite Element Modeling Study of Anterior Cervical Arthrodesis versus Cervical Arthroplasty with Bryan Disc or Prodisc C. *Mil. Med.* 186 (Suppl. 1), 737–744. doi:10.1093/milmed/usaa378

Devin Leahy, P., and Puttlitz, C. M. (2012). The Effects of Ligamentous Injury in the Human Lower Cervical Spine. *J. Biomechanics* 45 (15), 2668–2672. doi:10.1016/j.jbiomech.2012.08.012

Du, C. F., Guo, J. C., Huang, Y. P., and Fan, Y. B. (2015). "A New Method for Determining the Effect of Follower Load on the Range of Motions in the Lumbar Spine," in *World Congress on Medical Physics and Biomedical Engineering* (Toronto, Canada: Springer, Cham, 326–329. doi:10.1007/978-3-319-19387-8_78

Eck, J. C., Humphreys, S. C., Lim, T. H., Jeong, S. T., Kim, J. G., Hodges, S. D., et al. (2002). Biomechanical Study on the Effect of Cervical Spine Fusion on Adjacent-Level Intradiscal Pressure and Segmental Motion. *Spine (Phila Pa 1976)* 27 (22), 2431–2434. doi:10.1097/00007632-200211150-00003

Elsawaf, A., Mastronardi, L., Roperto, R., Bozzao, A., Caroli, M., and Ferrante, L. (2009). Effect of Cervical Dynamics on Adjacent Segment Degeneration After Anterior Cervical Fusion with Cages. *Neurosurg. Rev.* 32 (2), 215–224. doi:10.1007/s10143-008-0164-2

Findlay, C., Ayis, S., and Demetriades, A. K. (2018). Total Disc Replacement versus Anterior Cervical Discectomy and Fusion. *Bone & Jt. J.* 100-B (8), 991–1001. doi:10.1302/0301-620x.100b8.Bjj-2018-0120.R1

Goffin, J., Geusens, E., Vantomme, N., Quintens, E., Waerzeggers, Y., Depreitere, B., et al. (2004). Long-Term Follow-Up After Interbody Fusion of the Cervical Spine. *J. Spinal Disord.* 17 (2), 79–85. doi:10.1097/00024720-200404000-00001

Harada, G. K., Tao, Y., Louie, P. K., Basques, B. A., Galbusera, F., Niemeyer, F., et al. (2021). Cervical Spine MRI Phenotypes and Prediction of Pain, Disability and Adjacent Segment Degeneration/Disease after ACDF. *J. Orthop. Res.* 39 (3), 657–670. doi:10.1002/jor.24658

Herron, M. R., Park, J., Dailey, A. T., Brockmeyer, D. L., and Ellis, B. J. (2020). Febio Finite Element Models of the Human Cervical Spine. *J. Biomechanics* 113, 110077. doi:10.1016/j.jbiomech.2020.110077

Hua, W., Zhi, J., Ke, W., Wang, B., Yang, S., Li, L., et al. (2020). Adjacent Segment Biomechanical Changes After One- or Two-Level Anterior Cervical Discectomy and Fusion Using Either a Zero-Profile Device or Cage Plus Plate: A Finite Element Analysis. *Comput. Biol. Med.* 120, 103760. doi:10.1016/j.compbiomed.2020.103760

Hussain, M., Natarajan, R. N., An, H. S., and Andersson, G. B. J. (2010). Patterns of Height Changes in Anterior and Posterior Cervical Disc Regions Affects the Contact Loading at Posterior Facets During Moderate and Severe Disc Degeneration. *Spine (Phila Pa 1976)* 35 (18), E873–E881. doi:10.1097/BRS.0b013e3181dc60a9

Kallemeyn, N., Gandhi, A., Kode, S., Shivanna, K., Smucker, J., and Grosland, N. (2010). Validation of a C2-C7 Cervical Spine Finite Element Model Using Specimen-Specific Flexibility Data. *Med. Eng. Phys.* 32 (5), 482–489. doi:10.1016/j.medengphy.2010.03.001

Kumagai, G., Wada, K., Kudo, H., Asari, T., Chiba, D., Ota, S., et al. (2019). Associations Between Cervical Disc Degeneration and Muscle Strength in a Cross-Sectional Population-Based Study. *PloS One* 14 (1), e0210802. doi:10.1371/journal.pone.0210802

Li, H., Pei, B. Q., Yang, J. C., Hai, Y., Li, D. Y., and Wu, S. Q. (2015). Load Rate of Facet Joints at the Adjacent Segment Increased After Fusion. *Chin. Med. J. Engl.* 128 (8), 1042–1046. doi:10.4103/0366-6999.155080

Liu, N., Lu, T., Wang, Y., Sun, Z., Li, J., and He, X. (2019). Effects of New Cage Profiles on the Improvement in Biomechanical Performance of Multilevel Anterior Cervical Corpectomy and Fusion: A Finite Element Analysis. *World Neurosurg.* 129, e87–e96. doi:10.1016/j.wneu.2019.05.037

Lopez-Espina, C. G., Amirouche, F., and Havalad, V. (2006). Multilevel Cervical Fusion and its Effect on Disc Degeneration and Osteophyte Formation. *Spine (Phila Pa 1976)* 31 (9), 972–978. doi:10.1097/01.brs.0000215205.66437.c3

Lu, T., and Lu, Y. (2019). Comparison of Biomechanical Performance Among Posterolateral Fusion and Transforaminal, Extreme, and Oblique Lumbar Interbody Fusion: A Finite Element Analysis. *World Neurosurg.* 129, e890–e899. doi:10.1016/j.wneu.2019.06.074

Lu, T., and Lu, Y. (2020). Interlaminar Stabilization Offers Greater Biomechanical Advantage Compared to Interspinous Stabilization After Lumbar Decompression: A Finite Element Analysis. *J. Orthop. Surg. Res.* 15 (1), 291. doi:10.1186/s13018-020-01812-5

Lysell, E. (1969). Motion in the Cervical Spine: An Experimental Study on Autopsy Specimens. *Acta Orthop. Scand.* 40 (Suppl. 123), 1–61. doi:10.3109/ort.1969.40.suppl-123.01

Matsunaga, S., Kabayama, S., Yamamoto, T., Yone, K., Sakou, T., and Nakanishi, K. (1999). Strain on Intervertebral Discs After Anterior Cervical Decompression and Fusion. *Spine (Phila Pa 1976)* 24 (7), 670–675. doi:10.1097/00007632-199904010-00011

Miyazaki, M., Hong, S. W., Yoon, S. H., Zou, J., Tow, B., Alanay, A., et al. (2008). Kinematic Analysis of the Relationship Between the Grade of Disc Degeneration and Motion Unit of the Cervical Spine. *Spine (Phila Pa 1976)* 33 (2), 187–193. doi:10.1097/BRS.0b013e3181604501

Mo, Z., Zhao, Y., Du, C., Sun, Y., Zhang, M., and Fan, Y. (2015). Does Location of Rotation Center in Artificial Disc Affect Cervical Biomechanics? *Spine (Phila Pa 1976)* 40 (8), E469–E475. doi:10.1097/brs.0000000000000818

Oliver, J. D., Goncalves, S., Kerezoudis, P., Alvi, M. A., Freedman, B. A., Nassr, A., et al. (2018). Comparison of Outcomes for Anterior Cervical Discectomy and Fusion With and Without Anterior Plate Fixation. *Spine (Phila Pa 1976)* 43 (7), E413–E422. doi:10.1097/brs.0000000000002441

Östh, J., Brolin, K., Svensson, M. Y., and Linder, A. (2016). A Female Ligamentous Cervical Spine Finite Element Model Validated for Physiological Loads. *J. Biomech. Eng.* 138 (6), 061005. doi:10.1115/1.4032966

Panjabi, M. M., Crisco, J. J., Vasavada, A., Oda, T., Cholewicki, J., Nibu, K., et al. (2001). Mechanical Properties of the Human Cervical Spine as Shown by Three-Dimensional Load-Displacement Curves. *Spine (Phila Pa 1976)* 26 (24), 2692–2700. doi:10.1097/00007632-200112150-00012

Prasarn, M. L., Baria, D., Milne, E., Latta, L., and Sukovich, W. (2012). Adjacent-Level Biomechanics After Single versus Multilevel Cervical Spine Fusion. *J. Neurosurg. Spine* 16 (2), 172–177. doi:10.3171/2011.10.Spine11116

Tamai, K., Grisdela, P., Romanu, J., Paholpak, P., Nakamura, H., Wang, J. C., et al. (2019). The Impact of Cervical Spinal Muscle Degeneration on Cervical Sagittal Balance and Spinal Degenerative Disorders. *Clin. Spine Surg.* 32 (4), E206–E213. doi:10.1097/bsd.0000000000000789

Wada, K., Tanaka, T., Kumagai, G., Kudo, H., Asari, T., Chiba, D., et al. (2018). A Study of the Factors Associated with Cervical Spinal Disc Degeneration, with a Focus on Bone Metabolism and Amino Acids, in the Japanese Population: A Cross Sectional Study. *BMC Musculoskelet. Disord.* 19 (1), 153. doi:10.1186/s12891-018-2055-1

Wilke, H. J., Neef, P., Caimi, M., Hoogland, T., and Claes, L. E. (1999). New *In Vivo* Measurements of Pressures in the Intervertebral Disc in Daily Life. *Spine (Phila Pa 1976)* 24 (8), 755–762. doi:10.1097/00007632-199904150-00005

Wong, C. E., Hu, H. T., Hsieh, M. P., and Huang, K. Y. (2020). Optimization of Three-Level Cervical Hybrid Surgery to Prevent Adjacent Segment Disease: A Finite Element Study. *Front. Bioeng. Biotechnol.* 8, 154. doi:10.3389/fbioe.2020.00154

Yu, C. C., Liu, P., Huang, D. G., Jiang, Y. H., Feng, H., and Hao, D. J. (2016). A New Cervical Artificial Disc Prosthesis Based on Physiological Curvature of End Plate: A Finite Element Analysis. *Spine J.* 16 (11), 1384–1391. doi:10.1016/j.spinee.2016.06.019

Zhang, Q. H., Teo, E. C., Ng, H. W., and Lee, V. S. (2006). Finite Element Analysis of Moment-Rotation Relationships for Human Cervical Spine. *J. Biomechanics* 39 (1), 189–193. doi:10.1016/j.jbiomech.2004.10.029

Zhu, B., Xu, Y., Liu, X., Liu, Z., and Dang, G. (2013). Anterior Approach versus Posterior Approach for the Treatment of Multilevel Cervical Spondylotic Myelopathy: A Systemic Review and Meta-Analysis. *Eur. Spine J.* 22 (7), 1583–1593. doi:10.1007/s00586-013-2817-2

Conflict of Interest: The authors declare that the research was conducted in the absence of any commercial or financial relationships that could be construed as a potential conflict of interest.

frontiers | Frontiers in Bioengineering and Biotechnology

ORIGINAL RESEARCH
published: 28 June 2022
doi: 10.3389/fbioe.2022.891632

Biodegradability and Cytocompatibility of 3D-Printed Mg-Ti Interpenetrating Phase Composites

Xixiang Yang[1], Wanyi Huang[1], Desong Zhan[1], Dechun Ren[2], Haibin Ji[2], Zengqian Liu[2], Qiang Wang[1], Ning Zhang[1]* and Zhefeng Zhang[2]*

[1]*School and Hospital of Stomatology, China Medical University, Liaoning Provincial Key Laboratory of Oral Diseases, Shenyang, China,* [2]*Shi-Changxu Innovation Center for Advanced Materials, Institute of Metal Research, Chinese Academy of Sciences, Shenyang, China*

Orthopedic hybrid implants combining both titanium (Ti) and magnesium (Mg) have gained wide attraction nowadays. However, it still remains a huge challenge in the fabrication of Mg-Ti composites because of the different temperatures of Ti melting point and pure Mg volatilization point. In this study, we successfully fabricated a new Mg-Ti composite with bi-continuous interpenetrating phase architecture by infiltrating Mg melt into Ti scaffolds, which were prepared by 3D printing and subsequent acid treatment. We attempted to understand the 7-day degradation process of the Mg-Ti composite and examine the different Mg^{2+} concentration composite impacts on the MC3T3-E1 cells, including toxicity, morphology, apoptosis, and osteogenic activity. CCK-8 results indicated cytotoxicity and absence of the Mg-Ti composite during 7-day degradation. Moreover, the composite significantly improved the morphology, reduced the apoptosis rate, and enhanced the osteogenic activity of MC3T3-E1 cells. The favorable impacts might be attributed to the appropriate Mg^{2+} concentration of the extracts. The results on varying Mg^{2+} concentration tests indicated that Mg^{2+} showed no cell adverse effect under 10-mM concentration. The 8-mM group exhibited the best cell morphology, minimum apoptosis rate, and maximum osteogenic activity. This work may open a new perspective on the development and biomedical applications for Mg-Ti composites.

Keywords: 3D printing, Mg-Ti composite, degradation, Mg^{2+}, MC3T3-E1 cells

Edited by:
Liqiang Wang,
Shanghai Jiao Tong University, China

Reviewed by:
Shokouh Attarilar,
Shanghai Jiao Tong University, China
Chunguang Yang,
Institute of Metal Research (CAS), China
Peng Chen,
Tokyo Medical and Dental University, Japan

***Correspondence:**
Qiang Wang
mfqwang@cmu.edu.cn
Ning Zhang
zhangning_513@sohu.com

Specialty section:
This article was submitted to Biomaterials, a section of the journal Frontiers in Bioengineering and Biotechnology

Received: *08 March 2022*
Accepted: *19 May 2022*
Published: *28 June 2022*

Citation:
Yang X, Huang W, Zhan D, Ren D, Ji H, Liu Z, Wang Q, Zhang N and Zhang Z (2022) Biodegradability and Cytocompatibility of 3D-Printed Mg-Ti Interpenetrating Phase Composites. Front. Bioeng. Biotechnol. 10:891632. doi: 10.3389/fbioe.2022.891632

1 INTRODUCTION

In the last few decades, there has been an overwhelming increase in the research on medical devices and implants because of aging population and ever-increasing human life expectancy. In particular, in the field of orthopedics, the number of orthopedic implant surgeries is constantly increasing. Ideal orthopedic implant materials should be outlined with the following characteristics (Witte 2010; Attarilar et al., 2020a): 1) good biocompatibility, 2) sufficient mechanical strength without the stress shielding effect, and 3) biological activity to promote healing.

Metals, ceramics, polymers, and composites are the commonly used orthopedics. Among them, metals are most suitable for wide applications in clinical conditions (Kandala et al., 2021). Ti and its alloys represent a feasible choice among materials for metallic orthopedic implants because of their satisfactory biocompatibility, high corrosion resistance, and excellent mechanical properties (Geetha et al., 2009; He et al., 2015; Zhu et al., 2016). Despite the mentioned advantages, their further clinical application remains a challenge due to some major drawbacks such as the stress shielding effect and being biologically inert (Stanec et al., 2016; Bobbert et al., 2017). Various methods of fabricating less stiff modulus orthopedic implants have been reported (Ouyang et al., 2019; Esen et al., 2020; Liang et al., 2021; Xu et al., 2021), and the control of porosity is considered a promising method (Meenashisundaram et al., 2020; Zhang et al., 2020; Zhang et al., 2021). On one hand, the porous structure of Ti-based materials effectively reduced the stress shielding effect between the implant and the surrounding bone. On the other hand, it can induce blood supply to the scaffold to supply oxygen and nourishment needed for tissue repair, promoting the generation and calcification of new bone tissues (Liu et al., 2015; Claros et al., 2016; de Krijger et al., 2017). Furthermore, the bioactivity of Ti and Ti alloys can also be improved by adding other elements, such as magnesium and zinc, into the porous structure (Wong et al., 2017; Yao et al., 2022).

Recently, Mg and Mg alloys have been widely designed and reported as potential biodegradable orthopedic implant materials (Witte et al., 2005). Compared with other biomedical metals, Mg-based implants have become increasingly attractive because of their appropriate mechanical properties, such as low density, high specific strength, and low elastic modulus (Mps et al., 2006). The elastic modulus of Mg is close to that of the bone, and it can effectively decrease the stress shielding effect at the bone-implant interface (Li et al., 2016; Wang N et al., 2020). Moreover, as one of the most abundant elements in the human body, Mg can be degraded and absorbed along with the human body's self-healing. In addition, the functional effects of Mg include regulating bone metabolism, stimulating new bone formation, and increasing bone cell adhesion (Li et al., 2018).

For the aforementioned reasons, the combination of Ti and Mg seems a promising new idea for fabricating ideal biomedical materials. Martin et al. and Balog et al., (2019) successfully produced Ti+ (12, 17, and 24 vol.%) Mg composites by powder metallurgy. The mechanical and bioactive properties of the composites demonstrated immense potential for application as dental implants. However, Mg filaments were arrayed along the extrusion direction and embedded in the Ti matrix. In the case of low Mg content, the filaments could barely connect with each other. Ouyang et al. (2019) reported that a new Mg-Ti composite was manufactured through the process of spark plasma sintering (SPS). Despite the composite exhibiting good mechanical properties, the Mg-rich regions were non-uniformly distributed among the Ti matrix. In general, it is difficult to achieve ideal Mg-Ti composite biomedical materials using the traditional casting methods. In this context, 3D printing offers many advantages in manufacturing orthopedic implants, including free designation and high precision (Campanelli et al., 2017). Three-dimensional printing takes full advantage of the possibilities to realize the addition of functional elements in Ti alloys and the processing of implants with porous structures (Attarilar et al., 2020b; Fan et al., 2021). The type of repeating unit cell and its dimensions can be chosen to adjust the mechanical properties of the porous biomaterials to achieve an excellent match for the mechanical properties of bone (Eltorai, Nguyen and Daniels 2015; Stanec et al., 2016).

In our previous study (Zhang et al., 2020), we proposed a new fabrication approach to create a good combination of properties in a Mg-NiTi composite. This approach is also applicable in engineering other material systems to improve performance. In the present study, a pure Ti scaffold with three-dimensional (3D) interpenetrating phase architecture was fabricated by the 3D printing technology. We fabricated a Mg-Ti composite by pressureless infiltration of the Mg melt into the scaffold. The degradation behavior of the Mg-Ti interpenetrating phase composite *in vitro* and the bio-compatibility of the Mg-Ti composite degradation process were evaluated. Then, the effect of Mg^{2+}, produced in the degradation process, on MC3T3-E1 cells was investigated by various Mg^{2+} concentration tests.

2 MATERIALS AND METHODS

2.1 Material Preparation and Characterization

The fabrication methods of the Mg-Ti composite can be seen in our previous study (Zhang et al., 2020). In the following tests, we chose commercial pure Mg as the control material. Scanning electron microscope (SEM, Zeiss Merlin Compact, Zeiss, Germany) imaging coupled with energy-dispersive spectroscopy (EDS) analysis was performed to characterize the microstructure of the Mg-Ti composite and pure Mg specimens. All the specimens with a size of φ10 mm × 2 mm were prepared for the *in vitro* studies and immersion tests. Silicon carbide (SiC) papers were used to polish the samples to 800–2000 grit. Then, the disc samples were cleaned with distilled water for 10 min and sterilized with ultraviolet for 40–60 min, following ultrasonic etching in acetone and ethyl alcohol.

2.2 Immersion Test

All the samples for the immersion test were placed in 12-well cell culture plates and immersed in modified Eagle's medium alpha (α-MEM) supplemented with 10% fetal bovine serum (FBS) at 37°C for 1, 3, 5, and 7-days. The immersion ratio was fixed as $1.25\ cm^2/ml$ with the α-MEM medium refreshed every 24 h. The medium pH value at regular time points was determined by using a pH detection device (PHS-3C, Leica, China). The corrosion products produced in the process of degradation were dried by hot air, following the removal with a chromic acid solution (200 g/L CrO_3+ 10 g/L $AgNO_3$). Then, the samples' morphology was assessed by using a digital camera, and the microstructure was analyzed by SEM and EDS.

2.3 *In Vitro* Cell Tests

2.3.1 Extract Preparation and Cell Culture

The extracts were used for the *in vitro* tests. After 1, 3, 5, and 7-days of immersion, the Mg-Ti composite and pure Mg samples were immersed in an α-MEM medium containing 10% FBS for 72 h at 37°C in a humidified atmosphere of 5% CO_2. The immersion ratio was selected, as mentioned previously according to the standard ISO 10993. After filtrating with a filter (0.22 μm), the extracts were collected and then diluted six times with the α-MEM medium for *in vitro* tests.

MC3T3-E1 cells were chosen to test cell morphology, proliferation, apoptosis, and differentiation. The cells were cultured in α-MEM supplemented with 10% FBS and 1% penicillin and streptomycin in a humidified atmosphere at 37°C with 5% CO_2. When the monolayer reached sub-confluence, the cells were subcultured with 0.25% trypsin.

2.3.2 Cell Proliferation and Cytotoxicity Test

Cell-Counting Kit-8 (CCK-8, United States Everbright Inc., Silicon Valley, United States) assay was chosen to evaluate the effects of the Mg-Ti composite and pure Mg extracts on cell proliferation. Cells were seeded in 96-well plates at 3×10^3 cells/well for 24 h. They were washed twice with PBS, and the medium was replaced by 100 μl extracts or a normal culture medium after 24 h of attachment. After 1, 2, and 3-days of culturing, 100 μl α-MEM with 10% CCK-8 was added after rinsing twice with PBS; then, the plate was incubated for 2 h at 37°C. The 450 nm optical density was measured by using a microplate reader (Infinite M200, Tecan, Austria). Three replicates were chosen per group.

2.3.3 Cell Morphology Staining

To detect the effect of the Mg-Ti composite and pure Mg extracts on cell morphology, MC3T3-E1 cells were incubated on a 24-well cell culture plate with the diluted extracts at a density of 1×10^4 per well for 4 and 24 h. At each time point, the cells were permeabilized with 0.1% Triton X-100 after washing with PBS three times. Then, the permeabilized cells were supplemented with 100 nmol/L rhodamine-phalloidin (Cytoskeleton, Inc., Denver, CO, United States) for 30 min in the dark at room temperature. After that, the cells were stained with DAPI for 2 min coupled with washing with PBS three times before observation with a fluorescence microscope (ZEISS, Germany).

2.3.4 Cell Apoptosis

An Annexin V-FITC/PI kit (United States Everbright Inc., Silicon Valley, United States) was used to detect the effects of the sample extracts on cell apoptosis quantified through the standard flow cytometry test, according to the manufacturer's protocol. MC3T3-E1 cells were seeded in 12-well plates at 1×10^5 cells/well in a 1 ml medium for 24 h. The medium was replaced by prepared extracts or a normal culture medium, respectively, for 1 and 3-days. At each time point, the cells were digested with 0.25% trypsin and collected for the stain after washing with PBS three times. The collected cells were re-suspended with 100 μl binding buffer and stained with Annexin V-FITC and propidium iodide (PI) for 15 min in the dark. Before the flow cytometry (BD, LSRFortessa, United States) test, 300 μl binding buffer was added to each sample and blended evenly.

2.3.5 Alkaline Phosphatase (ALP) Activity

MC3T3-E1 cells were seeded in 12-well plates at 1×10^5 cells/well for 24 h. The culture medium was replaced with the prepared extracts, and the culture medium contained an osteogenesis-inducing component. The extracts were refreshed every 2-days. The activity of ALP was evaluated with an Alkaline Phosphatase Assay Kit, according to the manufacturer's instructions (Beyotime, China) after culture for 7 and 14-days. The protein content was measured following the protocol of the BCA protein assay kit (Beyotime, China). The ALP activity test of all samples was normalized using the protein concentration.

2.4 Cell Responses to Varying Mg^{2+} Concentrations

2.4.1 Preparation of the Medium With Varying Mg^{2+} Concentrations

To simulate the effect of 7-day degradation of Mg^{2+} production on MC3T3-E1 cells, we prepared α-MEM with varying Mg^{2+} concentrations. First, inductively coupled plasma mass spectrometry (7800 ICP-MS, Agilent, United States) was performed to detect the Mg^{2+} concentration of pure Mg and Mg-Ti composite extracts. Then, the sterilized Mg chloride solution was applied to elevate the α-MEM Mg^{2+} concentration, according to the result of the Mg^{2+} concentration test.

2.4.2 Effect of Varying Mg^{2+} Concentrations on MC3T3-E1 Cells

CCK-8 assay was performed to evaluate the effects of varying Mg^{2+} concentrations on MC3T3-E1 cells in cytotoxic and proliferation ability. The cell morphology was stained with phalloidin to observe the effect of varying Mg^{2+} concentrations on the intracellular F-actin cytoskeletal network for 4 and 24 h. The cell apoptosis rate of MC3T3-E1 cells incubated with varying Mg^{2+} concentrations was determined by Annexin V-FITC/PI double staining for the period of 1 and 3-days. To determine the effect of varying Mg^{2+} concentrations on the osteogenic differentiation ability, an ALP assay was carried out after incubation for 7-days and 14-days.

2.5 Statistical Analysis

All experiments were repeated by at least three times for statistical purposes. Statistical analysis was performed with SPSS 25.0 software. Differences between the groups were analyzed by one-way analysis of variance (ANOVA) followed by Tukey's test.

3 RESULTS

3.1 Morphology and Microstructure Characterization

Figure 1 shows the morphology and microstructures of the Mg-Ti composite. The microstructure and elemental composition of samples are analyzed *via* SEM coupled with EDS. SEM images show that the surface of the sample was smooth without obvious structural flaws, for example, pores or micro-cracks. It indicates that after the infiltration of the Mg melt into the Ti scaffold and subsequent solidification, the Mg-Ti composite materials are highly densified with the Mg and Ti phases interpenetrating the 3D space. In addition, the width of the Mg phase or the interspace between neighboring Ti struts is close to 700 μm in the sample. To further detect the element distribution, EDS is performed. The EDS analysis presents that Ti and Mg are the main elements in all tested specimens.

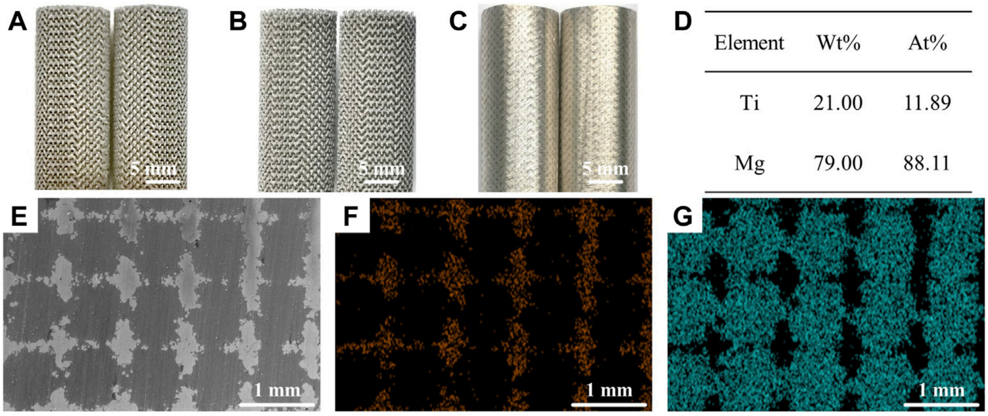

Element	Wt%	At%
Ti	21.00	11.89
Mg	79.00	88.11

FIGURE 1 | Morphology of the Mg-Ti composite. **(A–C) (A)** 3D-printed Ti scaffold. **(B)** Ti scaffold after acid treatment. **(C)** Mg melt infiltration into the Ti scaffold. EDS results **(D)** and the corresponding SEM images **(E–G)** of the Mg-Ti composite, **(F)** Ti, and **(G)** Mg.

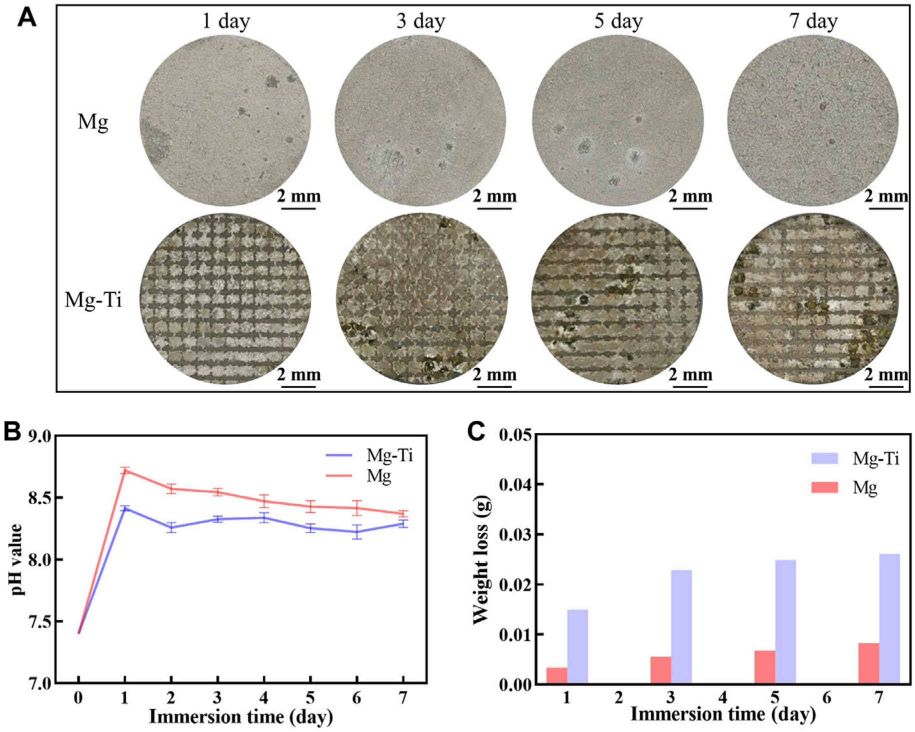

FIGURE 2 | (A) Corroded surface photographs of pure Mg and Mg-Ti composite (corrosion products were removed). **(B)** pH values of pure Mg and the Mg-Ti composite in the α-MEM solution with 10% FBS at 37°C and 5% CO_2. **(C)** Weight loss of pure Mg and Mg-Ti composite.

3.2 Immersion Test

Figure 2 shows the results of pH value, weight loss, and macroscopic morphology of pure Mg and Mg-Ti composites. It is observed that the pH values of the Mg-Ti composite and pure Mg extracts both reached the maximum on the first day. The pH values of the Mg-Ti group are higher than those of the Mg group at all the test time points. The degradation of Mg proceeds gradually, slows down with the immersion time, and then becomes saturated after 7-days for both the Mg-Ti composite and pure Mg. The weight loss of the Mg-Ti composite is much higher than that of pure Mg after immersion for 7-days. It reaches a saturation point for the Mg-Ti composite and pure Mg after 5-days of degradation. The macroscopic appearance of the pure Mg and Mg-Ti composite shows that the degradation starts from the edge and extends toward the center of the materials with the increase in immersion time.

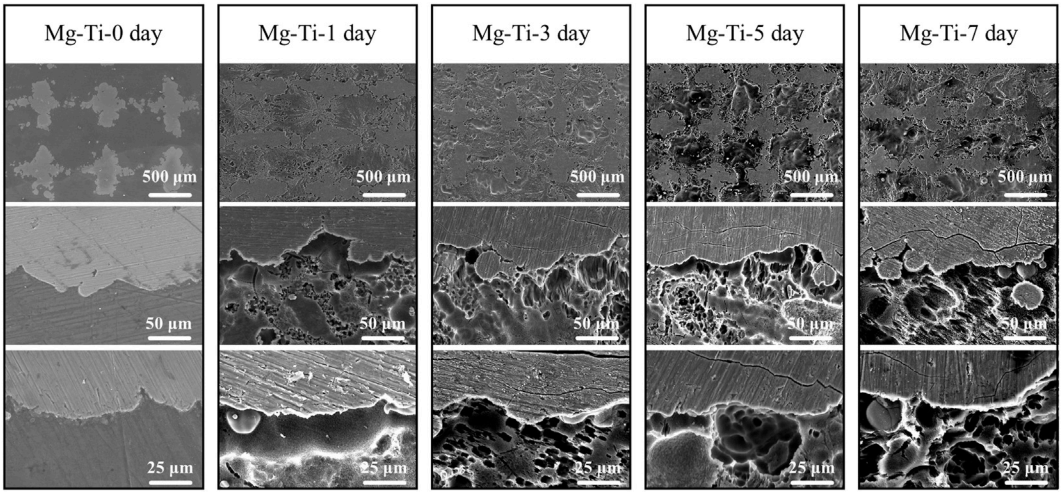

FIGURE 3 | Microscopic morphology of the Mg-Ti composite after 0, 1, 3, 5, and 7 days of degradation (corrosion products were removed).

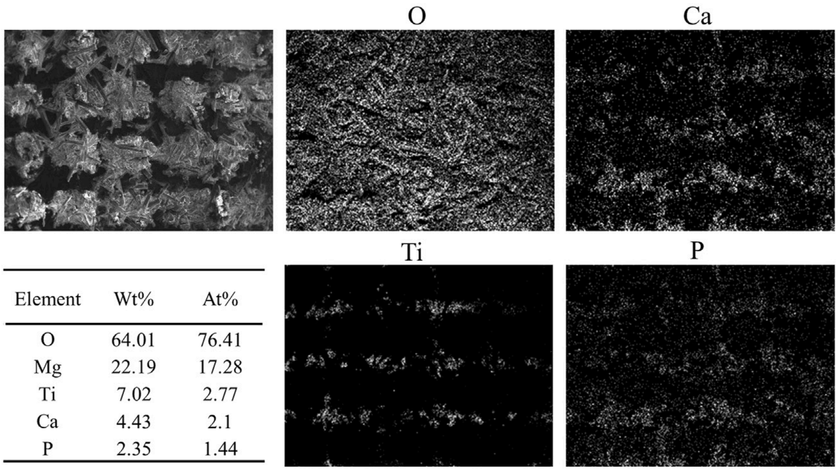

Element	Wt%	At%
O	64.01	76.41
Mg	22.19	17.28
Ti	7.02	2.77
Ca	4.43	2.1
P	2.35	1.44

FIGURE 4 | SEM images and EDS analysis of the Mg-Ti composite after 7 days of degradation.

Figure 3 shows the microscopic morphology of the Mg-Ti composite within 7-days of degradation. After removing the corrosion products, it can be observed that the Ti matrix in the Mg-Ti composite is almost integrated, whereas the Mg area is partially degraded. Several corrosion pits or cracks are basically observed in the Mg-rich area, whereas very few are observed in the Ti area. From the microscopic point of view, the degradation of the Mg-Ti composite starts from the interface of the Ti and Mg region, leading to a porous morphology of the corroded Mg area. With the prolongation of immersion time, the corroded area of the Mg region is extended and spreads to the central regions of Mg. **Figure 4** shows the SEM and EDS images of the corrosion product of the Mg-Ti composite after 7-days of degradation. The Ca/P rate is close to 1.4.

3.3 *In Vitro* Cytocompatibility of MC3T3-E1 Cells

3.3.1 Mg^{2+} Concentration of Extracts

Figure 5 shows the Mg^{2+} concentration of pure Mg and the Mg-Ti composite extracts at different periods of immersion time. The Mg-1 day group exhibits the highest Mg^{2+} concentration (9.6 mM). With the immersion time prolonged, the Mg^{2+} concentration for the pure Mg groups decreases gradually and eventually stabilizes for 5-days (3 mM). For the Mg-Ti group, the Mg^{2+} concentration remains stable around 8 mM in the process of 7-days of degradation. Thereby, we selected a range of concentrations (2, 4, 6, 8, and 10 mM) to detect the effect of various Mg^{2+} concentrations on MC3T3-E1 cells.

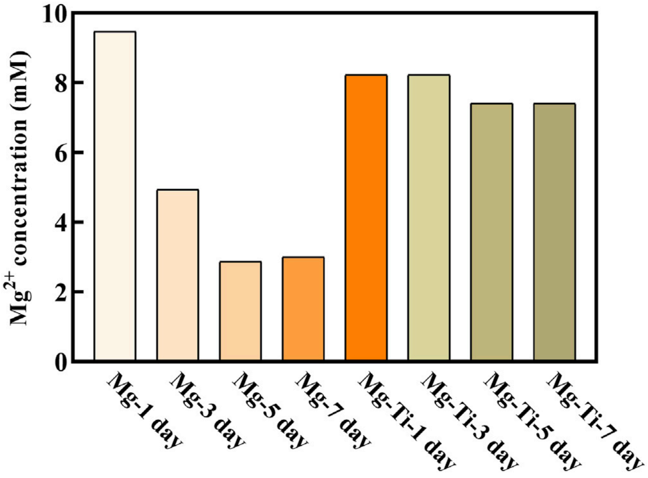

FIGURE 5 | Extract of the Mg^{2+} concentration of the degraded Mg-Ti composite and pure Mg after diluting six times.

3.3.2 Cell Proliferation and Cytotoxicity

The CCK-8 results (**Figure 6**) show that the cells proliferate well in the pure Mg and Mg-Ti groups during incubation for 3-days. It displays that the OD values of all the groups increase gradually over the incubation time. Within 3-days of culture, the Mg-3 day group displays higher proliferation than the control group ($p < 0.05$). The relative growth rates (RGR) of MC3T3-E1 cells are shown in **Table. 1**. The RGR is calculated by a formula, according to the standard United States Pharmacopeia. The cell viability results of all specimens are more than 75%, indicating no cytotoxicity of all groups through 3 days of culture. As shown in **Figure 7**, the effects of Mg^{2+} concentrations on the cell proliferation ability are observed. It can be seen that the OD values gradually increased over the incubation time. From 1-day to 3-days of culture, all groups showed no statistical difference within the RGR ranging from 0–1 (no toxicity).

3.3.3 Cell Morphology Staining

The fluorescence staining results of the intracellular F-actin cytoskeletal network with rhodamine-phalloidin and DAPI are shown in **Figure 8**. At the period of 4 h, the cells show obvious spindle morphology with little filopodia in both pure Mg and Mg-Ti groups. With the incubation time prolonged to 24 h, the cells present a fibrous structure with apparent F-actin, filopodia, and lamellipodia observed in the Mg-Ti group. Compared with pure Mg, cells provide more area in the Mg-Ti group, which suggests that the initial attachment behavior of MC3T3-E1 cells is better. As shown in **Figure 9**, the addition of Mg^{2+} promotes the expansion of MC3T3-E1 cells. Moreover, the cell exhibits a better shape configuration and displays better adhesion in the 8-mM group.

3.3.4 Apoptosis Analysis

The results of the cell apoptosis analysis are shown in **Figure 10** and **Figure 11**. Apoptosis is an active biological mechanism leading to programmed cell death. The decrease in the apoptosis rate indicates an increase in the proliferative activity of MC3T3-E1 cells. **Figure 10** demonstrates the cell apoptosis

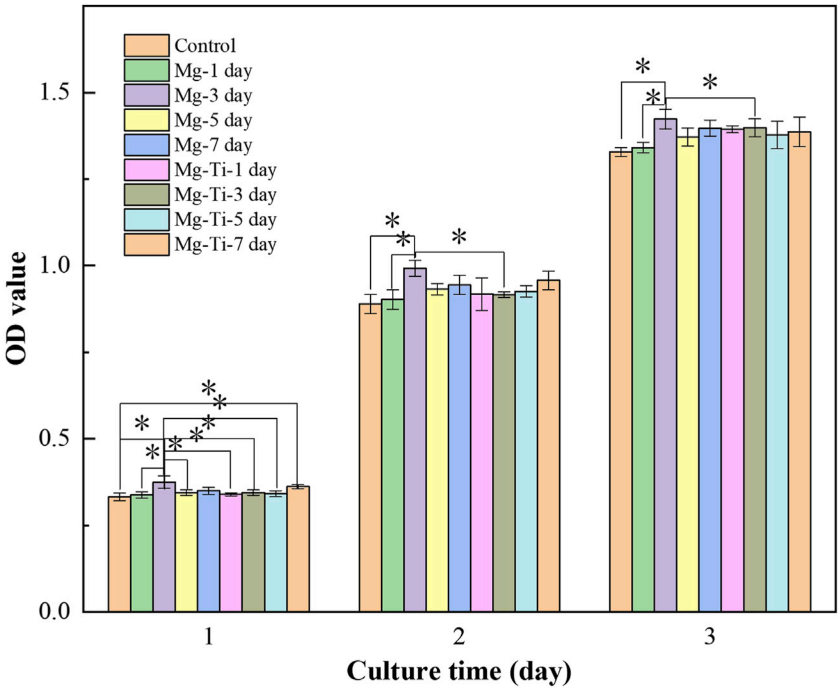

FIGURE 6 | Optical density value (OD value) of MC3T3-E1 cells cultured with extracts of the degraded Mg-Ti composite and pure Mg.

TABLE 1 | Relative growth rate (RGR) and cytotoxicity level of MC3T3-E1 cells cultured with extracts of the degraded Mg-Ti composite and pure Mg at different detection periods.

Sample	1 day		2 days		3 days	
	RGR (%)	Grade	RGR (%)	Grade	RGR (%)	Grade
Mg-1 day	101.88±0.01	0	101.42±0.03	0	100.89±0.01	0
Mg-3 days	112.89±0.02	0	111.56±0.02	0	107.12±0.03	0
Mg-5 day	103.80±0.01	0	104.77±0.02	0	103.21±0.03	0
Mg-7 day	105.40±0.01	0	106.15±0.03	0	105.18±0.02	0
Mg-Ti-1 day	102.40±0.01	0	103.23±0.05	0	104.92±0.01	0
Mg-Ti-3 day	103.77±0.01	0	102.97±0.01	0	105.22±0.03	0
Mg-Ti-5 day	102.95±0.01	0	104.08±0.02	0	103.66±0.04	0
Mg-Ti-7 day	108.97±0.01	0	107.60±0.03	0	104.33±0.04	0

RGR, relative growth rate; Grade, the cytotoxicity level of MC3T3-E1 cells.

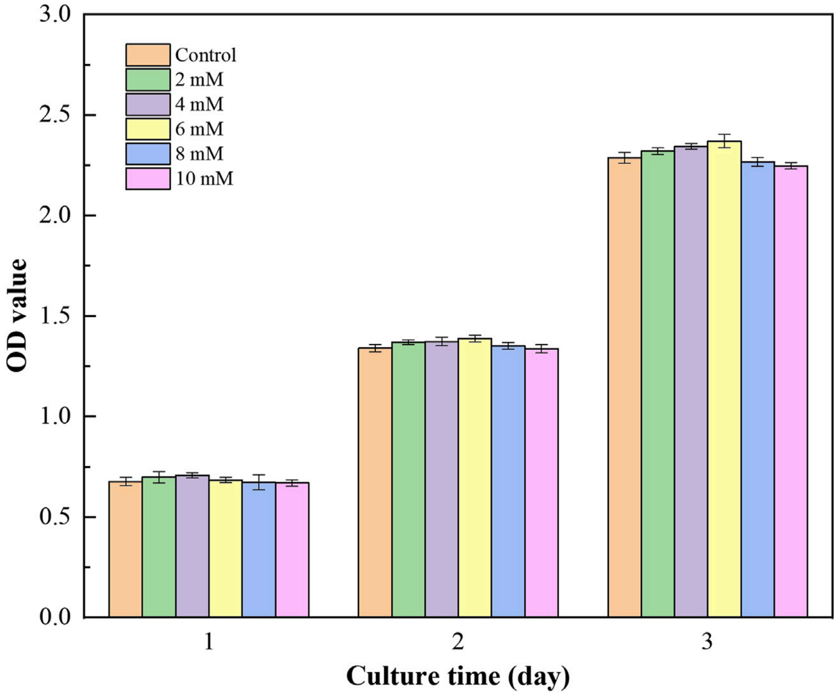

FIGURE 7 | OD value of MC3T3-E1 cells cultured with gradient Mg^{2+} concentrations.

culture in pure Mg and Mg-Ti composite extracts with different degradation times. After seeding for 1-day and 3-days, the apoptosis of all groups including pure Mg and the Mg-Ti composite is less than 10%, which is an acceptable range. On day 1, the apoptosis of the Mg-Ti group is lower than that of the pure Mg group but is slightly higher than that of the control group. On day 3, the apoptosis rates of pure Mg and Mg-Ti groups are both lower than those of the control group (**Table 2**). The apoptosis results of MC3T3-E1 cells on varying Mg^{2+} concentrations within 3-days are shown in **Figure 11**. After 3-days of incubation, the addition of Mg^{2+} reduces the apoptosis of MC3T3-E1 cells with the 8 mM Mg^{2+} exhibiting minimum apoptosis.

3.3.5 ALP Activity

The differentiation ability of MC3T3-E1 cells is used to describe the osteoblast maturation and can be assessed by an ALP test. **Figure 12A** shows that the ALP activity is promoted in the Mg-Ti composite and pure Mg groups on days 7 and 14. It can be found that the ALP content of both groups increased as the osteogenic induction time was extended. On days 7 and 14, the ALP content of the Mg-Ti group is significantly higher than that of the pure Mg group ($p < 0.05$). In the different immersion times of pure Mg and Mg-Ti groups, the results show little difference. **Figure 12B** shows the ALP activity of MC3T3-E1 cells incubated in a gradient Mg^{2+} concentration medium for 7-days and 14-days. It can be identified that the addition of Mg^{2+} to the medium promotes the

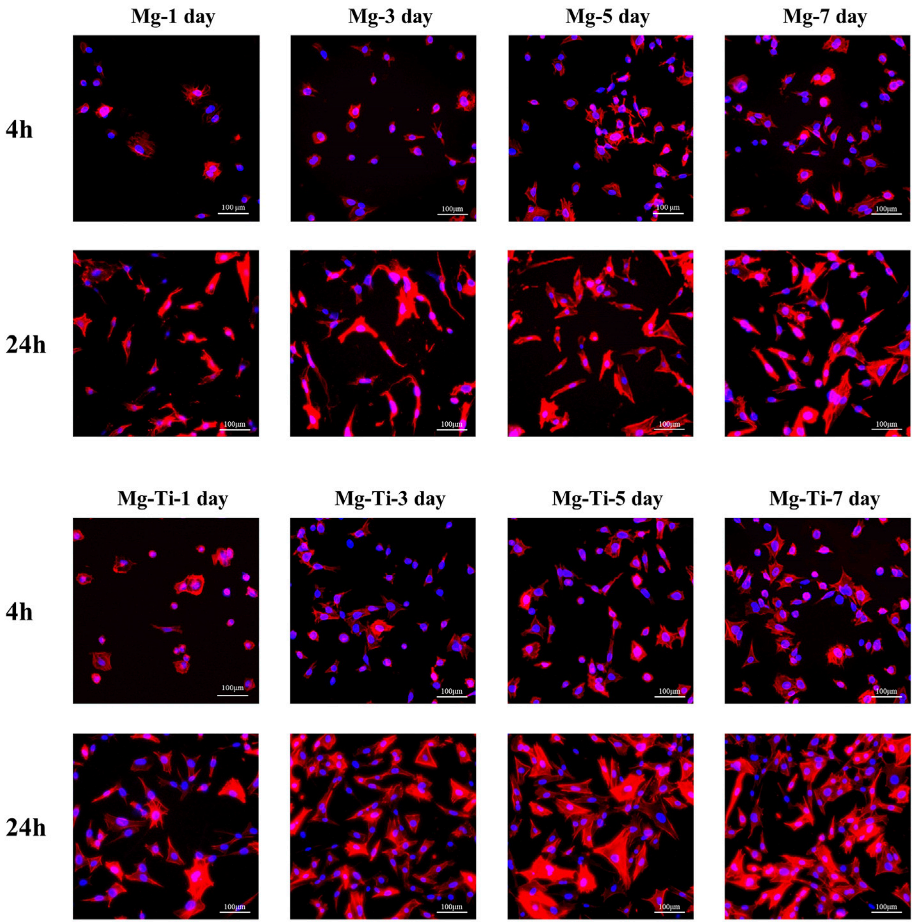

FIGURE 8 | Morphology staining of MC3T3-E1 cells cultured with extracts of the degraded Mg-Ti composite and pure Mg for 4 and 24 h.

ALP activity of cells. The ALP activity is the highest in the 8 mM Mg^{2+} medium within both groups.

4 DISCUSSION

4.1 Degradation Behavior

As is known, Mg is active and can react with moisture or water when exposed to aqueous environments, resulting in hydroxide ions (OH^-), hydrogen gas (H_2), and Mg^{2+} ions by the following reactions (Jin et al., 2020):

$$Mg + 2H_2O \rightarrow Mg^{2+} + 2OH^- + H_2\uparrow, \quad (1)$$

$$Mg^{2+} + 2OH^- \rightarrow Mg(OH)_2\downarrow. \quad (2)$$

Generally, the corrosive attack in pure Mg normally starts at the grain boundary. However, galvanic corrosion is induced by the electrode potential differences of Ti and Mg metals in the Mg-Ti composite. The Ti phase is protected as cathodic sites, and the Mg phase is selectively corroded as anodic sites.

Ideal Mg-Ti composites should maintain Ti scaffold integrity to provide the implant strength during the bone defect repair process after the Mg phase degradation. However, as the composites undergo degradation, hydrogen gas accumulation around the cathodic site (Ti skeleton) may cause adverse effects. Different amounts of hydrogen gas could be produced depending on the corrosion rate of the composites. The produced hydrogen could create stresses during corrosion, especially on the Ti skeleton. Moreover, sudden hydrogen gas evolution could also cause the initiation of micro-cracks in the Ti skeleton, resulting in catastrophic failure. Esen et al. (2020) fabricated Ti6Al4V-Mg/WE41/AZ27 composites through powder metallurgy. After immersion for 1-day, the Ti6Al4V-Mg composite samples were not able to preserve their Ti scaffold integrities. The loss of Ti scaffold integrities mainly resulted from the high pressure generated by hydrogen gas. The generated pressure overcame the local strength of sintering necks in the Ti6Al4V alloy skeleton. In the present work, although the degeneration rate of the Mg-Ti composite is higher than that of pure Mg, there is no obvious change in the macro-morphology of the sample with only a few cracks in the Ti regions close to Mg after 7-days of immersion. These all result from the unique design of the 3D interpenetrating phase architecture. By retaining the structural integrity and resisting the development of damage, the mechanical

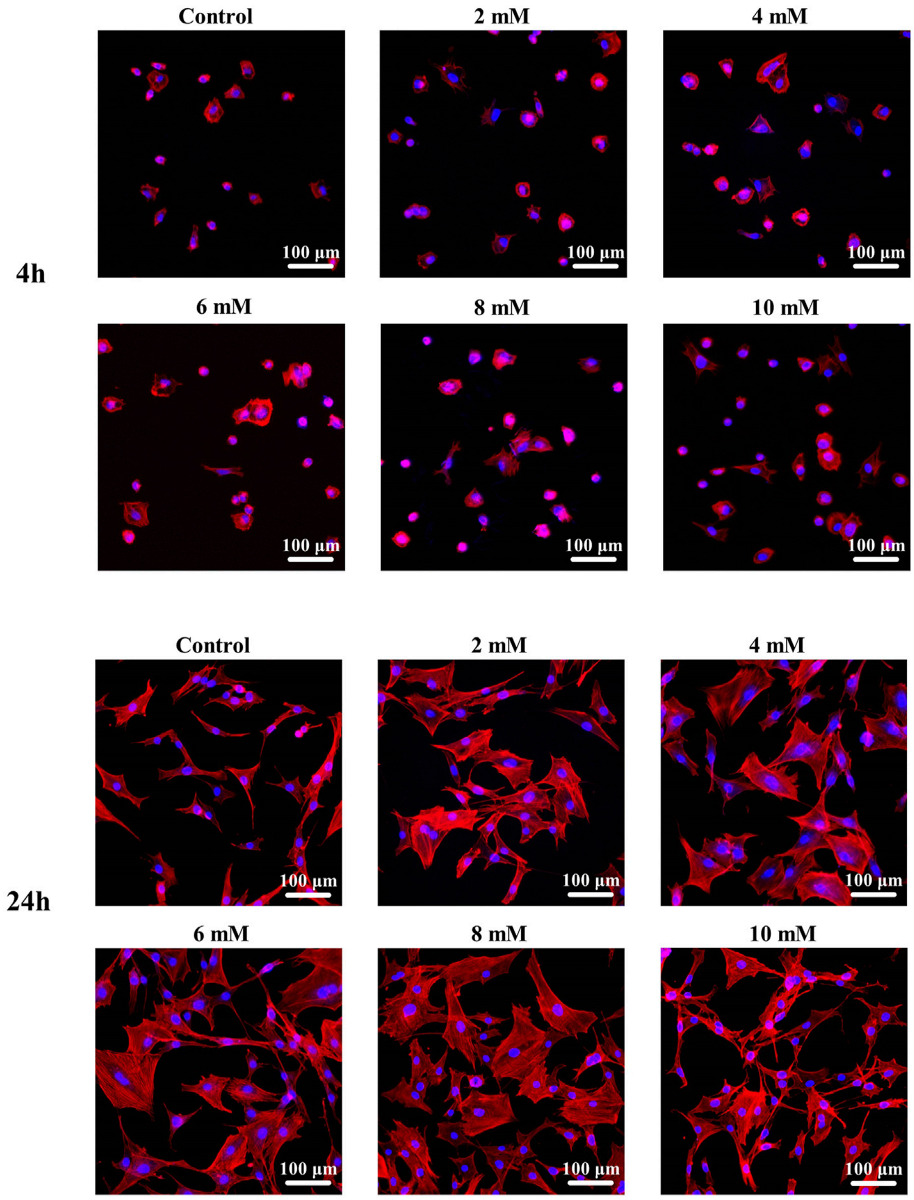

FIGURE 9 | Morphological staining of MC3T3-E1 cells cultured with gradient Mg^{2+} concentrations for 4 and 24 h.

properties of the Mg-Ti composite are enhanced by the interpenetrating phase architecture. The stresses caused by the accumulation of hydrogen gas during the process of corrosion are permitted effective transfer within each bi-continuity of the Ti and Mg phases to generate a substantial strengthening effect in the composite (Zhang et al., 2020).

In this work, the Mg-Ti composite exhibits a higher degradation rate than pure Mg during 7-days of degradation. The high degradation rate might mainly result from galvanic corrosion in the Mg-Ti composite. Because of the electrode potential difference of Ti and Mg metals, Mg with higher activity is preferentially corroded. As shown in **Figure 4**, the micromorphology image of the Mg-Ti composite shows that the corrosion of Mg regions in the composites preferentially starts from the Mg and Ti interface and gradually extends to the central regions of Mg over time. Apart from galvanic corrosion, the irregularly porous morphology of Mg after preferential corrosion may be another reason for the higher degradation rate. In addition, the irregularly porous corrosion morphology is similar to cancellous bone, thereby stimulating the growth of new bone tissue near the implant.

With regard to the Mg-based materials, the formation of corrosion products is generally characterized by the degradation process. Magnesium hydroxide, generated on the surface of materials, is characterized as the main corrosion product. As shown in **Figure 5**, the surface of the Mg-Ti

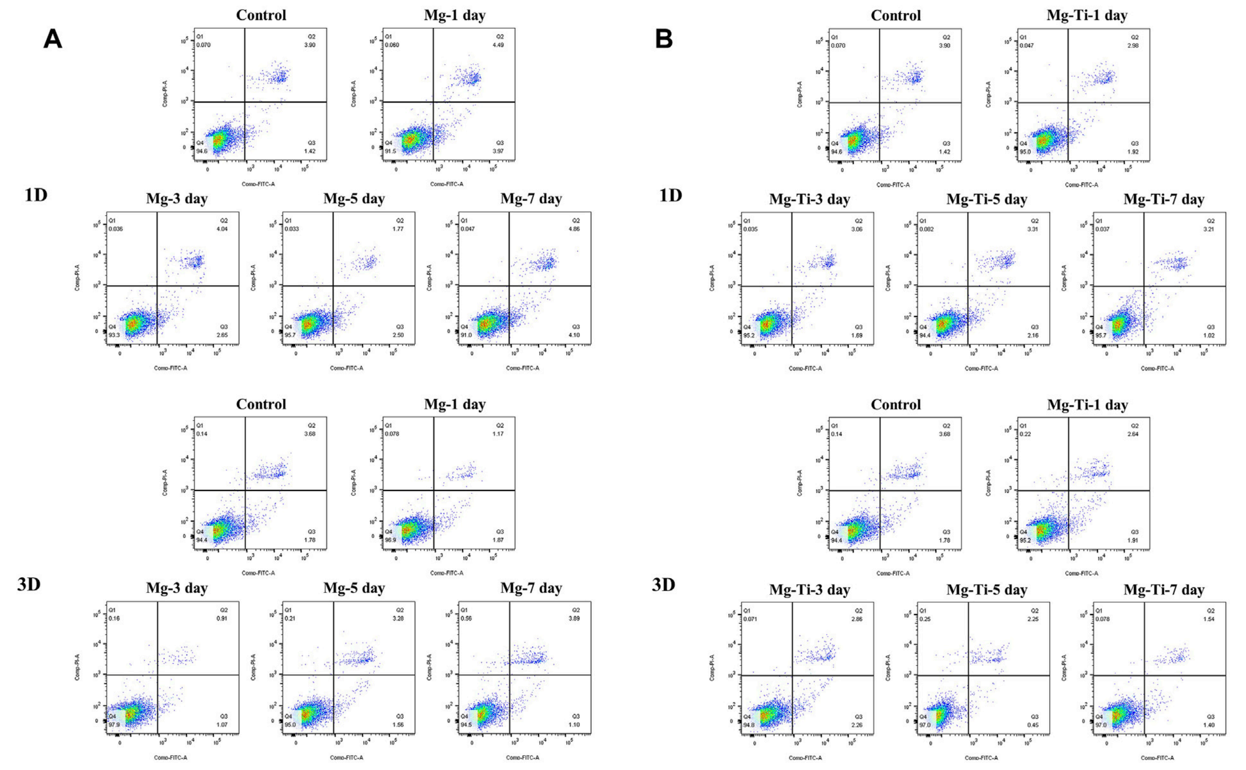

FIGURE 10 | Apoptosis of MC3T3-E1 cells cultured with extracts of degraded pure **(A)** Mg and **(B)** Mg-Ti composite for 1 day and 3 days.

composite was almost covered with corrosion product after 7 days of immersion, and the abundance in the Mg site is more than that of the Ti site. The reason for the $Mg(OH)_2$ formation promotion might be that Mg^{2+} and OH^- accumulate in the Mg region as it is the anodic site in galvanic corrosion. The $Mg(OH)_2$ film on the surface of the material could passivate Mg in basic environments as a protective layer and prevents further corrosion underneath Mg. However, the layer could not maintain long-term stability in aqueous environments, especially with the presence of bromide, chlorate, sulfate, and chloride. Soluble $MgCl_2$ converted from $Mg(OH)_2$ could further transform to magnesium phosphate and finally transform into apatite. This may be the reason why the pH values have remained steady in the immersion test.

4.2 *In Vitro* Cytocompatibility of MC3T3-E1 Cells

4.2.1 Cell Viability and Morphology

The reactions between Mg and the biological environment have to be taken into account when Mg-based materials are used as orthopedic implants. In the degradation process, especially at its early stage, the reaction of Mg with water molecules in the aqueous environment leads to the formation of hydroxide ions (OH^-), hydrogen gas (H_2), and a high concentration of Mg^{2+}. These three factors affect the biocompatibility of Mg-based materials. However, the degradation rate of Mg-based materials *in vivo* is not easy to be simulated by extracts obtained from the current ISO 10993 standards because of the large differences between *in vivo* and *in vitro* conditions. In the study by Gao, Su and Qin (2021), the results suggested that the immersion degradation rate *in vitro* was 2–4 times higher than the degradation rate of the *in vivo* implantation experiment. Similarly, the 1–5 correlation factors of the degradation rate can be predicted between *in vitro* and *in vivo* when an appropriate medium was used for the *in vitro* immersion test (Witte et al., 2006). Sanchez et al. (2015) also reported that the degradation rate *in vitro* reaches up to nine times higher than the *in vivo* degradation. Therefore, Wang et al. (2015)suggested that the extract of Mg-based materials should be diluted 6–9 times to test biocompatibility *in vitro*, according to the selection of implantation.

In this work, the extracts of the samples were diluted six times to evaluate the Mg-Ti composite and pure Mg availabilities for cell morphology, proliferation, and formation of alkaline phosphatase. Then, the Mg^{2+} concentrations of the diluted extracts were measured. These values were used as the basis for preparing culture media with various Mg^{2+} concentrations. As shown in **Figure 5**, the Mg^{2+} concentration of diluted pure Mg extracts decreases gradually over time, yet that of the Mg-Ti composite remains stable around 8 mM in the process of 7-days of degradation.

In general, the primary requirement of orthopedic implants is to be non-toxic to cells. The CCK-8 method is most commonly used to detect cell proliferation *in vitro*. According to CCK8 results, it can be found that Mg-Ti groups exhibit a similar cell proliferation ability of osteoblasts compared to pure Mg groups in the process of 7-days of degradation. In addition, both pure Mg

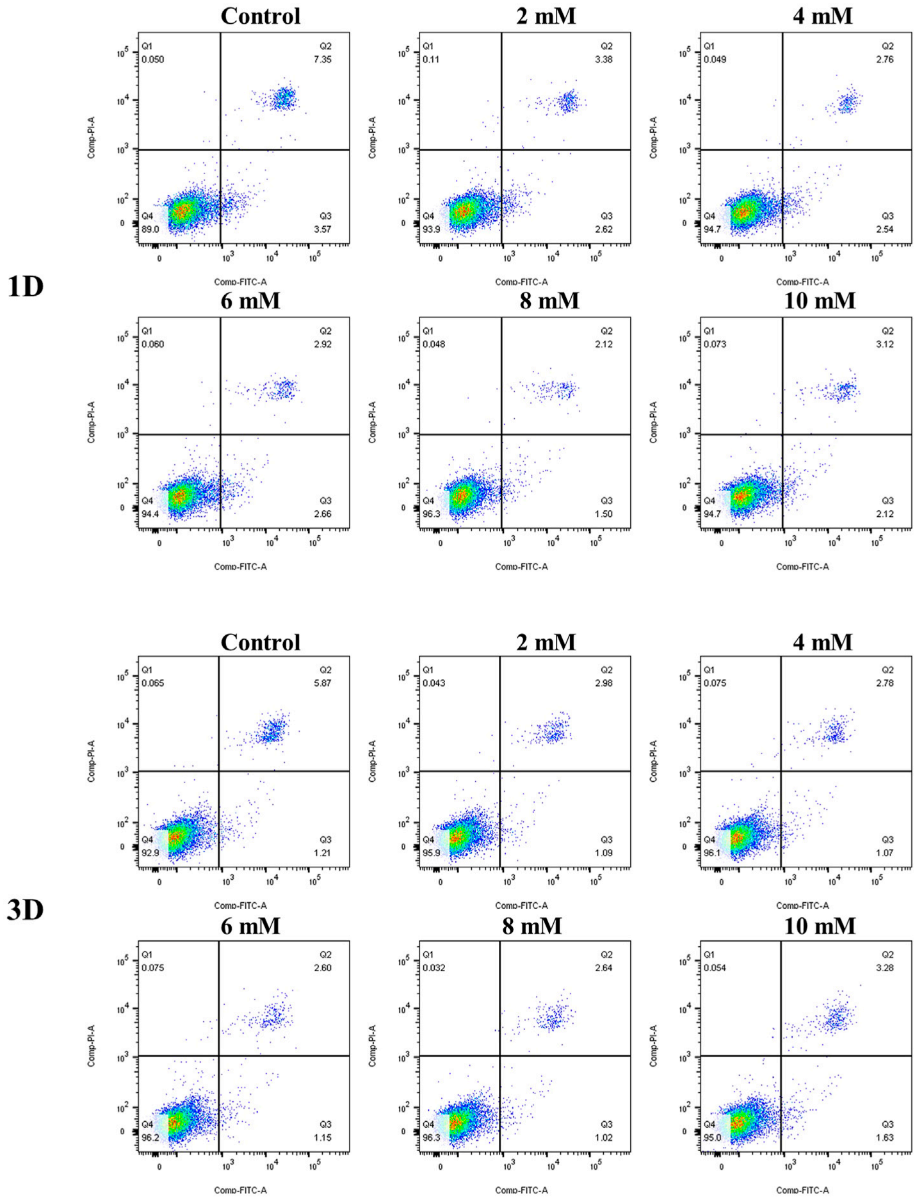

FIGURE 11 | Apoptosis of MC3T3-E1 cells cultured with gradient Mg^{2+} concentrations for 1 day and 3 days.

TABLE 2 | RGR and the cytotoxicity level of MC3T3-E1 cells cultured with gradient Mg^{2+} concentrations at different detection periods.

Sample (mM)	1 day		2 days		3 days	
	RGR (%)	Grade	RGR (%)	Grade	RGR (%)	Grade
2	103.14±0.03	0	102.21±0.01	0	101.45±0.02	0
4	104.47±0.01	0	102.46±0.02	0	102.48±0.01	0
6	101.13±0.01	0	103.53±0.02	0	103.66±0.03	0
8	99.49±0.04	1	100.90±0.02	0	99.10±0.02	1
10	98.91±0.02	1	99.75±0.02	1	98.26±0.02	1

RGR, relative growth rate; Grade, the cytotoxicity level of MC3T3-E1 cells.

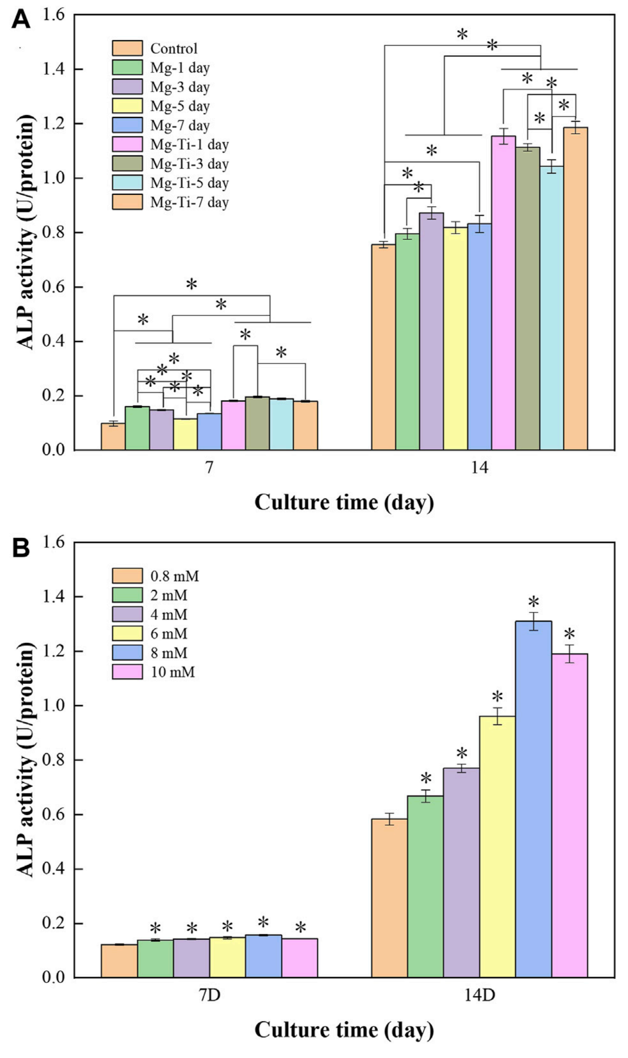

FIGURE 12 | (A) ALP activity of MC3T3-E1 cells cultured with extracts of the degraded Mg-Ti composite and pure Mg for 7 and 14 days (n=3 and $*p < 0.05$). **(B)** ALP activity of MC3T3-E1 cells cultured with gradient Mg^{2+} concentrations for 7 and 14 days (n=3 and $*p < 0.05$).

and Mg-Ti groups have positive effects on the proliferation ability of osteoblasts compared with the control group on days 1, 2, and 3, which indicated that all the extracts in this study are non-toxic and of excellent biocompatibility. Similar results are also obtained after 3 days of culture in media (0.8, 2, 4, 6, 8, and 10 mM Mg^{2+}) where the cell proliferation rates of all groups have no significant difference, showing that Mg^{2+} is non-toxic to cells under 10 mM.

In addition, Mg^{2+} also exerts an effect on cellular morphology. An appropriate Mg^{2+} concentration promotes the formation of the actin filament bundle and the expansion of cells, which is beneficial to cell adhesion and motility. It is widely accepted that the F-actin cytoskeletal network is a key regulator of cellular shape and force generation in cell migration with crucial roles in maintaining the cellular shape and elasticity. F-actin staining results (**Figure 9**) show that cell morphology with more filopodia was observed in the group with an Mg concentration at 8 mM. In the report by Maier and Haraszti (2015), Mg^{2+} has a significant influence on the global structure of the actin filament bundles. The addition of Mg^{2+} contributes to the changes in the elasticity of the actin network even at low concentrations (2–12 mM). Moreover, the speed and extent of bundle formation increase when elevating the Mg^{2+} concentration from 1 to 5–10 mM (Hu and Kuhn 2012). These all suggest that Mg^{2+} around 8 mM is an appropriate concentration benefiting the integration of implants and surrounding tissues. Moreover, as shown in **Figure 8**, the cell morphology of the Mg-Ti composite is better than that of pure Mg. This may result from the cooperated effect of Mg^{2+} concentration and corrosion products caused by different degradation modes and rates.

4.2.2 Cell Apoptosis

Apoptosis, occurring over several hours, is well known as cell programmed death since death results from the cell itself, eliminating damaged cells (Matsui et al., 2017). The apoptosis rate is an essential index when characterizing the biocompatibility of orthopedic implant materials. In the process of apoptosis, mitochondria play an essential role, which is associated with intracellular Ca^{2+} overload. Larger amounts of Ca^{2+} influx result in intracellular Ca^{2+} concentration rise and accumulation in the mitochondria (Thor, Hartzell and Orrenius 1984). The accumulation of Ca^{2+} contributes to the opening of a high-conductance pore in the inner mitochondrial membrane (IMM), which has been termed mitochondrial permeability transition (MPT) (Douglas et al., 1979). Then, the osmotic swelling of the mitochondria and rupture of the mitochondrial membrane occur which results in the mitochondrial proteins, including cytochrome C, releasing into the cytosol (Lemasters et al., 1999). In the cytosol, an apoptosome complex is formed by cytochrome C together with apoptosis activating factor-1 (Apaf-1) and pro-caspase-9. Cell apoptosis can be triggered by the apoptosome complex through intrinsic or extrinsic apoptosis pathways.

In the experiment of incubating MC3T3-E1 cells with a series of culture media in increasing Mg^{2+} concentrations, the results of the apoptosis analysis implied that the apoptosis rate gradually decreased with the increase in the Mg^{2+} concentration. The minimum apoptosis was observed in the 8-mM Mg^{2+} concentration culture medium. The reasons may be as follows: on one hand, the elevation of extracellular Mg^{2+}, as the well-known calcium competing ion, suppresses the increase in the intracellular Ca^{2+} concentration by competing with extracellular Ca^{2+} and inhibiting the release of intracellular calcium, thereby preventing cell damage and reducing apoptosis (Bojan et al., 2013). On the other hand, several *in vitro* studies implied that the elevation of intracellular Mg^{2+} was observed in the early phase of apoptosis (Zhang et al., 2005). However, in the research of Matsui et al. (2017), they developed a novel Mg^{2+} probe which achieved a long-term visualization of intracellular Mg^{2+} dynamics during apoptosis. The results showed that the increase in the Mg^{2+} concentration is associated with the decrease in the ATP concentration after apoptotic cell shrinkage, demonstrating that Mg-ATP is the main resource for the Mg^{2+} increase after cell shrinkage during apoptosis. Moreover, the same conclusion was drawn by Chien et al. (1999) that the elevation of cytosolic free Mg^{2+} was irrelevant to the extracellular Mg^{2+} concentration with the increase in intracellular Mg^{2+} derived from the mitochondria during the process of apoptosis. Together, Mg^{2+} concentration at an appropriate range tends to decrease the apoptosis rate of cells. A recent study has documented that the addition of Mg particles reduces the apoptosis caused by the Ti particles (Wang Y et al., 2020). However, the apoptosis results of experimental extracts were not completely consistent with the aforementioned trends. It might be attributed to the generation of other factors (pH, osmolality, and corrosion product) in the degradation process.

4.2.3 Cell Differentiation

ALP, as the key factor governing the process of osteogenesis, is expressed in the early stage of bone development and used as an early marker of osteoblast differentiation (Hu et al., 2021; Yi et al., 2021). In the present study, the ALP activities of the Mg-Ti and pure Mg groups with different degradation times were both higher than those of the control group. In addition, the ALP activity gradually decreased over time, which was consistent with the Mg^{2+} concentration trend of pure Mg extracts. It showed that the extracts of Mg-based materials could enhance the ALP activity of cells and the enhancing efficiency was closely related to the Mg^{2+} concentration of extracts. Moreover, the ALP activity of Mg-Ti groups was higher than that of pure Mg groups at all degradation times, which indicated that the extracts of the Mg-Ti composite could better promote the osteogenic differentiation of cells compared with pure Mg. The difference in the ALP activity of the two materials might be attributed to the following aspects. On one hand, the Mg^{2+} concentration of Mg-Ti composite extracts remained at around 8 mM in 7-days of degradation, which is regarded as an appropriate range for cell osteogenic differentiation. This assumption was verified by the experimental result of MC3T3-E1 cells incubated with varying Mg^{2+} concentrations. As shown in **Figure 12**, the ALP activity of the 8-mM group was significantly higher than that of the other five groups with the difference being statistically significant. On the other hand, the Mg-Ti composite exhibited a slightly higher pH value of less than 8.5 than that of pure Mg in the process of degradation. It was reported that suitable alkalinity (pH 7.8–8.5) had a beneficial effect on osteogenesis (Liu et al., 2016; Wu et al., 2019). However, the 7-day extract groups showed a similar Mg^{2+} concentration to 5-days, whereas they exhibited a higher ALP activity. This phenomenon may result from the production of more calcium phosphate after 7-days of degradation, which improves the osteogenic ability of cells.

In summary, the extracts of the Mg-Ti composite exhibit good biocompatibility and excellent osteogenic activity in the process of 7-days of degradation. However, because of the difference in degradation rates *in vitro* and *in vivo*, animal studies need to be carried out in the future to determine the suitability of the Mg-Ti composite as an orthopedic implant.

5 CONCLUSION

1) A new Mg-Ti interpenetrating phase composite is fabricated by printing a pure Ti scaffold through the 3D printing technology and then the pressureless infiltration of the Mg melt into it. The degradation of the Mg-Ti composite starts from the Mg matrix near the interface of the Ti and Mg region. The Ti-based skeleton remained intact, while Mg processively degraded during different periods. In the degradation process of the Mg-Ti composite, a slightly alkaline environment is formed which is conducive to the cell culture.

2) The extracts of the Mg-Ti composite were showed to be non-toxic to cells during 7 days of degradation. Compared with pure Mg extracts, it exhibited better cell morphology and higher osteogenic activity. Mg^{2+}, which was precipitated during degradation, had an impact on cell apoptosis, and the rates of apoptosis were overall within an acceptable range.

DATA AVAILABILITY STATEMENT

The original contributions presented in the study are included in the article/Supplementary Material; further inquiries can be directed to the corresponding author.

AUTHOR CONTRIBUTIONS

ZZ, QW, and ZL contribute to the conception and design of the study. XY performed the experiments and wrote the first draft of the manuscript. WH polished the language of the manuscript. NZ and DZ wrote sections of the manuscript. DR and HJ performed the statistical analysis. All authors contributed to the manuscript revision, read, and approved the submitted version.

ACKNOWLEDGMENTS

The authors are grateful for the financial support by the National Key R&D Program of China (2020YFA0710404), the National Natural Science Foundation of China (52173269 and 52101160), the Liaoning Province Education Department Program (ZF2019032), the Liaoning Revitalization Talents Program, and the Youth Innovation Promotion Association CAS.

REFERENCES

Attarilar, S., Ebrahimi, M., Djavanroodi, F., Fu, Y., Wang, L., and Yang, J. (2020a). 3D Printing Technologies in Metallic Implants: A Thematic Review on the Techniques and Procedures. *Int. J. Bioprint* 7, 21–46. doi:10.18063/ijb.v7i1.306

Attarilar, S., Yang, J., Ebrahimi, M., Wang, Q., Liu, J., Tang, Y., et al. (2020b). The Toxicity Phenomenon and the Related Occurrence in Metal and Metal Oxide Nanoparticles: A Brief Review from the Biomedical Perspective. *Front. Bioeng. Biotechnol.* 8, 1659–1683. doi:10.3389/fbioe.2020.00822

Balog, M., Ibrahim, A. M. H., Krizik, P., Bajana, O., Klimova, A., Catic, A., et al. (2019). Bioactive Ti + Mg Composites Fabricated by Powder Metallurgy: The

Relation between the Microstructure and Mechanical Properties. *J. Mech. Behav. Biomed. Mater.* 90, 45–53. doi:10.1016/j.jmbbm.2018.10.008

Bobbert, F. S. L., Lietaert, K., Eftekhari, A. A., Pouran, B., Ahmadi, S. M., Weinans, H., et al. (2017). Additively Manufactured Metallic Porous Biomaterials Based on Minimal Surfaces: A Unique Combination of Topological, Mechanical, and Mass Transport Properties. *Acta Biomater.* 53, 572–584. doi:10.1016/j.actbio.2017.02.024

Bojan, M., Peperstraete, H., Lilot, M., Tourneur, L., Vouhé, P., and Pouard, P. (2013). Cold Histidine-Tryptophan-Ketoglutarate Solution and Repeated Oxygenated Warm Blood Cardioplegia in Neonates with Arterial Switch Operation. *Ann. Thorac. Surg.* 95, 1390–1396. doi:10.1016/j.athoracsur.2012.12.025

Campanelli, L. C., Bortolan, C. C., da Silva, P. S. C. P., Bolfarini, C., and Oliveira, N. T. C. (2017). Effect of an Amorphous Titania Nanotubes Coating on the Fatigue and Corrosion Behaviors of the Biomedical Ti-6Al-4V and Ti-6Al-7Nb Alloys. *J. Mech. Behav. Biomed. Mater.* 65, 542–551. doi:10.1016/j.jmbbm.2016.09.015

Chien, M. M., Zahradka, K. E., Newell, M. K., and Freed, J. H. (1999). Fas-induced B Cell Apoptosis Requires an Increase in Free Cytosolic Magnesium as an Early Event. *J. Biol. Chem.* 274, 7059–7066. doi:10.1074/jbc.274.11.7059

Claros, C. A. E., Oliveira, D. P., Campanelli, L. C., Pereira da Silva, P. S. C., and Bolfarini, C. (2016). Fatigue Behavior of Ti-6Al-4V Alloy in Saline Solution with the Surface Modified at a Micro- and Nanoscale by Chemical Treatment. *Mater. Sci. Eng. C* 67, 425–432. doi:10.1016/j.msec.2016.04.099

de Krijger, J., Rans, C., Van Hooreweder, B., Lietaert, K., Pouran, B., and Zadpoor, A. A. (2017). Effects of Applied Stress Ratio on the Fatigue Behavior of Additively Manufactured Porous Biomaterials under Compressive Loading. *J. Mech. Behav. Biomed. Mater.* 70, 7–16. doi:10.1016/j.jmbbm.2016.11.022

Eltorai, A. E. M., Nguyen, E., and Daniels, A. H. (2015). Three-Dimensional Printing in Orthopedic Surgery. *Orthopedics* 38, 684–687. doi:10.3928/01477447-20151016-05

Esen, Z., Öcal, E. B., Akkaya, A., Gürçay, B., Özcan, C., Özgümüş, B. A., et al. (2020). Corrosion Behaviours of Ti6Al4V-Mg/Mg-Alloy Composites. *Corros. Sci.* 166, 108470. doi:10.1016/j.corsci.2020.108470

Fan, D.-Y., Yi, Z., Feng, X., Tian, W.-Z., Xu, D.-K., Cristino Valentino, A. M., et al. (2021). Antibacterial Property of a Gradient Cu-Bearing Titanium Alloy by Laser Additive Manufacturing. *Rare Mater.* 41, 580–593. doi:10.1007/s12598-021-01826-w

Gao, J., Su, Y., and Qin, Y.-X. (2021). Calcium Phosphate Coatings Enhance Biocompatibility and Degradation Resistance of Magnesium Alloy: Correlating *In Vitro* and *In Vivo* Studies. *Bioact. Mater.* 6, 1223–1229. doi:10.1016/j.bioactmat.2020.10.024

Geetha, M., Singh, A. K., Asokamani, R., and Gogia, A. K. (2009). Ti Based Biomaterials, the Ultimate Choice for Orthopaedic Implants - A Review. *Prog. Mater. Sci.* 54, 397–425. doi:10.1016/j.pmatsci.2008.06.004

He, X., Hartlieb, E., Rothmund, L., Waschke, J., Wu, X., Van Landuyt, K. L., et al. (2015). Intracellular Uptake and Toxicity of Three Different Titanium Particles. *Dent. Mater.* 31, 734–744. doi:10.1016/j.dental.2015.03.017

Hu, B., Chen, L., Chen, Y., Zhang, Z., Wang, X., and Zhou, B. (2021). Cyanidin-3-glucoside Regulates Osteoblast Differentiation via the ERK1/2 Signaling Pathway. *ACS Omega* 6, 4759–4766. doi:10.1021/acsomega.0c05603

Hu, X., and Kuhn, J. R. (2012). Actin Filament Attachments for Sustained Motility *In Vitro* Are Maintained by Filament Bundling. *Plos One* 7, e31385. doi:10.1371/journal.pone.0031385

Hunter, D. R., and Haworth, R. A. (1979). The Ca2+-Induced Membrane Transition in Mitochondria. III. Transitional Ca2+ Release. *Arch. Biochem. Biophys.* 195, 468–477. doi:10.1016/0003-9861(79)90371-010.1016/0003-9861(79)90373-4

Jin, S., Zhang, D., Lu, X., Zhang, Y., Tan, L., Liu, Y., et al. (2020). Mechanical Properties, Biodegradability and Cytocompatibility of Biodegradable Mg-Zn-Zr-Nd/Y Alloys. *J. Mater. Sci. Technol.* 47, 190–201. doi:10.1016/j.jmst.2020.02.017

Kandala, B. S. P. K., Zhang, G., Lcorriveau, C., Paquin, M., Chagnon, M., Begun, D., et al. (2021). Preliminary Study on Modelling, Fabrication by Photo-Chemical Etching and *In Vivo* Testing of Biodegradable Magnesium AZ31 Stents. *Bioact. Mater.* 6, 1663–1675. doi:10.1016/j.bioactmat.2020.11.012

Lemasters, J. J., Qian, T., Bradham, C. A., Brenner, D. A., Cascio, W. E., Trost, L. C., et al. (1999). Mitochondrial Dysfunction in the Pathogenesis of Necrotic and Apoptotic Cell Death. *J. Bioenergetics Biomembr.* 31, 305–319. doi:10.1023/a:1005419617371

Li, X., Liu, X., Wu, S., Yeung, K. W. K., Zheng, Y., and Chu, P. K. (2016). Design of Magnesium Alloys with Controllable Degradation for Biomedical Implants: From Bulk to Surface. *Acta Biomater.* 45, 2–30. doi:10.1016/j.actbio.2016.09.005

Li, Y., Zhou, J., Pavanram, P., Leeflang, M. A., Fockaert, L. I., Pouran, B., et al. (2018). Additively Manufactured Biodegradable Porous Magnesium. *Acta Biomater.* 67, 378–392. doi:10.1016/j.actbio.2017.12.008

Liang, L., Huang, Q., Wu, H., Ouyang, Z., Liu, T., He, H., et al. (2021). Stimulation of *In Vitro* and *In Vivo* Osteogenesis by Ti-Mg Alloys with the Sustained-Release Function of Magnesium Ions. *Colloids Surfaces B Biointerfaces* 197, 111360. doi:10.1016/j.colsurfb.2020.111360

Liu, W., Wang, T., Yang, C., Darvell, B. W., Wu, j., Lin, K., et al. (2016). Alkaline Biodegradable Implants for Osteoporotic Bone Defects-Importance of Microenvironment pH. *Osteoporos. Int.* 27, 93–104. doi:10.1007/s00198-015-3217-8

Liu, Y., Li, K., Luo, T., Song, M., Wu, H., Xiao, J., et al. (2015). Powder Metallurgical Low-Modulus Ti-Mg Alloys for Biomedical Applications. *Mater. Sci. Eng. C* 56, 241–250. doi:10.1016/j.msec.2015.06.010

Maier, T., and Haraszti, T. (2015). Reversibility and Viscoelastic Properties of Micropillar Supported and Oriented Magnesium Bundled F-Actin. *PloS One* 10, e0136432. doi:10.1371/journal.pone.0136432

Matsui, Y., Funato, Y., Imamura, H., Miki, H., Mizukami, S., and Kikuchi, K. (2017). Visualization of Long-Term Mg2+ Dynamics in Apoptotic Cells Using a Novel Targetable Fluorescent Probe. *Chem. Sci.* 8, 8255–8264. doi:10.1039/c7sc03954a

Meenashisundaram, G. K., Wang, N., Maskomani, S., Lu, S., Anantharajan, S. K., Dheen, S. T., et al. (2020). Fabrication of Ti + Mg Composites by Three-Dimensional Printing of Porous Ti and Subsequent Pressureless Infiltration of Biodegradable Mg. *Mater. Sci. Eng. C* 108, 110478. doi:10.1016/j.msec.2019.110478

Ouyang, S., Huang, Q., Liu, Y., Ouyang, Z., and Liang, L. (2019). Powder Metallurgical Ti-Mg Metal-Metal Composites Facilitate Osteoconduction and Osseointegration for Orthopedic Application. *Bioact. Mater.* 4, 37–42. doi:10.1016/j.bioactmat.2018.12.001

Sanchez, A. H. M., Luthringer, B. J. C., Feyerabend, F., and Willumeit, R. (2015). Mg and Mg Alloys: How Comparable Are *In Vitro* and *In Vivo* Corrosion Rates? A Review. *Acta Biomater.* 13, 16–31. doi:10.1016/j.actbio.2014.11.048

Staiger, M. P., Pietak, A. M., Huadmai, J., and Dias, G. (2006). Magnesium and its Alloys as Orthopedic Biomaterials: A Review. *Biomaterials* 27, 1728–1734. doi:10.1016/j.biomaterials.2005.10.003

Stanec, Z., Halambek, J., Maldini, K., Balog, M., Križik, P., Schauperl, Z., et al. (2016). Titanium Ions Release from an Innovative Titanium-Magnesium Composite: an *In Vitro* Study. *Acta Stomatol. Croat.* 50, 40–48. doi:10.15644/asc50/1/6

Thor, H., Hartzell, P., and Orrenius, S. (1984). Potentiation of Oxidative Cell Injury in Hepatocytes Which Have Accumulated Ca2+. *J. Biol. Chem.* 259, 6612–6615. doi:10.1016/s0021-9258(20)82186-3

Wang, J., Witte, F., Xi, T., Zheng, Y., Yang, K., Yang, Y., et al. (2015). Recommendation for Modifying Current Cytotoxicity Testing Standards for Biodegradable Magnesium-Based Materials. *Acta Biomater.* 21, 237–249. doi:10.1016/j.actbio.2015.04.011

Wang N, N., Maskomani, S., Meenashisundaram, G. K., Fuh, J. Y. H., Dheen, S. T., and Anantharajan, S. K. (2020). A Study of Titanium and Magnesium Particle-Induced Oxidative Stress and Toxicity to Human Osteoblasts. *Mater. Sci. Eng. C* 117, 111285. doi:10.1016/j.msec.2020.111285

Wang Y, Y., Fu, P., Wang, N., Peng, L., Kang, B., Zeng, H., et al. (2020). Challenges and Solutions for the Additive Manufacturing of Biodegradable Magnesium Implants. *Engineering* 6, 1267–1275. doi:10.1016/j.eng.2020.02.015

Witte, F., Fischer, J., Nellesen, J., Crostack, H.-A., Kaese, V., Pisch, A., et al. (2006). *In Vitro* and *In Vivo* Corrosion Measurements of Magnesium Alloys. *Biomaterials* 27, 1013–1018. doi:10.1016/j.biomaterials.2005.07.037

Witte, F., Kaese, V., Haferkamp, H., Switzer, E., Meyer-Lindenberg, A., Wirth, C. J., et al. (2005). *In Vivo* corrosion of Four Magnesium Alloys and the Associated Bone Response. *Biomaterials* 26, 3557–3563. doi:10.1016/j.biomaterials.2004.09.049

Witte, F. (2010). The History of Biodegradable Magnesium Implants: A Review☆. *Acta Biomater.* 6, 1680–1692. doi:10.1016/j.actbio.2010.02.028

Wong, P.-C., Tsai, P.-H., Li, T.-H., Cheng, C.-K., Jang, J. S. C., and Huang, J. C. (2017). Degradation Behavior and Mechanical Strength of Mg-Zn-Ca Bulk Metallic Glass Composites with Ti Particles as Biodegradable Materials. *J. Alloys Compd.* 699, 914–920. doi:10.1016/j.jallcom.2017.01.010

Wu, H., Yin, Y., Hu, X., Peng, C., Liu, Y., Li, Q., et al. (2019). Effects of Environmental pH on Macrophage Polarization and Osteoimmunomodulation. *ACS Biomater. Sci. Eng.* 5, 5548–5557. doi:10.1021/acsbiomaterials.9b01181

Xu, L., Qin, J., Li, Z., Ding, S., Wen, K., Zhang, Y., et al. (2021). A Primary Study of the Corrosion Behavior and Superior Structure Stability of Mg-Ti Composites Fabricated by High-Pressure Solid-State Sintering. *J. Mater. Res. Technol.* 15, 1705–1715. doi:10.1016/j.jmrt.2021.09.005

Yao, F., You, G., Wang, L., Li, Q., Zeng, S., and Ming, Y. (2022). Design, Fabrication, Microstructure, and Mechanical Properties of Interlayer-free Vacuum Diffusion Bonding Mg/Ti Composites. *Vacuum* 199, 110947. doi:10.1016/j.vacuum.2022.110947

Yi, Z., Liu, Y., Ma, Y., Liu, Z., Sun, H., Zhou, X., et al. (2022). Surface Treatment of 3D Printed Cu-Bearing Ti Alloy Scaffolds for Application in Tissue Engineering. *Mater. Des.* 213, 110350–110571. doi:10.1016/j.matdes.2021.110350

Zhang, M., Yu, Q., Liu, Z., Zhang, J., Jiao, D., Li, S., et al. (2021). Compressive Properties of 3-D Printed Mg-NiTi Interpenetrating-phase Composite: Effects of Strain Rate and Temperature. *Compos. Part B Eng.* 215, 108783. doi:10.1016/j.compositesb.2021.108783

Zhang, M., Yu, Q., Liu, Z., Zhang, J., Tan, G., Jiao, D., et al. (2020). 3D Printed Mg-NiTi Interpenetrating-phase Composites with High Strength, Damping Capacity, and Energy Absorption Efficiency. *Sci. Adv.* 6, 268–273. doi:10.1126/sciadv.aba5581

Zhang, X.-Y., Li, W.-G., Wu, Y.-J., Bai, D.-C., and Liu, N.-F. (2005). Proanthocyanidin from Grape Seeds Enhances Doxorubicin-Induced Antitumor Effect and Reverses Drug Resistance in Doxorubicin-Resistant K562/DOX Cells. *Can. J. Physiol. Pharmacol.* 83, 309–318. doi:10.1139/y05-018

Zhu, C., Lv, Y., Qian, C., Qian, H., Jiao, T., Wang, L., et al. (2016). Proliferation and Osteogenic Differentiation of Rat BMSCs on a Novel Ti/SiC Metal Matrix Nanocomposite Modified by Friction Stir Processing. *Sci. Rep.* 6, 38875. doi:10.1038/srep38875

Conflict of Interest: The reviewer CY declared a shared affiliation, with no collaboration, with the authors DR, HJ, ZL, and ZZ to the handling editor at the time of the review.

frontiers | Frontiers in Bioengineering and Biotechnology

ORIGINAL RESEARCH
published: 01 July 2022
doi: 10.3389/fbioe.2022.917812

Microstructural Origins of the Corrosion Resistance of a Mg-Y-Nd-Zr Alloy Processed by Powder Bed Fusion – Laser Beam

Hanna Nilsson Åhman[1,2]*, *Francesco D'Elia*[1], *Pelle Mellin*[2] *and Cecilia Persson*[1]

[1]*Division of Biomedical Engineering, Department of Materials Science and Engineering, Uppsala University, Uppsala, Sweden,*
[2]*Swerim AB, Stockholm, Sweden*

Magnesium alloys are biocompatible, biodegradable and have the ability to promote bone ingrowth, making them ideal candidate materials for replacing auto- and allografts in future treatments of large bone defects. Powder bed fusion–laser beam (PBF-LB) additive manufacturing of these alloys would further allow for the production of complex structures, optimized for bone grafting. However, the corrosion rates of structures processed by PBF-LB remain too high. An improved understanding of the influence of the microstructure generated during PBF-LB on the corrosion properties is considered key to their future implementation in implants. In this study, the effect of PBF-LB processing and subsequent hot isostatic pressing (HIP) on the microstructure and texture in different sample directions was studied and related to the corrosion behavior of a Mg-Y-Nd-Zr alloy. The results were compared with an extruded Mg-Y-Nd-Zr alloy. A higher amount of secondary phases resulted in a higher rate of localized corrosion for the PBF-LB processed material compared to that for the extruded one. Due to growth of the secondary phases, the corrosion rate was further increased after HIP. Moreover, a strong texture was observed in the PBF-LB material, and it was also enhanced in the HIP material. While this affected the electrochemical activity as measured by potentiodynamic polarization tests, any texture effect appeared to be masked by the contribution of the secondary phases in the longer-term mass change and hydrogen evolution tests. Future work should look further into the influence of individual process parameters on the microstructure and the resulting corrosion behavior of the material, to further clarify its interdependence.

Keywords: hot isostatic press (HIP), additive manufacturing, powder bed fusion, laser beam, WE43, magnesium, biodegradable metals, biodegradation

Edited by:
Nicole Sommer,
Medical University of Graz, Austria

Reviewed by:
Dong Bian,
Guangdong Provincial People's Hospital, China
Pei Feng,
Central South University, China

****Correspondence:***
Hanna Nilsson Åhman
hanna.nilsson-ahman@swerim.se

Specialty section:
This article was submitted to Biomaterials, a section of the journal Frontiers in Bioengineering and Biotechnology

Received: *11 April 2022*
Accepted: *14 June 2022*
Published: *01 July 2022*

Citation:
Nilsson Åhman H, D'Elia F, Mellin P and Persson C (2022) Microstructural Origins of the Corrosion Resistance of a Mg-Y-Nd-Zr Alloy Processed by Powder Bed Fusion – Laser Beam. Front. Bioeng. Biotechnol. 10:917812. doi: 10.3389/fbioe.2022.917812

INTRODUCTION

Bone tissue generally has a great ability to regenerate, and in the case of small fractures, it can heal without any outer intervention besides external support in the form of a cast. However, for the healing of large bone defects, such as comminuted long bone fractures, or defects related to the removal of diseased bone, surgical intervention is often needed (Einhorn and Gerstenfeld, 2015). Today, the gold standard for the treatment of large bone defects is autografting or allografting, where the missing bone is replaced with a piece of bone taken from another location of the patient's own body or from a donor. Nevertheless, the limited availability along with the risk of donor site morbidity or host rejection remains a problem (Giannoudis et al., 2005; Valtanen et al., 2021). Consequently, alternative treatments for the improved healing of large bone defects are needed.

Magnesium (Mg) and its alloys have been found to be some of the most promising materials for the production of biodegradable orthopedic implants (Plaaß et al., 2016; Han et al., 2019; Prasad et al., 2021). Magnesium is highly biocompatible, biodegradable, and known to promote osteogenic differentiation and enhance bone ingrowth (Castellani et al., 2011; Cao et al., 2020; Liang et al., 2021). Furthermore, Youngs's modulus of Mg alloys is closer to that of bone in comparison with the metal alloys traditionally used in orthopedics, such as the Ti-6Al-4V (Staiger et al., 2006; Kurdi et al., 2020). A mismatch in Young's modulus will affect the distribution of stresses in the bone surrounding the implant. This is important, as bone is a dynamic material, and an incorrect stress distribution can result in bone degradation and implant loosening (Engh et al., 1987; Hasegawa et al., 2021). The first clinically implemented biodegradable metal implant was a bone fixation device produced from a powder extruded Mg-Y-Nd-Zr alloy, which received its CE certification in 2013 (Syntellix., 2019; Han et al., 2019).

The establishment of the Mg-Y-Nd-Zr family of alloys (e.g., WE43) has enabled a broader use of Mg alloys in a large range of industrial applications (Luxfer MEL Aircraft interiors., 2003; Kainer, 2003). Such Mg-RE alloys often consist in low alloyed (Mg > 90 wt%), multi-phase systems (Kainer, 2003) given their high tendency to form intermetallic compounds with Mg. The improved corrosion property of the Mg-RE alloys in comparison with other commercial alloys such as the Mg-Al-Zn systems (AZ-series), can be derived from the corrosion potential of the intermetallic phases formed in the Mg-RE system being closer to that of the Mg-matrix (Südholz et al., 2011). There is also a positive shift in the corrosion potential of the Mg–matrix due to the relatively high solubility of Y in Mg (Ben-hamu et al., 2007; Südholz et al., 2011). Moreover, Y contributes to an enhanced corrosion resistance by improving the stability of the surface through the formation of Y2O3 (Du et al., 2011). New production routes such as powder extrusion, ensure a uniform distribution of secondary phases to further promote a more uniform and less severe degradation rate, which is desired for resorbable orthopedic fixation devices and stents (Biotronik; Syntellix). (Magnesium Scaffold, 2020)

Powder bed fusion–laser beam (PBF-LB) is an advanced manufacturing technique offering unique possibilities regarding design optimization for all types of applications (Gibson et al., 2015). In orthopedics, PBF-LB of metal alloys such as Ti-6Al-4V has allowed for the manufacturing of complex patient specific implants with optimized structures for cell viability and bone ingrowth (Revilla-León et al., 2020; McGregor et al., 2021; Yang et al., 2021; Zhao et al., 2021). Combining the unique possibilities provided by PBF-LB regarding design optimization, with the biodegradability and biocompatibility of Mg alloys, can lead to the development of a new generation of load-bearing biodegradable metal implants for the improved healing of large bone defects. However, for a successful development of Mg-based biodegradable bone grafts, the corrosion rate needs to be controlled. Firstly, the corrosion rate needs to be slow enough, so that the biodegradable implant maintains its mechanical properties and structural integrity during the load bearing phase. For this, a degradation rate of 0.5 mm/year is the current recommended limit (Ding, 2016). Secondly, Mg alloys degrade with H2 gas as one of the main corrosion products. The amount of H2 gas formed needs to be controlled, as too high gas evolution can have an adverse effect on the bone remodeling (Plaaß et al., 2016; Meier and Panzica, 2017). A limit of an average H2 gas evolution rate of 0.01 ml/cm^2/day has been suggested by Song et al. (Song et al., 2001).

The feasibility of processing Mg alloys by PBF-LB was first proven by Ng et al., in 2010 (Ng et al., 2010), while the first studies on the processing of a Mg-Y-Nd-Zr alloy specifically by PBF-LB were presented by Tandon et al. and Jauer et al., in 2015 and 2016, respectively (Tandon et al., 2015, 2016; Jauer et al., 2016). In the last couple of years there have been a number of studies on the microstructure and material properties of Mg-Y-Nd-Zr alloys processed by PBF-LB.

A few of these studies have focused on the corrosion properties of Mg-Y-Nd-Zr alloys processed by PBF-LB, including the effects of heat treatment (Esmaily et al., 2020) plasma electrolytic oxidation (PEO) surface treatments (Li et al., 2021), and lattice design (Kopp et al., 2019). A study on the *in vivo* degradation behavior of PBF-LB processed Mg-Y-Nd-Zr alloy has also been recently published (Liu J. et al., 2022). Esmaily et al. (Esmaily et al., 2020) evaluated the corrosion properties in 0.5% NaCl of a Mg-Y-Nd-Zr alloy processed by different PBF-LB parameters and subsequently treated by hot isostatic pressing (HIP) and heat treated. HIP treatment is commonly applied to remove defects (e.g., porosity) often found in PBF-LB materials in order to obtain a fully dense material (Gibson et al., 2015). Such defects can have detrimental effects on both corrosion and mechanical properties (Geenen et al., 2017). Esmaily et al. showed that HIP and heat treatment improved the short-term degradation rates, but the cast counterpart remained superior. Even though the study offered an important insight into the corrosion behavior of a Mg-Y-Nd-Zr alloy processed by PBF-LB, the study is limited to only short-term corrosion properties. Moreover, the corrosive medium did not contain neither Ca nor P, which have an important influence on the degradation properties of Mg alloys (Rettig and Virtanen, 2009; Esmaily et al., 2017; Py et al., 2020). In the case of surface treatments, although PEO has demonstrated the ability to mitigate the corrosion to some extent, the corrosion rates of the bulk Mg material remain too high (Benn et al., 2021; Li et al., 2021; Suchý et al., 2021). Additionally, the *in vivo* study further corroborated the need for further improvements of corrosion properties (Liu J. et al., 2022).

Finally, Mg-Y-Nd-Zr alloys produced by various routes, including PBF-LB, are known to produce a very strong texture (Esmaily et al., 2020; Li et al., 2021). Texture has previously been shown to affect the corrosion behavior of Mg alloys due to a difference in electrochemical activity of the different crystallographic planes (Song and Xu, 2012; Sabbaghian et al., 2019). Texture has also induced an anisotropic corrosion behavior in other metals processed by PBF-LB, such as Al

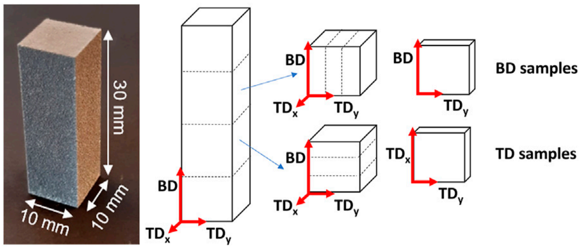

FIGURE 1 | Schematic of the cutting of the samples indicating build direction (BD) and transverse directions (TD), as well as the denomination used for the surfaces throughout the text.

(Chen et al., 2018) and Ti (Dai et al., 2016), but its effect on corrosion has not yet been evaluated for any Mg alloys.

With the aim of improving the corrosion properties of a Mg-Y-Nd-Zr alloy processed by PBF-LB, the porosities were removed through HIP. The resulting densification as well as its impact on the microstructure and texture and resulting corrosion properties for 28 days were investigated. The distribution and type of the secondary phases present in the Mg-Y-Nd-Zr alloy were characterized before and after HIP, along with grain size distribution and texture. Moreover, the influence of the resulting microstructure and texture on the long-term corrosion properties, including corrosion morphology and corrosion rate, was determined. Finally, the results were compared with those for a powder extruded Mg-Y-Nd-Zr alloy, which is the material from which the commercially available implants are currently being produced.

MATERIALS AND METHODS

Sample Preparation

A gas atomized Mg-Y3.9-Nd3.0-Zr0.49 (in wt%) alloy metal powder, with a fine particle size distribution (d10 = 25 μm, d50 = 42 μm and d90 = 67 μm), was purchased from NMD GmbH (Hemseen, Germany). The powder was processed by PBF-LB on an EOS M290 printer (EOS GmbH, Krailling, Germany). The process was carried out under argon atmosphere (O2 < 0.1%) to minimize oxidation during the process. A laminar flow of argon across the bed removed the evaporation products. A build plate of a commercial Mg-Al-Zn alloy (KG Fridman AB, Karlstad, Sweden) was used to ensure the weldability of the powder to the build plate. Previously optimized parameters (Nilsson Åhman et al., 2022), with a laser power of 200 W, scanning speed of 1111 mm/s, hatch distance of 0.1 mm and a layer thickness of 0.03 mm, were applied to produce rectangular samples with a measurement of 10*10*30 mm. The laser focus diameter is 90 μm. The scanning direction was rotated 67° between each layer to minimize the overlapping of scanning tracks between layers (Pakkanen, 2018), and no contouring was used.

To understand the impact of porosity, two samples were post processed by HIP, to remove the final porosity. During HIP, 520°C and 105 MPa of pure argon was applied for 3 h in a QIH9 HIP machine (Quintus, Västerås, Sweden) (Esmaily et al., 2020).

Commercially produced powder extruded Mg-Y3.9-Nd3.0-Zr0.49 (in wt%) alloy was purchased (Smiths, Biggleswade, United Kingdom) and used as reference, as it corresponds to the material used in the biodegradable metal implants found on the market today (Syntellix).

Compositional and Microstructural Characterization

The porosity of the as-built (AB) and HIP samples was established according to the standard ASTM B311-17, using the Sartorius YDK01 density determination kit (Sartorius AG, Goettingen, Germany). The density of the samples was measured before they were cut according to the scheme presented in **Figure 1**, with NAB = 5 and NHIP = 2. The density was then compared to the expected density of the alloy, 1.84 g/cm^3 (Cverna et al., 2001).

To study the microstructure of the surfaces in the build direction (BD) and the transverse direction (TD) the samples were cut according to the scheme presented in **Figure 1** to obtain 10 mm^2 surfaces. The BD surface is defined as the surface that is parallel to the build direction, i.e., the z axis, and perpendicular to the x and y axes. The TD surface is defined as being perpendicular to the z axis, and thus the BD surface. As the scanning direction was rotated with 67° in each layer, the x and y axes can be used interchangeably, i.e., TD = TDx and TDy.

For microstructural analysis, samples of the AB, HIP and extruded (Extr) material were mounted in Bakelite and ground with abrasive silicon carbide papers of grades P600, P1200, P2500 and P4000, and subsequently polished using oxidized porous silica (OPS) for 15 min. The microstructure of the samples was investigated using a light optical microscope (LOM) (Leica DM IRM, Leica Microsystems GmbH, Wetzlar, Germany), after 5 s of etching with 2% Nital (2 wt% nitric acid in methanol). Further characterization of the microstructure and the secondary phases was done by backscatter electron imaging (BSE) in a scanning electron microscope (SEM, AZtec 5.0, Oxford Instruments, Abingdon, United Kingdom).

Identification of secondary phases was also done using X-ray diffraction (XRD) (Bruker D8 Discover, Bruker, Billerica, MA, United States). The XRD was performed with Cu Kα (1.54 Å) radiation, and poly-capillary optics were used for parallel beam geometry with a collimator size of 2 mm. Data was collected between 10° and 120° (2θ) and analyzed using the Bruker software DIFFRAC.EVA (Bruker, Billerica, MA, United States).

Grain size and texture of the AB, HIP and Extr material were measured using electron backscatter diffraction imaging (EBSD, Nordlys HKL detector, Oxford Instruments, Abingdon, United Kingdom). A step size of 0.8 μm was used, and the grain boundaries were defined as having a misorientation greater than 15°. The grain size is defined as the area-weighted average of the equivalent circle diameter. The data was analyzed using Aztec Crystal 2.0 (Oxford Instruments, Abingdon, United Kingdom).

TABLE 1 | Salt concentration of Dulbecco's Phosphate Buffered Saline solution.

	CaCl2 ·H2O	MgCl2·H2O	KCl	KH2PO4	NaCl	Na2HPO4
g/L	0.133	0.1	0.2	0.2	8.0	1.15

Corrosion Measurements

For corrosion measurements, 1 mm of the AB surface of the 10*10*30 mm printed rectangle was removed to ensure that only bulk material was being evaluated. Samples were then cut into pieces measuring 8*8*2 mm according to the scheme presented in Figures.

Figure 1 to ensure that the surface investigated was the one mainly in contact with the corrosion medium. Samples of the same size were sectioned from the Extr material, investigating the surfaces in the extrusion direction. The surfaces were ground with abrasive silicon carbide papers of grades P600, P1200 and P2500, then washed with ethanol, dried with a hot air dryer, and stored in a desiccator for 24 h before evaluation. All corrosion tests were carried out in non deareated Dulbecco's Phosphate Buffered Saline solution (DPBS, Sigma Aldrich, St. Louis, MO, United States) with the concentrations given in **Table 1**. The ratio between the corrosion medium and the sample surface area was above 20 ml/cm^2, in accordance with ASTM G31 (ASTM G31-72 (2004))

Potentiodynamic polarization testing (PDP) was performed in triplicate using a flushed-port cell with a three-electrode set-up (ASTM G150) (ASTM G150-18, 2018), and a Parstat 3000A-DX potentiostat (Ametek Inc., Berwyn, PA, United States). A saturated calomel electrode was used as a reference, and Pt-wire as a counter electrode. Potentiodynamic scans were conducted at a rate of 1 mV/s, after 10 min of conditioning at open circuit potential (OCP) (Kirkland et al., 2012). The corrosion potential (Ecorr) and corrosion current (icorr) were determined by Tafel extrapolation using VersaStudio software (VersaStudio 2.60.6, Ametek Inc., Berwyn, PA, United States).

To further investigate the initial stages of the corrosion attack in the AB, HIP and Extr material, samples were ground with abrasive silicon carbide papers down to P4000, and subsequently polished using OPS for 15 min, before immersion in DPBS for 30 min. The resulting surface was investigated with BSE - SEM.

To study the corrosion morphology and the corrosion behavior over time, immersion tests in triplicate were also carried out in DPBS at 37°C for 28 days. An analytical balance (Mettler AE240, Mettler-Toledo, Columbus, OH, United States) with an accuracy of 0.05 mg was used to establish the weight of the samples before and after 28 days of immersion. To track the instantaneous corrosion rate, the hydrogen evolution was also measured over a period of 28 days using the volumetric method described by Song et al. (Song et al., 2001). The samples that were immersed for 28 days were washed with deionized water and dried with a hot air dryer, and their surfaces were then examined in LOM to establish the corrosion morphology.

Finally, the samples immersed for 28 days were mounted in Bakelite, and ground with abrasive silicon carbide papers of grades P600, P1200, P2500 and P4000, using ethanol, and subsequently polished with diamond carbon paste with grit size 3 and 0.25 μm. The resulting cross sections were characterized using BSE-SEM and EDS.

RESULTS AND DISCUSSION

Compositional and Microstructural Characterization

The result for the densities of the AB and HIP samples was 99.4 ± 0.05% and 99.9 ± 0.005% respectively. According to the Archimedes measurement there is a clear increase in density after HIP, and no pores are visible in the microscopy images of the HIP material (**Figure 2**). The LOM images of the AB and the HIP samples, both in BD and TD direction, as well as the Extr sample are presented in **Figure 2**. The individual melt pools are clearly visible in the LOM images of the AB sample in the BD direction (**Figure 2A**)), and conversely, the scanning lines from the laser are clearly visible for AB sample in the TD image (**Figure 2B**)). Examining the LOM images after HIP, the structure of the melt pools is still discernable in the images of the HIP material in the BD direction (**Figure 2C**)) and the scanning lines from the laser are still clearly visible in the HIP material in the TD direction (**Figure 2D**)). As there is usually a preferential etching taking place in areas surrounding secondary phases, one can from these images presume that there is a redistribution of secondary phases after HIP. In the Extr material, there is a segregation of secondary phases along the grain boundaries as well as typical necklace-type distribution of particles, and the individual recrystallized α-Mg grains are clearly visible (**Figure 2E**)).

The melt pools are also clearly visible in the BSE-SEM images, marked with a dashed red line in **Figure 3A**). In the same image, the area in the circle marked i) highlights a cellular structure that can be seen inside the melt pools, with lines of precipitates aligned parallel to the melt pool boundaries. The size of the precipitates ranges from a few nm up to 100 nm. At the melt pool boundaries is another region, highlighted by the circle marked ii), where precipitates are organized in lines perpendicular to the melt pool boundary. These regions coincide with the area marked with i) and ii) in the BSE-SEM images of the TD direction (**Figure 3B**), confirming the accumulation of secondary phases at the edges of the laser scanning track. Moreover, round precipitates with sizes around 200–400 nm are present throughout the material independently of the melt pool boundaries, as indicated in **Figure 3A**. EDS point analysis identified them as Zr-rich particles. Larger precipitates in the form of flakes measuring a few micrometers and high in Y and O are also visible throughout the microstructure. These oxide flakes are likely remains from oxide shells originating along the surface of powder particles during gas atomization. Due to the very high melting point of these oxide shells, it is unlikely that they are melted during PBF-LB, but rather, they are cracked and therefore remains inside the solidified material. Precipitates of HCP-Zr have been observed before, and have been predicted by thermodynamic calculations based on the Calphad method (Nilsson Åhman et al., 2022). These observations are in line with what has previously been

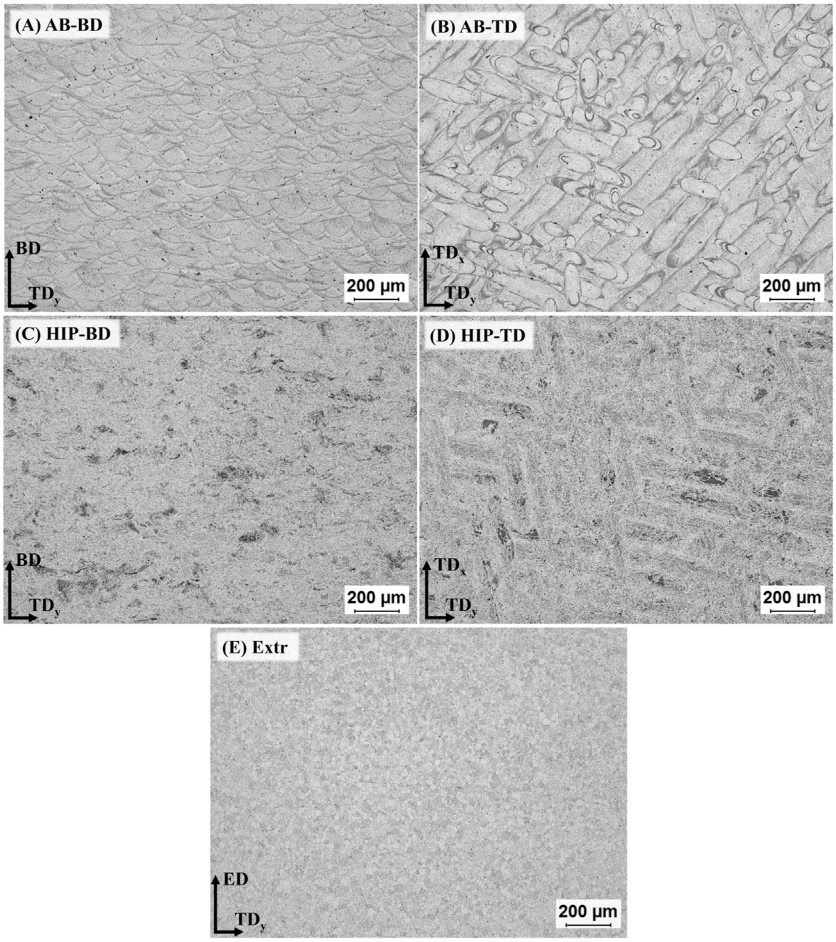

FIGURE 2 | LOM images of the samples after 5s etching in 2% Nital, for **(A)** AB-BD direction, **(B)** AB-TD direction, **(C)** HIP-BD direction, **(D)** HIP-TD and **(E)** Extr material.

observed for a Mg-Y-Nd-Zr processed by PBF-LB (Bär et al., 2019).

After HIP, the secondary phases coarsen considerably, and the melt pool boundaries are no longer visible in BSE-SEM images (**Figures 3C,D**). There are randomly distributed larger angular precipitates in the order of µm, rich in Nd and there are also smaller precipitates in the form of thin platelets and globular particles, ranging in size from a few to 100 nm. EDS found the area containing these precipitates to be enriched in Y and Nd. The oxides are still present after HIP, which was expected, as the solubility of O in Mg is very low (Hallstedt, 1993). Inspection of the BSE-SEM images of the Extr material reveals secondary phases rich in Y and Nd that are primarily present in the grain boundaries, whose distribution corresponds to that also observed in the LOM images in **Figure 2**. Some Zr-rich precipitates are also present, but none were found to contain large amounts of O.

The XRD spectra for the AB, HIP, Extr and powder material is presented in **Figure 4**. The main peaks all correspond to α-Mg in all spectra, and smaller peaks identified with Y2O3 were also present in all samples. Oxide particles were observed in the microstructure of the Extr material, originating from the production of the powder, but is also expected to be found as a thin layer on the surface. In the powder and in the AB material, peaks corresponding to the Mg3Nd phase were established. However, no peaks corresponding to the Mg3Nd phase were seen for the HIP material. Peaks that are not present in the powder sample but can be found in the spectra for both the AB and the HIP material are those corresponding to the intermetallic compounds Mg41Nd5 or Mg24Y5. It is not possible to determine which is present due their peaks overlapping in the XRD spectra, but both are expected to be present, together with ternary Mg-Y-Nd phases (Zumdick et al., 2019). These peaks also grow stronger after HIP, which could be related to the growth in size of these secondary phases observed in the BSE-SEM images (**Figure 3**). There are also a number of smaller peaks that were not identified.

The LOM and BSE-SEM microscopy images as well as the results from the XRD are in line with the microstructure observed for the AB and Extr material in previous studies (Bär et al., 2019; Zumdick et al., 2019; Esmaily et al., 2020). Mg3Nd is a meta-stable intermetallic phase, and the presence of the Mg3Nd precipitates in the powder, as well as in the AB material, is

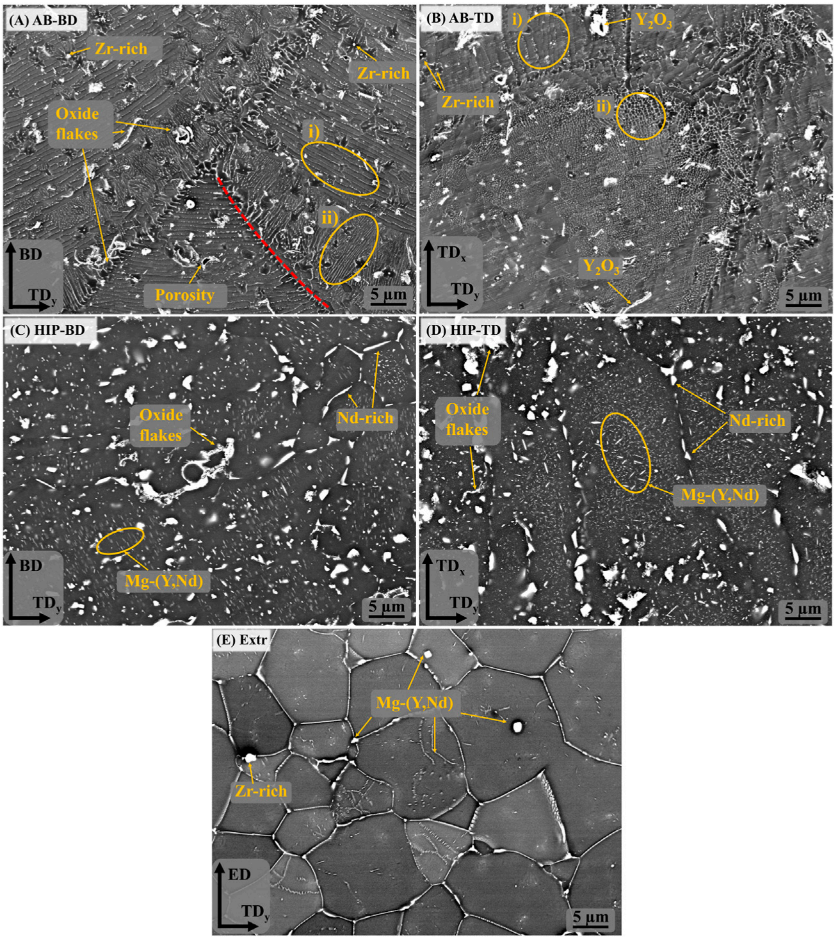

FIGURE 3 | BSE-SEM images of the **(A)** AB-BD direction, **(B)** AB-TD direction, **(C)** HIP-BD direction, **(D)** HIP-TD and **(E)** Extr material.

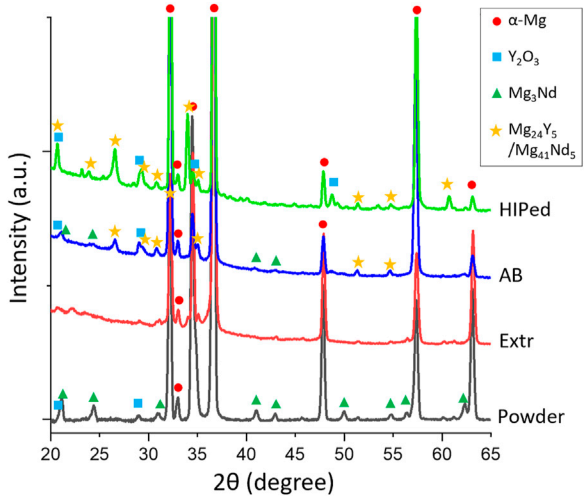

FIGURE 4 | XRD spectra of the powder, the Extr, AB and HIP samples.

also in agreement with the discussion on stability and thermodynamics of the secondary phases in Mg-Y-Nd-Zr alloys (Nie and Muddle, 2000). As it is a meta-stable phase, this can also explain why it is not present in the material after HIP. The intermetallic compounds Mg41Nd5 and Mg24Y5 have been confirmed as stable phases in a number of other studies on the Mg-Y-Nd systems, and are also the precipitates present in the HIP material (Gangireddy et al., 2018).

The result of the EBSD measurements of the AB, HIP and Extr material can be found in **Figure 5** in the form of inverse pole figures (IPF) and corresponding IPF color maps. The IPF color maps of the AB material in the BD and TD direction can be seen in **Figures 5A,B**. In both these images it can be observed that grains have to a large extent grown within the melt pool. It is especially evident in the IPF color map of the AB TD image, where larger grains with a strong basal texture grown within the laser tracks can be observed. The extension of the larger grains along the melt pool results in a larger grain size in the TD direction than in the BD direction. The average grain size in the BD direction was around 19 μm, while for the TD direction it was around 35 μm. The larger grains have a crystal structure whereby the

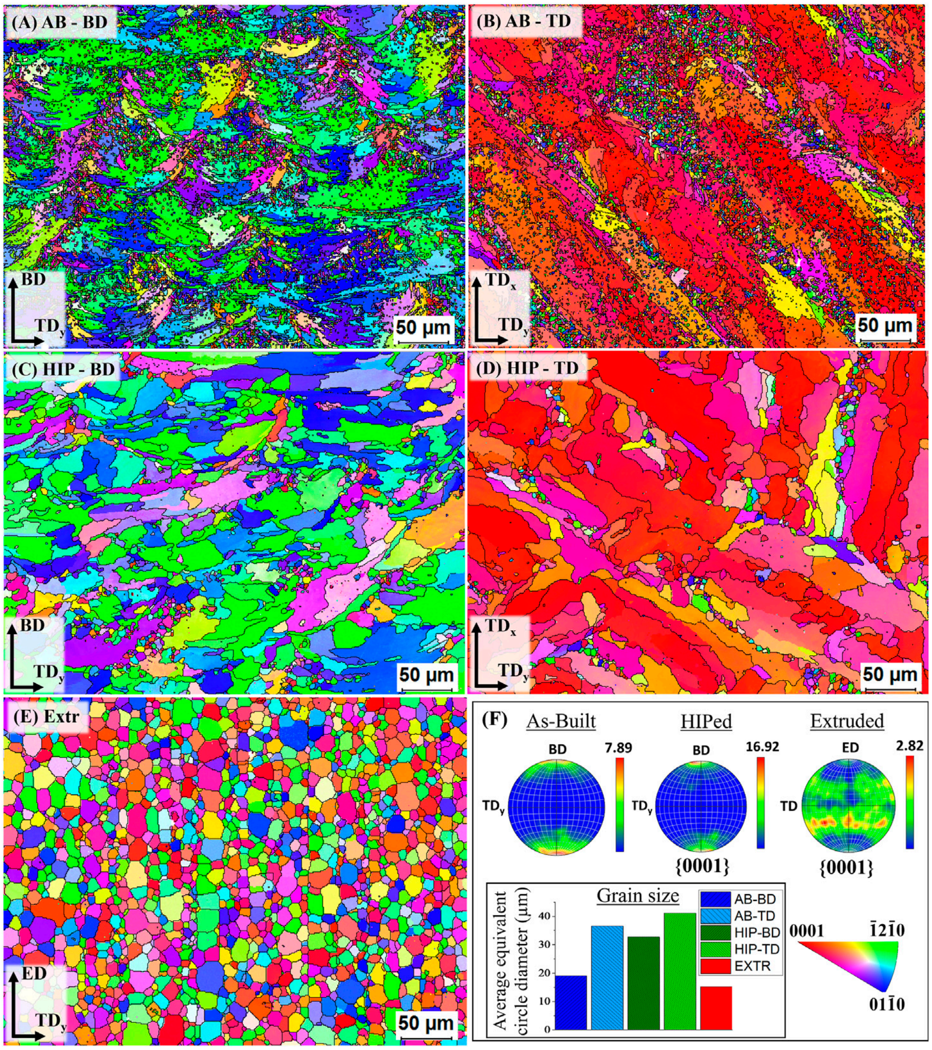

FIGURE 5 | IPF color maps of the AB **(A,B)** HIP **(C,D)** and Extr **(E)** material, together with the pole figures **(F)**.

[0001] axis of the HCP crystal grains is orientated parallel to the build direction. Along the boundaries of the laser scanning tracks, there are clusters of smaller equiaxed grains with random texture.

The two types of grain structures have been observed in previous work, with a varying distribution. Jauer et al. reported an average grain size of around 1 μm in the BD direction (Jauer et al., 2016), with the majority of the grains having equiaxed morphology and weak texture, and only a few large elongated grains having basal texture. The information given on the process parameters is however too limited to discuss the difference. Esmaily et al. on the other hand, reported average grain sizes (Esmaily et al., 2020) ranging from 18 to 36 μm in the TD depending on the processing parameters applied. The majority of the grains consisted in the larger grains with a strong basal structure, and only a limited amount of the smaller equiaxed grains with a weaker texture can be observed in the EBSD map for one of the sets of process parameters. Esmaily et al. also applied a different scan strategy, rotating 90° between the layers, as opposed to the 67° rotation used in this study. The difference in scanning rotation has resulted in a difference in grain growth in other metals processed by PBF-LB, such as in Ti alloys (Zheng et al., 2022) and in Ni alloys (Carter et al., 2014). However, no major difference was observed in the morphology of the larger grains in this study and the article by Esmaily et al. However, there is a large number of the smaller equiaxed grains present in this study. This could be related to the difference in hatch distance in relation to the focus diameter of the laser beam. Esmaily et al. used a hatch distance of 40 μm, which is much smaller than the focus diameter of 90 μm. Comparing these parameters to those used in this study, i.e., hatch distance of 100 μm and focus diameter of 90 μm, suggests that subsequent scanning lines in the study of Esmaily et al. were overlapping to a much larger extent. This larger overlapping of subsequent laser scanning tracks would result in increased remelting of the material and thus, a lower presence of smaller equiaxed grains. Moreover, there are differences in laser power and laser scanning

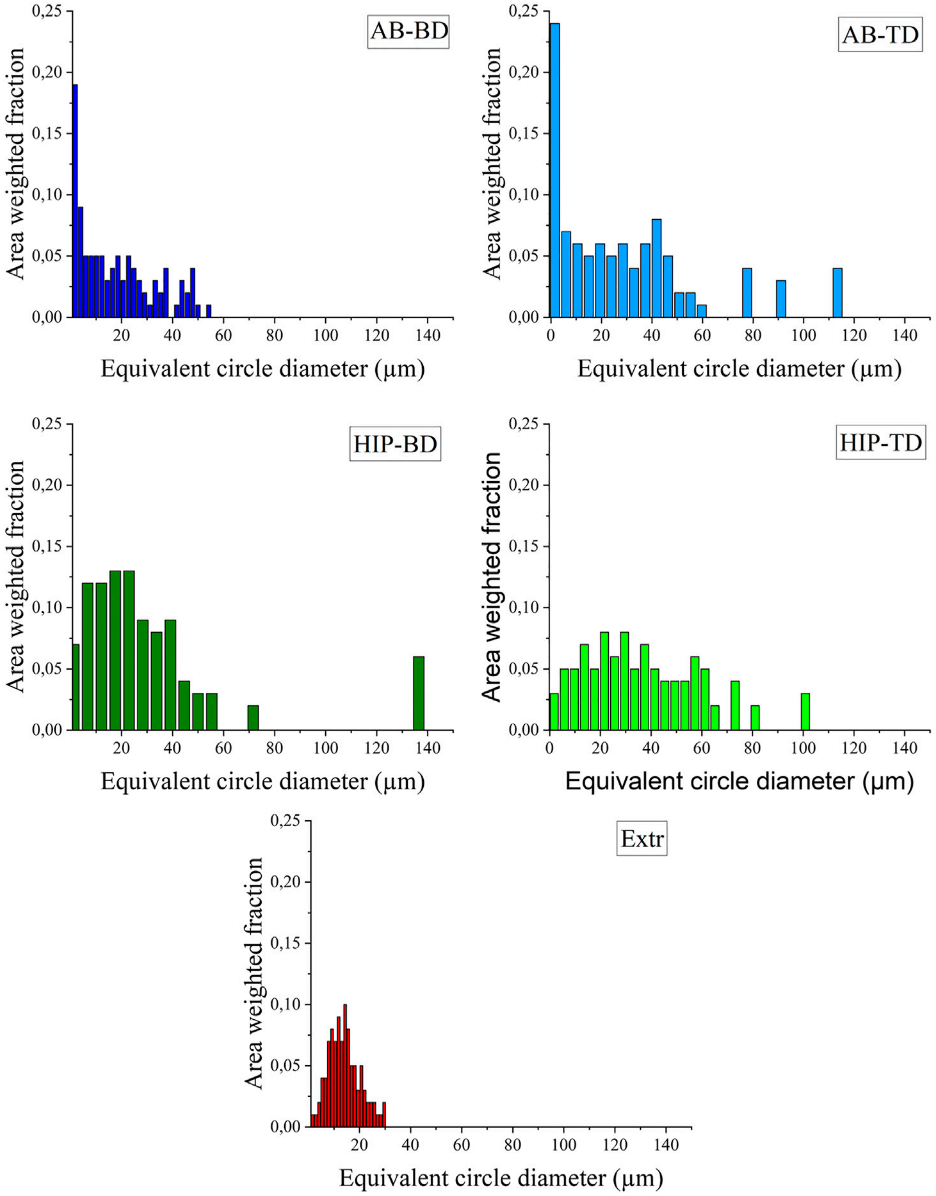

FIGURE 6 | Grain size distribution presented as equivalent circle diameter plotted against the area weighted fraction for the **(A)** AB-BD, **(B)** AB-TD, **(C)** HIP-BD, **(D)** HIP - TD and **(E)** Extr material.

speed, thereby making it difficult to conclude on the extent to which the various parameters affect the difference in microstructure between the two studies.

Neither Esmaily et al. nor Jauer et al. investigated the difference in grain morphology between TD and BD. Zumdick et al. (Zumdick et al., 2019) obtained an average grain size of 1.0 ± 0.4 µm and 1.1 ± 0.4 µm for the TDx and TDy respectively, and 1.1 µm in the BD plane, which is much smaller than those observed in this study. However, the authors only reported average grain sizes and did not regard the effect of grain orientation and texture in their study. Until now, the differences in grain size distribution depending on the build direction, has not been investigated.

The differences observed in reported microstructures between previous studies could be due to variations in both the processing parameters, as well as the original alloy content of the gas atomized powder. However, these are the only studies available that include characterization of the grain size of Mg-Y-Nd-Zr alloys processed by PBF-LB. Regardless, the difference in grain morphology observed in the above-mentioned studies, as well as the clear difference between the TD and BD direction observed in this study, highlights the need to further study the

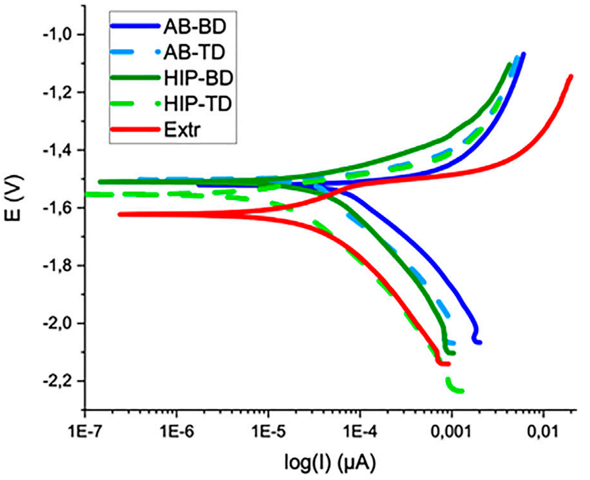

FIGURE 7 | Potentiodynamic testing curves for AB, HIP and Extr material.

TABLE 2 | OCP, corrosion potential, and corrosion current for respective material.

	OCP	Ecorr	Icorr
	[Vvs SCE]	[Vvs SCE]	[μA/cm2]
AB-BD	−1.56	−1.51 ± 0.006	119 ± 61.2
AB-TD	−1.58	−1.51 ± 0.007	37 ± 8.2
HIP-BD	−1.58	−1.49 ± 0.020	53 ± 15.9
HIP-TD	−1.60	−1.57 ± 0.04	25 ± 13.5
Extr	−1.65	−1.62 ± 0.002	30 ± 4.1

relationship between feedstock, processing parameters and microstructure, as well as its influence on material properties.

The IPF color maps of the HIP material can also be seen in **Figure 5**. In these images it can be observed that the smaller equiaxed grains have almost disappeared, and the grains with strong basal structure have grown, resulting in an increase in average grain size in both the BD (33 μm) and TD (41 μm). It should also be noted that the average grain size for AB-TD is larger than for HIP-BD. As a result of the growth of the larger grains with a strong basal structure, and the equiaxed grains with a random texture disappearing, the HIP material exhibits a much stronger texture than the AB material. These results show a larger change in grain structure as compared to what has previously been reported for the HIP Mg-Y-Nd-Zr alloys processed by PBF-LB and HIP with same parameters (Esmaily et al., 2020). Esmaily et al. also observed a larger amount of equiaxed grains remaining after HIP.

In the IPF color map of the Extr material, the same grain structure as observed in the LOM and the BSE-SEM images can be seen. The Extr material has an average grain size of 15 μm, with more homogenous grain size distribution, and a weaker texture than that of the PBF-LB material. These results are in line with what has previously been reported for extruded Mg-Y-Nd-Zr alloys (Zhang et al., 2020).

The observations made for the EBSD color maps presented in **Figure 5** can be corroborated by the graphs presenting the grain size distribution (**Figure 6**). For both the AB groups, a larger number of small grains are present than for the HIP material. The increase in larger grains can also be seen for the HIP material. The higher amount of large grains in the TD material compared to the BD material can also be observed for both the AB and HIP material. The extruded material is, as can be expected from the EBSD map, showing a normal distribution.

Corrosion Measurements

The corrosion properties of the samples were first evaluated by PDP, for which the results are presented in **Figure 7**, together with the averaged values of the open circuit potential (PCP) corrosion potential and the corrosion current in **Table 2**. In contrast to the printed material, the Extr material showed a slight tendency towards passivation, manifested as an inflection in the anodic branch of the curve, which could indicate an initial breakdown followed by a passivation of the surface. Neither the AB nor the HIP material showed a similar behavior. The BD and TD surfaces all show a similar anodic behavior, indicating high corrosion rates for all printed samples. However, at higher potentials the anodic current density was highest for the Extr material.

With regards to the cathodic branch of the curve, the AB materials show higher current densities than both the HIP and Extr material. The AB current densities are higher throughout the cathodic branch of the polarization curve than the HIP and this shift in the cathodic part of the curve is also reflected in the evaluated corrosion current densities (icorr), which are higher for AB than the corresponding HIP surface, indicating that the surface of the HIP material is more stable.

Comparing the current densities for the BD to the TD surfaces of the AB and HIP material, both BD surfaces exhibit a higher corrosion current than the corresponding TD surface. The difference was more pronounced for the AB than for the HIP material. Looking at the result obtained from EBSD, this is in line with the findings of Song et al. (Song and Xu, 2012) which showed that the strongly textured Mg-Al-Zn alloy exhibited a lower corrosion activity in the basal plane, as the close packed (0001) plane has a lower surface energy and is thus more stable and more corrosion resistant. Moreover, the variation in results for the printed samples were larger than for the Extr material, indicating a more inhomogeneous material.

The results from the hydrogen evolution and the mass change are presented in **Figure 8**. Looking at the hydrogen evolution, it is clear that the HIP material exhibited the highest hydrogen evolution rate, followed by the AB material. The results for the TD and BD surfaces were overlapping. The powder Extr material exhibited the lowest rate of hydrogen evolution, and also had the lowest divergence between the samples. The higher divergence indicates a more inhomogeneous material, which is in line with the corrosion current densities previously established (**Figure 7**). These results contradict the results for the PDP, which indicated that the AB material had a higher corrosion rate than the HIP one. A reason for this contradiction could be that the porosity in the AB material results in a higher surface area being exposed and has greater importance during the short-term PDP testing. Furthermore, the PDP is an accelerated test, and the formation of protective corrosion layers at the surface could make an appreciable contribution to the measured current

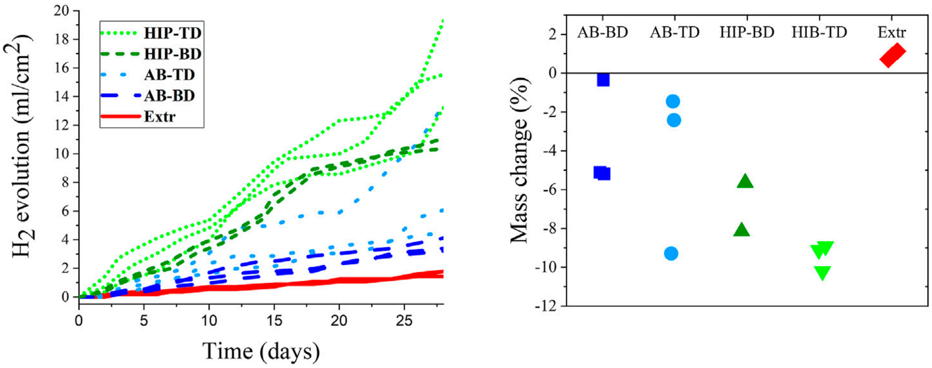

FIGURE 8 | Hydrogen evolution measured over a period of 28 days **(A)** together with a scatterplot for the change in mass after 28 days of immersion **(B)**. (*n* = 3 for all sample groups but HIP-BD, where *n* = 2).

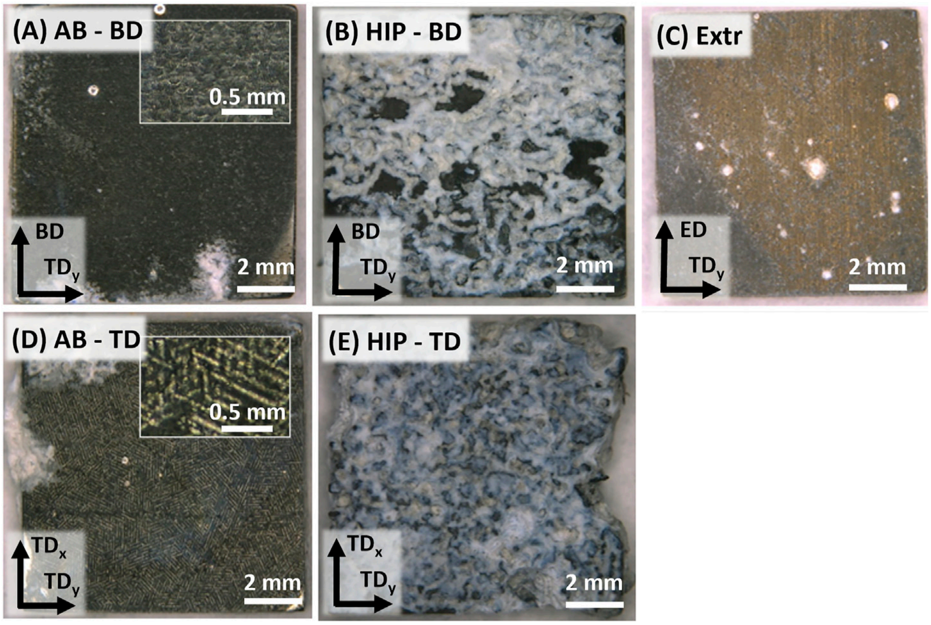

FIGURE 9 | Images of corroded samples after 28 days of immersion, with the AB surfaces in **(A,D)**, the HIP surfaces in **(B,E)**, and **(C)** the Extr material.

densities. The hydrogen evolution and mass change experiments are carried out for a much longer time and thus more closely reflect the expected performance as implants.

The mass change is also presented in **Figure 8** indicating similar results as the hydrogen evolution, with the HIP material having the highest corrosion rate followed by the AB material. The mass change results are affected by the buildup of corrosion products on the surface of the samples, which explains the positive mass change for the Extr material. There is also a large span in mass change, especially for the AB samples, which indicates an inhomogeneous material. Moreover, the number of samples available were limited, which limits drawing any strong conclusions regarding the difference BD and TD surfaces from the mass change measurements. Nevertheless, a clear difference between the samples could also be observed macroscopically in the LOM images of the samples after 28 days of immersion (**Figure 9**).

The images in **Figure 9** show the same trend as for the hydrogen evolution and mass change results, with the HIP material exhibiting the most severe corrosion attack, followed by the AB, and finally the Extr material. A thick layer of insoluble white corrosion products was formed on the surfaces of the HIP material (**Figure 9B**), and there was a large amount of corrosion products piled up at the bottom of the beaker for these samples. Even though some areas of the AB material also exhibited a buildup of the white corrosion products, and a small amount was collected at the bottom of the beaker, the AB and the Extr material both maintained a more homogenous surface (**Figures 9A,C**).

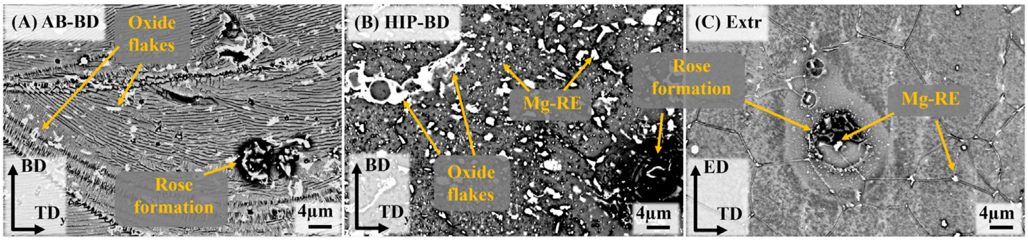

FIGURE 10 | BSE-SEM mages of the surfaces of **(A)** AB, **(B)** HIP and **(C)** Extr samples after 30 min immersion in DPBS.

Inserts of higher magnification for the AB material in **Figure 9A** still reveal the structure resulting from the laser scanning tracks (as observed in the LOM and BSE-SEM images of the AB material), especially in the TD direction. While the surface of the AB material turned dark, the surface of Extr material surface maintained a brighter gold-like color throughout the 28 days. Mg alloys darken as a thicker layer of corrosion products form on the surface, hence the difference in color indicates that the Extr material had a thinner layer of corrosion products built up on the surface (Taheri et al., 2014; Esmaily et al., 2017).

In order to achieve a better understanding of the corrosion mechanism at play, the surfaces of the samples were studied in the SEM after 30min immersion in DPBS (**Figure 10**). Local attack in the form of rose formations consisting in a buildup of corrosion products was observed in all materials. This type of formation has been previously observed to form around cathodically active intermetallic particles for both cast and Extr Mg-Y-Nd-Zr alloys (Kalb et al., 2012; Ascencio et al., 2015). This visibly local attack is in agreement with the behavior observed in the PDP curves, where the exponentially increasing anodic branch is indicating pitting corrosion (Kirkland et al., 2012). Although these rose formations are present also in the Extr material, the attack is less severe in other areas of the material, as can be seen in **Figure 10C**.

Comparing the Extr material (**Figure 10C**) with the AB material (**Figure 10A**), the corrosive attack, corresponding to the dark areas surrounding the intermetallic particles, is more severe in the AB material. Moreover, comparing the AB material to the HIP material, the dark areas surrounding the intermetallic particles are even larger for the HIP material. The difference between the printed materials and the Extr material can be related to the larger amount of intermetallic particles in the printed material as opposed to the extruded material, also resulting in a lower amount of alloying elements being dissolved in the Mg matrix. The difference between the AB and the HIP material was explained by the growth of the amount of intermetallic particles. It can also be observed that the localized attack is not as severe around the oxide flakes, suggesting that the internal oxides might not be the main cause for the poor corrosion resistance of the PBF-LB material, and that the Zr-rich and Mg-RE intermetallic particles are of greater relevance. However, even though the oxides do not appear to be a primary site of attack, a larger amount of Y2O3 would lead to a depletion of Y from the matrix, decreasing the corrosion resistance of the material (Davenport et al., 2007). Corrosion studies of Mg-Y-Nd-Zr alloys processed by PBF-LB and heat treated by other methods have exhibited similar results, with the heat-treated material generally possessing worse corrosion properties (Kopp et al., 2019; Li et al., 2021).

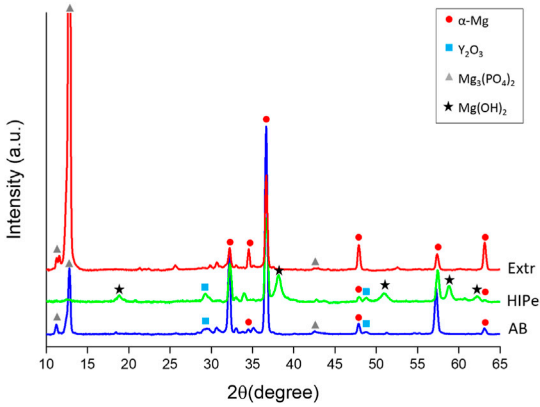

FIGURE 11 | XRD of the BD surfaces of the AB and HIP samples, as well as the Extr samples after 28 days of immersion in DPBS.

The XRD of the BD surfaces of the samples after 28 days of immersion in DPBS are presented in **Figure 11**. The spectra showed a strong peak of Mg3(PO4)2 for the Extr samples. Mg3(PO4)2 peaks were also present for the AB samples, while Mg(OH)2 peaks are mainly present for the HIP samples. MgO is also expected to be present to some extent, but MgO peaks overlap with those of hcp-Mg (Rettig and Virtanen, 2009). These results are in line with the results obtained from EDS, presented in **Figure 12**, with the cross sections of both the AB and the Extr material showing a surface layer rich in P and O for the AB material, corresponding to Mg3(PO4)2. The AB and the Extr material also have some Ca and Na present on the surface. Ca3(PO4)2 is also a common constituent forming on magnesium surfaces in Ca2+-containing corrosion mediums (Rettig and Virtanen, 2009). However, there is a morphological difference between the surface layers. The AB material exhibits a double layer structure, with one uneven layer measuring from a few µm and upwards, over a cracked surface where the beginning of the attack of the bulk material underneath can be seen. The cracked oxide layer is commonly observed in Mg alloys and their occurrence has been ascribed to the deformation of the metallic layer. This deformation is due to a combined effect from the volume expansion of the corrosion layer, the mismatch in the crystal structure between the cubic MgO and the HCP metallic Mg matrix, and the embrittlement of the

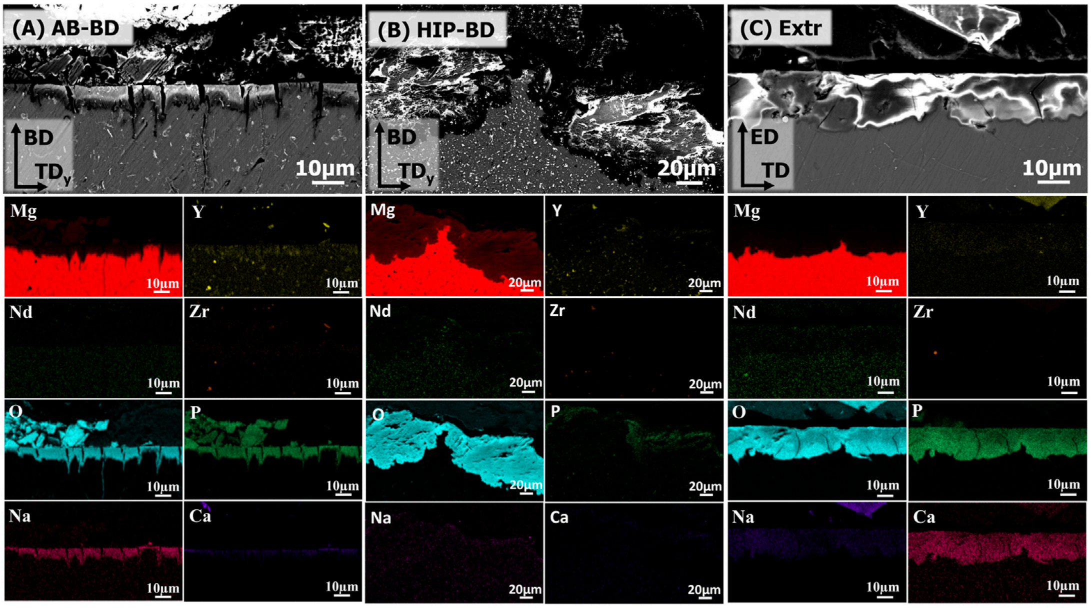

FIGURE 12 | BSE-SEM images of the cross-sections of the corroded **(A)** AB, **(B)** HIP and **(C)** Extr samples, after 28 days of immersion. The EDS maps of the main alloying elements (Mg, Y, Nd, Zr) together with the main elements found in the corrosion products (O, P, Na, Ca) are included below corresponding BSE-SEM image.

metallic layer due to an uptake of hydrogen (Xu et al., 2015; Esmaily et al., 2017). For the HIP material, an uneven layer of corrosion products is visible, with a thickness in the order of 100 µm. Here the corrosion is so severe that the cracked surface morphology is not observed. EDS mapping reveals a composition consisting mainly of O and Mg, thereby suggesting a strong presence of Mg(OH)2, with some P at the surface. The Extr material, on the other hand, shows a 10–20 µm denser, and more even layer, with few cracks in it, and with the material just below this layer virtually intact. A more homogeneous microstructure has previously been proven beneficial during the initial stages of degradation, as it allows for a more even and dense formation of oxide layer (Mraied et al., 2019). Moreover, the solubility of Mg3(PO4)2 and Ca3(PO4)2 is many times lower in aqueous solutions than that of Mg(OH)2 (Aylward and Findlay, 2007). This could also explain the semi passivating behavior exhibited by the Extr material in the PDP curves.

Kalb et al. (Kalb et al., 2012) described the mechanism behind the degradation of Mg alloys, with the corrosion starting with the reduction of water at the cathodic centers under the release of Mg2+, OH-, and H2 gas. As the pH shifts upwards due to the release of OH−, Mg(OH)2 becomes stable, and precipitates at the surface of the samples. They also describe how the Mg(OH)2 converts into Mg3(PO4)2 and Ca3(PO4)2 as Ca2+ and PO43- ions diffuse into the Mg(OH)2 layer. However, as the degradation rate of the HIP material is high, it could be that the conversion of Mg(OH)2 into more stable compounds is not fast enough. The result is a porous, inhomogeneous and a relatively soluble oxide/hydroxide layer that is not protective. A similar behavior can be observed for the AB material, but as the initial degradation rate is slightly slower, part of the Mg(OH)2 has time to convert into the more stable corrosion products Mg3(PO4)2 and Ca3(PO4)2. Thus, this would mean that an initially faster corrosion rate will have a negative of effect on the stability of the corroded surfaces over time.

Thus, the results show that the HIP material has the highest degradation rate, followed by the AB material and finally the Extr material, which means that the study failed to improve the corrosion properties in relation to previous studies. The reason is ascribed to the distribution of the alloying elements and the size of the secondary phases. The larger precipitates in the HIP material increase micro galvanic corrosion, which also hinders any passive oxide layer to form. The key role of the precipitates is also a possible reason for the contradictory results of some of the long-term tests (**Figure 8**), where the more closely packed TD surfaces tended to give higher corrosion rates. The importance of the secondary phases for the corrosion behavior of magnesium alloys processed by PBF-LB have been established for many other alloying systems. This includes the commercial Mg-Al-Zn alloys, where there are many studies confirming the detrimental effect of the Mg-Al intermetallics on the corrosion properties (Shuai et al., 2018; Gao et al., 2021). The electrochemical activity of secondary phases is also one of the main challenges of the new alloying systems being developed for biodegradable metal implants, including the Mg-Zn-Ca alloys (Yao et al., 2021)

Another important factor that might also have affected the corrosion results is the difference in grain size distribution. A smaller average grain size and more homogenous grain size distribution has previously been proven to be beneficial for the corrosion properties of Mg-RE alloys, affecting both the distribution of secondary phases, as well as the homogeneity of the surface oxide layers (Liu et al., 2014; Liu G et al., 2022). This could thus be a contributing factor to the better corrosion property of the Extr material, as well as the better corrosion properties of the AB material in comparison to the HIP material. Moreover, this could also be the reason for the higher corrosion rates in TD direction.

It may be noted that the experiment was carried out in a static environment, and that the corrosion media was not exchanged during the 28 days of immersion. As this will affect the corrosion behavior of the material, future work should the include investigation of the corrosion behavior of the material in non-static conditions. Moreover, the number of samples available was limited as there was no possibility to produce more samples in the PBF-LB system applied. A change of PBF-LB system also entails a change in a number of process parameters such as laser spot size and argon gas flow, thus it is not possible to reproduce the samples in other systems available. The large variations in set process parameters, such as laser spot size, between different PBF-LB systems further highlights the need of an enhanced understanding of the influence of the process on the microstructure and material properties. As previously mentioned, future work is suggested to first focus on the influence of individual PBF-LB process parameters on the microstructure and the amount of evaporated Mg in order to clarify their relationship. A particular focus should be on the resulting amount and distribution of secondary phases and its overall effect on the corrosion behavior of the material. Other effects such as the influence of the PBF-LB process on the stress state of the material should also be clarified, as this could also have an adverse effect on the corrosion properties. This is important as this will expand the knowledge regarding which microstructure to aim for future process parameter development and optimization.

Finally, when the relationship among process parameters, microstructure and corrosion behavior has been clarified, further development of the Mg alloys should seek to better adapt alloy concentration to the PBF-LB process in order to compensate for the possible negative effects, such as loss of Mg during processing, and the decreasing amount of Y in solid solution due to the oxide formation. A closed value chain from powder production to the processing of the powder using PBF-LB, keeping the material under inert atmosphere, could also minimize the oxide layer to be formed on the powder, and thus the depletion of Y due to this effect. However, this would also enhance the reactivity of the powder, and thus the hazards working with it. The effect of the concentration of alloying elements on the formation of Mg-RE intermetallic compounds should also be investigated. Even though heat treatments have been ineffective thus far at improving corrosion resistance, they have not been completely optimized for PBF-LB material. This is also the case for the HIP parameters applied in this study. Future HIP experiments on PBF-LB-processed Mg-Y-Nd-Zr alloy should also explore lower temperatures and faster cooling. Moreover, once corrosion properties have been improved, the influence of texture on corrosion rates should be revisited.

CONCLUSION

A typical microstructure for a Mg-Y-Nd-Zr alloy processed by PBF-LB as well as that for Mg-Y-Nd-Zr alloy processed by powder extrusion was studied. After HIP of the PBF-LB samples, a growth in secondary phases along with a larger grain size and a stronger texture was observed. While the surfaces of the AB samples showed a higher corrosion current density than that of the HIP samples, the corrosion resistance as measured by hydrogen evolution and mass change of the AB material was lower compared to the HIP material. The higher corrosion rate of the HIP samples was also confirmed by visual inspection, and BSE-SEM images of the sample cross sections. The reason for the higher degradation rates of the HIP material was attributed to the growth of secondary phases occurring during HIP, which leads to increased micro galvanic corrosion, as well as the larger grain size. To a certain extent, this indicates that the size and distribution of the secondary phases is more important than having a fully dense material. The Extr material exhibited the lowest corrosion rate, due to a higher amount of dissolved alloying elements in the matrix and less intermetallic particles and a more homogenous grain size distribution. The stability of the surface of the Extr material was further enhanced by the formation of a passivating layer of Mg3(PO4)2 and Ca3(PO4)2. Moreover, even though a stronger texture was observed along the BD, there was no significant difference in corrosion rate over time between the BD and TD surfaces. This suggests that the size and distribution of secondary phases are more critical to the corrosion resistance than the differences in electrochemical activity attributed to crystal orientation. However, further clarification of the importance of the texture as well as grain size is needed.

DATA AVAILABILITY STATEMENT

The original contributions presented in the study are included in the article/Supplementary Material, further inquiries can be directed to the corresponding author.

AUTHOR CONTRIBUTIONS

Conceptualization, CP; methodology HNÅ; formal analysis, HNÅ; investigation, HNÅ; resources, CP; PM writing—original draft preparation, HNÅ; writing—review and editing, FD'E., PM, and CP; visualization, HNÅ; supervision, PM, FD'E, and CP; project administration, HNÅ and PM, funding acquisition, PM and CP. All authors have read and agreed to the published version of the manuscript.

FUNDING

This research was funded by the Swedish Foundation for Strategic Research (SSF), project number FID17-0028, and by the Swedish Governmental Agency for Innovation Systems (Vinnova), project numbers 2019-05259 and 2019-00029 (Vinnova Competence Centre AM4Life).

ACKNOWLEDGMENTS

We would like to acknowledge the contribution of Lena Thorsson, Exmet AB, during the production of the samples, as well as Rachel Pettersson, KTH, for discussing the analysis of the results.

REFERENCES

Ascencio, M., Pekguleryuz, M., and Omanovic, S. (2015). An Investigation of the Corrosion Mechanisms of WE43 Mg Alloy in a Modified Simulated Body Fluid Solution: The Effect of Electrolyte Renewal. *Corros. Sci.* 91, 297–310. doi:10.1016/j.corsci.2014.11.034

ASTM G150-18 (2018). *Standard Test Method for Electrochemical Critical Pitting Temperature Testing of Stainless Steels and Related Alloys*. West Conshohocken, PA: ASTM International. doi:10.1520/G0150-18

ASTM G31-72 (2004). *Standard Practice for Laboratory Immersion Corrosion Testing of Metals ASTM International*. West Conshohocken, PA: ASTM International. doi:10.1520/G0031-72R04

Aylward, G., and Findlay, T. (2007). *SI Chemical Data*. 6th ed. Milton: John Wiley & Sons Australia Ltd.

Bär, F., Berger, L., Jauer, L., Kurtuldu, G., Schäublin, R., Schleifenbaum, J. H., et al. (2019). Laser Additive Manufacturing of Biodegradable Magnesium Alloy WE43: A Detailed Microstructure Analysis. *Acta Biomater.* 98, 36–49. doi:10.1016/j.actbio.2019.05.056

Ben-hamu, G., Eliezer, D., Shin, K. S., and Cohen, S. (2007). The Relation between Microstructure and Corrosion Behavior of Mg-Y-RE-Zr Alloys. *J. Alloys Compd.* 431, 269–276. doi:10.1016/j.jallcom.2006.05.075

Benn, F., Kröger, N., Zinser, M., van Gaalen, K., Vaughan, T. J., Yan, M., et al. (2021). Influence of Surface Condition on the Degradation Behaviour and Biocompatibility of Additively Manufactured WE43. *Mater. Sci. Eng. C* 124, 112016. doi:10.1016/j.msec.2021.112016

Cao, J., Lian, R., and Jiang, X. (2020). Magnesium and Fluoride Doped Hydroxyapatite Coatings Grown by Pulsed Laser Deposition for Promoting Titanium Implant Cytocompatibility. *Appl. Surf. Sci.* 515, 146069. doi:10.1016/j.apsusc.2020.146069

Carter, L. N., Martin, C., Withers, P. J., and Attallah, M. M. (2014). The Influence of the Laser Scan Strategy on Grain Structure and Cracking Behaviour in SLM Powder-Bed Fabricated Nickel Superalloy. *J. Alloys Compd.* 615, 338–347. doi:10.1016/j.jallcom.2014.06.172

Castellani, C., Lindtner, R. A., Hausbrandt, P., Tschegg, E., Stanzl-Tschegg, S. E., Zanoni, G., et al. (2011). Bone-implant Interface Strength and Osseointegration: Biodegradable Magnesium Alloy versus Standard Titanium Control. *Acta Biomater.* 7, 432–440. doi:10.1016/j.actbio.2010.08.020

Chen, Y., Zhang, J., Gu, X., Dai, N., Qin, P., and Zhang, L.-C. (2018). Distinction of Corrosion Resistance of Selective Laser Melted Al-12Si Alloy on Different Planes. *J. Alloys Compd.* 747, 648–658. doi:10.1016/j.jallcom.2018.03.062

Cverna, F., Dunigan, S., Nelson, T., Henry, S. D., and Scott, W. W. (2001). in *Worldwide Guide to Equivalent Nonferrous Metals and Alloys*. Editors F. Cverna, S. Dunigan, T. Nelson, S. D. Henry, and W. W. Scott. 4th ed. (Yukp Ohio: ASM International).

Dai, N., Zhang, L.-C., Zhang, J., Zhang, X., Ni, Q., Chen, Y., et al. (2016). Distinction in Corrosion Resistance of Selective Laser Melted Ti-6Al-4V Alloy on Different Planes. *Corros. Sci.* 111, 703–710. doi:10.1016/j.corsci.2016.06.009

Davenport, A. J., Padovani, C., Connolly, B. J., Stevens, N. P. C., Beale, T. A. W., Groso, A., et al. (2007). Synchrotron X-Ray Microtomography Study of the Role of Y in Corrosion of Magnesium Alloy WE43. *Electrochem. Solid-State Lett.* 10, C5–C10. doi:10.1149/1.2400727

Ding, W. (2016). Opportunities and Challenges for the Biodegradable Magnesium Alloys as Next-Generation Biomaterials. *Regen. Biomater.* 3, 79–86. doi:10.1093/RB/RBW003

Du, H., Wei, Z., Liu, X., and Zhang, E. (2011). Effects of Zn on the Microstructure, Mechanical Property and Bio-Corrosion Property of Mg-3Ca Alloys for Biomedical Application. *Mater. Chem. Phys.* 125, 568–575. doi:10.1016/j.matchemphys.2010.10.015

Einhorn, T. A., and Gerstenfeld, L. C. (2015). Fracture Healing: Mechanisms and Interventions. *Nat. Rev. Rheumatol.* 11, 45–54. doi:10.1038/nrrheum.2014.164

Engh, C., Bobyn, J., and Glassman, A. (1987). Porous-coated hip replacement. The factors governing bone ingrowth, stress shielding, and clinical results. *J. Bone Jt. Surg. Br. volume* 69-B, 45–55. doi:10.1302/0301-620X.69B1.3818732

Esmaily, M., Svensson, J. E., Fajardo, S., Birbilis, N., Frankel, G. S., Virtanen, S., et al. (2017). Fundamentals and advances in magnesium alloy corrosion. *Prog. Mater. Sci.* 89, 92–193. doi:10.1016/j.pmatsci.2017.04.011

Esmaily, M., Zeng, Z., Mortazavi, A. N., Gullino, A., Choudhary, S., Derra, T., et al. (2020). A detailed microstructural and corrosion analysis of magnesium alloy WE43 manufactured by selective laser melting. *Addit. Manuf.* 35, 101321–101334. doi:10.1016/j.addma.2020.101321

Gangireddy, S., Gwalani, B., Liu, K., Faierson, E. J., and Mishra, R. S. (2019). Microstructure and mechanical behavior of an additive manufactured (AM) WE43-Mg alloy. *Addit. Manuf.* 26, 53–64. doi:10.1016/j.addma.2018.12.015

Gao, C., Li, S., Liu, L., Bin, S., Yang, Y., Peng, S., et al. (2021). Dual alloying improves the corrosion resistance of biodegradable Mg alloys prepared by selective laser melting. *J. Magnesium Alloys* 9, 305–316. doi:10.1016/j.jma.2020.03.016

Geenen, K., Röttger, A., and Theisen, W. (2017). Corrosion behavior of 316L austenitic steel processed by selective laser melting, hot-isostatic pressing, and casting. *Mater. Corros.* 68, 764–775. doi:10.1002/maco.201609210

Giannoudis, P. V., Dinopoulos, H., and Tsiridis, E. (2005). Bone substitutes: an update. *Injury* 36 (Suppl. 3), S20–S27. doi:10.1016/j.injury.2005.07.029

Gibson, I., Rosen, D., and Stucker, B. (2015). *Additive Manufacturing Technologies*. 2nd Edn. New York, NY: Springer New York. doi:10.1007/978-1-4939-2113-3

Hallstedt, B. (1993). The Magnesium - Oxygen system. *Calphad* 17, 281–286. doi:10.1016/0364-5916(93)90006-W

Han, H.-S., Loffredo, S., Jun, I., Edwards, J., Kim, Y.-C., Seok, H.-K., et al. (2019). Current status and outlook on the clinical translation of biodegradable metals. *Mater. Today* 23, 57–71. doi:10.1016/j.mattod.2018.05.018

Hasegawa, M., Tone, S., Naito, Y., Wakabayashi, H., and Sudo, A. (2021). Minimum ten-year results in revision total hip arthroplasty using titanium fully porous long stem. *Int. Orthop. (SICOT)* 45, 1727–1733. doi:10.1007/s00264-021-05030-4

Jauer, L., Meiners, W., Vervoort, S., and Gayer, C. (2016). Selective Laser Melting of Magnesium Alloys. in *Proceedings World PM 2016 AM- Powder Bed Based Technologies*. Hamburg, Germany: October. doi:10.1007/978-3-319-48150-0_11

Kainer, K. U. (2003). *Magnesium - Alloys and Technologies*. Weinheim: Wiley VCH.

Kalb, H., Rzany, A., and Hensel, B. (2012). Impact of microgalvanic corrosion on the degradation morphology of WE43 and pure magnesium under exposure to simulated body fluid. *Corros. Sci.* 57, 122–130. doi:10.1016/j.corsci.2011.12.026

Kirkland, N. T., Birbilis, N., and Staiger, M. P. (2012). Assessing the corrosion of biodegradable magnesium implants: A critical review of current methodologies and their limitations. *Acta Biomater.* 8, 925–936. doi:10.1016/j.actbio.2011.11.014

Kopp, A., Derra, T., Müther, M., Jauer, L., Schleifenbaum, J. H., Voshage, M., et al. (2019). Influence of design and postprocessing parameters on the degradation behavior and mechanical properties of additively manufactured magnesium scaffolds. *Acta Biomater.* 98, 23–35. doi:10.1016/j.actbio.2019.04.012

Kurdi, O., RusnaldySuprihanto, A., SuprihantoRachma, A., Muchammad, A. R., Rachma, H., Leoni, A. R., et al. (2020). Determination of stress shielding due to magnesium internal bone fixation. *AIP Conf. Proc.* 2262. doi:10.1063/5.0016960

Li, M., Benn, F., Derra, T., Kröger, N., Zinser, M., Smeets, R., et al. (2021). Microstructure, mechanical properties, corrosion resistance and cytocompatibility of WE43 Mg alloy scaffolds fabricated by laser powder bed fusion for biomedical applications. *Mater. Sci. Eng. C* 119, 111623. doi:10.1016/j.msec.2020.111623

Liang, L., Huang, Q., Wu, H., Ouyang, Z., Liu, T., He, H., et al. (2021). Stimulation of In Vitro and In Vivo osteogenesis by Ti-Mg alloys with the sustained-release function of magnesium ions. *Colloids Surfaces B Biointerfaces* 197, 111360. doi:10.1016/j.colsurfb.2020.111360

Liu, D., Ding, Y., Guo, T., Qin, X., Guo, C., Yu, S., et al. (2014). Influence of fine-grain and solid-solution strengthening on mechanical properties and In Vitro degradation of WE43 alloy. *Biomed. Mat.* 9, 015014. doi:10.1088/1748-6041/9/1/015014

Liu, G., Xu, J., Feng, B., Liu, J., Qi, D., Huang, W., et al. (2022). Comparison of Corrosion Performance of Extruded and Forged WE43 Mg Alloy. *Materials* 15, 1622. doi:10.3390/ma15051622

Liu, J., Liu, B., Min, S., Yin, B., Peng, B., Yu, Z., et al. (2022). Biodegradable magnesium alloy WE43 porous scaffolds fabricated by laser powder bed fusion for orthopedic applications: Process optimization, In Vitro and In Vivo investigation. *Bioact. Mater.* 16, 301–319. doi:10.1016/j.bioactmat.2022.02.020

Luxfer MEL Aircraft interiors (2003).Aircraft-Interiors-Magnesium-Extrusion. Available at: https://www.luxfermeltechnologies.com/markets/aerospace/aircraft-interiors-magnesium-extrusion/ (Accessed November 5, 2020).

Magnesium Scaffold (2020). Biotronik Vascular Intervention// Coronary Resorbable Magnesium Scaffold (RMS). Available at: https://www.biotronik.com/en-ch/products/coronary/magmaris (Accessed April 26, 2020).

McGregor, M., Patel, S., McLachlin, S., and Vlasea, M (2021). Architectural bone parameters and the relationship to titanium lattice design for powder bed fusion additive manufacturing. *Addit. Manuf.* 47, 102273. doi:10.1016/j.addma.2021.102273

Meier, R., and Panzica, M. (2017). Erste Ergebnisse mit einer resorbierbaren MgYREZr-Kompressionsschraube bei der instabilen Kahnbeinfraktur zeigen eine massive Zystenbildung. *Handchir Mikrochir Plast. Chir.* 49, 37–41. doi:10.1055/s-0042-121416

Mraied, H., Wang, W., and Cai, W. (2019). Influence of chemical heterogeneity and microstructure on the corrosion resistance of biodegradable we43 magnesium alloys. *J. Mat. Chem. B* 7, 6399–6411. doi:10.1039/c9tb00388f

Ng, C. C., Savalani, M. M., Man, H. C., and Gibson, I. (2010). Layer manufacturing of magnesium and its alloy structures for future applications. *Virtual Phys. Prototyp.* 5, 13–19. doi:10.1080/17452751003718629

Nie, J. F., and Muddle, B. C. (2000). Characterisation of strengthening precipitate phases in a Mg-Y-Nd alloy. *Acta Mater.* 48, 1691–1703. doi:10.1016/S1359-6454(00)00013-6

Nilsson Åhman, H., Thorsson, L., Mellin, P., Lindwall, G., and Persson, C. (2022). An Enhanced Understanding of the Powder Bed Fusion–Laser Beam Processing of Mg-Y3.9wt%-Nd3wt%-Zr0.5wt% (WE43) Alloy through Thermodynamic Modeling and Experimental Characterization. *Mater. (Basel).* 15, 417. doi:10.3390/ma15020417

Pakkanen, J. (2018). *Designing for Additive Manufacturing Product and Process Driven Design for Metals and Polymers*. Washington: semanticscholar. doi:10.6092/polito/porto/2714732

Plaass, C., Ettinger, S., Sonnow, L., Koenneker, S., Noll, Y., Weizbauer, A., et al. (2016). Early results using a biodegradable magnesium screw for modified chevron osteotomies. *J. Orthop. Res.* 34, 2207–2214. doi:10.1002/jor.23241

Prasad, S. V. S., Prasad, S. B., Verma, K., Mishra, R. K., Kumar, V., and Singh, S. (2022). The role and significance of Magnesium in modern day research-A review. *J. Magnesium Alloys* 10, 1–61. doi:10.1016/j.jma.2021.05.012

Py, B., Johnston, S., Hardy, A., Shi, Z., Wolski, K., and Atrens, A. (2020). Quantifying the influence of calcium ion concentration on the corrosion of high-purity magnesium, AZ91, WE43 in modified Hanks' solutions. *Mat. Res. Express* 7, 096501. doi:10.1088/2053-1591/abb1f4

Rettig, R., and Virtanen, S. (2009). Composition of corrosion layers on a magnesium rare-earth alloy in simulated body fluids. *J. Biomed. Mat. Res.* 88A, 359–369. doi:10.1002/jbm.a.31887

Revilla-León, M., Sadeghpour, M., and Özcan, M. (2020). A Review of the Applications of Additive Manufacturing Technologies Used to Fabricate Metals in Implant Dentistry. *J. Prosthodont.* 29, 579–593. doi:10.1111/jopr.13212

Sabbaghian, M., Mahmudi, R., and Shin, K. S. (2019). Effect of texture and twinning on mechanical properties and corrosion behavior of an extruded biodegradable Mg-4Zn alloy. *J. Magnesium Alloys* 7, 707–716. doi:10.1016/j.jma.2019.11.001

Shuai, C., He, C., Feng, P., Guo, W., Gao, C., Wu, P., et al. (2018). Biodegradation mechanisms of selective laser-melted Mg-xAl-Zn alloy: grain size and intermetallic phase. *Virtual Phys. Prototyp.* 13, 59–69. doi:10.1080/17452759.2017.1408918

Song, G.-L., and Xu, Z. (2012). Effect of microstructure evolution on corrosion of different crystal surfaces of AZ31 Mg alloy in a chloride containing solution. *Corros. Sci.* 54, 97–105. doi:10.1016/j.corsci.2011.09.005

Song, G., Atrens, A., and StJohn, D. (2001). An hydrogen evolution method for the estimation of the corrosion rate of magnesium alloys. *TMS Annu. Meet.*, 254–262. doi:10.1002/9781118805497.ch44

Staiger, M. P., Pietak, A. M., Huadmai, J., and Dias, G. (2006). Magnesium and its alloys as orthopedic biomaterials: A review. *Biomaterials* 27, 1728–1734. doi:10.1016/j.biomaterials.2005.10.003

Suchý, J., Klakurková, L., Man, O., Remešová, M., Horynová, M., Paloušek, D., et al. (2021). Corrosion behaviour of WE43 magnesium alloy printed using selective laser melting in simulation body fluid solution. *J. Manuf. Process.* 69, 556–566. doi:10.1016/j.jmapro.2021.08.006

Südholz, A. D., Kirkland, N. T., Buchheit, R. G., and Birbilis, N. (2011). Electrochemical properties of intermetallic phases and common impurity elements in magnesium alloys. *Electrochem. Solid-State Lett.* 14, C5–C2012. doi:10.1149/1.3523229

Syntellix, M. M. (2019). Material Research. Available at: https://www.syntellix.de/en/products/technology.html (Accessed June 28, 2019).

Taheri, M., Kish, J. R., Birbilis, N., Danaie, M., McNally, E. A., and McDermid, J. R. (2014). Towards a physical description for the origin of enhanced catalytic activity of corroding magnesium surfaces. *Electrochimica Acta* 116, 396–403. doi:10.1016/j.electacta.2013.11.086

Tandon, R., Palmer, T., Gieseke, M., Noelke, C., and Kaierle, S. (2016). Additive manufacturing of magnesium alloy powders: Investigations into process development using elektron®MAP+43 via laser powder bed fusion and directed energy deposition. in *Proceedings World PM 2016 Congress and Exhibition*. Hamburg, Germany: October.

Tandon, R., Wilks, T., Gieseke, M., Noelke, C., Kaierle, S., and Palmer, T. (2015). Additive manufacturing of electron® 43 alloy using laser powder bed and directed energy deposition. in *International Powder Metallurgy Congress and Exhibition*. France: Reims.

Valtanen, R. S., Yang, Y. P., Gurtner, G. C., Maloney, W. J., and Lowenberg, D. W. (2021). Synthetic and Bone tissue engineering graft substitutes: What is the future? *Injury* 52, S72–S77. doi:10.1016/j.injury.2020.07.040

Xu, W., Birbilis, N., Sha, G., Wang, Y., Daniels, J. E., Xiao, Y., et al. (2015). A high-specific-strength and corrosion-resistant magnesium alloy. *Nat. Mater* 14, 1229–1235. doi:10.1038/nmat4435

Yang, N., Song, Y., Huang, J., Chen, Y., and Maskery, I. (2021). Combinational design of heterogeneous lattices with hybrid region stiffness tuning for additive manufacturing. *Mater. Des.* 209, 109955. doi:10.1016/j.matdes.2021.109955

Yao, X., Tang, J., Zhou, Y., Atrens, A., Dargusch, M. S., Wiese, B., et al. (2021). Surface modification of biomedical Mg-Ca and Mg-Zn-Ca alloys using selective laser melting: Corrosion behaviour, microhardness and biocompatibility. *J. Magnesium Alloys* 9, 2155–2168. doi:10.1016/j.jma.2020.08.011

Zhang, Y., Tan, L., Wang, Q., Gao, M., Etim, I. P., and Yang, K. (2020). Effects of microstructure on the torsional properties of biodegradable WE43 Mg alloy. *J. Mater. Sci. Technol.* 51, 102–110. doi:10.1016/j.jmst.2020.04.003

Zhao, D., Liang, H., Han, C., Li, J., Liu, J., Zhou, K., et al. (2021). 3D printing of a titanium-tantalum Gyroid scaffold with superb elastic admissible strain, bioactivity and *in-situ* bone regeneration capability. *Addit. Manuf.* 47, 102223. doi:10.1016/j.addma.2021.102223

Zheng, Z., Jin, X., Bai, Y., Yang, Y., Ni, C., Lu, W. F., et al. (2022). Microstructure and anisotropic mechanical properties of selective laser melted Ti6Al4V alloy under different scanning strategies. *Mater. Sci. Eng. A* 831, 142236. doi:10.1016/j.msea.2021.142236

Zumdick, N. A., Jauer, L., Kersting, L. C., Kutz, T. N., Schleifenbaum, J. H., and Zander, D. (2019). Additive manufactured WE43 magnesium: A comparative study of the microstructure and mechanical properties with those of powder extruded and as-cast WE43. *Mater. Charact.* 147, 384–397. doi:10.1016/j.matchar.2018.11.011

Conflict of Interest: The authors declare that the research was conducted in the absence of any commercial or financial relationships that could be construed as a potential conflict of interest.

frontiers | Frontiers in Materials

ORIGINAL RESEARCH
published: 22 July 2022
doi: 10.3389/fmats.2022.932007

Study on Stability and Elastic Properties of β-Ti*X* (*X*=Nb, Ta) Alloys From First-Principles Calculations

Hou Shuluo, Li Jiuxiao, Wang Yixue*, Yang Dongye and Wan Zhaomei*

School of Materials Engineering, Shanghai University of Engineering Science, Shanghai, China

In this article, the phase stability, elastic properties, and electronic structure of the β-Ti*X* (*X* = Nb, Ta) alloy body-centered cubic (bcc) structure were systematically studied with the aid of first-principles calculations. The results show that the phase stability and elastic properties of the β-Ti*X* alloys are closely related to the contents of alloying element *X*. For β-Ti*X* alloys, the contents of Nb and Ta that satisfy their mechanical stability are 10% and 13%, respectively; at room temperature, both β-TiNb and β-TiTa alloys can reach a thermodynamically stable state when the content of Nb or Ta is 25%. In terms of elastic properties, the content of alloying element *X* is positively correlated with the elastic constant, Young's modulus, and shear modulus of the β-Ti*X* alloys. The elastic modulus reaches its minimum when the *X* content is 25%, and the smallest direction of Young's modulus appears in the <111> direction. The calculation results of the electronic structure show that the bonding strength between the Ti atom and *X* atom increases with the content of alloying element *X*, which leads to improvement of phase stability and elastic modulus.

Keywords: β-Ti alloys, first-principles, phase stability, elastic properties, electronic structure

Edited by:
Daixiu Wei,
Tohoku University, Japan

Reviewed by:
Xiaojie Li,
Taizhou University, China
Fuxing Yin,
Hebei University of Technology, China

***Correspondence:**
Li Jiuxiao
lijiuxiao@126.com
Wang Yixue
sunnywang2013@sina.com

Specialty section:
This article was submitted to Biomaterials, a section of the journal Frontiers in Materials

Received: *29 April 2022*
Accepted: *30 May 2022*
Published: *22 July 2022*

Citation:
Shuluo H, Jiuxiao L, Yixue W, Dongye Y and Zhaomei W (2022) Study on Stability and Elastic Properties of β-TiX (X=Nb, Ta) Alloys From First-Principles Calculations. Front. Mater. 9:932007. doi: 10.3389/fmats.2022.932007

1 INTRODUCTION

Since the 1990s, β-Ti alloys with body-centered cubic (bcc) structure have become the primary research focus of biomedical Ti alloys due to their lower elastic modulus, better biocompatibility, higher strength, and corrosion resistance (Rack and Qazi, 2006; Geetha et al., 2009). β-Ti alloys can be obtained by adding transition metal (TM) elements, which can reduce the relatively high stiffness (Jackson and Dring, 2013; Hao et al., 2018). The alloying is an important way to improve the mechanical properties of titanium alloy and enhance the stability of the phase. The stability, biocompatibility, and non-toxicity of alloying elements are important for the selection of β-type biomedical titanium alloying elements. Nb and Ta are commonly added to β-type biomedical titanium alloys. On the one hand, as strong β-phase stable elements, Nb and Ta can inhibit the formation of non-equilibrium phases such as α', α'', and ω phase and effectively reduce the modulus of titanium alloy (Lee et al., 2002; Zhou et al., 2004). On the other hand, Nb and Ta have good biocompatibility and less toxicity and are considered to be safe biomedical alloying elements (Zhang et al., 2010). Generally speaking, thermoelastic martensite $\beta \rightarrow \alpha''$ transformation or thermal ω phase formation will proceed with low content of TM elements and poor phase stability (Formanoir et al., 2019; Kapoor et al., 2020). However, the elastic modulus of the bcc structure will be increased with the additional content of TM alloying elements (Banerjee and Williams, 2013; Huang et al., 2021). This contradiction is a problem that needs to be solved urgently.

Recently, with the rapid development of computer-aided material design, the first-principles methods based on density functional theory have been widely used to study the elastic properties, phase stability, and electronic structure of β-Ti alloys. The study by Yu et al. showed that the non-spherical distribution of electrons will lead to difficult plastic deformation of the alloy and high modulus. Koval et al., (2019) also analyzed the effect of electronic structure on the elastic properties of β-Ti alloys. Zhang et al., (2016) used the first-principles method to study the effect of alloying element content on the phase stability of binary titanium alloys. Moreno et al., (2017; Moreno et al., (2018) determined the most stable structure of $Ti_{1-x}Nb_x$ (x < 31.5%) alloy by using the energy minimization method and calculated its elastic constant by using the first-principles full potential supplemented plane wave. Jia et al., (2020) simulated the effect of doping trace transition metal elements on the stability of β-Ti alloys by density functional theory. However, the studies mentioned above ignored the effect of temperature on the thermodynamic stability of β-Ti alloys. In addition, the composition range of alloys adopted in those studies is too limited to carry out the alloy design. These shortcomings lead to lack of effective theoretical support for the composition design of β-Ti alloy, which is not conducive to further research.

Therefore, based on the first-principles method, this work researched the influence of Nb and Ta contents on the mechanical stability, thermodynamic stability, and elastic properties of β-Ti*X* (*X* = Nb, Ta) alloys. The supercell method is used to approximate disordered solid solution properties. In this study, the calculation has been performed systematically from the perspective of the structure, formation enthalpy, Gibbs free energy, elastic constant, and electronic structure of β-Ti*X* (*X* = Nb, Ta) alloys with different compositions. First, according to the Gibbs free energy, the alloy composition range satisfying the thermodynamic stability was determined. Second, based on the single-crystal elastic constants, Young's modulus and shear modulus of the β-Ti*X* (*X* = Nb, Ta) alloys were predicted and evaluated by the Hill arithmetic averaging method, and the elastic anisotropy was analyzed. Finally, in line with the electronic structure, the influence mechanism of alloying element content on the stability and elastic properties of β-Ti*X* (*X* = Nb, Ta) alloys was expounded from the electronic level.

2 COMPUTATIONAL METHODOLOGY

2.1 Computational Settings

In this research, density functional theory calculations were performed by means of the Vienna ab initio simulation package (VASP) (Kresse and Furthmüller, 1996a; b), which is based on the projected augmented wave (PAW) method (Blochl, 1994). The generalized gradient approximation parameterized by Perdew, Burke, and Ernzerhof (GGA-PBE) (Perdew et al., 1996) was used as the exchange–correlation function. The valence electron configurations of the PAW potentials were 3s23p63d24s2 for Ti, 4s24p64d45s1 for Nb, and 5s25p65d36s2 for Ta. The supercell method was used to calculate the total energy and the elastic moduli of the β-Ti*X* (*X* = Nb, Ta) binary alloys with different compositions. A 2 × 2 × 2 supercell containing eight β-Ti bcc unit cells (space group Im3m) was constructed, and the number of Ti atoms is 16. The Ti atoms in the supercell were replaced at intervals of 2 by Nb or Ta atoms. The nominal molecular formula of β-Ti*X* (*X* = Nb, Ta) alloys is $Ti_{16\text{-}n}X_n$ (*X* = Nb, Ta; n = 0, 2, 4, 6, 8, 10, 12, 14, 16), as shown in **Figure 1**.

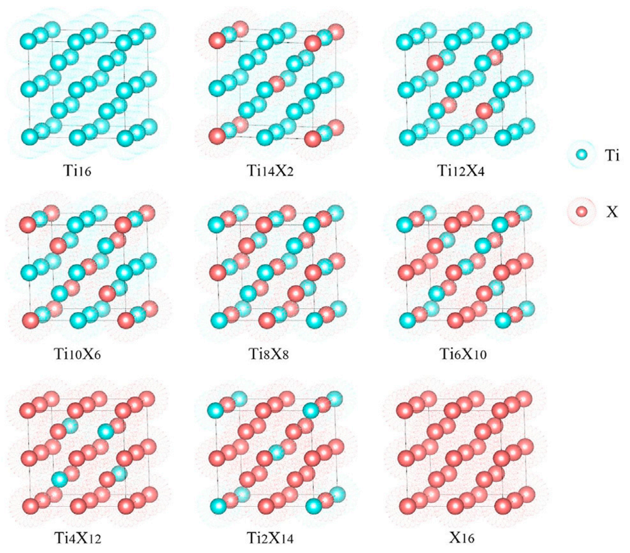

FIGURE 1 | Models of β-Ti*X* (*X* = Nb, Ta) alloys.

During the calculation, a plane-wave expansion of the wave functions with a cut-off energy of 500 eV, and the Brillouin Zone (BZ) was sampled with a Monkhorst-Pack k-point grid (Monkhorst and Pack, 1976). Then, a 10 × 10 × 10 k-point mesh was used for structure optimization. In calculations related to the density of states (DOS), the one-electron wave functions were expanded in a plane-wave basis set with an energy cut-off of 600 eV. For the usually sensitive calculations of the elastic tensor, the energy cut-off was increased to 700 eV. The energy convergence criterion of the electron step self-consistent cycle was 1.0 × 10−7 eV. The convergence criterion of the ion step is that the interatomic force was less than 0.01 eV/Å. Energy-volume fitting comprised the Birch–Murnaghan equation of state (Birch, 1947) so as to obtain the corresponding equilibrium volume of each component, and the calculations of the total energy were performed by using the tetrahedron method with Blöchel correction (Blöchl et al., 1994).

2.2 Calculation of Thermodynamic Stability

The formation enthalpy $\boldsymbol{\Delta H_f}$ can be described as follows:

$$\boldsymbol{\Delta H_f} = (\boldsymbol{D_{\mathrm{tot}}} - \boldsymbol{N_{\mathrm{Ti}}D_{\mathrm{Ti}}} - \boldsymbol{N_X D_X}) \big/ (\boldsymbol{N_{\mathrm{Ti}}} + \boldsymbol{N_X}), \quad (1)$$

where $\boldsymbol{D_{tot}}$, $\boldsymbol{D_{Ti}}$, and $\boldsymbol{D_X}$ represent the total energy of the system, the energy of a single Ti atom, and the energy of a single *X* atom, respectively and $\boldsymbol{N_{Ti}}$ and $\boldsymbol{N_X}$ correspond to the number of Ti atoms and *X* atoms in the system according to its subscript, respectively.

TABLE 1 | Strains used to calculate the elastic constants of β-Ti*X* (X = Nb, Ta) alloys.

Applied Strain (unlisted $e_{ij} = 0$)	The energy of the cubic crystal subjected to the strain on the left column	$\Delta D/V_0$
$e_4 = e_5 = e_6 = \delta$	$D_1 = D_0 + \frac{V_0}{2}(C_{44}e_4e_4 + C_{44}e_5e_5 + C_{44}e_5e_5)$	$\frac{3}{2}C_{44}\,\delta^2$
$e_1 = e_2 = \delta$	$D_2 = D_0 + \frac{V_0}{2}(C_{11}e_1e_1 + C_{11}e_2e_2 + C_{12}e_1e_2 + C_{12}e_2e_1)$	$(C_{11} + C_{12})\delta^2$
$e_1 = e_2 = e_3 = \delta$	$D_3 = D_0 + \frac{V_0}{2}(C_{11}e_1e_1 + C_{11}e_2e_2 + C_{11}e_3e_3 + C_{12}e_1e_2 + C_{12}e_1e_3 + C_{12}e_2e_1 + C_{12}e_2e_3 + C_{12}e_3e_1 + C_{12}e_3e_2)$	$\frac{3}{2}(C_{11} + 2C_{12})\delta^2$

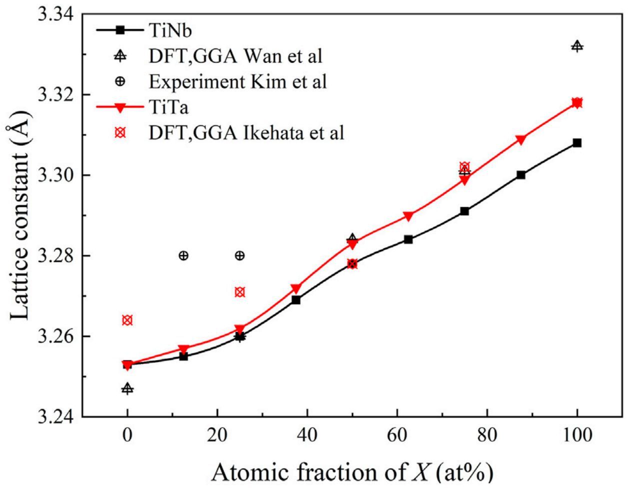

FIGURE 2 | Lattice constants (Å) of β-Ti*X* (X = Nb, Ta) alloys. (Wan et al., 2014) (Kim et al., 2006); (Ikehata et al., 2004)

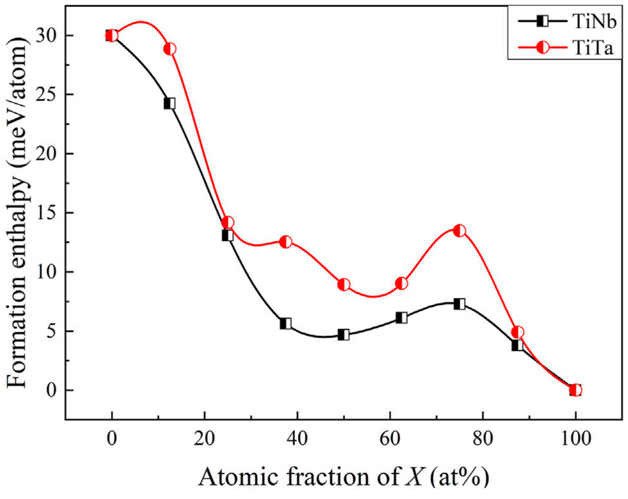

FIGURE 3 | Formation enthalpy of β-Ti*X* (X = Nb, Ta) alloys.

The Gibbs free energy ΔG can be expressed by

$$\Delta G(T) = \Delta H_f - T\Delta S + \Delta F_{vib}(T), \tag{2}$$

where ΔS stands for the mixing entropy of the alloys, ΔF_{vib} is the free energy of lattice vibration of the alloys, and T represents the temperature. The mixing entropy of the alloys can be calculated by

$$\Delta S = -k_B[x\ln x + (1-x)\ln(1-x)], \tag{3}$$

where x is the atomic percentage of alloying element X (Nb, Ta) and k_B is the Boltzmann constant. For stable structure alloys, the effect of lattice vibration on Gibbs free energy is generally much less than that of the mixing entropy (Benisek et al., 2014). Therefore, in this case, the influence of ΔF_{vib} is ignored. Based on **Eqs 1**, **2**, **3**, the Gibbs free energy of the β-Ti*X* (X = Nb, Ta) alloys can be obtained at a range of temperatures.

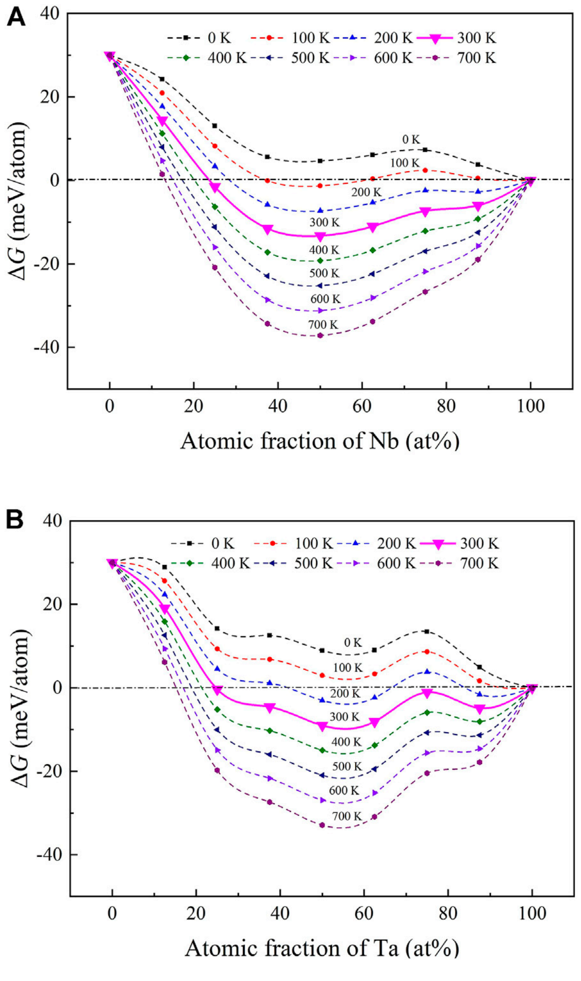

FIGURE 4 | Gibbs free energies of **(A)** β-TiNb and **(B)** β-TiTa alloys.

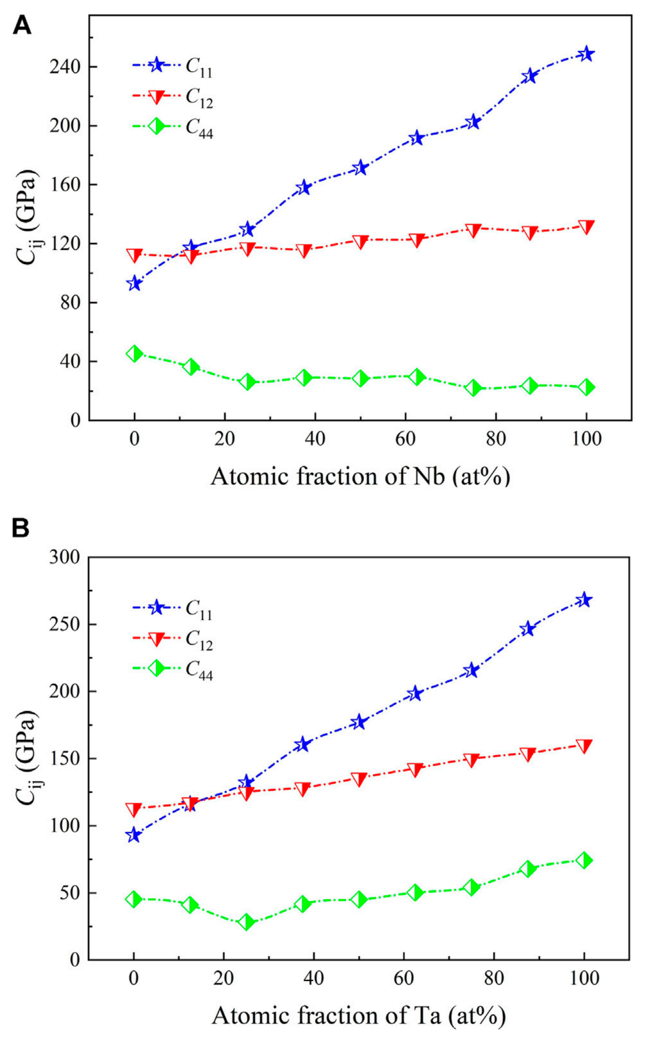

FIGURE 5 | Single-crystal constants of **(A)** β-TiNb and **(B)** β-TiTa alloys.

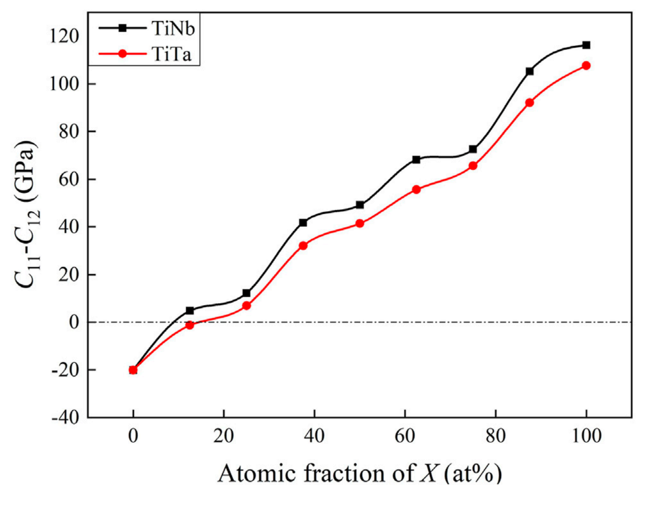

FIGURE 6 | Mechanical stability of β-Ti*X* (*X* = Nb, Ta) alloys.

2.3 Calculation of the Elastic Properties

The elastic constant of the single crystal can be obtained by the relationship between stress and strain. Hooke's law can be expressed as

$$(\boldsymbol{\sigma}_i) = \left(\boldsymbol{C}_{ij}\right)\left(\boldsymbol{\varepsilon}_j\right). \tag{4}$$

$(\boldsymbol{C}_{ij})$ represents the 6 × 6 stiffness matrix. $(\boldsymbol{\sigma}_i)$ represents the stress tensor, and $(\boldsymbol{\varepsilon}_j)$ represents the strain tensor. Both $(\boldsymbol{\sigma}_i)$ and $(\boldsymbol{\varepsilon}_j)$ were given by the Viogt notation. The Viogt notation is a representation method that converts two indexes into one index: 11→1, 22→2, 33→3, 32 (23)→4, 13 (31)→5, and 12 (21)→6. Also, the strain tensor ε is defined as

$$\boldsymbol{\varepsilon} = \begin{bmatrix} e_1 & \frac{1}{2}e_6 & \frac{1}{2}e_5 \\ \frac{1}{2}e_6 & e_2 & \frac{1}{2}e_4 \\ \frac{1}{2}e_5 & \frac{1}{2}e_4 & e_3 \end{bmatrix}. \tag{5}$$

The number of independent elastic constants is different if crystal structures vary. The higher the degree of symmetry of the crystal structure, the less the number of independent elastic constants will be. So, there are only three independent elements $\boldsymbol{C}_{11}$, $\boldsymbol{C}_{12}$, and $\boldsymbol{C}_{44}$ which exist in β-Ti*X* (*X* = Nb, Ta) alloys to account for cubic symmetry.

All the elastic constants of the crystal structure can be obtained by calculating the total energy change after elastic strain which can be expanded by the Taylor formula as (Giustino, 2014):

$$\boldsymbol{D}(V,\ \boldsymbol{\varepsilon}) = \boldsymbol{D}_0 + \boldsymbol{V}_0\left(\sum_{i=1}^{6}\boldsymbol{\sigma}_i\boldsymbol{e}_i + \frac{1}{2}\sum_{i,j=1}^{6}\boldsymbol{C}_{ij}\boldsymbol{e}_i\boldsymbol{e}_j\right), \tag{6}$$

where $\boldsymbol{D}_0$ and $\boldsymbol{D}$ represent the total energy of the system before and after strain, respectively, and $\boldsymbol{V}_0$ represents the crystal volume before strain. Since the number of independent elastic constants in the bcc structure is three, the same amount of cubic crystal strains needs to be applied, as shown in **Table 1**. Each independent elastic constant is contained in the second-order coefficients of the Taylor expansion. Several strain values ($\boldsymbol{\varepsilon} = -0.04, -0.02, 0, 0.02, 0.04$) are selected to fit the total energy.

In addition, since the independent elastic constants are included in the quadratic coefficient, the energy change after strain must be a positive value, which can determine whether the dynamics of the cubic crystal is stable:

$$\boldsymbol{C}_{11} + \boldsymbol{C}_{12} > \boldsymbol{0},\ \boldsymbol{C}_{11} - \boldsymbol{C}_{12} > \boldsymbol{0},\ \boldsymbol{C}_{44} > \boldsymbol{0}. \tag{7}$$

The elastic constants of polycrystalline materials, such as bulk (B) modulus and Young's (E) modulus, can be derived from the independent elastic constants calculated in the previous section. The maximum and minimum values of the elastic constants are given by the Voigt and Reuss averaging procedures, respectively, (Voigt, 1910; Reuss, 1929).

In order to reduce the deviation, the Hill arithmetic averaging is adopted in this work (Hill, 1952). The formula for calculating the bulk modulus of the bcc structure is the same under the three

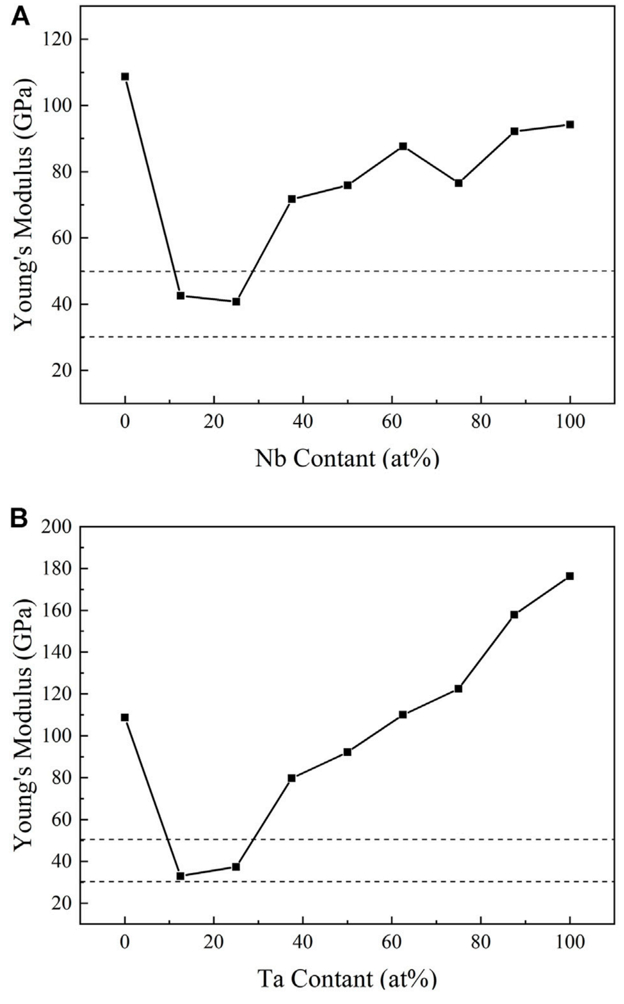

FIGURE 7 | Young's moduli of **(A)** β-TiNb and **(B)** β-TiTa alloys.

methods (Hill arithmetic average, Voigt, and Reuss averaging procedures):

$$B = B_V = B_R = \frac{C_{11} + 2C_{12}}{3}. \tag{8}$$

Also, the theoretical polycrystalline Young's modulus and shear modulus can be obtained by the Hill average method as follows:

$$E = \frac{9BG}{3B + G}, \tag{9}$$

$$G = \left(\frac{G_R + G_V}{2}\right), \tag{10}$$

where G_R and G_V are the Reuss and Voigt averages, respectively, which can be described in the following forms:

$$G_V = \frac{C_{11} - C_{12} + 3C_{44}}{3}. \tag{11}$$

$$G_R = \frac{5(C_{11} - C_{12})C_{44}}{4C_{44} + 3(C_{11} - C_{12})}. \tag{12}$$

In addition, the effects of Nb or Ta content on the critical stress for the slips of <111> on {011}, {112}, or {123} planes were evaluated. The shear modulus along <111> on {011},{112}, or {123} of the bcc structure alloys is estimated based on the elastic constants by the following equation:

$$G_{111} = \frac{3C_{44}(C_{11} - C_{12})}{(C_{11} - C_{12}) + 4C_{44}}. \tag{13}$$

Then, the ideal shear strength τ_{max} can be expressed as

$$\tau_{max} = 0.11G_{111}. \tag{14}$$

3 RESULTS AND DISCUSSION

3.1 Lattice Constants

Calculating lattice constants can estimate the effectiveness of structural optimization. **Figure 2** illustrates the curve of the lattice constant of the β-Ti*X* (*X* = Nb, Ta) alloys with the content of alloy elements *X*. For comparison, lattice parameter data from several other experimental or simulated works (Ikehata et al., 2004; Kim et al., 2006; Wan et al., 2014) are also presented in **Figure 2**. Among them, the black marks represent related work on TiNb alloys, and the red marks represent related work on TiTa alloys. It can be clearly seen that the lattice constant of β-Ti*X* (*X* = Nb, Ta) alloys increases linearly with the increase of the alloying element *X* content. With the increase of the alloying element Nb and Ta content, the lattice constants of β-TiNb and β-TiTa increased by about 1.7% and 2%, respectively. This is because the atomic radius of Nb and Ta are larger than that of Ti, and the atomic radius of Ta is slightly larger than that of Nb.

3.2 Thermodynamic Stability

It is well known that the thermodynamic stability of materials can be determined by calculating the formation enthalpy and Gibbs free energy. **Figure 3** shows the relationship between the formation enthalpy and the content of alloying elements. The formation enthalpies of β-Ti*X* (*X* = Nb, Ta) alloys are greater than 0. Moreover, as the content of alloying elements increases, the formation enthalpies all show a downward trend. In addition, the formation enthalpy of the β-TiTa alloy is always higher than that of the β-TiNb alloy, which indicates that Nb can provide better β-phase stability than Ta as an alloying element.

The Gibbs free energy of the β-Ti*X* (*X* = Nb, Ta) alloys is shown in **Figure 4**. If ΔG is less than zero, the alloy is thermodynamically stable at the corresponding temperature. It can be clearly seen that as the temperature increases, the Gibbs free energy of β-Ti*X* (*X* = Nb, Ta) decreases. Also, the Gibbs free energy of β-TiNb is always lower than that of β-TiTa at the same composition and temperature, which also interprets that Nb provides stronger phase stability than Ta. Among other things, the Gibbs free energy of β-Ti*X* (*X* = Nb, Ta) alloys almost always reaches its minimum value when the alloying element content is about 50% because the mixing

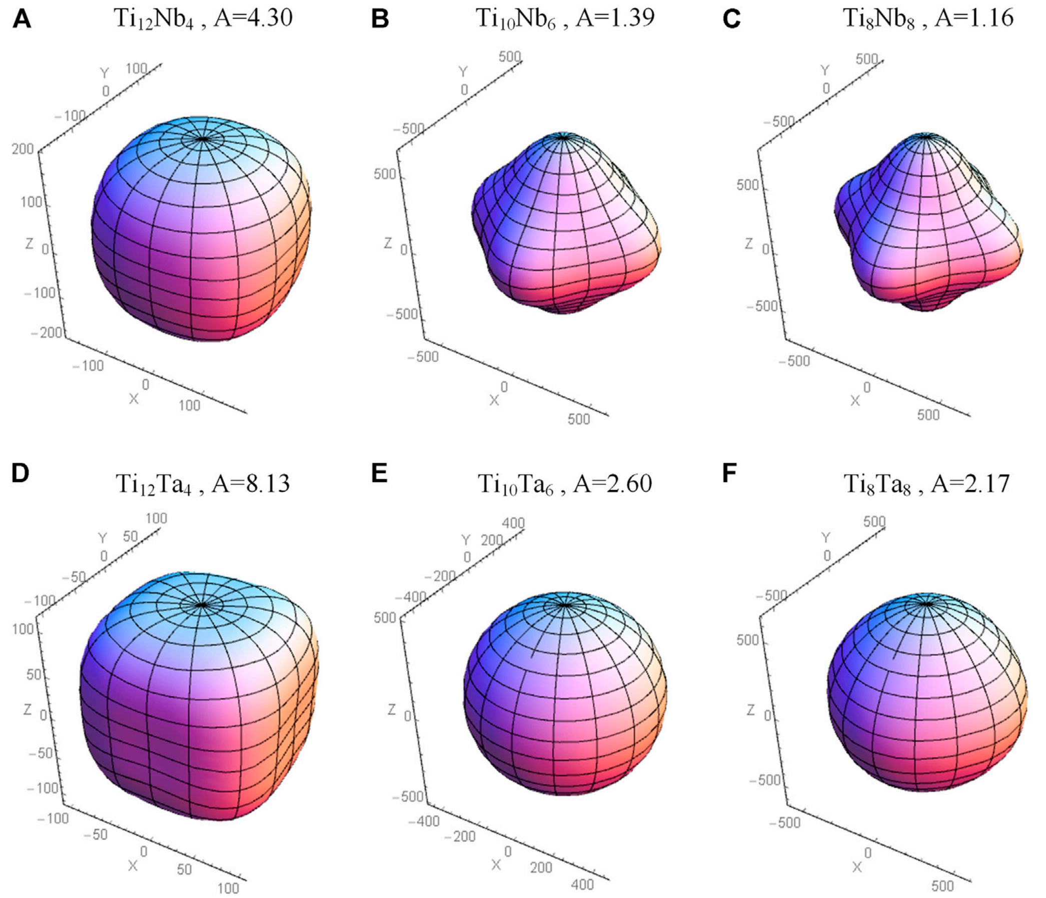

FIGURE 8 | Young's moduli of **(A)** $Ti_{12}Nb_4$, **(B)** Ti10Nb6, **(C)** Ti8Nb8, **(D)** Ti12Ta, **(E)** Ti10Ta, and **(F)** Ti8Ta8. (The Zener ratio $A = 2C_{44} / (C_{11} - C_{12})$ is a measure of the elastic anisotropy.)

entropy of the alloys has the maximum value when the composition is similar, whereas at the position of about 75% alloying element content, the Gibbs free energy curve of the β-TiTa alloy shows a peak. Therefore, in the range of 200–600 K, there are two troughs in the Gibbs free energy curve of the β-TiTa alloy, which is due to the amplitude modulation decomposition of the β-TiTa alloy in this temperature range. It should be pointed out that the dotted line in **Figure 4** is at the position of $\Delta G = 0$. As a matter of fact, at room temperature (about 300 K), both β-TiNb and β-TiTa can reach a thermodynamically stable state when the alloying element content is more than 25%.

3.3 Elastic Properties

3.1.1 Elastic Constants

The C_{11}, C_{12}, and C_{44} of β-TiX (X = Nb, Ta) alloys change with alloying element content as shown in **Figure 5**. Both C_{11} and C_{12} increase with the increase of alloying element content. In the case of C_{44}, the calculation results have different degrees of underestimation. This phenomenon also exists in other transition metal simulation calculations, and some reports have pointed out that it is caused by the existence of Van Hove singularity (Katahara et al., 1979; Koči et al., 2008; Nagasako et al., 2010). Moreover, the anomalies of C_{44} have been captured experimentally at low temperatures in transition metals (Talmor et al., 1977; Walker, 1978; Walker and Bujard, 1980), which also indicates that the calculation results are reasonable.

Both $C_{11} + C_{12} > 0$ and $C_{44} > 0$ are automatically met because C_{ij} is always positive. Hence, the mechanical stability of the alloys depends on $C_{11} - C_{12}$. **Figure 6** shows the change of the $C_{11} - C_{12}$ in the β-TiX (X = Nb, Ta) alloys. The value of $C_{11} - C_{12}$ increases with the increase of the alloying element's content, and the value of $C_{11} - C_{12}$ is 0 when Nb element content is 10% or Ta element content is 13%. In other words, the bcc structure β-TiX (X = Nb, Ta) alloys can satisfy the mechanical stability requirements when Nb content is greater than 10% in the β-TiNb alloy or Ta content is greater than 13% in the β-TiTa alloy.

3.3.2 Young's Modulus and Shear Modulus

The Young's modulus of β-TiX (X = Nb, Ta) alloys is shown in **Figure 7**. For β-TiNb, Young's modulus reaches the minimum value of 40.75 GPa when the Nb content is about 25%. Then,

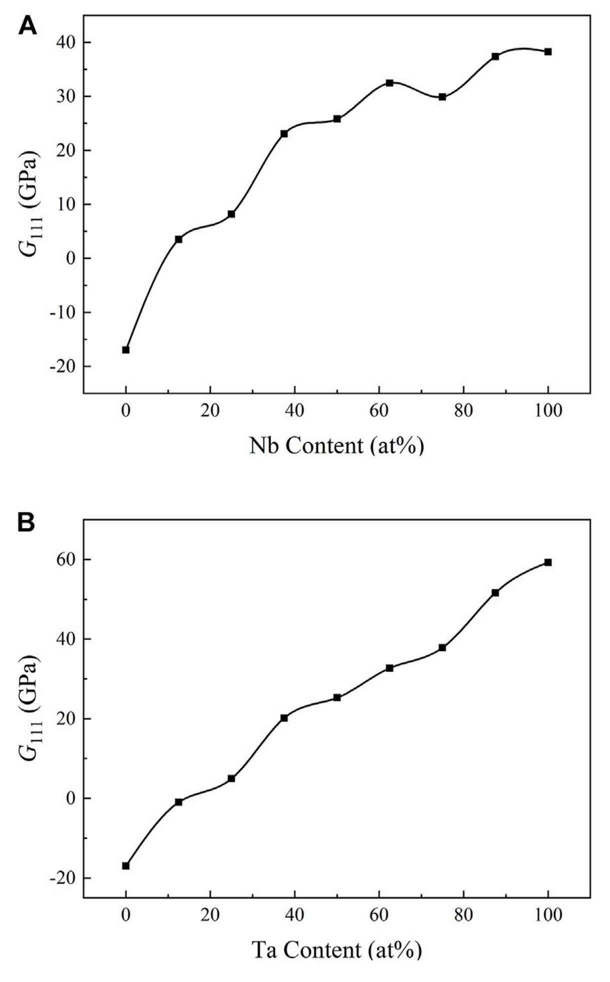

FIGURE 9 | Shear moduli of **(A)** β-TiNb and **(B)** β-TiTa alloys.

Young's modulus increases with the increase of Nb content. But, Young's modulus slightly decreases when the Nb content is about 75%. For β-TiTa, when the Ta content is 12.5% and 25%, Young's modulus is basically equivalent. After that, Young's modulus kept increasing monotonously. The mechanical stability of 12.5% Ta does not meet the requirements. Therefore, the minimum Young's modulus of β-TiTa is obtained when the Ta content is 25%, and its value is 37.36 GPa.

The DFT method can also be used to calculate the anisotropy of Young's modulus (Wróbel et al., 2012). It has been pointed out that the direction of low Young's modulus is more conducive to the formation of texture and the nucleation of metastable martensite (Hanada et al., 2014; Guo et al., 2015; Hou et al., 2016). Therefore, the analysis of elastic anisotropy and the direction of the minimum value of Young's modulus is helpful in further regulating the elastic properties of β-TiX (X = Nb, Ta) alloys. **Figure 8** shows the distribution of Young's modulus of β-TiX (X = Nb, Ta) alloys with 25%, 37.5%, and 50% alloying elements. The closer to the origin of the space coordinate system, the smaller Young's modulus will be. Young's modulus of $Ti_{12}Nb_4$ has a minimum value in the <100> direction in **Figure 8A**. In **Figure 8C**, the minimum value of Young's modulus shifts from the <100> direction to the <111> direction. Also, Young's modulus of $Ti_{10}Nb_6$ has a minimum value in the <111> direction in **Figure 8B**. Later, as the Nb content increases, the minimum value of Young's modulus remains in the <111> direction. For β-TiTa alloy in **Figures 8D–F**, Young's modulus of $Ti_{12}Ta_4$ has a minimum value in the <100> direction, but when the Ta element content reaches 37.5%, Young's modulus in all directions is basically the same, and the subsequent change is small. Overall, as the atomic ratio of β-TiX (X = Nb, Ta) alloys gradually increases to 1, its elastic anisotropy gradually increases.

Figure 9 shows the shear moduli of β-TiX (X = Nb, Ta) alloys. With the increases in alloying element content, the G_{111} value has increased to varying degrees. The G_{111} value of β-TiTa basically keeps increasing linearly, while the growth of the G_{111} value of β-TiNb gradually becomes slow. Moreover, Ta has a stronger influence on the shear modulus of β-TiX (X = Nb, Ta) alloys than Nb. The result shows that the higher the content of β-phase stabilizing elements in the titanium alloys, the higher the critical stress required for slip deformation.

3.4 Electronic Structure

In this section, the total density of states (TDOS) and partial density of states (PDOS) of β-TiX (X = Nb, Ta) alloys are calculated to reveal the influence mechanism of alloying element X content on the phase stability and mechanical properties of β-TiX alloys, as shown in **Figure 10**. The dotted line in **Figure 10** represents the position of the Fermi level, at x = 0. The left side of the Fermi level is the valence band and the right side is the conduction band. First, it can be seen that the TDOS near the Fermi level of both β-TiNb and β-TiTa alloys mainly originates from the contribution of Ti-d and X-d orbital electrons. This indicates that the phase stability and mechanical properties of the β phase of titanium alloy are closely related to the d-orbital electrons, which is consistent with the report of Kuroda et al., (1998). Second, the TDOS value corresponding to the position of the Fermi level is related to phase stability, and the lower the value is, the more stable the structure is (Guo and Wang, 2000). It can be seen from **Figure 10** that as the content of alloy element X increases, the value corresponding to the position of the Fermi level on the TDOS image of β-TiX alloys gradually decreases. This indicates that the phase stability of β-TiX alloys is improved with the increase of the content of Nb and Ta elements, which can be attributed to the fact that alloying elements Nb and Ta can provide additional d-orbital electrons. In addition, dp valence state orbital hybridization of the alloying element X and Ti is found in the conduction band near the Fermi level. This hybridization phenomenon can increase the bonding strength, which is not only beneficial to improve the phase stability of β-TiX alloys but also to improve their tensile

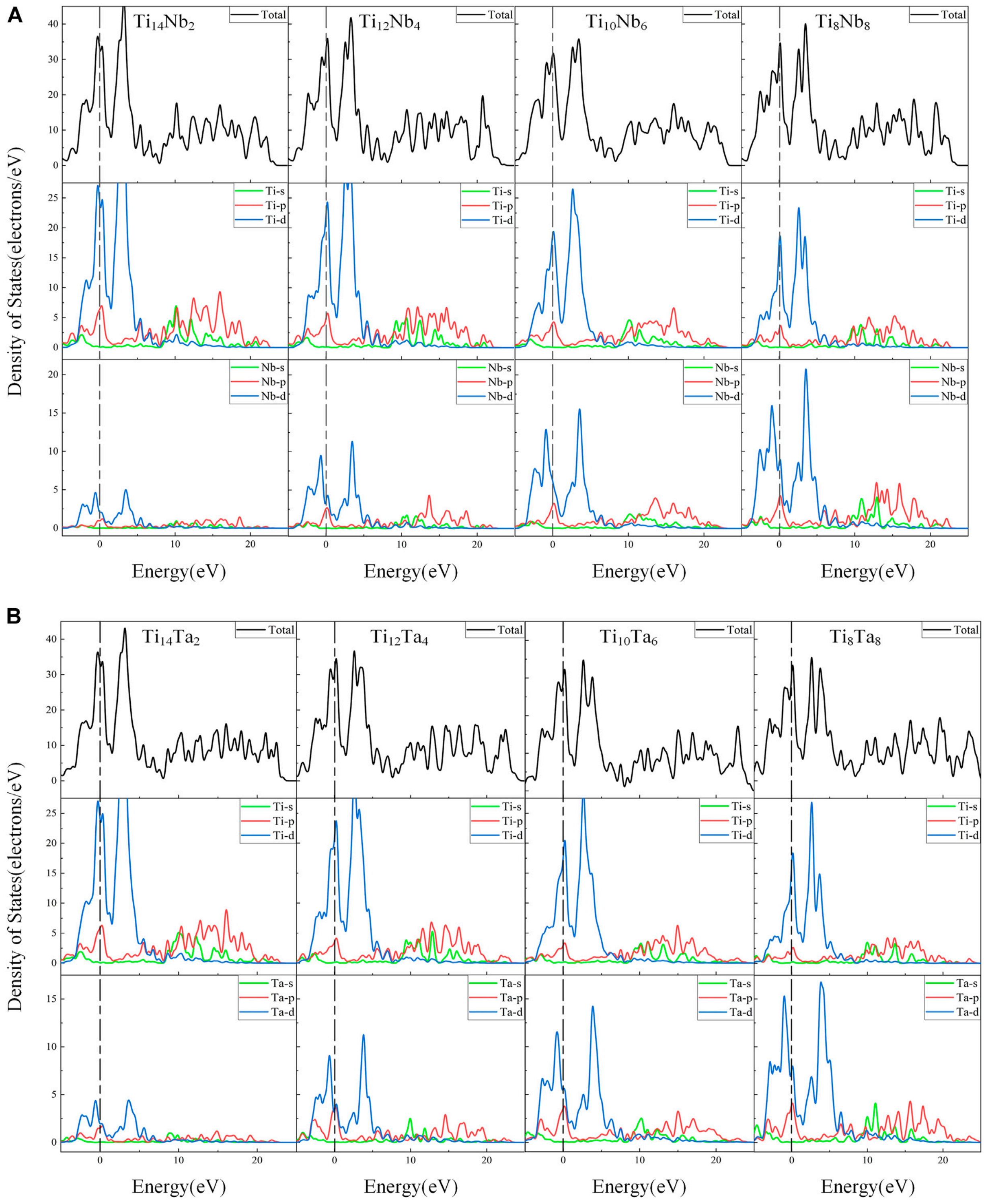

FIGURE 10 | TDOS and PDOS of **(A)** *β*-TiNb and **(B)** *β*-TiTa alloys.

strength. The abovementioned points also explain why the elastic modulus of *β*-Ti*X* alloys increases when the alloying element *X* content exceeds 25%.

To understand the bonding characteristic more intuitively and vividly, the three-dimensional difference charge densities map of *β*-Ti*X* alloys is plotted by the VESTA package (Momma

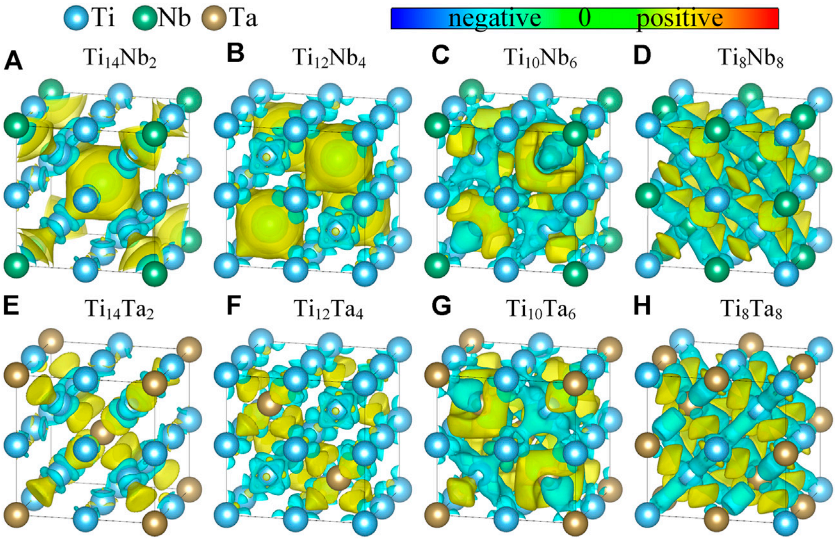

FIGURE 11 | Difference charge densities of *β*-Ti*X* (*X* = Nb, Ta) alloys. **(A)** $Ti_{14}Nb_2$; **(B)** $Ti_{12}Nb_4$; **(C)** $Ti_{10}Nb_6$; **(D)** Ti_8Nb_8; **(E)** $Ti_{14}Ta_2$; **(F)** $Ti_{12}Ta_4$; **(G)** $Ti_{10}Ta_6$; **(H)** Ti_8Ta_8. The value of all the isosurface level is 0.0051e/Å^3.

and Izumi, 2008) and shown in **Figure 11**. In each plot, the atomic positions of all alloying elements are the same as in the model in **Figure 1**. The yellow area represents the gain of electrons, while the blue area represents the loss of electrons. It can be seen from **Figure 11** that the Ti atom in *β*-Ti*X* alloys loses electrons and the alloying element *X* gains electrons. Also, there is almost no difference in charge density between Ti–Ti atomic pairs and *X*–*X* atomic pairs, showing typical metallic properties. When the content of alloying elements is low, as shown in **Figures 11A,B,E,F**, the charge density profile between Ti-*X* atoms is symmetrically distributed, which indicates the existence of weak metallic bonds between Ti-*X* atoms (Ouadah et al., 2020). As the content of alloying element *X* increases, the bonding electron density between Ti atoms and *X* atoms is obviously increased and forms the ring-type features, leading to an increase in bond strength and indicating an effective solid-solution strengthening the effect. When alloying element *X* content is 37.5%, as shown in **Figures 11C,G**, the distribution of electron cloud between solute atom *X* and solvent atom Ti is asymmetrical. The non-spherical distribution of electrons will act as a barrier to make deformation difficult and high modulus in the plastic deformation process of the material, while this is consistent with the research results of Yu et al., (2021). When the alloying element *X* content reaches 50%, as shown in **Figures 11D,H**, the Ti-*X* bond is strengthened by sharing electron pairs to form a covalent bond, and the bonding direction is obviously concentrated in the <111> direction. This result is consistent with that of the previous studies on thermodynamic stability and elastic anisotropy. Moreover, by comparing the difference charge density of *β*-TiNb and *β*-TiTa alloys with the same content of alloying elements, it can be seen that the bonding effect of *β*-TiNb alloys is better than that of *β*-TiTa alloys, which is consistent with the conclusion of formation enthalpy.

4 CONCLUSION

This article presents an ab initio study of phase stability and elastic properties of *β*-Ti*X* (*X* = Nb, Ta) alloys. The phase stability of the *β*-Ti*X* (*X* = Nb, Ta) alloys was determined from two aspects of mechanical stability and thermodynamic stability. The elastic modulus was estimated by the Hill arithmetic averaging, and the elastic anisotropy was analyzed. Also, the influence mechanism of the content of alloying element *X* (*X* = Nb, Ta) on the phase stability and elastic properties of *β*-Ti*X* (*X* = Nb, Ta) alloys was expounded from the electronic level. The conclusions of this study are as follows:

1) The mechanical stability of the *β*-Ti*X* (*X* = Nb, Ta) alloys meets the requirements when the Nb element content is 10% in the *β*-TiNb alloy or when the Ta element content is 13% in the *β*-TiTa alloy.
2) The formation enthalpy of *β*-Ti*X* (*X* = Nb, Ta) alloys decreases with the increase of alloying element Nb or Ta content. At room temperature (about 300 K), *β*-TiNb and *β*-TiTa alloys are thermodynamically stable when the content of alloying elements Nb or Ta is more than 25%.
3) The minimum Young's modulus of *β*-Ti*X* (*X* = Nb, Ta) alloys was obtained when the content of alloying elements is 25%. The minimum Young's modulus of the *β*-TiNb alloy is 40.75 GPa and that of the *β*-TiTa alloy is 37.36 GPa.
4) As the alloy element's content increases, the minimum value of Young's modulus of *β*-Ti*X* (*X* = Nb, Ta) alloys shifts from the <100> direction to the <111> direction. Also, Young's

modulus anisotropy of the β-TiTa alloy is smaller than that of β-TiNb alloy.

5) Alloying element X (X = Nb, Ta) can provide additional d-orbital electrons, that is to say, the increase of alloying element X content will lead to the increase of valence electron concentration and bonding strength, thus improving the phase stability and elastic modulus of β-TiX (X = Nb, Ta) alloys.

In summary, the β-TiX (X = Nb, Ta) alloys with an alloying element content of 25% meet the requirements of mechanical stability and thermodynamic stability and have the lowest elastic modulus. The optimum content of β-TiNb and β-TiTa alloying elements determined in this work is 25%, and the corresponding elastic moduli under this composition are 40.75 and 37.36 GPa, respectively.

DATA AVAILABILITY STATEMENT

The original contributions presented in the study are included in the article/Supplementary Material; further inquiries can be directed to the corresponding authors.

AUTHOR CONTRIBUTIONS

HSL, LJX, and WYX contributed to the conception and design of the study. HSL organized the database and performed the statistical analysis. HSL and WZM wrote the first draft of the manuscript. LJX, WYX, and YDY wrote sections of the manuscript. All authors contributed to manuscript revision, read, and approved the submitted version.

REFERENCES

Banerjee, D., and Williams, J. C. (2013). Perspectives on Titanium Science and Technology. *Acta Mater.* 61 (3), 844–879. doi:10.1016/j.actamat.2012.10.043

Benisek, A., Dachs, E., Salihović, M., Paunovic, A., and Maier, M. E. (2014). The Vibrational and Configurational Entropy of α-brass. *J. Chem. Thermodyn.* 71, 126–132. doi:10.1016/j.jct.2013.11.012

Birch, F. (1947). Finite Elastic Strain of Cubic Crystals. *Phys. Rev.* 71 (11), 809–824. doi:10.1103/PhysRev.71.809

Blöchl, P. E., Jepsen, O., and Andersen, O. K. (1994). Improved Tetrahedron Method for Brillouin-Zone Integrations. *Phys. Rev. B* 49 (23), 16233. doi:10.1103/PhysRevB.49.16223

Blochl, P. E. (1994). Projector Augmented-Wave Method. *Phys. Rev. B* 50 (24), 17979. doi:10.1103/PhysRevB.50.17953

de Formanoir, C., Martin, G., Prima, F., Allain, S. Y. P., Dessolier, T., Sun, F., et al. (2019). Micromechanical Behavior and Thermal Stability of a Dual-phase α+α' Titanium Alloy Produced by Additive Manufacturing. *Acta Mater.* 162, 149–162. doi:10.1016/j.actamat.2018.09.050

Geetha, M., Singh, A. K., Asokamani, R., and Gogia, A. K. (2009). Ti Based Biomaterials, the Ultimate Choice for Orthopaedic Implants – A Review. *Prog. Mater. Sci.* 54 (3), 397–425. doi:10.1016/j.pmatsci.2008.06.004

Giustino, F. (2014). *Materials Modelling Using Density Functional Theory: Properties and Predictions*. New York: Oxford University Press.

Guo, G. Y., and Wang, H. H. (2000). Calculated Elastic Constants and Electronic and Magnetic Properties of Bcc, Fcc, and Hcp Cr Crystals and Thin Films. *Phys. Rev. B* 62 (8), 5136–5143. doi:10.1103/PhysRevB.62.5136

Guo, S., Meng, Q., Zhao, X., Wei, Q., and Xu, H. (2015). Design and Fabrication of a Metastable β-type Titanium Alloy with Ultralow Elastic Modulus and High Strength. *Sci. Rep.* 5 (1), 1–8. doi:10.1038/srep14688

Hanada, S., Masahashi, N., Jung, T. K., Miyake, M., Sato, Y. S., and Kokawa, H. (2014). Effect of Swaging on Youngs Modulus of β Ti–33.6Nb–4Sn Alloy. *J. Mech. Behav. Biomed. Mater.* 32, 310–320. doi:10.1016/j.jmbbm.2013.10.027

Hao, Y. L., Gong, D. L., Li, T., Wang, H. L., Cairney, J. M., Wang, Y. D., et al. (2018). Continuous and Reversible Atomic Rearrangement in a Multifunctional Titanium Alloy. *Materialia* 2, 1–8. doi:10.1016/j.mtla.2018.08.013

Hill, R. (1952). The Elastic Behaviour of a Crystalline Aggregate. *Proc. Phys. Soc. A* 65 (5), 349–354. doi:10.1088/0370-1298/65/5/307

Hou, Y. P., Guo, S., Qiao, X. L., Tian, T., Meng, Q. K., Cheng, X. N., et al. (2016). Origin of Ultralow Young' S Modulus in a Metastable β-Type Ti–33Nb–4Sn Alloy. *J. Mech. Behav. Biomed. Mater.* 59, 220–225. doi:10.1016/j.jmbbm.2015.12.037

Huang, S., Zhao, Q., Wu, C., Lin, C., Zhao, Y., Jia, W., et al. (2021). Effects of β-Stabilizer Elements on Microstructure Formation and Mechanical Properties of Titanium Alloys. *J. Alloys Compd.* 876, 160085. doi:10.1016/j.jallcom.2021.160085

Ikehata, H., Nagasako, N., Furuta, T., Fukumoto, A., Miwa, K., and Saito, T. (2004). First-principles Calculations for Development of Low Elastic Modulus Ti Alloys. *Phys. Rev. B* 70 (17), 174113. doi:10.1103/PhysRevB.70.174113

Jackson, M., and Dring, K. (2013). A Review of Advances in Processing and Metallurgy of Titanium Alloys. *Mater. Sci. Technol.* 22 (8), 881–887. doi:10.1179/174328406X111147

Jia, S., Wang, L., Zhang, L., Wu, K., Wu, W., and Gao, Z. (2020). Structures and Properties of β-Titanium Doping Trace Transition Metal Elements: a Density Functional Theory Study. *Russ. J. Phys. Chem.* 94 (10), 2055–2063. doi:10.1134/s0036024420100283

Kapoor, K., Ravi, P., Naragani, D., Park, J.-S., Almer, J. D. J., and Sangid, M. D. (2020). Strain Rate Sensitivity, Microstructure Variations, and Stress-Assisted β→α″ Phase Transformation Investigation on the Mechanical Behavior of Dual-phase Titanium Alloys. *Mater. Charact.* 166, 110410. doi:10.1016/j.matchar.2020.110410

Katahara, K. W., Manghnani, M. H., and Fisher, E. S. (1979). Pressure Derivatives of the Elastic Moduli of BCC Ti-V-Cr, Nb-Mo and Ta-W Alloys. *J. Phys. F. Metall. Phys.* 9 (5), 773–790. doi:10.1088/0305-4608/9/5/006

Kim, H. Y., Ikehara, Y., Kim, J. I., Hosoda, H., and Miyazaki, S. (2006). Martensitic Transformation, Shape Memory Effect and Superelasticity of Ti–Nb Binary Alloys. *Acta Mater.* 54 (9), 2419–2429. doi:10.1016/j.actamat.2006.01.019

Koči, L., Ma, Y., Oganov, A. R., Souvatzis, P., and Ahuja, R. (2008). Elasticity of the Superconducting Metals V, Nb, Ta, Mo, and W at High Pressure. *Phys. Rev. B* 77 (21), 214101. doi:10.1103/PhysRevB.77.214101

Koval, N. E., Juaristi, J. I., Díez Muiño, R., and Alducin, M. (2019). Elastic Properties of the TiZrNbTaMo Multi-Principal Element Alloy Studied from First Principles. *Intermetallics* 106, 130–140. doi:10.1016/j.intermet.2018.12.014

Kresse, G., and Furthmüller, J. (1996a). Efficiency of Ab-Initio Total Energy Calculations for Metals and Semiconductors Using a Plane-Wave Basis Set. *Comput. Mater. Sci.* 6 (1), 15–50. doi:10.1016/0927-0256(96)00008-0

Kresse, G., and Furthmüller, J. (1996b). Efficient Iterative Schemes for Ab Initio Total-Energy Calculations Using a Plane-Wave Basis Set. *Phys. Rev. B* 54 (16), 11169–11186. doi:10.1103/PhysRevB.54.11169

Kuroda, D., Niinomi, M., Morinaga, M., Kato, Y., and Yashiro, T. (1998). Design and Mechanical Properties of New Type Titanium Alloys for Implant Materials. *Mater. Sci. Eng. A* 243 (1-2), 244–249. doi:10.1016/S0921-5093(97)00808-3

Lee, C. M., Ju, C. P., and Chern Lin, J. H. (2002). Structure–property Relationship of Cast Ti–Nb Alloys. *J. Oral Rehabil.* 29 (4), 314–322. doi:10.1046/j.1365-2842.2002.00825.x

Momma, K., and Izumi, F. (2008). VESTA: a Three-Dimensional Visualization System for Electronic and Structural Analysis. *J. Appl. Cryst.* 41 (3), 653–658. doi:10.1107/S0021889808012016

Monkhorst, H. J., and Pack, J. D. (1976). Special Points for Brillouin-Zone Integrations. *Phys. Rev. B* 13 (12), 5188–5192. doi:10.1103/PhysRevB.13.5188

Moreno, J., Papageorgiou, D. G., Evangelakis, G. A., and Lekka, C. E. (2018). An ab initio Study of the Structural and Mechanical Alterations of Ti-Nb Alloys. *J. Appl. Phys.* 124 (24), 245102. doi:10.1063/1.5025926

Moreno, J. J. G., Bönisch, M., Panagiotopoulo, N. T., Calin, M., Papageorgiou, D. G., Gebert, A., et al. (2017). Ab-Initio and Experimental Study of Phase Stability of Ti-Nb Alloys. *J. Alloys Compd.* 696, 481–489. doi:10.1016/j.jallcom.2016.11.231

Nagasako, N., Jahnátek, M., Asahi, R., and Hafner, J. (2010). Anomalies in the Response of V, Nb, and Ta to Tensile and Shear Loading: Ab Initio Density Functional Theory Calculations. *Phys. Rev. B* 81 (9), 094108. doi:10.1103/PhysRevB.81.094108

Ouadah, O., Merad, G., Saidi, F., Mendi, S., and Dergal, M. (2020). Influence of Alloying Transition Metals on Structural, Elastic, Electronic and Optical Behaviors of γ-TiAl Based Alloys: A Comparative DFT Study Combined with Data Mining Technique. *Mater. Chem. Phys.* 242, 122455. doi:10.1016/j.matchemphys.2019.122455

Perdew, J. P., Burke, K., and Ernzerhof, M. (1996). Generalized Gradient Approximation Made Simple. *Phys. Rev. Lett.* 77 (18), 3865–3868. doi:10.1103/PhysRevLett.77.3865

Rack, H. J., and Qazi, J. I. (2006). Titanium Alloys for Biomedical Applications. *Mater. Sci. Eng. C* 26 (8), 1269–1277. doi:10.1016/j.msec.2005.08.032

Reuss, A. (1929). Berechung der Fliessgrenze von Mischkristallen auf grund der plastizitätsbedingung für einkristalle. *Z. Angew. Math. Mech.* 9 (1), 49–58. doi:10.1002/zamm.19290090104

Talmor, Y., Walker, E., and Steinemann, S. (1977). Elastic Constants of Nionium up to the Melting Point. *Solid State Commun.* 23 (9), 649–651. doi:10.1016/0038-1098(77)90541-5

Voigt, W. (1910). *Lehrbuch der kristallphysik:(mit ausschluss der kristalloptik)*. Ann Arbor: BG Teubner.

Walker, E. (1978). Anomalous Temperature Behaviour of the Shear Elastic Constant C44 in Vanadium. *Solid State Commun.* 28 (7), 587–589. doi:10.1016/0038-1098(78)90495-7

Walker, E., and Bujard, P. (1980). Anomalous Temperature Behaviour of the Shear Elastic Constant C44 in Tantalum. *Solid State Commun.* 34 (8), 691–693. doi:10.1016/0038-1098(80)90957-6

Wan, X., Wu, C., Tan, C., and Lin, J. (2014). Structure Stability and Elastic Properties of β Type Ti-X (X=Nb, Mo) Alloys from First-Principles Calculations. *Rare Metal Mater. Eng.* 43 (3), 553–558. doi:10.1016/S1875-5372(14)60075-8

Wróbel, J., Hector, L. G., Wolf, W., Shang, S. L., Liu, Z. K., and Kurzydłowski, K. J. (2012). Thermodynamic and Mechanical Properties of Lanthanum–Magnesium Phases from Density Functional Theory. *J. Alloys Compd.* 512 (1), 296–310. doi:10.1016/j.jallcom.2011.09.085

Yu, W., Zhou, Y., Chong, X., Wei, Y., Hu, C., Zhang, A., et al. (2021). Investigation on Elastic Properties and Electronic Structure of Dilute Ir-Based Alloys by First-Principles Calculations. *J. Alloys Compd.* 850, 156548. doi:10.1016/j.jallcom.2020.156548

Zhang, M. H., Yu, Z. T., Zhang, D. Z., and Jing, W. S. (2010). Biocompatibility Evaluation of β-type Titanium Alloys. *J. Clin. Rehabilitative Tissue Eng. Res.* 14 (42)**,** 7849–7853. doi:10.3969/j.issn.1673-8225.2010.42.014

Zhang, S.-Z., Cui, H., Li, M.-M., Yu, H., Vitos, L., Yang, R., et al. (2016). First-principles Study of Phase Stability and Elastic Properties of Binary Ti-xTM (TM = V,Cr,Nb,Mo) and Ternary Ti-15TH-yAl Alloys. *Mater. Des.* 110, 80–89. doi:10.1016/j.matdes.2016.07.120

Zhou, Y. L., Niinomi, M., and Akahori, T. (2004). Effects of Ta Content on Young's Modulus and Tensile Properties of Binary Ti–Ta Alloys for Biomedical Applications. *Mater. Sci. Eng. A* 371 (1-2), 283–290. doi:10.1016/j.msea.2003.12.011

Conflict of Interest: The authors declare that the research was conducted in the absence of any commercial or financial relationships that could be construed as a potential conflict of interest.

frontiers | Frontiers in Bioengineering and Biotechnology

TYPE Review
PUBLISHED 11 August 2022
DOI 10.3389/fbioe.2022.952536

OPEN ACCESS

EDITED BY
Jianxun Ding,
Changchun Institute of Applied Chemistry (CAS), China

REVIEWED BY
Nenad Filipovic,
University of Kragujevac, Serbia
Silvia Spriano,
Politecnico di Torino, Italy

*CORRESPONDENCE
Jia Liu,
liujia@ymcn.edu.cn
Yujin Tang,
tangyujin@ymcn.edu.cn
Liqiang Wang,
wang_liqiang@sjtu.edu.cn

SPECIALTY SECTION
This article was submitted to Biomaterials,
a section of the journal Frontiers in Bioengineering and Biotechnology

RECEIVED 25 May 2022
ACCEPTED 20 July 2022
PUBLISHED 11 August 2022

CITATION
Liu C, Yang C, Liu J, Tang Y, Lin Z, Li L, Liang H, Lu W and Wang L (2022), Medical high-entropy alloy: Outstanding mechanical properties and superb biological compatibility. *Front. Bioeng. Biotechnol.* 10:952536.
doi: 10.3389/fbioe.2022.952536

Medical high-entropy alloy: Outstanding mechanical properties and superb biological compatibility

Changxi Liu[1,2], Chengliang Yang[2,3], Jia Liu[2,3]*, Yujin Tang[2,3]*, Zhengjie Lin[4], Long Li[5], Hai Liang[5], Weijie Lu[1,2] and Liqiang Wang[1,2]*

[1]State Key Laboratory of Metal Matrix Composites, School of Material Science and Engineering, Shanghai Jiao Tong University, Shanghai, China, [2]National Center for Translational Medicine, Shanghai Jiao Tong University, Shanghai, China, [3]Department of Orthopaedics, Affiliated Hospital of Youjiang Medical University for Nationalities, Guangxi Key Laboratory of Basic and Translational Research of Bone and Joint Degenerative Diseases, Baise, China, [4]3D Printing Clinical Translational and Regenerative Medicine Center, Shenzhen Shekou People's Hospital, Shenzhen, China, [5]Department of Stomatology, Shenzhen Shekou People's Hospital, Shenzhen, China

Medical metal implants are required to have excellent mechanical properties and high biocompatibility to handle the complex human environment, which is a challenge that has always existed for traditional medical metal materials. Compared to traditional medical alloys, high entropy alloys (HEAs) have a higher design freedom to allow them to carry more medical abilities to suit the human service environment, such as low elastic modulus, high biocompatible elements, potential shape memory capability. In recent years, many studies have pointed out that bio-HEAs, as an emerging medical alloy, has reached or even surpassed traditional medical alloys in various medical properties. In this review, we summarized the recent reports on novel bio-HEAs for medical implants and divide them into two groups according the properties, namely mechanical properties and biocompatibility. These new bio-HEAs are considered hallmarks of a historic shift representative of a new medical revolution.

KEYWORDS

bio-heas, mechanical properties, corrosion resistance, cytocompatibility, friction resistance

Introduction

Currently, numerous biomaterials, including polymer materials, composite materials, and metal materials, have been developed for disease visualization, drug toxicity assessment and detection, tissue repair and substitution (Gaharwar et al., 2020; Eliaz, 2019; Fenton et al., 2018; Qu et al., 2019; Mitrousis et al., 2018; Wang et al., 2021a; Liu et al., 2022). With excellent mechanical properties and good corrosion resistance, metal medical implants undertake the function of repairing and replacing human diseased tissues and organs, which are widely used in artificial heart valves, bone implants and

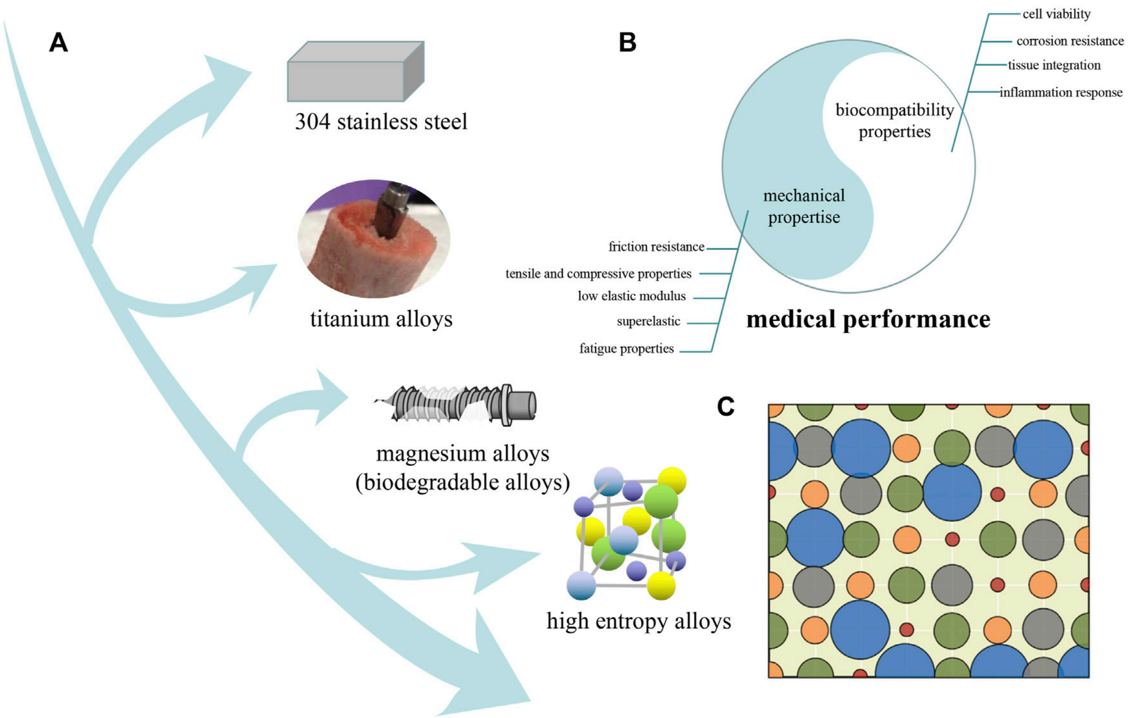

FIGURE 1
(A) Schematic showing several different medical metal implant development sequences. **(B)** Mechanical properties and biocompatibility constitute the performance evaluation criteria for medical metal implants. **(C)** Schematic diagram showing the elemental arrangement model of HEA (the circles in different colors and varying sizes represent the mixed atoms), in this case, the configurational entropy is determined not only by chemical composition but also by atomic size (Ye et al., 2016).

scaffolds, and tooth repair and replacement (Eivazzadeh-Keihan et al., 2020; Sharma et al., 2020; Wang et al., 2022a; Guo et al., 2022; Mao et al., 2022; Qiao et al., 2022) Figure 1A illustrates the several stages of metal implant development and improvement. The earliest metal implant material is 304 stainless steel (Verran and Whitehead, 2005), which is used in artificial joints. Stainless steel material has high strength but also has a high elastic modulus (193 GPa), which is much higher than human bones 10–40 GPa). Such mismatched elastic moduli will prevent the load from smoothly transferring from the implant to the surrounding bone tissue, resulting in a stress shielding phenomenon when the implant is implanted into human bone (Mi et al., 2007). The stress shielding phenomenon can lead to the degeneration and atrophy of the bone tissue and eventually cause the implant to loosen and even fail, which does not meet the requirements of long-term service. Subsequently, compared with other metal materials, titanium and titanium alloys have the characteristics of high specific strength, strong corrosion resistance and good biocompatibility and have become preferred materials for bone tissue repair and replacement (Wang et al., 2021b; Wang et al., 2022b; Cui et al., 2022; Lv et al., 2022; Zhang et al., 2022). For instance, Wang developed a Ti-35Nb-2Ta-3Zr (wt%) alloy with a low Young's modulus of approximately 48 GPa (Wang et al., 2017).

High-entropy alloys have received a great amount of attention in recent years because of their unique composition (five or more metal elements) and homogeneous microstructure (Cantor et al., 2004; Hemphill et al., 2012; Gludovatz et al., 2014; Yu et al., 2014; Ye et al., 2015a; Xia et al., 2015; Miracle and Senkov, 2017). Compared to conventional alloys with relatively simple compositions, HEAs have two significant features: 1) enormous room for performance optimization and improvement derives from multielemental combinations, which ensure that HEAs have a variety of ingredients and complex microstructures, and 2) the various elements mixed will exhibit properties that are not possessed by any pure metal element, which provides HEAs with new properties (Tsai and Yeh, 2014; Lu et al., 2015; George et al., 2019).

With the excellent performance of HEAs, a good approach is to put HEAs into the medical field to explore the potential of HEAs as medical implants. Furthermore, HEAs represented by Ti, Ta, Nb, Zr, and Hf systems have good application and development potential in medical implants, as shown in Figure 1B (Raducanu et al., 2011; Wang and Xu, 2017; Tüten et al., 2019; Yang et al., 2020). For instance, bio-HEAs could be designed to possess high strength following rational guidance due to their complex elemental composition and richness of design (Wang et al., 2020a; Su et al., 2022; Xu et al., 2022). On the other hand, bio-HEAs are designed to have low toxicity because the elements in bio-HEAs have excellent biocompatibility (Nagase et al., 2020). This review aimed to discuss recent advances in bio-HEA mechanical properties and biocompatibility.

High entropy alloy concept

The current mainstream concept is that the high entropy alloy should contain 5–13 main elements, and the mole fraction of each element should be between 5 and 35 at% (Cantor et al., 2004; Yeh et al., 2004). The term "high-entropy alloy" is defined because the relationship of individual atoms can be modelled as an ideal solution, as illustrated in Figure 1C.

The atomic radius difference range (δ) (1) is used to describe the radius relative radius of each element ($\bar{}$r is the average atomic radius and r_i is the atomic radius of element i). It claims that only solid solutions are formed when the δ value is lower than 4% (Zhang and Lv, 2008).

$$\delta = 100\sqrt{\sum c_i\left(1-\frac{r_i}{\bar{r}}\right)} \tag{1}$$

Configuration entropy (ΔS_{am}) 2) is used to describe the mixing entropy of alloys, which high entropy alloys require the ΔS_{mix} value are higher than 11 J/mol K, where c_i is the molar fraction of the *i*th element, R is the constant (8.314 J/mol K), and n is the total number of constituent elements.

The enthalpy of mixing (ΔH_{am}) 3) range of the HEA is a key parameter, which requires between −11.6 and 3.2 kJ/mol, where ΔH_{ij} is the binary enthalpy of elements i and j (Zhang and Lv, 2008).

$$\Delta S_{am} = -R\sum c_i \ln c_i \tag{2}$$

$$\Delta \mathrm{Ham} = \sum c_j \Delta \mathrm{Hij} \tag{3}$$

The parameter *O* 4) involves ΔS_{am} and ΔH_{am}, which can predict the composition of the final HEA phase, where T_{top} is the melting temperature calculated using 5. Usually, only solid solutions are formed when $\Omega > 1.1$ and $\delta < 3.6\%$, and only solid solutions and intermetallic compounds are formed when $1.1 < O < 10$ and $3.6\% < d < 6.6\%$; furthermore, only solid solutions are formed when $\Omega > 10$ (Yang and Zhang, 2012).

$$\Omega = T_{top}\Delta S_{am} \big/ |\Delta \mathrm{Ham}| \tag{4}$$

$$T_{top} = \sum c_i T_{top\,i} \tag{5}$$

The difference in electronegativity $\Delta\chi$ 6) is also used as the criterion for judging whether a single solid solution can be formed, where χ is the average electronegativity and χ_i is the electronegativity of element i. Only solid solutions are formed when the components of the alloy elements are between 3 and 6%.

$$\Delta\chi = 100\sqrt{\sum c_i\left(1-\frac{\chi_i}{\chi}\right)2} \tag{6}$$

Although there may be some differences in the above criteria in the current research on high-entropy alloys, these criteria are useful for predicting the solid phase and composition selection and determination of the atomic fraction ratio for bio-HEAs (Takeuchi et al., 2013; Ye et al., 2015b).

HEAs design and numerical simulation

Compared with traditional alloys, bio-HEAs have a high freedom in element design, which also means more factors need to be considered. Multi-element of bio-HEAs not only induce strong chemical fluctuation to random phase, but also have important effects on the stacking fault energy, second phase and dislocation core structure. In fact, numerical simulations could reflect the bio-HEAs properties independent of material test, which is very beneficial for guiding the design of alloys with high freedom such as bio-HEAs (Yin et al., 2020; Xu et al., 2021). In recent years, Monte Carlo (Zhou et al., 2021), molecular dynamics (Jian et al., 2020; Li et al., 2020), first-principles calculations (Rao et al., 2019), and deep learning (Kostiuchenko et al., 2019) is widely applied in modeling and prediction of bio-HEAs.

Lee (Lee et al., 2020) predicted the Young's modulus (E), bulk modulus (K) and shear modulus (G) of the material by First-principles calculations, showing excellent agreement with the experimental values. Moreover, Yao (Yao et al., 2016) established phase diagrams of NbTaTiV, NbTaVW, and NbTaTiVW through CALPHAD modeling, which predicted the state of NbTaV(TiW) in different temperature ranges. Liu (Liu et al., 2021) used Monte Carlo to predict order-disorder transitions caused by W and Nb. By comparing with experiments, the simulation results provide insight into the role of chemical ordering in the strength and ductility of HEAs.

In fact, HEAs with so many element combinations means huge data and this is a perfect example of deep learning. With the rapid development of computer science, deep learning is becoming more and more accurate for analyzing data patterns and predicting development from samples (Lecun et al., 2015; Guo et al., 2016). For the design of HEAs, the optimal HEA potential element ratio could be output by a deep learning network trained on HEA experimental data (Yan et al., 2021). For instance, wen (Wen et al., 2021a) collected experimental data on AlCoCrFeNi, CoCrFeNiMn, HfNbTaTiZr, and MoNbTaWV, and trained a deep learning network for these types of HEAs to

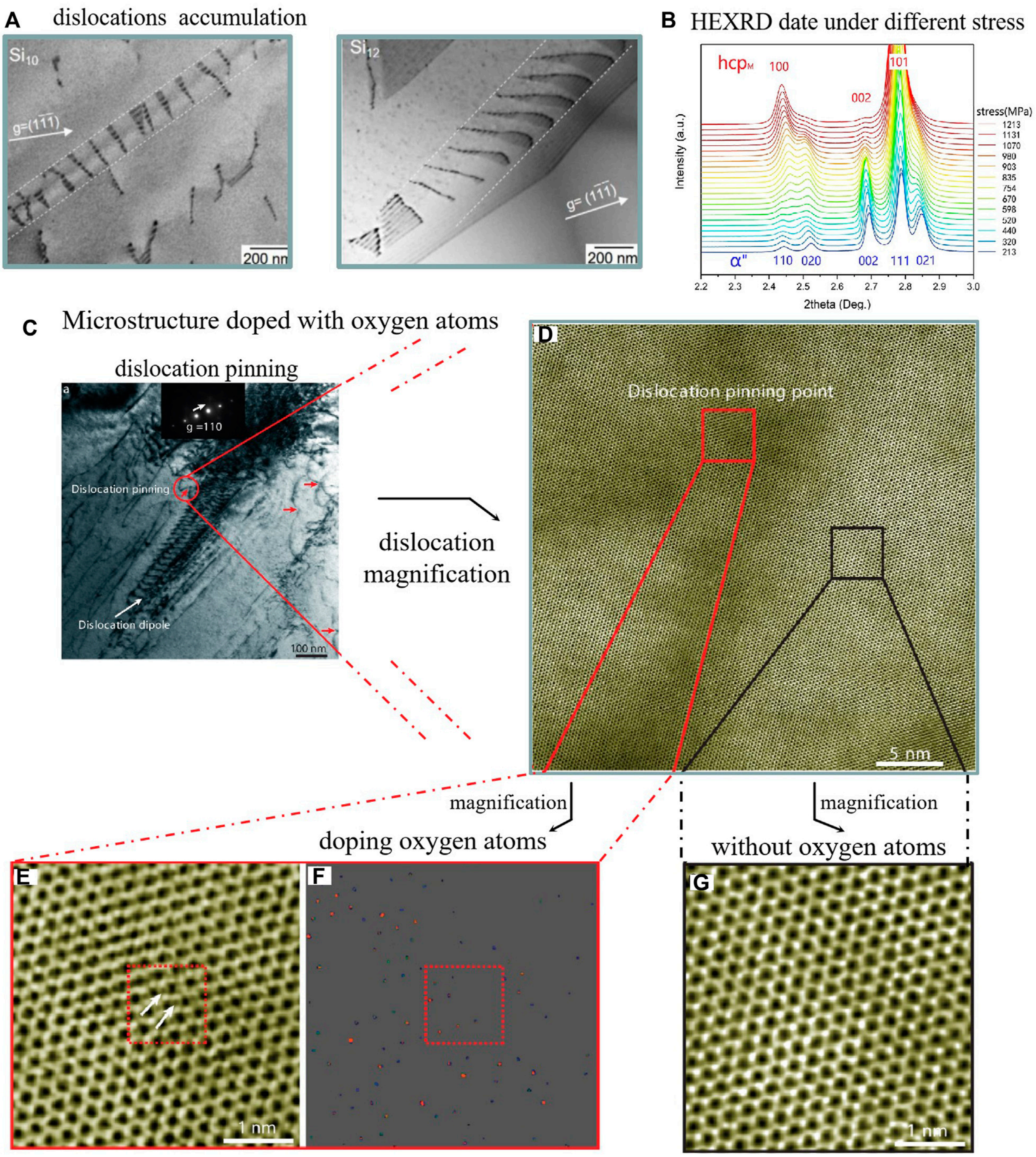

FIGURE 2
(A) Two-beam BF images show the frequently observed accumulation of dislocations on the {111}-type FCC slip planes in $Co_{22}Cr_{22}Fe_{22}Ni_{22}Si_{10}$ and $Co_{10}Cr_{10}Fe_{10}Ni_{10}Mn_{10}Si_{10}$HEA (Wei et al., 2022b). **(B)** the (100) peak of hcpM could be found when the stress was over 520 MPa **(C)** Dislocations in the 8% strained O-2 HEA, imaged under {1a11}-type diffraction conditions (Wang et al., 2020b). **(D)** The dislocation pinning point (red circle) in **(C)** was chosen for further STEM characterization. **(E)** Aberration-corrected STEM-ABF images of the local atomic structure of pinning sites. White arrows point to the pillars of oxygen atoms. **(F)** STEM-HADDF also indicates ordered oxygen complexes near the dislocation pinning point **(G)** Aberration-corrected STEM-ABF images far from the pinning point (Lei et al., 2018).

predict the potential of solid solution strengthening. In the future, deep learning might play a guiding role in the design and prediction of potential properties of HEAs.

Mechanical properties

Compared with traditional medical metal implants, HEAs have excellent mechanical properties (Picak et al., 2021; Wei et al., 2022a). The strength, ductility, elastic modulus and fatigue properties of bio-HEAs should be considered. The excellent mechanical properties of these medical high-entropy alloys are inextricably connected with their microstructures. In fact, the microstructures of HEAs are numerous and complex, and the final microstructure is not the same even for HEAs with the same elements but different ratios, furthermore, heat treatment and thermal deformation also affect the structure (Dirras et al., 2016; Zhang et al., 2018; Li et al., 2019). It is critical to obtain an overall view and summarize the properties of bio-HEAs at this stage, as well as to determine the design ideas of future bio-HEAs.

Tensile and compressive properties

Tensile and compression tests are some of the most intuitive criteria to detect the mechanical properties of materials, which can obtain a series of material performance data, such as yield strength, breaking strength, and elongation, from stress–strain diagrams. Furthermore, many HEAs with excellent mechanical properties have been developed in recent years, which yield strength exceeding 1000 MPa and the elastic modulus lower than 70 GPa These HEAs often have high tensile strength and excellent elongation data, achieving simultaneous improvement of material strength and plasticity. Wei (Wei et al., 2022b) replaced part of the metal elements in HEAs with the metalloid element Si, in which the metalloid element is between metals and nonmetals, and it is easy to induce complex subnanometre-scale structures in the substrate. Figure 2A illustrates the accumulation of dislocations on the {111}-type FCC slip planes. The mechanical properties of -Si HEAs are improved due to these defects, which is consistent with the results of first-principles calculations and Monte Carlo simulations. It shows the elevation of ductility simultaneously with strength in macroscopic performance. Su (Su et al., 2019) designed a hierarchical microstructural for HEA by introducing grains and textures with different size gradients and substructures, which enhanced transformation-induced plasticity (TRIP) and twinning-induced plasticity (TWIP) effects. The material exhibits bimodal microstructures, which were produced consisting of nanograins (~50 nm) in the vicinity of shear bands and recovered parent grains (10–35 μm) with preexisting nanotwins after tempering. Compared with the 95% recrystallized specimen's yield strength of 555 MPa, the HEA yield strength of the bimodal microstructures is increased to 1.3 GPa.

The equiatomic HfNbTaTiZr achieves a tensile yield strength of 974 MPa and has an elongation of 20%. Furthermore, there are numerous dislocations with restricted movement at grain boundaries in HfNbTaTiZr, due to grain refinement (Juan et al., 2016). The O element doped TiZrHfNb exhibited a yield strength of 1,300 MPa and an elongation of 30% in the room temperature tensile test. The strong ordered oxygen complexes in Figures 2C–G are the key reason to achieve such performance. The strength improvement is due to the O solid solution strengthening, more interestingly, the plasticity improvement is due to O changing the plastic deformation mode from plane slip to wave slip, which is different from conventional alloys (Lei et al., 2018). This study shows that the presence of interstitial oxygen elements in a nano-ordered manner could successfully overcome the strength–ductility trade-off.

Chen (Chen et al., 2022a) found that the WNbMoTaZr HEA has a significant increase in strength and toughness with increasing Zr content; the yield strength in the compression test is 1,223 ± 20.1 MPa, and the fracture strain is 6.4 ± 0.66%. In addition, TiZrNbTa doped with N also achieved high strength and high toughness of the material. The yield strength and fracture strain of the tensile test reached 1,196 ± 8 MPa and 17.5 ± 0.3%, respectively (Wang et al., 2022c). The introduction of N in the original matrix resulted in dendritic structures and simultaneously led to dislocation pinning and reduce diffusion rate.

In recent years, some studies on the microstructure and mechanism of bio-HEAs may provide theoretical support for high-strength mechanical properties. Lee believes that unlike traditional body-centered cubic (BCC) structure metals and dilute alloys, in which the strain strengthening depends on screw dislocation, plastic flows in HEAs mainly contribute to edge dislocation (Lee et al., 2021). Furthermore, TWIP and TRIP are still the main methods to enhance the mechanical properties of bio-HEAs. During the tensile process, TWIP and TRIP occur sequentially in the ß phase. $Ti_{16}Zr_{35}Hf_{35}Ta_{14}$ was found to exhibit a new stress-induced martensitic transformation (SIMT) α”-to-hcpM by *in situ* high energy X-ray diffraction (HEXRD), as shown in Figure 2B. The peak of hcpM starts to appear when the stress is 520 MPa, and the peak of α” gradually weakens and finally disappears when the stress is 800 MPa. In addition, SIMT improves the yield strength-ductility of Ti16Zr35Hf35Ta14 [72]. Wen (Wen et al., 2021b) found that the Nb content in $HfNbTa_{0.2}TiZr$ HEA affects the stability of the BCC phase. With the decrease in Nb content, the martensite tends to transform from the BCC structure to the HCP structure, as shown in Figure 3A. A large number of twins are observed during the transition, which may be due to the lower SFE of the HCP structure, and the material finally exhibits a dual increase in strength and plasticity, as shown in Figure 3B. In addition, the

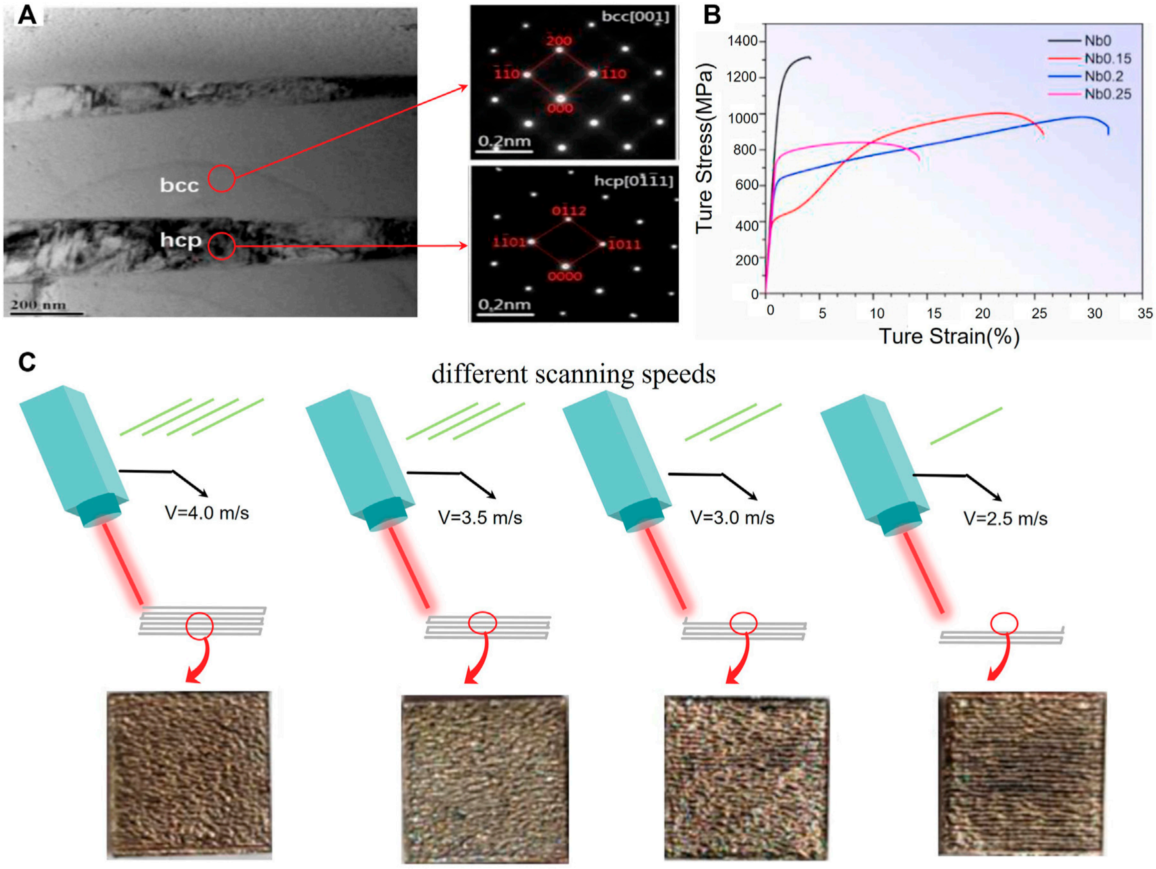

FIGURE 3
(A) TEM bright-field images of the co-existed BCC and HCP phase (Wen et al., 2021b). **(B)** Selected area diffraction show the extra twinning spots **(C)** Four different scanning speeds at 4.0 m/s, 3.5 m/s, 3.0 m/s, 2.5 m/s for the SLM (Xiao et al., 2022).

fine precipitates in $Hf_{20}Nb_{10}Ti_{35}Zr_{35}$ formed by ageing cooperate with TWIP and TRIP and improve the mechanical properties of the material (Su et al., 2022).

Additive manufacturing (AM) is a new type of manufacturing method that has a great impact on medical implant fabrication and its ability to produce complex, porous configurations and structure-specific implants (Herzog et al., 2016; Bourell et al., 2017). Additively manufactured porous materials fabricated by AM could well mimic the skeletal environment in which cells grow (Hafeez et al., 2020; Zhang et al., 2021a). Compared with the HEAs prepared by cold crucible suspension, the microstructure fabricated by AM may be different due to different cooling rates during fabrication; furthermore, the final mechanical properties of the material are also different. Defects caused by AM are an important factor that affects the performance of bio-HEAs because the elements used in bio-HEAs not only have high melting points but also have a wide range of melting points between different elements. Zhang (Zhang et al., 2021b) found that a mixed powder of NbMoTa has a high defect rate after fabrication. Consequently, the printed material has higher formability and strength for SLM after adding Ti and Ni elements. Compared with NbMoTa, the $NbMoTaTi_{0.5}Ni_{0.5}$ HEA has a large amount of extended dislocation at the grain boundary, which strengthens the grain boundary of the crystal. Xiao (Xiao et al., 2022) studied the effect of selected laser melting (SLM) on the microstructure and mechanical properties of WMoTaNbTi HEAs. Several different scan speeds, including 4.0 m/s, 3.5 m/s, 3.0 m/s and 2.5 m/s, were collected and are illustrated in Figure 3C. The material exhibited the highest compressive strength of 1,312 MPa and exhibited good local ductility when the scanning speed was 2.5 m/s.

Low elastic modulus HEAs

Reducing the elastic modulus of metal implants to match human bone to prevent potential stress shielding risks is an important goal for medical metal implants. TiZrNb, $Ti_{40}Zr_{40}Nb_{20}$, $Ti_{45}Zr_{35}Nb_{20}$, $Ti_{45}Zr_{45}Nb_{10}$, and $Ti_{50}Zr_{40}Nb_{10}$

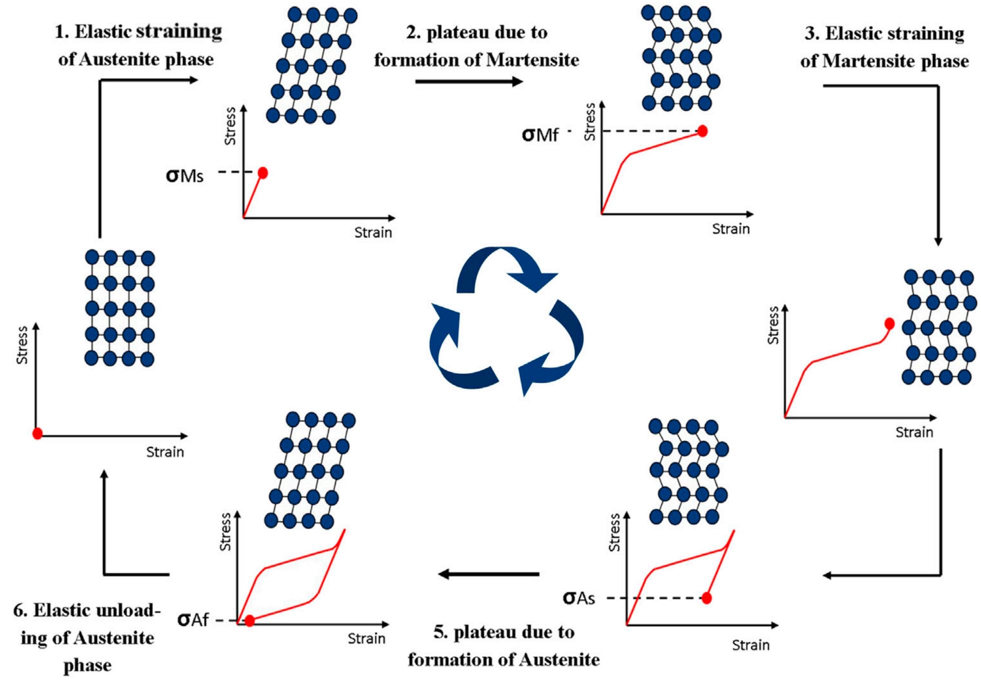

FIGURE 4
The schematic diagram for mental superelasticity by martensitic transformation (Ramezannejad et al., 2019).

all exhibit low elastic moduli (Hu et al., 2022). In particular, the TiZrNb HEA, at room temperature, is composed of dendritic crystals with a single BCC, whose elastic moduli range from 73 ± 3 GPa to 52 ± 2 GPa and are very close to the elastic moduli of large human bones. Schönecker (Schönecker et al., 2022) proposed a new idea for reducing the elastic modulus of TiZrNbMoTa. Considering the service conditions of the bones, including walking, running, and climbing, the load direction of the leg is along the long-bone (longitudinal direction). For this unidirectional loading situation, the anisotropy of the material is used to reduce the elastic modulus. Single crystals and textured polycrystals have lower elastic moduli than isotropic materials in a certain direction.

In fact, the elastic modulus of a material is affected by the chemical bond, crystal structure, chemical composition, etc. The bio-HEAs could form numerous types according to different ratios and selected elements. Such a large number of samples undoubtedly provides sufficient samples for machine learning to calculate and predict the final performance of materials. In recent years, with the rapid development of computer science, machine learning, as a product of the development of computer science, has been widely used in the calculation of big data (Dove et al., 2017; Wei et al., 2019). Roy (Roy et al., 2020) used the gradient boost for a regression model to predict 26 high-entropy alloys with different compositions, in which the deviation from the test value of the sample did not exceed 20%, and the elastic modulus of TaTiZr was predicted to be 98.33 GPa. Compared with blindly arranging and combining element types, machine learning can provide a relatively clear path in designing materials.

Superelastic HEA

In 1963, the Naval Ordnance Laboratory discovered superelasticity in TiNi alloys with nearly equiatomic proportions (Buehler et al., 1963). To date, supereelastic metals have been widely used in aerospace, marine and cable communications (Hoh et al., 2009). In medical metal implants, bone scaffolds fabricated by superelastic materials have better flexibility and better fit the complex structure inside the human body.

SIMT could improve the mechanical properties of HEAs; for instance, TRIP could improve the plasticity of HEAs. In addition, SIMT is a prerequisite for superelasticity effects and shape memory of mental materials. The *ß* phase in the superelastic alloy transforms into orthorhombic α'' martensite when loaded up to a certain critical stress (s_{SIM}). The α'' martensite grows through several variants that yield to the maximum strain along the loading direction. These repeatedly loaded trajectories exhibit a cyclic shape in the stress–strain curve in Figure 4 (Ramezannejad et al., 2019). Upon unloading, α'' martensite is able to totally transform back to *ß* under the ideal scenario.

Some bio-HEAs have also been shown to have superelastic properties. Peltier (Peltier et al., 2021) pointed out that for $(TiHfZr)_{74}(NbTa)_{26}$, its superelasticity originates from the transition of β↔α” when deformation occurs. The superelastic temperature range is 40–200°C, which is compatible with the human service environment temperature. Furthermore, Wang (Wang et al., 2019) utilized *in situ* XRD to characterize the superelastic behavior of TiZrHfAlNb and found β↔α” during unloading in experiments on uniaxial tension. In addition, the plastic deformation is also recovered during this process. The discovery of these superelastic bio-HEAs will encourage more scholarly interest and attention.

Fatigue properties of HEA

Fatigue fracture often occurs when the material is under the action of alternating loads for a long time, and the material is broken by a stress lower than the breaking strength. Fatigue fracture is due to the initiation of internal cracks, and the cracks gradually propagate under alternating loads until failure. Metal medical implants are often under alternating loads during service. For instance, artificial teeth undergo hundreds of times of chewing every day. These chewing movements can be regarded as materials that are under the alternating stress environment.

HfNbTaTiZr exhibits good performance in fatigue tests. The maximum stress required to exceed the yield stress causes fatigue failure of HfNbTaTiZr even in the high cycle fatigue regime (Guennec et al., 2018a). In the microstructure, the fatigue strength of the material is affected by the mobility of dislocations, which increases with mobility. This feature has also been observed in other alloys (Mughrabi and Wüthrich, 1976; Magnin and Driver, 1979; Guiu et al., 1982; Guennec et al., 2015). In the low-cycle regime of HfNbTaTiZr, the resistance to fatigue is through the accumulation of dislocations at the crack tip, which can lead to the closure of the crack (Chen et al., 2022b).

In fact, currently, more fatigue research on HEAs focuses on FeCoNi systems (Hemphill et al., 2012; Tang et al., 2015; Thurston et al., 2017; Guennec et al., 2018b), and research on medical high-entropy alloys is still lacking. To date, medical high-entropy alloys are mainly aimed at strength and toughness, as well as low modulus. Fatigue performance is an important medical indicator; therefore, fatigue behaviour investigations on bio-HEAs are suggested to obtain a wider range of bio-HEAs with good fatigue performance.

Biocompatibility properties of Bio-HEAs

Compared with the HEA materials used in the manufacturing industry and aerospace industry, which require metals to have excellent mechanical properties, bio-HEAs not only require good mechanical properties but also require additional materials with excellent biocompatibility properties. Furthermore, the purpose of testing biocompatibility is to explore the potential biological risks when medical high-entropy alloys are used as implants. In recent years, many scholars have extensively studied the biocompatibility of HEAs and found many bio-HEAs with excellent biocompatibility. The biocompatibility of bio-HEAs, including cytocompatibility, corrosion resistance, friction resistance, and bio-HEAs with these three excellent properties, is summarized.

Cytocompatibility

The cell viability experiment is the most intuitive test to analyze the biocompatibility of bio-HEAs. The purpose of the cell viability experiment was to simulate cell growth and differentiation and to observe whether the cells still have normal functions on the implant surface. For instance, osteoblasts are often cultured on the implant surface to observe osteoblast division, differentiation, and the final mineral deposition quality (McBeth et al., 2017). At present, many studies have shown that medical high-entropy alloys exhibit high cell viability and provide a good environment for cell work.

Todai (Todai et al., 2017) found that TiNbTaZrMo HEA exhibited excellent biocompatibility, and the osteoblast activity attached to the surface was closely related to the microstructure of HEA. SUS316L, CP-Ti, and TiNbTaZrMo HEAs in the as-cast and annealed samples were tested in total, and it was pointed out that the osteoblast density of TiNbTaZrMo in the as-cast and annealed samples was higher than that of SUS316L and CP-Ti. In addition, TiNbTaZrMo in the annealed sample exhibited the highest cell density and was superior to SUS316L in cell size and cell spreading, which are important for cell migration and protein synthesis. Furthermore, this study also pointed out that the annealed TiNbTaZrMo has better cytocompatibility due to the redistribution and grain growth of the annealed grains. Shittu (Shittu et al., 2020) showed that MoNbTaTiZr HEA not only has good mechanical properties, in which the elastic modulus is 30% lower than that of SS304 but also has good cytocompatibility. Stem cells were cultured onto MoNbTaTiZr and tissue culture polystyrene (TCPS) surfaces, and fluorescence microscopy was used to show cellular coverage. The cell coverage of MoNbTaTiZr and TCPS reached 89 and 100%, respectively. Furthermore, numerous long cytoplasmic extensions forming a network in contact with adjacent cells were observed on the bio-HEA surface, indicating that the MoNbTaTiZr surface supports cell attachment by filopodia extensions and provides strong support for the growth of cells (Hasan et al., 2017).

The TiNbTaZrMo fabricated by SLM not only has superior mechanical properties but also has great biocompatibility.

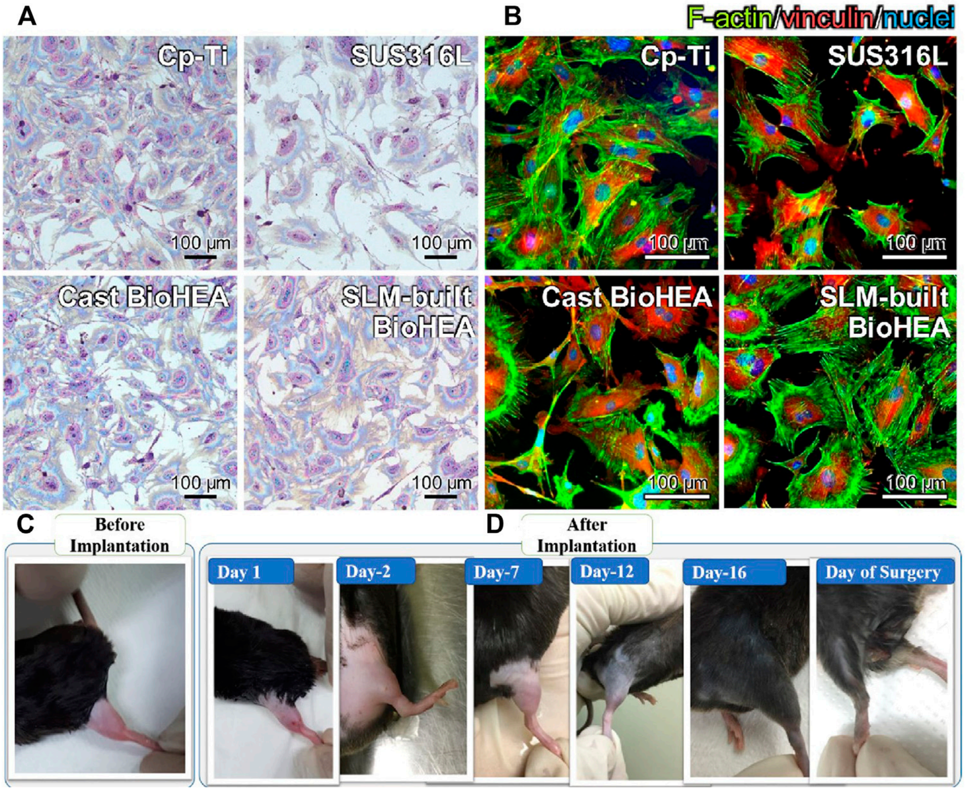

FIGURE 5
(A) Giemsa staining images of osteoblasts cultured on the surface of SLM-built BioHEA and CP-Ti, SS316L, and cast BioHEA counterpar (Ishimoto et al., 2021)t. **(B)** Fluorescent images of osteoblast adhesion on SLM-built bio-HEA, CP-Ti, SS316L, and cast bio-HEA (Akmal et al., 2021). **(C,D)** Visual evidence of mice thigh before and d after implantation (MoTa)0.2NbTiZr alloy (Akmal et al., 2021).

Giemsa staining images showed that the cell growth density of bio-HEAs fabricated by SLM was the same as that of CP-Ti and much higher than that of SS316L, as shown in Figure 5A. Furthermore, fluorescent images demonstrate the cell cytoskeletal components and focal adhesions of osteoblasts adhered to the specimens in Figure 5B. The cells exhibited a uniform distribution on the bio-HEA surface, which had an obvious advantage of cell spreading. Such great mechanical and biological properties of bio-HEAs are due to the rapid solidification in the SLM fabrication process, which can effectively inhibit the segregation of components (Ishimoto et al., 2021).

Animal models are an effective approach to evaluate the service status of materials in the *in vivo* environment. Akmal (Akmal et al., 2021) demonstrated $(MoTa)_xNbTiZr$ implantation inside a mouse thigh and counted the changes in the mouse thigh over 16 days, as shown in Figures 5C,D. The mouse thigh was inflamed after implantation, and after Day 7, the inflammation subsided without abnormal neurobehaviour. However, host response experiments including inflammatory response, osteoinductive and bioactive behavior still lack additional investigation, and *in vitro* experiments should be further discussed.

Corrosion resistance

Metal implants may have a potential risk of corrosion in the human body, which may lead to a decrease in implant performance and failure. Bio-HEAs have shown good potential in corrosion resistance properties, and research on corrosion resistance will broaden bio-HEA applications in medical materials.

In a corrosive environment, bio-HEAs are oxidized, and a passive oxide film grows on the surface. The density of the oxide film is a key factor in preventing further corrosion and avoiding material failure. Yang (Yang et al., 2020) pointed out that the corrosion rate of TiZrHfNbTa HEA is 10–4 mm/year under an environment of a low passive current density of approximately 10–2 A/m2, comparable to the traditional Ti6Al4V alloy. Through X-ray photoelectron spectroscopy (XPS) tests, it was found that TiO2, ZrO2, HfO2, and Ta2O5 were formed during

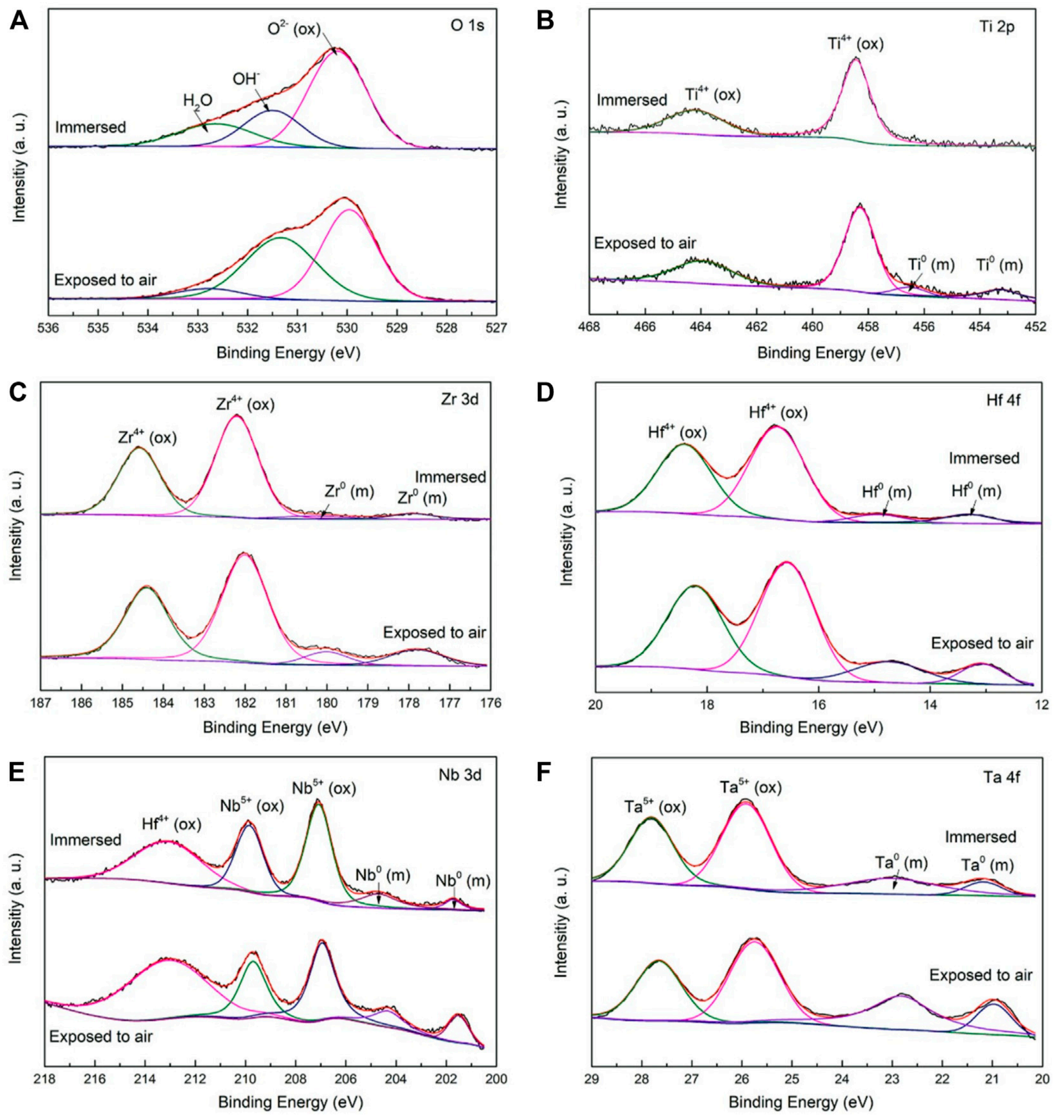

FIGURE 6
XPS spectra of the surface films formed on the TiZrHfNbTa [**(A)** O 1s, **(B)** Ti 2p, **(C)** Zr 3d, **(D)** Hf 4f, **(E)** Nb 3d, and **(F)** Ta 4f], which exposed to air and after the 7-days immersion in the Hank's solution at 310 K[33].

the corrosion process, which played an important role in resisting corrosion, as shown in Figures 6A–F. Furthermore, Wang (Wang et al., 2022d) replaced the element Ta in TiZrHfNbTa with element Fe to test the effect of different volume fractions of Fe elements (0, 0.25, 0.5, 0.75, 1, 1.5, 2) on the material corrosion resistance. It should be noted that the corrosion potential first decreased and then increased with increasing Fe content. $Fe_{0.5}$ exhibited the best corrosion resistance, and no corrosion pits were observed after polarization. Hua pointed out that TiZrNbTaMo also has great corrosion resistance. TiZrNbTaMo has better corrosion potential than traditional Ti6Al4V, which means that the passivation film produced by TiZrNbTaMo has higher stability (Hua et al., 2021).

Friction resistance performance

Metal implants inevitably contact the surrounding tissue when implanted into the human body. Wear behaviour is unavoidable and must be considered for metal medical implants. Especially in bone implants, the high amount of frictional behaviour puts the material at risk of wear failure.

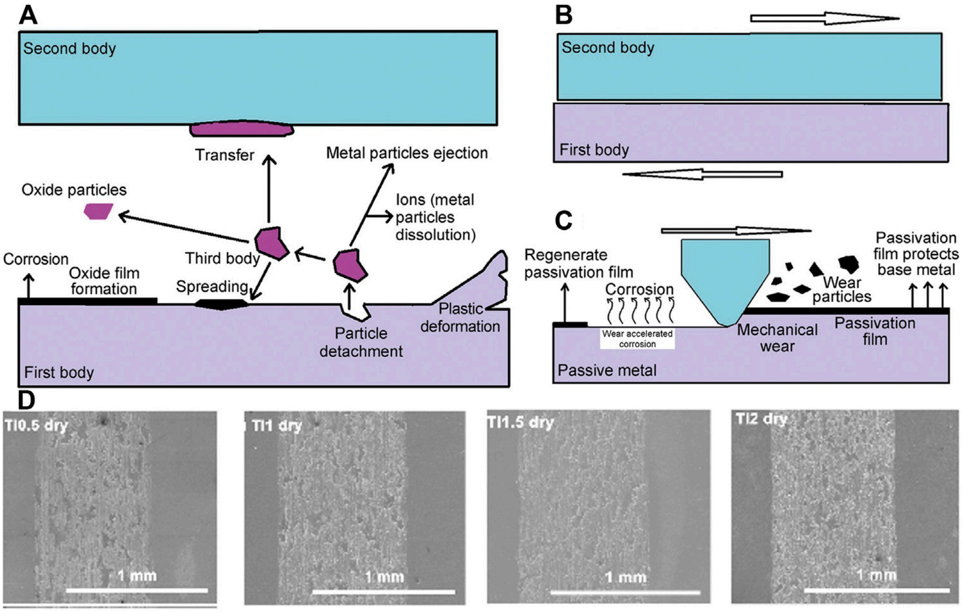

FIGURE 7
Schematic diagram of friction corrosion mechanism of implant surface: **(A)** three-body wear; **(B)** two-body wear; **(C)** removal process of the passivation film (Li et al., 2021). **(D)** SEM images of wear scars of the $Ti_{0.5}$ZrNbTaMo, TiZrNbTaMo, $Ti_{1.5}$ZrNbTaMo, and Ti_2ZrNbTaMo HEAs under the dry wear condition (Hua et al., 2021).

Furthermore, implant wear may lead to inflammation and osteolysis, which affect implant longevity and increase the patient's risk of secondary injury. Tribocorrosion includes the interaction of corrosion with sliding wear, biological solutions, solid particle erosion, frictional oxidation, cavitation erosion, abrasion, and fretting (Wood, 2007). Figures 7A–C shows two types of medical mental implants wear in the human body environment, namely, two-body wear and three-body wear. Compared with two-body wear, three-body wear has an additional interaction with particles that are dropped by wear, and two-body wear will eventually transform into three-body wear over time (Li et al., 2021).

Bhardwaj designed AlxTiZrNbHf (x = 0, 0.25, 0.50, 0.75, 1) bio-HEA to explore the effect of Al on the friction resistance. The reason why the addition of Al can enhance the wear resistance is because Al improves the mechanical properties of the material. Furthermore, an oxide film with higher friction resistance grows on the surface of AlTiZrNbHf due to the Al element, which is found without any elemental separation in the friction track in EDS analysis (Bhardwaj et al., 2021).

In fact, the friction and corrosion behaviour of metal implants often occur in combination. The corrosion behaviour may accelerate the wear situation of the material; conversely, the peeling of the oxide film due to wear may accelerate the corrosion of the material. TiZrHfNbFe bio-HEA exhibited good wear resistance in the dry friction test. Although corrosive wear occurs in a phosphate buffer saline (PBS) solution, the final performance is better than that of Ti6Al4V (Wang et al., 2022d). In addition, Hua (Hua et al., 2021) pointed out that the friction resistance of TiZrNbTaMo increases with decreasing Ti content. The wear is worse in the dry environment than in the PBS environment. The reason is that the oxide films formed in the dry environment are brittle and are more likely to fall off during friction, as shown in Figure 7D. The peeled oxide film changes the wear environment from two-body wear to three-body wear.

Surface modification is a common and effective method to improve bio-HEA surfaces and reduce friction loss. The film with a laminated structure of NbMoWTa has good friction resistance, especially when the film height is 2.5 nm; it exhibits excellent friction resistance, and the coefficient of friction (COF) is significantly lower than that of the monolithic NbMoWTa film (Luo et al., 2021).

Conclusion

In recent years, many studies have aimed to determine the biomedical potential of HEAs to design excellent medical metal implants and expand the application range of bio-HEA. Compared with traditional medical metals, bio-HEAs have more freedom in composition selection and could be widely used in medical implants, especially in bone scaffolds, bone plates, and bone nails. The microstructure and morphology of bio-HEAs are closely affected by the selected elements or the proportion of each element. Strategies for designing reasonable and excellent HEA systems need to be further investigated.

In this review, the superior mechanical properties and biocompatibility of bio-HEAs are summarized. For mechanical properties, bio-HEAs could both have high yield strength and low modulus, which meet the strength requirements and avoid stress shielding. Furthermore, some bio-HEAs with superelasticity could be developed in the medical field. However, fatigue experiments are still lacking in bio-HEAs and need to be further evaluated. For biocompatibility, the elements selected by bio-HEAs focus on having excellent biocompatibility and low biotoxicity, for instance, Ti, Ta, Nb, Zr, and Hf. More importantly, the cytocompatibility of some bio-HEAs was even higher than that of CP-Ti and Ti6Al4V. However, the current cell viability tests of bio-HEAs focus on *in vitro* cell viability, lacking relevant *in vivo* animal experiments.

Although bio-HEAs have made significant progress, the availability of new bio-HEAs still has many properties to test. In addition, many medical properties of bio-HEAs have surpassed those of traditional medical metals. However, most of these studies only show a certain medical performance of bio-HEAs, and there is a lack of systematic and complete research on all the medical implant indices possessed by a certain material. In the future, one approach to obtain excellent bio-HEAs is by designing the bio-HEA composition and regulating the microstructure and morphology. The new bio-HEA is expected to become a new generation of metal medical implants with excellent performance.

Author contributions

CL and LW are responsible for the framework and overall content of the article; CY, JL, and YT are responsible for material biological properties; WL is responsible for the content of mechanical properties; ZL, LL, and HL are responsible for corrosion resistance and friction resistance.

Funding

National Natural Science Foundation of China under (Grant Nos.51831011, 52011530181), Shanghai Science and Technology Commission under Grant No.20S31900100, Guangxi Science and Technology Programe. The central government guides the local science and technology development science and technology innovation base project [Guike Jizi (2020)No.198]: Basic Research and Transformation Technology Innovation Base of Bone and Joint Degenerative Diseases.

Conflict of interest

The authors declare that the research was conducted in the absence of any commercial or financial relationships that could be construed as a potential conflict of interest.

Publisher’s note

References

Akmal, M., Hussain, A., Afzal, M., Lee, Y. I., and Ryu, H. J. (2021). Systematic study of (MoTa) NbTiZr medium- and high-entropy alloys for biomedical implants- *in vivo* biocompatibility examination. *J. Mat. Sci. Technol.* 78, 183–191. doi:10.1016/j.jmst.2020.10.049

Bhardwaj, V., Zhou, Q., Zhang, F., Han, W., Du, Y., Hua, K., et al. (2021). Effect of Al addition on the microstructure, mechanical and wear properties of TiZrNbHf refractory high entropy alloys. *Tribol. Int.* 160, 107031. doi:10.1016/j.triboint.2021.107031

Bourell, D., Kruth, J. P., Leu, M., Levy, G., Rosen, D., Beese, A. M., et al. (2017). Materials for additive manufacturing. *CIRP Ann.* 66, 659–681. doi:10.1016/j.cirp.2017.05.009

Buehler, W. J., Gilfrich, J. V., and Wiley, R. C. (1963). Effect of low-temperature phase changes on the mechanical properties of alloys near composition TiNi. *J. Appl. Phys.* 34, 1475–1477. doi:10.1063/1.1729603

Cantor, B., Chang, I. T. H., Knight, P., and Vincent, A. J. B. (2004). Microstructural development in equiatomic multicomponent alloys. *Mater. Sci. Eng. A* 375–377, 213–218. doi:10.1016/j.msea.2003.10.257

Chen, S. H., Zhang, J., Guan, S., Li, T., Liu, J., Wu, F., et al. (2022). Microstructure and mechanical properties of WNbMoTaZrx (x = 0.1, 0.3, 0.5, 1.0) refractory high entropy alloys. *Mater. Sci. Eng. A* 835, 142701. doi:10.1016/j.msea.2022.142701

Chen, S., Li, W., Wang, L., Yuan, T., Tong, Y., Tseng, K. K., et al. (2022). Stress-controlled fatigue of HfNbTaTiZr high-entropy alloy and associated deformation and fracture mechanisms. *J. Mat. Sci. Technol.* 114, 191–205. doi:10.1016/j.jmst.2021.10.026

Cui, Y., Chen, L. Y., Qin, P., Li, R., Zang, Q., Peng, J., et al. (2022). Metastable pitting corrosion behavior of laser powder bed fusion produced Ti-6Al-4V in Hank’s solution. *Corros. Sci.* 203, 110333. doi:10.1016/j.corsci.2022.110333

Dirras, G., Lilensten, L., Djemia, P., Laurent-Brocq, M., Tingaud, D., Couzinie, J. P., et al. (2016). Elastic and plastic properties of as-cast equimolar TiHfZrTaNb high-entropy alloy. *Mater. Sci. Eng. A* 654, 30–38. doi:10.1016/j.msea.2015.12.017

Dove, G., Halskov, K., Forlizzi, J., and Zimmerman, J. (2017). “UX design innovation: Challenges for working with machine learning as a design material,” in Proceedings of the 2017 CHI conference on human factors in computing systems (CHI ’17), Association for computing machinery, New York, NY, USA, 278–288.

Eivazzadeh-Keihan, R., Bahojb Noruzi, E., Khanmohammadi Chenab, K., Jafari, A., Radinekiyan, F., Hashemi, S. M., et al. (2020). Metal-based nanoparticles for bone tissue engineering. *J. Tissue Eng. Regen. Med.* 14, 1687–1714. doi:10.1002/term.3131

Eliaz, N. (2019). Corrosion of metallic biomaterials: A review. *Materials* 12, 407. doi:10.3390/ma12030407

Fenton, O. S., Olafson, K. N., Pillai, P. S., Mitchell, M. J., and Langer, R. (2018). Advances in biomaterials for drug delivery. *Adv. Mat.* 30, 1705328–1705329. doi:10.1002/adma.201705328

Gaharwar, A. K., Singh, I., and Khademhosseini, A. (2020). Engineered biomaterials for *in situ* tissue regeneration. *Nat. Rev. Mat.* 5, 686–705. doi:10.1038/s41578-020-0209-x

George, E. P., Raabe, D., and Ritchie, R. O. (2019). High-entropy alloys. *Nat. Rev. Mat.* 4, 515–534. doi:10.1038/s41578-019-0121-4

Gludovatz, B., Hohenwarter, A., Catoor, D., Chang, E. H., George, E. P., and Ritchie, R. O. (2014). A fracture-resistant high-entropy alloy for cryogenic applications. *Science* 345, 1153–1158. doi:10.1126/science.1254581

Guennec, B., Kentheswaran, V., Perriere, L., Ueno, A., Guillot, I., Couzinie, J. P., et al. (2018). Four-point bending fatigue behavior of an equimolar BCC HfNbTaTiZr high-entropy alloy: Macroscopic and microscopic viewpoints. *Materialia* 4, 348–360. doi:10.1016/j.mtla.2018.09.040

Guennec, B., Nobori, T., Kuwahara, H., and Ueno, A. (2018). Effect of the stress ratio on the fatigue behavior of Zr55Al10Ni5Cu30 bulk metallic glass part I—analysis of the fatigue resistance. *Intermetallics* 92, 72–78. doi:10.1016/j.intermet.2017.09.023

Guennec, B., Ueno, A., Sakai, T., Takanashi, M., Itabashi, Y., and Ota, M. (2015). Dislocation-based interpretation on the effect of the loading frequency on the fatigue properties of JIS S15C low carbon steel. *Int. J. Fatigue* 70, 328–341. doi:10.1016/j.ijfatigue.2014.10.006

Guiu, F., Dulniak, R., and Edwards, B. C. (1982). On the nucleation of fatigue cracks in pure polycrystalline α-iron. *Fatigue Fract. Eng. Mat. Struct.* 5, 311–321. doi:10.1111/j.1460-2695.1982.tb01240.x

Guo, L., Ataollah Naghavi, S., Wang, Z., Nath Varma, S., Han, Z., Yao, Z., et al. (2022). On the design evolution of hip implants: A review. *Mat. Des.* 216, 110552. doi:10.1016/j.matdes.2022.110552

Guo, Y., Liu, Y., Oerlemans, A., Lao, S., Wu, S., and Lew, M. S. (2016). Deep learning for visual understanding: A review. *Neurocomputing* 187, 27–48. doi:10.1016/j.neucom.2015.09.116

Hafeez, N., Liu, J., Wang, L., Wei, D., Tang, Y., Lu, W., et al. (2020). Superelastic response of low-modulus porous beta-type Ti-35Nb-2Ta-3Zr alloy fabricated by laser powder bed fusion. *Addit. Manuf.* 34, 101264. doi:10.1016/j.addma.2020.101264

Hasan, J., Jain, S., and Chatterjee, K. (2017). Nanoscale topography on black titanium imparts multi-biofunctional properties for orthopedic applications. *Sci. Rep.* 7, 41118–41213. doi:10.1038/srep41118

Hemphill, M. A., Yuan, T., Wang, G., Yeh, J., Tsai, C., Chuang, A., et al. (2012). Fatigue behavior of Al 0.5CoCrCuFeNi high entropy alloys. *Acta Mater.* 60, 5723–5734. doi:10.1016/j.actamat.2012.06.046

Herzog, D., Seyda, V., Wycisk, E., and Emmelmann, C. (2016). Additive manufacturing of metals. *Acta Mater.* 117, 371–392. doi:10.1016/j.actamat.2016.07.019

Hoh, D. J., Hoh, B. L., Amar, A. P., and Wang, M. Y. (2009). Shape memory alloys: Metallurgy, biocompatibility, and biomechanics for neurosurgical applications. *Oper. Neurosurg.* 64, ons199–ons215. doi:10.1227/01.neu.0000330392.09889.99

Hu, S., Li, T., Su, Z., and Liu, D. (2022). Research on suitable strength, elastic modulus and abrasion resistance of Ti–Zr–Nb medium entropy alloys (MEAs) for implant adaptation. *Intermetallics* 140, 107401. doi:10.1016/j.intermet.2021.107401

Hua, N., Wang, W., Wang, Q., Ye, Y., Lin, S., Zhang, L., et al. (2021). Mechanical, corrosion, and wear properties of biomedical Ti–Zr–Nb–Ta–Mo high entropy alloys. *J. Alloys Compd.* 861, 157997. doi:10.1016/j.jallcom.2020.157997

Ishimoto, T., Ozasa, R., Nakano, K., Weinmann, M., Schnitter, C., Stenzel, M., et al. (2021). Development of TiNbTaZrMo bio-high entropy alloy (BioHEA) super-solid solution by selective laser melting, and its improved mechanical property and biocompatibility. *Scr. Mater.* 194, 113658. doi:10.1016/j.scriptamat.2020.113658

Jian, W. R., Xie, Z., Xu, S., Su, Y., Yao, X., and Beyerlein, I. J. (2020). Effects of lattice distortion and chemical short-range order on the mechanisms of deformation in medium entropy alloy CoCrNi. *Acta Mater.* 199, 352–369. doi:10.1016/j.actamat.2020.08.044

Juan, C.-C., Tsai, M. H., Tsai, C. W., Hsu, W. L., Lin, C. M., Chen, S. K., et al. (2016). Simultaneously increasing the strength and ductility of a refractory high-entropy alloy via grain refining. *Mater. Lett.* 184, 200–203. doi:10.1016/j.matlet.2016.08.060

Kostiuchenko, T., Körmann, F., Neugebauer, J., and Shapeev, A. (2019). Impact of lattice relaxations on phase transitions in a high-entropy alloy studied by machine-learning potentials. *npj Comput. Mat.* 5, 55–57. doi:10.1038/s41524-019-0195-y

Lecun, Y., Bengio, Y., and Hinton, G. (2015). Deep learning. *Nature* 521, 436–444. doi:10.1038/nature14539

Lee, C., Kim, G., Chou, Y., Musico, B. L., Gao, M. C., An, K., et al. (2020). Temperature dependence of elastic and plastic deformation behavior of a refractory high-entropy alloy. *Sci. Adv.* 6, eaaz4748. doi:10.1126/sciadv.aaz4748

Lee, C., Maresca, F., Feng, R., Chou, Y., Ungar, T., Widom, M., et al. (2021). Strength can be controlled by edge dislocations in refractory high-entropy alloys. *Nat. Commun.* 12, 5474. doi:10.1038/s41467-021-25807-w

Lei, Z., Liu, X., Wu, Y., Wang, H., Jiang, S., Wang, S., et al. (2018). Enhanced strength and ductility in a high-entropy alloy via ordered oxygen complexes. *Nature* 563, 546–550. doi:10.1038/s41586-018-0685-y

Li, H. F., Huang, J. Y., Lin, G. C., and Wang, P. Y. (2021). Recent advances in tribological and wear properties of biomedical metallic materials. *Rare Met.* 40, 3091–3106. doi:10.1007/s12598-021-01796-z

Li, L., Li, Z., Kwiatkowski da Silva, A., Peng, Z., Zhao, H., Gault, B., et al. (2019). Segregation-driven grain boundary spinodal decomposition as a pathway for phase nucleation in a high-entropy alloy. *Acta Mater.* 178, 1–9. doi:10.1016/j.actamat.2019.07.052

Li, X. G., Chen, C., Zheng, H., Zuo, Y., and Ong, S. P. (2020). Complex strengthening mechanisms in the NbMoTaW multi-principal element alloy. *npj Comput. Mat.* 6, 70. doi:10.1038/s41524-020-0339-0

Liu, C., Wang, L., Lu, W., Liu, J., Yang, C., Fan, C., et al. (2022). Computer vision-aided bioprinting for bone research. *Bone Res.* 10, 21–14. doi:10.1038/s41413-022-00192-2

Liu, X., Zhang, J., Yin, J., Bi, S., Eisenbach, M., and Wang, Y. (2021). Monte Carlo simulation of order-disorder transition in refractory high entropy alloys: A data-driven approach. *Comput. Mater. Sci.* 187, 110135. doi:10.1016/j.commatsci.2020.110135

Lu, Z. P., Wang, H., Chen, M., Baker, I., Yeh, J., Liu, C., et al. (2015). An assessment on the future development of high-entropy alloys: Summary from a recent workshop. *Intermetallics* 66, 67–76. doi:10.1016/j.intermet.2015.06.021

Luo, D., Zhou, Q., Ye, W., Ren, Y., Greiner, C., He, Y., et al. (2021). Design and characterization of self-lubricating refractory high entropy alloy-based multilayered films. *ACS Appl. Mat. Interfaces* 13, 55712–55725. doi:10.1021/acsami.1c16949

Lv, Y., Lang, X., Su, C., Cao, L., and Wang, L. (2022). Stacking fault and nano-twins dominating strengthening mechanism of (CuZnMnNi)100-xSnx high entropy brass alloy prepared by mechanical alloying and fast hot pressing sintering. *Mater. Lett.* 312, 131614. doi:10.1016/j.matlet.2021.131614

Magnin, T., and Driver, J. H. (1979). The influence of strain rate on the low cycle fatigue properties of single crystals and polycrystals of two ferritic alloys. *Mater. Sci. Eng.* 39, 175–185. doi:10.1016/0025-5416(79)90057-0

Mao, C., Yu, W., Jin, M., Wang, Y., Shang, X., Lin, L., et al. (2022). Mechanobiologically optimized Ti–35Nb–2Ta–3Zr improves load transduction and enhances bone remodeling in tilted dental implant therapy. *Bioact. Mater.* 16, 15–26. doi:10.1016/j.bioactmat.2022.03.005

McBeth, C., Lauer, J., Ottersbach, M., Campbell, J., Sharon, A., and Sauer-Budge, A. F. (2017). 3D bioprinting of GelMA scaffolds triggers mineral deposition by primary human osteoblasts. *Biofabrication* 9, 015009. doi:10.1088/1758-5090/aa53bd

Mi, Z. R., Shuib, S., Hassan, A. Y., Shorki, A. A., and Ibrahim, M. M. (2007). Problem of stress shielding and improvement to the hip implat designs: A review. *J. Med. Sci.* 7, 460–467. doi:10.3923/jms.2007.460.467

Miracle, D. B., and Senkov, O. N. (2017). A critical review of high entropy alloys and related concepts. *Acta Mater.* 122, 448–511. doi:10.1016/j.actamat.2016.08.081

Mitrousis, N., Fokina, A., and Shoichet, M. S. (2018). Biomaterials for cell transplantation. *Nat. Rev. Mat.* 3, 441–456. doi:10.1038/s41578-018-0057-0

Mughrabi, H., and Wüthrich, C. (1976). Asymmetry of slip and shape changes during cyclic deformation of α-iron single crystals. *Philos. Mag.* 33, 963–984. doi:10.1080/14786437608221928

Nagase, T., Iijima, Y., Matsugaki, A., Ameyama, K., and Nakano, T. (2020). Design and fabrication of Ti–Zr-Hf-Cr-Mo and Ti–Zr-Hf-Co-Cr-Mo high-entropy alloys as metallic biomaterials. *Mater. Sci. Eng. C* 107, 110322. doi:10.1016/j.msec.2019.110322

Peltier, L., Berveiller, S., Meraghni, F., Lohmuller, P., and Laheurte, P. (2021). Martensite transformation and superelasticity at high temperature of (TiHfZr)74(NbTa)26 high-entropy shape memory alloy. *Shap. Mem. Superelasticity* 7, 194–205. doi:10.1007/s40830-021-00323-4

Picak, S., Yilmaz, H. C., and Karaman, I. (2021). Simultaneous deformation twinning and martensitic transformation in CoCrFeMnNi high entropy alloy at high temperatures. *Scr. Mater.* 202, 113995. doi:10.1016/j.scriptamat.2021.113995

Qiao, K., Zhang, T., Wang, K., Yuan, S., Wang, L., Chen, S., et al. (2022). Effect of multi-pass friction stir processing on the microstructure evolution and corrosion behavior of ZrO2/AZ31 magnesium matrix composite. *J. Mater. Res. Technol.* 18, 1166–1179. doi:10.1016/j.jmrt.2022.02.127

Qu, H., Fu, H., Han, Z., and Sun, Y. (2019). Biomaterials for bone tissue engineering scaffolds: A review. *RSC Adv.* 9, 26252–26262. doi:10.1039/c9ra05214c

Raducanu, D., Vasilescu, E., Cojocaru, V., Cinca, I., Drob, P., Vasilescu, C., et al. (2011). Mechanical and corrosion resistance of a new nanostructured Ti–Zr–Ta–Nb alloy. *J. Mech. Behav. Biomed. Mater.* 4, 1421–1430. doi:10.1016/j.jmbbm.2011.05.012

Ramezannejad, A., Xu, W., Xiao, W., Fox, K., Liang, D., and Qian, M. (2019). New insights into nickel-free superelastic titanium alloys for biomedical applications. *Curr. Opin. Solid State Mater. Sci.* 23, 100783. doi:10.1016/j.cossms.2019.100783

Rao, S. I., Akdim, B., Antillon, E., Woodward, C., Parthasarathy, T., and Senkov, O. (2019). Modeling solution hardening in BCC refractory complex concentrated alloys: NbTiZr, Nb 1.5 TiZr 0.5 and Nb 0.5 TiZr 1.5. *Acta Mater.* 168, 222–236. doi:10.1016/j.actamat.2019.02.013

Roy, A., Babuska, T., Krick, B., and Balasubramanian, G. (2020). Machine learned feature identification for predicting phase and Young's modulus of low-medium- and high-entropy alloys. *Scr. Mater.* 185, 152–158. doi:10.1016/j.scriptamat.2020.04.016

Schönecker, S., Li, X., Wei, D., Nozaki, S., Kato, H., Vitos, L., et al. (2022). Harnessing elastic anisotropy to achieve low-modulus refractory high-entropy alloys for biomedical applications. *Mat. Des.* 215, 110430. doi:10.1016/j.matdes.2022.110430

Sharma, A., Oh, M. C., Kim, J.-T., Srivastava, A. K., and Ahn, B. (2020). Investigation of electrochemical corrosion behavior of additive manufactured Ti–6Al–4V alloy for medical implants in different electrolytes. *J. Alloys Compd.* 830, 154620. doi:10.1016/j.jallcom.2020.154620

Shittu, J., Pole, M., Cockerill, I., Sadeghilaridjani, M., Reddy, L. V. K., Manivasagam, G., et al. (2020). Biocompatible high entropy alloys with excellent degradation resistance in a simulated physiological environment. *ACS Appl. Bio Mat.* 3, 8890–8900. doi:10.1021/acsabm.0c01181

Su, I. A., Tseng, K. K., Yeh, J. W., El-Sayed, B., Liu, C. H., and Wang, S. H. (2022). Strengthening mechanisms and microstructural evolution of ductile refractory medium-entropy alloy Hf20Nb10Ti35Zr35. *Scr. Mater.* 206, 114225–114313. doi:10.1016/j.scriptamat.2021.114225

Su, J., Raabe, D., and Li, Z. (2019). Hierarchical microstructure design to tune the mechanical behavior of an interstitial TRIP-TWIP high-entropy alloy. *Acta Mater.* 163, 40–54. doi:10.1016/j.actamat.2018.10.017

Takeuchi, A., Amiya, K., Wada, T., Yubuta, K., Zhang, W., and Makino, A. (2013). Entropies in alloy design for high-entropy and bulk glassy alloys. *Entropy* 15, 3810–3821. doi:10.3390/e15093810

Tang, Z., Yuan, T., Tsai, C. W., Yeh, J. W., Lundin, C. D., and Liaw, P. K. (2015). Fatigue behavior of a wrought Al0. 5CoCrCuFeNi two-phase high-entropy alloy. *Acta Mater.* 99, 247–258. doi:10.1016/j.actamat.2015.07.004

Thurston, K. V. S., Gludovatz, B., Hohenwarter, A., Laplanche, G., George, E. P., and Ritchie, R. O. (2017). Effect of temperature on the fatigue-crack growth behavior of the high-entropy alloy CrMnFeCoNi. *Intermetallics* 88, 65–72. doi:10.1016/j.intermet.2017.05.009

Todai, M., Nagase, T., Hori, T., Matsugaki, A., Sekita, A., and Nakano, T. (2017). Novel TiNbTaZrMo high-entropy alloys for metallic biomaterials. *Scr. Mater.* 129, 65–68. doi:10.1016/j.scriptamat.2016.10.028

Tsai, M.-H., and Yeh, J.-W. (2014). High-entropy alloys: A critical review. *Mater. Res. Lett.* 2, 107–123. doi:10.1080/21663831.2014.912690

Tüten, N., Canadinc, D., Motallebzadeh, A., and Bal, B. (2019). Microstructure and tribological properties of TiTaHfNbZr high entropy alloy coatings deposited on Ti6Al4V substrates. *Intermetallics* 105, 99–106. doi:10.1016/j.intermet.2018.11.015

Verran, J., and Whitehead, K. (2005). Factors affecting microbial adhesion to stainless steel and other materials used in medical devices. *Int. J. Artif. Organs* 28, 1138–1145. doi:10.1177/039139880502801111

Wang, J. C., Liu, Y., Liang, S., Zhang, Y., Wang, L., Sercombe, T., et al. (2022). Comparison of microstructure and mechanical behavior of Ti-35Nb manufactured by laser powder bed fusion from elemental powder mixture and prealloyed powder. *J. Mat. Sci. Technol.* 105, 1–16. doi:10.1016/j.jmst.2021.07.021

Wang, L., Cao, T., Liu, X., Wang, B., Jin, K., Liang, Y., et al. (2020). A novel stress-induced martensitic transformation in a single-phase refractory high-entropy alloy. *Scr. Mater.* 189, 129–134. doi:10.1016/j.scriptamat.2020.08.013

Wang, L., Fu, C., Wu, Y., Li, R., Hui, X., and Wang, Y. (2019). Superelastic effect in Ti-rich high entropy alloys via stress-induced martensitic transformation. *Scr. Mater.* 162, 112–117. doi:10.1016/j.scriptamat.2018.10.035

Wang, L., Xie, L., Lv, Y., Zhang, L. C., Chen, L., Meng, Q., et al. (2017). Microstructure evolution and superelastic behavior in Ti-35Nb-2Ta-3Zr alloy processed by friction stir processing. *Acta Mater.* 131, 499–510. doi:10.1016/j.actamat.2017.03.079

Wang, R., Tang, Y., Lei, Z., Ai, Y., Tong, Z., Li, S., et al. (2022). Achieving high strength and ductility in nitrogen-doped refractory high-entropy alloys. *Mat. Des.* 213, 110356. doi:10.1016/j.matdes.2021.110356

Wang, S. P., and Xu, J. (2017). TiZrNbTaMo high-entropy alloy designed for orthopedic implants: As-cast microstructure and mechanical properties. *Mater. Sci. Eng. C* 73, 80–89. doi:10.1016/j.msec.2016.12.057

Wang, S., Wu, M., Shu, D., Zhu, G., Wang, D., and Sun, B. (2020). Mechanical instability and tensile properties of TiZrHfNbTa high entropy alloy at cryogenic temperatures. *Acta Mater.* 201, 517–527. doi:10.1016/j.actamat.2020.10.044

Wang, W., Yang, K., Wang, Q., Dai, P., Fang, H., Wu, F., et al. (2022). Novel Ti-Zr-Hf-Nb-Fe refractory high-entropy alloys for potential biomedical applications. *J. Alloys Compd.* 906, 164383. doi:10.1016/j.jallcom.2022.164383

Wang, Y., Chen, G., Zhang, H., Zhao, C., Sun, L., and Zhao, Y. (2021). Emerging functional biomaterials as medical patches. *ACS Nano* 15, 5977–6007. doi:10.1021/acsnano.0c10724

Wang, Y., Shi, H., Zhou, P., Tang, Y., Liu, J., Wang, L., et al. (2021). Microstructure evolution and mechanical properties of TiC/Ti6Al4V medical composite processed by severe plastic deformation. *J. Mater. Res. Technol.* 15, 6442–6452. doi:10.1016/j.jmrt.2021.11.090

Wang, Y., Wei, D., Wang, L., Zhang, L., Liu, J., Tang, Y., et al. (2022). Surface modification and twinning behavior in gradient graphene-based TiC/Ti6Al4V composite. *Appl. Surf. Sci.* 583, 152495. doi:10.1016/j.apsusc.2022.152495

Wei, D., Gong, W., Wang, L., Tang, B., Kawasaki, T., Harjo, S., et al. (2022). Strengthening of high-entropy alloys via modulation of cryo-pre-straining-induced defects. *J. Mater. Sci. Technol.* 129, 251–260. doi:10.1016/j.jmst.2022.04.055

Wei, D., Wang, L., Zhang, Y., Gong, W., Tsuru, T., Lobzenko, I., et al. (2022). Metalloid substitution elevates simultaneously the strength and ductility of face-centered-cubic high-entropy alloys. *Acta Mater.* 225, 117571. doi:10.1016/j.actamat.2021.117571

Wei, J., Chu, X., Sun, X., Xu, K., Deng, H., Chen, J., et al. (2019). Machine learning in materials science. *InfoMat* 1, 338–358. doi:10.1002/inf2.12028

Wen, C., Wang, C., Zhang, Y., Antonov, S., Xue, D., Lookman, T., et al. (2021). Modeling solid solution strengthening in high entropy alloys using machine learning. *Acta Mater.* 212, 116917. doi:10.1016/j.actamat.2021.116917

Wen, X., Wu, Y., Huang, H., Jiang, S., Wang, H., Liu, X., et al. (2021). Effects of Nb on deformation-induced transformation and mechanical properties of HfNbxTa0.2TiZr high entropy alloys. *Mater. Sci. Eng. A* 805, 140798. doi:10.1016/j.msea.2021.140798

Wood, R. J. K. (2007). Tribo-corrosion of coatings: A review. *J. Phys. D. Appl. Phys.* 40, 5502–5521. doi:10.1088/0022-3727/40/18/s10

Xia, S. Q., Yang, X., Yang, T. F., Liu, S., and Zhang, Y. (2015). Irradiation resistance in AlxCoCrFeNi high entropy alloys. *Jom* 67, 2340–2344. doi:10.1007/s11837-015-1568-4

Xiao, B., Jia, W., Tang, H., Wang, J., and Zhou, L. (2022). Microstructure and mechanical properties of WMoTaNbTi refractory high-entropy alloys fabricated by selective electron beam melting. *J. Mat. Sci. Technol.* 108, 54–63. doi:10.1016/j.jmst.2021.07.041

Xu, S., Su, Y., Jian, W. R., and Beyerlein, I. J. (2021). Local slip resistances in equal-molar MoNbTi multi-principal element alloy. *Acta Mater.* 202, 68–79. doi:10.1016/j.actamat.2020.10.042

Xu, Z. Q., Ma, Z. L., Tan, Y., and Cheng, X. W. (2022). Designing TiVNbTaSi refractory high-entropy alloys with ambient tensile ductility. *Scr. Mater.* 206, 114230–114236. doi:10.1016/j.scriptamat.2021.114230

Yan, Y., Lu, D., and Wang, K. (2021). Accelerated discovery of single-phase refractory high entropy alloys assisted by machine learning. *Comput. Mater. Sci.* 199, 110723. doi:10.1016/j.commatsci.2021.110723

Yang, W., Liu, Y., Pang, S., Liaw, P. K., and Zhang, T. (2020). Bio-corrosion behavior and *in vitro* biocompatibility of equimolar TiZrHfNbTa high-entropy alloy. *Intermetallics* 124, 106845. doi:10.1016/j.intermet.2020.106845

Yang, X., and Zhang, Y. (2012). Prediction of high-entropy stabilized solid-solution in multi-component alloys. *Mater. Chem. Phys.* 132, 233–238. doi:10.1016/j.matchemphys.2011.11.021

Yao, H. W., Qiao, J., Gao, M., Hawk, J., Ma, S., Zhou, H., et al. (2016). NbTaV-(Ti, W) refractory high-entropy alloys: Experiments and modeling. *Mater. Sci. Eng. A* 674, 203–211. doi:10.1016/j.msea.2016.07.102

Ye, Y. F., Wang, Q., Lu, J., Liu, C. T., and Yang, Y. (2015). Design of high entropy alloys: A single-parameter thermodynamic rule. *Scr. Mater.* 104, 53–55. doi:10.1016/j.scriptamat.2015.03.023

Ye, Y. F., Wang, Q., Lu, J., Liu, C. T., and Yang, Y. (2016). High-entropy alloy: Challenges and prospects. *Mater. Today* 19, 349–362. doi:10.1016/j.mattod.2015.11.026

Ye, Y. F., Wang, Q., Lu, J., Liu, C. T., and Yang, Y. (2015). The generalized thermodynamic rule for phase selection in multicomponent alloys. *Intermetallics* 59, 75–80. doi:10.1016/j.intermet.2014.12.011

Yeh, J. W., Chen, S. K., Lin, S. J., Gan, J. Y., Chin, T. S., Shun, T. T., et al. (2004). Nanostructured high-entropy alloys with multiple principal elements: Novel alloy design concepts and outcomes. *Adv. Eng. Mat.* 6, 299–303. doi:10.1002/adem.200300567

Yin, S., Ding, J., Asta, M., and Ritchie, R. O. (2020). *Ab initio* modeling of the energy landscape for screw dislocations in body-centered cubic high-entropy alloys. *npj Comput. Mat.* 6, 110. doi:10.1038/s41524-020-00377-5

Yu, Z., Wen-Gan, M., Ren-You, Z., Chong, C., and Lei, G. (2014). QCD NLO and EW NLO corrections to tt~H production with top quark decays at hadron collider. *Phys. Lett. Sect. B Nucl. Elem. Part. High-Energy Phys.* 738, 1–5. doi:10.1016/j.physletb.2014.09.022

Zhang, H., Zhao, Y., Cai, J., Ji, S., Geng, J., Sun, X., et al. (2021). High-strength NbMoTaX refractory high-entropy alloy with low stacking fault energy eutectic phase via laser additive manufacturing. *Mat. Des.* 201, 109462. doi:10.1016/j.matdes.2021.109462

Zhang, M., Zhou, X., Zhu, W., and Li, J. (2018). Influence of annealing on microstructure and mechanical properties of refractory CoCrMoNbTi0.4 high-entropy alloy. *Metall. Mat. Trans. A* 49, 1313–1327. doi:10.1007/s11661-018-4472-z

Zhang, T., Wei, D., Lu, E., Wang, W., Wang, K., Li, X., et al. (2022). Microstructure evolution and deformation mechanism of α+ β dual-phase Ti-xNb-yTa-2Zr alloys with high performance. *J. Mat. Sci. Technol.* 131, 68–81. doi:10.1016/j.jmst.2022.04.052

Zhang, Y., Attarilar, S., Wang, L., Lu, W., Yang, J., and Fu, Y. (2021). A review on design and mechanical properties of additively manufactured NiTi implants for orthopedic applications. *Int. J. Bioprint.* 7, 340. doi:10.18063/ijb.v7i2.340

Zhang, Y., and Lv, Y. neng. (2008). On the nonisospectral modified Kadomtsev-Peviashvili equation. *J. Math. Analysis Appl.* 342, 534–541. doi:10.1016/j.jmaa.2007.12.032

Zhou, X., He, S., and Marian, J. (2021). Cross-kinks control screw dislocation strength in equiatomic bcc refractory alloys. *Acta Mater.* 211, 116875. doi:10.1016/j.actamat.2021.116875

frontiers | Frontiers in Bioengineering and Biotechnology

TYPE Review
PUBLISHED 16 August 2022
DOI 10.3389/fbioe.2022.953344

OPEN ACCESS

EDITED BY
T. S. Sampath Kumar,
Indian Institute of Technology Madras,
India

REVIEWED BY
Xiao Lin,
Soochow University, China
Wei Ye,
Huaiyin Institute of Technology, China

*CORRESPONDENCE
Jia Liu,
liujia@ymcn.edu.cn
Kuaishe Wang,
wangkuaishe888@126.com

SPECIALTY SECTION
This article was submitted to
Biomaterials,
a section of the journal
Frontiers in Bioengineering and
Biotechnology

RECEIVED 26 May 2022
ACCEPTED 11 July 2022
PUBLISHED 16 August 2022

CITATION
Zhang T, Wang W, Liu J, Wang L, Tang Y
and Wang K (2022), A review on
magnesium alloys for
biomedical applications.
Front. Bioeng. Biotechnol. 10:953344.
doi: 10.3389/fbioe.2022.953344

A review on magnesium alloys for biomedical applications

Ting Zhang[1], Wen Wang[1], Jia Liu[2]*, Liqiang Wang[3], Yujin Tang[2] and Kuaishe Wang[1]*

[1]School of Metallurgical Engineering, Xi'an University of Architecture and Technology, Xi'an, China, [2]Department of Orthopaedics, Affiliated Hospital of Youjiang Medical University for Nationalities, Baise, Guangxi, China, [3]State Key Laboratory of Metal Matrix Composites, School of Material Science and Engineering, Shanghai Jiao Tong University, Shanghai, China

Magnesium (Mg) and Mg alloys are considered as potential candidates for biomedical applications because of their high specific strength, low density, and elastic modulus, degradability, good biocompatibility and biomechanical compatibility. However, the rapid corrosion rate of Mg alloys results in premature loss of mechanical integrity, limiting their clinical application in load-bearing parts. Besides, the low strength of Mg alloys restricts their further application. Thus, it is essential to understand the characteristics and influencing factors of mechanical and corrosion behavior, as well as the methods to improve the mechanical performances and corrosion resistance of Mg alloys. This paper reviews the recent progress in elucidating the corrosion mechanism, optimizing the composition, and microstructure, enhancing the mechanical performances, and controlling the degradation rate of Mg alloys. In particular, the research progress of surface modification technology of Mg alloys is emphasized. Finally, the development direction of biomedical Mg alloys in the future is prospected.

KEYWORDS

magnesium alloy, biomedical applications, corrosion resistance, surface modification, microsturcture and properties

1 Introduction

Biomaterials are used for diagnosing, treating, repairing or replacing damaged tissues, and further enhancing the function of organisms (Liu et al., 2021a). Bone implant materials are an important part of biomedical materials, and about 70%–80% of implants are made of biomedical alloys (Hafeez et al., 2019; Liu et al., 2020c). The demand for biomedical alloys is rapidly increasing as the world population is getting older. The most representative biomedical alloys include stainless steel (Du et al., 2022), cobalt (Co)-chromium (Cr) alloys (Yamanaka et al., 2016; Zhou et al., 2020b), titanium (Ti) and its alloys (StráskŶ et al., 2022; Zhang et al., 2022), showing great biological and mechanical performances. However, a second surgery is required to remove the aforementioned implant materials after the bone has healed, which is extremely painful to the patient.

Magnesium (Mg) with biodegradability has gradually attracted extensive attention in biomedical filed (Zhang et al., 2021a; Dong et al., 2022a). It not only exhibits mechanical performances similar to human bone (density of 1.74 g/cm^3 and elastic modulus of

41–45 GPa), but also shows good biocompatibility (Chen et al., 2018; Dong et al., 2022a). Mg is an essential nutrient for the human body to keep healthy, which can promote bone growth, enhances cell adhesion to biomaterials, and assists the differentiation and biomineralization of osteoblasts (Schwalfenberg and Genuis, 2017). Furthermore, Mg alloys are easily corroded in physiological environment due to their active chemical performances, so they can degrade to produce magnesium hydroxide [$Mg(OH)_2$] and hydrogen (H_2) (Johnson et al., 2012; Agarwal et al., 2016). Compared with the other metal implants, the corrosion products of Mg alloys have been proved to be non-toxic and can be excreted through human metabolism (Wang et al., 2020a).

However, the development of Mg alloy for biomedical applications faces great challenges. The high corrosion rate of Mg in the human body leads to extremely rapid degradation, loss of mechanical integrity, and implant failure prior to the healing process (Banerjee et al., 2019). In addition, corrosion products such as H_2 gas and OH^- ions can affect the biocompatibility of material. H_2 will accumulate in the neighboring tissue in the form of air holes, causing tissue layers to separate (Jung et al., 2019). OH^- ions will lead to surface alkalization and potentially damage cells (Chin et al., 2020). Furthermore, the mechanical performances of Mg alloys, including the hardness, ductility, strength, wear resistance, and toughness, should be improved to satisfy various biomedical applications.

Recently, numerous efforts have been made to improve the mechanical and biological performances of Mg alloys, which are mainly divided into metallurgical modification and surface modification. Metallurgical modification is an effective method to optimize composition and microstructure by alloying, composite fabrication, and heat treatment. While it significantly enhances the mechanical performances and degradation resistance, the release of some toxic elements during the process damages neighboring tissues (Li et al., 2021). In comparison, surface modification is a more promising approach of tuning the microstructure and improving performances, which is accomplished by preparing protective coatings or changing the surface features of materials. The mechanical integrity, biodegradability, and biocompatibility of Mg alloys have been improved considerably through various surface modification processes (Lin et al., 2019; Yao et al., 2020; Zhang et al., 2021b). At present, surface modification methods mainly include mechanical, physical, chemical, and biochemical methods (Zhang et al., 2020b). To fully understand the biological and mechanical behaviors of biomedical alloys, it is essential to carried out a thorough analysis of their structures and modification mechanisms.

This review first introduces the development and characteristics of Mg and Mg alloys for biomedical applications, and then compares main methods and technologies for controlling the degradation rate as well as improving the corrosion resistance and biocompatibility of Mg alloys. Furthermore, the performances and applications of biomedical Mg alloys modified by these methods are discussed. Finally, the directions for future research and possibilities are also illustrated.

2 Magnesium and magnesium alloys for biomedical applications

2.1 Applications of magnesium alloys for biomedical applications

The application of Mg alloys in biomedical field has a long history. Mg was first used as ligatures for bleeding vessels in 1878, and since then Mg alloys have been extensively studied in medical and surgical fields, including cardiovascular, musculoskeletal, and general surgery (Witter, 2010). Currently, the applications of biomedical Mg alloys mainly include cardiovascular stents and bone implants. Mg as a vascular stent is beneficial to regulate heart rhythm, improve blood flow, inhibit platelet activation, and prevent vasoconstriction (Banjanin and Belojevic, 2018). Moreover, Mg-based vascular stent can widen the narrowed arteries and maintain them until the vessel completes remodeling, then gradually degrades and is replaced by neovascular tissue (Liu et al., 2019b).

As an orthopedic implant, Mg alloy is a novel medical material, which can replace bone implants such as steel nails in traditional medicine, and better match the mechanical performances of human bone and avoid stress shielding effects than Ti alloys (Wang et al., 2008; Amukarimi and Mozafari, 2021). Furthermore, Mg alloys can be degraded into non-toxic and harmless small molecules after the human bones are basically healed, and are excreted through the human circulatory system, avoiding the pain of patients suffering from the second surgery to remove the implant. It has been reported that Mg as an orthopedic biomaterial promotes bone remodeling and healing (O'Neill et al., 2018; Zhou et al., 2021). In summary, Mg and its alloys are extremely valuable and potential biomaterials, especially for orthopedic applications.

2.2 Characteristics of magnesium alloys for biomedical applications

Mg alloys have been widely applied in biomedical field due to their high strength, low density, and good biocompatibility (Table 1). However, due to the high corrosion rate caused by the lowest standard electrode potential of Mg (−2.37 V), the excessively fast degradation rate of Mg alloys after implantation in the human body destroys the mechanical support before the reconstruction of damaged bone tissue (Cai et al., 2022). The

TABLE 1 Advantages of Mg alloys for biomedical applications.

Advantages	Description	References
Low density and elastic modulus	Density and elastic modulus are similar to those of cortical bone	Sezer et al. (2018)
High specific strength	The strength to weight ratio is approximately 35–260 kNm/kg	Seetharaman et al. (2022)
Machinability	Mg has excellent machinability, is easy to achieve stable dimensions and can be easily processed into complex shapes	Kirkland et al. (2011)
Stress shielding effect	The elastic modulus of Mg is very close to that of bone, many problems associated with implant stress shielding can be greatly reduced	Seetharaman et al. (2022)
Biocompatibility	Mg is biocompatible and has been shown to have osteogenic functions	Amukarimi and Mozafari, (2021)
Degradability	Mg eventually degrade completely in the body, which is beneficial to the patient	Kumar et al. (2018)

TABLE 2 Disadvantages of Mg alloys for biomedical applications.

Disadvantages	Description	References
Low mechanical properties	Implants generally need to be able to withstand a certain load and deformation. At present, it is difficult for most Mg alloys to meet clinical needs in both strength and plasticity	Seetharaman et al. (2022)
High degradation rate	It is easy to cause premature loss of mechanical integrity and support of implants, which restricts its application in clinical treatment, especially in orthopedic load-bearing parts	Ding, (2016)
Hydrogen (H_2)	H_2 released during Mg degradation accumulates in the surrounding soft tissue	Razavi and Huang, (2019)

disadvantages of Mg alloys for biomedical applications are listed in Table 2.

Among them, the corrosion behavior of Mg alloy implants needs to be paid the most attention. When Mg is placed in an aqueous solution, Mg^{2+} cations are generated on the Mg surface due to the anodic reaction of Mg, as shown in Eq. 1 (Amukarimi and Mozafari, 2021). Meanwhile, a cathodic reaction occurs when protons are reduced at the cathode, producing H_2 gas and OH^- ions (Eq. 2). Eventually, the $Mg(OH)_2$ film covers the Mg surface (Eq. 3).

$$\text{Anodic reaction: } Mg \rightarrow Mg^{2+} + 2e^- \tag{1}$$

$$\text{Cathodic reaction: } 2H_2O + 2e^- \rightarrow 2OH^- + H_2 \tag{2}$$

$$\text{Product formation: } Mg + 2H_2O \rightarrow Mg(OH)_2 + H_2 \tag{3}$$

The corrosion behavior of Mg in the human body is more complex. Despite considerable efforts by researchers, it is still not fully understood. The corrosion degradation process of biomedical Mg alloys in body fluids can be shown in Figure 1. Electrochemical reactions (Eqs 1–4) occur arbitrarily across the surface, resulting in galvanic coupling because of different potentials between the Mg substrate and intermetallic phases or grain boundaries (Figure 1A). Moreover, some organic molecules may be adsorbed on the surface of Mg alloys, affecting the corrosion process of the material (Figures 1A,B). The OH^- ions generated during the reaction process will cause the local environment to be alkaline, resulting in a $Mg(OH)_2$ film covering the Mg substrate surface, separating the Mg from the surrounding environment. However, the produced $Mg(OH)_2$ film is loose and porous, and the external corrosion medium can further corrode the fresh Mg substrate through these holes, forming corrosion pits and producing a large amount of $Mg(OH)_2$ (Amukarimi and Mozafari, 2021). It is worth noting that the human environment contains numerous chloride ions (Cl^-), and when the Cl^- ions concentration reaches 30 mmol/L, it will lead to the conversion of $Mg(OH)_2$ into soluble $MgCl_2$ (Dong et al., 2022a). The concentration of Cl^- ions in the human body is about 150 mmol/L, and these Cl^- will damage the $Mg(OH)_2$ layer and cause local corrosion defects (Figure 1C). The reactions as shown in Eqs 4, 5 (Seetharaman et al., 2022).

$$\text{Product formation: } Mg(OH)_2 + 2Cl^- \rightarrow MgCl_2 \tag{4}$$

$$\text{Product formation: } Mg^{2+} + 2Cl^- \rightarrow MgCl_2 \tag{5}$$

As $Mg(OH)_2$ layer is destroyed, the Mg substrate is further exposed, the local alkalinity increases, the Ca^{2+} and PO_4^{3-} ions contained in the body fluid use the residual $Mg(OH)_2$ as the nucleation sites to form calcium phosphate based apatite. Carbonates also be formed in the presence of carbonic acid or CO_2, and these products co-deposit onto the surface of Mg substrate, forming a corrosion products layer. Cells are also found to adhere on the Mg surface. As the implantation time increased, the adhered cells proliferate, forming new tissues close to the corrosion product layer. In addition, corroded Mg may

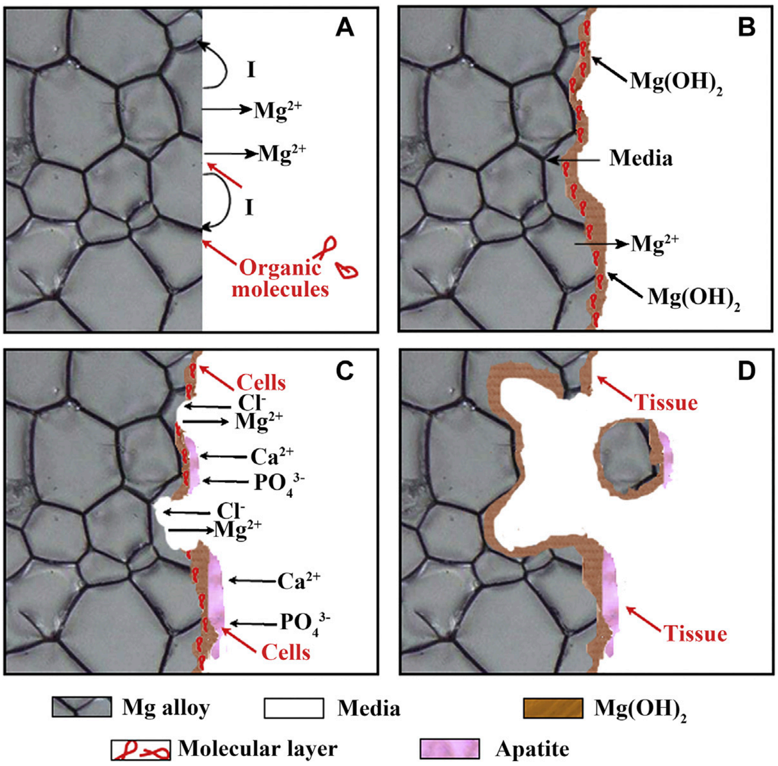

FIGURE 1
(A–D) Schematic illustration of the biocorrosion at the interface between Mg and medium. Reprinted with permission from reference (Zheng et al., 2014), Elsevier.

separate and fall off the substrate in the form of particles. The particles may be surrounded and swallowed by the fibrous tissue or macrophages until complete degradation (Figure 1D).

2.3 Factors affecting performances of magnesium alloys for biomedical applications

The service environment of biomedical Mg alloys is complicated, and its mechanical performances and corrosion behaviors mainly depend on alloy composition, microstructure, environmental medium as well as stress.

2.3.1 Alloy composition

Despite the many advantages of Mg as a biomedical material, the application of pure Mg is limited because of its low corrosion resistance and insufficient mechanical performances. Although its corrosion in aqueous solution can be used for cathodic protection of batteries, corrosion resistance is required in structural applications. In addition, pure Mg shows low ductility and strength owing to the lack of the slip system inherent in the HCP structure, which can be improved by selecting appropriate alloying elements (Seetharaman et al., 2022).

Alloy composition can change the microstructure of Mg alloys, as well as the potential difference and surface potential between phases, thereby affecting mechanical performances and corrosion resistance. The alloying elements most commonly added to Mg are aluminum (Al) and zinc (Zn), since they increase the hardness, strength, and castability (Seetharaman et al., 2022). Lithium (Li) is a potential element for developing novel Mg alloys due to its low density and high solid solubility. It has been reported that the addition of Li more than 11.5% can change the crystal structure from HCP to BCC of Mg, thereby improving the formability (Pekguleryuz et al., 2013). In addition, alloy composition also affects the formation of oxide film or corrosion product film on the alloy surface. It was demonstrated that Mg-9.29Li-0.88Ca (Zeng et al., 2014) added with Li and Ca and Mg-4Zn-0.5Ca (Cho et al., 2017) added with Mn could form protective films in simulated body fluids, thus increasing the corrosion resistance of the alloys.

2.3.2 Surface morphology

Since the surfaces of Mg alloys are in direct contact the surrounding environment in the human body, the surface conditions such as roughness and microstructure are also the main factors affecting their biomedical performances. Generally, the surface roughness plays a role on the corrosion behaviour of metallic materials. An increase in the surface roughness of stainless steels has been reported to increase the pitting susceptibility and corrosion rate (Amiriafshar et al., 2020). A similar trend occurred in copper (Xia et al., 2022) and Ti-based alloys (Pal et al., 2021). For Mg alloys, Xu et al. (2020) reported that the continuous protective film formed on alloys with smooth surfaces is higher than that on irregular surfaces, and the increase in surface roughness of Mg alloys affects the passivation tendency, thereby increasing the pitting susceptibility of the alloys.

Numerous researches have shown that the fine grain can enhance the mechanical performances and corrosion resistance of Mg alloys (Cui et al., 2021; Dobkowska et al., 2021; Klu et al., 2022). In particular, grain refinement promotes the increase of grain boundaries as corrosion barriers, which can more effectively block the expansion of pitting corrosion. The grains are refined and the microstructure is more uniform, and a more uniform and dense passivation layer can be formed (Ralston et al., 2010). Twining and texture also have obvious impact on the performances of Mg alloys. Liu et al. (2018a) carried out solution and then extrusion (T3) and solution (T4) treatments on EW75 alloy, and found that the T3 alloy with twinning structure showed better corrosion resistance. Luo et al. (2020) studied the corrosion behavior of Mg-6Gd-2Y-0.2Zr alloy and found that the $(11\,\bar{2}\,0)$ and $(10\,\bar{1}\,0)$ planes with higher atomic density were more prone to corrosion.

Besides, the second phase is also one of the key factors affecting the corrosion resistance of Mg alloys. The second phases with different types, shapes, and distributions will be produced by adding different types and contents of elements and using different processes. The most common influence mechanism is that the corrosion potential of the substrate is lower than that of the second phase, the two form a micro-battery, and the substrate acts as the anode to corrode first. However, the electrode potential of the second phase is lower does not mean that its corrosion rate is better (Zhang et al., 2020a). The corrosion of Mg alloys is also related to the morphology and distribution of the second phase. Jönsson et al. (2006) found that the potential difference in AZ91D reached 220 mV, but the corrosion rate was lower than that of pure Mg. Because a large amount of network second phases at the grain boundaries covers the substrate and act as a corrosion barrier to prevent the propagation of corrosion to the substrate, thereby reducing the corrosion rate.

2.3.3 Environmental medium

The composition of physiological solutions affects the biological activity of Mg alloys. The main components that affect the corrosion of Mg alloys are inorganic ions, proteins, and cells. Jang et al. (2013) studied the effect of different inorganic ions on the degradation of Mg alloys in the human environment. The research showed: 1) When there were only two anions of Cl^- and OH^- in the environment, the corrosion product layer does not contain calcium; 2) When HPO_4^{2-} and Cl^- co-exist in solution, the phosphate could induce the formation of a dense amorphous magnesium phosphate corrosion product layer; 3) When HPO_4^{2-} and Ca^{2+} existed together in NaC1 solution, octacalcium phosphate, and hydroxyapatite layers would be formed on the Mg alloy surface, which could inhibit local corrosion and improve overall corrosion resistance; 4) The degradation rate was accelerated by HCO_3^- ions.

In addition to inorganic ions, there are various proteins in human plasma. The research results show that the effect of protein on the corrosion rate of Mg alloys is related to the alloy type, time, and concentration (Virtanen, 2011). Although albumin has little effect on the electrochemical behavior of AZ31 alloy, it greatly promotes the anodic dissolution of pure Mg and LAE442 alloy (Mueller et al., 2009). When the AZ31 alloy is exposed to serum protein, serum protein increases the corrosion rate of the substrate within the first 3 days (Gu et al., 2009). Although the protein adsorption layer generally acts as a barrier between the metal surface and the surrounding environment, hindering corrosion to a certain extent (Yang et al., 2012), this protein adsorption layer is not very dense. Moreover, the performances of the protein adsorption layer can change dramatically over time due to Mg corrosion, for example, high pH on the Mg surface can lead to protein denaturation or even exfoliation.

The mechanism of the effect of cells on the corrosion of Mg alloys *in vitro* is not very clear. The adhered cell layer acts as a barrier to slow down the corrosion process (Seuss et al., 2011). However, Zhang et al. (2014) demonstrated that human umbilical vein endothelial cells can accelerate the corrosion rate of Mg, which may be due to the process of cell metabolism and proliferation that promotes protein desorption and storage of Mg^{2+} ions in the medium.

2.3.4 Stress conditions

As a biomedical material, after being implanted into the human body, Mg faces different stress conditions at different implant sites, which also affects the corrosion of the substrate. For example, after the Mg alloy vascular stent is implanted into the human body, it is exposed to blood fluid in the initial stage, and the stent is mainly subjected to the shear force of blood flow. In the subsequent stage of tissue coating the stent, the growth of the intima on the surface of the stent is again influenced by fluid diffusion. Fluid flow has a major effect on the degradation of Mg scaffolds, which can increase the overall corrosion rate of the implant due to the presence of shear stress (Wang et al., 2014; Saad et al., 2017). Simultaneously, the thickness of the corrosion layer, the area and depth of localized corrosion and the exfoliation of corrosion products in the corrosion pit also further expanded by shear stress (Wang et al., 2014).

3 Modification of magnesium alloys for biomedical applications

Although Mg has the advantages of mechanical performances close to bone and the best biocompatibility among biodegradable metals (Chen et al., 2018; Qin et al., 2019), the high corrosion rate in the human body greatly hinders its development and application. Therefore, improving the corrosion resistance of Mg is the key to overcome the above-mentioned drawbacks in biomedical applications. There are two methods for controlling the corrosion behavior of Mg alloys. One is to tun the composition of Mg alloys through high purification or alloying, and the other is to change the microstructure of metal surface or form a protective coating on the surface through surface treatment (Rendon et al., 2019; Amukarimi and Mozafari, 2021). Recently, researchers have made a lot of efforts to achieve optimal corrosion resistance of Mg biomaterials by devising novel Mg alloys and surface modification techniques.

3.1 Optimization of alloy composition

3.1.1 Purification

The corrosion of Mg alloys is related to the content of impurity elements (Cao et al., 2013). Commercially pure Mg often contains a large amount of impurity elements (Fe, Ni, Cu, etc.), the corrosion potential of these elements is much higher than that of Mg, which is easy to cause galvanic corrosion, thereby accelerating the dissolution of Mg and the hydrogen evolution reaction (Atrens et al., 2018). Therefore, it is possible to reduce the corrosion rate and enhance the mechanical performances by improving the purity of biomedical Mg alloys and controlling the content of harmful elements to keep them at the allowable limit concentration (Yamamoto and Hiromoto, 2009). At present, the main method to improve the purity is by selecting high-purity raw materials, optimizing the smelting process and adding Mn, Zr, and other elements to reduce impurities (Prasad et al., 2013). Although the degradation of Mg alloys can be effectively slowed down by purifying, the corresponding mechanical performances are reduced while impurities are removed, which limits its further application (Qiao et al., 2012).

3.1.2 Alloying

Alloying is one of the main ways to advance the mechanical performances of metals (Chen et al., 2015; Wei et al., 2022). In particular, the addition of appropriate alloying elements can refine grains, optimize the type and size as well as distribution of second phase, thereby enhancing the corrosion resistance of Mg alloys. Moreover, elements can form passive films or corrosion product layers to inhibit the further expansion of corrosion. Currently, aluminum (Al), zinc (Zn), manganese (Mn), calcium (Ca), strontium (Sr), strontium (Zr), neodymium (Nd) elements are widely used as alloying elements. The effects of these elements on performances of Mg alloys are shown in Table 3.

Al is the most added element in commercial Mg alloys, which can not only refine the grains, but also improve the corrosion resistance (Mirza et al., 2017). After adding Al, the Al-rich layer, and β-phase ($Mg_{17}Al_{12}$) network formed on the corrosion surface can effectually prevent further corrosion of Mg alloys. Many Mg alloys containing Al element, such as AE21, AZ31, and AZ91, have been used in biomedical fields due to their good mechanical performances and corrosion resistance. However, Al is considered to be neurotoxic and may cause Alzheimer's disease (Agarwal et al., 2016; Mirza et al., 2017).

Zn, as an essential trace element for the human body, can also effectively improve the mechanical performances of materials (Becerra et al., 2020), which is usually added in Mg-Al alloys. As one of the main research interests of novel medical materials, Mg-Zn alloys exhibit good biocompatibility (Bîrcă et al., 2018). The addition of Zn has a great effect on the corrosion properties of Mg alloys. For instance, Koç et al. (2015) reported that in Mg-Zn alloys, the increase of Zn content resulted in grain refinement, the formation of passivation films, and the formation of Zn oxide layers and the precipitation of eutectic phases, which significantly slowed down the degradation rate. Yan et al. (2017) investigated the microstructure and corrosion behavior of Mg-6Zn, Mg-14.5Zn, Mg-25.3Zn, and Mg-40.3Zn (wt.%) alloys. They found that the MgZn phase was the dominant intermetallic phase when Zn was added at 6 and 14.5 wt.%, respectively. When the addition of Zn reached 25.3 and 40.3 wt.%, a large number of $MgZn_2$ phases and Zn particles were formed. The higher the Zn concentration, the larger the intermetallic phase. The more Zn particles, the more serious the microgalvanic corrosion. The concentration of Zn has a great impact on biomedical effects of Mg alloys, but there is still no systematic study to define the concentration limit of Zn in biodegradable Mg alloys (Tian et al., 2016). Therefore, more research on the content limitation of Zn is required in the future to improve the clinical application of Mg-Zn alloys.

Mn is one of the essential trace elements for the human body. It can refine the grains, and can convert the impurity elements such as Fe, Ni into intermetallic compounds to precipitate, and may also form a Mn-containing oxide film to prevent the infiltration of Cl^- ions, thus it is widely used in biomedical Mg alloys (Cho et al., 2017; Liu et al., 2021b). Liu et al. (2021c) a added Mn to as-extruded Mg-0.5Bi-0.5Sn alloys, and demonstrated that the addition of Mn resulted in a decrease in the average grain size, and the corrosion rate of the alloy reduced from 0.59 mm/a to 0.22 mm/a when only 0.5% Mn was added in the simulated body fluid. Compared with the alloy without Mn element, the alloy exhibited a more uniform corrosion morphology, which provided favorable conditions for the dynamic balance between the formation and destruction of the corrosion product film, and hindered the further corrosion of

TABLE 3 Effects of common alloying elements on performances of Mg alloys.

Alloying elements	Biocompatibility	Corrosion resistance	Mechanical performances	References
Al	Ai is neurotoxic, it may cause Alzheimer's disease and damages muscle fibers	It is beneficial for corrosion resistance	The addition of Al increases the strength and plasticity	Agarwal et al. 2016; Mirza et al. 2017
Zn	Zn is an essential trace element for human body, with non-cytotoxic and good biocompatibility	It makes the corrosion resistance decreases with the increase of Zn content	Zn mainly plays the role of solid solution strengthening, and the strength increases with the increase of Zn content	Tian et al. 2016; Becerra et al. 2020
Mn	Mn is an essential trace element for human body. However, it has been reported that Mn is cytotoxic and neurotoxic	It is beneficial for the corrosion resistance	It increases yield strength, and decreases tensile strength and elongation	Cho et al. 2017; Liu et al. 2021b
Ca	Ca is an important component of human bone, with non-cytotoxic	It makes the corrosion resistance reduces with increasing Ca content	It makes the strength increases and plasticity reduces with increasing Ca content	Zhang et al. 2017b; Mohamed et al. 2019
Sr	Sr is an important component of human bone, with non-cytotoxic. It can promote bone formation	It makes the corrosion resistance of Mg alloys reduces with increasing Sr content	It makes the strength increases with increasing Sr conten.t	Dong et al. (2022a)
Zr	Zr has good biocompatibility and bone bonding ability	It makes the corrosion resistance reduces with increasing Zr content	It makes the grains refine, strength and plasticity increase	Agarwal et al. 2016; Zhou et al. 2020a
Si	Si is an essential trace element for human body	It reduces the corrosion resistance	It produces coarse Mg_2Si phase, increases strength and decreases plasticity	Qin et al. (2019)
Li	Li may cause malformation of human cardiovascular system	It reduces the corrosion resistance	When the addition amount of Li exceeds 5.5%, the microstructure changes, the strength decreases and the plasticity increases	Wu et al. 2017; Kumar et al. 2018
Nd	Nd is cytotoxic at high concentration, while it has good biosafety at low concentration	It improves the corrosion resistance	It makes the new phases form, microstructure refine, mechanical performances improve	Xie et al. (2021)
Y	Y has good biocompatibility	It improves the corrosion resistance	It increases the strength and plasticity	Ren et al. 2017; Nie et al. 2021
Ce	Ce is high cytotoxic	It improves the corrosion resistance, while more amount reduces corrosion resistance	It improves the strength and fatigue resistance	Amukarimi and Mozafari (2021)
La	La is higher cytotoxic	It improves the corrosion resistance	It improves the strength and creep resistance	Ding et al. (2014)
Er	Er is cytotoxic	It improves the corrosion resistance	It improves strength and plasticity	Zhang et al. 2010; Zhang et al. 2012a
Gd	Gd is cytotoxic	It improves corrosion resistance, which decreases when Gd content is high	It improves strength due to solid solution strengthening	Chen et al. (2019b)

Mg substrate. Rosalbino et al. (2010) studied the corrosion resistance of Mg-2Zn-0.2X (X = Ca, Mn, Si) alloys in simulated body fluids, and the results showed that Mg-2Zn-0.2Mn had better corrosion resistance. However, the cytotoxicity and neurotoxicity of Mn have been reported (Ding et al., 2011; Zheng et al., 2014). Mn damages the sensory epithelial cells and auditory nerves of organisms, and causes severe lesions in neurons and hair cells.

Ca is an essential element for human body and an important component of bone, the density is close to that of human bone (Ding et al., 2014), which makes Mg-Ca alloy exhibit greater advantageous as a bone implant material. The addition of Ca with an appropriate amount can refine grains, inhibit grain boundary compounds, reduce the potential difference between the second phase and the substrate, and improve the density of oxide film, thereby hindering corrosion and increasing the corrosion resistance of Mg alloys (Zhang et al., 2017b; Mohamed et al., 2019). Zheng et al. (2010) prepared Mg-Ca alloys with 1 ~10 wt.% Ca content and analyzed their corrosion resistant. Electrochemical tests and *in vitro* simulation tests showed that the corrosion resistance of Mg-Ca alloys with 5 wt.% and 10 wt.% Ca content was significantly reduced compared to 1 wt.% Ca. Zhang et al. (2011) found that the addition of Ca (0.2 wt.%) decreased the degradation rate of as-cast Mg-4Zn alloy (~30%), because Ca reduced the potential difference between the second phase and the substrate. Studies have shown that for Mg-Ca alloys, increasing the Ca content is beneficial to increase the Mg_2Ca phase as well as the compressive strength, elastic modulus, and hardness, but reduce the plasticity, corrosion resistance, and biocompatibility (Li et al., 2011; Agarwal et al., 2016). It is worth noting that the mechanical performances, corrosion resistance, and biocompatibility of the alloy are better when the Ca content is low (less than 1 wt.%) (Li et al., 2011).

Sr is one of the trace elements in the human body. Almost all of the Sr exists in the bones. Strontium salts can promote the formation of bones (Bornapour et al., 2013). The chemical performances of Sr, Mg, and Ca are similar. The addition of Sr to Mg alloys can effectively refine grains and improve comprehensive properties. Therefore, Sr elements are often added to Mg alloys for bone implantation in recent years. Mg-Sr alloys also exhibit good biocompatibility. For instance, Ragamouni et al. (2013) indicated that Mg-Zr alloy with Sr addition fuses better with new bone tissue in bone tissue of rabbit.

In addition, Zr, Si, Li elements are often added to Mg alloys for biomedical applications. The good biocompatibility and bone bonding ability of Zr element have been reported (Agarwal et al., 2016; Zhou et al., 2020a). As an alloying element, Zr can refine grains and effectually increase the corrosion resistance of Mg alloys (Xing et al., 2021). Si is also one of the essential trace elements for the human body. It is often added together with other elements to improve the performances of Mg alloys, because the Mg_2Si phase produced in Mg-Si binary alloys greatly reduces the ductility and corrosion resistance (Qin et al., 2019). Although Li may cause malformation of the human cardiovascular system, Mg-Li-based alloys exhibit good ductility, which can fulfill the requirements of expandable vascular stents (Kumar et al., 2018). Moreover, observed that Mg-Li-Zn ternary alloys showed good biocompatibility.

Low alloying of rare Earths is a direction to develop high-performance Mg alloys. The addition of a small amount of rare Earth elements can significantly affect the microstructure and performances of Mg alloys. At present, rare Earth elements commonly added in biomedical Mg alloy include Nd (Xie et al., 2021), Y (Ren et al., 2017; Nie et al., 2021), Ce (Amukarimi and Mozafari, 2021), La (Ding et al., 2014), Er (Zhang et al., 2010; Zhang et al., 2012a), Gd (Chen et al., 2019b; Luo et al., 2020), etc. Nd can form new phases with Mg and other chemical elements in Mg alloys, thereby refining the microstructure and improving the mechanical performances of the alloys (Xu et al., 2014). In particular, Zhang et al. (2012b) and Xie et al. (2021) reported that the Mg-Nd-Zn-Zr alloys developed by adding elements such as Nd exhibit good mechanical performances (> 200 MPa), corrosion resistance (corrosion rate is ~0.125 mm/a), and better biocompatibility. The addition of Y improves the corrosion resistance of Mg alloys. Ren et al. (2017) observed that when the Y content is less than 1%, the corrosion resistance of the alloy increases with the increase of the Y content due to the grains refinement. However, too much Y added to the alloy will lead to the formation of the MgY phase, forming many micro-batteries and accelerating the corrosion of the alloy. Although Ce, La, and Er have high cytotoxicity among rare Earth elements (Feyerabend et al., 2010; Zhang et al., 2012a), the addition of a small amount of above elements to Mg alloys will not damage human body, and can significantly improve mechanical performances and corrosion resistance (Zhang et al., 2010). Chen et al. (2019b) observed that when a low content of Gd (0%–1%) was added to the Mg-2Zn-0.5Zr alloy, the second phase was uniformly distributed, and the addition of Gd stabilized the degradation layer and reduced the degradation rate of the alloy. However, when the addition of Gd was increased to 2%, large and thick second phases formed along the grain boundaries, which increased the alloy corrosion rate due to electrochemical corrosion.

With the in-depth study of alloying, the mechanism of improving the corrosion resistance of Mg alloys by alloying has gradually become clear. Only a small amount of alloying elements are added to biomedical Mg alloys to obtain great performances, and excessive elements will deteriorate the corrosion properties. Moreover, the more elements added, the more uncertain factors in the performance determination of medical Mg alloys, and the greater challenges in biosafety assessment. Therefore, the comprehensive properties of biomedical Mg alloys including corrosion degradation, mechanical performances, and biosafety should be comprehensively considered to add appropriate alloying element.

3.2 Surface modification

In addition to changing the corrosion resistance of Mg alloys, surface modification is also an important means to advance their corrosion resistance. Appropriate surface modification methods can not only enhance the mechanical performances and corrosion resistance of Mg alloys, but also simultaneously improve the biological function of the alloys such as biocompatibility and bioactivity (Yu et al., 2018; Wu et al., 2019). Currently, a variety of surface modification technologies have been developed for biomedical Mg alloys, which can be divided into surface coating preparation and surface microstructure modification.

3.2.1 Surface coating preparation

Since the oxide film formed on the Mg surface is relatively loose, it cannot protect the alloy for a long time. Therefore, it is effective to prepare a protective layer on the Mg surface by chemical, physical, mechanical, and biological or biomimetic techniques (Yin et al., 2020).

3.2.1.1 Chemical conversion coatings

Chemical conversion coatings are formed by the electrochemical or chemical reaction of Mg-based materials, and the bath usually includes fluoride, phosphates, carbonate, and chromate (Wandelt, 2018; Rahim et al., 2022). An insoluble compound film with good adhesion can be formed on the Mg surface by chemical conversion treatment, which can not only protect Mg alloy from water and other corrosive environments,

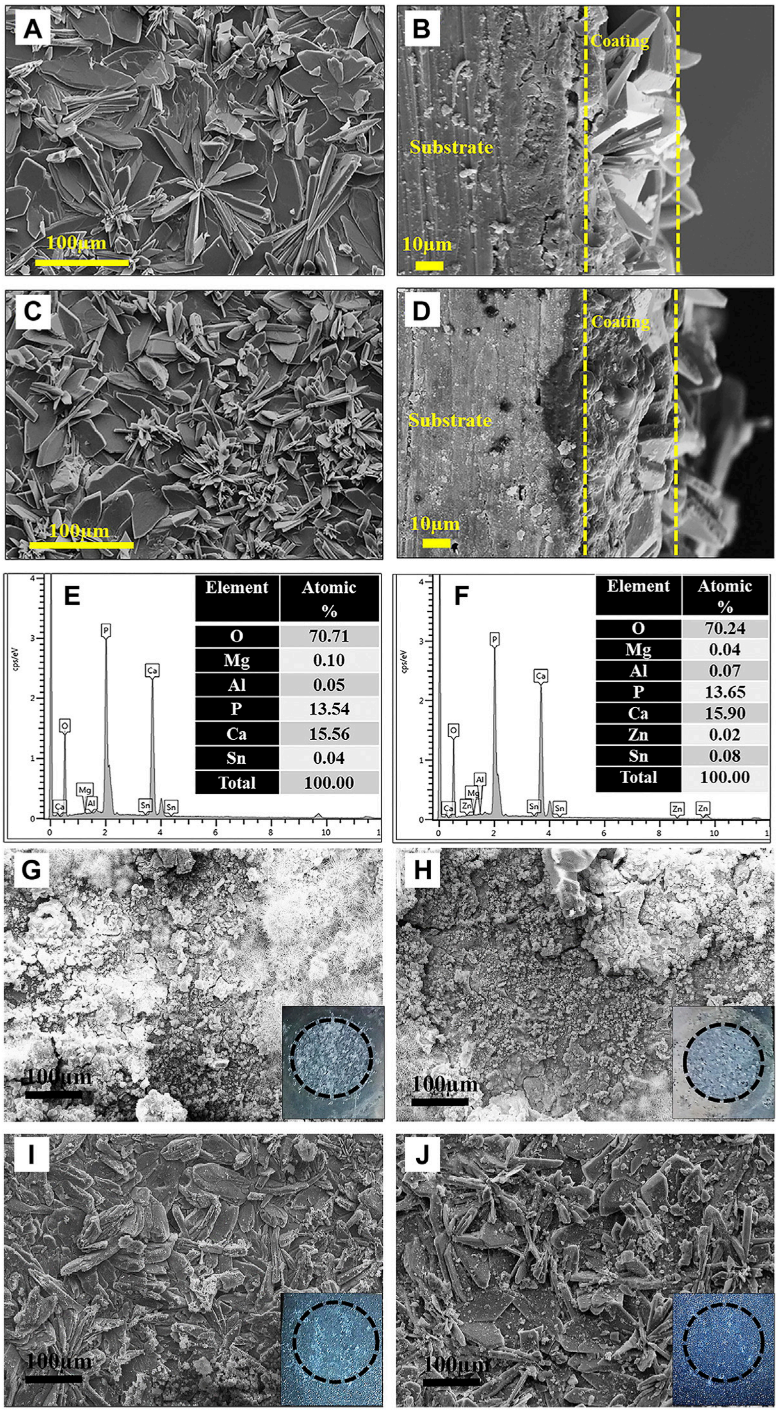

Element	Atomic %
O	70.71
Mg	0.10
Al	0.05
P	13.54
Ca	15.56
Sn	0.04
Total	100.00

Element	Atomic %
O	70.24
Mg	0.04
Al	0.07
P	13.65
Ca	15.90
Zn	0.02
Sn	0.08
Total	100.00

FIGURE 2
SEM images: **(A,C)** PCC coated surface and **(B,D)** cross-section of LAT971 and LATZ9531; EDS spectrum: **(E)** LAT971 and **(F)** LATZ9531 alloy; SEM images after corrosion test: **(G,H)** uncoated and **(I,J)** PCC coated LAT971 and LAT9531, respectively. Reprinted with permission from reference (Maurya et al., 2018), Elsevier.

but also improve the adhesion of subsequent coatings. The method is easy to operate, which is widely used for biomedical applications. Among them, fluoride coatings (Pereda et al., 2011) and phosphates coatings (Chen et al., 2014a; Willbold et al., 2015) for biomedical Mg alloy surfaces have attracted extensive attention.

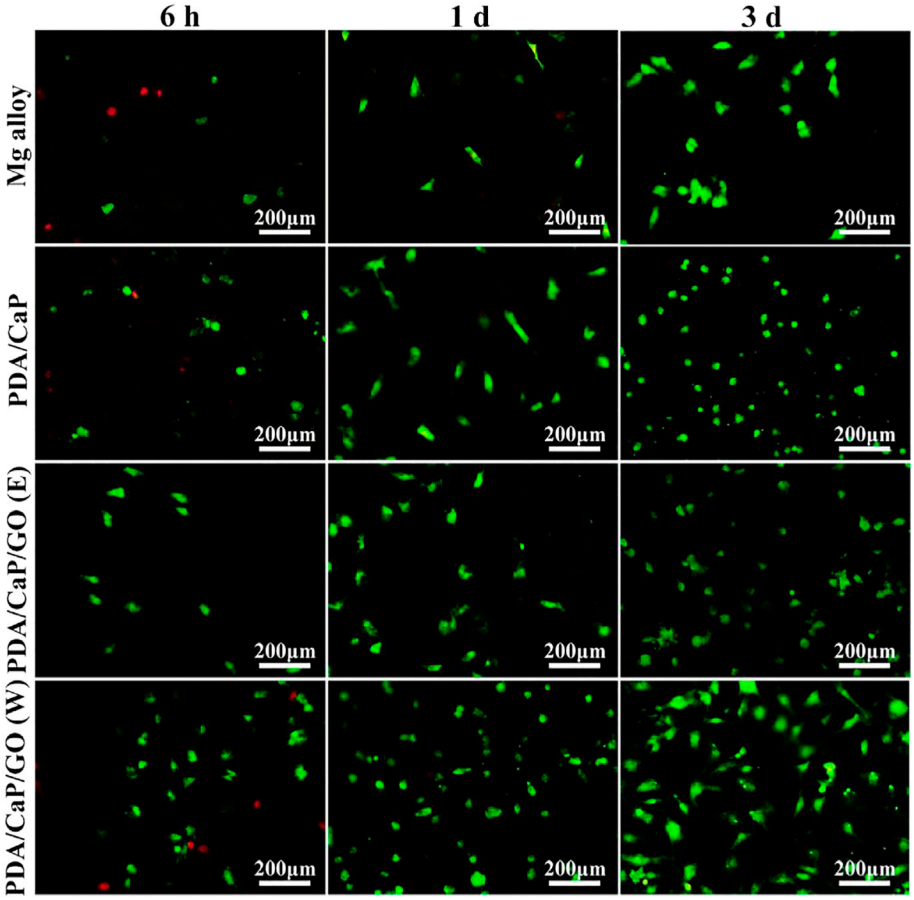

FIGURE 3
Fluorescence images of live/dead staining of cells after cultured on the different samples. Reprinted with permission from reference (Dong et al., 2022b), Elsevier.

Typically, fluoride conversion coatings are performed in hydrofluoric acid (HF) solutions by chemical reactions with Mg alloys (Lin et al., 2013; Yan et al., 2014). The main component of the fluorine conversion coating is magnesium fluoride (MgF_2), which is insoluble in water and easily deposited on the Mg surface. MgF_2 films have been used in biomedical Mg alloys due to their good corrosion resistance, improved cellular response, and biocompatibility (Liu et al., 2015b). Barajas et al. (2019) prepared a magnesium hydroxyfluoride coating on the AZ31 alloy surface using 4% and 10% HF solution respectively. The corrosion current density of the fluorinated samples is reduced by about three orders of magnitude, which improves the corrosion resistance of the alloy and biocompatibility. Furthermore, Fintová et al. (2019) fabricated fluoride conversion coatings though immersing AZ61 Mg alloy into sodium fluoroborate [Na (BF_4)] molten salt under different temperature, and then boiling in distilled water to remove the residual salts and the outer layer. The obtained coating exhibited a double layer structure with a thick inner Mg-F (MgF_2) layer and a thin outer Na-Mg-F ($NaMgF_3$) layer. The corrosion current density i_{corr} of the coatings decreased with increasing treatment time, indicating an increase in corrosion resistance in SBF solution. Therefore, fluoride conversion coatings are a good way for improving the corrosion resistance of Mg alloys.

Recently, phosphate conversion coatings such as zinc phosphate (Zeng et al., 2011), calcium phosphate (Chen et al., 2014b) have been reported due to their water insolubility, high temperature resistance, corrosion resistance, and great biocompatibility. For instance, Zeng et al. (2011) prepared two phosphate conversion coatings on the surface of AZ31 alloy, both of which showed higher corrosion resistance than the substrate. The flower-like Zn-Ca coating was denser than the rod-like Zn coating, which significantly reduced the corrosion current density. Besides, Maurya et al. (2018) improved the corrosion resistance of Mg-9Li-7Al-1Sn (LAT971) and Mg-9Li-5Al-3Sn-1Zn (LAT9531) by preparing the phosphate chemical conversion coatings. The microstructure of phosphate chemical conversion (PCC) coatings and the corrosion morphologies are shown in

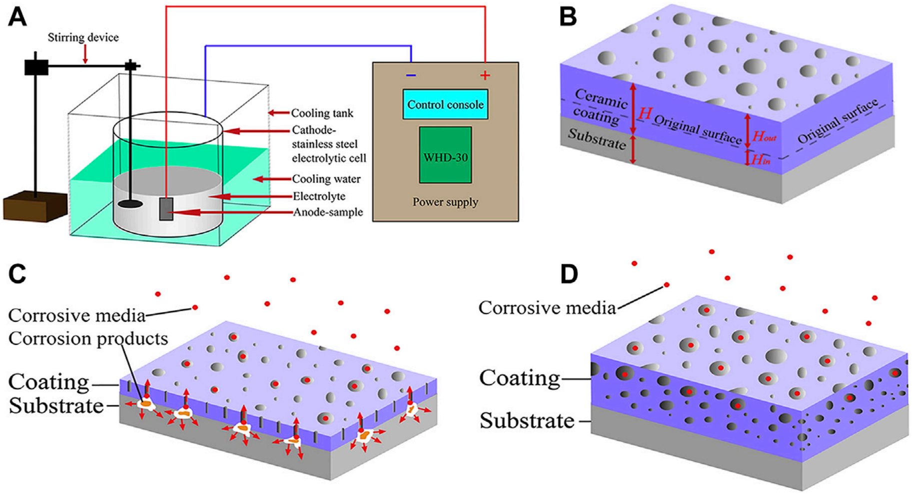

FIGURE 4
The schematic diagrams of **(A)** MAO device, **(B)** growth model; the corrosion mechanism of MAO coating: **(C)** thin coating with through-pores; **(D)** thicker coating with complex pores. Reprinted with permission from reference (Liu et al., 2020a), Elsevier.

Figure 2. Since the coating could slow down the generation of degradation productions and hinder the occurrence of pitting corrosion, the degradation rates of coated-LA971/LAT9351 was reduced.

In summary, an insoluble compound film with good adhesion can be formed on the Mg surface by chemical conversion treatment, which can protect Mg alloy from water and other corrosive environments. In the future, chemical conversion coatings should be combined with other surface modification techniques to produce biofunctional coatings with excellent mechanical properties.

3.2.1.2 Biomimetic deposition

Biomimetic deposition is a method developed in recent years to simulate the process of physiological apatite mineralization in nature and spontaneously deposit bioceramic membranes on the surface of substrates. The advantages of the biomimetic technique are as follows (Lin et al., 2015): First, the coating composition, phase, and crystallinity are easy to adjust; Second, the method can also produce biomimetic apatite coatings on porous or complex-shaped implants; Third, it is a simple and effective method of incorporating biologically active agents or drugs into apatite coatings through coprecipitation rather than *via* mere adsorption on the surface. Therefore, biomimetic method has been extensively applied for the modification of metallic biomaterials. For example, Hernandez et al. (2022) successfully deposited bioactive hydroxyapatite (HAp) coatings on pure Mg surfaces based on immersion of Mg substrates in supersaturated calcification solution (SCS). Gao et al. (2015) used biomimetic method to prepare bioactive hydroxyapatite/graphene oxide (HA/GO) hybrid coatings on Mg alloys, and they found that the formed HA/GO coating could significantly improve the corrosion resistance. Dong et al. (2022b) prepared polydopamine (PDA)-based calcium phosphate (CaP)/graphene oxide (GO) composite coatings on AZ60 Mg alloy. First, PDA was used as a pretreatment layer to induce the biomimetic deposition of CaP, and then GO as a sealing layer was spin-coated with ethanol and water as dispersants, respectively. Electrochemical and immersion test results showed that the corrosion resistance of the PDA/CaP/GO composite coating was significantly increased. The results of *in vitro* cell experiments showed that the composite coating could promote cell adhesion and improve biocompatibility (Figure 3). In addition, the corrosion resistance and biocompatibility of the PDA/CaP/GO composite coating with water as dispersant were better than those with ethanol, which was significantly improved compared with the Mg alloy.

In summary, the preparation of bioactive coatings on the surface of Mg and Mg alloys by biomimetic deposition can effectively improve the corrosion resistance and biocompatibility. However, the technology is still in the experimental stage at present, and there are few material systems that can be deposited. In the future, In-depth research should be carried out to promote the development of this technology.

3.2.1.3 Micro-arc oxidation coating

Micro-arc oxidation (MAO), also known as plasma electrolytic oxidation (PEO), is a high voltage plasma-assisted anodic oxidation process developed from traditional anodizing to form ceramic-like coatings (Lu et al., 2016). The schematic

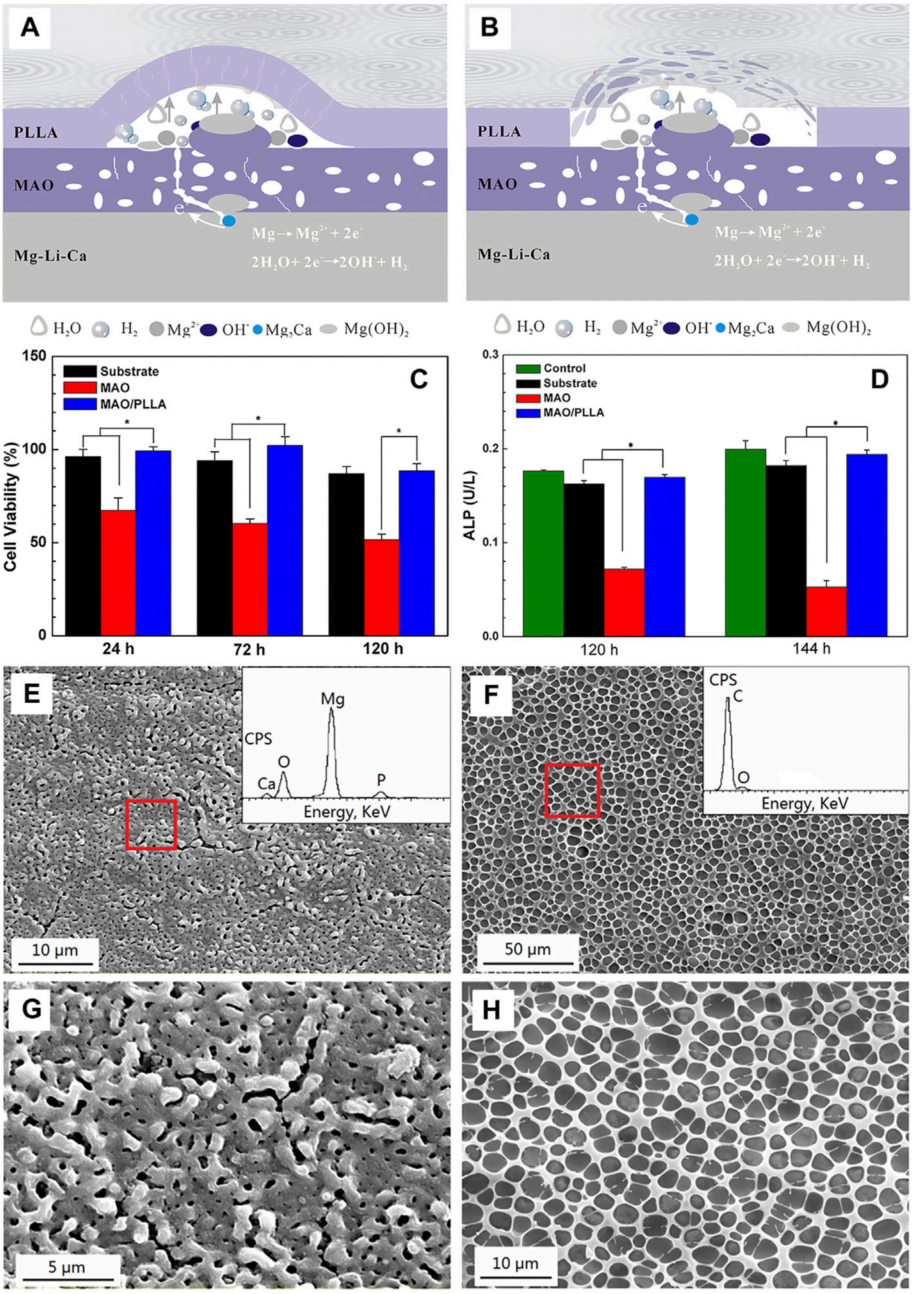

FIGURE 5
Schematic diagrams of the degradation mechanism of porous MAO/PLLA composite coatings on Mg-1Li-1Ca alloys: **(A)** swelling of PLLA and corrosion of the substrate, and **(B)** blistering and final peeling-off of PLLA; **(C)** RGR and **(D)** proliferation and differentiation of MC3T3-E1 cells cultured for different times in different extracts. Error bars represent ± S for $n = 5$ and 3, respectively, and $p < 0.05$, as indicated by the asterisk (*); SEM images of **(E)** the MAO coatings; **(F)** the MAO/PLLA composite coatings, **(G,H)** the high magnification view of e and f, respectively. Reprinted with permission from reference (Zeng et al., 2016), American Chemical Society.

diagram is indicated in Figure 4. MAO has been widely investigated innumerous fields because of its high efficiency, high bonding strength between coating and substrate, no limitation on the surface shape of the workpiece and so on (Liu et al., 2019a; Liu et al., 2020a).

The microstructure and performances of the MAO coating on the surfaces of biomedical Mg alloys have been extensively investigated. Liu et al. (2019a) observed that the prepared porous ceramic coating consists of dense inner and porous outer layers. Generally, a lower voltage produces a fine porous structure, while

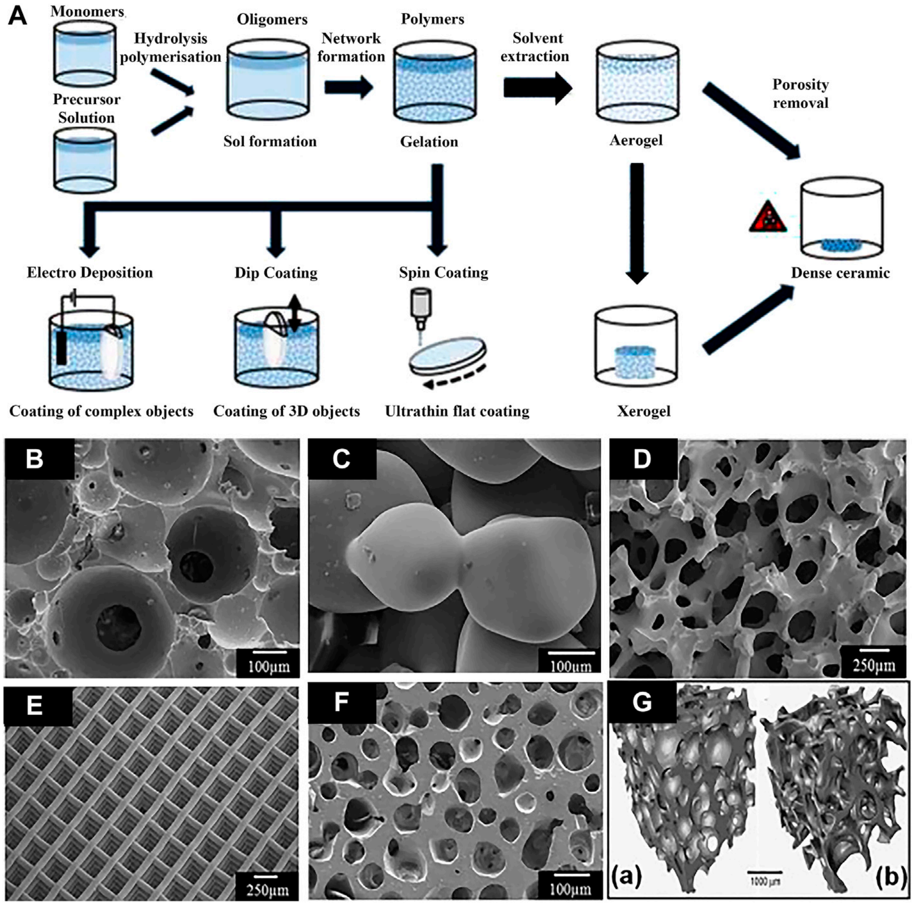

FIGURE 6
(A) Schematic illustration of preparation processes of the sol-gel coatings; **(B–F)** bioactive glass scaffolds with porous structure produced by sol-gel methods, and **(G)** micro-computed tomography image of typical scaffold and human trabecular bone. Reprinted with permission from reference (Owens et al., 2016), Elsevier.

the pore dimension increases with treatment time and voltage. Therefore, a large number of micropores or high porosity is the main drawback for MAO coatings to realize long-term surface protection (Lu et al., 2016). Wang et al. (2020d) fabricated a dense MAO coating through a two-step current decreasing mode, which decreased the corrosion rate of material from 0.9690 to 0.1559 g/m^{2}h in NaCl solution. Lin et al. (2021) prepared Li-added MAO coatings on pure Mg surface. The results showed that the corrosion resistance of the coated alloy was significantly higher than that of pure Mg, and the addition of Li reduced the number of micropores and cracks on the MAO coating, which made the alloy to exhibit better corrosion resistance. Furthermore, Liu et al. (2020a) prepared a protective MAO coating on the surface of Mg-based composite to reduce their degradation rate. They found that the corrosion resistance of the composite was significantly improved by the coating, and the corrosion resistance of the coating increased with oxidation time.

For biocompatibility and biological activity, the MAO coating exhibits high bonding strength with the substrate due to the dense interior, and the porous outer layer is helpful to protein adsorption, osteoblast adhesion, and bone tissue regeneration, which is potential for biological applications. Wei et al. (2015) obtained a dense PEO/PLLA composite coating by sealing PEO with PLLA on AZ31Mg alloy. The results from *in vitro* tests showed that the degradation kinetics were obviously reduced, the hemolysis ratio was as low as 0.80%, and MC3T3-E1 cells displayed good adhesion and proliferation ability on the coating. Zeng et al. (2016) investigated the effects of MAO/PLA composite coatings on the corrosive behavior of Mg-1Li-1Ca alloys. They found that the MAO coatings could only provide limited protection to the substrate. Although it could protect the substrate during the initial immersion stage, the difference of free corrosion potential between the coating and substrate caused galvanic corrosion due to the presence of pores and microcracks during the subsequent immersion. Moreover,

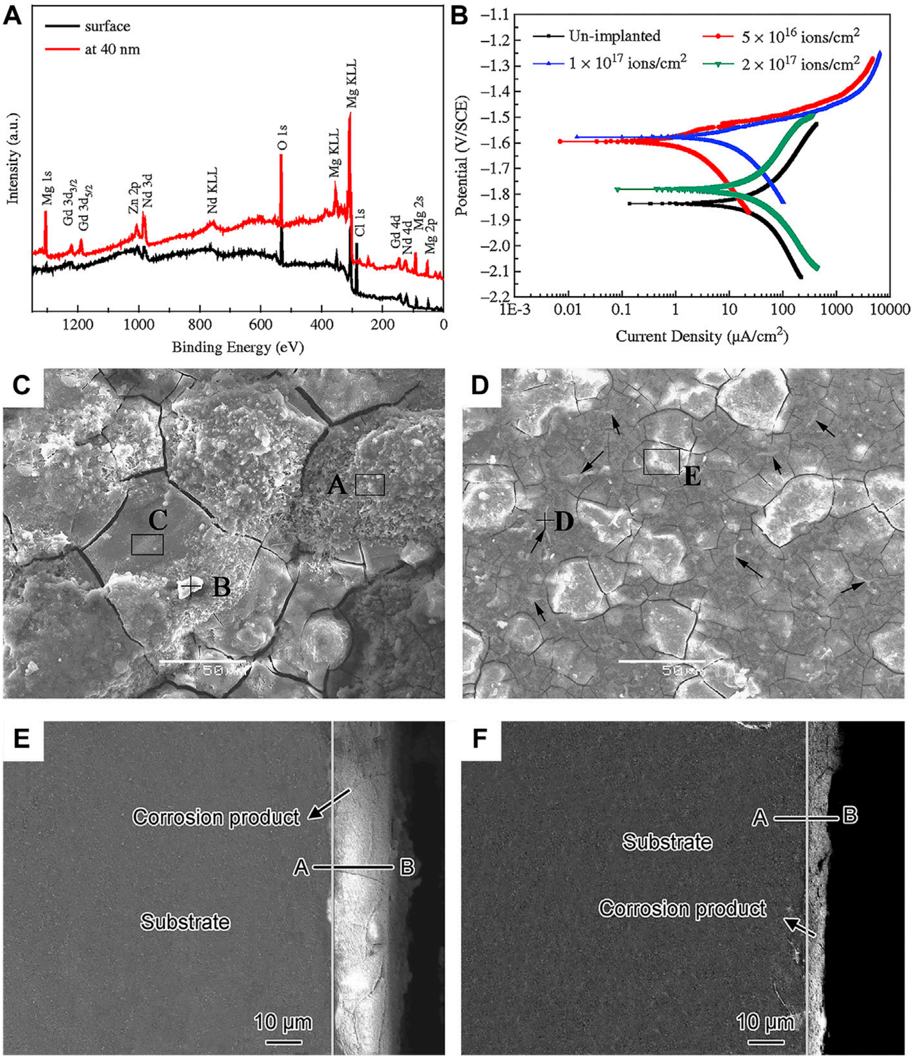

FIGURE 7
(A) XPS spectra of implanted alloy at different depths; **(B)** polarisation curves of Mg-Gd-Zn-Zr alloy with various doses in SBF solution; surface and cross-section morphology after corrosion test **(C,E)** unimplanted and **(D,F)** Nd implanted alloy. Reprinted with permission from reference (Wang et al., 2015b), Elsevier.

the top layer of PLLA on the MAO coating experienced swelling and subsequent delamination or peeling off under the pressure of H_2 gas and corrosion products (Figures 5A,B). The results of biocompatibility test using fresh rabbit arterial blood showed that the hemolysis ratio decreased from 61.35% to 0.17% for the MAO/PLLA composite coated on Mg-Li-Ca alloy (Figures 5C,D). The composite coating with porous microstructure (Figures 5E–H) also promoted the attachment of MC3T3-E1 cells.

In summary, the bioactive coating prepared by micro-arc oxidation is beneficial to protein adsorption, osteoblast adhesion, and bone tissue regeneration. In the future, micro-arc oxidation technology should be developed for multilayered micro-nanostructured coatings for cell adhesion and proliferation, and to construct multifunctional coatings with biological activity and antibacterial properties.

3.2.1.4 Sol-gel coating

The sol-gel process, also known as chemical solution deposition, has been extensively applied in materials science and ceramic engineering. The method is mainly used for synthesis of materials starting from a chemical solution that acts as the precursor for an integrated network (or gel) of either discrete particles or network polymers (Figueira et al., 2016). In general, sol-gel formation follows four steps: 1) hydrolysis, 2) condensation and polymerization of monomers to form chains

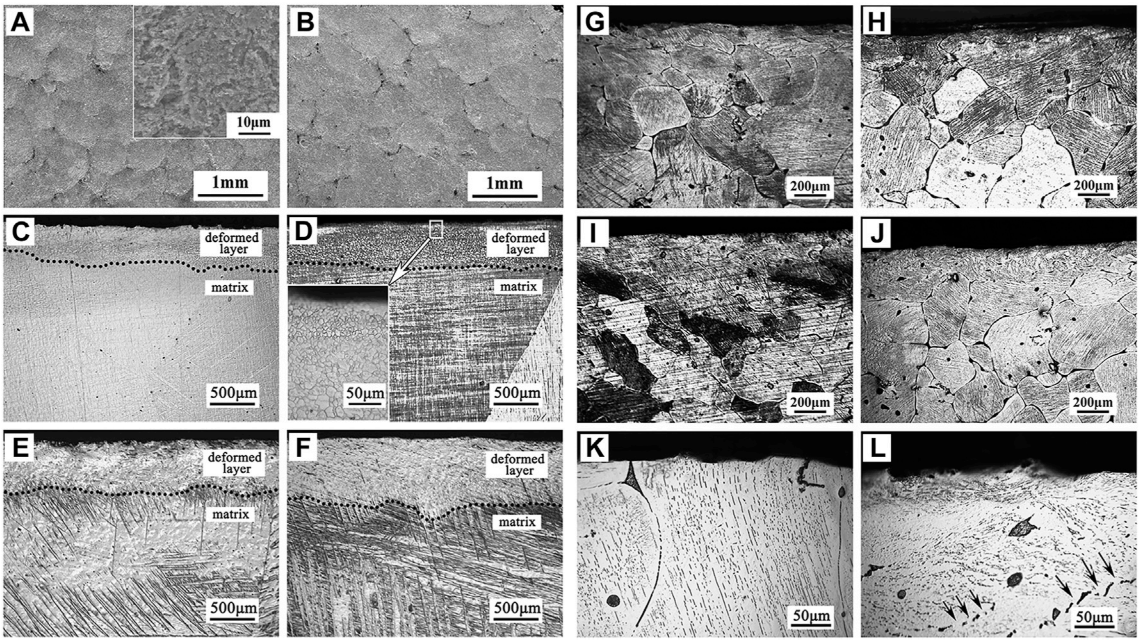

FIGURE 8
Surface morphologies of **(A)** SMATed pure Mg, and **(B)** SMATed Mg-1Ca alloy; cross-section morphologies of **(C–F)** SMATed pure Mg for different time, **(G–J)** SMATed Mg-1Ca alloy for different time, and high magnification images of **(K)** untreated and **(L)** SMATed Mg-1Ca alloy. Reprinted with permission from reference (Chen et al., 2019a), Elsevier.

and particles, 3) particle growth, and 4) agglomeration of the polymer structures followed by the network formation throughout in liquid medium which increases the viscosity to form a gel (Owens et al., 2016). The schematic illustration of preparation process of the sol-gel coatings is show in Figure 6A. The method has the advantages of low cost, low processing temperature, and the ability to coat a variety of materials into complex shapes, which is favorable for biomedical applications (Figueira, 2020). The porous scaffolds of a few bioglasses (BGs) has been prepared by the method, such as the glass designated 58S [60 SiO_2-36 CaO-4 P_2O_5 (mol%)] by Sepulveda et al. (2002). The scaffolds with porous structures made of bioactive glasses produced by sol-gel processes in recent years are displayed in Figures 6B–F.

Combining the changes in the coating preparation process and adding other functional components, different functional coatings can be obtained. In addition, how to shorten the processing time and improve the bonding between the surface and the substrate by changing the processing parameters seems to be the main research direction in the future.

The microstructure and corrosion resistance of the sol-gel coatings have been investigated. Kania et al. (2020) observed that the 300 nm thick TiO_2 films with an anatase structure were deposited on MgCa4Zn1Gd1 alloy by magnetron sputtering and spin coating methods respectively. Compared to the film prepared by spin coating, the surface of TiO_2 film prepared using the magnetron sputtering method exhibits finer and more uniform grains. The alloy with TiO_2 film deposited by sol-gel exhibits better corrosion resistant. Nezamdoust et al. (2018) demonstrated that the silica coating prepared on the surface of AM60B Mg alloy by sol-gel method improved the surface roughness, corrosion resistance, and the hydrophobicity. Hu et al. (2011) used sol-gel method to prepare a nano TiO_2 coating on AZ31 alloy, and reported that the degradation rate was lower when the size of nano-spherical TiO_2 particles was smaller. Omar et al. (2020) synthesized 58S and 68S bioactive silica glasses by the sol-gel method, and dip-coated them on the AZ91D alloy. Results showed that the coatings improved corrosion resistance in Hank's solution, and the cells were well adhered, spread, and elongated on the coated materials.

3.2.1.5 Ion implantation

Ion implantation is a surface modification technique in which target elements are formed into an ion beam in a vacuum, and then sputtered onto the modified material, and finally a layer with specific composition and structure is formed on the substrate surface (Jamesh et al., 2014). Implantation of appropriated ions into Mg substrate can reduce its corrosion rate and improve mechanical performances and biocompatibility. Recently, the main researches include metal ion such as iron (Fe), cerium (Ce), zinc (Zn), zirconium (Zr), strontium (Sr), as well as the non-metallic ions such as carbon (C), oxygen (O),

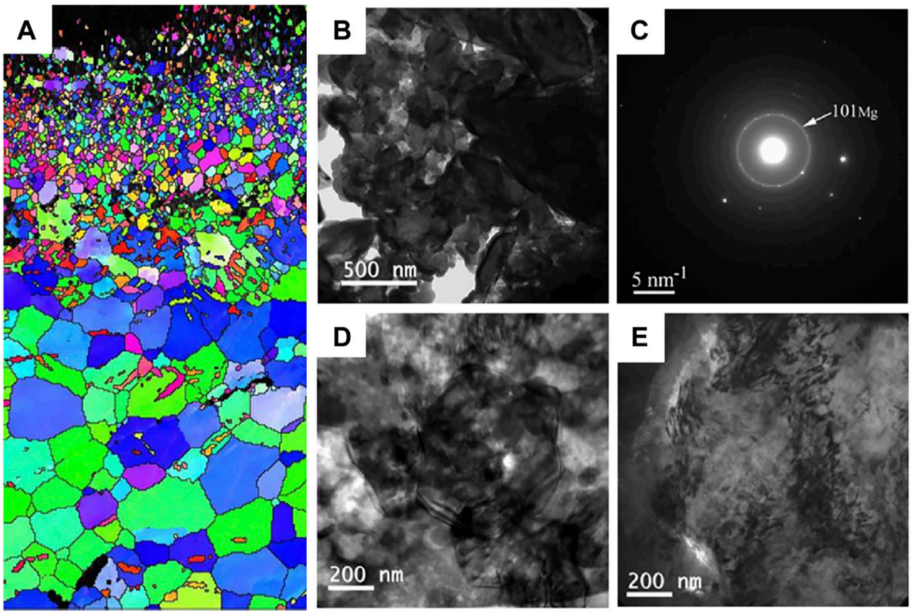

FIGURE 9
(A) EBSD map of the cross section of AZ31 samples after shot peening; TEM images **(B)** bright field image and **(C)** the corresponding SAED pattern of the shot peening sample just under the topmost layer, bright field images at the depth of **(D)** 30 μm and **(E)** 150 μm. Reprinted with permission from reference (Bagherifard et al., 2018; Bagherifard et al., 2019), Elsevier.

Nitrogen (N) (Liu et al., 2017; Somasundaram et al., 2018; Zhu et al., 2018). Jia et al. (2018) observed that after implanting Sr ions into Mg alloys, the elastic modulus and hardness are improved, and meanwhile the corrosion potential is increased. Zhu et al. (2018) implanted N ions on the surface of AZ31 alloy, followed by magnetron sputtering to generate double-layer amorphous hydrogenated diamond-like carbon (DLC:H)/SiNx, which effectively improves the long-term corrosion resistance of the substrate. Wang et al. (2015b) implanted Nd ions on the Mg-Gd-Zn-Zr alloy, and found that a mixed layer consist of Nd_2O_3, Gd_2O_3, and metal Nd was produced on the surface (Figure 7A). The Nd_2O_3 and Gd_2O_3 are relatively stable in the aqueous solution, preventing the inward transport of Cl^-, which can increase the corrosion resistance of the alloy under the appropriate condition (Figure 7B). Figures 7C–F show the surface and cross-sectional morphologies of the corrosion product layer on the alloy before and after ion implantation. It is worth noting that the thickness of the corrosion product layer becomes smaller after ion implantation, and the alloy is uniformly etched before and after implantation. Liu et al. (2017) modified Mg alloys by metal vapor vacuum arc plasma deposition after implanting Zn ions on the surface of Mg-1Ca alloys. A relatively uniform ZnO coating was produced on the Mg alloy surface, which promoted the proliferation and adhesion of MC3T3-E1 cells and significantly increased the corrosion potential.

As one of the most important methods for surface modification of Mg alloys, ion implantation is convenience, controllability, and flexibility. Currently, single ion implantation is limited in improving the performance of materials. The implantation of ions with various functions can not only effectively improve the physical and chemical properties or biological activity of alloys, but also improve the antibacterial ability. With the development of composite ion implantation technology, it will be a trend to simultaneously implant multiple ions to obtain multifunctional Mg materials.

3.2.2 Surface microstructural modification

Surface microstructural modification technique induces the deformation of the metal surface through mechanical processing, so that the material surface obtains a different microstructure and performance from the matrix material. Mechanical processing improves the mechanical performances and corrosion resistance of Mg alloys by refining grains, changing the distribution of second phases or intermetallic compounds, and enhancing surface hardness (Yin et al., 2020). The process usually does not involve chemical reactions. This part mainly introduces the research status of surface mechanical attrition, shot peening, laser surface modification, and friction stir processing (FSP) in improving the performances of Mg alloys for biomedical applications.

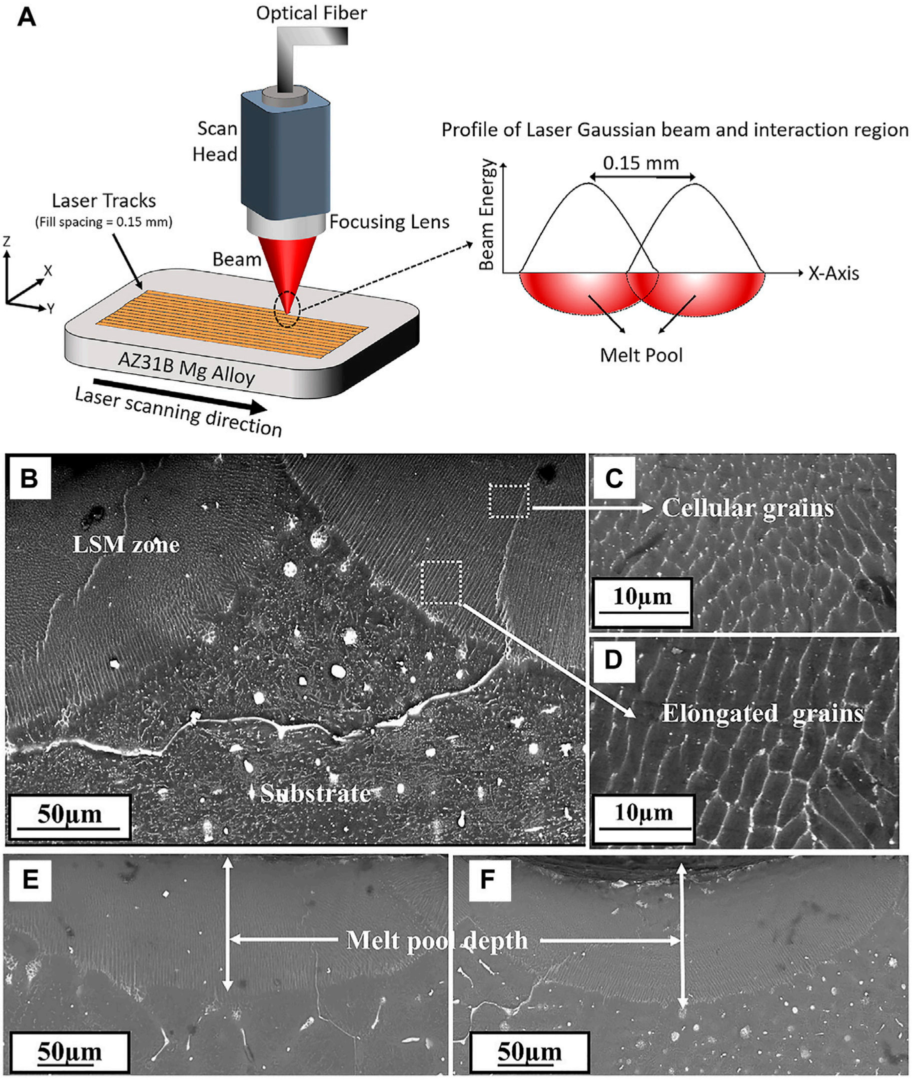

FIGURE 10
(A) Schematic of laser surface modification process; SEM images of cross section microstructure **(B)** laser melted Mg-Zn-Dy alloy, **(C)** and **(D)** enlarged views, **(E)** and **(F)** meltpool depth of the alloy processed at different conditions respectively. Reprinted with permission from reference (Rakesh et al., 2019), Elsevier.

3.2.2.1 Surface mechanical attrition

Surface mechanical grinding treatment (SMAT) is a promising surface nanocrystallization technique, which can refine grains to nanoscale and form gradient nanostructures without changing the composition of materials. It has a significant effect on the improvement of the corrosion resistance of Mg alloys. After SMAT, the microstructure of Mg alloys is fine and uniform, the surface is relatively smoother, and the corrosion rate is significantly reduced (Xia et al., 2016). The surface and cross-section morphologies of Mg and Mg alloy after SMAT as indicated in Figure 8. For instance, Laleh and Kargar (2011) performed SMAT process on AZ91D Mg alloy and found that the corrosion rate was significantly reduced. However, studies have been shown that the degradation resistance of Mg after SMAT decreases due to the increased crystal defect density after grain refinement and surface contamination caused by the attrition balls (Li et al., 2014; Skowron et al., 2020). Similarly, Chen et al. (2019a) reported that the H_2 release, weight loss, and the corrosion rate of the alloy after SMAT were twice as high as those of the untreated alloy due to the increased surface roughness. In summary, it can be considered that SMAT is less effective for improving the performances of biomedical Mg alloys. In the future, composite technology should be developed towards combining SMAT with other effective surface coating techniques.

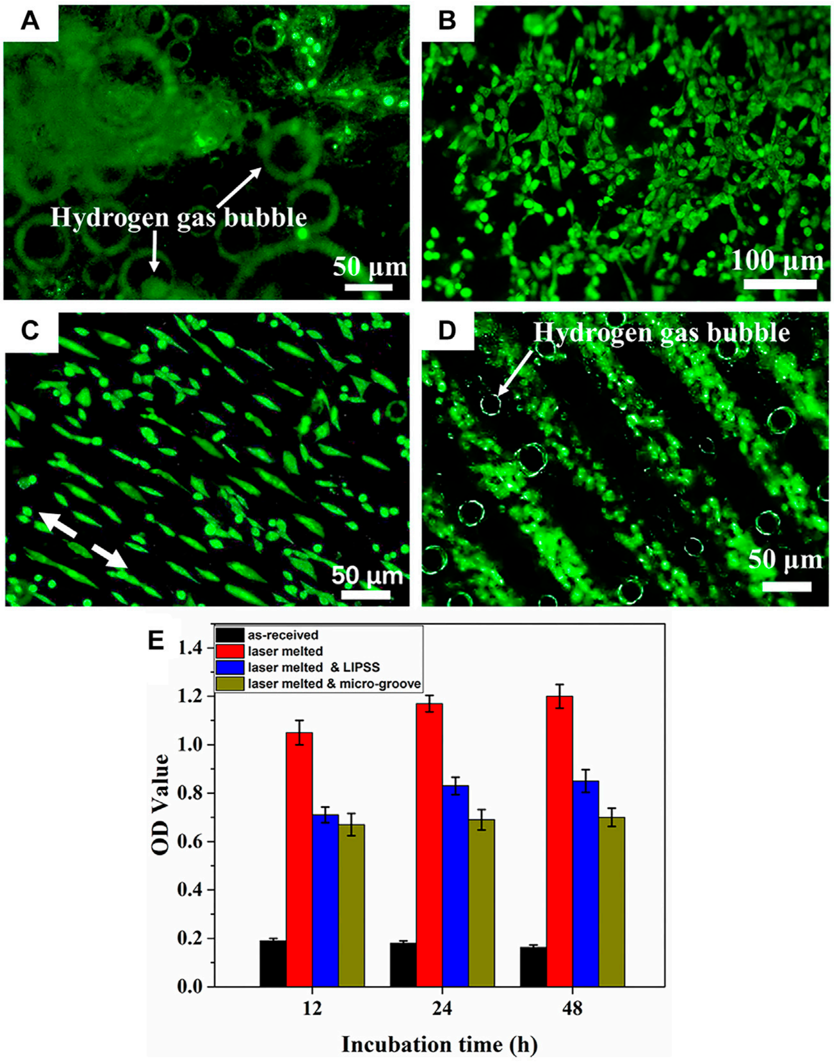

FIGURE 11
Fluorescence images of the MC3T3-E1 cell on **(A)** as-received, **(B)** laser melted, **(C)** laser melted and LIPSS, **(D)** laser melted and micro-groove surface and **(E)** cell proliferation after cultured for 48 h. Reprinted with permission from reference (Zhang et al., 2019), Elsevier.

3.2.2.2 Shot peening

Shot peening is also a common surface modification technique that introduce compressive residual stress to the Mg surface through a similar principle to SMAT technique. The plastically deformed zone formed by the shot peening process has an extended and refined grain structure (Kovacı et al., 2019). The representative microstructure of Mg alloys after shot peening is show in Figure 9. Mhaede et al. (2014) found that shot peening is a good way to improve microhardness and degradation resistance by refining grains and increasing the density of coating. Similarly, Yao et al. (2021) performed shot peening on AZ91 alloys after zinc coating and demonstrated that shot peening increased the densification of Zn coating, increasing the microhardness, and corrosion resistance. The H_2 release and weight loss were reduced significantly for the shot-peened Zn-coated samples, compared to the bare sample. In addition, Bagherifard et al. (2018) investigated the effects of sever shot peening on the properties of AZ31 Mg alloy. They observed higher i_{corr} values, the cell viability was no obvious improvement for different shot-peened samples, which could be attributed to the rough surface layer after shot peening. Similarly, Peral et al. (2020) also demonstrated that higher surface roughness during shot peening promoted the rapid degradation. Therefore, similar to SMAT, shot peening is limited for improving the biological function of Mg alloys. In the future, we should focus on the development of composite techniques combining shot peening and coating preparation processes.

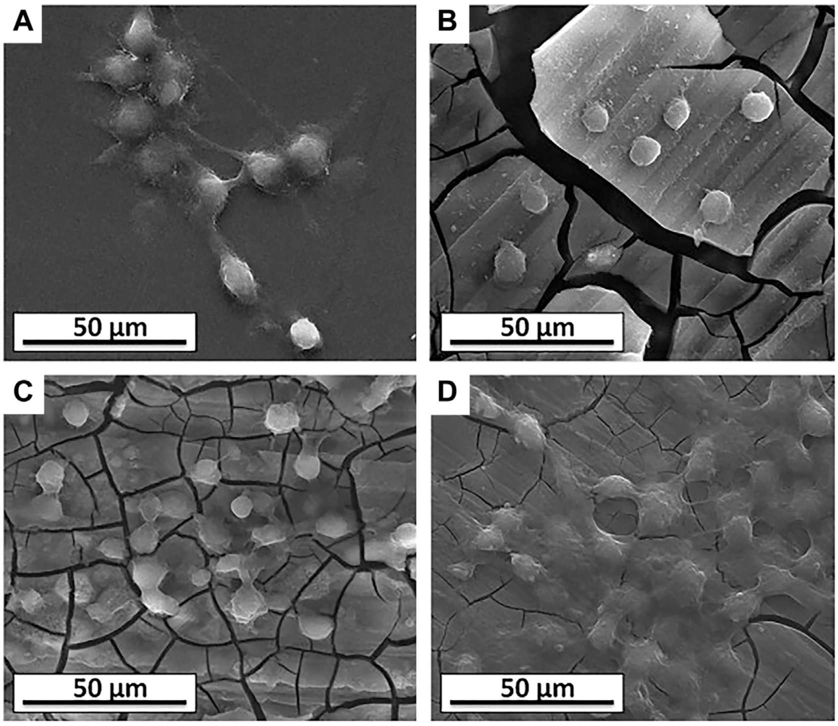

FIGURE 12
SEM morphologies of the L6 cells on the surface of the samples: **(A)** control, **(B)** Mg, **(C)** FSP-Mg, and **(D)** FSP-Mg-nHA. Reprinted with permission from reference (Sunil et al., 2014a), Elsevier.

3.2.2.3 Laser surface modification

Laser surface modification technology is an effective method to modify the material surface through melting by high intensity laser beam due to its high efficiency, no pollution, and low material consumption (Liu et al., 2020b; Hafeez et al., 2021). The schematic of laser surface modification is illustrated in Figure 10A. After laser surface modification, the microstructure of the alloy surface is changed significantly, such as the formation of fine dendritic grain layer without obvious porosity (Figures 10B–E). Nowadays, laser surface modification, mainly including the laser surface melting (Mistry and Vadali, 2022), laser cladding (Gao et al., 2022), and laser surface alloying (Yang et al., 2022), have been extensively applied in surface engineering.

In particular, Among these techniques, laser surface melting has attracted extensive attention to enhance the mechanical performances and corrosion resistance of Mg alloys due to the absence of additional alloying elements and a natural metallurgical bonding interface (Afzal et al., 2015). Numerous studies have been conducted on the microstructure and mechanical performances of Mg alloys after LSM treatment. For instance, Wu et al. (2021) used LSM for surface modification of AZ31B alloy, and found that the grain growth along the Z direction and form a cellular/dendritic microstructure, with the $Mg_{17}Al_{12}$ phase uniformly distributed along the grain boundaries. Liu et al. (2015a) also found that the microstructure of AM60B Mg alloy was composed of refined α-Mg grains and uniformly distributed secondary phases after laser surface melting. Guan et al. (2010) observed that the β-$Mg_{17}Al_{12}$ phases refined and Al concentration increased in AZ91 Mg alloy after laser melting, causing a decrease of corrosion rate by 70%.

In addition, the effect of surface texture formed during the LSM process on the degradation behavior of Mg alloys has been reported by Zhang et al. (2019). The LSM-treated Mg alloys not only improved mechanical performances and the degradation resistance, but also promoted cells adhesion and proliferation along the direction of LSM-induced nanotexture (Figure 11). Manne et al. (2018) investigated the effect of different laser powers and scanning speeds of LSM on Mg-2.2Zn alloy, and found that the most refined morphology was obtained at a power of 125 W and a scanning speed of 30 mm/s. The corrosion rate of Mg-2.2Zn alloy in HBSS was reduced by more than 40%, and the biomineralization was improved due to the enhanced surface energy for the LSM-treated substrate. In summary, laser surface modification can improve the cytocompatibility and corrosion resistance of Mg alloys by improving the surface microstructure of the substrate, efforts should be devoted to optimizing the process parameters and carrying out more in-depth research in the future.

3.2.2.4 Friction stir processing

A microstructural modification method called friction stir processing (FSP), with a principle similar to friction stir welding (FSW), which is developed by Mishra (Mishra and Ma, 2005), is generally used for mechanical property enhancement and surface composite fabrication of light alloy (Cao et al., 2018; Gu et al., 2019; Wang et al., 2020b). FSP is an effective technique that can produce fine grains and uniform microstructures and improve mechanical performances in base materials (Wang et al., 2015a; Wang et al., 2017). Darras et al. (2007) obtained fine grains and homogenous microstructure by a single-pass FSP. Similarly, Cavaliere and De Marco (2007) observed that the AZ91 alloy exhibited superplasticity with an elongation of 1,050% at 300°C and 10^{-4} s^{-1} due to the grain refinement after FSP. In addition, FSP is also beneficial to the corrosion resistance of Mg alloys, which has been applied to optimize surface microstructure or to prepare a composite layer on the substrate surface in biomedical field (Liu et al., 2018b; Liu et al., 2019a). For instance, Zhu et al. (2013) found that the Mg-Zn-Y-Nd alloy after FSP exhibited uniform equiaxed fine grains (~5 μm), and the intermetallic compounds were refined to nanoscale due to the dynamic recrystallization. Similarly, Liu et al. (2018b) obtained the fine grains and intermetallic compounds in AZ91 Mg alloy by FSP (Figure 11). Besides, they investigated the corrosion resistance of AZ91 alloy before and after FSP, and observed that a dense and continuous β phase layer was formed on the surface of the FSPed sample due to the segregation of fine β phase, which effectually improved the stability and passivity of corrosion product film. Argade et al. (2012) observed that the pitting corrosion potential of Mg-Y-RE alloy after FSP is higher than that of base metal because of the grain refinement and uniform second phase distribution during FSP.

Recently, a large number of researches have been carried out on the fabrication of surface metal composites by FSP (Ding et al., 2016; Saikrishna et al., 2018; Yang et al., 2018; Wang et al., 2021). Three ways of adding reinforcing particles to the alloy surface have been reported (Zhang et al., 2017a; Ran et al., 2018; Wang et al., 2020c; Wang et al., 2022). One is to fill the processed grooves or holes with reinforcing particles, the other is to fill the reinforcing particles between two plates to form a sandwich-like structure, and the third is to pre-assemble the reinforcing particles in a stirring tool with a hollow structure. Generally, surface composites exhibit the combination of grain refinement by FSP and reinforcement particle when the reinforcing phase is incorporated into a substrate (Qin et al., 2018; Qiao et al., 2021). For instance, Jiang et al. (2013) fabricated nano-SiO_2/AZ31 Mg composites with FSP and found the addition of nano-SiO_2 could refine the grain to nanoscale and increase the composite hardness.

Nowadays, Sunil et al. (2014a) and Sunil et al. (2014b) used FSP to embed the nano-hydroxyapatite (nHA) powder (~32 nm) on the Mg surface and successfully prepared a fine-grained Mg-nHA composites for degradable bone implants. After FSP, the grains are obvious refined and the nHA distribution is uniform at the surface of pure Mg. Compared with unprocessed Mg, the Mg-nHA composite exhibits superior bioactivity from *in vitro* bioactivity tests because the presence of apatite formed from nHA particles on the composite surface enhances the biomineralization and reduces the corrosion rate. Cell culture studies indicate that the better cell adhesion and proliferation on the FSP-Mg-nHA composites compared with unprocessed Mg and FSP-Mg (Figure 12). Similarly, Hanas et al. (2018) prepared HA-enhanced AZ31 composites by FSP to obtain better biological activity. Qin et al. (2018) promoted the uniform dispersion of hydroxyapatite to the ZK60 Mg alloy by two-pass FSP, and obtained a surface composite with enhanced corrosion resistance. Similarly, Qiao et al. (2022) used multi-pass FSP to prepare the ZrO_2 particles reinforced AZ31 Mg composites, and found that with the increase of the pass, the distribution of strengthening particles was more uniform, and the mechanical performances and corrosion resistance were significantly improved.

As a solid-state microstructure modification technology, FSP plays a great role in improving the properties of Mg alloys. On the one hand, the grains are refined and surface defects are eliminated due to the sever plastic deformation during FSP. On the other hand, it can be combined with other technologies or reinforcement materials to simultaneously improve the mechanical and biological properties of materials. In summary, it is a promising research direction for developing FSP technology to modify the microstructure and prepare Mg-based composites for biomedical applications.

4 Conclusion

Mg alloys are considered to be a promising biodegradable implant material due to their biodegradability, good biocompatibility, and biomechanical compatibility, which is should be further investigated to develop the Mg and Mg alloys for biomedical applications. This review mainly summaries the degradation mechanism of Mg alloys under the action of various condition and stress, and the commonly emphasized surface modification methods, such as chemical conversion, micro-arc oxidation, sol-gel, ion implantation, surface mechanical attrition, shot peening, laser surface modification, and FSP. For biomedical Mg alloys, the rapid degradation rate, and insufficient mechanical performances limit their clinical application as load-bearing parts. Therefore, it is necessary to clarify the degradation mechanism of Mg alloys under the action of complex condition and stress. Secondly, it is need to realize the controllability of the degradation rate of Mg alloys on the basis of ensuring biocompatibility and safety. Ultimately, it should be combined with surface modification technology to improve the mechanical performances and corrosion resistance in the future.

Author contributions

TZ: organized the data and drafted the full manuscript. WW, JL, LW, YT, and KW: contributed to the sections and critically revised the manuscript. All authors contributed to the manuscript revision and read and approved the submitted revision.

Funding

The authors would like to acknowledge the financial support provided by the National Science Foundation under Grant Nos. 51831011, Guangxi Science and Technology Program [Guike Jizi (2020) No. 198], Guangxi key R&D Project (Guike AB18050008).

Conflict of interest

Publisher’s note

References

Afzal, M., Khan, A. N., Mahmud, T. B., Khan, T., and Ajmal, M. (2015). Effect of laser melting on plasma sprayed WC-12 wt.% Co coatings. *Surf. Coat. Technol.* 266, 22–30. doi:10.1016/j.surfcoat.2015.02.004

Agarwal, S., Curtin, J., Duffy, B., and Jaiswal, S. (2016). Biodegradable magnesium alloys for orthopaedic applications: A review on corrosion, biocompatibility and surface modifications. *Mater. Sci. Eng. C* 68, 948–963. doi:10.1016/j.msec.2016.06.020

Amiriafshar, M., Rafieazad, M., Duan, X., and Nasiri, A. (2020). Fabrication and coating adhesion study of superhydrophobic stainless steel surfaces: The effect of substrate surface roughness. *Surf. Interfaces* 20, 100526. doi:10.1016/j.surfin.2020.100526

Amukarimi, S., and Mozafari, M. (2021). Biodegradable magnesium-based biomaterials: An overview of challenges and opportunities. *MedComm* 2, 123–144. doi:10.1002/mco2.59

Argade, G., Kandasamy, K., Panigrahi, S., and Mishra, R. (2012). Corrosion behavior of a friction stir processed rare-Earth added magnesium alloy. *Corros. Sci.* 58, 321–326. doi:10.1016/j.corsci.2012.01.007

Atrens, A., Johnston, S., Shi, Z., and Dargusch, M. S. (2018). Viewpoint - understanding Mg corrosion in the body for biodegradable medical implants. *Scr. Mat.* 154, 92–100. doi:10.1016/j.scriptamat.2018.05.021

Bagherifard, S. (2019). Enhancing the structural performance of lightweight metals by shot peening. *Adv. Eng. Mat.* 21, 1801140. doi:10.1002/adem.201801140

Bagherifard, S., Hickey, D. J., Fintová, S., Pastorek, F., Fernandez-Pariente, I., Bandini, M., et al. (2018). Effects of nanofeatures induced by severe shot peening (SSP) on mechanical, corrosion and cytocompatibility properties of magnesium alloy AZ31. *Acta Biomater.* 66, 93–108. doi:10.1016/j.actbio.2017.11.032

Banerjee, P., Saadi, S., Choudhary, L., Harandi, S. E., and Singh, R. (2019). Magnesium implants: Prospects and challenges. *Materials* 12, 136. doi:10.3390/ma12010136

Banjanin, N., and Belojevic, G. (2018). Changes of blood pressure and hemodynamic parameters after oral magnesium supplementation in patients with essential hypertension—An intervention study. *Nutrients* 10, 581. doi:10.3390/nu10050581

Barajas, J., Joya, J., Durán, K., Hernández-Barrios, C., Coy, A., Viejo, F., et al. (2019). Relationship between microstructure and formation-biodegradation mechanism of fluoride conversion coatings synthesised on the AZ31 magnesium alloy. *Surf. Coat. Technol.* 374, 424–436. doi:10.1016/j.surfcoat.2019.06.010

Becerra, L. H. C., Rodríguez, M. A. L. H., Solís, H. E., Arroyo, R. L., and Castro, A. T. (2020). Bio-inspired biomaterial Mg–Zn–Ca: A review of the main mechanical and biological properties of Mg-based alloys. *Biomed. Phys. Eng. Express* 6, 042001. doi:10.1088/2057-1976/ab9426

Bîrcă, A. C., Neacşu, I. A., Vasile, O. R., Ciucă, I., Vasile, I. M., Fayeq, M. A., et al. (2018). Mg–Zn alloys, most suitable for biomedical applications. *Rom. J. Morphol. Embryol.* 59, 49–54.

Bornapour, M., Muja, N., Shum-Tim, D., Cerruti, M., and Pekguleryuz, M. (2013). Biocompatibility and biodegradability of Mg–Sr alloys: The formation of Sr-substituted hydroxyapatite. *Acta Biomater.* 9, 5319–5330. doi:10.1016/j.actbio.2012.07.045

Cai, L., Mei, D., Zhang, Z. Q., Huang, Y., Cui, L.-Y., Guan, S.-K., et al. (2022). Advances in bioorganic molecules inspired degradation and surface modifications on Mg and its alloys. *J. Magnesium Alloys* 10, 670–688. doi:10.1016/j.jma.2022.02.005

Cao, F., Shi, Z., Hofstetter, J., Uggowitzer, P. J., Song, G., Liu, M., et al. (2013). Corrosion of ultra-high-purity Mg in 3.5% NaCl solution saturated with $Mg\,(OH)_2$. *Corros. Sci.* 75, 78–99. doi:10.1016/j.corsci.2013.05.018

Cao, X., Shi, Q., Liu, D., Feng, Z., Liu, Q., Chen, G., et al. (2018). Fabrication of *in situ* carbon fiber/aluminum composites via friction stir processing: Evaluation of microstructural, mechanical and tribological behaviors. *Compos. Part B Eng.* 139, 97–105. doi:10.1016/j.compositesb.2017.12.001

Cavaliere, P., and De Marco, P. (2007). Superplastic behaviour of friction stir processed AZ91 magnesium alloy produced by high pressure die cast. *J. Mat. Process. Technol.* 184, 77–83. doi:10.1016/j.jmatprotec.2006.11.005

Chen, G., Fu, Y., Cui, Y., Gao, J., Guo, X., Gao, H., et al. (2019a). Effect of surface mechanical attrition treatment on corrosion fatigue behavior of AZ31B magnesium alloy. *Int. J. Fatigue* 127, 461–469. doi:10.1016/j.ijfatigue.2019.06.031

Chen, J., Tan, L., Yu, X., Etim, I. P., Ibrahim, M., Yang, K., et al. (2018). Mechanical properties of magnesium alloys for medical application: A review. *J. Mech. Behav. Biomed. Mat.* 87, 68–79. doi:10.1016/j.jmbbm.2018.07.022

Chen, J., Tan, L., Yu, X., and Yang, K. (2019b). Effect of minor content of Gd on the mechanical and degradable properties of as-cast Mg-2Zn-xGd-0.5 Zr alloys. *J. Mat. Sci. Technol.* 35, 503–511. doi:10.1016/j.jmst.2018.10.022

Chen, K., Dai, J., and Zhang, X. (2015). Improvement of corrosion resistance of magnesium alloys for biomedical applications. *Corros. Rev.* 33, 101–117. doi:10.1515/corrrev-2015-0007

Chen, X. B., Nisbet, D. R., Li, R. W., Smith, P., Abbott, T. B., Easton, M. A., et al. (2014a). Controlling initial biodegradation of magnesium by a biocompatible strontium phosphate conversion coating. *Acta Biomater.* 10, 1463–1474. doi:10.1016/j.actbio.2013.11.016

Chen, X. B., Yang, H. Y., Abbott, T. B., Easton, M. A., and Birbilis, N. (2014b). Corrosion protection of magnesium and its alloys by metal phosphate conversion coatings. *Surf. Eng.* 30, 871–879. doi:10.1179/1743294413Y.0000000235

Chin, P., Cheok, Q., Glowacz, A., and Caesarendra, W. (2020). A review of *in-vivo* and *in-vitro* real-time corrosion monitoring systems of biodegradable metal implants. *Appl. Sci. (Basel).* 10, 3141. doi:10.3390/app10093141

Cho, D. H., Lee, B. W., Park, J. Y., Cho, K. M., and Park, I. M. (2017). Effect of Mn addition on corrosion properties of biodegradable Mg-4Zn-0.5 Ca-xMn alloys. *J. Alloys Compd.* 695, 1166–1174. doi:10.1016/j.jallcom.2016.10.244

Cui, X., Fu, W., Fang, D., Bi, G., Ren, Z., Guo, S., et al. (2021). Mechanical properties and deformation mechanisms of a novel fine-grained Mg-Gd-Y-Ag-Zr-Ce alloy with high strength-ductility synergy. *J. Mat. Sci. Technol.* 66, 64–73. doi:10.1016/j.jmst.2020.05.028

Darras, B., Khraisheh, M., Abu-Farha, F., and Omar, M. (2007). Friction stir processing of commercial AZ31 magnesium alloy. *J. Mat. Process. Technol.* 191, 77–81. doi:10.1016/j.jmatprotec.2007.03.045

Ding, D., Roth, J., and Salvi, R. (2011). Manganese is toxic to spiral ganglion neurons and hair cells *in vitro*. *Neurotoxicology* 32, 233–241. doi:10.1016/j.neuro.2010.12.003

Ding, W. (2016). Opportunities and challenges for the biodegradable magnesium alloys as next-generation biomaterials. *Regen. Biomater.* 3, 79–86. doi:10.1093/rb/rbw003

Ding, Y., Wen, C., Hodgson, P., and Li, Y. (2014). Effects of alloying elements on the corrosion behavior and biocompatibility of biodegradable magnesium alloys: A review. *J. Mat. Chem. B* 2, 1912–1933. doi:10.1039/c3tb21746a

Ding, Z., Zhang, C., Xie, L., Zhang, L. C., Wang, L., Lu, W., et al. (2016). Effects of friction stir processing on the phase transformation and microstructure of TiO2-compounded Ti-6Al-4V alloy. *Metall. Mat. Trans. A* 47, 5675–5679. doi:10.1007/s11661-016-3809-8

Dobkowska, A., Adamczyk–Cieślak, B., Koralnik, M., Chromiński, W., Kubasek, J., Ciftci, J., et al. (2021). Corrosion behavior of fine-grained Mg-7.5 Li-3Al-1Zn fabricated by extrusion with a forward-backward rotating die (KoBo). *J. Magnesium Alloys* 10, 811–820. doi:10.1016/j.jma.2021.08.020

Dong, J., Lin, T., Shao, H., Wang, H., Wang, X., Song, K., et al. (2022a). Advances in degradation behavior of biomedical magnesium alloys: A review. *J. Alloys Compd.* 908, 164600. doi:10.1016/j.jallcom.2022.164600

Dong, Y., Wang, T., Xu, Y., Guo, Y., Li, G., Lian, J., et al. (2022b). A polydopamine-based calcium phosphate/graphene oxide composite coating on magnesium alloy to improve corrosion resistance and biocompatibility for biomedical applications. *Materialia* 21, 101315. doi:10.1016/j.mtla.2022.101315

Du, X., Xi, T., Yang, C., Zhao, H., and Yang, K. (2022). Cu addition retards the static recrystallization of cold-deformed 316L biomedical stainless steel. *J. Mater. Res. Technol.* 19, 1673–1677. doi:10.1016/j.jmrt.2022.05.155

Feyerabend, F., Fischer, J., Holtz, J., Witte, F., Willumeit, R., Drücker, H., et al. (2010). Evaluation of short-term effects of rare Earth and other elements used in magnesium alloys on primary cells and cell lines. *Acta Biomater.* 6, 1834–1842. doi:10.1016/j.actbio.2009.09.024

Figueira, R. B., Fontinha, I. R., Silva, C. J., and Pereira, E. V. (2016). Hybrid sol-gel coatings: Smart and green materials for corrosion mitigation. *Coatings* 6, 12. doi:10.3390/coatings6010012

Figueira, R. B. (2020). Hybrid sol–gel coatings for corrosion mitigation: A critical review. *Polymers* 12, 689. doi:10.3390/polym12030689

Fintová, S., Drábiková, J., Pastorek, F., Tkacz, J., Kuběna, I., Trško, L., et al. (2019). Improvement of electrochemical corrosion characteristics of AZ61 magnesium alloy with unconventional fluoride conversion coatings. *Surf. Coat. Technol.* 357, 638–650. doi:10.1016/j.surfcoat.2018.10.038

Gao, F., Xu, C., Hu, H., Wang, Q., Gao, Y., Chen, H., et al. (2015). Biomimetic synthesis and characterization of hydroxyapatite/graphene oxide hybrid coating on Mg alloy with enhanced corrosion resistance. *Mat. Lett.* 138, 25–28. doi:10.1016/j.matlet.2014.09.088

Gao, M., Li, S., Guan, W., Xie, H., Wang, X., Liu, J., et al. (2022). Excellent thermal shock resistance of NiCrAlY coatings on copper substrate via laser cladding. *J. Mat. Sci. Technol.* 130, 93–102. doi:10.1016/j.jmst.2022.05.011

Gu, H., Ding, Z., Yang, Z., Yu, W., Zhang, W., Lu, W., et al. (2019). Microstructure evolution and electrochemical properties of TiO2/Ti-35Nb-2Ta-3Zr micro/nano-composites fabricated by friction stir processing. *Mat. Des.* 169, 107680. doi:10.1016/j.matdes.2019.107680

Gu, X., Zheng, Y., and Chen, L. (2009). Influence of artificial biological fluid composition on the biocorrosion of potential orthopedic Mg–Ca, AZ31, AZ91 alloys. *Biomed. Mat.* 4, 065011. doi:10.1088/1748-6041/4/6/065011

Guan, Y., Zhou, W., Zheng, H., and Li, Z. (2010). Solidification microstructure of AZ91D Mg alloy after laser surface melting. *Appl. Phys. A* 101, 339–344. doi:10.1007/s00339-010-5880-0

Hafeez, N., Liu, S., Lu, E., Wang, L., Liu, R., lu, W., et al. (2019). Mechanical behavior and phase transformation of β-type Ti-35Nb-2Ta-3Zr alloy fabricated by 3D-Printing. *J. Alloys Compd.* 790, 117–126. doi:10.1016/j.jallcom.2019.03.138

Hafeez, N., Wei, D., Xie, L., Tang, Y., Liu, J., Kato, H., et al. (2021). Evolution of microstructural complex transitions in low-modulus β-type Ti-35Nb-2Ta-3Zr alloy manufactured by laser powder bed fusion. *Addit. Manuf.* 48, 102376. doi:10.1016/j.addma.2021.102376

Hanas, T., Kumar, T. S., Perumal, G., Doble, M., and Ramakrishna, S. (2018). Electrospun PCL/HA coated friction stir processed AZ31/HA composites for degradable implant applications. *J. Mat. Process. Technol.* 252, 398–406. doi:10.1016/j.jmatprotec.2017.10.009

Hernandez, L., Gonzalez, J. E., Barranco, V., Veranes-Pantoja, Y., Galván, J., Gattorno, G. R., et al. (2022). Biomimetic hydroxyapatite (HAp) coatings on pure Mg and their physiological corrosion behavior. *Ceram. Int.* 48, 1208–1222. doi:10.1016/j.ceramint.2021.09.206

Hu, J., Zhang, C., Cui, B., Bai, K., Guan, S., Wang, L., et al. (2011). *In vitro* degradation of AZ31 magnesium alloy coated with nano TiO2 film by sol–gel method. *Appl. Surf. Sci.* 257, 8772–8777. doi:10.1016/j.apsusc.2011.03.148

Jamesh, M. I., Wu, G., Zhao, Y., Jin, W., McKenzie, D. R., Bilek, M. M., et al. (2014). Effects of zirconium and nitrogen plasma immersion ion implantation on the electrochemical corrosion behavior of Mg–Y–RE alloy in simulated body fluid and cell culture medium. *Corros. Sci.* 86, 239–251. doi:10.1016/j.corsci.2014.05.020

Jang, Y., Collins, B., Sankar, J., and Yun, Y. (2013). Effect of biologically relevant ions on the corrosion products formed on alloy AZ31B: An improved understanding of magnesium corrosion. *Acta Biomater.* 9, 8761–8770. doi:10.1016/j.actbio.2013.03.026

Jia, Y., Ba, Z., Dong, Q., Li, Z., and Kuang, J. (2018). Surface properties of magnesium improved by Sr ion implantation. *Mat. Res. Express* 5, 066546. doi:10.1088/2053-1591/aacc12

Jiang, Y., Yang, X., Miura, H., and Sakai, T. (2013). Particles reinforced magnesium alloy produced by friction stir processing. *Rev. Adv. Mat. Sci.* 33, 29–32.

Johnson, I., Perchy, D., and Liu, H. (2012). *In vitro* evaluation of the surface effects on magnesium-yttrium alloy degradation and mesenchymal stem cell adhesion. *J. Biomed. Mat. Res. A* 100, 477–485. doi:10.1002/jbm.a.33290

Jönsson, M., Thierry, D., and LeBozec, N. (2006). The influence of microstructure on the corrosion behaviour of AZ91D studied by scanning Kelvin probe force microscopy and scanning Kelvin probe. *Corros. Sci.* 48, 1193–1208. doi:10.1016/j.corsci.2005.05.008

Jung, O., Porchetta, D., Schroeder, M.-L., Klein, M., Wegner, N., Walther, F., et al. (2019). *In vivo* simulation of magnesium degradability using a new fluid dynamic bench testing approach. *Int. J. Mol. Sci.* 20, 4859. doi:10.3390/ijms20194859

Kania, A., Pilarczyk, W., and Szindler, M. M. (2020). Structure and corrosion behavior of TiO2 thin films deposited onto Mg-based alloy using magnetron sputtering and sol-gel. *Thin Solid Films* 701, 137945. doi:10.1016/j.tsf.2020.137945

Kirkland, N., Kolbeinsson, I., Woodfield, T., Dias, G., and Staiger, M. (2011). Synthesis and properties of topologically ordered porous magnesium. *Mater. Sci. Eng. B* 176, 1666–1672. doi:10.1016/j.mseb.2011.04.006

Klu, E. E., Song, D., Li, C., Wang, G., Gao, B., Ma, A., et al. (2022). Achieving ultra-fine grains and high strength of Mg–9Li alloy via room-temperature ECAP and post rolling. *Mater. Sci. Eng. A* 833, 142371. doi:10.1016/j.msea.2021.142371

Koç, E., Kannan, M. B., Ünal, M., and Candan, E. (2015). Influence of zinc on the microstructure, mechanical properties and *in vitro* corrosion behavior of magnesium–zinc binary alloys. *J. Alloys Compd.* 648, 291–296. doi:10.1016/j.jallcom.2015.06.227

Kovacı, H., Bozkurt, Y. B., Yetim, A. F., Aslan, M., and Çelik, A. (2019). The effect of surface plastic deformation produced by shot peening on corrosion behavior of a low-alloy steel. *Surf. Coat. Technol.* 360, 78–86. doi:10.1016/j.surfcoat.2019.01.003

Kumar, K., Gill, R., and Batra, U. (2018). Challenges and opportunities for biodegradable magnesium alloy implants. *Mat. Technol. (N. Y. N. Y).* 33, 153–172. doi:10.1080/10667857.2017.1377973

Laleh, M., and Kargar, F. (2011). Effect of surface nanocrystallization on the microstructural and corrosion characteristics of AZ91D magnesium alloy. *J. Alloys Compd.* 509, 9150–9156. doi:10.1016/j.jallcom.2011.06.094

Li, N., Li, Y., Li, Y., Wu, Y., Zheng, Y., Han, Y., et al. (2014). Effect of surface mechanical attrition treatment on biodegradable Mg–1Ca alloy. *Mater. Sci. Eng. C* 35, 314–321. doi:10.1016/j.msec.2013.11.010

Li, W., Qiao, W., Liu, X., Bian, D., Shen, D., Zheng, Y., et al. (2021). Biomimicking bone–implant interface facilitates the bioadaption of a new degradable magnesium alloy to the bone tissue microenvironment. *Adv. Sci.* 8, 2102035. doi:10.1002/advs.202102035

Li, Y., Hodgson, P. D., and Wen, C. (2011). The effects of calcium and yttrium additions on the microstructure, mechanical properties and biocompatibility of biodegradable magnesium alloys. *J. Mat. Sci.* 46, 365–371. doi:10.1007/s10853-010-4843-3

Lin, B., Zhong, M., Zheng, C., Cao, L., Wang, D., Wang, L., et al. (2015). Preparation and characterization of dopamine-induced biomimetic hydroxyapatite coatings on the AZ31 magnesium alloy. *Surf. Coat. Technol.* 281, 82–88. doi:10.1016/j.surfcoat.2015.09.033

Lin, J., Chen, W., Tang, Q., Cao, L., and Su, S. (2021). Lithium-modified MAO coating enhances corrosion resistance and osteogenic differentiation for pure magnesium. *Surf. Interfaces* 22, 100805. doi:10.1016/j.surfin.2020.100805

Lin, M., Yuan, G., Niu, J., Yang, Z., and Ding, W. (2013). *In vitro* degradation behavior and biocompatibility of Mg-Nd-Zn-Zr alloy by hydrofluoric acid treatment. *Mater. Sci. Eng. C* 33, 242–250. doi:10.1016/j.msec.2012.08.036

Lin, Z., Wu, S., Liu, X., Qian, S., Chu, P. K., Zheng, Y., et al. (2019). A surface-engineered multifunctional TiO2 based nano-layer simultaneously elevates the corrosion resistance, osteoconductivity and antimicrobial property of a magnesium alloy. *Acta Biomater.* 99, 495–513. doi:10.1016/j.actbio.2019.09.008

Liu, C., Liang, J., Zhou, J., Wang, L., and Li, Q. (2015a). Effect of laser surface melting on microstructure and corrosion characteristics of AM60B magnesium alloy. *Appl. Surf. Sci.* 343, 133–140. doi:10.1016/j.apsusc.2015.03.067

Liu, E., Niu, Y., Yu, S., Liu, L., Zhang, K., Bi, X., et al. (2020a). Micro-arc oxidation behavior of fly ash cenospheres/magnesium alloy degradable composite and corrosion resistance of coatings. *Surf. Coat. Technol.* 391, 125693. doi:10.1016/j.surfcoat.2020.125693

Liu, J., Han, E., Song, Y., and Shan, D. (2018a). Effect of twins on the corrosion behavior of Mg–5Y–7Gd–1Nd–0.5 Zr Mg alloy. *J. Alloys Compd.* 757, 356–363. doi:10.1016/j.jallcom.2018.05.105

Liu, J., Zheng, Y., Bi, Y., Li, Y., and Zheng, Y. (2017). Improved cytocompatibility of Mg-1Ca alloy modified by Zn ion implantation and deposition. *Mat. Lett.* 205, 87–89. doi:10.1016/j.matlet.2017.06.055

Liu, Q., Ma, Q., Chen, G., Cao, X., Zhang, S., Pan, J., et al. (2018b). Enhanced corrosion resistance of AZ91 magnesium alloy through refinement and homogenization of surface microstructure by friction stir processing. *Corros. Sci.* 138, 284–296. doi:10.1016/j.corsci.2018.04.028

Liu, S., Han, S., Zhang, L., Chen, L. Y., Wang, L., Zhang, L., et al. (2020b). Strengthening mechanism and micropillar analysis of high-strength NiTi–Nb eutectic-type alloy prepared by laser powder bed fusion. *Compos. Part B Eng.* 200, 108358. doi:10.1016/j.compositesb.2020.108358

Liu, S., Liu, J., Wang, L., Ma, L. W., Zhang, L. C., Lu, W., et al. (2020c). Superelastic behavior of *in-situ* eutectic-reaction manufactured high strength 3D porous NiTi-Nb scaffold. *Scr. Mat.* 181, 121–126. doi:10.1016/j.scriptamat.2020.02.025

Liu, W., Liu, S., and Wang, L. (2019a). Surface modification of biomedical titanium alloy: Micromorphology, microstructure evolution and biomedical applications. *Coatings* 9, 249. doi:10.3390/coatings9040249

Liu, X., Wu, K., Gao, L., Wang, L., and Shi, X. (2021a). Biomaterial strategies for the application of reproductive tissue engineering. *Bioact. Mat.* 14, 86–96. doi:10.1016/j.bioactmat.2021.11.023

Liu, X., Zhen, Z., Liu, J., Xi, T., Zheng, Y., Guan, S., et al. (2015b). Multifunctional MgF2/polydopamine coating on Mg alloy for vascular stent application. *J. Mat. Sci. Technol.* 31, 733–743. doi:10.1016/j.jmst.2015.02.002

Liu, Y., Cheng, W., Gu, X., Liu, Y., Cui, Z., Wang, L., et al. (2021b). Tailoring the microstructural characteristic and improving the corrosion resistance of extruded dilute Mg–0.5 Bi–0.5 Sn alloy by microalloying with Mn. *J. Magnesium Alloys* 9, 1656–1668. doi:10.1016/j.jma.2020.07.010

Liu, Y., Lu, B., and Cai, Z. (2019b). Recent progress on Mg-and Zn-based alloys for biodegradable vascular stent applications. *J. Nanomater.* 2019, 1–16. doi:10.1155/2019/1310792

Liu, Y., Zhang, Y., Wang, Y. L., Tian, Y.-Q., and Chen, L. S. (2021c). Research progress on surface protective coatings of biomedical degradable magnesium alloys. *J. Alloys Compd.* 885, 161001. doi:10.1016/j.jallcom.2021.161001

Lu, X., Mohedano, M., Blawert, C., Matykina, E., Arrabal, R., Kainer, K. U., et al. (2016). Plasma electrolytic oxidation coatings with particle additions–A review. *Surf. Coat. Technol.* 307, 1165–1182. doi:10.1016/j.surfcoat.2016.08.055

Luo, Y., Deng, Y., Guan, L., Ye, L., Guo, X., Luo, A., et al. (2020). Effect of grain size and crystal orientation on the corrosion behavior of as-extruded Mg-6Gd-2Y-0.2 Zr alloy. *Corros. Sci.* 164, 108338. doi:10.1016/j.corsci.2019.108338

Manne, B., Thiruvayapati, H., Bontha, S., Rangarasaiah, R. M., Das, M., Balla, V. K., et al. (2018). Surface design of Mg-Zn alloy temporary orthopaedic implants: Tailoring wettability and biodegradability using laser surface melting. *Surf. Coat. Technol.* 347, 337–349. doi:10.1016/j.surfcoat.2018.05.017

Maurya, R., Siddiqui, A. R., and Balani, K. (2018). An environment-friendly phosphate chemical conversion coating on novel Mg-9Li-7Al-1Sn and Mg-9Li-5Al-3Sn-1Zn alloys with remarkable corrosion protection. *Appl. Surf. Sci.* 443, 429–440. doi:10.1016/j.apsusc.2018.02.254

Mhaede, M., Pastorek, F., and Hadzima, B. (2014). Influence of shot peening on corrosion properties of biocompatible magnesium alloy AZ31 coated by dicalcium phosphate dihydrate (DCPD). *Mater. Sci. Eng. C* 39, 330–335. doi:10.1016/j.msec.2014.03.023

Mirza, A., King, A., Troakes, C., and Exley, C. (2017). Aluminium in brain tissue in familial Alzheimer's disease. *J. Trace Elem. Med. Biol.* 40, 30–36. doi:10.1016/j.jtemb.2016.12.001

Mishra, R. S., and Ma, Z. (2005). Friction stir welding and processing. *Mater. Sci. Eng. R Rep.* 50, 1–78. doi:10.1016/j.mser.2005.07.001

Mistry, U., and Vadali, M. (2022). A steady-state semi-analytical approximation of melt pool evolution in pulsed laser surface melting. *J. Manuf. Process* 74, 123–135. doi:10.31224/osf.io/2kzca

Mohamed, A., El-Aziz, A. M., and Breitinger, H. G. (2019). Study of the degradation behavior and the biocompatibility of Mg–0.8 Ca alloy for orthopedic implant applications. *J. Magnesium Alloys* 7, 249–257. doi:10.1016/j.jma.2019.02.007

Mueller, W.-D., Fernandez Lorenzo de Mele, M., Nascimento, M. L., and Zeddies, M. (2009). Degradation of magnesium and its alloys: Dependence on the composition of the synthetic biological media. *J. Biomed. Mat. Res. A* 90, 487–495. doi:10.1002/jbm.a.32106

Nezamdoust, S., Seifzadeh, D., and Rajabalizadeh, Z. (2018). PTMS/OH-MWCNT sol-gel nanocomposite for corrosion protection of magnesium alloy. *Surf. Coat. Technol.* 335, 228–240. doi:10.1016/j.surfcoat.2017.12.044

Nie, Y., Dai, J., Li, X., and Zhang, X. (2021). Recent developments on corrosion behaviors of Mg alloys with stacking fault or long period stacking ordered structures. *J. Magnesium Alloys* 9, 1123–1146. doi:10.1016/j.jma.2020.09.021

Omar, S. A., Ballarre, J., Castro, Y., Campos, E. M., Schreiner, W., Durán, A., et al. (2020). 58S and 68S sol-gel glass-like bioactive coatings for enhancing the implant performance of AZ91D magnesium alloy. *Surf. Coat. Technol.* 400, 126224. doi:10.1016/j.surfcoat.2020.126224

O'Neill, E., Awale, G., Daneshmandi, L., Umerah, O., and Lo, K. W. H. (2018). The roles of ions on bone regeneration. *Drug Discov. Today* 23, 879–890. doi:10.1016/j.drudis.2018.01.049

Owens, G. J., Singh, R. K., Foroutan, F., Alqaysi, M., Han, C.-M., Mahapatra, C., et al. (2016). Sol–gel based materials for biomedical applications. *Prog. Mat. Sci.* 77, 1–79. doi:10.1016/j.pmatsci.2015.12.001

Pal, S., Finšgar, M., Bončina, T., Lojen, G., Brajlih, T., Drstvenšek, I., et al. (2021). Effect of surface powder particles and morphologies on corrosion of Ti-6Al-4 V fabricated with different energy densities in selective laser melting. *Mat. Des.* 211, 110184. doi:10.1016/j.matdes.2021.110184

Pekguleryuz, M. O., Kainer, K., and Kaya, A. (2013). *Fundamentals of magnesium alloy metallurgy*. Elsevier. doi:10.1533/9780857097293.backmatter

Peral, L., Zafra, A., Bagherifard, S., Guagliano, M., and Fernández-Pariente, I. (2020). Effect of warm shot peening treatments on surface properties and corrosion behavior of AZ31 magnesium alloy. *Surf. Coat. Technol.* 401, 126285. doi:10.1016/j.surfcoat.2020.126285

Pereda, M. D., Alonso, C., Gamero, M., Del Valle, J., and De Mele, M. F. L. (2011). Comparative study of fluoride conversion coatings formed on biodegradable powder metallurgy Mg: The effect of chlorides at physiological level. *Mater. Sci. Eng. C* 31, 858–865. doi:10.1016/j.msec.2011.01.010

Prasad, A., Uggowitzer, P. J., Shi, Z. M., and Atrens, A. (2013). Production of high purity Mg-X rare Earth binary alloys using Zr. *Mat. Sci. Forum.* 765, 301–305. doi:10.4028/www.scientific.net/MSF.765.301

Qiao, K., Zhang, T., Wang, K., Yuan, S., Wang, L., Chen, S., et al. (2022). Effect of multi-pass friction stir processing on the microstructure evolution and corrosion behavior of ZrO2/AZ31 magnesium matrix composite. *J. Mater. Res. Technol.* 18, 1166–1179. doi:10.1016/j.jmrt.2022.02.127

Qiao, K., Zhang, T., Wang, K., Yuan, S., Zhang, S., Wang, L., et al. (2021). Mg/ZrO2 metal matrix nanocomposites fabricated by friction stir processing: Microstructure, mechanical properties, and corrosion behavior. *Front. Bioeng. Biotechnol.* 9, 605171. doi:10.3389/fbioe.2021.605171

Qiao, Z., Shi, Z., Hort, N., Abidin, N. I. Z., and Atrens, A. (2012). Corrosion behaviour of a nominally high purity Mg ingot produced by permanent mould direct chill casting. *Corros. Sci.* 61, 185–207. doi:10.1016/j.corsci.2012.04.030

Qin, D., Shen, H., Shen, Z., Chen, H., and Fu, L. (2018). Manufacture of biodegradable magnesium alloy by high speed friction stir processing. *J. Manuf. Process.* 36, 22–32. doi:10.1016/j.jmapro.2018.09.019

Qin, Y., Wen, P., Guo, H., Xia, D., Zheng, Y., Jauer, L., et al. (2019). Additive manufacturing of biodegradable metals: Current research status and future perspectives. *Acta Biomater.* 98, 3–22. doi:10.1016/j.actbio.2019.04.046

Ragamouni, S., Kumar, J. M., Mushahary, D., Nemani, H., and Pande, G. (2013). Histological analysis of cells and matrix mineralization of new bone tissue induced in rabbit femur bones by Mg–Zr based biodegradable implants. *Acta Histochem.* 115, 748–756. doi:10.1016/j.acthis.2013.03.004

Rahim, S. A., Joseph, M., Sampath Kumar, T., and Hanas, H. (2022). Recent progress in surface modification of Mg alloys for biodegradable orthopedic applications. *Front. Mat.* 9, 848980. doi:10.3389/fmats.2022.848980

Rakesh, K., Bontha, S., Ramesh, M., Das, M., and Balla, V. K. (2019). Laser surface melting of Mg-Zn-Dy alloy for better wettability and corrosion resistance for biodegradable implant applications. *Appl. Surf. Sci.* 480, 70–82. doi:10.1016/j.apsusc.2019.02.167

Ralston, K., Birbilis, N., and Davies, C. (2010). Revealing the relationship between grain size and corrosion rate of metals. *Scr. Mat.* 63, 1201–1204. doi:10.1016/j.scriptamat.2010.08.035

Ran, R., Liu, Y., Wang, L., Lu, E., Xie, L., Lu, W., et al. (2018). α" Martensite and amorphous phase transformation mechanism in TiNbTaZr alloy incorporated with TiO_2 particles during friction stir processing. *Metall. Mat. Trans. A* 49, 1986. doi:10.1007/s11661-018-4577-4

Razavi, M., and Huang, Y. (2019). Assessment of magnesium-based biomaterials: From bench to clinic. *Biomater. Sci.* 7, 2241–2263. doi:10.1039/C9BM00289H

Ren, X. D., Li, X. S., Yang, Y., Yang, Y., and Wu, H. (2017). Corrosion behavior and electrochemical properties of as-cast Mg-2Zn-0.5 Ca-Y series magnesium alloys in Hank's solution and NaCl solution. *Rare Metal Mater. Eng.* 46, 45–50. doi:10.1016/S1875-5372(17)30075-9

Rendon, M., Allain, J. P., Robledo, S. M., Echeverria, F., and Harmsen, M. C. (2019). Coatings for biodegradable magnesium-based supports for therapy of vascular disease: A general view. *Mater. Sci. Eng. C* 102, 150–163. doi:10.1016/j.msec.2019.04.032

Rosalbino, F., De Negri, S., Saccone, A., Angelini, E., and Delfino, S. (2010). Bio-corrosion characterization of Mg–Zn–X (X= Ca, Mn, Si) alloys for biomedical applications. *J. Mat. Sci. Mat. Med.* 21, 1091–1098. doi:10.1007/s10856-009-3956-1

Saad, A. P. M., Rahim, R. A. A., Harun, M. N., Basri, H., Abdullah, J., Kadir, M. R. A., et al. (2017). The influence of flow rates on the dynamic degradation behaviour of porous magnesium under a simulated environment of human cancellous bone. *Mat. Des.* 122, 268–279. doi:10.1016/j.matdes.2017.03.029

Saikrishna, N., Reddy, G. P. K., Munirathinam, B., Dumpala, R., Jagannatham, M., Sunil, B. R., et al. (2018). An investigation on the hardness and corrosion behavior of MWCNT/Mg composites and grain refined Mg. *J. Magnesium Alloys* 6, 83–89. doi:10.1016/j.jma.2017.12.003

Schwalfenberg, G. K., and Genuis, S. J. (2017). The importance of magnesium in clinical healthcare. *Scientifica*, 1–14. doi:10.1155/2017/4179326

Seetharaman, S., Jayalakshmi, S., Arvind Singh, R., and Gupta, M. (2022). The potential of magnesium-based materials for engineering and biomedical applications. *J. Indian Inst. Sci.* 102, 421–437. doi:10.1007/s41745-021-00274-w

Sepulveda, P., Jones, J. R., and Hench, L. L. (2002). Bioactive sol-gel foams for tissue repair. *J. Biomed. Mat. Res.* 59, 340–348. doi:10.1002/jbm.1250

Seuss, F., Seuss, S., Turhan, M., Fabry, B., and Virtanen, S. (2011). Corrosion of Mg alloy AZ91D in the presence of living cells. *J. Biomed. Mat. Res.* 99, 276–281. doi:10.1002/jbm.b.31896

Sezer, N., Evis, Z., Kayhan, S. M., Tahmasebifar, A., and Koç, M. (2018). Review of magnesium-based biomaterials and their applications. *J. Magnesium Alloys* 6, 23–43. doi:10.1016/j.jma.2018.02.003

Skowron, K., Dryzek, E., Wróbel, M., Nowak, P., Marciszko-Wiąckowska, M., Le Joncour, L., et al. (2020). Gradient microstructure induced by surface mechanical attrition treatment (SMAT) in magnesium studied using positron annihilation spectroscopy and complementary methods. *Materials* 13, 4002. doi:10.3390/ma13184002

Somasundaram, S., Ionescu, M., and Mathan, B. K. (2018). Ion implantation of calcium and zinc in magnesium for biodegradable implant applications. *Metals* 8, 30. doi:10.3390/met8010030

StráskÝ, J., Preisler, D., Seiner, H., Bodnárová, L., Janovská, M., Košutová, T., et al. (2022). Achieving high strength and low elastic modulus in interstitial biomedical Ti–Nb–Zr–O alloys through compositional optimization. *Mater. Sci. Eng. A* 839, 142833. doi:10.1016/j.msea.2022.142833

Sunil, B. R., Kumar, T. S., Chakkingal, U., Nandakumar, V., and Doble, M. (2014a). Friction stir processing of magnesium–nanohydroxyapatite composites with controlled *in vitro* degradation behavior. *Mater. Sci. Eng. C* 39, 315–324. doi:10.1016/j.msec.2014.03.004

Sunil, B., Sampath Kumar, T., Chakkingal, U., Nandakumar, V., and Doble, M. (2014b). Nano-hydroxyapatite reinforced AZ31 magnesium alloy by friction stir processing: A solid state processing for biodegradable metal matrix composites. *J. Mat. Sci. Mat. Med.* 25, 975–988. doi:10.1007/s10856-013-5127-7

Tian, P., Xu, D., and Liu, X. (2016). Mussel-inspired functionalization of PEO/PCL composite coating on a biodegradable AZ31 magnesium alloy. *Colloids Surfaces B Biointerfaces* 141, 327–337. doi:10.1016/j.colsurfb.2016.02.004

Virtanen, S. (2011). Biodegradable Mg and Mg alloys: Corrosion and biocompatibility. *Mater. Sci. Eng. B* 176, 1600–1608. doi:10.1016/j.mseb.2011.05.028

Wandelt, K. (2018). *Encyclopedia of interfacial chemistry: Surface science and electrochemistry*. Elsevier.

Wang, J., Giridharan, V., Shanov, V., Xu, Z., Collins, B., White, L., et al. (2014). Flow-induced corrosion behavior of absorbable magnesium-based stents. *Acta Biomater.* 10, 5213–5223. doi:10.1016/j.actbio.2014.08.034

Wang, J. L., Xu, J. K., Hopkins, C., Chow, D. H. K., and Qin, L. (2020a). Biodegradable magnesium-based implants in orthopedics—A general review and perspectives. *Adv. Sci.* 7, 1902443. doi:10.1002/advs.201902443

Wang, L., Lu, W., Qin, J., Zhang, F., and Zhang, D. (2008). Microstructure and mechanical properties of cold-rolled TiNbTaZr biomedical β titanium alloy. *Mater. Sci. Eng. A* 490, 421–426. doi:10.1016/j.msea.2008.03.003

Wang, L., Qu, J., Chen, L., Meng, Q., Zhang, L. C., Qin, J., et al. (2015a). Investigation of deformation mechanisms in β-type Ti-35Nb-2Ta-3Zr alloy via FSP leading to surface strengthening. *Metall. Mat. Trans. A* 46, 4813–4818. doi:10.1007/s11661-015-3089-8

Wang, L., Wang, Y., Huang, W., Liu, J., Tang, Y., Zhang, L., et al. (2020b). Tensile and superelastic behaviors of Ti-35Nb-2Ta-3Zr with gradient structure. *Mat. Des.* 194, 108961. doi:10.1016/j.matdes.2020.108961

Wang, L., Xie, L., Lv, Y., Zhang, L. C., Chen, L., Meng, Q., et al. (2017). Microstructure evolution and superelastic behavior in Ti-35Nb-2Ta-3Zr alloy processed by friction stir processing. *Acta Mat.* 131, 499–510. doi:10.1016/j.actamat.2017.03.07910.1016/j.actamat.2017.03.079

Wang, W., Han, P., Peng, P., Zhang, T., Liu, Q., Yuan, S.-N., et al. (2020c). Friction stir processing of magnesium alloys: A review. *Acta Metall. sin-engl.* 33, 43–57.

Wang, Y., Shi, H., Zhou, P., Tang, Y., Liu, J., Wang, L., et al. (2021). Microstructure evolution and mechanical properties of TiC/Ti6Al4V medical composite processed by severe plastic deformation. *J. Mater. Res. Technol.* 15, 6442–6452. doi:10.1016/j.jmrt.2021.11.090

Wang, Y., Wei, D., Wang, L., Zhang, L., Liu, J., Tang, Y., et al. (2022). Surface modification and twinning behavior in gradient graphene-based TiC/Ti6Al4V composite. *Appl. Surf. Sci.* 583, 152495. doi:10.1016/j.apsusc.2022.152495

Wang, Z., Tao, X., Zhang, X., Ba, Z., and Wang, Q. (2015b). Corrosion behaviour of Nd ion implanted Mg–Gd–Zn–Zr alloy in simulated body fluid. *Mat. Technol. (N. Y. N. Y).* 30, 321–326. doi:10.1179/1753555715Y.0000000004

Wang, Z. X., Zhang, J. W., Ye, F., Lv, W. G., Lu, S., Sun, L., et al. (2020d). Properties of micro-arc oxidation coating fabricated on magnesium under two steps current-decreasing mode. *Front. Mat.* 261. doi:10.3389/fmats.2020.00261

Wei, D., Wang, L., Zhang, Y., Gong, W., Tsuru, T., Lobzenko, I., et al. (2022). Metalloid substitution elevates simultaneously the strength and ductility of face-centered-cubic high-entropy alloys. *Acta Mat.* 225, 117571. doi:10.1016/j.actamat.2021.117571

Wei, Z., Tian, P., Liu, X., and Zhou, B. (2015). *In vitro* degradation, hemolysis, and cytocompatibility of PEO/PLLA composite coating on biodegradable AZ31 alloy. *J. Biomed. Mat. Res.* 103, 342–354. doi:10.1002/jbm.b.33208

Willbold, E., Gu, X., Albert, D., Kalla, K., Bobe, K., Brauneis, M., et al. (2015). Effect of the addition of low rare Earth elements (lanthanum, neodymium, cerium) on the biodegradation and biocompatibility of magnesium. *Acta Biomater.* 11, 554–562. doi:10.1016/j.actbio.2014.09.041

Witter, F. (2010). The history of biodegradable magnesium implants: A review☆. *Acta Biomater.* 6, 1680–1692. doi:10.1016/j.actbio.2010.02.028

Wu, J., Zhao, D., Ohodnicki, J. M., Lee, B., Roy, A., Yao, R., et al. (2017). *In vitro* and *in vivo* evaluation of multiphase ultrahigh ductility Mg–Li–Zn alloys for cardiovascular stent application. *ACS Biomater. Sci. Eng.* 4, 919–932. doi:10.1021/acsbiomaterials.7b00854

Wu, S., Wang, S., Wang, G., Yu, X., Liu, W., Chang, Z., et al. (2019). Microstructure, mechanical and corrosion properties of magnesium alloy bone plate treated by high-energy shot peening. *Trans. Nonferrous Metals Soc. China* 29, 1641–1652. doi:10.1016/S1003-6326(19)65071-5

Wu, T. C., Joshi, S. S., Ho, Y. H., Pantawane, M. V., Sinha, S., Dahotre, N. B., et al. (2021). Microstructure and surface texture driven improvement in *in-vitro* response of laser surface processed AZ31B magnesium alloy. *J. Magnesium Alloys* 9, 1406–1418. doi:10.1016/j.jma.2020.11.002

Xia, S., Liu, Y., Fu, D., Jin, B., and Lu, J. (2016). Effect of surface mechanical attrition treatment on tribological behavior of the AZ31 alloy. *J. Mat. Sci. Technol.* 32, 1245–1252. doi:10.1016/j.jmst.2016.05.018

Xia, Y., Fan, G., Chen, K., Chen, Y., He, Z., Ou, J., et al. (2022). Preparation and anti-corrosion performances of grass-like microstructured superhydrophobic surface on copper via solution-immersion. *Mat. Lett.* 323, 132482. doi:10.1016/j.matlet.2022.132482

Xie, K., Wang, L., Guo, Y., Zhao, S., Yang, Y., Dong, D., et al. (2021). Effectiveness and safety of biodegradable Mg-Nd-Zn-Zr alloy screws for the treatment of medial malleolar fractures. *J. Orthop. Transl.* 27, 96–100. doi:10.1016/j.jot.2020.11.007

Xing, F., Guo, F., Su, J., Zhao, X., and Cai, H. (2021). The existing forms of Zr in Mg-Zn-Zr magnesium alloys and its grain refinement mechanism. *Mat. Res. Express* 8, 066516. doi:10.1088/2053-1591/ac083c

Xu, C., Wang, X., Zhang, J., and Zhang, Z. (2014). Effect of Nd and Yb on the microstructure and mechanical properties of Mg-Zn-Zr alloy. *Rare Metal Mater. Eng.* 43, 1809–1814. doi:10.1016/S1875-5372(14)60136-3

Xu, F., Luo, L., Xiong, L., and Liu, Y. (2020). Microstructure and corrosion behavior of ALD Al2O3 film on AZ31 magnesium alloy with different surface roughness. *J. Magnesium Alloys* 8, 480–492. doi:10.1016/j.jma.2019.06.003

Yamamoto, A., and Hiromoto, S. (2009). Effect of inorganic salts, amino acids and proteins on the degradation of pure magnesium *in vitro*. *Mater. Sci. Eng. C* 29, 1559–1568. doi:10.1016/j.msec.2008.12.015

Yamanaka, K., Mori, M., and Chiba, A. (2016). Developing high strength and ductility in biomedical Co–Cr cast alloys by simultaneous doping with nitrogen and carbon. *Acta Biomater.* 31, 435–447. doi:10.1016/j.actbio.2015.12.011

Yan, T., Tan, L., Zhang, B., and Yang, K. (2014). Fluoride conversion coating on biodegradable AZ31B magnesium alloy. *J. Mat. Sci. Technol.* 30, 666–674. doi:10.1016/j.jmst.2013.12.015

Yan, Y., Cao, H., Kang, Y., Yu, K., Xiao, T., Luo, J., et al. (2017). Effects of Zn concentration and heat treatment on the microstructure, mechanical properties and corrosion behavior of as-extruded Mg-Zn alloys produced by powder metallurgy. *J. Alloys Compd.* 693, 1277–1289. doi:10.1016/j.jallcom.2016.10.017

Yang, L., Hort, N., Willumeit, R., and Feyerabend, F. (2012). Effects of corrosion environment and proteins on magnesium corrosion. *Corros. Eng. Sci. Technol.* 47, 335–339. doi:10.1179/1743278212y.0000000024

Yang, Y., Cristino, V., Tam, L., Lo, K., and Kwok, C. (2022). Laser surface alloying of copper with Cr/Ti/CNT for enhancing surface properties. *J. Mater. Res. Technol.* 17, 560–573. doi:10.1016/j.jmrt.2021.12.129

Yang, Z., Gu, H., Sha, G., Lu, W., Yu, W., Zhang, W., et al. (2018). TC4/Ag metal matrix nanocomposites modified by friction stir processing: Surface characterization, antibacterial property, and cytotoxicity *in vitro*. *ACS Appl. Mat. Interfaces* 10, 41155–41166. doi:10.1021/acsami.8b16343

Yao, H. L., Hu, X. Z., Yi, Z. H., Xia, J., Tu, X. Y., Li, S. B., et al. (2021). Microstructure and improved anti-corrosion properties of cold-sprayed Zn coatings fabricated by post shot-peening process. *Surf. Coat. Technol.* 422, 127557. doi:10.1016/j.surfcoat.2021.127557

Yao, X., Tang, J., Zhou, Y., Atrens, A., Dargusch, M. S., Wiese, B., et al. (2020). Surface modification of biomedical Mg-Ca and Mg-Zn-Ca alloys using selective laser melting: Corrosion behaviour, microhardness and biocompatibility. *J. Magnesium Alloys* 9, 2155–2168. doi:10.1016/j.jma.2020.08.011

Yin, Z. Z., Qi, W. C., Zeng, R. C., Chen, X. B., Gu, C. D., Guan, S. K., et al. (2020). Advances in coatings on biodegradable magnesium alloys. *J. Magnesium Alloys* 8, 42–65. doi:10.1016/j.jma.2019.09.008

Yu, X., Ibrahim, M., Liu, Z., Yang, H., Tan, L., Yang, K., et al. (2018). Biofunctional Mg coating on PEEK for improving bioactivity. *Bioact. Mat.* 3, 139–143. doi:10.1016/j.bioactmat.2018.01.007

Zeng, R. C., Cui, L., Jiang, K., Liu, R., Zhao, B. D., Zheng, Y. F., et al. (2016). *In vitro* corrosion and cytocompatibility of a microarc oxidation coating and poly (l-lactic acid) composite coating on Mg–1Li–1Ca alloy for orthopedic implants. *ACS Appl. Mat. Interfaces* 8, 10014–10028. doi:10.1021/acsami.6b00527

Zeng, R. C., Sun, L., Zheng, Y. F., Cui, H. Z., and Han, E. H. (2014). Corrosion and characterisation of dual phase Mg–Li–Ca alloy in Hank's solution: The influence of microstructural features. *Corros. Sci.* 79, 69–82. doi:10.1016/j.corsci.2013.10.028

Zeng, R., Lan, Z., Kong, L., Huang, Y., and Cui, H. (2011). Characterization of calcium-modified zinc phosphate conversion coatings and their influences on corrosion resistance of AZ31 alloy. *Surf. Coat. Technol.* 205, 3347–3355. doi:10.1016/j.surfcoat.2010.11.027

Zhang, B., Hou, Y., Wang, X., Wang, Y., and Geng, L. (2011). Mechanical properties, degradation performance and cytotoxicity of Mg–Zn–Ca biomedical alloys with different compositions. *Mater. Sci. Eng. C* 31, 1667–1673. doi:10.1016/j.msec.2011.07.015

Zhang, C., Ding, Z., Xie, L., Zhang, L. C., Wu, L., Fu, Y., et al. (2017a). Electrochemical and *in vitro* behavior of the nanosized composites of Ti-6Al-4V and TiO_2 fabricated by friction stir process. *Appl. Surf. Sci.* 423, 331–339. doi:10.1016/j.apsusc.2017.06.141

Zhang, J., Fang, C., and Yuan, F. (2012a). Grain refinement of as cast Mg–Mn alloy by simultaneous addition of trace Er and Al. *Int. J. Cast Metals Res.* 25, 335–340. doi:10.1179/1743133612y.0000000016

Zhang, J., Guan, Y., Lin, W., and Gu, X. (2019). Enhanced mechanical properties and biocompatibility of Mg-Gd-Ca alloy by laser surface processing. *Surf. Coat. Technol.* 362, 176–184. doi:10.1016/j.surfcoat.2019.01.063

Zhang, J., Jiang, B., Yang, Q., Huang, D., Tang, A., Pan, F., et al. (2020a). Role of second phases on the corrosion resistance of Mg-Nd-Zr alloys. *J. Alloys Compd.* 849, 156619. doi:10.1016/j.jallcom.2020.156619

Zhang, J., Kong, N., Shi, Y., Niu, J., Mao, L., Li, H., et al. (2014). Influence of proteins and cells on *in vitro* corrosion of Mg–Nd–Zn–Zr alloy. *Corros. Sci.* 85, 477–481. doi:10.1016/j.corsci.2014.04.020

Zhang, J., Ma, Q., and Pan, F. (2010). Effects of trace Er addition on the microstructure and mechanical properties of Mg–Zn–Zr alloy. *Mat. Des.* 31, 4043–4049. doi:10.1016/j.matdes.2010.05.008

Zhang, J., Zhang, B., Zhang, J., Lin, W., and Zhang, S. (2021a). Magnesium promotes the regeneration of the peripheral nerve. *Front. Cell Dev. Biol.* 2169, 717854. doi:10.3389/fcell.2021.717854

Zhang, L. C., Chen, L. Y., and Wang, L. (2020b). Surface modification of titanium and titanium alloys: Technologies, developments, and future interests. *Adv. Eng. Mat.* 22, 2070017. doi:10.1002/adem.202070017

Zhang, T., Wei, D., Lu, E., Wang, W., Wang, K., Li, X., et al. (2022). Microstructure evolution and deformation mechanism of α+ β dual-phase Ti-xNb-yTa-2Zr alloys with high performance. *J. Mat. Sci. Technol.* 131, 68–81. doi:10.1016/j.jmst.2022.04.052

Zhang, X., Yuan, G., Mao, L., Niu, J., and Ding, W. (2012b). Biocorrosion properties of as-extruded Mg–Nd–Zn–Zr alloy compared with commercial AZ31 and WE43 alloys. *Mat. Lett.* 66, 209–211. doi:10.1016/j.matlet.2011.08.079

Zhang, Y., Li, J., and Li, J. (2017b). Effects of calcium addition on phase characteristics and corrosion behaviors of Mg-2Zn-0.2 Mn-xCa in simulated body fluid. *J. Alloys Compd.* 728, 37–46. doi:10.1016/j.jallcom.2017.08.264

Zhang, Z. Q., Yang, Y. X., Li, J. A., Zeng, R. C., and Guan, S.-K. (2021b). Advances in coatings on magnesium alloys for cardiovascular stents–a review. *Bioact. Mat.* 6, 4729–4757. doi:10.1016/j.bioactmat.2021.04.044

Zheng, Y. F., Gu, X. N., and Witte, F. (2014). Biodegradable metals. *Mater. Sci. Eng. R Rep.* 77, 1–34. doi:10.1016/j.mser.2014.01.001

Zheng, Y., Gu, X., Xi, Y., and Chai, D. (2010). *In vitro* degradation and cytotoxicity of Mg/Ca composites produced by powder metallurgy. *Acta Biomater.* 6, 1783–1791. doi:10.1016/j.actbio.2009.10.009

Zhou, H., Hou, R., Yang, J., Sheng, Y., Li, Z., Chen, L., et al. (2020a). Influence of Zirconium (Zr) on the microstructure, mechanical properties and corrosion behavior of biodegradable zinc-magnesium alloys. *J. Alloys Compd.* 840, 155792. doi:10.1016/j.jallcom.2020.155792

Zhou, H., Liang, B., Jiang, H., Deng, Z., and Yu, K. (2021). Magnesium-based biomaterials as emerging agents for bone repair and regeneration: From mechanism to application. *J. Magnesium Alloys* 9, 779–804. doi:10.1016/j.jma.2021.03.004

Zhou, Y., Sun, Q., Dong, X., Li, N., Shen, Z. J., Zhong, Y., et al. (2020b). Microstructure evolution and mechanical properties improvement of selective laser melted Co-Cr biomedical alloys during subsequent heat treatments. *J. Alloys Compd.* 840, 155664. doi:10.1016/j.jallcom.2020.155664

Zhu, H., Zhao, T., Wei, Q., Liu, N., Ma, L., Hu, Z., et al. (2018). Corrosion resistance improvement of Mg alloy AZ31 by combining bilayer amorphous DLC: H/SiNx film with N+ ions implantation. *J. Alloys Compd.* 762, 171–183. doi:10.1016/j.jallcom.2018.05.217

Zhu, S., Jin, J., Wang, J., Sun, Y., Chen, J., Wang, L., et al. (2013). "Effect of friction stir processing on microstructures and corrosive properties in simulated body fluid of biological Mg-Zn-Y-Nd alloy," in Proceedings of the 1st International Joint Symposium on Joining and Welding (Elsevier), 411–415. doi:10.1533/978-1-78242-164-1.411

frontiers | Frontiers in Bioengineering and Biotechnology

TYPE Review
PUBLISHED 08 September 2022
DOI 10.3389/fbioe.2022.977282

OPEN ACCESS

EDITED BY
Daixiu Wei,
Tohoku University, Japan

REVIEWED BY
Yuting Lv,
Shandong University of Science and Technology, China
Qiang Wang,
China Medical University, China

*CORRESPONDENCE
Yujin Tang,
tangyujin@ymcn.edu.cn
Jia Liu,
liujia@ymcn.edu.cn
Peilei Zhang,
peilei@sues.edu.cn

SPECIALTY SECTION
This article was submitted to Biomaterials, a section of the journal Frontiers in Bioengineering and Biotechnology

RECEIVED 24 June 2022
ACCEPTED 01 August 2022
PUBLISHED 08 September 2022

CITATION
Feng J, Tang Y, Liu J, Zhang P, Liu C and Wang L (2022), Bio-high entropy alloys: Progress, challenges, and opportunities. *Front. Bioeng. Biotechnol.* 10:977282. doi: 10.3389/fbioe.2022.977282

Bio-high entropy alloys: Progress, challenges, and opportunities

Junyi Feng[1], Yujin Tang[2]*, Jia Liu[2]*, Peilei Zhang[1]*, Changxi Liu[3] and Liqiang Wang[3]

[1]School of Materials Engineering, Shanghai University of Engineering Science, Shanghai, China, [2]State Key Laboratory of Metal Matrix Composites, School of Materials Science and Engineering, Shanghai Jiao Tong University, Shanghai, China, [3]Affiliated Hospital of Youjiang Medical University for Nationalities, Baise, China

With the continuous progress and development in biomedicine, metallic biomedical materials have attracted significant attention from researchers. Due to the low compatibility of traditional metal implant materials with the human body, it is urgent to develop new biomaterials with excellent mechanical properties and appropriate biocompatibility to solve the adverse reactions caused by long-term implantation. High entropy alloys (HEAs) are nearly equimolar alloys of five or more elements, with huge compositional design space and excellent mechanical properties. In contrast, biological high-entropy alloys (Bio-HEAs) are expected to be a new bio-alloy for biomedicine due to their excellent biocompatibility and tunable mechanical properties. This review summarizes the composition system of Bio-HEAs in recent years, introduces their biocompatibility and mechanical properties of human bone adaptation, and finally puts forward the following suggestions for the development direction of Bio-HEAs: to improve the theory and simulation studies of Bio-HEAs composition design, to quantify the influence of composition, process, post-treatment on the performance of Bio-HEAs, to focus on the loss of Bio-HEAs under actual service conditions, and it is hoped that the clinical application of the new medical alloy Bio-HEAs can be realized as soon as possible.

KEYWORDS

biological high-entropy, compositon design, mechanical properties, implant, biocompatibility

Introduction

As one of the material foundations of human production and life, metal materials have always played an essential role in the development history of human civilization. In recent decades, with the continuous development of science and technology, people have put forward higher and higher requirements for the comprehensive properties of metal materials. People have been changing the properties of materials by adding relatively small amounts of secondary elements to the primary elements. For example, C and Cr elements are added to steel to improve strength and corrosion resistance, and Al-Mn and Al-Mg alloys formed by adding Mn and Mg to aluminum have good corrosion resistance and

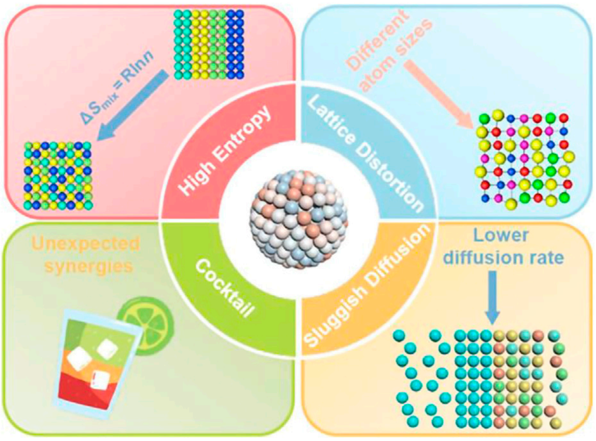

FIGURE 1
Schematic illustration of the properties and characteristics of HEAs (Xin et al., 2020).

plasticity (Zhang et al., 2008; Serda, 2013; Liu et al., 2021; Zhou et al., 2022). However, such a primary-element approach dramatically limits the total number of possible element combinations and, therefore, the total number of alloys, most of which have been identified and exploited. New approaches are needed if the compositional space for exploration is significantly enlarged. To obtain alloy materials with better properties, in the 1990s, researchers got alloys with high mixing entropy by adding alloy components (Peker and Johnson, 1993; Choi-Yim and Johnson, 1997). In 2004, Ye et al. (Yeh et al., 2004) prepared multi-principal composition alloys with equal or nearly equal molar ratios, and named such multi-principal alloys as high entropy alloys (HEAs) for the first time. And unlike conventional alloys, the properties of HEAs are jointly influenced by multiple constituent elements. High entropy alloys have advantages not found in conventional alloys, such as high strength, high-temperature resistance, corrosion resistance, etc. (Yeh, 2006, 2013; Senkov et al., 2010, 2011; Miracle et al., 2014; Zhang et al., 2014, 2018; George et al., 2019; Xin et al., 2020).

At present, high-entropy alloys refer to a class of alloys composed of five or more elements, and the atoms of each component are smelted and alloyed according to an equal atomic ratio or close to an equal atomic ratio and have high mixing entropy and solid solution formation tendency (Schopphoven et al., 2016; Liang et al., 2022). Scholars have conducted a lot of research on HEA and have concluded four core effects: high entropy effect, sluggish diffusion, lattice distortion, and cocktail effect, as shown in Figure 1 (Xin et al., 2020). Among them, high lattice distortion and high mixing entropy will lead to a large degree of atomic disorder in the alloy. This allows HEA to have low Gibbs free energy, which significantly improves the stability of the single solid solution phase and inhibits the formation of intermetallic compounds (Wang B. et al., 2018; Huo et al., 2018; Nong et al., 2018). Structural "lattice distortion effect," that is, the difference in atomic size among various elements, can cause severe lattice distortion, which is considered to be the primary reason for the high strength of high-entropy alloys and has an essential impact on the morphology and movement of dislocation lines (Ma Y. et al., 2020; Xie et al., 2020). The cocktail effect refers to the fact that HEA is an alloy formed by mixing multiple elements and will exhibit properties that a single pure metal element does not have (Lin C. L. et al., 2021). These properties give HEA a more comprehensive range of applications (Wang et al., 2019; Wei et al., 2021; Jiang et al., 2022a, 2022b; Cheng et al., 2022).

Currently, potential applications for HEAs include corrosion-resistant materials, nuclear materials, molds, and biomedicine (George et al., 2020; Soto et al., 2020). Among these, HEAs have great potential in the biomedical field, and biomaterials science continues to be at the forefront of research and innovation in clinical and biomedical applications as medical technology advances and the needs of the population increase. An illustrative example of the significant impact is that degenerative diseases of the bones and joints, such as osteoporosis, affect many people worldwide, mainly middle-aged and postmenopausal women (Cohen et al., 2022; Iki et al., 2022; Mattia et al., 2022). Growing clinical demand for reconstructive joint replacements is prompting researchers to develop implants with better function, biocompatibility, and improved clinical outcomes. Alloys have been used as bone implants for many years. Among them, stainless steel, cobalt-based alloys (CoCrMo), and titanium and their alloys are widely used for their good biocompatibility, sufficient mechanical strength, and excellent corrosion resistance (Gross et al., 2020; Shipilova et al., 2020). However, implants made from these materials are usually much stiffer than natural bone, leading to stress shielding - a significant source of bone resorption and eventual failure of such implants. The human skeleton can be divided into dense bone (cortical bone) and trabecular bone (cancellous bone). Dense bone is almost solid, while the porosity of trabecular bone varies between 50 and 90%, and the mechanical properties of the bone vary significantly with age, anatomical location, and bone mass (Lei et al., 2013; Al-Hafidh et al., 2020; Gaffuri et al., 2021). Such complex mechanical property modulation is difficult to achieve with a single principal element alloy, which requires substantial elemental modulation by HEA to meet specific bone-implant needs. Such complex mechanical property modulation is difficult to achieve with a single primary element alloy, which requires significant elemental modulation of HEA to meet specific bone-implant needs.

We call this HEA with biomedical application potential Biological High Entropy Alloy (Bio-HEAs) [41], and many scholars have already researched the related direction. Metal biomaterials must be composed of raw materials with good biocompatibility, such as non-toxic and non-allergenic

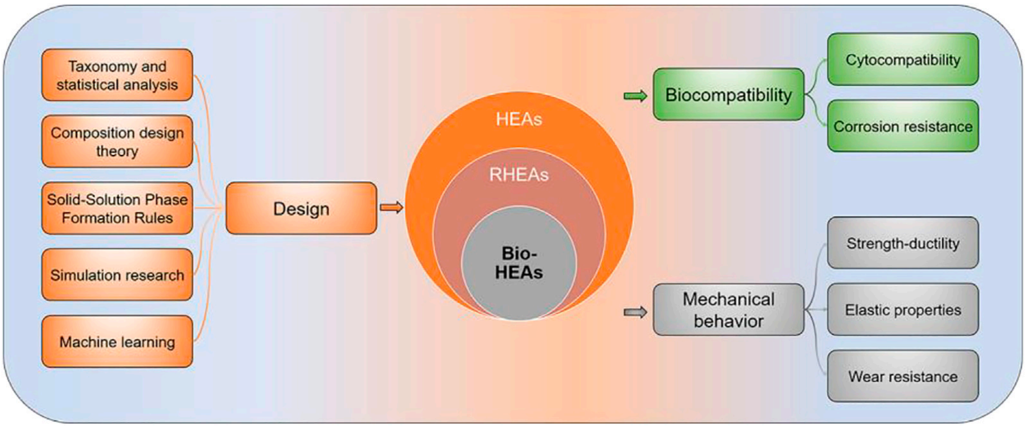

FIGURE 2
A mind map to explore the design theory, biocompatibility, and mechanical properties of Bio-HEAs in this paper.

materials (Meloni et al., 2019; Kazemi et al., 2020; Spataru et al., 2021). The selection of constituent elements is particularly critical for Bio-HEA. Bio-HEA is mainly composed of Ti, Zr, Hf, Nb, Ta, V, Mo, and W. These elements do not cause side effects to the tissue cells at the implantation site or are within the safe range of side effects to the body throughout the service phase. High-entropy alloys have become one of the most promising medical metal materials in recent years due to their biological safety, high strength, high corrosion resistance, high wear resistance, and ease of forming simple objects. Since high entropy alloys are tunable in terms of properties, the desired properties can be obtained by changing the type or content of the elements in the HEAs, which gives the HEAs a broader scope of application. In the field of biomedicine, high-entropy alloys have a similar hardness to the bone, high specific strength, good corrosion, and wear resistance, and these characteristics are in line with the typical attributes of biomedical metal materials, which means that there is a good potential for its application in the medical health field.

Figure 2 shows the structure and main content of the paper. The second section reviews the composition design theory of Bio-HEAs. It presents the progress of research on developing Bio-HEAs compositions based on the first principles of density functional theory (DFT) simulations calculation. The third section discusses the biocompatibility of the designed and developed Bio-HEAs, including cytocompatibility and corrosion resistance. The fourth section compares the mechanical properties of Bio-HEAs with human bone and commonly used bio-alloys, including strength-ductility, elastic properties, and wear resistance. The fifth section discusses the future development prospects of Bio-HEAs and explores the possibility of high-entropy alloys in biomedicine.

Component design theory and simulation studies

The proposal of the concept of the high-entropy alloy not only improves the freedom of alloy material composition but also dramatically increases the difficulty of its composition exploration and performance optimization. Selecting alloying elements and the appropriate proportions are particularly important to obtain high-entropy alloys with specific phase structures or properties (Pradeep et al., 2015; Takeuchi et al., 2015; Tian et al., 2015; Ye et al., 2015). The core problems involved in the current high entropy alloys research can often be summarized as the problem of alloy composition design and property optimization (LaRosa et al., 2019; George et al., 2020; Soto et al., 2020).

As one of the members of high-entropy alloys, Bio-HEA has the same component design concept as high-entropy alloys. Due to the large number of optional components of HEAs and the high content of each component, the complex physical properties and chemical synergism between various alloying elements will ultimately significantly affect the mechanical properties and microstructure of high-entropy alloys (Cann et al., 2021; Ostovari Moghaddam et al., 2021). This chapter summarizes the research on Bio-HEAs in recent years as a composition system. The combined effects of all the components are considered from composition design theory. The phase formation laws and mechanisms are discussed through solid-solution phase formation rules. The Bio-HEAs alloy properties are predicted by simulation, such as first principles and molecular dynamics. Machine learning is introduced to provide a reference database for the composition design guidelines of new high-entropy alloys.

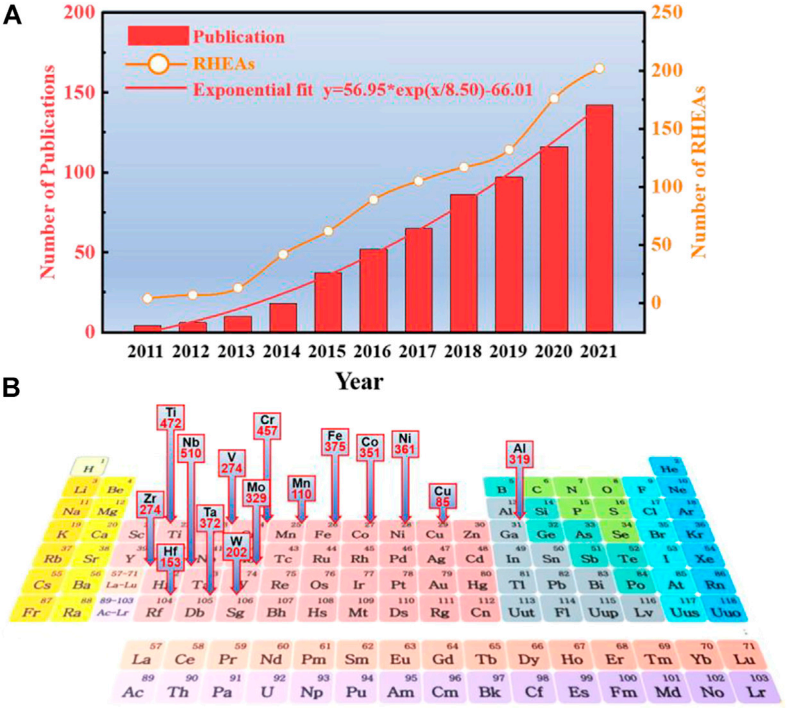

FIGURE 3
(A). The number of RHEA publications from 2011 to 2021 and the frequency of RHEA occurrences involved. The number of RHEA articles can be described by exponential growth $y = 56.95 * \exp(x/8.50) - 66.01$. **(B)**. The frequency of occurrence and the distribution of their positions on the periodic table of elements in the 953 RHEAs counted.

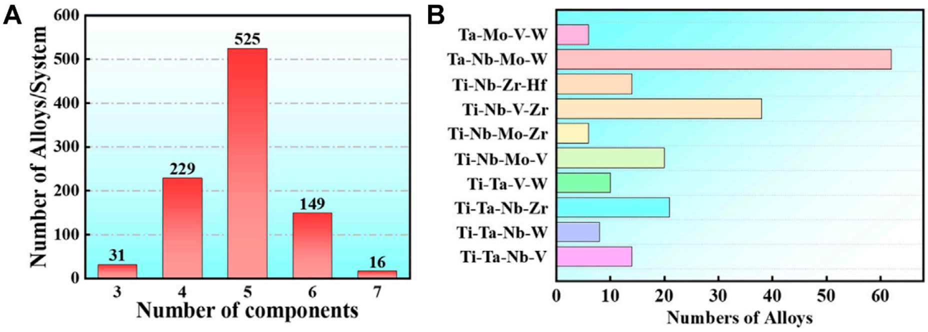

FIGURE 4
In the statistical publications, the frequencies of RHEAs of 3,4,5,6,7 group elements, respectively **(A)**, while the frequencies of RHEAs based on the most common 4 group element systems of Ta-Nb-Mo-W, Ti-Nb-V-Zr, Ti-Nb-Mo-V, and Ti-Ta-Nb-V are in **(B)**.

Taxonomy and statistical analysis

Bio-HEA alloys were developed based on the research of refractory high-entropy alloys (RHEAs). In 2010, Senkov et al. (Senkov et al., 2010) synthesized near-equivalent atoms WTaMoNb and WTaMoNbV alloys with single-phase body-centered cubic (BCC) lattice using the vacuum arc melting technique. Since then, many other HEAs based on refractory elements (Ti, Zr, Hf, V, Nb, Ta, Cr, Mo, and W) have been the focus of experimental studies (Gu P. et al., 2022; Chen S. H. et al., 2022; Huang et al., 2022; Peng et al., 2022; Zhou et al., 2022). The original RHEA was designed based on five refractory elements (Ta, Nb, Mo, W, and V). The broader elemental system of RHEAs includes Group IV (Ti, Zr, and Hf), Group V (V, Nb, and Ta), and Group VI (Cr, Mo, and W). There are also non-refractory metals such as Al, Si, Co, Cu, or Ni; the number of studies on RHEA is steadily increasing, as shown in Figure 3. Overall, the number of publications shows a roughly exponential relationship with year trends: $y = 56.95 * \exp(x/8.50) - 66.01$. By the end of December 2021, described 953 RHEAs alloys involved in 633 studies, among which 31 are 3-component, 229 are 4-component, 525 are 5-component, 149 are 6-component and 16 are 7-component (Figure 4). The most common elements in RHEAs are Nb(present in 510 alloys),Ti (472), Cr (457), Fe (375), Ta (372), Ni(361), Co(351), Mo (329), Al (319), V (274), Zr (274), W (202), Hf(153), Mn (110), Cu(85), and some other non-metallic elements Si, C and N are also included, providing more ideas for the composition design of HEA.

Bio-HEAs are based on the study of RHEAs, and the selected metal elements require no cytotoxicity or low cytotoxicity. The following eight alloy compositions are commonly used: Ti, Ta, Nb, Mo, V, W, Hf, and Zr. The refractory high-entropy alloys with four or more group elements are usually designed based on Ta-Nb-Mo-W, Ti-Nb-Zr-Hf, Ti-Nb-V-Zr, Ti-Nb-Mo-V, Ti-Ta-Nb-Zr, and Ti-Ta-Nb-V, as shown in Figure 4. In addition, alloys can contain Al or Si to reduce the alloy density to improve Bio-HEAs performance, and there are also studies to improve the wear performance of Bio-HEAs by adding Cr elements (Tong et al., 2020).

Composition design theory

Bio-HEAs have excellent mechanical properties, and their strong solid solution strengthening mechanism plays an important role. The phase formation mode of HEAs was investigated to explore the composition design of different HEAs and many empirical parameters, such as atomic radius difference, mixing entropy, valence electron concentration, mixing enthalpy, etc. These parameters are usually constructed based on different perspectives such as thermodynamics, lattice distortion, and electronic behavior to explain the stability of the solid solution phase in HEAs. These empirical parameters can distinguish solid solution from intermetallic compound phases, discriminate the formation of phases such as FCC/BCC/HCP, and predict the single-phase and multi-phase structures of HEAs [8]. The researchers have summarized a large amount of data and proposed some semi-empirical criteria for the formation of simple solid solutions:

(1) The mixing entropy ($\Delta S_{mix)}$ is 12–17.5 J/(molK), and the calculation formula of ΔS_{mix} is (Zhou et al., 2022):

$$\Delta S_{mix} = -R\sum\nolimits_{i=1}^{n} c_i ln c_i \tag{1}$$

where R is the gas constant, and c_i is the mole fraction of the *i*th element.

(2) The mixing enthalpy (ΔH_{mix}) is −15–5 kJ/mol, and the calculation formula of ΔH_{mix} is (Zhou et al., 2022):

$$\Delta H_{mix} = -R\sum\nolimits_{i=1}^{n} 4H_{AB}c_i c_j \,(\mathrm{i} \neq \mathrm{j}) \tag{2}$$

where c_j denotes the mole fraction of the *j*th element; H_{AB} is the enthalpy of mixing between the A and B elements.

(3) The atomic size difference $\delta \le 6.5\%$, and the calculation formula of δ is (Zhou et al., 2022):

$$\delta = \sqrt{\sum\nolimits_{i=1}^{n} c_i \left(1 - \frac{r_i}{\bar{r}}\right)^2} \tag{3}$$

where r_i denotes the atomic radius of the *i*th component; is the molar average atomic radius.

In addition, the formulae for calculating the three relevant features of HEAs are added (Lilensten et al., 2018), including valence electron concentration (VEC), electronegativity difference ($\Delta\chi$), and melting temperature (T_m), and the calculation formula is as follows:

$$VEC = \sum\nolimits_{i=1}^{n} c_i VEC_i \tag{4}$$

$$\Delta\chi = \sqrt{\sum\nolimits_{i=1}^{n} c_i \left(\chi_i - \bar{\chi}\right)^2} \tag{5}$$

$$T_m = \sum\nolimits_{i=1}^{n} c_i T_{mi} \tag{6}$$

Where c_i denotes the atomic concentrations for the *i*th element, VEC_i is the valence electron concentration of the *i*th element. T_{mi} is the melting point and Pauling electronegativity of the *i*th element. The structure and properties of Bio-HEA elements are listed in Table 1.

Based on the six eigenvalues of the designed HEAs, Zhu et al. (Zhu et al., 2022) used an Artificial neural network (ANN) to count a dataset containing 529 HEAs. The Pearson correlation coefficients between the six eigenvalues are listed in Figure 5. The values in the matrix describe the correlation of the two eigenvalues, and the correlations quantitatively vary from 1 to −1, indicating a highly positive or negative relationship (After removing the autocorrelation value of 1, the matrix elements range from −0.65 to 0.65). For example, the atomic size difference is negatively correlated with the mixing enthalpy, which means that as the mixing enthalpy decreases, the atomic size difference appears larger. The electronegativity difference is positively correlated with the melting temperature. Overall, the absence of a strong positive or negative correlation matrix between any two features implies that each of these six feature values has a unique influence on the final properties of the alloy, which needs to be taken into account when designing new group element alloys.

Solid-solution phase formation rules

The solid solution-phase structure of Bio-HEAs is a hot topic of research. For conventional binary solid solution materials, the

TABLE 1 Structure and properties of Bio-HEA elements.

Metals	T_m(K)	VEC	r(Å)	Structure at RT	Structure at T_m	χ	ρ(g/cm^3)
Ti	1941	4	1.47	HCP	BCC	1.54	4.50
Zr	2,128	4	1.6	HCP	BCC	1.33	6.50
Hf	2,506	4	1.56	HCP	BCC	1.30	13.31
Nb	2,750	5	1.47	BCC	BCC	1.60	8.57
Ta	3,290	5	1.47	BCC	BCC	1.50	16.65
V	2,183	5	1.35	BCC	BCC	1.63	5.96
W	3,695	6	1.37	BCC	BCC	2.36	19.35
Mo	2,896	6	1.4	BCC	BCC	2.16	10.22

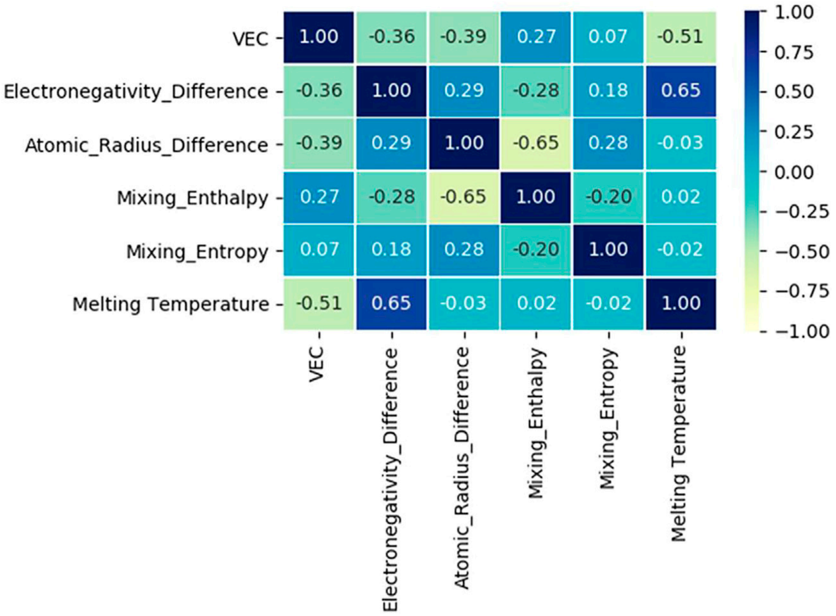

	VEC	Electronegativity_Difference	Atomic_Radius_Difference	Mixing_Enthalpy	Mixing_Entropy	Melting Temperature
VEC	1.00	-0.36	-0.39	0.27	0.07	-0.51
Electronegativity_Difference	-0.36	1.00	0.29	-0.28	0.18	0.65
Atomic_Radius_Difference	-0.39	0.29	1.00	-0.65	0.28	-0.03
Mixing_Enthalpy	0.27	-0.28	-0.65	1.00	-0.20	0.02
Mixing_Entropy	0.07	0.18	0.28	-0.20	1.00	-0.02
Melting Temperature	-0.51	0.65	-0.03	0.02	-0.02	1.00

FIGURE 5
Heatmap of the correlation matrix between six relevant features, including VEC, electronegativity difference, mixing enthalpy, atomic size difference, mixing entropy, and melting temperature (Zhu et al., 2022).

classical Hume-Rothery criterion predicts the phase composition of the alloy from the atomic size, electronic structure, and other elemental properties (Ye et al., 2016). The alloys should have a high mixing entropy, low atomic size difference, and mixing enthalpies with small absolute values to form solid solutions (Zhang et al., 2008). In addition to the Hume-Rothery criterion, materials workers have proposed many simple but practical parameters to determine the phase composition tendency of high entropy alloys according to the properties of the alloy's atoms. From Figure 6, it can be seen that Ω and ϕ affect the phase of HEAs, respectively, and a single eigenvalue cannot predict the trend of solid solution phase formation of HEAs. Still, it should be combined with the interaction of multiple eigenvalues. For example, several criteria have been proposed by experts and scholars to predict the formation conditions of solid solutions effectively. Zhang et al. (Zhang et al., 2008) indicated that the favorable conditions for the formation of the solid solution phase are $-20 \le \Delta H\text{mix} \le 5$ kJ/mol, $\delta \le 6.4$, and $12 \le \Delta S\text{mix} \le 17.5$ J/(mol K). Guo et al. (Guo et al., 2013) demonstrated that the parameter ranges for forming the solid solution phase are $-11.6 \le \Delta H\text{mix} \le 3.2$ kJ/mol and $\delta \le 6.6$. Yang and Zhang (Yang and Zhang, 2012) noted that the favorable criteria for predicting the formation conditions of the solid solution phase are $\Omega \ge 1.1$ and $\delta \le 6.6$. The possibility of forming a solid solution phase can be

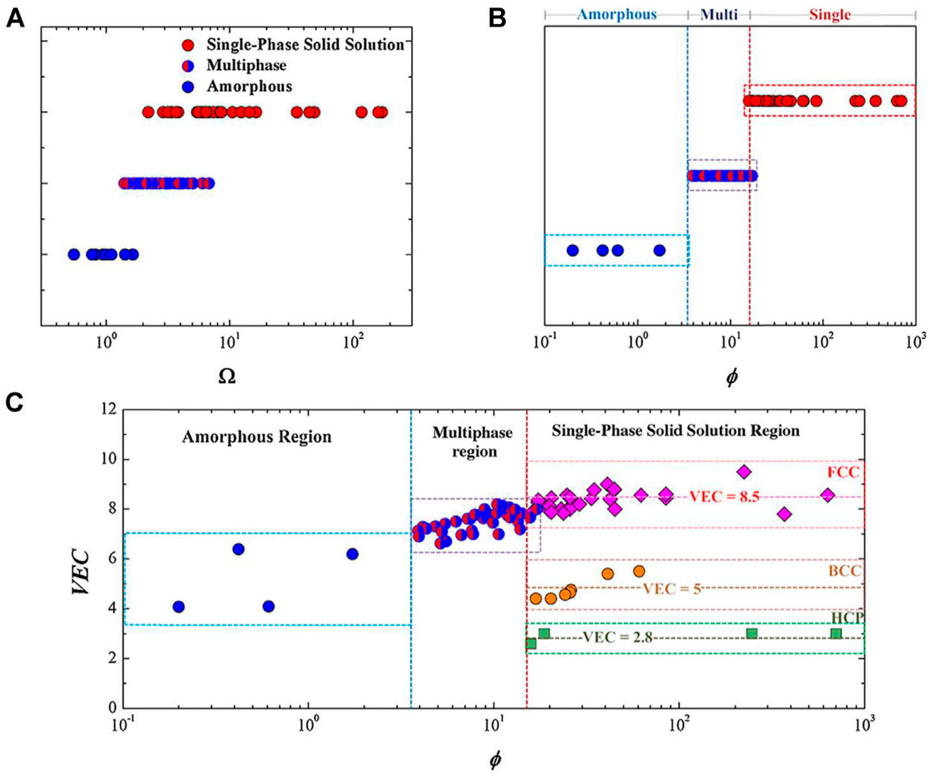

FIGURE 6
The plot of **(A)** the Ω values versus phases and **(B)** the ϕ values versus phases for the HEAs. **(C)** The plot of the VEC versus ϕ for different HEAs. The FCC solid solution mainly forms around a VEC of 8.5, BCC around a VEC of 5, and HCP around a VEC of 2.8, each within a narrow band (Ye et al., 2016)

notably enhanced during the design process of HEAs, reflecting on the criteria as mentioned above.

For the whole alloy system of HEAs, the valence electron concentration (VEC) is the key parameter affecting the crystallization of the solid solution phase in the absence of strong atomic size effects, and a generalization work on the impact of VEC on Bio-HEAs in the literature is presented. To reduce the difficulty of computational work caused by multicomponent alloys, we use the cluster formula approach A cluster formula approach to simplify the calculation based on chemical short-range orders (CSROs). We can consider the solute atoms with similar properties in a multicomponent alloy as a cluster and the remaining solvent atoms with similar properties as a class of gum atoms, and most of the HEAs can be expressed as [cluster](gum atom)$_x$ (Yang W. et al., 2022). In Bio-HEAs, the BCC solid solution structure is predominant, guided by Friedel oscillation theory, the gum atomic number is ideally calculated as x = 1–5, with a stable electronic structure. In the Bio-HEAs system, Ti, Zr, and Hf could be regarded as an averaged virtual element, M, since they are in the same group in the periodic table of elements, the value of VEC is four, and the $\Delta H_{Ti\text{-}Zr}$, $\Delta H_{Ti\text{-}Hf}$, and $\Delta H_{Hf\text{-}Zr}$ are zero. Ta, Nb, and V can also be considered an average virtual element, A, while Mo and V can be regarded as another average virtual element, B. We use $M_xA_yB_z$ to generalize all $[Ti\text{-}Zr\text{-}Hf]_x$~ $(Ta\text{-}Nb\text{-}V)_y$~$(Mo\text{-}W)_z$, and based on existing studies, we make a classification including $[Ti\text{-}Zr\text{-}Hf]_x$~ $(Ta\text{-}Nb\text{-}V)_y$ $[Ti\text{-}Zr\text{-}Hf]_x$~ $(Mo\text{-}W)_z$ and $[Ta\text{-}Nb\text{-}V]_y$ ~$(Mo\text{-}W)_z$, and $[Ti\text{-}Zr\text{-}Hf]_x$~ $(Ta\text{-}Nb\text{-}V)_y$~$(Mo\text{-}W)_z$, where $x,y,z \neq 0$. As can be seen from Figure 7, the VECs of the discussed Bio-HEAs range from 4.0 to 5.8, among which $[Ti\text{-}Zr\text{-}Hf]_x$~ $(Ta\text{-}Nb\text{-}V)_y$ fluctuate between 4.2 and 4.8 due to the generally low VECs of their constituent elements, and are primarily single BCC solid solution phases. The VEC of Bio-HEAs $[Ta\text{-}Nb\text{-}V]_y$ ~$(Mo\text{-}W)_z$ in the high VEC element group is concentrated in the range of 5.2–5.6, mainly in the BCC phase and multiphase, where the multiphase components include Laves phase, BCC2 phase, B2 phase, FCC phase and other precipitated phases (Wang et al., 2020; Mao et al., 2022). The interesting point is that alloys of the system $[Ti\text{-}Zr\text{-}Hf]_x$~ $(Mo\text{-}W)_z$ hardly appear in the surveyed literature, implying that for Bio-HEAs, the V-subgroup elements Ta, Nb, and V with BCC lattice and high mutual solubility are indispensable.

The relationship between VEC and the solid solution phase has been studied thoroughly throughout the high entropy alloy system. The VEC of the alloy plays a crucial role in determining

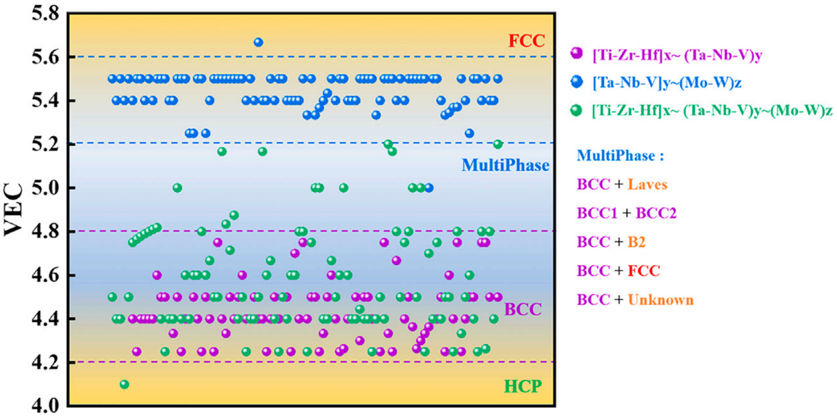

FIGURE 7
Statistical correspondence between VEC and phase composition in Bio-HEAs, Bio-HEAs are classified by [Ti-Zr-Hf]$_x$~ (Ta-Nb-V)$_y$ [Ti-Zr-Hf]$_x$~ (Mo-W)$_z$ and [Ti-Zr-Hf]$_x$~ (Ta-Nb-V)$_y$~ (Mo-W)$_z$, where x,y,z ≠ 0.

the crystallinity of the solid solution phase, especially for single-phase solid solutions. As mentioned earlier, the predominance of the BCC phase in the reported Bio-HEAs is quite reasonable, as the alloy is based on the V-subgroup elements and the IV-subgroup elements (Ti, Zr, and Hf), which are also BCC-phase structures at high temperatures. However, they undergo isotropic transformations and are HCP structures at RT, like Ti and Zr, as shown in Table 1. The phases included in the high VEC Bio-HEAs vary depending on the elemental composition and ratio and the effects of the process. Since the elements used are BCC, the generated solid solution phases are still based on the BCC phase, and the synergistic precipitation phases contain other solid solution phases such as Laves phase, BCC2 phase, B2, and FCC phase (Wei et al., 2022b).

The molybdenum equivalent (Mo$_{eq}$) has been widely used to measure the β-phase stability in the multicomponent Ti-based alloy quantitatively. In addition, it has been shown that the Mo$_{eq}$ parameter is also reliable for predicting the phase stability of solid solution in HEA, especially for the BCC/HCP phase (Wang et al., 2015); Ishida (Ishida, 2017) suggested a new Mo$_{eq}$ based on the thermodynamic database of the Ti alloys, as shown in Eq. 7

$$\begin{aligned}Moeq = {} & [Mo] + 0.26[Au] + 0.43[Bi] + 12.62[Be] + 2.93[Co] + 1.65[Cr] + \\ & 0.85[Cu] + 4.17[Fe] + 0.05[Hf] + 0.17[Mg] + 3.28[Mn] + 0.64[Nb] + \\ & 1.75[Ni] + 0.23[Os] + 0.71[Pd] + 0.64[Pt] + 0.29[Pu] + 1.72[Re] + 2.89[Rh] + \\ & 1.67[Ru] + 0.97[Si] + 0.23[Ta] + 0.32[U] + 0.80[V] + 0.56[W] + 1.13[Y] + \\ & 0.16[Zr]\end{aligned} \tag{7}$$

Where [M] is the weight percent concentration of element M. The inclusion of Ti, Zr, Hf, Nb, Ta, V, Mo, and W, the basic elements of Bio-HEAs, implies that the Mo$_{eq}$ index is a guide to determining the desired stability of the solid solution phase in Bio-HEAs. Yang et al. (Yang W. et al., 2022) used Mo$_{eq}$ to predict the phase stability of BCC/HCP solid solution in the Ti-Zr-Hf-Nb-Ta HEAs system. According to Yang's calculations, the values of Mo$_{eq}$ for Ti-Zr-Hf-Nb-Ta HEAs were in the range of 13.5–21.1 wt%, representing a high trend of BCC solid solution

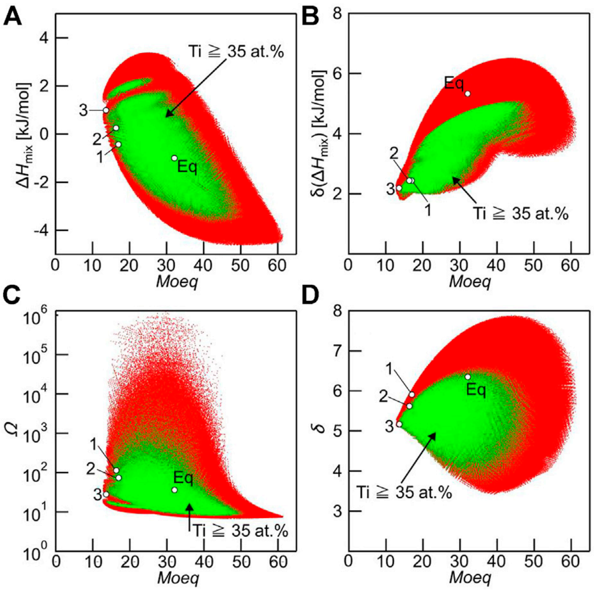

FIGURE 8
Relationship between Mo$_{eq}$ and various empirical alloy parameters used to predict solid solution formation, including ΔHmix, δ (ΔHmix), Ω, and δ parameters in Ti-Zr-Hf-Nb-Ta-Mo alloys with ΔSmix ≥1.5 R (red dots). The green dot indicates the alloys whose Ti concentration was at and above 35 at% and considered the Ti-rich alloys. Hollow black circles (○) indicate the Ti−Zr−Hf−Nb−Ta−Mo alloy investigated in the present study. **(A)** Mo$_{eq}$ vs ΔH$_{mix}$, **(B)** Mo$_{eq}$ vs δ(ΔH$_{mix}$), **(C)** Mo$_{eq}$ vs Ω, and **(D)** Mo$_{eq}$ vs δ parameters (Iijima et al., 2021).

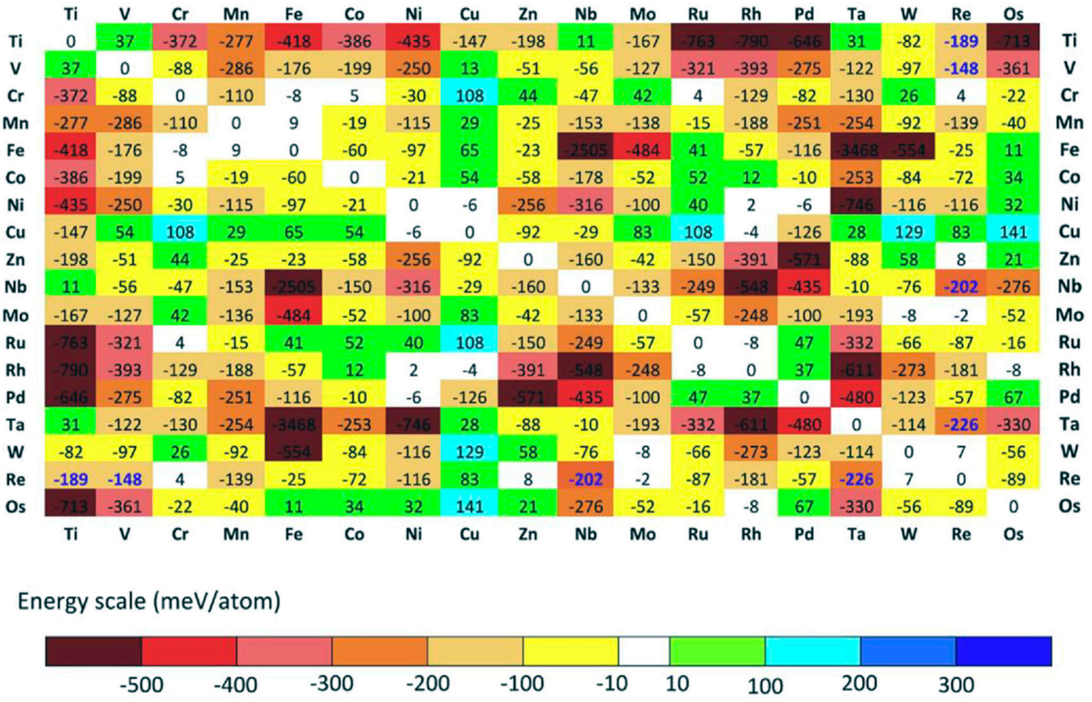

	Ti	V	Cr	Mn	Fe	Co	Ni	Cu	Zn	Nb	Mo	Ru	Rh	Pd	Ta	W	Re	Os
Ti	0	37	-372	-277	-418	-386	-435	-147	-198	11	-167	-763	-790	-646	31	-82	**-189**	-713
V	37	0	-88	-286	-176	-199	-250	13	-51	-56	-127	-321	-393	-275	-122	-97	**-148**	-361
Cr	-372	-88	0	-110	-8	5	-30	108	44	-47	42	4	-129	-82	-130	26	4	-22
Mn	-277	-286	-110	0	9	-19	-115	29	-25	-153	-138	-15	-188	-251	-254	-92	-139	-40
Fe	-418	-176	-8	9	0	-60	-97	65	-23	-2505	-484	41	-57	-116	-3468	-554	-25	11
Co	-386	-199	5	-19	-60	0	-21	54	-58	-178	-52	52	12	-10	-253	-84	-72	34
Ni	-435	-250	-30	-115	-97	-21	0	-6	-256	-316	-100	40	2	-6	-746	-116	-116	32
Cu	-147	54	108	29	65	54	-6	0	-92	-29	83	108	-4	-126	28	129	83	141
Zn	-198	-51	44	-25	-23	-58	-256	-92	0	-160	-42	-150	-391	-571	-88	58	8	21
Nb	11	-56	-47	-153	-2505	-150	-316	-29	-160	0	-133	-249	-548	-435	-10	-76	**-202**	-276
Mo	-167	-127	42	-136	-484	-52	-100	83	-42	-133	0	-57	-248	-100	-193	-8	-2	-52
Ru	-763	-321	4	-15	41	52	40	108	-150	-249	-57	0	-8	47	-332	-66	-87	-16
Rh	-790	-393	-129	-188	-57	12	2	-4	-391	-548	-248	-8	0	37	-611	-273	-181	-8
Pd	-646	-275	-82	-251	-116	-10	-6	-126	-571	-435	-100	47	37	0	-480	-123	-57	67
Ta	31	-122	-130	-254	-3468	-253	-746	28	-88	-10	-193	-332	-611	-480	0	-114	**-226**	-330
W	-82	-97	26	-92	-554	-84	-116	129	58	-76	-8	-66	-273	-123	-114	0	7	-56
Re	**-189**	**-148**	4	-139	-25	-72	-116	83	8	**-202**	-2	-87	-181	-57	**-226**	7	0	-89
Os	-713	-361	-22	-40	11	34	32	141	21	-276	-52	-16	-8	67	-330	-56	-89	0

FIGURE 9
The DFT calculates the formation energy of the lowest energy structures in various binary relative to their phase separation into pure elements. If the numbers are in bold blue, the energies are evaluated relative to the respective solid solution (Troparevsky et al., 2015)

phase formation, which is consistent with the actual results. Iijima et al. (Iijima et al., 2021) used the Mo_{eq} parameter to predict various characteristic quantities of solid solution formation, including ΔH_{mix}, Ω, and δ parameters, as shown in Figure 8. The calculations included 1.5×10^7 Ti-Zr-Hf-Nb-Ta-Mo Bio-HEAs, and it was found that there was no clear relationship between the Mo_{eq} parameter and other eigenvalues. The Mo_{eq} parameter can be considered independent of other empirical alloy parameters, which can directly be predicted for the Bio-HEAs solid solution phase.

Simulation research

Bio-HEA has a “cocktail” effect and is characterized by a multi-component synergistic effect. The design and development of new Bio-HEAs biomaterials require continuous changes in elemental composition and content (Li J. et al., 2021; Ostovari Moghaddam et al., 2021). However, Bio-HEAs have too many permutations of elemental composition and content ratios, and the elements used contain and are not only Ti, Zr, Hf, Nb, Ta, Mo, V, and W, which are expensive. Therefore, direct experimental verification of Bio-HEA alloys’ design is laborious and expensive. DFT has become one of the main methods for exploring material properties in theoretical solid-state physics. Over time, DFT calculations have entered the Bio-HEA field, and the number of corresponding studies has gradually increased (Yang F. et al., 2022; Biermair et al., 2022). Simulations based on the first principles of DFT are an essential method for designing Bio-HEA compositions. They are widely used to predict material properties such as energy band density, electronic structure, and charge density from atomic and electrical scales (Yu et al., 2019; Zhao, 2020; Wu et al., 2022).

Troparevsky et al. (Troparevsky et al., 2015) evaluated the energy of formation of binary compounds by DFT calculations and therefore did not require experimentally or empirical inputs as shown in Figure 9. The model correctly ranks the combinations of elements of known single-phase HEAs based on statistics from numerous studies and eliminates combinations that are not single-phase. The constructed elemental matrix can predict all currently known single-phase HEAs. In addition, this method can predict feasible five-, six-, and seven-component alloys, thus guiding exploring new HEAs.

As the most important influencing factor of Bio-HEA biocompatibility, the selection of elements plays a significant role in the simulation design. Bai et al. (Bai et al., 2021) predicted the impact of Ti elements on the mechanical properties of iso-atomic NbMoTaW HEA from the first-principles calculation based on DFT. The phase structure, density, lattice constant, elastic, and electrical properties of

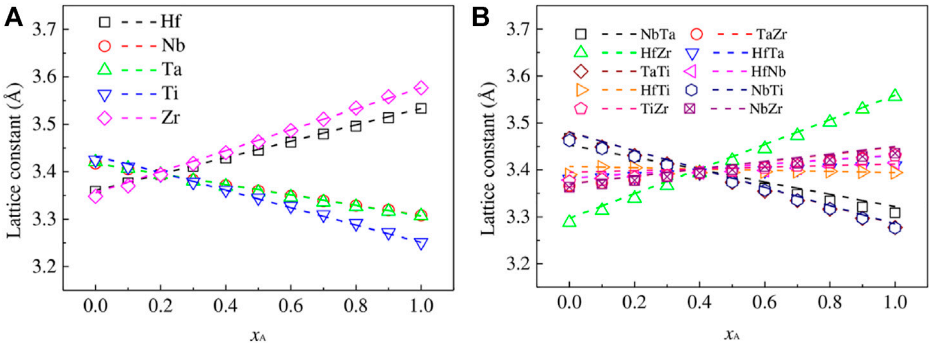

FIGURE 10
The final members of the lattice constants of the 1–4 **(A)** and 2–3 **(B)** pseudo-binary A_xB_{1-x} alloys as a function of the molar fraction. In subfigure **(A)**, A represents one of the Hf-Nb-Ta-Ti-Zr elements, and B represents the other four elements. In subfigure **(B)**, A represents two elements of Hf-Nb-Ta-Ti-Zr, while B represents the other three. The lattice constants that conform to Vegard's law are shown as dashed lines (Chen S. M. et al., 2022)

NbMoTaW HEA by Ti elements were calculated. The energy band, total and partial densities of states, and charge density were calculated to investigate the strength and ductility enhancement mechanism of NbMoTaW alloy using Ti alloying. Tong et al. (Tong et al., 2020) used DFT calculations to simulate the effects of Ti, Zr, Cr, V, Hf, and Re additions on the properties of NbMoTaW HEAs and further analyzed the role played by various strengthening mechanisms. Chen et al. (Chen S. M. et al., 2022) used the first-principles approach combined with a thermodynamic model to study phase decomposition in alloys by considering HEA as various pseudo-binary systems, as shown in Figure 10, which predicts that phase decomposition in Hf-Nb-Ti-Zr alloys with a BCC structure occurs at temperatures below the critical temperature of 1298 K. The HEA decomposes most favorably into NbTa-rich and HfZr-rich BCC phases, while the BCC-rich HfZr phase is transferred to the hexagonal compact stacking structure (HCP) phase at low temperatures. (Chen X. et al., 2022; Chen Z. W. et al., 2022). In addition, the effects of solid solution and precipitation strengthening mechanisms on the strength of HEA were calculated based on the predicted phase decomposition results, combined with experimental data.

In the simulation studies of HEAs, apart from DFT simulations, molecular dynamics also occupy a relatively large proportion, and molecular dynamics-based simulations are more reliable in analyzing the microscopic deformation mechanism of HEAs. Progress has been made in using molecular dynamics simulations to explain the deformation mechanisms and mechanical properties of 3D transition group HEAs (Liu et al., 2020). This approach has significant implications for predicting the performance of HEAs, especially for assessing complex service conditions of Bio-HEAs. Simulation methods still have great research potential in the composition design of Bio-HEAs, and more research is needed to discover the intrinsic connections.

Machine learning

With the increasing number of high-entropy components, the composition design becomes more and more complex, and the traditional empirical trial-and-error method, first-principles calculations, and molecular dynamics simulations introduced earlier gradually fail to meet the needs of the growing performance-oriented high-entropy alloy composition. Build machine learning models to predict the performance of various target alloys for fast and cost-effectively solved material performance evaluation (Kumar et al., 2021). Using a multi-objective genetic algorithm to find the Pareto Frontier of multi-objective performance in the prediction results can solve the problem of searching for elements of material composition (Bao et al., 2022). Combined with adaptive iterative methods for model uncertainty-based material screening, optimized material compositions or processes can be identified, guiding materials research (Chen H. et al., 2022; Thebelt et al., 2022). In the context of multi-objective performance requirements, the application of machine learning to the field of high-entropy alloys is particularly critical, such as the co-optimization of strength and corrosion resistance of high-strength and corrosion-resistant high-entropy alloys, the co-optimization of density and strong toughness properties of lightweight high-entropy alloys, the co-optimization of high-temperature strength and oxidation resistance properties needed for refractory high-entropy alloys, and the co-optimization of biocompatibility, mechanical properties matching those of living organisms, and excellent corrosion resistance required for biological high-entropy alloys.

Machine learning is applied to the strength and hardness properties of HEAs with data and set samples, either derived

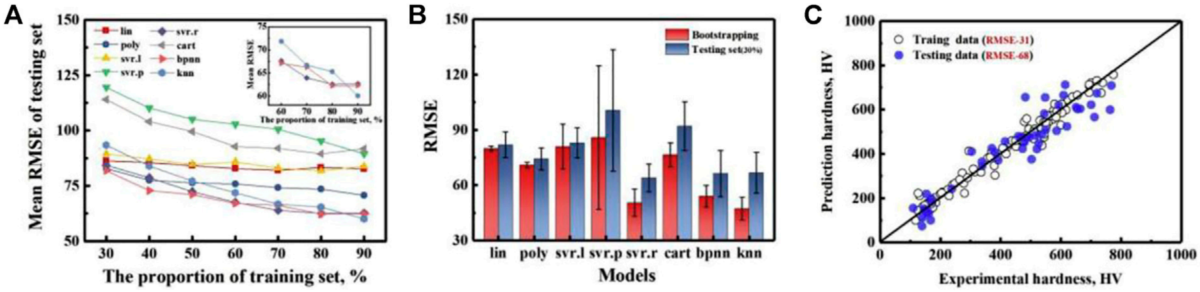

FIGURE 11
Test error evaluation of three different models, **(A)** a holdout method and **(B)** bootstrapping methods, indicating sur. r outperforms the bpnn and knn model. **(C)** The predicted values as a function of the measured values of the svr. r model for training data (randomly chosen 70%) and testing data (the rest 30%) (Wen et al., 2019)

from experimental studies or obtained with the help of computational simulations (Bakr et al., 2022; Chen Z. W. et al., 2022; Hou et al., 2022). The research mainly focuses on machine learning to accurately predict the strength and hardness properties of new alloys and to guide the design of alloy compositions based on the property prediction results. Klimenko (Klimenko et al., 2021) and Bhandari (Bhandari et al., 2021) et al. developed support vector machine and random forest machine learning models for accurate prediction of yielding of HEAs with an accuracy of more than 95% based on a sample of high-entropy alloy data with characteristic parameters such as composition, modulus, density, mixing entropy, and atomic radius difference of HEAs as inputs. Several well-known machine learning models, including a radial basis function kernel (svr. r), a regression tree model (cart), a back propagation neural network model (bpnn), and a k-nearest neighbor model (knn) to produce a non-convex input/output fitness function to estimate the hardness (Wen et al., 2019). As shown in Figure 11, 42 newly synthesized HEAs were designed based on machine learning and experimental feedback results, with 35 of them having alloy hardness values higher than the best values in the training dataset.

In addition to the prediction of properties such as strength and hardness of HEAs, machine learning has also done a lot of work on elastic properties, which are the most critical concern for medical high-entropy alloys, to achieve the design of Bio-HEAs compositions corresponding to modulus and strength requirements based on the model's prediction of elastic properties. Chanda et al. (Chanda et al., 2021) trained a neural network model using 140 samples of high-entropy alloy data with seven characteristic quantities such as electronegativity difference, mixing enthalpy, and mixing entropy as inputs and predicted the alloy elastic modulus with an accuracy of 94%. Roy et al. (Roy et al., 2020) trained gradient boosted tree regression models based on 89 high-entropy alloy data samples with ten empirical parameters as input characteristic parameters to predict the elastic modulus for 26 equimolar high-entropy alloys with low, medium, and high entropy compositions of the MoTaTiWZr system, and the agreement with the experimental results was high. The correlation coefficients revealed that the enthalpy of mixing and alloy melting point is the most critical for the prediction of elastic modulus, which provides a theoretical database for the subsequent design of Bio-HEAs with specific Young's modulus to solve the stress shielding problem.

As a new type of medical alloy, Bio-HEAs have the characteristics of biosafety, high strength, high corrosion resistance, high wear resistance, etc. It has recently become the most promising medical metal material for research (Liu et al., 2022b; 2022a). Biocompatibility is the focus of attention for Bio-HEAs in clinical applications, but the long development cycle of biomaterials (about 20 years) limits the speed of development of new materials. Rapid interaction between Biological Omics and Material attributes through machine learning will significantly shorten this process (Basu et al., 2022). It revealed the relationship between biological data and material properties through the concept of biomaterialomics, as shown in Figure 12. Therefore, material design measurement methods that integrate machine learning, search algorithms, and adaptive iteration are essential to guide the efficient design of Bio-HEAs with small data samples, large cost space, and multi-objective performance requirements.

Biocompatibility

Due to the frequent occurrence of diseases, and other human injuries, the demand for implant materials has increased, and more attention has been paid to medical metal materials. In contrast, high-entropy alloys have become one of the most promising new medical materials in recent years due to their

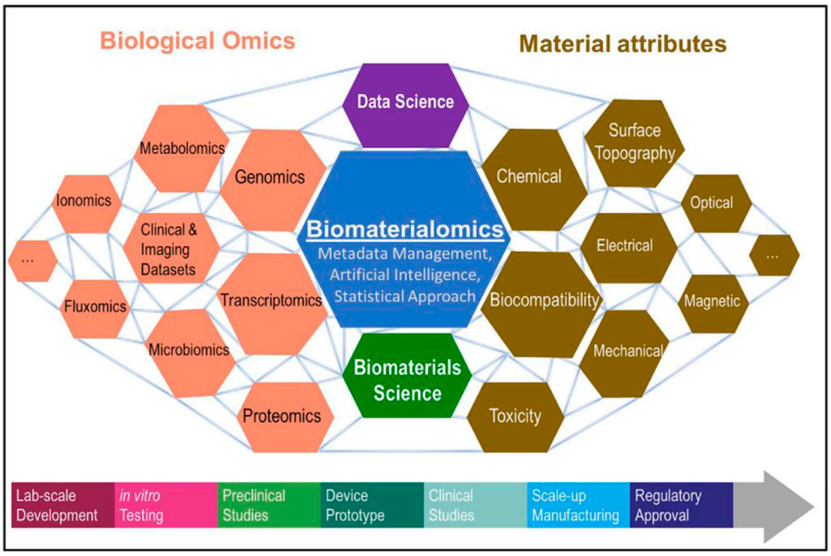

FIGURE 12
Introducing the concept of biomaterialomics, an interdisciplinary study unraveling the relationship between biological data and material properties (Basu et al., 2022).

FIGURE 13
The primary factors are affecting the functional biocompatibility of a biomedical implant.

excellent performance and have been explored and researched by many scholars at home and abroad (Nagase et al., 2020). Bio-HEAs use Ti, Ta, Zr, Nb, and Hf elements with high biosafety and good biocompatibility. As a new bio-alloy material, Bio-HEAs require a series of biosafety assessments before they can be implanted in organisms, and the common factors affecting the biology of biomedical implants are shown in Figure 13. For Bio-HEA to be truly used in the clinical field as a biomedical implant, its biocompatibility needs to be experimentally proven by the mechanical, physical, and degradation properties, by sterilization (freeing the implant surface from all types of microorganisms), by toxicological aspects (examination and treatment of any toxins or toxic substances), by surgery, implant site and load-bearing capacity (Davis et al., 2022). Based on the existing research work, this chapter summarizes the biocompatibility performance of Bio-HEAs in terms of their cytocompatibility and corrosion resistance in physiological solutions.

Cytocompatibility

Most of the research on Bio-HEA biocompatibility currently focuses on evaluating the cytocompatibility of HEA alloys by the direct cell contact method (Wang J. C. et al., 2022; Wei et al., 2022a; Guo et al., 2022). The cytocompatibility of alloy materials includes cell adhesion ability and cytotoxicity (Ma N. et al., 2020); cell adhesion is essential to maintain the stability of tissue structure and is a regulator of cell motility and function, with significant effects on cell proliferation and differentiation (Yang et al., 2011). Cytotoxicity is an indicator to assess the biological activity of cells on the surface of the alloy, which is one of the critical indicators for the *in vitro* evaluation of Bio-HEAs. The commonly used cell lines are human aortic smooth muscle cell,

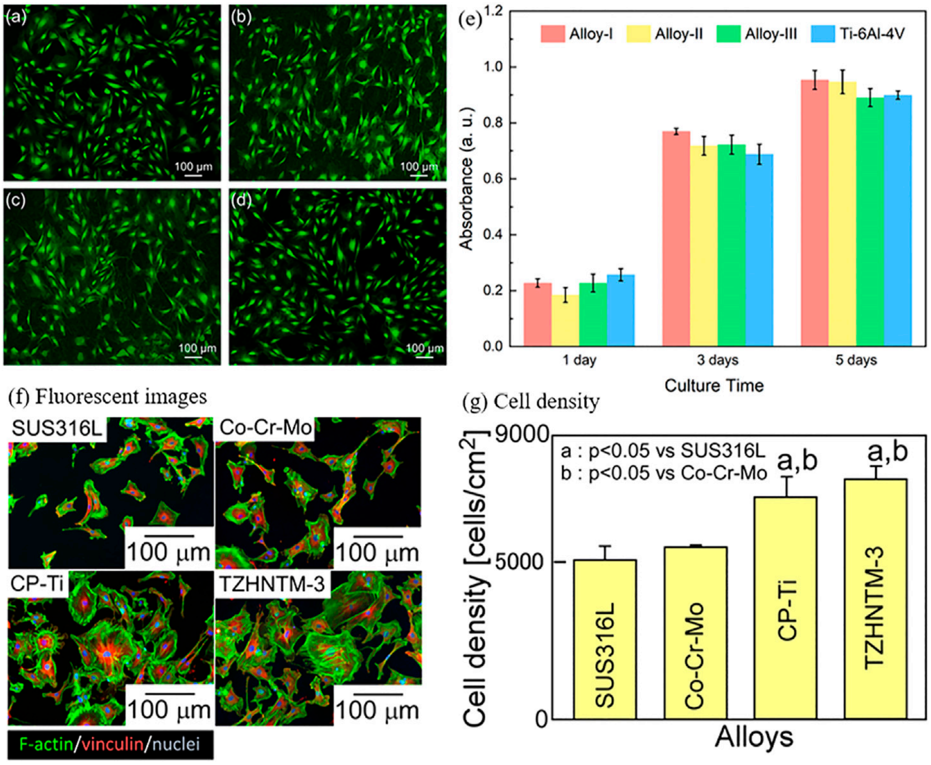

FIGURE 14
Live/dead staining of MC3T3-E1 cells on **(A)** Alloy-I, **(B)** Alloy-II, **(C)** Alloy-III, and **(D)** Ti64 after 72 h of incubation. **(E)** The proliferation of MC3T3-E1 cells on Alloy-I, Alloy-II, Alloy-III, and Ti64 after 1, 3, and 5 days of cell culture, respectively (Yang W. et al., 2022). Biocompatibility of the arc-melted isoatomic TiNbTaZrMo (TZHNTM-Eq) and non-isoatomic $Ti_{28.32}Zr_{28.32}Hf_{28.32}Nb_{6.74}Ta_{6.74}Mo_{1.55}$ (TZHNTM-3) and SUS316L stainless steel, ASTM F1537-08 of Co-Cr-Mo alloy and commercially pure titanium (CP-Ti) were used as references. **(F)** Quantitative analysis of the density of osteoblasts cultured on the fabricated specimens by staining images with Giemsa and **(G)** fluorescent images of osteoblast adhesion on the fabricated specimens (Iijima et al., 2021).

osteoblast, human osteosarcoma cell, human epithelial fibroblast, L929 mouse fibroblast cells, and Mouse embryo osteoblast precursor cells。

Currently, the cytotoxicity tests on Bio-HEAs are conducted by culturing cells *in vitro* and measuring their survival rate on the alloy surface to assess their biological properties. Todai et al. (Todai et al., 2017) cultured human osteoblasts on the surface of TiNbTaZrMo Bio-HEA, which exhibited superior biological activity to pure Ti. Yang et al. (Yang W. et al., 2022) used MC3T3-E1 cells on $Ti_{20}Zr_{20}Hf_{20}Nb_{20}Ta_{20}$ (Alloy-I), $Ti_{25}Zr_{25}Hf_{25}Nb_{12.5}Ta_{12.5}$ (Alloy-II), $Ti_{27.78}Zr_{27.78}Hf_{27.78}Nb_{8.33}Ta_{8.33}$ (Alloy- III) and Ti6Al4V substrates were incubated to evaluate the biocompatibility of Ti-Zr-Hf-Nb-Ta HEA, as shown in Figure 14. The biological activities of HEA and Ti-6Al-4V were observed by fluorescence staining after 72 h of culture, as shown in Figure 14. It was found that a large number of MC3T3-E1 cells adhered to the surface of HEA and Ti-6Al-4V with a high survival rate of adherent cells, indicating that MC3T3-E1 cells had a high survival rate and good initial adhesion on this HEA. In addition, the survival numbers of cells in HEA and Ti-6Al-4V were counted on the first, second, and third days, respectively, and no statistically significant differences were found, indicating that TiZrHfNbTa HEA has the same level of biocompatibility as Ti-6Al-4V. Iijima et al. (Iijima et al., 2021) used mouse primary osteoblasts cultured on TiZrHfNbTaMo surface for 24 h. After 24 h in a humidified atmosphere of 5% CO2, the cells were fixed in methanol, stained with 5% Giemsa aqueous solution for staining, and observed under a light microscope, as shown in Figure 14. In addition, Bio-HEAs such as TiZrNbHfTa (Braic et al., 2012; Motallebzadeh et al., 2018) have good mechanical properties and excellent friction and wear resistance, showing close to or even better biocompatibility than conventional medical alloys such as Ti-6Al-4V.

Corrosion resistance

Bio-HEAs have been shown to have excellent cytocompatibility. Still, the application of the material should also consider the working service environment, where all metals and alloys are subject to corrosion when in contact with body

TABLE 2 Electrochemical parameters of the relevant Bio-HEAs in simulated human solutions.

Bio-HEA	Solution	E_{corr}(V)	I_{corr} (× 10^{-3}A/m^{-2})	Epit(V)	Refs
$Ti_{20}Zr_{20}Hf_{20}Nb_{20}Ta_{20}$	Hank's	−0.302 ± 0.014	0.8 ± 0.20		Yang et al. (2022b)
$Ti_{25}Zr_{25}Hf_{25}Nb_{12.5}Ta_{12.5}$	Hank's	−0.407 ± 0.021	1.19 ± 0.42		Yang et al. (2022b)
$Ti_{27.78}Zr_{27.78}Hf_{27.78}Nb_{8.33}Ta_{8.33}$	Hank's	−0.437 ± 0.062	1.22 ± 0.37	1.238	Yang et al. (2022b)
TC4	Hank's	−0.347 ± 0.014	0.61 ± 0.14		Yang et al. (2022b)
Pure Ti film	Hank's	−0.252	1.101	> 2	Lai et al. (2018)
$Ta_{57}Ti_{17}Zr_{15}Si_{11}$ film	Hank's	−0.304	0.77	> 2	Lai et al. (2018)
$Ta_{75}Ti_{10}Zr_{8}Si_{7}$ film	Hank's	−0.336	0.83	> 2	Lai et al. (2018)
Pure Ta film	Hank's	−0.432	0.61	> 2	Lai et al. (2018)
TiZrNbTaMo	PBS	−0.607	0.3	2	Wang and Xu, (2017)
316L SS	PBS	−0.234		0.675	Wang and Xu, (2017)
CoCrMo	PBS	−0.320		0.435	Wang and Xu, (2017)
TiZrHfNbTa	Hank's	−0.395	0.8		Yang et al. (2020)
TiZrHfNb	PBS	−0.39 ± 0.03	10.93 ± 2.77		Wang et al. (2022c)
$TiZrHfNbFe_{0.25}$	PBS	−0.42 ± 0.05	9.33 ± 1.61		Wang et al. (2022c)
$TiZrHfNbFe_{0.5}$	PBS	−0.30 ± 0.01	2.80 ± 0.77		Wang et al. (2022c)
$TiZrHfNbFe_{0.75}$	PBS	−0.27 ± 0.01	1.66 ± 0.27	1.36 ± 0.02	Wang et al. (2022c)
TiZrHfNbFe	PBS	−0.33 ± 0.02	5.18 ± 1.81	1.22 ± 0.12	Wang et al. (2022c)
$TiZrHfNbFe_{1.5}$	PBS	−0.49 ± 0.04	15.5 ± 0.25	1.16 ± 0.16	Wang et al. (2022c)
$TiZrHfNbFe_{2}$	PBS	−0.51 ± 0.01	27.1 ± 2.21	0.82 ± 0.03	Wang et al. (2022c)
TiZrTaHfNb	PBS	−0.396	0.72		Motallebzadeh et al. (2019)
$Ti_{1.5}ZrTa_{0.5}Hf_{0.5}Nb_{0.5}$	PBS	−0.396	0.56		Motallebzadeh et al. (2019)

fluids because the body environment is very aggressive due to the presence of hydrogen ions and chloride ions, and proteins (Khodaei et al., 2020). Bio-HEAs, as metal implants, undergo various chemical reactions with body fluids, where the metal components of the alloy are oxidized to ionic form and dissolved oxygen is reduced to hydroxide ions, causing various forms of corrosion damage (Cui et al., 2022). For the study of the corrosion resistance of Bio-HEAs, the solutions commonly used to simulate the physiological environment include saline (0.9% NaCl solution), Hank's solution (with a composition of 0.137 M of NaCl, 5.4 mM of KCl, 0.25 mM of Na_2HPO_4, 0.44 mM of KH_2PO_4, 1.3 mM of $CaCl_2$, 1.0 mM of $MgSO_4$, and 4.2 mM of $NaHCO_3$, pH = 7.4), phosphate buffer saline (PBS) and fetal bovine serum (FBS).

Potentiodynamic polarization curve measurement is one of the most widely used measurements in electrochemical corrosion (Gu M. et al., 2022; Li et al., 2022), which can provide information on the corrosion rate and corrosion mechanism of bio-alloy materials under a simulated physiological environment and evaluate the bio-suitability of Bio-HEAs by chemical corrosion conditions. In the corrosion reaction, corrosion potential (E_{corr}), corrosion current density (I_{corr}), and AC impedance are essential parameters for analyzing the corrosion resistance of the material, and the relevant parameters of some Bio-HEAs are listed as shown in Table 2. For Bio-HEAs with Ti and Ta elements, their lower E_{corr} indicates that they will both readily form protective passivation layers (usually oxides) (Zheng et al., 2018). Most Bio-HEAs have no pitting reaction until 2V, which means promising applications in human environments around 0–0.2 V. No pitting and no localized corrosion due to the breakdown of the protective passivation films, dramatically increasing the lifetime of alloy implants (Hwang et al., 2019; Li T. et al., 2021). The corrosion current density indicates the corrosion rate of the material. The lower the I_{corr} value, the lower the corrosion rate of the material, and the low I_{corr} value of Bio-HEAs indicates that it is preferable in medical alloy implant applications (Zhu et al., 2021; Feng H. et al., 2022).

The Ti-Zr-Ta-Hf-Nb system of Bio-HEAs has promising properties as a novel superior metallic biomaterial with an ideal combination of wear resistance, wettability, pitting, and resistance to general corrosion outperforming the conventional metallic biomaterials 316L, CoCrMo, and Ti-6Al-4V in these aspects (Cui et al., 2022). Wang et al. (Wang and Xu, 2017) investigated the electrochemical behavior of HEA in PBS by kinetic potential polarization test. They initially evaluated its corrosion resistance in a physiological environment and compared it with Ti6Al4V, 316L SS, and CoCrMo alloys, as shown in Figure 15. TiZrNbTaMo HEA exhibits an extensive passive plateau in the curve up to 1.2 VSCE without pitting or

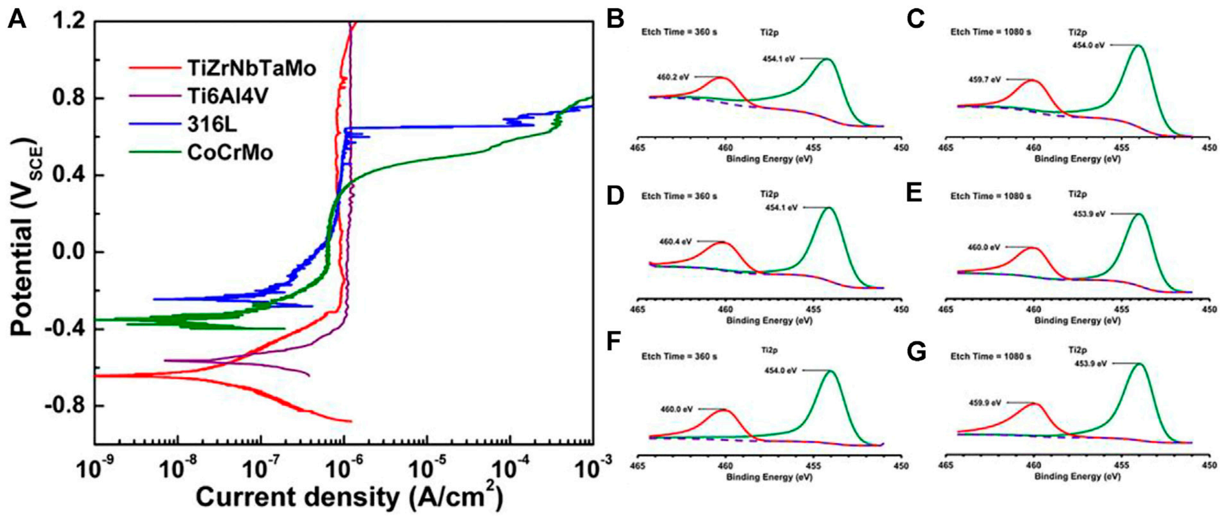

FIGURE 15
(A) Potentiodynamic polarization curves of arc-melted TiZrNbTaMo HEA, as well as Ti-6Al-4V, 316L, and CoCrMo alloys in PBS for comparison of biocompatibility (Wang and Xu, 2017). Ti2p peaks after etching times of 360 and 1,080 s immersed in FBS for 28 days: **(B)** and **(C)** for TiTaHfNb, **(D)** and **(E)** for TiTaHfNbZr, **(F)** and **(G)** for TiTaHfMoZr (Gurel et al., 2021).

turning passivation. Such a response is similar to that of Ti-6Al-4V, except for a more positive E_{corr} and a slightly higher pass for Ti-6Al-4V. TiZrNbTaMo HEA exhibited excellent corrosion resistance comparable to Ti6Al4V alloy and significantly better-pitting resistance than 316 L SS and CoCrMo alloys in a physiological environment simulated by PBS media. TiZrNbTaMo HEA exhibited excellent corrosion resistance comparable to Ti6Al4V alloy and significantly better-pitting resistance than 316 L SS and CoCrMo alloys in a physiological environment simulated by PBS media. Gurel et al. (Gurel et al., 2021) studied the biocompatibility of three TiTaHf-based high-entropy alloys, namely TiTaHfNb, TiTaHfNbZr, and TiTaHfMoZr alloys, using FBS as a test environment to compare their corrosion resistance as bone implants by the level of ions released from HEA etched by FBS solution, TiTaHfNb HEA exhibited the highest corrosion resistance to FBS, as shown in Figure 15. In addition, after 28 days of immersion in FBS solution, the three HEA were found to produce hydroxyapatite on their surfaces when in contact with FBS, further demonstrating their great potential for use in orthopedic implants.

Antibacterial property

In addition to applications in human implants, Bio-HEAs have great potential for medical devices. Conventional medical devices, despite their strict sterilization procedures, are still subject to bacterial infections, which greatly threaten the health of patients (Grischke et al., 2016; Zhang et al., 2021). Antibacterial metals and alloys are more suitable metal materials for medical devices, prepared by elemental alloying and processing processes, exhibiting strong inhibition of bacterial adhesion, growth, and proliferation. Currently, common antibacterial medical devices are antibacterial stainless steel, antibacterial magnesium alloy and antibacterial titanium alloy, and the elements that play an antibacterial role are mainly Cu, Ag and Zn (Chopra, 2007; Tie et al., 2013; Nan and Yang, 2016). Biological HEAs with antibacterial properties usually contain these antibacterial elements, and Chen et al. (Chen C. et al., 2022) designed CrFeNiCuSi HEA with antibacterial properties, which achieved 97.45% inhibition of *E. coli*. Similarly, the synergistic effect of copper ions and copper-rich phase greatly improved the antibacterial performance of Bio-HEAs, and CoFeCrCu HEA showed superior antibacterial performance with 99.97% inhibition of *E. coli* and 99.96% inhibition of *Staphylococcus aureus* after 24 h, much higher than conventional antibacterial alloy materials (Ren et al., 2022).

The antibacterial mechanism exhibited by Bio-HEAs containing Cu elements has been explored and verified (Sarell et al., 2010; Squitti et al., 2015; Zhang et al., 2019). On the one hand, the electrostatic force of Cu^{2+} can directly disrupt the adhesion of bacteria and rupture their cell walls, leading to cell rupture and death. On the other hand, in HEA, Cu and other elements (such as Fe) form a potential difference to form a miniature galvanic cell, releasing a large amount of Cu^{2+}, which further exerts the bactericidal effect of Cu ions. In addition, according to Ren et al. (Ren et al., 2022), direct contact of bacteria with the copper-rich phase in Bio-HEAs produces an effective concentration of ROS (H_2O_2) during incubation, which induces oxidative stress, resulting in an antibacterial effect.

HEAs with antibacterial ability not only have strong and long-lasting bactericidal ability but also have good corrosion resistance and mechanical properties, indicating that Bio-HEAs also have great potential in the field of medical devices. Bio-HEAs containing Cu ions or Ag ions show stronger antibacterial ability, but the release of Cu^{2+} and Ag + may cause some damage to human body, which requires finding the right combination of elements to make Bio-HEAs have antibacterial ability and at the same time have basically no side effects on human body.

Mechanical properties

In addition to the biological safety of the material, meeting specific medical functions is a fundamental requirement of Bio-HEA. The implant generally serves as a replacement for damaged bone or as extra support. For different disease sites, an alloy with mechanical properties appropriate to the tissue is required. The mechanical match between the material and the biological organism during the implantation and functionalization of the material also influences the service effect of the implant in the damaged area. Too low modulus of elasticity can reduce the medical therapeutic impact of the alloy, while the too high modulus of elasticity can lead to stress shielding problems (Uppal et al., 2022; Xing et al., 2022). Therefore, Bio-HEA should not be pursued for high-strength mechanical properties but should be consistent with human tissues, close to or complete the therapeutic effect before failure. The natural selection of Bio-HEAs for implants is due to the multiple biomaterials advantages, including high strength, low density (high specific strength), high corrosion resistance, complete inertness to the body environment, and enhanced biocompatibility, low modulus, and increased capacity to join with bone and other tissues. These properties fit with the specific properties of biomedical metal materials, which means there is a good potential for its application in the medical field.

Strength and ductility

From an engineering perspective, the multi-component nature of HEAs predestines the strengthening mechanism of HEAs to be equally multidimensional. Current research on HEAs is characterized by numerous discoveries, intense discussions, and illuminating scientific research questions (Chen X. et al., 2022; Jin et al., 2022). Strength and ductility are widely studied as core mechanical properties of metallic materials. Complex alloying and thermo-mechanical processing affect the microstructure of HEAs, which has a dramatic effect on strength and ductility (Wu and Fan, 2020; He et al., 2021).

Several factors may influence the strength and ductility of Bio-HEA. Undoubtedly, the elemental composition is the most critical factor. Moreover, the strength and ductility may be changed by various factors such as microstructure, processing method, and post-heat treatment (Liu Z. et al., 2022; Jin et al., 2022). At the same time, these influencing factors interact with each other. For example, the microstructure manifests the combined effect of elemental composition and processing routes of Bio-HEAs. This composition-processing route-microstructure-property study idea, widely applied in conventional alloys, is also applicable in HEAs alloy systems. Still, the challenges are enormous, and the verification is more complex.

The elements composition of Bio-HEAs has the most critical effect on its strength and ductility. First, alloying elements determine the elastic behavior and atomic interactions of Bio-HEA, affecting the strength and ductility of the alloy at the atomic level. In addition, the ratio of elements can determine the phase composition and fraction of Bio-HEAs. In multi-component Bio-HEAs, the type and content of modulating elements can have a significant impact on the mechanical properties of the HEA, and common element additions include metallic and non-metallic elements (Tancret, 2021).

As the most common element in Bio-HEAs, Nb can provide an effective strengthening effect. The strengthening effect of Nb is due to its large atomic radius, which produces severe lattice distortion when added. It is widely used as a precipitation hardening element in the Bio-HEAs system (Li W. et al., 2021). Like Nb, Ti element with a larger atomic radius also strengthens solid solution in Bio-HEAs (Zhang et al., 2017). Still, the difference is that the strengthening effect of Ti on Bio-HEAs occurs mainly at low Ti content. Low Ti element concentration promotes solid solution formation, strengthened BCC phase, and hard Laves phase. In contrast, high Ti concentration leads to the precipitation of intermetallic compounds in HEAs to embrittle the alloy (Zhou et al., 2007). The strengthening mechanism of element Ta (Mohd Pauzi et al., 2016) for $Al_{0.5}FeCrNiMnCo$ (the primary phase is BCC + FCC) is mainly characterized by the precipitation strengthening effect and the presence of more Laves intermetallic phase precipitation. In addition, the strengthening effects of W (Waseem and Ryu, 2017), Zr (Yurchenko et al., 2017), and Cr (Stepanov et al., 2015) in Bio-HEAs were analyzed separately, and the compressive and tensile strengths increased to varying degrees with the addition of small amounts of the elements. Still, their strength benefits were compromised as the elements were alloyed. On the other hand, ductility tends to be the opposite of strength, and depending on the type of alloy, strength and ductility may vary roughly linear or nonlinearly with element concentration.

Small amounts of non-metallic elements, such as O, B, C, N, and Si, are usually added to Bio-HEAs to improve the overall performance of the alloy. According to the traditional experience, adding C elements to steel materials can greatly improve the

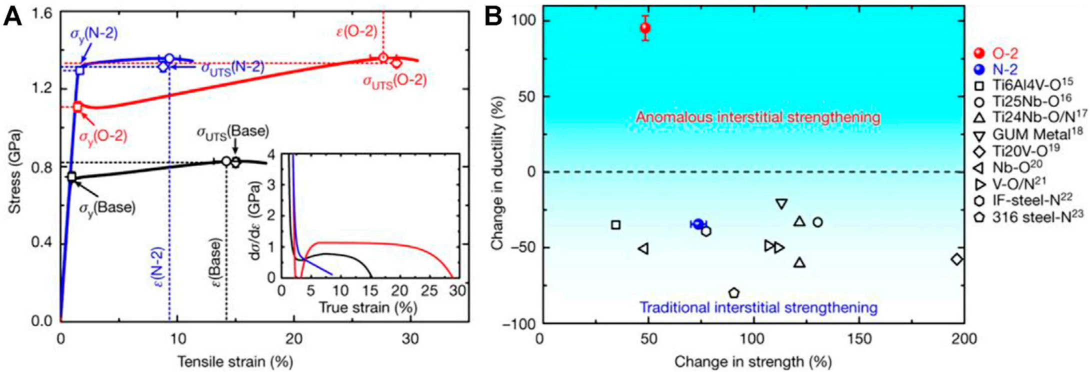

FIGURE 16
(A) Room-temperature tensile stress-strain curves for TiZrHfNb $(TiZrHfNb)_{98}O_2$, and $(TiZrHfNb)_{98}N_2$ HEA. The inset shows the corresponding strain-hardening response (dσ/dε) **(B)** Variation in strength and ductility of the HEA presented here, relative to several established high-performance alloys (Lei et al., 2018).

mechanical properties of steel, and this method is also applicable to Bio-HEAs. The trace addition of C elements will form MC-type alloy carbides on the BCC matrix of $Hf_{0.5}Mo_{0.5}NbTiZr$, and the work-hardening ability and plastic strain of the alloy is enhanced (Gao et al., 2021). Chen et al. (Chen et al., 2018) investigated the effect of O element content on the microstructure and compressive properties of $ZrTiHfNb_{0.5}Ta_{0.5}$ Bio-HEAs. O atoms were present in the lattice of $ZrTiHfNb_{0.5}Ta_{0.5}$ Bio-HEAs and did not precipitate the MO alloy oxide phase. With the increase of the O element, the interstitial solid solution strengthening effect of the O atom increases, and the yield strength of the alloy gradually increases but the plasticity decreases. Further, Lei et al. (Lei et al., 2018) used ordered oxygen complexes to replace O atoms in the gap enhancement, changed the dislocation shear mode from planar slip to wave slip through ordered gap complexes, and promoted double cross-slip through the formation of Frank-Read sources (a mechanism to explain the generation of multiple dislocations), thus promoting dislocation proliferation, deformation, and stretching to achieve a massive increase in strength and plasticity of TiZrHfNb Bio-HEAs, as shown in Figure 16, the tensile strength is enhanced (by 48.5 ± 1.8 percent), and ductility is substantially improved (by 95.2 ± 8.1 percent). As with metallic elements, small amounts of specific non-metallic elements have a strengthening effect on Bio-HEAs, while transitional doping deteriorates the strengthening effect.

Processing is another crucial factor affecting the strength and ductility of the alloy under the premise that the compositions of the Bio-HEAs group elements are clearly defined. Common preparation methods for Bio-HEAs include vacuum arc melting (Chen et al., 2016), electromagnetic induction melting (George et al., 2020), powder metallurgy techniques (Hu et al., 2022), magnetron sputtering (Dvurečenskij et al., 2022), laser electron beam melting (Arif et al., 2022), and 3D printing additive manufacturing (Wang S. et al., 2022). Smelting is the most common preparation method for Bio-HEA, followed by powder metallurgy and additive manufacturing (Arif et al., 2021). The preparation of homogeneous bulk bioethanol by conventional arc melting is challenging, it requires several post-processing (such as remelting), which is a complex process and only yields samples of simple shapes (Cieslak et al., 2019; Güler et al., 2022). As a fabrication process that overcomes the limitations of traditional machining methods, additive manufacturing (AM) is considered as an advanced machining method for generating low-defect HEA specimens, which has the advantage of producing parts with complex geometries with high precision and achieving large-scale customization to maximize material, energy and time savings (Cui et al., 2021; Du et al., 2021). Recently, AM techniques commonly used for Bio-HEA preparation include directed energy deposition (DED) and powder bed fusion (PBF) (Lin Y. C. et al., 2021; Hassan et al., 2021). Directed energy deposition (DED) is an advanced preparation method based on powder feeding technology that allows higher precision shape customization. The advantages of DED are material design, preparation of different types of coatings and fast repair (Yadav et al., 2021; Yang F. et al., 2022). In contrast, selective laser melting (SLM) and selective electron beam melting (SEBM) offer higher processing accuracy and minimal surface roughness. In addition, in PBF technology, due to the extremely high cooling rate (10^5–10^7 K/s), smaller microstructures can be obtained compared to the conventional casting process (100 K/s), which greatly improves the mechanical properties of the part (Huang et al., 2021; Muftah et al., 2021; Ocak and Goller, 2021). For HEAs, the high cooling rate can greatly inhibit the segregation of elements and make it easier to achieve a solid solution structure with a strengthening effect (Zhu et al., 2021).

A change from one preparation technique to another can dramatically affect strength and ductility (Feng et al., 2021, Feng et al., 2022 J.; Wei et al., 2022b). Even for the same technology, the influence of the processing route on the product forming has to be taken into account. Adjusting the processing time and the processing temperature can cause changes in the microstructure and internal defects of the alloy. In addition, the as-prepared alloy samples may have undergone extensive post-treatment processes, such as homogenization, forging, cold and hot rolling, annealing, tempering, aging, etc. This complex process situation, coupled with the elemental diversity of Bio-HEAs, makes it nearly impossible to quantify the effect of processing on the strength and ductility of the alloy, and more precise characterization and analytical tools are needed to address this issue.

The microstructure that most directly affects the mechanical properties of Bio-HEAs also has various forms, including phase composition, grain size, dislocation density, twinning, layer dislocations, size and distribution of precipitated phases, etc. The main phase structures in Bio-HEAs mentioned earlier include BCC, FCC, HCP, Laves, B2, and IC, and MB, MC, MN, MO, and MSi formed by doping with non-metallic elements, as shown in Figure 7. Most single-phase Bio-HEAs are BCC structures, where the elements randomly occupy lattice positions and start BCC phases under the effect of high entropy. The atomic packing density of the BCC phase is 68%, smaller than that of the FCC phase (74%) and the HCP phase (74%). The spatial structure of the BCC phase structure has a higher gap, which makes it easier for small radius solute atoms to enter between the BCC lattice to form interstitial reinforcements, such as the non-metallic elements mentioned previously, without changing the phase structure. Dual solid solution phases Bio-HEAs involve BCC1+BCC2, BCC + HCP, BCC + FCC, BCC + Laves, BCC + B2, and BCC + TC, usually with the B2 phase or BCC phase as the matrix, and the second phase is induced in the alloy by composition adjustment or heat treatment. The multi-phase structure of Bio-HEAs still mainly uses a single-phase or a double phase as the dominant phase and the rest of the phases as the precipitating phases, which play a role in regulating the strength and ductility of Bio-HEAs. To date, there have been many studies on reconciling the strength and ductility of HEAs, including inducing transformation-induced plasticity (TRIP) by stressing (Radi et al., 2022), and creating specially tailored eutectic structures (Ostovari Moghaddam and Trofimov, 2021), introducing interstitially ordered oxygen complexes, and producing nanoscale precipitates or lamellar structures.

Even though Bio-HEAs have a large scope for compositional tuning, it is still difficult to design materials with both high strength and good ductility. At the same time, a large number of researchers have also worked on the strength-ductility conflict, for example, in the case of sacrificing a small amount of strength, the ductility can be greatly improved, or a certain ductility can be guaranteed so that the strength of the alloy is greatly enhanced. Various selectable alloying elements, sophisticated processing methods, and microstructure design allow Bio-HEAs to have more strength-ductility options to design specific alloys according to actual needs (Sheikh et al., 2016).

Elastic properties

Elastic properties characterize the reversible stress-strain of material when sufficient load is applied (Lv et al., 2022). These parameters are essential for analyzing complex mechanical properties (e.g., ductile-brittle behavior), and studying the elastic properties of Bio-HEAs is necessary because they open up an almost unlimited compositional space in material design. And as a new medical alloy material, elastic properties are also an essential factor in determining the application prospects of Bio-HEAs.

Metals and alloys have a long history of use as bone implants. Still, implants made of traditional medical metal material types are usually much harder than natural bone, leading to stress shielding effects, which is the primary factor in bone resorption and eventual failure of such implants (Wang et al., 2016). The stress shielding effect refers to the fact that when metal implants are aligned parallel to human bone, the modulus of the metal is often more than ten times that of the bone. The huge difference in modulus makes the stresses mainly borne by the alloy. At the same time, the human bone is left unstressed, or under less stress for a long period, bone regeneration is inhibited, and bone atrophy occurs, which leads to implant failure. The modulus of elasticity of human cortical bone (dense bone) is 3–30 Gpa, while the modulus of elasticity of bone trabeculae (cancellous bone) is even lower at 0.02–2 GPa (Wu et al., 2018). Most current metallic materials for implants have a much higher modulus than bone. For example, Ti-6Al-4V has a modulus of about 110 Gpa, while CoCrMo alloys have a modulus of 210 GPa (Che Ghani et al., 2020) and Table 3 shows the modulus of elasticity of various biomedical alloys compared to bone. Therefore, new materials with low Young's modulus and other bone-adapted mechanical properties need to be developed to avoid stress shielding at the bone-implant interface.

A high-priority goal in designing new metallic materials for load-bearing implant applications is to reduce Young's modulus in the major loading direction approximating that of cortical bone. In recent years, some biological HEAs and MEAs have been developed (Wang et al., 2017; Wang L. et al., 2018), and the elastic moduli of TiZrHf (HCP), TiZrNbHfTa (BCC), TiZrNbHf (BCC), and TiZrTaHf (BCC) alloys are 111, 103, 83, and 86GPa, respectively (Hu et al., 2021). The elastic modulus of these alloys

TABLE 3 Mechanical properties of human bone, traditional biomaterials, and Bio-HEAs.

Classification	Materials	Young's modulus (GPa)	σ_y (MPa)	Phase	σ_y/ρ (MPa*cm^{3}*g^{-1})	Ref
Human bone	Cortical bone	15–30	30–70			Wu et al. (2018)
	Cancellous bone	0.01–1.57	4–12			Uppal et al. (2022)
Traditional biomaterials	Co-Cr alloys	210–253	448–1,606			Moghadasi et al. (2022)
	Stainless steel	210–253	221–1,213			Moghadasi et al. (2022)
	Pure Ti	110	485			Moghadasi et al. (2022)
	Ti-6Al-4V	116	896–1,034			Moghadasi et al. (2022)
	Mg alloys	30–50	100–235			Moghadasi et al. (2022)
Bio-HEAs	$Hf_{0.4}Nb_{1.54}Ta_{1.54}Ti_{0.89}Zr_{0.64}$	125.0	822	BCC	79.1	Feuerbacher et al. (2015)
	$Hf_{0.5}Mo_{0.5}NbTiZr$	123.1	1,150	BCC	149.4	Guo et al. (2016)
	$HfMo_{0.25}NbTaTiZr$	121.0	1,112	BCC	112.2	Juan et al. (2016)
	$HfMo_{0.5}NbTaTiZr$	131.9	1,260	BCC	140.4	Liu et al. (2017)
	HfMoNbTaTiZr	147.0	1,512	BCC	152.1	Juan et al. (2015)
	HfMoNbTiZr	139.2	1,575	BCC	181.3	Guo et al. (2015)
	HfNbTaTiZr	110.6	1,073	BCC	108.4	Lin et al. (2015)
	$Mo_{0.1}NbTiV_{0.3}Zr$	106	932	BCC	141.2	Huang et al. (2017)
	MoNbTaTiW	229.4	1,455	BCC	123.8	Han et al. (2018)
	MoNbTaVW	231.8	1,246	BCC	100.7	Senkov et al. (2011)
	MoNbTaW	257.8	996	BCC	72.9	Han et al. (2018)
	$MoNbTiV_{0.25}Zr$	152.9	1750	BCC	241.2	Zhang et al. (2012)
	MoTaTiV	189.8	1,221	BCC	127.4	Qiao et al. (2017)
	NbTaTiV	133.8	965	BCC	105.2	Qiao et al. (2017)
	NbTiVZr	104.3	1,104	BCC	170.9	Wu et al. (2015)

(Where σ_y is the yield strength, σ_y/ρ represents the specific strength of the Bio-HEAs).

is relatively low, about half that of CoCr alloys and stainless steel, which is closer to human bone and can effectively reduce the effect of stress shielding.

To further verify the advantages of elastic properties, in addition to the research on Young's modulus, the current research on Bio-HEAs involves single-crystal elastic constant, polycrystalline elastic modulus, and Debye temperature (Huang and Vitos, 2022). The single-crystal elastic constant C_{ij} describes the response of a material to an external load and can be determined from the stress-strain and or energy-strain relationships (Chanda et al., 2021). The single-crystal elastic constants and polycrystalline elastic moduli of Bio-HEAs can be studied experimentally (*in situ* neutron diffraction, tensile tests, and ultrasonic resonance frequency techniques) and computationally (first-principles calculations) (Diao et al., 2017). For Bio-HEAs cubic crystals, there are three fundamental, independent modes of elastic deformation, namely expansion due to hydrostatic stress, shearing along the cubic crystal axis on the cubic plane of the crystal, and the shear resulting from the plane rotated 45° about the cube axis from the cube face is sheared in a direction perpendicular to that axis. The single-crystal elastic constants describe the relationship between the measured h, k, and l-specific elastic lattice strains, using neutron diffraction and the macroscopic stresses applied to the polycrystalline HEA material. The polycrystalline elastic modulus is calculated by the Voigt–Reuss–Hill method based on the single-crystal elastic coefficients to obtain Young's modulus E, bulk modulus B, shear modulus G, microhardness H, Poisson's ratio υ, and Cauchy pressure of Bio-HEAs, and thus further evaluate the mechanical properties of Bio-HEAs such as strength, hardness, and elastic anisotropy.

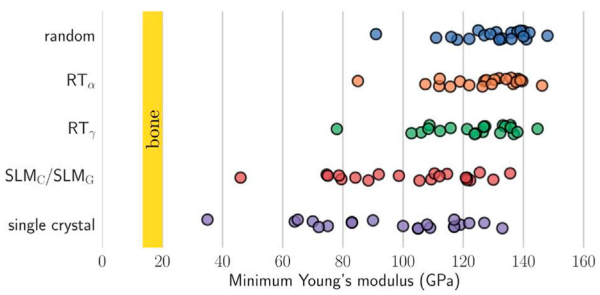

FIGURE 17
Higher single crystal elastic anisotropy for the present HEAs typically implies a lower minimum Young's modulus. For comparison, the vertical yellow bars indicate the targeted Young's modulus of cortical bone (Schönecker et al., 2022).

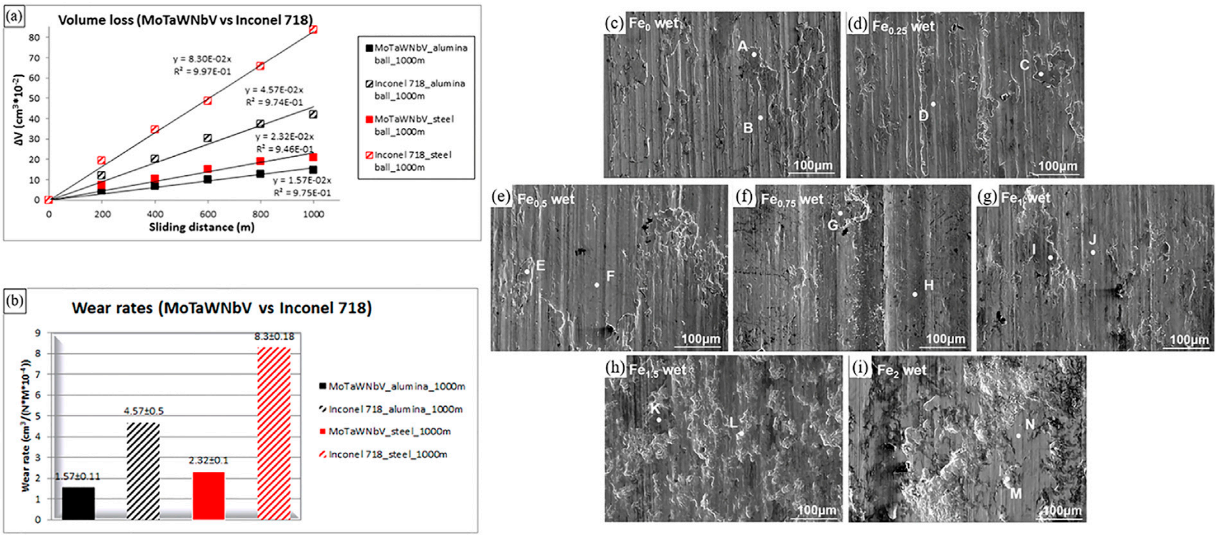

FIGURE 18
(A, B) Comparison of frictional properties of MoTaWNbV high entropy alloy and Inconel 718 conventional high-temperature alloy, using aluminum oxide and steel balls as counter body materials (Poulia et al., 2016). **C–I** SEM images of worn-scar surfaces of the Ti-Zr-Hf-Nb-Fe_x HEAs under PBS wet wear conditions (Wang et al., 2022c).

The elastic anisotropy is related to the formation of microcracks in the material and impacts the mechanical durability of Bio-HEAs. The study of the elastic anisotropy of Bio-HEAs was examined theoretically and experimentally (Duesbery and Vitek, 1998; Fazakas et al., 2014; Tian et al., 2014; Dirras et al., 2016; Lilensten et al., 2018; Laplanche et al., 2019; Akdim et al., 2021; Raturi et al., 2022). Virtual crystal approximation (VCA), coherent potential approximation (CPA), and special quasi-random structure (SQS) simulations by calculating the BCC HEA with elastic stiffness constants (Fazakas et al., 2014; Tian et al., 2014). For example, Tian et al. (Tian et al., 2014) showed that molybdenum-containing alloys are almost isotropic compared to molybdenum-free alloys of the $TiZrNbMoV_x$ system. By studying the single-crystal elastic properties of 21 Bio-HEAs, as shown in Figure 17, Schonecher et al. (Schönecker et al., 2022) verified that the valence electron number has a dominant effect on the elastic anisotropy and crystal orientation of low Young's modulus and high torsional modulus in HEAs, and discussed the potential of using single crystals or woven aggregates to reduce Young's modulus in Bio-HEAs.

Wear resistance

When conventional biomedical alloys are implanted, friction and wear are usually accelerated due to the corrosive physiological environment, resulting in considerable corrosion and wear of the material, severely reducing the service period (Chiba et al., 2007). Therefore, biomedical metal implant alloys need excellent biocompatibility, high corrosion, and good wear resistance. However, due to the low wear resistance of Ti-based alloys, particle diseases resulting from the wear debris may occur when they are performing in physiological environments (Long and Rack, 1998; Geetha et al., 2009). Ti-Zr-Nb-based refractory HEAs typically exhibit a body-centered cubic (BCC) solid solution structure and thus have higher hardness, yield strength, and wear resistance than Ti-6Al-4V, making them highly resistant to plastic deformation and fracture under high loads.

The wear resistance of Bio-HEAs is the key to their service life (Moazzen et al., 2022; Zhang et al., 2022). Poulia et al. (Poulia et al., 2016) analyzed the influence mechanism of the solid solution phase on relative wear resistance. They found that MoTaWNbV high-entropy alloy with a single-phase BCC structure could effectively absorb the energy during wear due to the abundant slip system in the BCC structure of the alloy, the BCC structure of this alloy possesses more slip systems. However, MoTaNbZrTi high-entropy alloy with a dual-phase BCC + HCP structure will form an oxide on the surface during wear to lubricate the surface and improve wear resistance. Both alloys have higher wear resistance than conventional high-temperature alloys. Figure 18 shows the wear resistance of MoTaWNbV and MoTaNbZrTi alloys compared to conventional high temperature alloys. To further investigate the wear resistance of Bio-HEAs under physiological environments, some researchers used PBS solutions to test the wear resistance of $TiZrHfNbFe_x$ HEAs under real service conditions (Wang W. et al., 2022). Figure 18 shows the fatigue wear of Bio-HEAs under applied load, where the deformed layer of the alloy surface is stripped off, and the exposed fresh metal surface reacts with the PBS solution and exhibits better resistance to wet wear than Ti-6Al-4V. In addition, the content of Fe elements was found to affect the wear mechanism of these Bio-HEAs, from abrasive and corrosive wear of Fe_0 to Fe_1 alloy to fatigue and corrosion wear of $Fe_{1.5}$ and Fe_2 alloys after sliding in PBS solution.

Conclusion and outlook

In conclusion, Bio-HEAs have potential applications in the biomedical field but are still in the laboratory stage. The immature preparation process, high cost, and clinical experiments have not yet been realized, making it difficult for Bio-HEAs to be widely used. The design theory, mechanical properties, and biocompatibility of Bio-HEAs are summarized, and their future directions are partially discussed as follows:

(1). There are currently relatively systematic design theories for HEAs, including semi-empirical guidelines for characteristic quantities such as mixing entropy, valence electron concentration, atomic radius difference, mixing enthalpy, and electronegativity. However, a great deal of validation work is still required for Bio-HEAs to design novel alloys. A simulation is an essential approach for the composition design of Bio-HEAs to predict material properties from electronic and atomic scales. Combined with machine learning, it can significantly reduce the time and cost of designing Bio-HEAs with new compositions.

(2). The phase structure of Bio-HEAs is dominated by the single phase of BCC, and the second phases of multi-phase Bio-HEAs include FCC, HCP, Laves, B2, and IC phases. Still, not all of these precipitated phases exhibit beneficial effects on the alloy, and excessive doping will destroy the continuity of the matrix. It is necessary to verify the reinforcement mechanism of precipitated relative Bio-HEAs through continuous exploratory experiments to achieve the goal of multiphase synergistic reinforcement.

(3). In the biomedical field, the application trend of Bio-HEAs is biased towards metal implants, which requires rigorous experimental to demonstrate the biosafety and service life of Bio-HEAs, and the continuous efforts of several research teams.

Author contributions

JF mainly wrote this review paper, YT and JL provided writing ideas for the article, PZ and LW provided guidance and revisions for the article, and CL provided writing suggestions for the article.

Funding

The authors thankfully acknowledge the financial support listed as below: National Natural Science Foundation of China under (Grant Nos.51831011, 52011530181, 52075317), Shanghai Science and Technology Commission under Grant No. 20S31900100, Science Foundation of Institute of Plasma Physics Chinese Academy of Sciences (No. DSJJ-18-01), Guangxi Science and Technology Program [Guike Jizi (2020) No. 198], Guangxi key R & D Project (Guike AB18050008).

Conflict of interest

The authors declare that the research was conducted in the absence of any commercial or financial relationships that could be construed as a potential conflict of interest.

Publisher's note

References

Akdim, B., Woodward, C., Rao, S., and Antillon, E. (2021). Predicting core structure variations and spontaneous partial kink formation for ½ screw dislocations in three BCC NbTiZr alloys. *Scr. Mater.* 199, 113834. doi:10.1016/j.scriptamat.2021.113834

Al-Hafidh, N. N., Al-Khatib, A. R., and Al-Hafidh, N. N. (2020). Assessment of the cortical bone thickness by CT-scan and its association with orthodontic implant position in a young adult eastern mediterranean population: A cross sectional study. *Int. Orthod.* 18, 246–257. doi:10.1016/J.ORTHO.2020.02.001

Arif, Z. U., Khalid, M. Y., Al Rashid, A., ur Rehman, E., and Atif, M. (2022). Laser deposition of high-entropy alloys: A comprehensive review. *Opt. Laser Technol.* 145, 107447. doi:10.1016/J.OPTLASTEC.2021.107447

Arif, Z. U., Khalid, M. Y., ur Rehman, E., Ullah, S., Atif, M., and Tariq, A. (2021). A review on laser cladding of high-entropy alloys, their recent trends and potential applications. *J. Manuf. Process.* 68, 225–273. doi:10.1016/J.JMAPRO.2021.06.041

Bai, L., Hu, Y., Liang, X., Tong, Y., Liu, J., Zhang, Z., et al. (2021). Titanium alloying enhancement of mechanical properties of NbTaMoW refractory high-Entropy alloy: First-principles and experiments perspective. *J. Alloys Compd.* 857, 157542. doi:10.1016/J.JALLCOM.2020.157542

Bakr, M., Syarif, J., and Hashem, I. A. T. (2022). Prediction of phase and hardness of HEAs based on constituent elements using machine learning models. *Mater. Today Commun.* 31, 103407. doi:10.1016/J.MTCOMM.2022.103407

Bao, L., Zheng, M., Zhou, Q., Gao, P., Xu, Y., and Jiang, H. (2022). Multi-objective optimization of partition temperature of steel sheet by NSGA-II using response surface methodology. *Case Stud. Therm. Eng.* 31, 101818. doi:10.1016/J.CSITE.2022.101818

Basu, B., Gowtham, N. H., Xiao, Y., Kalidindi, S. R., and Leong, K. W. (2022). Biomaterialomics: Data science-driven pathways to develop fourth-generation biomaterials. *Acta Biomater.* 143, 1–25. doi:10.1016/J.ACTBIO.2022.02.027

Bhandari, U., Zhang, C., Zeng, C., Guo, S., Adhikari, A., and Yang, S. (2021). Deep learning-based hardness prediction of novel refractory high-entropy alloys with experimental validation. *Crystals* 11, 46. doi:10.3390/CRYST11010046

Biermair, F., Razumovskiy, V. I., and Ressel, G. (2022). Influence of alloying on thermodynamic properties of AlCoCrFeNiTi high entropy alloys from DFT calculations. *Comput. Mater. Sci.* 202, 110952. doi:10.1016/J.COMMATSCI.2021.110952

Braic, V., Balaceanu, M., Braic, M., Vladescu, A., Panseri, S., and Russo, A. (2012). Characterization of multi-principal-element (TiZrNbHfTa)N and (TiZrNbHfTa)C coatings for biomedical applications. *J. Mech. Behav. Biomed. Mater.* 10, 197–205. doi:10.1016/J.JMBBM.2012.02.020

Cann, J. L., De Luca, A., Dunand, D. C., Dye, D., Miracle, D. B., Oh, H. S., et al. (2021). Sustainability through alloy design: Challenges and opportunities. *Prog. Mater. Sci.* 117, 100722. doi:10.1016/J.PMATSCI.2020.100722

Chanda, B., Jana, P. P., and Das, J. (2021). A tool to predict the evolution of phase and Young's modulus in high entropy alloys using artificial neural network. *Comput. Mater. Sci.* 197, 110619. doi:10.1016/J.COMMATSCI.2021.110619

Che Ghani, S. A., Mohamed, S. R., Sha'ban, M., Wan Harun, W. S., and Md Noar, N. A. Z. (2020). Experimental investigation of biological and mechanical properties of CoCrMo based selective laser melted metamaterials for bone implant manufacturing. *Procedia CIRP* 89, 79–91. doi:10.1016/J.PROCIR.2020.05.122

Chen, C., Chen, J., Yuan, S., Li, W., Wang, W., Li, X., et al. (2022a). Microstructure, mechanical properties, corrosion resistance and anti-bacterial behavior of novel Co-free high entropy alloys. *J. Alloys Compd.* 902, 163714. doi:10.1016/J.JALLCOM.2022.163714

Chen, H., Deng, T., Du, T., Chen, B., Skibniewski, M. J., and Zhang, L. (2022b). An RF and LSSVM-NSGA-II method for the multi-objective optimization of high-performance concrete durability. *Cem. Concr. Compos.* 129, 104446. doi:10.1016/J.CEMCONCOMP.2022.104446

Chen, H., Kauffmann, A., Gorr, B., Schliephake, D., Seemüller, C., Wagner, J. N., et al. (2016). Microstructure and mechanical properties at elevated temperatures of a new Al-containing refractory high-entropy alloy Nb-Mo-Cr-Ti-Al. *J. Alloys Compd.* 661, 206–215. doi:10.1016/J.JALLCOM.2015.11.050

Chen, S. H., Zhang, J. S., Guan, S., Li, T., Liu, J. Q., Wu, F. F., et al. (2022c). Microstructure and mechanical properties of WNbMoTaZrx (x = 0.1, 0.3, 0.5, 1.0) refractory high entropy alloys. *Mater. Sci. Eng. A* 835, 142701. doi:10.1016/J.MSEA.2022.142701

Chen, S. M., Ma, Z. J., Qiu, S., Zhang, L. J., Zhang, S. Z., Yang, R., et al. (2022d). Phase decomposition and strengthening in HfNbTaTiZr high entropy alloy from first-principles calculations. *Acta Mater.* 225, 117582. doi:10.1016/J.ACTAMAT.2021.117582

Chen, X., Lu, Q., Gao, Y., Tian, W., Wang, H., Zhou, H., et al. (2022e). Bidirectional improvement of strength and ductility of CoCrFeNiTi (Co40Cr16Fe35Ni8Ti1) high-entropy alloys suitable for coronary stents. *J. Mater. Res. Technol.* 18, 1934–1946. doi:10.1016/J.JMRT.2022.03.084

Chen, Y., Li, Y., Cheng, X., Xu, Z., Wu, C., Cheng, B., et al. (2018). Interstitial strengthening of refractory ZrTiHfNb0.5Ta0.5Ox (x = 0.05, 0.1, 0.2) high-entropy alloys. *Mater. Lett.* 228, 145–147. doi:10.1016/J.MATLET.2018.05.123

Chen, Z. W., Chen, L. X., Gariepy, Z., Yao, X., and Singh, C. V. (2022f). High-throughput and machine-learning accelerated design of high entropy alloy catalysts. *Trends Chem.* 4, 577–579. doi:10.1016/J.TRECHM.2022.03.010

Cheng, Q., Shi, H., Jiang, Q., Yu, Z., Zhang, P., and Ye, X. (2022). Effect of phase composition on microstructure and wear resistance of (Al16.80Co20.74Cr20.49Fe21.28Ni20.70)99.5Ti0.5 high-entropy alloy coatings. *Mater. Today Commun.* 31, 103765. doi:10.1016/J.MTCOMM.2022.103765

Chiba, A., Kumagai, K., Nomura, N., and Miyakawa, S. (2007). Pin-on-disk wear behavior in a like-on-like configuration in a biological environment of high carbon cast and low carbon forged Co-29Cr-6Mo alloys. *Acta Mater.* 55, 1309–1318. doi:10.1016/J.ACTAMAT.2006.10.005

Choi-Yim, H., and Johnson, W. L. (1997). Bulk metallic glass matrix composites. *Appl. Phys. Lett.* 71, 3808–3810. doi:10.1063/1.120512

Chopra, I. (2007). The increasing use of silver-based products as antimicrobial agents: A useful development or a cause for concern? *J. Antimicrob. Chemother.* 59, 587–590. doi:10.1093/JAC/DKM006

Cieslak, J., Tobola, J., Przewoznik, J., Berent, K., Dahlborg, U., Cornide, J., et al. (2019). Multi-phase nature of sintered vs. arc-melted CrxAlFeCoNi high entropy alloys - experimental and theoretical study. *J. Alloys Compd.* 801, 511–519. doi:10.1016/J.JALLCOM.2019.06.121

Cohen, A., Hostyk, J., Baugh, E. H., Buchovecky, C. M., Aggarwal, V. S., Recker, R. R., et al. (2022). Whole exome sequencing reveals potentially pathogenic variants in a small subset of premenopausal women with idiopathic osteoporosis. *Bone* 154, 116253. doi:10.1016/J.BONE.2021.116253

Cui, Y., Shen, J., Geng, K., and Hu, S. (2021). Fabrication of FeCoCrNiMnAl0.5-FeCoCrNiMnAl gradient HEA coating by laser cladding technique. *Surf. Coatings Technol.* 412, 127077. doi:10.1016/J.SURFCOAT.2021.127077

Cui, Y. W., Chen, L. Y., Qin, P., Li, R., Zang, Q., Peng, J., et al. (2022). Metastable pitting corrosion behavior of laser powder bed fusion produced Ti-6Al-4V in Hank's solution. *Corros. Sci.* 203, 110333. doi:10.1016/J.CORSCI.2022.110333

Davis, R., Singh, A., Jackson, M. J., Coelho, R. T., Prakash, D., Charalambous, C. P., et al. (2022). A comprehensive review on metallic implant biomaterials and their subtractive manufacturing. *Int. J. Adv. Manuf. Technol.* 120, 1473–1530. doi:10.1007/S00170-022-08770-8

Diao, H. Y., Feng, R., Dahmen, K. A., and Liaw, P. K. (2017). Fundamental deformation behavior in high-entropy alloys: An overview. *Curr. Opin. Solid State Mater. Sci.* 21, 252–266. doi:10.1016/J.COSSMS.2017.08.003

Dirras, G., Lilensten, L., Djemia, P., Laurent-Brocq, M., Tingaud, D., Couzinié, J. P., et al. (2016). Elastic and plastic properties of as-cast equimolar TiHfZrTaNb high-entropy alloy. *Mater. Sci. Eng. A* 654, 30–38. doi:10.1016/j.msea.2015.12.017

Du, C., Hu, L., Ren, X., Li, Y., Zhang, F., Liu, P., et al. (2021). Cracking mechanism of brittle FeCoNiCrAl HEA coating using extreme high-speed laser cladding. *Surf. Coatings Technol.* 424, 127617. doi:10.1016/J.SURFCOAT.2021.127617

Duesbery, M. S., and Vitek, V. (1998). Plastic anisotropy in b.c.c. transition metals. *Acta Mater.* 46, 1481–1492. doi:10.1016/S1359-6454(97)00367-4

Dvurečenskij, A., Cigáň, A., Lobotka, P., Radnóczi, G., Škrátek, M., Benyó, J., et al. (2022). Colloids of HEA nanoparticles in an imidazolium-based ionic liquid prepared by magnetron sputtering: Structural and magnetic properties. *J. Alloys Compd.* 896, 163089. doi:10.1016/J.JALLCOM.2021.163089

Fazakas, E., Zadorozhnyy, V., Varga, L. K., Inoue, A., Louzguine-Luzgin, D. V., Tian, F., et al. (2014). Experimental and theoretical study of Ti20Zr20Hf20Nb20X20 (X = V or Cr) refractory high-entropy alloys. *Int. J. Refract. Metals Hard Mater.* 47, 131–138. doi:10.1016/j.ijrmhm.2014.07.009

Feng, H., Li, H.-B., Dai, J., Han, Y., Qu, J.-D., Jiang, Z.-H., et al. (2022a). Why CoCrFeMnNi HEA could not passivate in chloride solution? - a novel strategy to significantly improve corrosion resistance of CoCrFeMnNi HEA by N-alloying. *Corros. Sci.* 204, 110396. doi:10.1016/J.CORSCI.2022.110396

Feng, J., Zhang, P., Jia, Z., Yu, Z., Fang, C., Yan, H., et al. (2021). Microstructures and mechanical properties of reduced activation ferritic/martensitic steel fabricated by laser melting deposition. *Fusion Eng. Des.* 173, 112865. doi:10.1016/J.FUSENGDES.2021.112865

Feng, J., Zhang, P., Jia, Z., Yu, Z., Fang, C., Yan, H., et al. (2022b). Laser additive manufacturing and post-heat treatment on microstructure and mechanical properties of 9Cr steel. *Int. J. Press. Vessels Pip.* 198, 104681. doi:10.1016/J.IJPVP.2022.104681

Feuerbacher, M., Heidelmann, M., and Thomas, C. (2015). Plastic deformation properties of Zr-Nb-Ti-Ta-Hf high-entropy alloys. *Philos. Mag.* 95, 1221–1232. doi:10.1080/14786435.2015.1028506

Gaffuri, F., Cossellu, G., Maspero, C., Lanteri, V., Ugolini, A., Rasperini, G., et al. (2021). Correlation between facial growth patterns and cortical bone thickness assessed with cone-beam computed tomography in young adult untreated patients. *Saudi Dent. J.* 33, 161–167. doi:10.1016/J.SDENTJ.2020.01.009

Gao, X., Wang, L., Guo, N., Luo, L., Zhu, G., Shi, C., et al. (2021). *In-situ* development of MB2 and their effect on microstructure and mechanical properties of refractory Hf0.5Mo0.5NbTiZr high entropy alloy matrix composites. *Int. J. Refract. Metals Hard Mater.* 96, 105473. doi:10.1016/J.IJRMHM.2021.105473

Geetha, M., Singh, A. K., Asokamani, R., and Gogia, A. K. (2009). Ti based biomaterials, the ultimate choice for orthopaedic implants - a review. *Prog. Mater. Sci.* 54, 397–425. doi:10.1016/J.PMATSCI.2008.06.004

George, E. P., Curtin, W. A., and Tasan, C. C. (2020). High entropy alloys: A focused review of mechanical properties and deformation mechanisms. *Acta Mater.* 188, 435–474. doi:10.1016/J.ACTAMAT.2019.12.015

George, E. P., Raabe, D., and Ritchie, R. O. (2019). High-entropy alloys. *Nat. Rev. Mat.* 4, 515–534. doi:10.1038/S41578-019-0121-4

Grischke, J., Eberhard, J., and Stiesch, M. (2016). Antimicrobial dental implant functionalization strategies -A systematic review. *Dent. Mat. J.* 35, 545–558. doi:10.4012/DMJ.2015-314

Gross, C., Bergfeldt, T., Fretwurst, T., Rothweiler, R., Nelson, K., and Stricker, A. (2020). Elemental analysis of commercial zirconia dental implants - is "metal-free" devoid of metals? *J. Mech. Behav. Biomed. Mater.* 107, 103759. doi:10.1016/J.JMBBM.2020.103759

Gu, M., Gong, Y., Wu, X., Dong, Y., and Wang, G. L. (2022a). Surface polarization of BiOI to boost photoelectrochemical signal transduction for high-performance bioassays. *Chem. Commun.* 58, 4651–4654. doi:10.1039/D2CC00019A

Gu, P., Qi, T., Chen, L., Ge, T., and Ren, X. (2022b). Manufacturing and analysis of VNbMoTaW refractory high-entropy alloy fabricated by selective laser melting. *Int. J. Refract. Metals Hard Mater.* 105, 105834. doi:10.1016/J.IJRMHM.2022.105834

Güler, S., Alkan, E. D., and Alkan, M. (2022). Vacuum arc melted and heat treated AlCoCrFeNiTiX based high-entropy alloys: Thermodynamic and microstructural investigations. *J. Alloys Compd.* 903, 163901. doi:10.1016/J.JALLCOM.2022.163901

Guo, L., Ataollah Naghavi, S., Wang, Z., Nath Varma, S., Han, Z., Yao, Z., et al. (2022). On the design evolution of hip implants: A review. *Mater. Des.* 216, 110552. doi:10.1016/J.MATDES.2022.110552

Guo, N. N., Wang, L., Luo, L. S., Li, X. Z., Chen, R. R., Su, Y. Q., et al. (2016). Microstructure and mechanical properties of refractory high entropy (Mo 0.5 NbHf 0.5 ZrTi) BCC/M 5 Si 3 *in-situ* compound. *J. Alloys Compd.* 660, 197–203. doi:10.1016/j.jallcom.2015.11.091

Guo, N. N., Wang, L., Luo, L. S., Li, X. Z., Su, Y. Q., Guo, J. J., et al. (2015). Microstructure and mechanical properties of refractory MoNbHfZrTi high-entropy alloy. *Mater. Des.* 81, 87–94. doi:10.1016/j.matdes.2015.05.019

Guo, S., Hu, Q., Ng, C., and Liu, C. T. (2013). More than entropy in high-entropy alloys: Forming solid solutions or amorphous phase. *Intermetallics* 41, 96–103. doi:10.1016/J.INTERMET.2013.05.002

Gurel, S., Nazarahari, A., Canadinc, D., Cabuk, H., and Bal, B. (2021). Assessment of biocompatibility of novel TiTaHf-based high entropy alloys for utility in orthopedic implants. *Mater. Chem. Phys.* 266, 124573. doi:10.1016/J.MATCHEMPHYS.2021.124573

Han, Z. D., Luan, H. W., Liu, X., Chen, N., Li, X. Y., Shao, Y., et al. (2018). Microstructures and mechanical properties of Ti NbMoTaW refractory high-entropy alloys. *Mater. Sci. Eng. A* 712, 380–385. doi:10.1016/J.MSEA.2017.12.004

Hassan, M. A., Ghayad, I. M., Mohamed, A. S. A., El-Nikhaily, A. E., and Elkady, O. A. (2021). Improvement ductility and corrosion resistance of CoCrFeNi and AlCoCrFeNi HEAs by electroless copper technique. *J. Mater. Res. Technol.* 13, 463–485. doi:10.1016/J.JMRT.2021.04.083

He, M. Y., Shen, Y. F., Jia, N., and Liaw, P. K. (2021). C and N doping in high-entropy alloys: A pathway to achieve desired strength-ductility synergy. *Appl. Mater. Today* 25, 101162. doi:10.1016/J.APMT.2021.101162

Hou, S., Sun, M., Bai, M., Lin, D., Li, Y., and Liu, W. (2022). A hybrid prediction frame for HEAs based on empirical knowledge and machine learning. *Acta Mater.* 228, 117742. doi:10.1016/J.ACTAMAT.2022.117742

Hu, S., Li, T., Su, Z., Meng, S., Jia, Z., and Liu, D. (2021). A novel TiZrNb medium entropy alloy (MEA) with appropriate elastic modulus for biocompatible materials. *Mater. Sci. Eng. B* 270, 115226. doi:10.1016/J.MSEB.2021.115226

Hu, X., Liu, X., Yan, D., and Li, Z. (2022). A high-density non-equiatomic WTaMoNbV high-entropy alloy: Alloying behavior, microstructure and mechanical properties. *J. Alloys Compd.* 894, 162505. doi:10.1016/J.JALLCOM.2021.162505

Huang, H., Wu, Y., He, J., Wang, H., Liu, X., An, K., et al. (2017). Phase-transformation ductilization of brittle high-entropy alloys via metastability engineering. *Adv. Mat.* 29, 1701678. doi:10.1002/ADMA.201701678

Huang, K., Peng, D., Yao, Z., Xia, J., Zhang, B., Liu, H., et al. (2021). Cathodic plasma driven self-assembly of HEAs dendrites by pure single FCC FeCoNiMnCu nanoparticles as high efficient electrocatalysts for OER. *Chem. Eng. J.* 425, 131533. doi:10.1016/J.CEJ.2021.131533

Huang, S., and Vitos, L. (2022). High entropy alloys: Elastic parameters and trends. *Encycl. Mat. Metall. Alloy.* 2, 427–434. doi:10.1016/B978-0-12-803581-8.11714-X

Huang, W., Wang, X., Qiao, J., and Wu, Y. (2022). Microstructures and mechanical properties of TiZrHfNbTaWx refractory high entropy alloys. *J. Alloys Compd.* 914, 165187. doi:10.1016/J.JALLCOM.2022.165187

Huo, W., Zhou, H., Fang, F., Zhou, X., Xie, Z., and Jiang, J. (2018). Microstructure and properties of novel CoCrFeNiTax eutectic high-entropy alloys. *J. Alloys Compd.* 735, 897–904. doi:10.1016/j.jallcom.2017.11.075

Hwang, E. H., Park, J. S., Seong, H. G., and Kim, S. J. (2019). Analysis on surface film formed on high-strength carbon steels in acidic phosphate solution and its relationship with localized corrosion in a 3.5% NaCl solution. *J. Mat. Res. Technol.* 8, 1419–1426. doi:10.1016/J.JMRT.2018.10.007

Iijima, Y., Nagase, T., Matsugaki, A., Wang, P., Ameyama, K., and Nakano, T. (2021). Design and development of Ti-Zr-Hf-Nb-Ta-Mo high-entropy alloys for metallic biomaterials. *Mater. Des.* 202, 109548. doi:10.1016/J.MATDES.2021.109548

Iki, M., Fujimori, K., Nakatoh, S., Tamaki, J., Ishii, S., Okimoto, N., et al. (2022). Delayed initiation of anti-osteoporosis medications increases subsequent hip and vertebral fractures in patients on long-term glucocorticoid therapy: A nationwide health insurance claims database study in Japan. *Bone* 160, 116396. doi:10.1016/J.BONE.2022.116396

Ishida, K. (2017). Schaeffler-type phase diagram of Ti-based alloys. *Metall Mat Trans A* 48, 4990–4998. doi:10.1007/S11661-017-4218-3

Jiang, Q., Zhang, P., Tan, J., Yu, Z., Tian, Y., Ma, S., et al. (2022a). Influence of the microstructure on mechanical properties of SLM additive manufacturing Fe-based bulk metallic glasses. *J. Alloys Compd.* 894, 162525. doi:10.1016/J.JALLCOM.2021.162525

Jiang, Q., Zhang, P., Yu, Z., Tian, Y., and Ma, S. (2022b). AlCoCrFeNi high entropy alloy fabricated via selective laser melting reinforced by Fe-based metallic glass. *Mater. Lett.* 307, 130994. doi:10.1016/J.MATLET.2021.130994

Jin, Z.-Z., Zha, M., Wang, S.-Q., Wang, S.-C., Wang, C., Jia, H.-L., et al. (2022). Alloying design and microstructural control strategies towards developing Mg alloys with enhanced ductility. *J. Magnesium Alloys* 10, 1191–1206. doi:10.1016/J.JMA.2022.04.002

Juan, C. C., Tsai, M. H., Tsai, C. W., Lin, C. M., Wang, W. R., Yang, C. C., et al. (2015). Enhanced mechanical properties of HfMoTaTiZr and HfMoNbTaTiZr refractory high-entropy alloys. *Intermetallics* 62, 76–83. doi:10.1016/j.intermet.2015.03.013

Juan, C. C., Tseng, K. K., Hsu, W. L., Tsai, M. H., Tsai, C. W., Lin, C. M., et al. (2016). Solution strengthening of ductile refractory HfMo x NbTaTiZr high-entropy alloys. *Mater. Lett.* 175, 284–287. doi:10.1016/j.matlet.2016.03.133

Kazemi, M., Ahangarani, S., Esmailian, M., and Shanaghi, A. (2020). Investigation on the corrosion behavior and biocompatibility of Ti-6Al-4V implant coated with HA/TiN dual layer for medical applications. *Surf. Coatings Technol.* 397, 126044. doi:10.1016/J.SURFCOAT.2020.126044

Khodaei, M., Nejatidanesh, F., Shirani, M. J., Iyengar, S., Sina, H., Valanezhad, A., et al. (2020). Optimum temperature and chlorine ion concentration for hydrogen peroxide treatment of titanium dental implant material. *J. Mater. Res. Technol.* 9, 13312–13319. doi:10.1016/J.JMRT.2020.09.040

Klimenko, D. N., Yurchenko, N. Y., Stepanov, N. D., and Zherebtsov, S. V. (2021). Prediction of strength characteristics of high-entropy alloys Al-Cr-Nb-Ti-V-Zr systems. *Mater. Today Proc.* 38, 1535–1540. doi:10.1016/J.MATPR.2020.08.145

Kumar, D., Gangwar, N., Rathore, A. S., and Ramteke, M. (2021). Multi-objective optimization of monoclonal antibody production in bioreactor. *Chem. Eng. Process. - Process Intensif.* 13, 108720. doi:10.1016/J.CEP.2021.108720

Lai, J. J., Lin, Y. S., Chang, C. H., Wei, T. Y., Huang, J. C., Liao, Z. X., et al. (2018). Promising Ta-Ti-Zr-Si metallic glass coating without cytotoxic elements for bio-implant applications. *Appl. Surf. Sci.* 427, 485–495. doi:10.1016/J.APSUSC.2017.08.065

Laplanche, G., Gadaud, P., Perrière, L., Guillot, I., and Couzinié, J. P. (2019). Temperature dependence of elastic moduli in a refractory HfNbTaTiZr high-entropy alloy. *J. Alloys Compd.* 799, 538–545. doi:10.1016/j.jallcom.2019.05.322

LaRosa, C. R., Shih, M., Varvenne, C., and Ghazisaeidi, M. (2019). Solid solution strengthening theories of high-entropy alloys. *Mater. Charact.* 151, 310–317. doi:10.1016/J.MATCHAR.2019.02.034

Lei, J., Liu, M. Q., Yap, A. U. J., and Fu, K. Y. (2013). Condylar subchondral formation of cortical bone in adolescents and young adults. *Br. J. Oral Maxillofac. Surg.* 51, 63–68. doi:10.1016/J.BJOMS.2012.02.006

Lei, Z., Liu, X., Wu, Y., Wang, H., Jiang, S., Wang, S., et al. (2018). Enhanced strength and ductility in a high-entropy alloy via ordered oxygen complexes. *Nature* 563, 546–550. doi:10.1038/s41586-018-0685-y

Li, C., Li, X., Shi, Z., Wu, P., Fu, J., Tang, J., et al. (2022). Exosomes from LPS-preconditioned bone marrow MSCs accelerated peripheral nerve regeneration via M2 macrophage polarization: Involvement of TSG-6/NF-κB/NLRP3 signaling pathway. *Exp. Neurol.* 356, 114139. doi:10.1016/J.EXPNEUROL.2022.114139

Li, J., Meng, X., Wan, L., and Huang, Y. (2021a). Welding of high entropy alloys: Progresses, challenges and perspectives. *J. Manuf. Process.* 68, 293–331. doi:10.1016/J.JMAPRO.2021.05.042

Li, T., Wu, J., and Frankel, G. S. (2021b). Localized corrosion: Passive film breakdown vs. Pit growth stability, Part VI: Pit dissolution kinetics of different alloys and a model for pitting and repassivation potentials. *Corros. Sci.* 182, 109277. doi:10.1016/J.CORSCI.2021.109277

Li, W., Xie, D., Li, D., Zhang, Y., Gao, Y., and Liaw, P. K. (2021c). Mechanical behavior of high-entropy alloys. *Prog. Mater. Sci.* 118, 100777. doi:10.1016/J.PMATSCI.2021.100777

Liang, C., Wang, C., Zhang, K., Tan, H., Liang, M., Xie, Y., et al. (2022). Mechanical and tribological properties of (FeCoNi)88-x(AlTi)12Mox high-entropy alloys. *Int. J. Refract. Metals Hard Mater.* 105, 105845. doi:10.1016/j.ijrmhm.2022.105845

Lilensten, L., Couzinié, J. P., Perrière, L., Hocini, A., Keller, C., Dirras, G., et al. (2018). Study of a bcc multi-principal element alloy: Tensile and simple shear properties and underlying deformation mechanisms. *Acta Mater.* 142, 131–141. doi:10.1016/j.actamat.2017.09.062

Lin, C. L., Lee, J. L., Kuo, S. M., Li, M. Y., Gan, L., Murakami, H., et al. (2021a). Investigation on the thermal expansion behavior of FeCoNi and Fe30Co30Ni30Cr10-xMnx high entropy alloys. *Mater. Chem. Phys.* 271, 124907. doi:10.1016/j.matchemphys.2021.124907

Lin, C. M., Juan, C. C., Chang, C. H., Tsai, C. W., and Yeh, J. W. (2015). Effect of Al addition on mechanical properties and microstructure of refractory AlxHfNbTaTiZr alloys. *J. Alloys Compd.* 624, 100–107. doi:10.1016/j.jallcom.2014.11.064

Lin, Y. C., Chao, C. M., Wang, D. K., Liu, K. M., and Tseng, H. H. (2021b). Enhancing the antifouling properties of a PVDF membrane for protein separation by grafting branch-like zwitterions via a novel amphiphilic SMA-HEA linker. *J. Membr. Sci.* 624, 119126. doi:10.1016/J.MEMSCI.2021.119126

Liu, B., Lei, S., Li, Y., Shan, A., and Dong, B. (2021). Deep periocular recognition method via multi-angle data augmentation. *Int. J. Adv. Netw. Monit. Control* 6, 11–17. doi:10.21307/IJANMC-2021-002

Liu, C., Liu, J., Yang, C., Tang, Y., Lin, Z., Li, L., et al. (2022a). Computer vision-aided 2D error assessment and correction for helix bioprinting. *Int. J. Bioprint* 8, 174–186. doi:10.18063/IJB.V8I2.547

Liu, C., Wang, L., Lu, W., Liu, J., Yang, C., Fan, C., et al. (2022b). Computer vision-aided bioprinting for bone research. *Bone Res.* 10, 21. doi:10.1038/S41413-022-00192-2

Liu, C., Yang, Y., and Xia, Z. (2020). Deformation mechanism in Al0.1CoCrFeNi Σ3(111)[110] high entropy alloys - molecular dynamics simulations. *RSC Adv.* 10, 27688–27696. doi:10.1039/D0RA01885F

Liu, Y., Zhang, Y., Zhang, H., Wang, N., Chen, X., Zhang, H., et al. (2017). Microstructure and mechanical properties of refractory HfMo0.5NbTiV0.5Six high-entropy composites. *J. Alloys Compd.* 694, 869–876. doi:10.1016/j.jallcom.2016.10.014

Liu, Z., Zhao, D., Wang, P., Yan, M., Yang, C., Chen, Z., et al. (2022c). Additive manufacturing of metals: Microstructure evolution and multistage control. *J. Mater. Sci. Technol.* 100, 224–236. doi:10.1016/J.JMST.2021.06.011

Long, M., and Rack, H. J. (1998). Titanium alloys in total joint replacement-a materials science perspective. *Biomaterials* 19, 1621–1639. doi:10.1016/S0142-9612(97)00146-4

Lv, Y., Liu, G., Wang, B., Tang, Y., Lin, Z., Liu, J., et al. (2022). Pore strategy design of a novel NiTi-Nb biomedical porous scaffold based on a triply periodic minimal surface. *Front. Bioeng. Biotechnol.* 10, 910475. doi:10.3389/FBIOE.2022.910475

Ma, N., Liu, S., Liu, W., Xie, L., Wei, D., Wang, L., et al. (2020a). Research progress of titanium-based high entropy alloy: Methods, properties, and applications. *Front. Bioeng. Biotechnol.* 8, 1303. doi:10.3389/FBIOE.2020.603522/BIBTEX

Ma, Y., Liu, X., Dong, W., Li, R., Zhang, Y., Lu, Y., et al. (2020b). Interstitial carbide synergistically strengthening high-entropy alloy CoCrFeNiV0.5C. *Mater. Sci. Eng. A* 792, 139802. doi:10.1016/j.msea.2020.139802

Mao, C., Yu, W., Jin, M., Wang, Y., Shang, X., Lin, L., et al. (2022). Mechanobiologically optimized Ti-35Nb-2Ta-3Zr improves load transduction and enhances bone remodeling in tilted dental implant therapy. *Bioact. Mater.* 16, 15–26. doi:10.1016/J.BIOACTMAT.2022.03.005

Mattia, L., Davis, S., Mark-Wagstaff, C., Abrahamsen, B., Peel, N., Eastell, R., et al. (2022). Utility of PINP to monitor osteoporosis treatment in primary care, the POSE study (PINP and Osteoporosis in Sheffield Evaluation). *Bone* 158, 116347. doi:10.1016/J.BONE.2022.116347

Meloni, M., Balzaretti, S., and Ceriotti, L. (2019). Medical devices biocompatibility assessment on HCE: Evidences of delayed cytotoxicity of preserved compared to preservative free eye drops. *Regul. Toxicol. Pharmacol.* 106, 81–89. doi:10.1016/J.YRTPH.2019.04.022

Miracle, D. B., Miller, J. D., Senkov, O. N., Woodward, C., Uchic, M. D., and Tiley, J. (2014). Exploration and development of high entropy alloys for structural applications. *Entropy* 16, 494–525. doi:10.3390/E16010494

Moazzen, P., Toroghinejad, M. R., Zargar, T., and Cavaliere, P. (2022). Investigation of hardness, wear and magnetic properties of NiCoCrFeZrx HEA prepared through mechanical alloying and spark plasma sintering. *J. Alloys Compd.* 892, 161924. doi:10.1016/J.JALLCOM.2021.161924

Moghadasi, K., Mohd Isa, M. S., Ariffin, M. A., Mohd jamil, M. Z., Raja, S., Wu, B., et al. (2022). A review on biomedical implant materials and the effect of friction stir based techniques on their mechanical and tribological properties. *J. Mater. Res. Technol.* 17, 1054–1121. doi:10.1016/J.JMRT.2022.01.050

Mohd Pauzi, S. S., Harun, M. K., and Talari, M. K. (2016). Effect of Ta addition on microstructure and hardness of FeCrNiMnCoTax and Al0.5FeCrNiMnCoTax high-entropy alloys. *Msf* 846, 13–19. doi:10.4028/WWW.SCIENTIFIC.NET/MSF.846.13

Motallebzadeh, A., Peighambardoust, N. S., Sheikh, S., Murakami, H., Guo, S., and Canadinc, D. (2019). Microstructural, mechanical and electrochemical characterization of TiZrTaHfNb and Ti1.5ZrTa0.5Hf0.5Nb0.5 refractory high-entropy alloys for biomedical applications. *Intermetallics* 113, 106572. doi:10.1016/J.INTERMET.2019.106572

Motallebzadeh, A., Yagci, M. B., Bedir, E., Aksoy, C. B., and Canadinc, D. (2018). Mechanical properties of TiTaHfNbZr high-entropy alloy coatings deposited on NiTi shape memory alloy substrates. *Metall Mat Trans A* 49, 1992–1997. doi:10.1007/S11661-018-4605-4

Muftah, W., Allport, J., and Vishnyakov, V. (2021). Corrosion performance and mechanical properties of FeCrSiNb amorphous equiatomic HEA thin film. *Surf. Coatings Technol.* 422, 127486. doi:10.1016/J.SURFCOAT.2021.127486

Nagase, T., Iijima, Y., Matsugaki, A., Ameyama, K., and Nakano, T. (2020). Design and fabrication of Ti-Zr-Hf-Cr-Mo and Ti-Zr-Hf-Co-Cr-Mo high-entropy alloys as metallic biomaterials. *Mater. Sci. Eng. C* 107, 110322. doi:10.1016/J.MSEC.2019.110322

Nan, L., and Yang, K. (2016). Effect of Cu addition on antibacterial property of type 200 stainless steel. *Mater. Technol.* 31, 44–47. doi:10.1179/1753555715Y.0000000025

Nong, Z. S., Lei, Y. N., and Zhu, J. C. (2018). Wear and oxidation resistances of AlCrFeNiTi-based high entropy alloys. *Intermetallics* 101, 144–151. doi:10.1016/j.intermet.2018.07.017

Ocak, B. C., and Goller, G. (2021). Investigation the effect of FeNiCoCrMo HEA addition on properties of B4C ceramic prepared by spark plasma sintering. *J. Eur. Ceram. Soc.* 41, 6290–6301. doi:10.1016/J.JEURCERAMSOC.2021.06.003

Ostovari Moghaddam, A., Shaburova, N. A., Samodurova, M. N., Abdollahzadeh, A., and Trofimov, E. A. (2021). Additive manufacturing of high entropy alloys: A practical review. *J. Mater. Sci. Technol.* 77, 131–162. doi:10.1016/j.jmst.2020.11.029

Ostovari Moghaddam, A., and Trofimov, E. A. (2021). Toward expanding the realm of high entropy materials to platinum group metals: A review. *J. Alloys Compd.* 851, 156838. doi:10.1016/J.JALLCOM.2020.156838

Peker, A., and Johnson, W. L. (1993). A highly processable metallic glass: Zr41.2Ti13.8Cu12.5Ni10.0Be22.5. *Appl. Phys. Lett.* 63, 2342–2344. doi:10.1063/1.110520

Peng, S., Xu, J., Xie, Z. H., and Munroe, P. (2022). Titanium bipolar plates augmented by nanocrystalline TiZrHfMoW coatings for application in proton exchange membrane fuel cells. *Appl. Surf. Sci.* 591, 153200. doi:10.1016/J.APSUSC.2022.153200

Poulia, A., Georgatis, E., Lekatou, A., and Karantzalis, A. E. (2016). Microstructure and wear behavior of a refractory high entropy alloy. *Int. J. Refract. Metals Hard Mater.* 57, 50–63. doi:10.1016/J.IJRMHM.2016.02.006

Pradeep, K. G., Tasan, C. C., Yao, M. J., Deng, Y., Springer, H., and Raabe, D. (2015). Non-equiatomic high entropy alloys: Approach towards rapid alloy screening and property-oriented design. *Mater. Sci. Eng. A* 648, 183–192. doi:10.1016/J.MSEA.2015.09.010

Qiao, D. X., Jiang, H., Chang, X. X., Lu, Y. P., and Li, T. J. (2017). Microstructure and mechanical properties of VTaTiMoAlx refractory high entropy alloys. *Msf* 898, 638–642. doi:10.4028/WWW.SCIENTIFIC.NET/MSF.898.638

Radi, A., Asghari-Rad, P., Kim, H. S., and Yapici, G. G. (2022). On the development of a novel multi-phase high entropy alloy with transformation-induced plasticity effect. *J. Alloys Compd.* 905, 164014. doi:10.1016/J.JALLCOM.2022.164014

Raturi, A., Biswas, K., and Gurao, N. P. (2022). Elastic and plastic anisotropy in a refractory high entropy alloy utilizing combinatorial instrumented indentation and electron backscatter diffraction. *J. Alloys Compd.* 896, 162902. doi:10.1016/J.JALLCOM.2021.162902

Ren, G., Huang, L., Hu, K., Li, T., Lu, Y., Qiao, D., et al. (2022). Enhanced antibacterial behavior of a novel Cu-bearing high-entropy alloy. *J. Mater. Sci. Technol.* 117, 158–166. doi:10.1016/J.JMST.2022.02.001

Roy, A., Babuska, T., Krick, B., and Balasubramanian, G. (2020). Machine learned feature identification for predicting phase and Young's modulus of low-, medium- and high-entropy alloys. *Scr. Mater.* 185, 152–158. doi:10.1016/J.SCRIPTAMAT.2020.04.016

Sarell, C. J., Wilkinson, S. R., and Viles, J. H. (2010). Substoichiometric levels of Cu2+ ions accelerate the kinetics of fiber formation and promote cell toxicity of amyloid-β from alzheimer disease. *J. Biol. Chem.* 285, 41533–41540. doi:10.1074/JBC.M110.171355

Schönecker, S., Li, X., Wei, D., Nozaki, S., Kato, H., Vitos, L., et al. (2022). Harnessing elastic anisotropy to achieve low-modulus refractory high-entropy alloys for biomedical applications. *Mater. Des.* 215, 110430. doi:10.1016/J.MATDES.2022.110430

Schopphoven, T., Gasser, A., Wissenbach, K., and Poprawe, R. (2016). Investigations on ultra-high-speed laser material deposition as alternative for hard chrome plating and thermal spraying. *J. Laser Appl.* 28, 022501. doi:10.2351/1.4943910

Senkov, O. N., Wilks, G. B., Miracle, D. B., Chuang, C. P., and Liaw, P. K. (2010). Refractory high-entropy alloys. *Intermetallics* 18, 1758–1765. doi:10.1016/J.INTERMET.2010.05.014

Senkov, O. N., Wilks, G. B., Scott, J. M., and Miracle, D. B. (2011). Mechanical properties of Nb25Mo25Ta25W25 and V20Nb20Mo20Ta20W20 refractory high entropy alloys. *Intermetallics* 19, 698–706. doi:10.1016/J.INTERMET.2011.01.004

Serda, M. (2013). Synteza i aktywność biologiczna nowych analogów tiosemikarbazonowych chelatorów żelaza. *Uniw. śląski* 3, 343–354. doi:10.2/JQUERY.MIN.JS

Sheikh, S., Shafeie, S., Hu, Q., Ahlström, J., Persson, C., Veselý, J., et al. (2016). Alloy design for intrinsically ductile refractory high-entropy alloys. *J. Appl. Phys.* 120, 164902. doi:10.1063/1.4966659

Shipilova, O. I., Gorbunov, S. P., Paperny, V. L., Chernykh, A. A., Dresvyansky, V. P., Martynovich, E. F., et al. (2020). Fabrication of metal-dielectric nanocomposites using a table-top ion implanter. *Surf. Coatings Technol.* 393, 125742. doi:10.1016/J.SURFCOAT.2020.125742

Soto, A. O., Salgado, A. S., and Niño, E. B. (2020). Thermodynamic analysis of high entropy alloys and their mechanical behavior in high and low-temperature conditions with a microstructural approach - a review. *Intermetallics* 124, 106850. doi:10.1016/J.INTERMET.2020.106850

Spataru, M. C., Butnaru, M., Sandu, A. V., Vulpe, V., Vlad, M. D., Baltatu, M. S., et al. (2021). In-depth assessment of new Ti-based biocompatible materials. *Mater. Chem. Phys.* 258, 123959. doi:10.1016/J.MATCHEMPHYS.2020.123959

Squitti, R., Tecchio, F., and Ventriglia, M. (2015). The role of copper in human diet and risk of dementia. *Curr. Nutr. Rep.* 4, 114–125. doi:10.1007/S13668-015-0121-Y

Stepanov, N. D., Yurchenko, N. Y., Skibin, D. V., Tikhonovsky, M. A., and Salishchev, G. A. (2015). Structure and mechanical properties of the AlCrxNbTiV (x = 0, 0.5, 1, 1.5) high entropy alloys. *J. Alloys Compd.* 652, 266–280. doi:10.1016/j.jallcom.2015.08.224

Takeuchi, A., Amiya, K., Wada, T., and Yubuta, K. (2015). Alloy design for high-entropy alloys based on Pettifor map for binary compounds with 1:1 stoichiometry. *Intermetallics* 66, 56–66. doi:10.1016/J.INTERMET.2015.06.014

Tancret, F. (2022). Materials design: Computational alloy design by combinatorial optimization. *Encycl. Mat. Metall. Alloy.*, 596–608. doi:10.1016/B978-0-12-819726-4.00061-2

Thebelt, A., Tsay, C., Lee, R. M., Sudermann-Merx, N., Walz, D., Tranter, T., et al. (2022). Multi-objective constrained optimization for energy applications via tree ensembles. *Appl. Energy* 306, 118061. doi:10.1016/J.APENERGY.2021.118061

Tian, F., Varga, L. K., Chen, N., Shen, J., and Vitos, L. (2014). *Ab initio* design of elastically isotropic TiZrNbMoV high-entropy alloys. *J. Alloys Compd.* 599, 19–25. doi:10.1016/j.jallcom.2014.01.237

Tian, F., Varga, L. K., Chen, N., Shen, J., and Vitos, L. (2015). Empirical design of single phase high-entropy alloys with high hardness. *Intermetallics* 58, 1–6. doi:10.1016/J.INTERMET.2014.10.010

Tie, D., Feyerabend, F., Feyerabend, W.-D., Müller, R., Schade, K., Liefeith, K., et al. (2013). Antibacterial biodegradable Mg-Ag alloys. *eCM* 25, 284–298. doi:10.22203/ECM.V025A20

Todai, M., Nagase, T., Hori, T., Matsugaki, A., Sekita, A., and Nakano, T. (2017). Novel TiNbTaZrMo high-entropy alloys for metallic biomaterials. *Scr. Mater.* 129, 65–68. doi:10.1016/J.SCRIPTAMAT.2016.10.028

Tong, Y., Bai, L., Liang, X., Chen, Y., Zhang, Z., Liu, J., et al. (2020). Influence of alloying elements on mechanical and electronic properties of NbMoTaWX (X = Cr, Zr, V, Hf and Re) refractory high entropy alloys. *Intermetallics* 126, 106928. doi:10.1016/J.INTERMET.2020.106928

Troparevsky, M. C., Morris, J. R., Kent, P. R. C., Lupini, A. R., and Stocks, G. M. (2015). Criteria for predicting the formation of single-phase high-entropy alloys. *Phys. Rev. X* 5, 011041. doi:10.1103/PHYSREVX.5.011041/FIGURES/2/MEDIUM

Uppal, G., Thakur, A., Chauhan, A., and Bala, S. (2022). Magnesium based implants for functional bone tissue regeneration - a review. *J. Magnesium Alloys* 10, 356–386. doi:10.1016/J.JMA.2021.08.017

Wang, B., Huang, X., Fu, A., Liu, Y., and Liu, B. (2018a). Serration behavior and microstructure of high entropy alloy CoCrFeMnNi prepared by powder metallurgy. *Mater. Sci. Eng. A* 726, 37–44. doi:10.1016/j.msea.2018.04.071

Wang, G., Liu, Q., Yang, J., Li, X., Sui, X., Gu, Y., et al. (2019). Synthesis and thermal stability of a nanocrystalline MoNbTaTiV refractory high-entropy alloy via mechanical alloying. *Int. J. Refract. Metals Hard Mater.* 84, 104988. doi:10.1016/J.IJRMHM.2019.104988

Wang, J. C., Liu, Y. J., Liang, S. X., Zhang, Y. S., Wang, L. Q., Sercombe, T. B., et al. (2022a). Comparison of microstructure and mechanical behavior of Ti-35Nb manufactured by laser powder bed fusion from elemental powder mixture and prealloyed powder. *J. Mater. Sci. Technol.* 105, 1–16. doi:10.1016/J.JMST.2021.07.021

Wang, L., Wang, Y., Huang, W., Liu, J., Tang, Y., Zhang, L., et al. (2020). Tensile and superelastic behaviors of Ti-35Nb-2Ta-3Zr with gradient structure. *Mater. Des.* 194, 108961. doi:10.1016/J.MATDES.2020.108961

Wang, L., Xie, L., Lv, Y., Zhang, L. C., Chen, L., Meng, Q., et al. (2017). Microstructure evolution and superelastic behavior in Ti-35Nb-2Ta-3Zr alloy processed by friction stir processing. *Acta Mater.* 131, 499–510. doi:10.1016/J.ACTAMAT.2017.03.079

Wang, L., Xie, L., Zhang, L. C., Chen, L., Ding, Z., Lv, Y., et al. (2018b). Microstructure evolution and superelasticity of layer-like NiTiNb porous metal prepared by eutectic reaction. *Acta Mater.* 143, 214–226. doi:10.1016/J.ACTAMAT.2017.10.021

Wang, Q., Dong, C., and Liaw, P. K. (2015). Structural stabilities of β-Ti alloys studied using a new Mo equivalent derived from [β/(α + β)] phase-boundary slopes. *Metall Mat Trans A* 46, 3440–3447. doi:10.1007/S11661-015-2923-3/FIGURES/3

Wang, S., Li, Y., Zhang, D., Yang, Y., Marwana Manladan, S., and Luo, Z. (2022b). Microstructure and mechanical properties of high strength AlCoCrFeNi2.1 eutectic high entropy alloy prepared by selective laser melting (SLM). *Mater. Lett.* 310, 131511. doi:10.1016/J.MATLET.2021.131511

Wang, S. P., and Xu, J. (2017). TiZrNbTaMo high-entropy alloy designed for orthopedic implants: As-cast microstructure and mechanical properties. *Mater. Sci. Eng. C* 73, 80–89. doi:10.1016/J.MSEC.2016.12.057

Wang, W., Yang, K., Wang, Q., Dai, P., Fang, H., Wu, F., et al. (2022c). Novel Ti-Zr-Hf-Nb-Fe refractory high-entropy alloys for potential biomedical applications. *J. Alloys Compd.* 906, 164383. doi:10.1016/J.JALLCOM.2022.164383

Wang, X., Xu, S., Zhou, S., Xu, W., Leary, M., Choong, P., et al. (2016). Topological design and additive manufacturing of porous metals for bone scaffolds and orthopaedic implants: A review. *Biomaterials* 83, 127–141. doi:10.1016/J.BIOMATERIALS.2016.01.012

Waseem, O. A., and Ryu, H. J. (2017). Powder metallurgy processing of a WxTaTiVCr high-entropy alloy and its derivative alloys for fusion material applications. *Sci. Rep.* 7, 1926. doi:10.1038/S41598-017-02168-3

Wei, D., Gong, W., Wang, L., Tang, B., Kawasaki, T., Harjo, S., et al. (2022a). Strengthening of high-entropy alloys via modulation of cryo-pre-straining-induced defects. *J. Mater. Sci. Technol.* 129, 251–260. doi:10.1016/J.JMST.2022.04.055

Wei, D., Wang, L., Zhang, Y., Gong, W., Tsuru, T., Lobzenko, I., et al. (2022b). Metalloid substitution elevates simultaneously the strength and ductility of face-centered-cubic high-entropy alloys. *Acta Mater.* 225, 117571. doi:10.1016/J.ACTAMAT.2021.117571

Wei, X., Zhang, P., Yu, Z., Yan, H., Wu, D., Shi, H., et al. (2021). Effect of phase transformation on mechanical properties of Al16.80Co20.74Cr20.49Fe21.28Ni20.70 high entropy alloy coatings processed by laser cladding. *J. Alloys Compd.* 862, 158563. doi:10.1016/J.JALLCOM.2020.158563

Wen, C., Zhang, Y., Wang, C., Xue, D., Bai, Y., Antonov, S., et al. (2019). Machine learning assisted design of high entropy alloys with desired property. *Acta Mater.* 170, 109–117. doi:10.1016/J.ACTAMAT.2019.03.010

Wu, D., Isaksson, P., Ferguson, S. J., and Persson, C. (2018). Young's modulus of trabecular bone at the tissue level: A review. *Acta Biomater.* 78, 1–12. doi:10.1016/J.ACTBIO.2018.08.001

Wu, H., and Fan, G. (2020). An overview of tailoring strain delocalization for strength-ductility synergy. *Prog. Mater. Sci.* 113, 100675. doi:10.1016/J.PMATSCI.2020.100675

Wu, Y. D., Cai, Y. H., Chen, X. H., Wang, T., Si, J. J., Wang, L., et al. (2015). Phase composition and solid solution strengthening effect in TiZrNbMoV high-entropy alloys. *Mater. Des.* 83, 651–660. doi:10.1016/j.matdes.2015.06.072

Wu, Z., Li, B., Chen, M., Yang, Y., Zheng, R., Yuan, L., et al. (2022). Tailoring magnetic property and corrosion resistance of FeCoNiCuAl high-entropy alloy with Ce additive. *J. Alloys Compd.* 901, 163665. doi:10.1016/J.JALLCOM.2022.163665

Xie, J., Zhang, S., Sun, Y., Hao, Y., An, B., Li, Q., et al. (2020). Microstructure and mechanical properties of high entropy CrMnFeCoNi alloy processed by electopulsing-assisted ultrasonic surface rolling. *Mater. Sci. Eng. A* 795, 140004. doi:10.1016/j.msea.2020.140004

Xin, Y., Li, S., Qian, Y., Zhu, W., Yuan, H., Jiang, P., et al. (2020). High-entropy alloys as a platform for catalysis: Progress, challenges, and opportunities. *ACS Catal.* 10, 11280–11306. doi:10.1021/ACSCATAL.0C03617/ASSET/IMAGES/LARGE/CS0C03617_0015

Xing, F., Li, S., Yin, D., Xie, J., Rommens, P. M., Xiang, Z., et al. (2022). Recent progress in Mg-based alloys as a novel bioabsorbable biomaterials for orthopedic applications. *J. Magnesium Alloys* 10, 1428–1456. doi:10.1016/J.JMA.2022.02.013

Yadav, S., Zhang, Q., Behera, A., Haridas, R. S., Agrawal, P., Gong, J., et al. (2021). Role of binder phase on the microstructure and mechanical properties of a mechanically alloyed and spark plasma sintered WC-FCC HEA composites. *J. Alloys Compd.* 877, 160265. doi:10.1016/J.JALLCOM.2021.160265

Yang, C. H., Wang, Y. T., Tsai, W. F., Ai, C. F., Lin, M. C., and Huang, H. H. (2011). Effect of oxygen plasma immersion ion implantation treatment on corrosion resistance and cell adhesion of titanium surface. *Clin. Oral Implants Res.* 22, 1426–1432. doi:10.1111/J.1600-0501.2010.02132.X

Yang, F., Wang, J., Zhang, Y., Wu, Z., Zhang, Z., Zhao, F., et al. (2022a). Recent progress on the development of high entropy alloys (HEAs) for solid hydrogen storage: A review. *Int. J. Hydrogen Energy* 47, 11236–11249. doi:10.1016/J.IJHYDENE.2022.01.141

Yang, W., Liu, Y., Pang, S., Liaw, P. K., and Zhang, T. (2020). Bio-corrosion behavior and *in vitro* biocompatibility of equimolar TiZrHfNbTa high-entropy alloy. *Intermetallics* 124, 106845. doi:10.1016/J.INTERMET.2020.106845

Yang, W., Pang, S., Liu, Y., Wang, Q., Liaw, P. K., and Zhang, T. (2022b). Design and properties of novel Ti-Zr-Hf-Nb-Ta high-entropy alloys for biomedical applications. *Intermetallics* 141, 107421. doi:10.1016/J.INTERMET.2021.107421

Yang, X., and Zhang, Y. (2012). Prediction of high-entropy stabilized solid-solution in multi-component alloys. *Mater. Chem. Phys.* 132, 233–238. doi:10.1016/J.MATCHEMPHYS.2011.11.021

Ye, Y. F., Wang, Q., Lu, J., Liu, C. T., and Yang, Y. (2015). Design of high entropy alloys: A single-parameter thermodynamic rule. *Scr. Mater.* 104, 53–55. doi:10.1016/J.SCRIPTAMAT.2015.03.023

Ye, Y. F., Wang, Q., Lu, J., Liu, C. T., and Yang, Y. (2016). High-entropy alloy: Challenges and prospects. *Mater. Today* 19, 349–362. doi:10.1016/J.MATTOD.2015.11.026

Yeh, J. W. (2013). Alloy design strategies and future trends in high-entropy alloys. *JOM* 65, 1759–1771. doi:10.1007/S11837-013-0761-6

Yeh, J. W., Chen, S. K., Lin, S. J., Gan, J. Y., Chin, T. S., Shun, T. T., et al. (2004). Nanostructured high-entropy alloys with multiple principal elements: Novel alloy design concepts and outcomes. *Adv. Eng. Mat.* 6, 299–303. doi:10.1002/ADEM.200300567

Yeh, J. W. (2006). Recent progress in high-entropy alloys. *Ann. Chim. Sci. Mat.* 31, 633–648. doi:10.3166/ACSM.31.633-648

Yu, P., Feng, R., Du, J., Shinzato, S., Chou, J. P., Chen, B., et al. (2019). Phase transformation assisted twinning in a face-centered-cubic FeCrNiCoAl high entropy alloy. *Acta Mater.* 181, 491–500. doi:10.1016/J.ACTAMAT.2019.10.012

Yurchenko, N. Y., Stepanov, N. D., Zherebtsov, S. V., Tikhonovsky, M. A., and Salishchev, G. A. (2017). Structure and mechanical properties of B2 ordered refractory AlNbTiVZrx (x = 0-1.5) high-entropy alloys. *Mater. Sci. Eng. A* 704, 82–90. doi:10.1016/J.MSEA.2017.08.019

Zhang, E. L., Fu, S., Wang, R. X., Li, H. X., Liu, Y., Ma, Z. Q., et al. (2019). Role of Cu element in biomedical metal alloy design. *Rare Metall.* 38, 476–494. doi:10.1007/S12598-019-01245-Y

Zhang, E., Zhao, X., Hu, J., Wang, R., Fu, S., and Qin, G. (2021). Antibacterial metals and alloys for potential biomedical implants. *Bioact. Mater.* 6, 2569–2612. doi:10.1016/J.BIOACTMAT.2021.01.030

Zhang, M., Wang, D., He, L., Ye, X., Ouyang, W., Xu, Z., et al. (2022). Microstructure and elevated temperature wear behavior of laser-cladded AlCrFeMnNi high-entropy alloy coating. *Opt. Laser Technol.* 149, 107845. doi:10.1016/J.OPTLASTEC.2022.107845

Zhang, M., Zhou, X., and Li, J. (2017). Microstructure and mechanical properties of a refractory CoCrMoNbTi high-entropy alloy. *J. Materi Eng Perform* 26, 3657–3665. doi:10.1007/S11665-017-2799-Z

Zhang, W., Liaw, P. K., and Zhang, Y. (2018). Science and technology in high-entropy alloys. *Sci. China Mat.* 61, 2–22. doi:10.1007/S40843-017-9195-8

Zhang, Y., Yang, X., and Liaw, P. K. (2012). Alloy design and properties optimization of high-entropy alloys. *JOM* 64, 830–838. doi:10.1007/S11837-012-0366-5

Zhang, Y., Zhou, Y. J., Lin, J. P., Chen, G. L., and Liaw, P. K. (2008). Solid-solution phase formation rules for multi-component alloys. *Adv. Eng. Mat.* 10, 534–538. doi:10.1002/ADEM.200700240

Zhang, Y., Zuo, T. T., Tang, Z., Gao, M. C., Dahmen, K. A., Liaw, P. K., et al. (2014). Microstructures and properties of high-entropy alloys. *Prog. Mater. Sci.* 61, 1–93. doi:10.1016/J.PMATSCI.2013.10.001

Zhao, S. (2020). Defect properties in a VTaCrW equiatomic high entropy alloy (HEA) with the body centered cubic (bcc) structure. *J. Mater. Sci. Technol.* 44, 133–139. doi:10.1016/J.JMST.2019.10.025

Zheng, S., Li, J., Zhang, J., Jiang, K., Liu, X., Chang, C., et al. (2018). Effect of Si addition on the electrochemical corrosion and passivation behavior of Fe-Cr-Mo-C-B-Ni-P metallic glasses. *J. Non-Crystalline Solids* 493, 33–40. doi:10.1016/J.JNONCRYSOL.2018.04.036

Zhou, J., Cheng, Y., Chen, Y., and Liang, X. (2022). Composition design and preparation process of refractory high-entropy alloys: A review. *Int. J. Refract. Metals Hard Mater.* 105, 105836. doi:10.1016/J.IJRMHM.2022.105836

Zhou, Y. J., Zhang, Y., Wang, Y. L., and Chen, G. L. (2007). Solid solution alloys of AlCoCrFeNiTix with excellent room-temperature mechanical properties. *Appl. Phys. Lett.* 90, 181904. doi:10.1063/1.2734517

Zhu, M., Zhao, B., Yuan, Y., Guo, S., and Wei, G. (2021). Study on corrosion behavior and mechanism of CoCrFeMnNi HEA interfered by AC current in simulated alkaline soil environment. *J. Electroanal. Chem.* 882, 115026. doi:10.1016/J.JELECHEM.2021.115026

Zhu, W., Huo, W., Wang, S., Wang, X., Ren, K., Tan, S., et al. (2022). phase formation prediction of high-entropy alloys: A deep learning study. *J. Mater. Res. Technol.* 18, 800–809. doi:10.1016/J.JMRT.2022.01.172